NUREG/CR-4683
EGG-2413
August 1986

PBF Severe Fuel Damage Scoping Test— Test Results Report

Alan D. Knipe
Scott A. Ploger
Daniel J. Osetek

F O R M A L R E P O R T

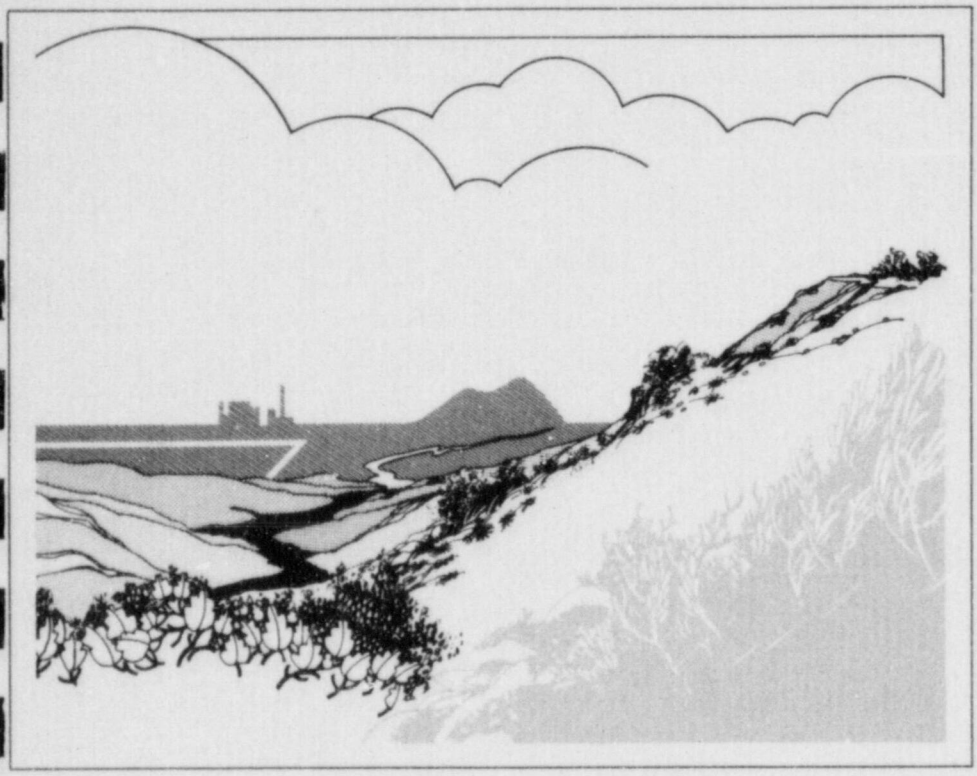

EG&G Idaho

Work performed under
DOE Contract No. DE-AC07-76ID01570

for the U.S. Nuclear Regulatory Commission

Idaho National Engineering Laboratory

Managed by the U.S. Department of Energy

8609300386 860831
PDR NUREG
CR-4683 R PDR

Available from

Superintendent of Documents
U.S. Government Printing Office
Post Office Box 37082
Washington, D.C. 20013-7982

and

National Technical Information Service
Springfield, VA 22161

NOTICE

This report was prepared as an account of work sponsored by an agency of the United States Government. Neither the United Sates Government nor any agency thereof, nor any of their employees, makes any warranty, expressed or implied, or assumes any legal liability or responsibility for any third party's use, or the results of such use, of any information, apparatus, product or process disclosed in this report, or represents that its use by such third party would not infringe privately owned rights.

NUREG/CR-4683
EGG-2413
Distribution Category: R3

PBF SEVERE FUEL DAMAGE SCOPING TEST—TEST RESULTS REPORT

Alan D. Knipe[a]
Scott A. Ploger
Daniel J. Osetek

Published August 1986

EG&G Idaho, Inc.
Idaho Falls, Idaho 83415

a. United Kingdom Atomic Energy Authority

Prepared for the
Division of Accident Evaluation
Office of Nuclear Regulatory Research
U.S. Nuclear Regulatory Commission
Washington, D.C. 20555
Under DOE Contract No. DE-AC07-76ID01570
FIN No. A6305

ABSTRACT

This report presents a comprehensive evaluation of the Severe Fuel Damage Scoping Test (SFD-ST) performed in the Power Burst Facility (PBF) at the Idaho National Engineering Laboratory. The test is part of an internationally sponsored light water reactor severe accident research program, initiated by the U.S. Nuclear Regulatory Commission. The experiment was the first of four, in-pile, multifuel rod tests performed in the PBF. The SFD-ST fuel bundle comprised 32, 0.9-m long, trace-irradiated (91 MWd/T) fuel rods. The bundle was surrounded by an insulating shroud, with the region maintained at a pressure of 7 MPa. The experiment consisted of a transient in which the inlet coolant flow to the test bundle was reduced to 16 g/s, and the nuclear power increased, until the peak temperature approached fuel melting. The ∿3 h transient was terminated by scram of the reactor, with the inlet coolant reflooding and cooling the bundle to saturation temperature within 8 min. The overall technical objective of the test was to contribute to the understanding of fuel bundle dynamics, and the related hydrogen and fission product behavior, during a high temperature transient. The report provides a description of the major observed phenomena. Interpretation of the test was based upon the response of on-line instruments, posttest fission product sample analysis, nondestructive and destructive postirradiation examination of the fuel bundle, and a calculational study using the Severe Core Damage Analysis Package (SCDAP).

FIN No. A6305—TFBP Severe Fuel Damage Studies

EXECUTIVE SUMMARY

The Severe Fuel Damage Scoping Test (SFD-ST) was conducted in the Power Burst Facility (PBF) at the Idaho National Engineering Laboratory on 28 October 1982. It was the first of four in-pile tests performed in the PBF as part of an internationally sponsored[a] light water reactor severe fuel damage research program, initiated by the U.S. Nuclear Regulatory Commission. The objective of the program is to develop a data base and models for the range of conditions covered in severe accidents to enable prediction of (a) the overall response of the core and associated structures, (b) the rate of hydrogen generation from the interaction of coolant with the fuel, cladding and reactor structure, (c) the rate of release of fission products and their chemical forms, and (d) the coolability of the damaged fuel under reflood.

The SFD-ST was the first light water reactor multifuel rod experiment of its kind. A prime aim was to gain experience in performing such tests in preparation for the subsequent series of experiments. To that end the test proved invaluable and influenced test procedures and instrumentation requirements, both in PBF and other facilities, and provided guidance to the posttest examinations and analyses of these tests. The overall technical objective of the SFD-ST was to contribute to the understanding of fuel bundle dynamics, and the related hydrogen generation and fission product behavior, during a high temperature transient.

The fuel bundle consisted of 32, 0.9 m-long, fresh fuel rods, and was surrounded by an insulating shroud. Prior to the high temperature transient the fuel was trace-irradiated (91 MWd/T) to achieve a suitable fission product inventory.

The transient phase commenced with boildown of the bundle coolant. The experiment was performed at a system pressure of 7 MPa and a nominal inlet flow rate of 16 g/s. The power was ramped over a 151 min period to provide nuclear heating rates of 0.10 to 0.15 K/s. The coolant level reduced from 0.42 m above the base of the fuel to 0.17 m during the initial 145 min, with fuel temperatures increasing to about 2100 K. During the final 6 min of the transient, zircaloy oxidation energy increased the heating rate to at least 10 K/s, with peak fuel temperatures rising from 2100 K to fuel melting (~3000 K). During this final phase there were redistributions of (U,Zr,O) melts, a large increase in the hydrogen production rate, significant changes in pressure, a coolant level decrease to about 0.1 m and an indicated reduction in the bundle inlet flow rate of about 25%. The inlet flow reduction, decline in the coolant level, and the rapid increase in zircaloy oxidation and temperature during the final minutes of the transient were all strongly interrelated, with positive feedback effects. The exact sequence of events could not be positively established, but it is probable that the high temperatures and melt relocation achieved during the Scoping Test were a direct consequence of the unplanned reduction in the bundle inlet flow rate.

The transient was terminated by scram of the reactor, and the inlet flow reflooded and cooled the bundle to saturation temperature (556 K) within 8 min, after which time it was continually flushed. All effluent from the bundle during the transient, reflood and flushing phases was routed to a fission product sampling and monitoring system.

Interpretation of the test was based upon the response of on-line instruments (e.g., thermocouples, pressure transducers, flowmeters, fission chambers, spectrometers), posttest fission product sample analysis, nondestructive and destructive postirradiation examination of the test bundle, and a calculational study using the Severe Core Damage Analysis Package (SCDAP).

As the first light water reactor fuel bundle high temperature experiment, the test provided valuable data for evaluation of SCDAP. Despite uncertainties in some of the measured parameters, particularly those related to input boundary conditions, the analysis provided a general confirmation of thermal-hydraulic models in the code. The principal uncertainties in the input data were related to the bundle nuclear power distribution, inlet flow rate and heat loss through the insulator.

---

a. Sponsors of the program include Belgium, Canada, Federal Republic of Germany, Italy, Japan, Netherlands, Republic of China (Taiwan), Republic of Korea, Spain, Sweden, United Kingdom, and United States.

A reliable measurement of the two-phase/steam interface elevation throughout the transient was overpredicted by SCDAP by about 0.1 m during the initial phase, reducing during the boildown to about 0.05 m.

The fuel rods were well instrumented with thermocouples, and provided accurate spatial and time dependent temperature data, up to values of about 2000 K. The maximum deviation of individual measurements from the radially averaged temperature profile at a given elevation was about ± 50 K, with no evidence of any general radial temperature gradient. SCDAP generally underpredicted ($\sim$100 K) both cladding and fuel centerline thermocouple measurements.

The steam thermocouple measurements generally showed larger radial variations than those within the fuel rods, but again indicated no specific trends. Radiation heat transfer from the fuel rod surfaces to the thermocouple shields, and from the shields to the thermocouples, may have resulted in higher apparent steam temperatures as these were not well predicted by SCDAP.

Fuel rod rupture and the associated release of fission products occurred over a 20 min period, at maximum cladding temperatures of about 1100 to 1200 K. The ballooning and rupture model in SCDAP predicted cladding failure outside this temperature range. In the final calculation, rupture of one component representing the central four rods occurred at a temperature of 1000 K, with the remaining components failing about 37 min later at 1240 K.

Fuel rod and steam thermocouples failed at temperatures below about 2000 K and 1400 K, respectively. Peak temperatures within the fuel bundle were estimated from posttest examination on the basis of metallurgical phase distributions and elemental composition differences. Thermocouples outside the test bundle provided additional information, and indicated when the bundle was cooled to saturation temperature. The final high temperature and cooldown phases, where peak temperatures of about 2100 K increased to fuel melting by the end of the transient before being cooled to saturation temperature, were not well represented by the SCDAP calculations. This was due to uncertainties in the steam generation rate and shroud behavior, and phenomena outside the scope of SCDAP models.

The widespread presence of Inconel constituents, in both U-rich and Zr-rich solidified melts, suggested that cladding interactions with middle or upper spacer grids may have been important in initiating fuel liquefaction and melt relocation processes.

Porous pellet regions, indicating peak temperatures near fuel melting, were found to contain substantial Zr cladding and Inconel grid constituents. Therefore, pellet liquefaction was chemically assisted and the porosity was probably associated with melt shrinkage. Melting of stoichiometric UO_2 (3120 K) could have occurred at many bundle elevations without leaving definite traces, due to subsequent melt interactions. However, at least one conspicuous densification zone survived that indicated incipient fuel melting without chemical alterations. The highest fuel temperatures almost certainly occurred adjacent to melts, with pellet interiors remaining considerably cooler from the strong temperature gradients across melt-fuel interfaces.

Molten cladding typically attacked UO_2 and ZrO_2 by reduction, often dynamically while slumping or while penetrating cracks. Some oxygen uptake also occurred by direct reactions with steam. Bulk oxidized melt generally arrived at the lower bundle region in a partially oxidized condition, and continued to react with fuel rods until solidification occurred or complete oxidation was achieved. High liquefied fuel concentrations measured in oxidized melt samples indicated temperatures greater than 2673 K.

A metallic melt formed late in the slumping sequence and relocated downward without dissolving significant quantities of fuel. The metallic melt reacted with the previously solidified bulk oxidized melt at approximately the time of reactor scram. The dominant mechanism for altering the bundle geometry was the formation and slumping of high temperature Zr-rich melts, accompanied by liquefaction of $\sim$15% of the original fuel volume. Bundle geometry was extensively disrupted due to steam embrittlement over the central bundle region.

The signals from an array of fission chambers were used to provide a qualitative assessment of material motion. Slowly varying deviations during the minute prior to reactor scram were interpreted as movement of fuel-bearing melt. The most significant melt depletion occurred at the 0.50-m elevation, with smaller depletions being detected at the 0.70-m elevation. The majority of melt accumulated at the bottom elevation (0.17 m), with smaller accumulations indicated by the fission chambers at the 0.30-m and 0.35-m locations.

A qualitative assessment of the posttest bundle geometry was provided by tomographic reconstruction from multiangle radiographs. An upward fuel stack displacement of over 0.11 m, creating several axial gaps in the bundle, was observed in the neutron radiographs. The approximate area fractions of UO_2, Zr-rich metallic melt and U-rich oxidized melt (mostly liquefied fuel) were derived by planimetry from macrophotographs of seven metallographic cross sections. The intact geometry flow area of 43% (which includes shroud insulation) was estimated to have reduced to between 32% and 37% from the lower six metallographic cross sections (0.055 m to 0.495 m). The flow area at the upper cross section location of 0.915 m was found to be about double the intact value.

An on-line thermal conductivity analyzer provided a time-dependent measurement of hydrogen release from the test train. Integration of the data prior to the final rapid oxidation provided a reliable hydrogen generation value of 113 ± 10 g. After this time the experimental uncertainties, both in the absolute value and timing of hydrogen release (i.e., transit time corrections), resulted in limited correlation of oxidation and bundle behavior in the temperature range of 2000 to 3000 K.

Postirradiation examination of the test bundle and shroud zirconium oxide thicknesses resulted in a total hydrogen generation estimate of 172 ± 40 g. The examination also indicated the presence hyperstoichiometric uranium oxides both inside fuel pellets and within adjacent uranium bearing melts. An upper limit estimate, based on two-thirds of the fuel oxidized to $UO_{2.6}$, provided an additional 48 g of hydrogen.

Hydrogen generation was reasonably simulated by SCDAP prior to the final rapid oxidation. Up to that time the code predicted a total hydrogen production of 74 g, in agreement with the measured hydrogen release of 113 g when corrected for zirconium regions not modelled in SCDAP.

Fission product release from the bundle during the SFD-ST could be approximately characterized in six phases. Transport effects not accounted for in the analysis complicated attempts to relate the experimental data to fuel release. The gap release and low temperature (peak fuel temperature <1700 K) diffusion phases amounted to only 0.15% of the integral activity measured up to about one hour after reactor scram. High temperature diffusion, between peak fuel temperatures of 1700 and 2100 K, accounted for about 4%. Fuel liquefaction before reactor scram increased the release to 10%, with an additional unquantified contribution from liquefaction during the cooldown phase. The total amount of fuel liquefied was estimated to be 15%, resulting in an upper limit of 20% fission product release from this mechanism.

During the ~8 min cooldown and reflood period, major release occurred due to a combination of the continued liquefaction, fuel oxidation, grain growth/separation and formation of shrinkage cracks within porous prior-molten regions. By the time the bundle had been reflooded and cooled to saturation temperature, 54% of the total activity had been recorded. However, due to transit time uncertainties, it is probable that a fraction of the cooldown contribution was released from the fuel during the high temperature liquefaction phase. The flushing process continued to extract further fission products from the bundle, in addition to resuspending species deposited within the system.

Effective release rate coefficients measured for the noble gas isotopes may have been influenced by holdup in the fuel-cladding gap or stagnation in the transport system, but they were not complicated by deposition processes. The measured noble gas release rate as a function of time was over three orders of magnitude below that predicted using NUREG-0772 constants (correctly applied to account for local variations in bundle temperature and fission product inventory) at low temperatures, and about one order of magnitude when peak and average bundle temperatures were about 2100 K and 1500 K, respectively. The low burnup of

the SFD-ST fuel, where open porosity and release paths had not developed, was the probable major reason for the lower release rates. Due to uncertainties in the transit time from the test bundle to the spectrometers, effective release rate coefficients were not correlated to peak temperatures above 2100 K.

The measured iodine release fraction was 0.51 ± 0.08, the cesium and tellurium release fractions were 0.32 ± 0.05 and 0.40 ± 0.07 respectively, the barium release was about 0.01, and very small release fractions (10^{-4} - 10^{-6}) of low volatile fission products Ru, Sr, Nb, and Ce were detected downstream of the bundle. The integral noble gas release was not measured directly, but integration of the spectrometer measurements of noble gas isotopes yielded an approximate average value of 0.5. All volatile fission products released, except tellurium, were transported efficiently in the high velocity, steam rich effluent stream. One fourth of the released tellurium was found irreversibly deposited on steamline walls, one half in the liquidline particle filler, and the remaining one fourth in the collection tank liquid.

Retained fission product estimates indicated appreciable release of ^{90}Sr, ^{95}Zr, ^{106}Ru, ^{125}Sb, ^{137}Cs, and ^{144}Ce from fuel pellets that remained solid. Ostensibly nonvolatile fission products (^{90}Sr, ^{106}Ru, ^{144}Ce, etc.) that were released evidently migrated only short distances before irreversibly depositing, as they were not detected downstream of the bundle in significant quantities.

SCDAP spatial and time dependent temperature histories were input to the fission product release code FASTGRASS. Release rates were underpredicted by several orders of magnitude during the early low temperature phase (peak temperatures < 1700 K) of the transient, but this accounted for << 1% of the total fractional release. Following this period, and prior to when temperatures became ill-defined, the release rates were reasonably predicted. On the basis of liquefaction occurring in 15% of the fuel bundle, which increased predicted release rates by about an order of magnitude above 2400 K, and the assumption that all grain boundaries eventually became connected to free surfaces, fractional releases were in general agreement with the measurements. The mechanism for separating fuel grains has not been positively identified, although there was evidence of microcrack networks associated with fuel oxidation.

The data from this analysis of the Scoping Test are being combined with those from the subsequent three tests performed in PBF, other integral and separate-effects experiments, and the TMI-2 core examination. A substantial data base related to severe fuel damage, melt progression, hydrogen generation and fission product behavior is becoming established. The identification of key phenomena and processes, and a consistent interpretation of the data from all the available sources, will greatly assist the development and validation of accident analysis models. This will permit more reliable, plant-specific, probabilistic risk assessment and will be instrumental in the development of regulatory policy on severe accidents.

ACKNOWLEDGMENTS

The authors are extremely appreciative of the organizations, and their staff, that have contributed to this program. It has taken about five years from conception of the Scoping Test to the issuance of this report, and the planning, execution, and analysis is a credit to all those individuals involved. The project covered a wide range of disciplines and, within EG&G Idaho, Inc., engaged groups from LWR research, engineering and physics, PBF facility and technical support, data acquisition, reduction, and graphics, the Test Reactor Area hot cells and associated laboratories, and code development. In addition, other organizations have participated in this collaborative program. The design and construction of the test train was undertaken by Battelle Northwest Laboratories, neutron radiography was performed at Argonne National Laboratory-West, metallographic analysis was greatly assisted by Kernforschungszentrum Karlsruhe, SEM/EDS and SAS measurements were carried out by Westinghouse Idaho Nuclear Company and Westinghouse Hanford, and code calculations were performed by workers from Argonne National Laboratory-East and the Japanese Atomic Energy Research Institute. One of the authors (A. D. Knipe) acknowledges the support of the United Kingdom Atomic Energy Authority during his assignment at INEL and the cooperation of the EG&G staff.

CONTENTS

ABSTRACT ii

EXECUTIVE SUMMARY iii

ACKNOWLEDGMENTS vii

1. INTRODUCTION 1

2. SYSTEM DESCRIPTION 4

   2.1 Overview 4

   2.2 The Facility 4

   2.3 Test Train and Fuel Bundle 4

   2.4 Fission Product and Hydrogen Sampling and Monitoring System 9

   2.5 Instrumentation 9

3. TEST CONDUCT 14

   3.1 Overview 14

   3.2 Test Loop Heat-Up 14

   3.3 Fuel Conditioning, Power Calibration and Fission Product Inventory Build-Up 14

   3.4 Shutdown Phase 14

   3.5 Short-lived Fission Product Build-Up 14

   3.6 High Temperature Transient 16

   3.7 Cooldown Phase 17

4. TEST BUNDLE THERMAL, HYDRAULIC, AND MECHANICAL BEHAVIOR 18

   4.1 Overview 18

   4.2 Boundary Conditions 18

   4.3 Bundle Nuclear Power 20

   4.4 Coolant Level 23

   4.5 Fuel Rod Temperatures 24

   4.6 Coolant Temperatures 28

   4.7 Shroud Behavior 32

4.8 Structural Changes 41

4.9 Hydrogen Production 59

4.10 The Final High Temperature Phase 63

5. FISSION PRODUCT BEHAVIOR 73

5.1 Overview 73

5.2 Fission Product Transit Time From Fuel Bundle to Detectors 74

5.3 Isotopic Fission Product Release 76

5.4 Fission Product Release During the Final High Temperature Phase 82

5.5 Total Fission Product Release 84

5.6 Tellurium Behavior 88

5.7 Retained Fission Products 90

6. POSTTEST ANALYSIS 94

6.1 Overview 94

6.2 SCDAP Calculations and Comparisons 94

6.3 Fission Product Release Model Calculations 111

7. SUMMARY 114

7.1 Hydraulic and Thermal Behavior 114

7.2 Bundle Structural Changes 115

7.3 Oxidation and Hydrogen Generation 116

7.4 Fission Product Behavior 117

7.5 Conclusion 119

8. REFERENCES 120

APPENDIX A—FUEL ROD CHARACTERISTICS A-1

APPENDIX B—INSTRUMENT LOCATION, TESTING, AND PERFORMANCE B-1

APPENDIX C—TEST TRAIN POWER SOURCES AND CALIBRATION C-1

APPENDIX D—THE HYDROGEN THERMAL CONDUCTIVITY ANALYZER MEASUREMENT D-1

APPENDIX E—POSTIRRADIATION EXAMINATION DATA E-1

APPENDIX F—ANALYSIS OF BUNDLE-RETAINED FISSION PRODUCTS F-1

APPENDIX G—FISSION PRODUCT AVERAGE AGE TRANSIT CALCULATIONS G-1

APPENDIX H—THE SCDAP MODEL FOR THE ANALYSIS OF THE SFD SCOPING TEST H-1

APPENDIX I—DOCUMENTATION AND RECORDS TRACEABILITY I-1

APPENDIX J—SFD-ST DATA PLOTS J-1

PBF SEVERE FUEL DAMAGE SCOPING TEST—TEST RESULTS REPORT

1. INTRODUCTION

The light water reactor (LWR) accident at the Three Mile Island Nuclear Station-Unit 2 (TMI-2)[1] in 1979, demonstrated the risk significance of severe core damage accidents. The multiple-failure accident sequence resulted in core damage beyond the limits associated with design-basis loss-of-coolant accidents. At the time of the TMI-2 accident the severe fuel damage and melt progression data base for the assessment of risk and consequences was very limited. The United States Nuclear Regulatory Commission (USNRC) therefore initiated an internationally sponsored[a] Severe Fuel Damage (SFD) research program.[2] The objective of the program is to develop a data base and models for the range of conditions covered in severe accidents to enable prediction of: (a) the overall response of the core and associated structures, (b) the rate of hydrogen generation from the interaction of coolant with the fuel, cladding and reactor structure, (c) the rate of release of fission products and their chemical forms, and (d) the coolability of the damaged fuel under reflood. A significant portion of the program, encompassing both experimental and model development aspects, was undertaken at the Department of Energy's Idaho National Engineering Laboratory (INEL).

The major test program at the INEL consisted of a series of four, in-pile, multifuel rod experiments performed in the Power Burst Facility (PBF). Each experiment consisted of a transient in which the test fuel bundle inlet coolant flow was reduced, and the nuclear power increased, until high temperatures in the bundle were achieved. Peak temperatures are known to have approached fuel melting in the first two tests, and similar values are anticipated to be established by postirradiation examination for the final tests. Parameters that were varied during the four experiments were the heat-up rate, coolant inlet flow rate, cooldown procedure, fuel rod burnup, and the presence of control rod material. The influence of these parameters on the experimental data collected during each test relates to the understanding of LWR fuel bundle behavior, hydrogen generation, and the release, transport and deposition of fission products. The principal test conditions are summarized in Table 1, and preliminary overviews of each test were provided in References 3 to 6. The data from the PBF tests are being combined with that from other integral and separate-effects tests, and the TMI-2 core examination, to facilitate the identification of key phenomena and processes, the development of deterministic models, the performance of appropriate sequence analyses, and the definition of fission product source terms. This will allow more reliable, plant-specific, probabilistic risk assessment and will be instrumental in the development of regulatory policies on severe accidents.

The SFD Scoping Test (SFD-ST) was the first large scale severe fuel damage experiment performed in PBF. A major objective was to gain experience in performing such tests in preparation for the subsequent series of experiments. To that end the test proved invaluable and influenced future procedures and instrumentation requirements. In addition, however, the test provided a wide range of useful severe fuel damage research data in its own right that have been brought together in this report. The overall technical objective of the SFD-ST was to contribute to the understanding of fuel bundle dynamics, and the related hydrogen generation and fission product behavior, during a high temperature transient. Furthermore, it was the only test of the series to simulate rapid steam/water cooling of degraded core materials and,therefore,of special interest to the TMI-2 core examination.

Following the initial interpretation of the Scoping Test data, five reports have been prepared covering analysis of the neutron detector signals,[7] results from the effluent system sample analyses,[8] preliminary examination of the test bundle,[9] metallographic examination of bundle cross sections,[10] and fission product behavior.[11] This document provides a comprehensive report of the SFD-ST and subsequent analyses,

---

a. Sponsors of the program include Belgium, Canada, Federal Republic of Germany, Italy, Japan, Netherlands, Republic of China (Taiwan), Republic of Korea, Spain, Sweden, United Kingdom, and United States.

Table 1. The SFD test series

Test	Bundle Description	Nominal Inlet Flowrate (g/s)	Approximate Steam Production Rate (g/s)	Approximate Heating Rate Prior to Rapid Oxidation[a] (K/s)	Cooldown Procedure
SFD-ST (28 Oct 1982)	32 fresh rods	16	16	0.1 to 0.15	Reactor scram, 16 g/s reflood increasing to ~30 g/s after 4 min. Whole bundle at T_{sat} after ~8 min.
SFD 1-1 (8 Sept 1983)	32 fresh rods	0.6	0.7 to 1.0	0.3 below 1300 K 0.9 above 1300 K	Power reduction and associated cooldown over 20 min prior to 17 g/s reflood.
SFD 1-3 (3 Aug 1984)	26 irradiated rods 2 fresh rods 4 guide tubes	0.6	0.6 to 2.4	0.5 below 1200 K 1.9 above 1200 K	Power reduction and argon associated cooldown over at least 50 min.
SFD 1-4 (7 Feb 1985)	26 irradiated rods 2 fresh rods 4 Ag-In-Cd control rods in guide tubes.	0.6	0.6 to 1.5[b]	0.4 below 1200 K[b] 1.4 above 1200 K	Power reduction and argon associated cooldown over at least 50 min.

a. Above ~1500 K to 2000 K (depending on axial location) in SFD ST, and about 1600 K in other three tests, the heating rate was extremely rapid and driven by the metal-water reaction.

b. Preliminary data.

including a reevaluation of the on-line test data, the results of the recent bundle composition and retained fission product analyses and best-estimate computer code predictions of the major phenomena. Assimilation of all the available information for the first time in the present report has resulted in several deviations from previous interpretations.

Descriptions of the PBF, the test train and fuel bundle configuration, the fission product and hydrogen sampling and monitoring system, and the on-line instrumentation are given in Section 2. A summary of the test conduct, including the fuel conditioning, power calibration, and fission product inventory build-up phases, is provided in Section 3. Section 4 is a detailed description of thermal, hydraulic, and mechanical behavior during the high temperature transient. An overview of the fission product behavior is given in Section 5, including a summary of previously reported results and the new retained fission product data. Analysis of the SFD-ST was performed with the Severe Core Damage Analysis Package (SCDAP) in an attempt to simulate major phenomena such as the fuel rod temperature response, cladding ballooning, oxidation, and meltdown. Fission product release was predicted with the mechanistic based code FASTGRASS. The calculational analyses are reported in Section 6. Section 7 provides an assessment of the SFD-ST in terms of the information that the experiment provided, and where it will assist severe accident regulatory policy decisions through confirmation or development of calculational models and by providing an indication of limitations in the current data base.

The report contains ten appendices. Appendix A specifies the test fuel rod characteristics and Appendix B provides a detailed description of instrument location, testing, and performance. The major individual contributions to the energy deposition within the test train, and an outline of the power balance resulting from the overall heat transfer process, is given in Appendix C. On-line hydrogen data measured with a thermal conductivity analyzer is discussed in Appendix D. Two appendices provide detailed accounts of the posttest examinations that characterized the fuel bundle (Appendix E) and obtained retained fission product

data (Appendix F). A procedure to assess the transit time for fission products released from the fuel to reach the various detectors using spectral data is presented in Appendix G. The SCDAP calculational model used for the analysis of the test is described in Appendix H. Appendix I provides instructions for retrieving information related to the SFD-ST and Appendix J includes a set of the on-line test data.

2. SYSTEM DESCRIPTION

2.1 Overview

This section contains a description of the Power Burst Facility (PBF), test train and fuel bundle, test train instrumentation, and effluent sampling and monitoring system. The nominal design characteristics of the fuel rods and bundle are provided in Appendix A. The experimental instrumentation is itemized, and the performance of each instrument discussed, in Appendix B.

2.2 The Facility

The PBF reactor, shown in Figure 1, consists of a driver core and a central flux trap contained in an open tank reactor vessel. An independent pressurized water coolant loop can provide a wide range of thermal-hydraulic conditions within the flux trap test space.

The PBF core is a right-circular annulus, 1.3 m in diameter and 0.91 m in length, enclosing the vertical flux trap that is 0.21 m in diameter. The core was designed for steady state and power burst operation, containing eight control rods for reactivity control during steady state operation and four transient rods for dynamic control during rapid reactivity transients. Each of the control and transient rods consists of a stainless steel canister containing a cylindrical annulus of boron carbide and is operated within an air-filled shroud.

An in-pile tube fits in the central flux trap region and houses the test train assembly. A nitrogen gas annulus is provided between the in-pile tube wall and an aluminum core filler piece because of the temperature gradient between the two components. The in-pile tube is a thick-walled (0.20 m outside diameter, 0.15 m inside diameter), Inconel 718, high strength tube designed to contain the steady state operating pressure and feasible pressure surges.

2.3 Test Train and Fuel Bundle

The test train for the SFD-ST was designed and built by the Pacific Northwest Laboratory (PNL) and assembled at the INEL. An elevation view of the test train within the in-pile tube is shown in Figure 2. The major components are the closure head assembly, the flow tube assembly, the outlet assembly, the insulated shroud assembly, the bundle assembly, and the inlet assembly.

The fuel bundle consisted of 32 fuel rods arranged in a 6 x 6 array with the four corner rods removed as shown in Figure 3. The figure also shows the identification system used for the rod positions. The active fuel length in the bundle was 0.9144 m and the fuel rods were of typical pressurized water reactor (PWR) design. The fuel bundle was assembled using three Inconel grid spacers to maintain a typical 17 x 17 PWR fuel rod pitch of 12.75 $\pm$ 0.25 mm. The rods were fixed to a lower support plate but were free to expand upwards.

The fuel bundle was contained within an insulating shroud constructed from a zirconia insulator sandwiched between zircaloy structural components. The insulation was fabricated from low density ZrO_2 fiberboard, with cylindrical ZrO_2 strengthening tubes to provide compressive strength, as illustrated in Figure 3. The insulation was provided to reduce the radial heat loss through the shroud wall and hence the power required to raise the test rods to the high target temperature. Use of the insulation also minimized radial temperature variations in the fuel bundle. The insulating shroud extended above and below the active fuel length. A high temperature ceramic insulator positioned within the shroud near the lower end inhibited the loss of possible molten material out of the test train. The insulator region was pressurized to protect the insulator, but was maintained at a constant negative pressure differential relative to the bundle region in order to prevent the liner from being forced into the fuel. The region was pressurized using argon gas from a

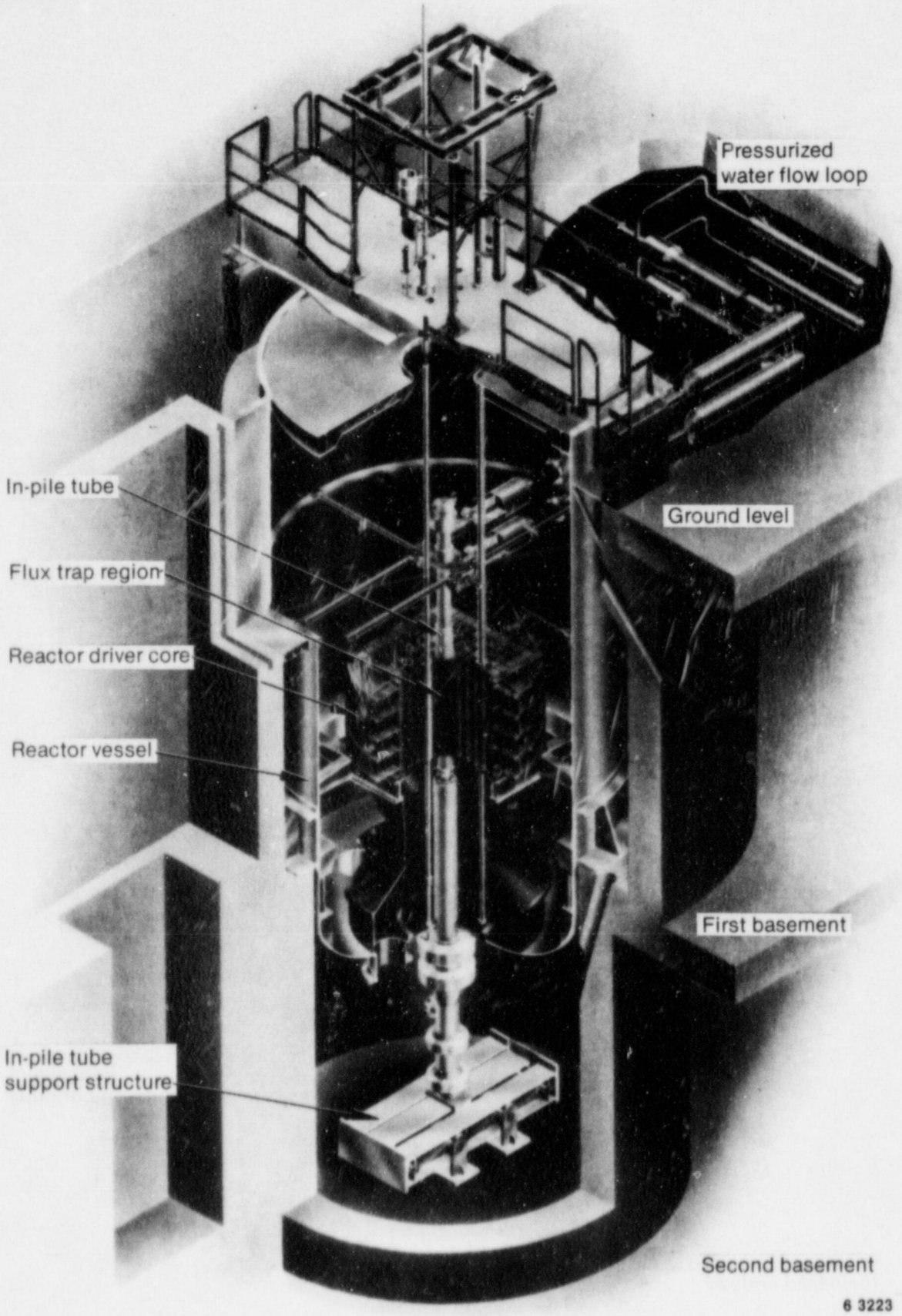

Figure 1. Power Burst Facility reactor cutaway view.

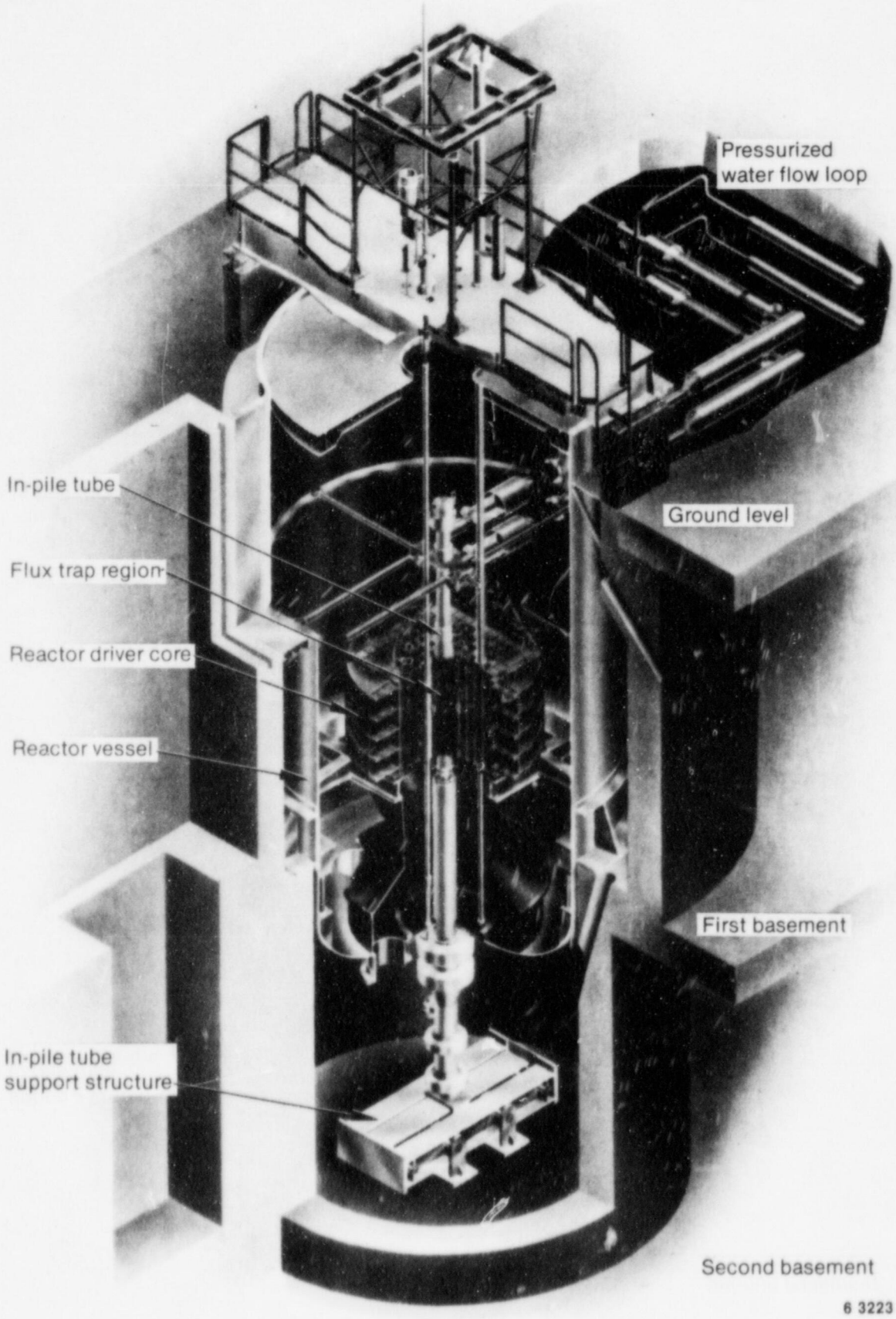

Figure 1. Power Burst Facility reactor cutaway view.

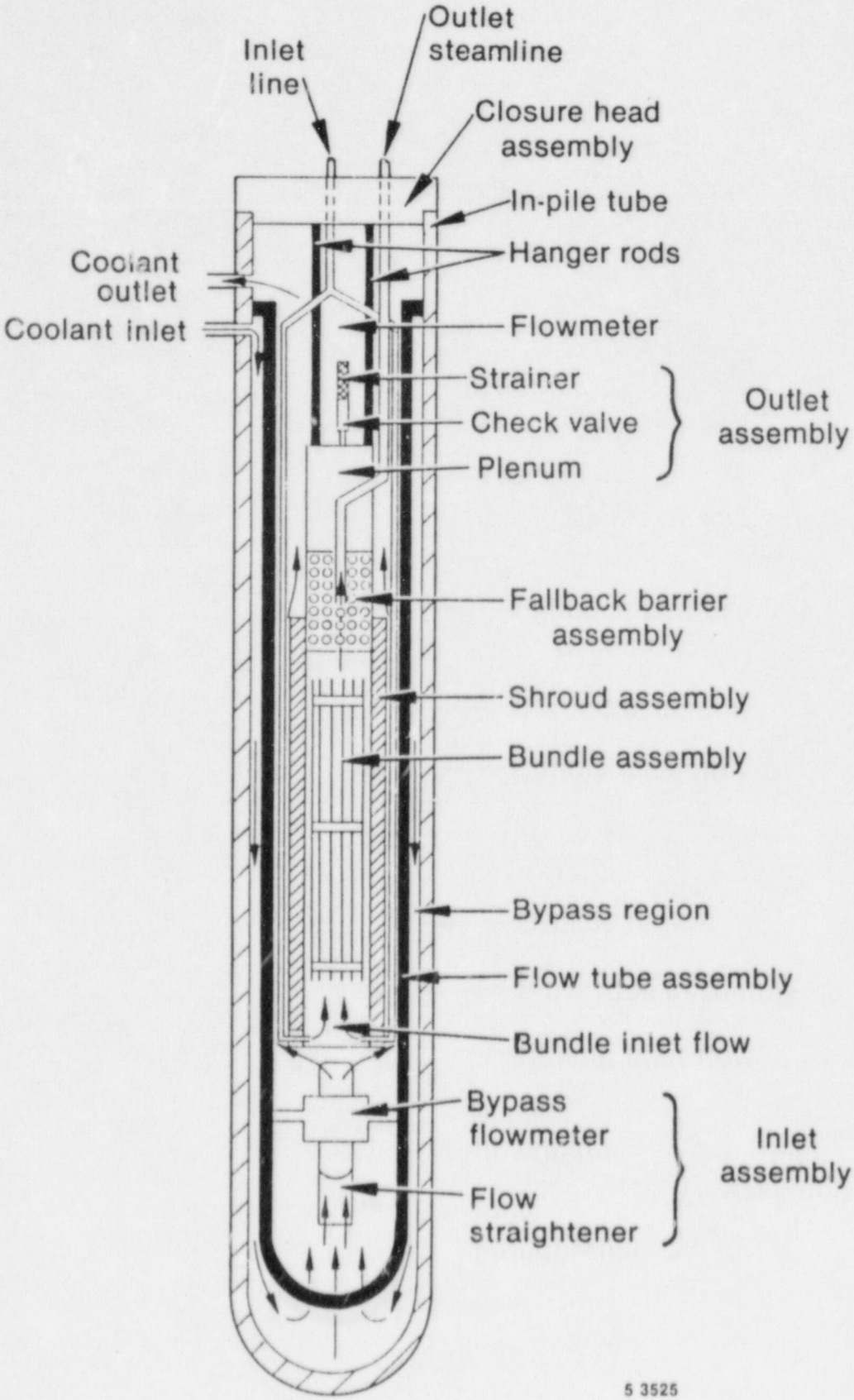

Figure 2. Elevation view of SFD-ST test train.

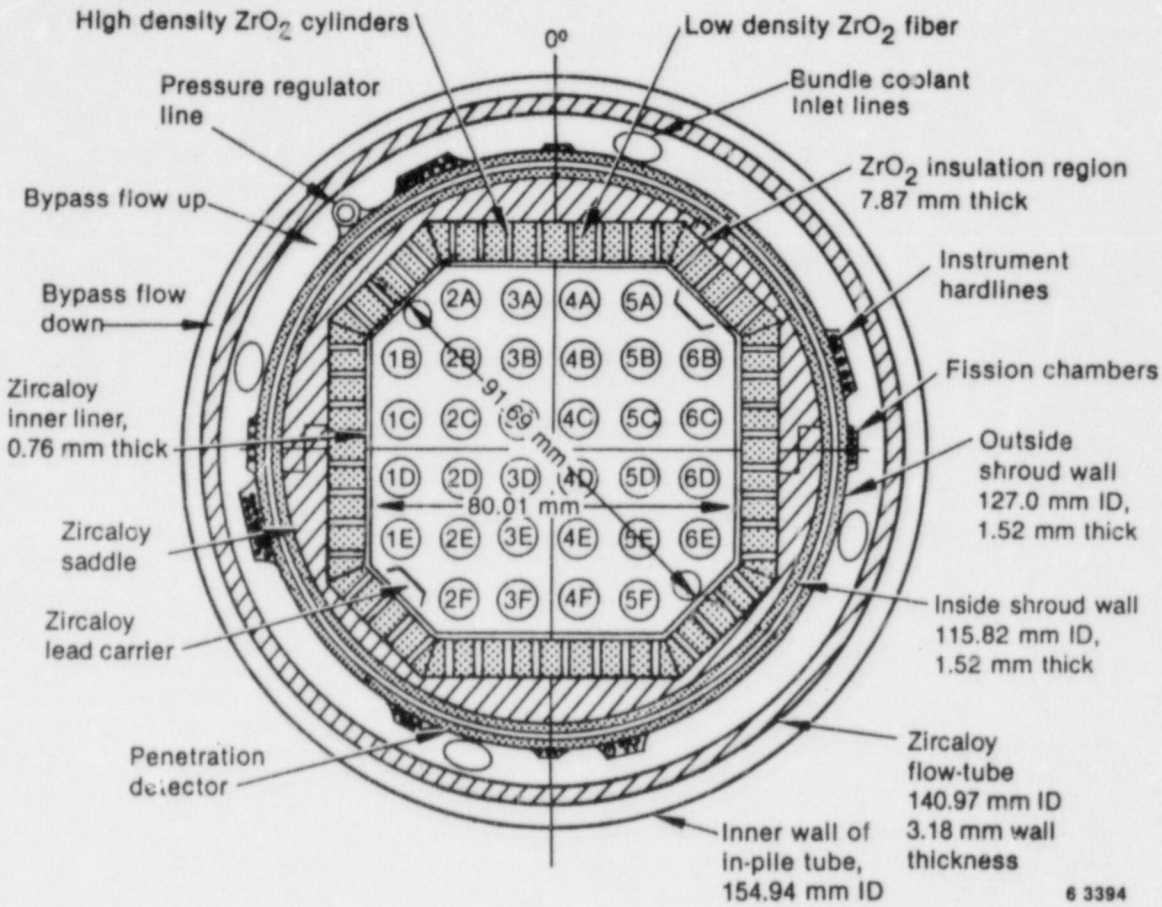

Figure 3. Cross-sectional view of SFD-ST shroud and bundle.

line that passed through the closure head assembly into the bottom of the insulating shroud, as shown schematically in Figure 4. Shroud pressure was measured through a similar line connected to the top of the shroud. During most of the high temperature transient the pressure in the bundle region of the test train was maintained at a slightly lower pressure than the bypass region (<15 kPa). The pressure difference between these two regions (Figure 4) was used to close the check valve in the outlet assembly and control the backpressure for the fission product and hydrogen sampling and monitoring system. This is discussed further in Subsection 2.4.

The bundle, shroud, inlet, and outlet assemblies were all contained within a flow tube assembly that directed the flow of the PBF loop coolant system within the in-pile tube, as shown in Figure 2. The flow tube comprised an upper stainless steel section, a center zircaloy-2 section for neutron economy in the test fuel, and a lower catch basket section to act as a heat sink and container for fuel fragments. The coolant entered the top of the in-pile tube above the reactor core and circulated down the annulus between the in-pile tube wall and the flow tube, a region that is termed the bypass. The flow reversed at the bottom where it passed through a flow straightener and flowmeter. The coolant was then directed up along the outside surface of the shroud and the outlet assembly, providing cooling for the superheated steam exiting the bundle through the outlet steamline.

The loop coolant system provided cooling water to the in-pile tube at controllable pressure, temperature, and flow rate in order to simulate accident conditions. The system is shown schematically in Figure 4 and includes a pressurizer, a pump, electrical heaters to control inlet temperature, a flow control valve, acoustic filters, and heat exchangers for removing the energy transferred to the coolant by the test fuel. Instrumentation in the inlet line provided measurements of initial conditions.

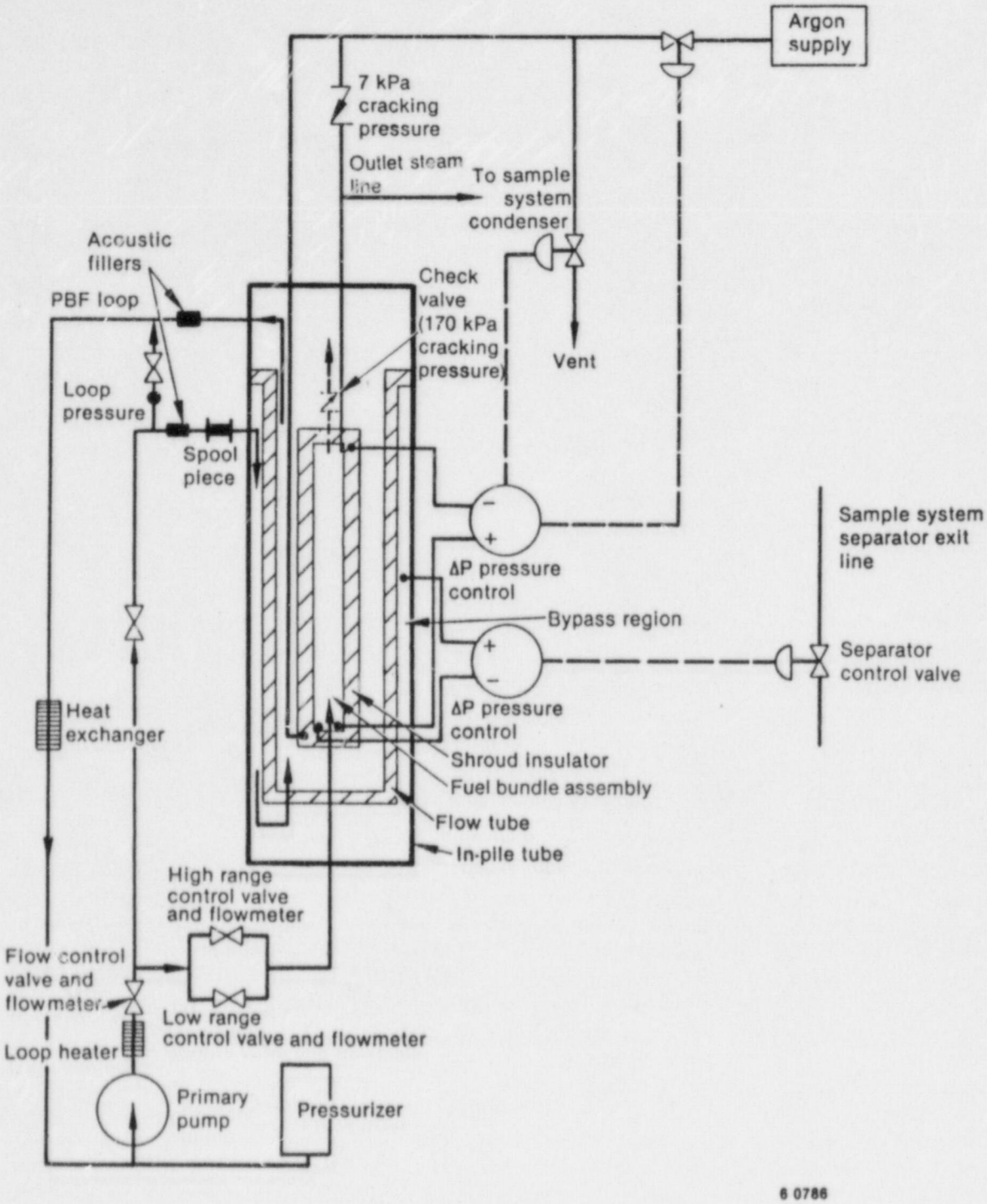

Figure 4. Schematic of the test train coolant and pressure control system.

A separate coolant line provided inlet flow to the test bundle region. At operating temperature and pressure this coolant line provided an inlet flow up to 2.2 L/s using a high range control valve and up to 0.2 L/s using a low range control valve (Figure 4). The line included inlet flow transducers to monitor the flow into the bundle region. The inlet flow line entered the test train through the closure head assembly as shown in Figure 2. The flow was divided into four small lines (two shown in diagram) that lead into the interior of the bundle inlet region. This flow passed through the bundle and up into the outlet assembly. The outlet assembly included both an exit steamline and a check valve. At high bundle flow rates during the

pretransient phase, the coolant flow through the bundle exited through the check valve into the bypass flow. During the low flow, high temperature transient, the check valve was closed and the coolant exiting the bundle was routed through the fallback barrier assembly to the outlet steamline that passed through the closure head. The fallback barrier, constructed of zircaloy plates and zirconia pellets, was designed to minimize condensate from returning to the fuel bundle. A particle screen was located in the flowpath through the check valve to catch fuel fragments >0.4 mm and prevent them from being swept into the PBF loop.

2.4 Fission Product and Hydrogen Sampling and Monitoring System

The effluent sampling and monitoring system, shown schematically in Figure 5, was used to collect and sample the bundle effluent throughout the experiment. The steam, fission products, and noncondensible gases exited the test train through the closure head of the in-pile tube flowed into an insulated steamline. This line routed the effluent into a shielded experimental area referred to as *Cubicle 13*. In Cubicle 13 the effluent line first passed through a manifold containing six grab samplers and into a condenser. The condensed coolant and noncondensible gases flowed into a separation vessel where the entrained gas was allowed to separate from the liquid. Nitrogen control gas was bled into the separation vessel at a constant flow rate to provide control of the backpressure in the system. A pressure control system regulated the gas flow leaving the separator through a pressure control valve to effectively maintain a fixed differential pressure between the bundle and the separation vessel. The gas flowing through this valve consisted of both the gases separated from the test coolant and the nitrogen control gas. The separated gases were carried past an on-line gamma

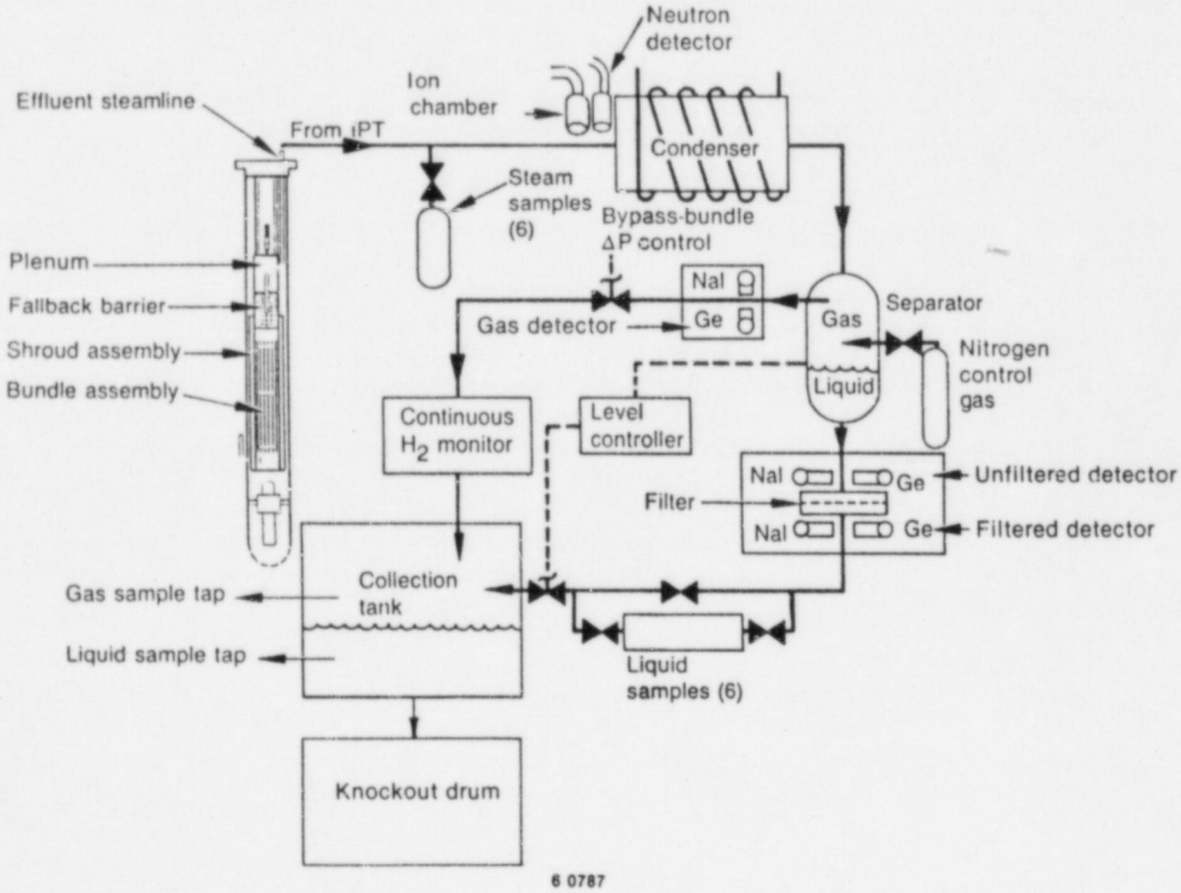

Figure 5. Schematic of the effluent sampling and monitoring system.

spectrometer and into the collection vessel. A continuous sample of this gas was passed through a thermal conductivity type hydrogen monitor (Appendix D).

The liquid drained from the separation vessel flowed past two on-line gamma spectrometers separated by a filter that was used to catch small particulate matter. The first spectrometer monitored the total activity in the liquid coolant. The second spectrometer monitored activity after filtration of the coolant. A bypass system was also provided to maintain flow in the event that the filter became clogged. Downstream of the on-line fission product monitors was a manifold with six flow-through sample containers to take grab samples of the condensed coolant. The coolant finally passed through a level control valve before entering into the collection vessel. Flow control of coolant into the collection vessel was provided by a flow control valve operated by a level control signal from the separator vessel.

2.5 Instrumentation

The test bundle was instrumented with six fuel rod centerline thermocouples, 25 fuel rod cladding thermocouples, 10 steam temperature probes and eight fuel rod pressure sensors. The shroud contained an additional 28 thermocouples and a penetration detector. Test conditions were monitored with thermocouples, pressure transducers, flowmeters, flux wires, and fission chambers associated with the test train. This section provides a brief description of the location of all these devices and the additional instrumentation related to the plant and the Fission Product Detection System (FPDS). Detailed tables and diagrams, identifying each instrument, and categorizing performance, are given in Appendix B. Performance categories were assigned by thorough measurement-by-measurement examination of the test data. As a result of examination, one or more categories (defined in Appendix B) were assigned to each measurement as a function of time. Data referred to as *Qualified* are absolute values and have been assigned uncertainty limits. The pretransient checks and the posttest data qualification procedures are also described in Appendix B. Throughout this report elevations are referenced to the bottom of the active fuel in the fuel rods.

2.5.1 Fuel Rod Instrumentation. The instrumentation for measurement of fuel rod parameters consisted of the following:

1. Twenty-five interior cladding surface thermocouples with their hot junctions spot welded at one of three elevations: 0.35, 0.50, or 0.70 m. There were seven junctions at both the 0.35- and 0.70-m levels and 11 junctions at the 0.50-m level. A total of nine fuel rods had cladding thermocouples.

2. There were six thermocouples located along fuel rod centerlines, with their hot junctions at the 0.70-m level.

3. Three gas pressure transducers, to indicate rod pressure up until cladding rupture, were connected to the bottom of fuel Rods 3A, 3D, and 5E (-0.27-m level). Two additional transducers, mounted on Rods 4B and 1E, failed prior to installation of the test train.

4. Five gas pressure switches to indicate cladding rupture were installed on the bottom of Rods 2B, 6B, 4C, 6D, and 3E at the -0.27-m level.

2.5.2 Shroud Instrumentation. The thermocouples for measuring shroud temperatures, and additional instrumentation mounted on the shroud, were as follows:

1. Six thermocouples were located on the outside of the shroud inner liner (the dry side) with two measurement junctions at each of the elevations 0.35, 0.50, and 0.70 m. These are referred to as the *inside* thermocouples.

2. There were ten thermocouples located within the shroud at the outer surface of the insulation; four each at 0.50 and 0.70 m, and two at 0.91 m. These are referred to as the *middle* thermocouples.

3. Twelve thermocouples were used to measure the temperature on the outer surface of the shroud outer wall (i.e., inner surface of the bypass coolant channel). Four were located at 90-degree intervals around the shroud at elevations of 0.35. 0.50, and 0.70 m. These are referred to as the *outside* thermocouples.

4. Four sheathed and insulated wires were wound tightly around the inner portion of the shroud double outer wall and constituted the shroud melt-through detector. Indications of the shroud outer wall temperature were derived from the change in the insulation resistance between the wire and sheath of the detector.

5. Two aluminum-cobalt alloy flux wires were located on the outer shroud wall, one at 0- and one at 180-degrees to provide an indication of the integral axial power profile.

2.5.3 Test Train Fission Chambers. Twelve fission chambers were installed external to the fuel bundle assembly in the bypass flow region between the flow tube assembly and the in-pile tube. The primary objectives of using these detectors were to measure the axial power distribution within the test bundle and to nonintrusively determine the temporal position of the boiling liquid boundary (two-phase coolant/steam). Other objectives included two-phase coolant velocity measurements and investigation of the potential for cladding and fuel motion detection and analysis.

The fission chambers were located in two strings on opposite sides of the test bundle. At the 270-degree orientation (see Figure 3) five detectors were mounted at axial elevations of 0.81, 0.70, 0.50, 0.35, and 0.17 m. The 90-degree orientation had five detectors at the same elevations, plus two additional ones located at 0.76 and 0.30 m. These extra detectors were added for coolant velocity determination measurements.

The fission chamber signal conditioning and control system consisted of 12 ac (noise) data channels, 12 dc data channels, a microcomputer controller, and a remote terminal.

2.5.4 Water and Steam Parameters Instrumentation. Instruments to measure the water and steam parameters within the in-pile tube were as follows:

1. Two thermocouples were used to measure the bundle water inlet temperature, both located at an elevation of -0.305 m.

2. Two thermocouples were used to measure the bypass water inlet temperature at an elevation of -0.31 m as it flowed up around the shroud.

3. Four differential thermocouples were used to measure the temperature rise of the water flowing upward through the bypass region on the outside of the shroud. The lower legs were located at -0.31 m at 90-degree intervals around the shroud. The upper legs were located at the 0.91-m level.

4. There were 14 steam probes that measured the temperature within and above the fuel bundle; five at the 0.50-m elevation, five at 0.91 m, two at 1.11 m, and two at 1.19 m.

5. The temperature on the outer wall of the steamline was monitored with two thermocouples at 1.5 and 1.8 m.

6. Two turbine flowmeters were used to measure water flow within the in-pile tube. One flowmeter was located at the bottom of the shroud and measured the volumetric flow rate through the bypass region. The other flowmeter, located above the bundle, measured the water flow through the bundle during preconditioning.

7. There were two temperature profile detectors intended to determine the location of a particular temperature in a vertical direction. The detectors were located in opposite corners of the bundle at 135- and 315-degrees.

8. Three differential pressure transducers located outside the in-pile tube measured pressure through sensing tubes. One transducer measured the pressure difference between the bypass region and the bundle region with sense tube elevations of 0.50 and -0.30 m, respectively. Another transducer measured the coolant pressure difference across the bundle region from inlet (-0.30 m) to outlet (1.77 m). The remaining transducer measured the pressure difference between the top of the shroud insulation and the bundle region at the -0.30-m level.

9. Two pressure transducers of different maximum ranges were used to monitor normal test train system operating pressures and to monitor any high pressure pulses. A 10.3 MPa transducer physically located outside the reactor was connected by a sense tube to the bypass region at the 0.50-m level. A high pressure (69 MPa) transducer was located at the -0.30-m level in the bundle coolant flow region.

10. Two flowmeters were used to measure the bundle inlet coolant flow. These devices were located in the coolant monitoring and control system. One was used for preconditioning and the other for the low flow transient.

2.5.5 Fission Product Detection System Instrumentation. The instruments used in the FPDS were as follows:

1. Four gamma detectors were used to measure gross gamma activity and three additional gamma detectors were used to measure the gamma spectral activity. Three NaI (gross gamma) and three germanium detectors (gamma spectral) were used, one each on the gasline leaving the separator and one each on either side of the filter on the liquidline leaving the separator. The fourth gross gamma detector was an ion chamber located at the condenser.

2. A delayed neutron monitor (moderated-BF_3 tube-type) was used to measure the delayed neutron flux on the liquidline downstream of the condenser.

3. A thermal conductivity-type hydrogen analyzer was used to measure the concentration of hydrogen gas leaving the separator.

4. There were two pressure transducers in the system, one on the separation vessel, and one on the collection vessel (*blowdown tank*).

5. Temperature measurements were made with a thermocouple located on the inlet steamline and a second thermocouple located on the fluid line leaving the condenser.

6. A flowmeter was used to measure liquid flow out of the separator.

7. A pressure switch was located across the filter bypass on the liquid outlet of the separation vessel to indicate when the filter was being bypassed.

8. There was a level indicator on the collection vessel (blowdown tank) to monitor liquid level.

2.5.6 Plant Instrumentation. Plant instrumentation used in this test is listed below.

1. Five ion chambers were used to measure reactor power; PPS01, PPS02, NMS03, NMS04, and TR1.

2. The loop pressure was measured by the Model 7788 Ashcroft pressure gauge commonly referred to as the *Heise* gauge.

3. The loop flow rate was measured with a Venturi flowmeter.

4. A Radiation Area Monitor was used to indicate radiation levels in the vicinity of the sample system.

5. There were three instruments on the inlet spool piece; a pressure transducer, a temperature transducer, and a turbine flowmeter.

6. The reactor primary coolant flow rate was measured.

7. The reactor primary coolant heat exchanger differential temperatures were measured.

Interpretation of the test was to a large extent based upon detailed examination of the on-line data from the bundle, shroud, test train, FPDS, and plant instrumentation. Subsequent sections discuss the measured responses for the majority of instruments. The complete qualified test data recorded during the SFD-ST are provided in Appendix J.

3. TEST CONDUCT

3.1 Overview

The Severe Fuel Damage Scoping Test consisted of a hydrostatic loop test and loop heat-up, three power ramps, and a constant high power (350 kW) irradiation period of 66 h, a 10 day shutdown, two constant low power (85 kW) irradiation periods of 4 h that were separated by a 14 h shutdown, and finally the high temperature transient.

The following subsections provide an outline of the sequence of events during the test, details of the high temperature transient and cooldown being provided in later sections. A chronological summary of the test is provided in Table 2 and, for convenience, the high temperature transient data are referred to a zero time of 23:00 on October 28, 1982.

3.2 Test Loop Heat-Up

Following hydrostatic testing of the loop, the required coolant conditions were established to perform the nuclear phase of the test. These conditions were 518 K inlet coolant temperature, 6.9 MPa system pressure, 2.2 L/s bundle coolant flow and 2.5 L/s bypass coolant flow. Instrument checks were made during both the hydrostatic testing and the loop heat-up.

3.3 Fuel Conditioning, Power Calibration, and Fission Product Inventory Build-Up

Fuel conditioning and power calibration consisted of three power ramps to the peak permissible reactor power of 26 MW at a maximum rate of 3.7 MW/min. The peak bundle nuclear power of ∿370 kW was held constant for about 2 h and then reduced to 1 kW. Following the third reduction, the power was again raised and constant reactor operation was maintained for 66 h with an average bundle power of ∿350 kW. The purpose of this long steady state irradiation period was to build up a sufficient inventory of intermediate- and long-lived fission products to ensure suitable yields for the FPDS.

During the initial power ramp phase, the PBF reactor thermal power and the bundle nuclear power were intercalibrated under single-phase liquid coolant conditions. The procedure, and comparison with pretest predictions, are discussed in Subsection 4.3.

3.4 Shutdown Phase

The 66 h fission product build-up phase was followed by a 10-day shut down period, with test train and loop depressurized and cooled to ambient conditions. The shutdown period allowed the fission product inventory to decay such that the cesium-to-iodine mass ratio was approximately eight during the transient, which is close to the nominal value for LWR fuel.

3.5 Short-Lived Fission Product Build-Up

The in-pile coolant loop was again pressurized to 6.9 MPa and heated to 518 K for this phase of the test. The reactor power was increased to provide a bundle power of ∿90 kW, held constant for 4 h to generate short-lived fission products, and finally reduced to 1 kW. Following a 2 h preparation period the power was raised to 24 kW for the high temperature transient (Transient-1 in Table 2). There were, however, problems in pressurizing the FPDS and after about 3 h the reactor was shut down. A 14 h delay was incurred while the

Table 2. SFD-ST event sequence

Event	Time	Time Relative to Transient Zero Time (min)	Date
Fuel Conditioning, Power Calibration, Fission Product Inventory Build-up:			
Nuclear operation initiated	0004	—	10/13/82
Heat exchanger alarm failed; reactor shutdown	0130	—	—
Reactor restarted	0556	—	—
Bundle inlet flowmeter failed; reactor shutdown	1218	—	—
Reactor restarted; low flow alarm changed to outlet flowmeter	2022	—	—
First power ramp to 370 kW completed; core and bundle thermal power measured	0637	—	10/14/82
Second power ramp to 370 kW completed	0934	—	—
Third power ramp to 370 kW completed	1310	—	—
Average 350 kW steady-state operation started	1411	—	—
66-h run completed; reactor shutdown	0811	—	10/17/82
Ten-Day Fission Product Cooling Period Completed	—	—	10/27/82
Short-Lived Fission Product Generation-1:			
Average 90 kW steady state operation started	0447	—	10/27/82
4-h run completed; power reduced to 1 kW	0905	—	—
High Temperature Transient-1:			
Flow reduction started	0918	—	—
Power ramp to 24 kW started	1118	—	—
Collection system problem noted; could not obtain 6.9 MPa; reactor shutdown	1438	—	—
Short-Lived Fission Product Generation-2:			
Collection system problem fixed; reactor critical; power ramp to 75 kW	0504	—	10/28/82
Commercial power failed; reactor scrammed	0827	—	—
Reactor critical	0945	—	—
4-h run at 90 kW completed; power reduced to 1 kW	1622	—	—
High Temperature Transient-2:			
Flow reduction started	1650	—	10/28/82
Power ramp to 25 kW started	1747	—	—
Collection system turned on; power at 25 kW	1834	—	—
Power at 32 kW	2028	—	—
Flow rate problem being worked	2238	—	—
Zero time for high temperature transient	2300	0	
Flow adjusted to 0.02 L/s; check valve closed	2322	22	—
Instrument checks performed	2330	30	—
Power at 39 kW; power ramp started	2355	55	—
Fission product system indicated rod failure, clad temperatures 1050 K to 1200 K.	0024-0044	84-104	10/29/82
Rod pressure switches indicated rod failure	0037-0044	97-104	—
Temperature ramp rate 0.13 to 0.15 K/s	0136-204	156-184	—
Shroud inner liner failed	0204	184	—
Temperature ramp rate = 0.16 to 0.18 K/s	0206-0217	186-197	—
Bundle inlet flow started to decrease, separator pressure started to increase	0215	195	—
Temperature ramp rate ~10 K/s	0220-226	200-206	—
Bundle inlet flow started to increase, separator pressure peaked at 6.84 MPa	0224-225	204-205	—
Reactor manually scrammed at 8.10 MW	0225:47.7	205.795	—
Bundle flow rate increased to 0.035 L/s	0230	210	—
Entire bundle at saturation temperature	0234	214	—
Bundle pressure drop measurements completed	0600-0630	420-450	—

problem was overcome, necessitating a repeat of the 4 h fission product build-up period. During the power increase to 90 kW there was a momentary failure of the commercial power supply and the reactor scrammed. A further start-up was required to complete the fission product inventory phase.

3.6 High Temperature Transient

Du[illegible] nuclear phase of the Scoping Test prior to the high temperature transient, a pressure differential of about 340 kPa was maintained between the bundle coolant and the bypass region, which allowed the bundle coolant to flow out the check valve (Figures 2 and 4). For the transient it was planned to lower the bundle pressure slightly below the bypass pressure, thereby forcing the check valve to close and routing the effluent from the bundle through the outlet steamline to the sampling and monitoring system. It was proposed to control the bundle pressure by the backpressure from the separator. Prior to initiation of the transient, with the reactor power at 100 kW, the flow rate through the bundle was set at 0.016 L/s. The collection system was activated after the reactor power was increased and the bundle coolant boildown had started. When the backpressure to the bundle was reduced below the bypass pressure in order to close the check valve, the flow rate increased to about 0.034 L/s. The flow rate was reduced to 0.016 L/s by increasing the backpressure from the collection system to the bundle. However, at this flow rate, the bundle-to-bypass pressure differential did not appear sufficient to keep the check valve closed. The lowest bundle flow rate that could be achieved with the check valve closed was about 0.020 L/s, which resulted in a small positive pressure difference between the bypass and the bundle.

The final power ramp, from a bundle nuclear power of 39 kW to a maximum value of about 93 kW, was initiated 55 min after the zero time of 23:00 h on 28 October 1982. The coolant level at the start of the power ramp was about 0.42 m above the base of the fuel. At ∿84 min the first indication of fuel rod failure was obtained from the FPDS ion chamber. The functional rod pressure indicators showed rod failures between ∿97 and 104 min. Over the 20 min failure period, the maximum measured cladding temperatures increased from approximately ∿1100 to 1200 K.

Once the two-phase/steam interface was below the lowest bundle thermocouples, at ∿90 min into the transient, the temperature rise-rates at all elevations were very similar, ranging from 0.10 to 0.15 K/s.

At 184 min, when the bundle nuclear power was ∿86 kW, the shroud inner zircaloy liner failed, as expected, and the inside shroud pressurization system was shut off. Coincident with the shroud inner liner failure, the heat transfer across the shroud to the bypass coolant increased considerably.

At about 200 min into the transient, when the peak cladding temperature was ∿2000 K and the coolant level was at 0.17 m, the bundle thermocouples indicated large increases in the temperature rise rate (∿10 K/s). All remaining fuel rod thermocouples failed during the rapid rise, so that maximum temperatures could not be measured on-line. Posttest analysis, using metallographic indicators, showed temperatures in a small fraction of the bundle reached fuel melting temperatures of up to ∿3100 K. The posttest examination also revealed extensive redistribution of (U,Zr,O) melts. During the final high temperature phase, a large increase in the hydrogen production rate was observed along with a significant increase (260 kPa) in the separator pressure, an indicated reduction in the bundle inlet flow rate from 0.020 to ∿0.015 L/s and a reduction in the coolant level to about 0.10 m. The maximum bundle nuclear power was calculated to be 93 kW, with the energy from oxidation significantly increasing the overall bundle power.

Throughout the high temperature transient the coolant level in the bundle, as a function of time, was determined from the 12 test train fission chambers as discussed in Subsection 4.4. At selected times during the transient the gas and liquid grab samples were collected as outlined in Subsection 2.4.

3.7 Cooldown Phase

The high temperature transient was terminated at 205.8 min by manually scramming the reactor. Following reactor shutdown, at a flow rate of about 0.020 L/s, a minimum of 2.5 min would be required to fully flood the fuel region. About 4 min after scram the flow rate began to increase to a value of about 0.035 L/s without operator intervention. The thermocouple data indicated that the saturation temperature of 556 K was achieved throughout the bundle ~8 min after scram. Data were recorded for 8 h after reactor scram.

4. TEST BUNDLE THERMAL, HYDRAULIC, AND MECHANICAL BEHAVIOR

4.1 Overview

This section describes the bundle behavior during the high temperature transient in terms of the various control parameters, referred to as the test *boundary conditions*, and the resultant two-phase/steam interface level, temperature distribution, changes in bundle geometry and hydrogen production.

The qualified test data recorded during the SFD-ST are provided in Appendix J. Due to the large number of thermocouple measurements, average values have been used to describe the thermal response of the bundle where possible.

4.2 Boundary Conditions

Figures 6 and 7 provide data plots of the major time dependent boundary conditions for the SFD Scoping Test; namely the bundle inlet and bypass flow rates, the bundle inlet temperature (single qualified thermocouple at -0.305 m), bypass temperature (mean value of four thermocouples at -0.31 m), and the bundle pressure. The significances of variations from the specified values are discussed in later subsections. The transient bundle nuclear power, and its derivation, is described in Subsection 4.3.

The flowmeter in the separator liquidline also provided data throughout the high temperature transient but, due to the separator level control system, exhibited rapid wide range fluctuations. The mean flow rate, integrated over 1 min intervals, was derived from this data and a posttest calibration applied. The average high temperature transient bundle outlet flow rate based on the separator flowmeter output was determined to be $\sim$10 g/s, compared with the inlet flowmeter value of 16 g/s $\pm$ 13% (2σ). Evidence from the FPDS and hydrogen thermal conductivity analyzer measurements indicate that the quantity of liquid routed through the separator gas exit line was small, and therefore the difference of $\sim$6 g/s required investigation. An independent evaluation of the bundle flow rate using the loop pressurizer level provided an estimate of 12.6 g/s, with an uncertainty range of $\pm$ 1.5 g/s on the basis of three measurements.

The possibility of coolant leakage between the inlet flowmeter and the separator flowmeter was examined. The absence of water and high fission product activities exterior to the FPDS and associated pipework ruled out the escape of coolant downstream of the test train. Similarly, on the basis of limited contamination of the loop, the transfer of coolant from the bundle and upper regions to the bypass coolant did not occur. However, leakage from the inlet region below the fuel bundle would not necessarily have resulted in significant contamination of the loop. Following the test, damage to the bundle inlet region was observed and, during disassembly, the braze joints on three of the four inlet coolant lines were discovered to be loose. Although leakage of a few g/s from the bundle inlet to the bypass appears credible, it is not consistent with the small positive bypass-minus-bundle differential pressure measured throughout most of the transient. However, as described in Subsection 4.10, a leak may have developed during the final minutes of the test.

The uncertainty in the bundle flow rate during the Scoping Test had considerable impact on the thermal-hydraulic analysis and the estimated transport times for fission products from the bundle to the various detectors. However, the most reliable measurement was provided by the inlet turbine flowmeter (Figure 6) and, in the absence of positive evidence of a leak, was used for the analysis presented in this report.

The thermal conductivity of the shroud, as a function of temperature, was determined pretest using bench-measured values and a theoretical interpretation for the composite ZrO_2 fiberboard and strengthening tubes. In the posttest analysis, the effective thermal conductivity was calculated using the measured temperature drop across the shroud assembly and the heat flux through the shroud. The two sets of values are near each other at low temperatures but, with increasing temperature, the *measured* effective

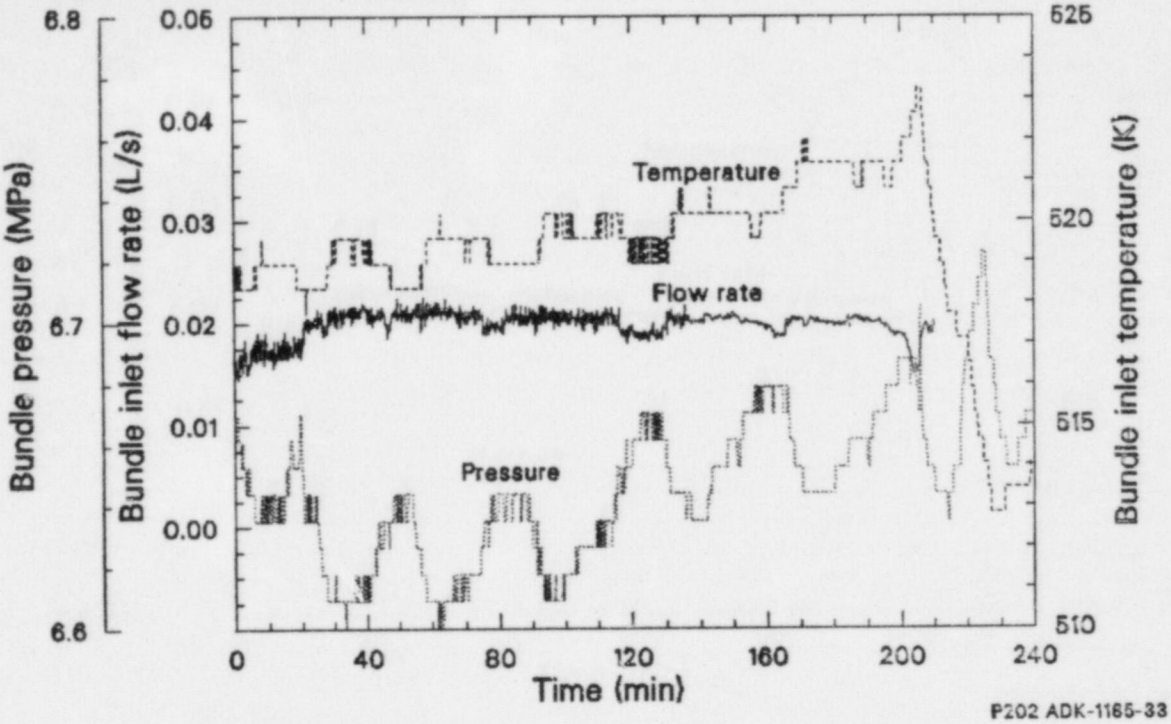

Figure 6. Bundle inlet coolant flow rate, inlet temperature and pressure.

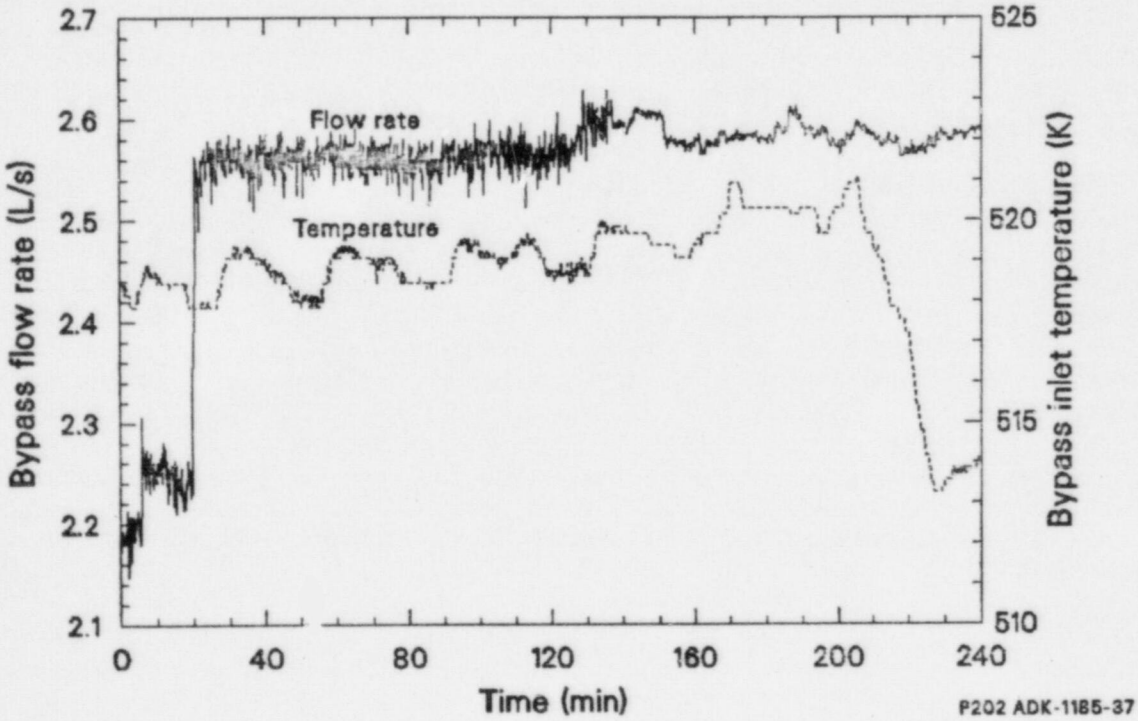

Figure 7. Bypass inlet flow rate and temperature.

shroud thermal conductivity was considerably larger than the pretest value. A partial explanation for the apparent enhanced conductivity that was estimated to be about a factor of three higher at 1200 K, was fiberboard compaction, which can be observed in the neutron radiographs (Subsection 4.8.2). The shroud conductivity data used in the SCDAP analysis is discussed in Appendix H and Subsection 6.2.

4.3 Bundle Nuclear Power

The PBF reactor ion chambers provided a measurement of the nominal reactor power. Under steady state conditions, with a water-filled bundle, the monitors were calibrated to allow derivation of the reactor thermal power. Reactor physics calculations[12] were performed to establish a pretest relationship between the reactor thermal power and the bundle nuclear power. The major contributions to the nuclear energy deposition within the test train components, and the relationship to the reactor power, are summarized in Appendix C.

The posttest analysis utilized thermal-hydraulic measurements to derive the bundle nuclear power. The method was based upon the premise that, under equilibrium conditions, the power generated by the fuel bundle was equal to the rate at which heat was transferred to the coolant flowing through the bundle plus any losses through the shroud. The heat loss was calculated with the use of the Dittus-Boelter[13] correlation. The bundle coolant heat gain rate was determined from the average inlet and outlet temperature measurements and from the inlet coolant flow rate and pressure. The computed bundle power history for the SFD-ST from the start of nuclear operation, is shown in Figures 8 and 9 (note zero times). This analysis, however, is not valid during bundle coolant boildown because of nonequilibrium conditions (see Appendix C).

The bundle nuclear power history throughout the high temperature transient was established using the following approach. A constant power hold (between 31.5 min and 54.7 min), prior to the start of the final power ramp, provided equilibrium conditions for the calculation of the bundle nuclear power. Towards the end of this period, when steady state was achieved, the rate of heat gain by the bundle coolant was measured to be 38.1 kW. The rate of heat gain by the bypass coolant throughout the high temperature transient, derived from the means of the four differential temperature measurements, is shown in Figure 10. The gamma-ray and neutron energy deposition in the shroud and bypass coolant, discussed in Appendix C, were obtained from the reactor physics calculations. The net power derived from these nuclear sources that were additional to those in the bundle, and the rate of heat gain by the bypass coolant, amounted to 0.9 kW. The total bundle nuclear power at this time was therefore calculated to be 39.0 kW.

To a good approximation, the test train fission chambers provided a measure of the relative power throughout the transient. The time dependent count rates from each chamber were scaled by the appropriate chamber sensitivity, obtained from calibrations performed in the Battelle NW Reactor,[14] to provide relative fission rates. At defined time steps a simple fit was made to the seven axial fission rate data points, a mean value being used where a pair of chambers occupied the same axial position. An extrapolation of the fit to the ends of the bundle was estimated on the basis of the reactor physics calculations. Integration of each axial power shape provided the relative bundle power as a function of time. The relative power profile established from the fission chamber data was normalized at the end of the power hold to the calibration point of 39.0 kW. It was confirmed that the above calibration was valid over the power range encountered during the transient phase by comparison of the normalization factor with values derived from the nominal 24 kW steady state period and the two 90 kW periods. The bundle nuclear power throughout the high temperature transient is presented in Figure 11 and can be seen to rise from the 39.0 kW calibration point to a maximum power of 93 kW.

The fundamental premise with the above approach to defining the bundle nuclear power history is that the integrated fission rate, measured by the chambers located outside the shroud, bears a direct constant relationship throughout the transient to the energy released as a result of nuclear processes within the bundle and coolant. It was assumed that the sensitivity of the fission chambers remained unchanged during the boildown. The measured axial fission distribution responded to variations in the coolant level, and to a much lesser extent to fuel rod relocation, but was strongly influenced by the approximately cosine power shape

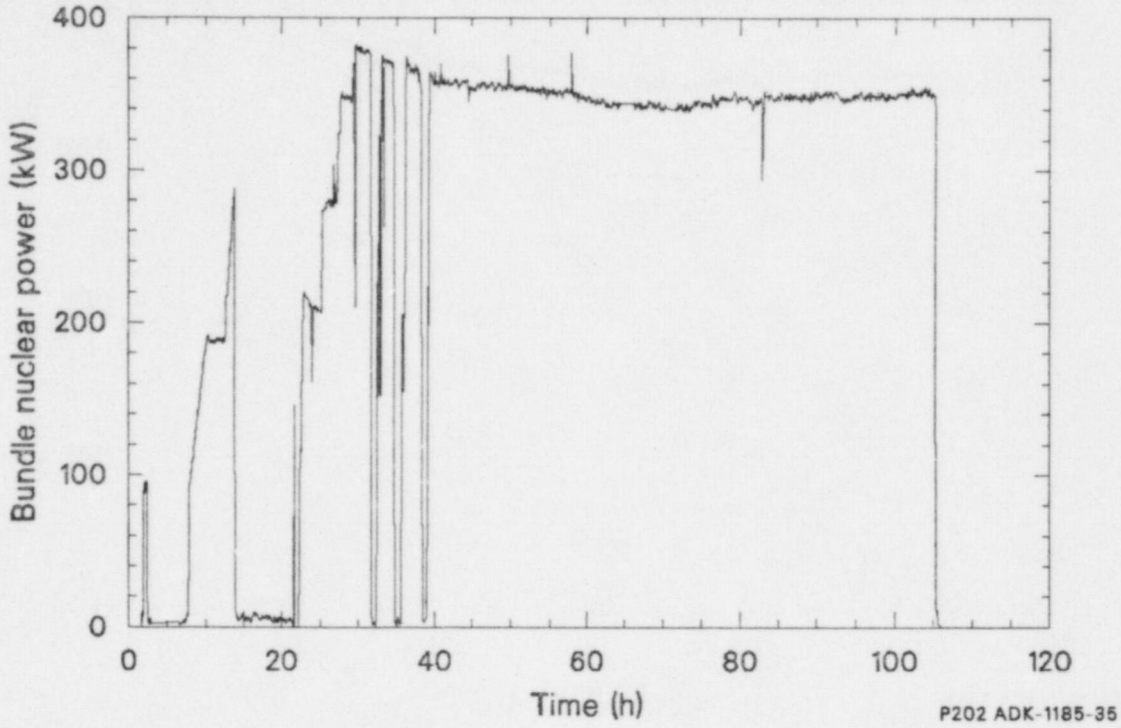

Figure 8. Bundle nuclear power history during calibration and fuel conditioning phases (zero time 23:00 October 12).

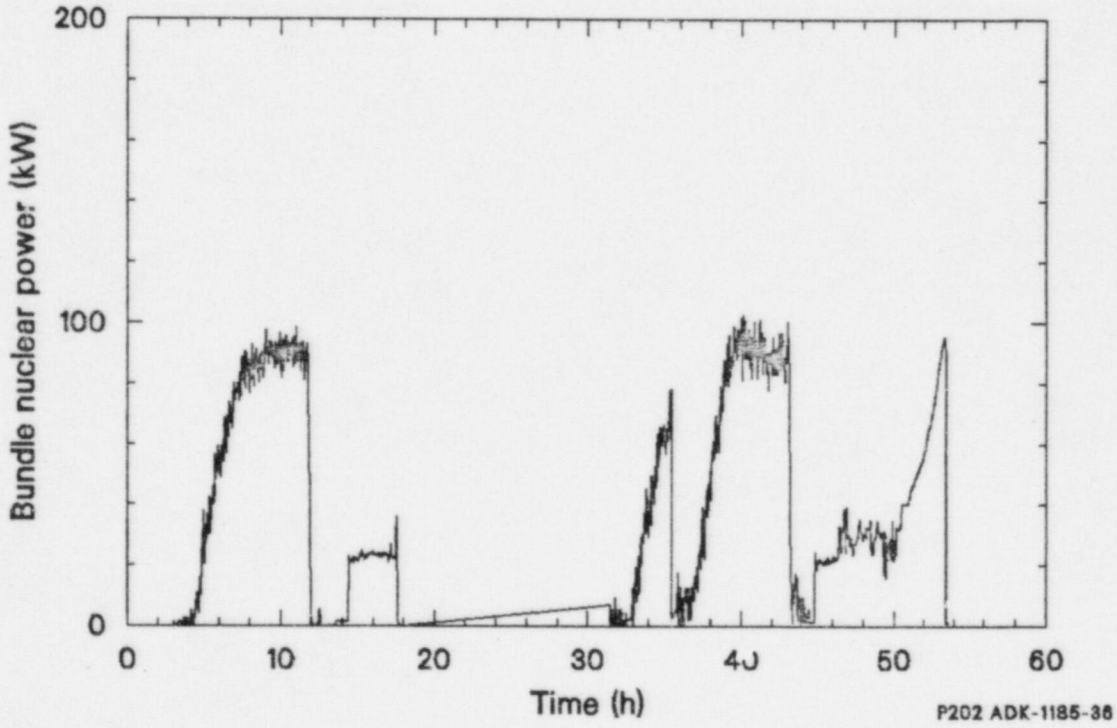

Figure 9. Bundle nuclear power history during short-lived fission product generation and transient phases (zero time 21:00 October 26).

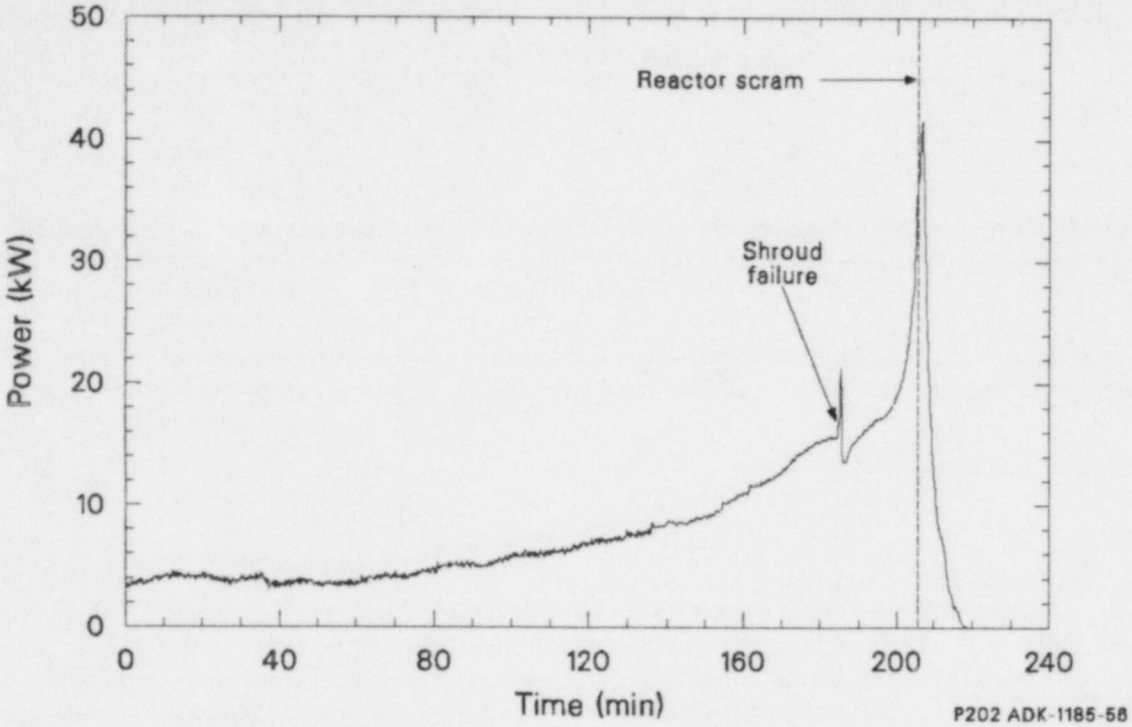

Figure 10. Rate of heat gain by the bypass coolant throughout high temperature transient.

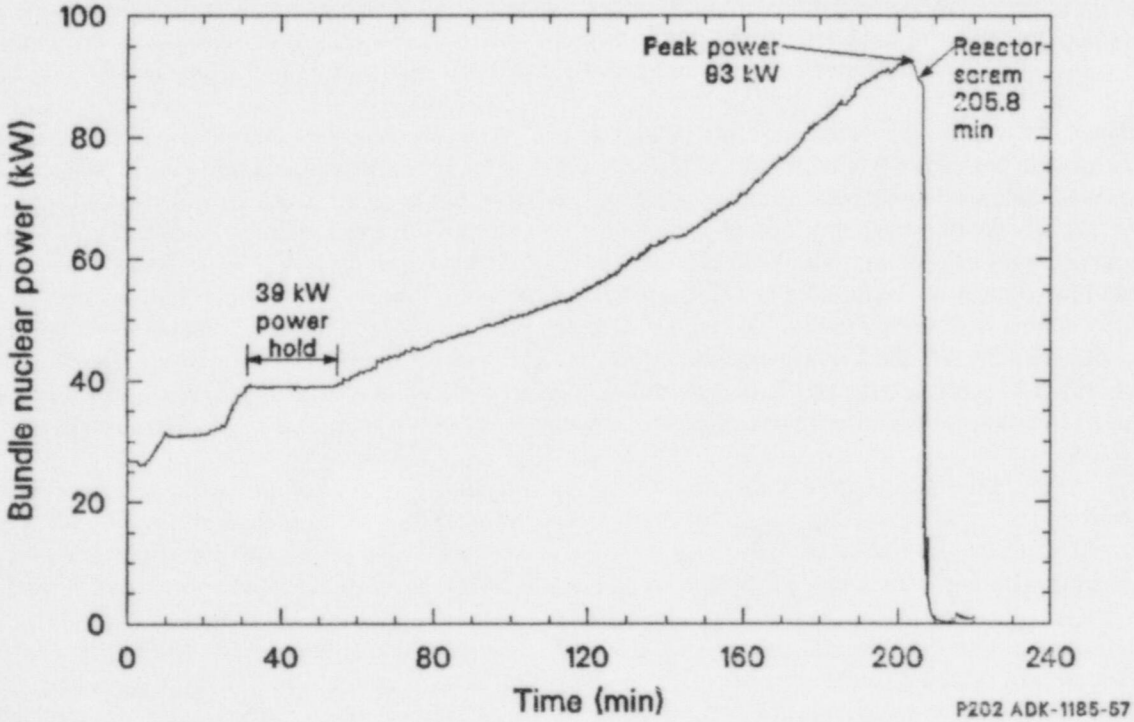

Figure 11. Bundle nuclear power throughout high temperature transient.

imposed by the reactor. The uncertainties associated with the derivation of the bundle nuclear power are assessed in Appendix C and it is concluded that an overall uncertainty level of ± 10% is appropriate during the 39.0 kW steady state power hold, increasing to about ± 15% at the maximum power.

4.4 Coolant Level

A knowledge of the two-phase/steam boundary is important for comparison with code predictions under transient conditions (see Subsection 6.2). Due to the relatively low inlet coolant flow rate a comparatively distinct boundary was formed between the lower liquid phase, which was primarily water but with some two-phase coolant near the interface, and the upper steam phase. The rate of change of the boundary elevation within the test bundle resulted from the evaporation rate at the boundary and the inlet coolant flow rate. It should be noted that a second *boiling-boundary* existed between the liquid phase, which may have had nucleate boiling, and the two-phase region with large heterogeneities of liquid and gaseous phases. However, this interface proved difficult to define and measure with any degree of accuracy. Analysis of the data from the test train fission chambers (Subsection 2.5.3) to establish the elevation of the two-phase/steam boundary, and an approximate location of the boiling boundary, is described in Reference 7 and has not been repeated in this report.

Figure 12 provides an overlay of the deduced two-phase/steam boundary elevation, the bundle nuclear power and the inlet flow rate as a function of time. At time zero the boundary was passing an elevation 0.50 m above the bottom of the fuel. The modulation in the steam interface level prior to the 39 kW steady state power hold was a consequence of the variations in the power and flow rate. With a steady state power of 39 kW and inlet flow rate of 0.020 L/s the two-phase/steam boundary stabilized at an elevation of 0.42 m. The level decrease that commenced about 55 min into the transient corresponds to the steady rise in bundle power. The fluctuation in level at about 184 min results from failure of the shroud inner liner (discussed in Subsection 4.7). The rapid decrease in level from about 200 min until reactor scram can be seen to coincide with a decrease in flow rate.

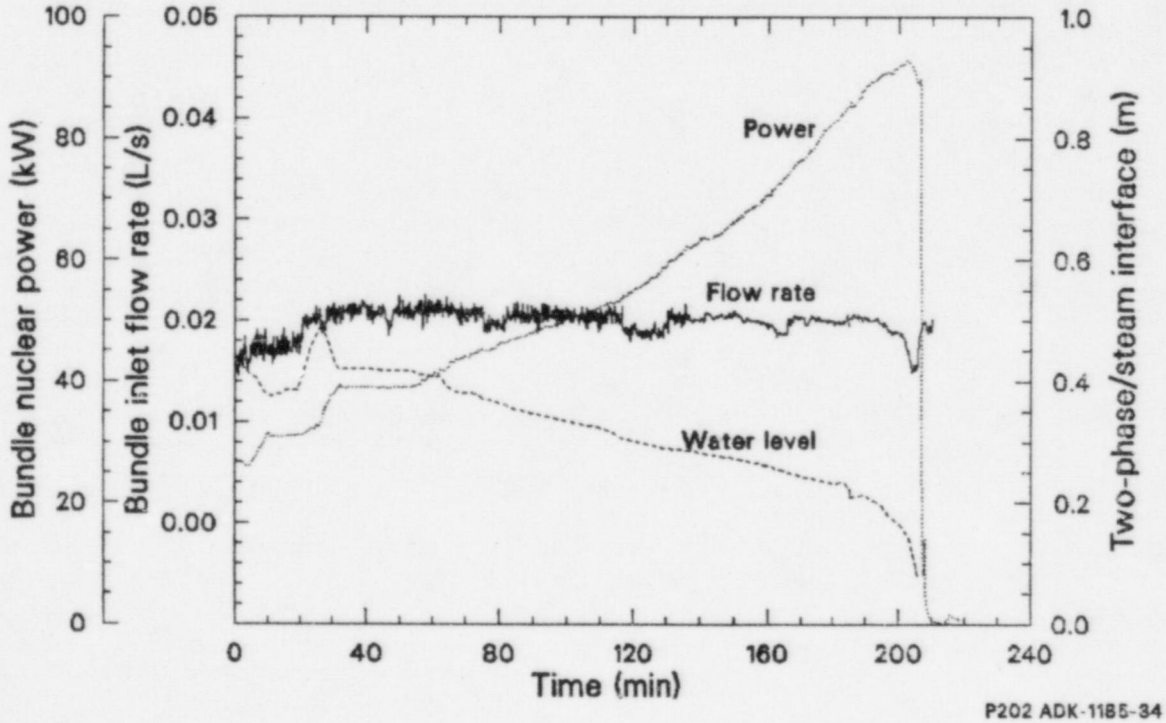

Figure 12. Bundle nuclear power, inlet coolant flow rate and two-phase/steam interface throughout high temperature transient.

The uncertainties associated with the level profile derived from the fission chamber data are estimated to amount to about ± 0.02 m. Confidence in the measurements is provided by the temperature rise on thermocouple dry-out, as discussed in the following sections.

4.5 Fuel Rod Temperatures

A radially averaged temperature profile for each of the 0.35-m, 0.50-m and 0.70-m elevations has been computed from the qualified data measured by the thermocouples located on the cladding inside surface of the instrumented fuel rods distributed throughout the bundle. These average temperature profiles are presented in Figure 13, with the deviation from the mean for the individual rods shown in Figure 14.

The plots show that the cladding was at saturation temperature at the 0.35-m elevation for the first 100 min, and the 0.50-m elevation at time zero and for about 5 min prior to the steady state power hold. It is of interest to note that the deviation from the mean during these periods when the thermocouple elevation is below the two-phase/liquid coolant level is a maximum of ± 10 K, whereas in the steam region prior to the commencement of the rapid temperature rise, the deviation at all elevations is about ± 50 K. The dry-out times for the 0.35-m and 0.50-m elevations indicate that the level profile derived from the fission chamber data is possibly low by about 0.01 m but within the overall estimated uncertainty of ± 0.02 m.

The deviation plots show no evidence of any general radial temperature gradients within the ± 50 K distribution. During the rapid temperature excursion, and prior to thermocouple failure, individual rod temperature measurements deviate from the mean value by up to ± 100 K.

Figure 15 compares the average cladding temperature and fuel centerline temperature at the 0.70-m elevation. The six instrumented fuel rods containing the centerline thermocouples again agreed to within ± 50 K for most of the transient, the variation increasing during the rapid temperature rise prior to reactor scram. It should be noted that the fuel centerline temperatures exceeded the cladding temperatures by about 50 K while the thermocouples were operational.

The temperature profile at the upper two elevations prior to the 39 kW hold resulted from the variations in power and flow rate. During the steady state power hold the average cladding temperature at 0.50 m was about 750 K, and 900 K at 0.70 m.

Table 3 summarizes the bundle nuclear power history and the associated estimated temperature rates-of-change at the three cladding thermocouple elevations for the time period between the end of the steady state power hold and shroud inner liner failure. The temperature increase rates were influenced by three step changes in the reactor power ramp (see first footnote on Table 3) and the events noted in column two of the table. The rise-rate at the 0.35 m elevation following coolant uncovery of the thermocouples was about twice that of the upper thermocouples. However, after that initial period the rate of temperature increase at all three elevations were very similar, ranging from 0.10 to 0.15 K/s.

Failure of the shroud inner liner at 184 min into the transient resulted in a small depressurization of the bundle and an associated cooling (discussed in Subsection 4.7). Following the brief temperature decrease, the rate of rise increased significantly at all elevations, compared with that prior to shroud liner failure.

None of the cladding thermocouples are considered to have provided reliable data throughout the entire high temperature transient, although four thermocouples at the 0.35 m elevation did not become questionable until about 2 min prior to reactor scram (exact times listed in Table B-2, Appendix B). During this final period the temperature rise-rate increased to about 6.5 K/s. In general, the 0.50-m elevation thermocouples became unreliable before those at 0.35 m. A rapid temperature rise-rate commenced at the 0.50-m elevation $\sim$2.5 min before to the lower elevation. Four of the five 0.70-m elevation thermocouples became unreliable about 23 to 44 min before shroud failure. However, a single thermocouple (Rod 3D) provided data until 9.7 min before reactor scram, at which time the temperature rise-rate was about 0.4 K/s.

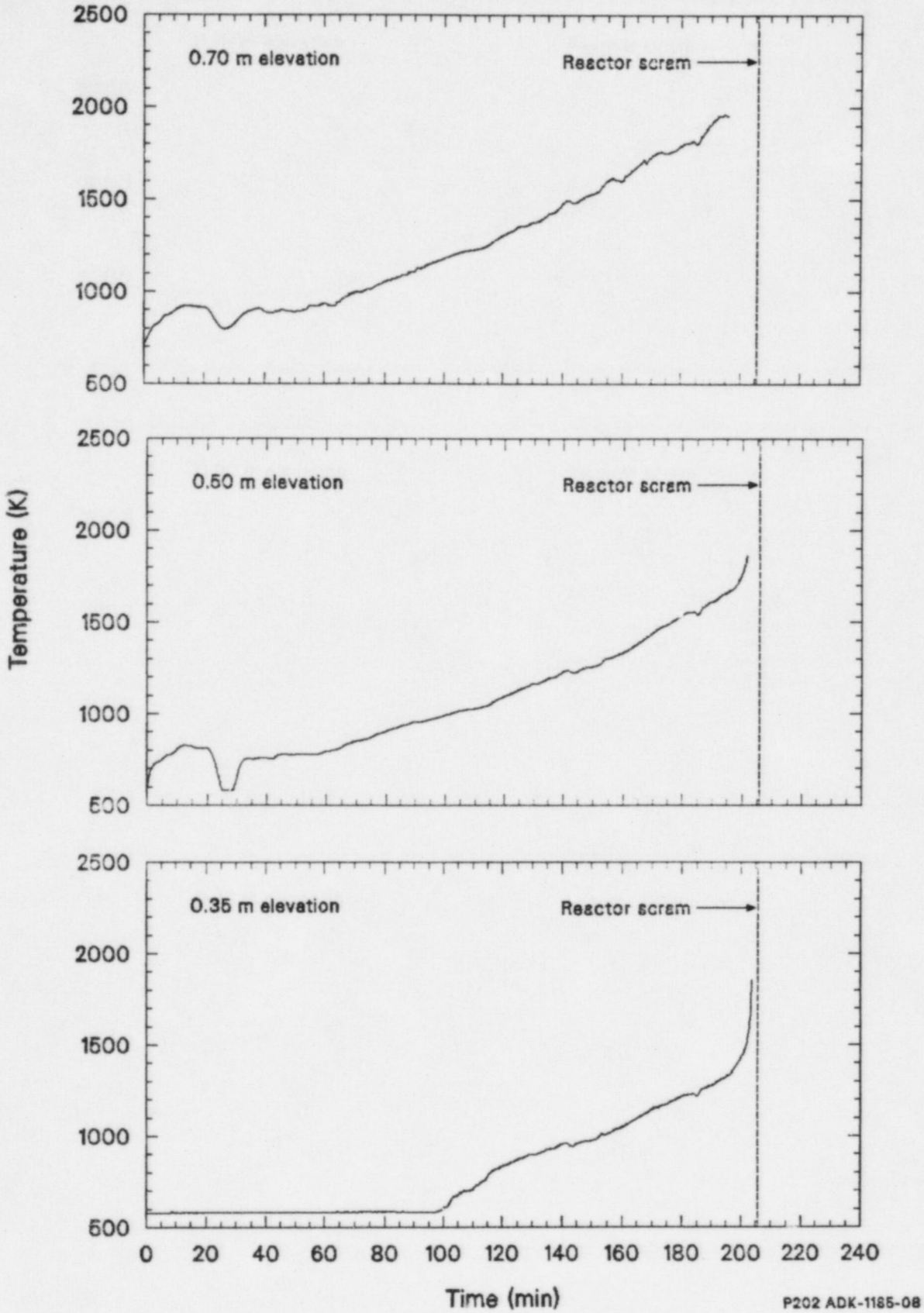

Figure 13. Radially averaged thermocouple measurements of cladding temperature.

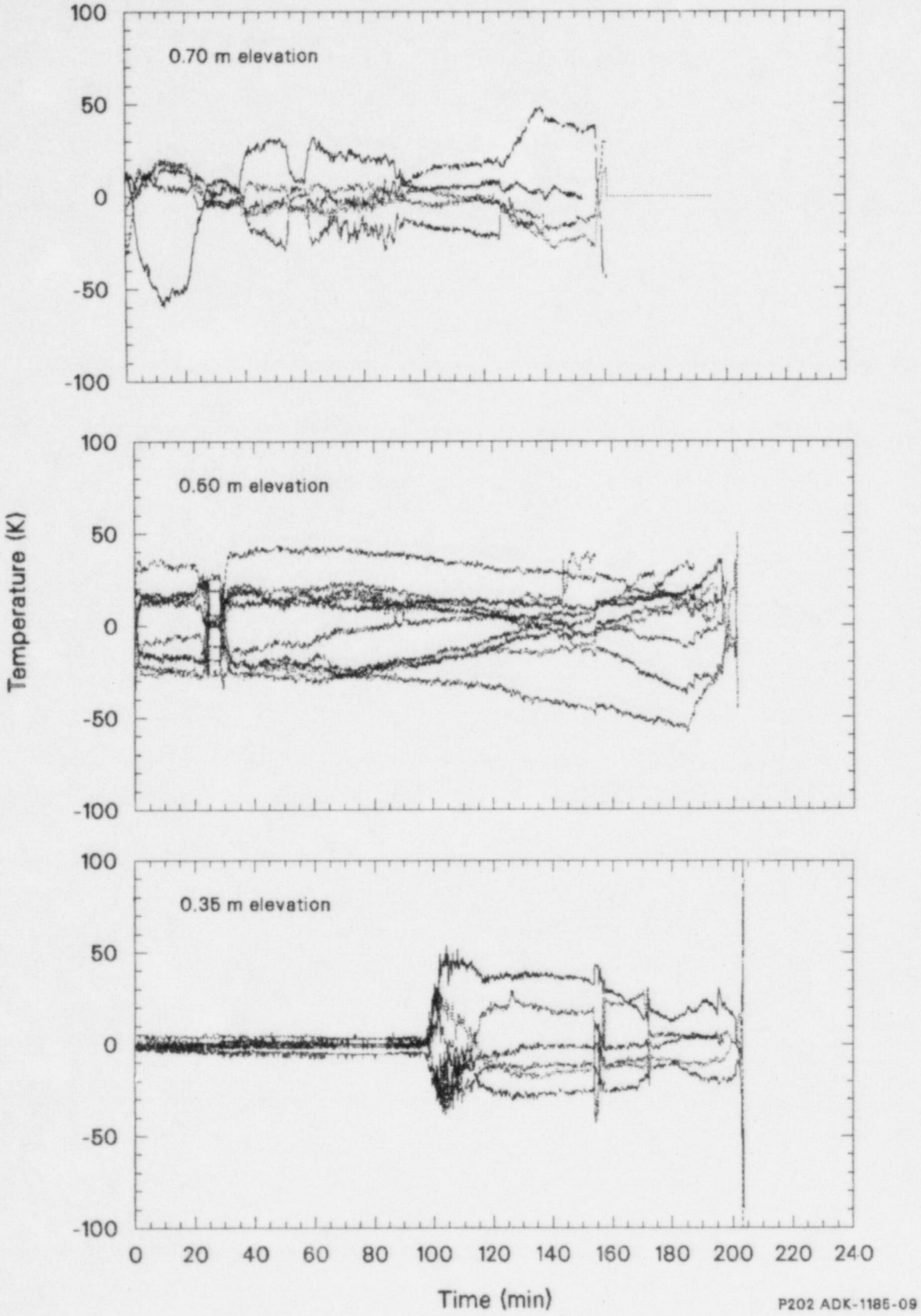

Figure 14. Deviation of thermocouple measurements from average cladding temperature.

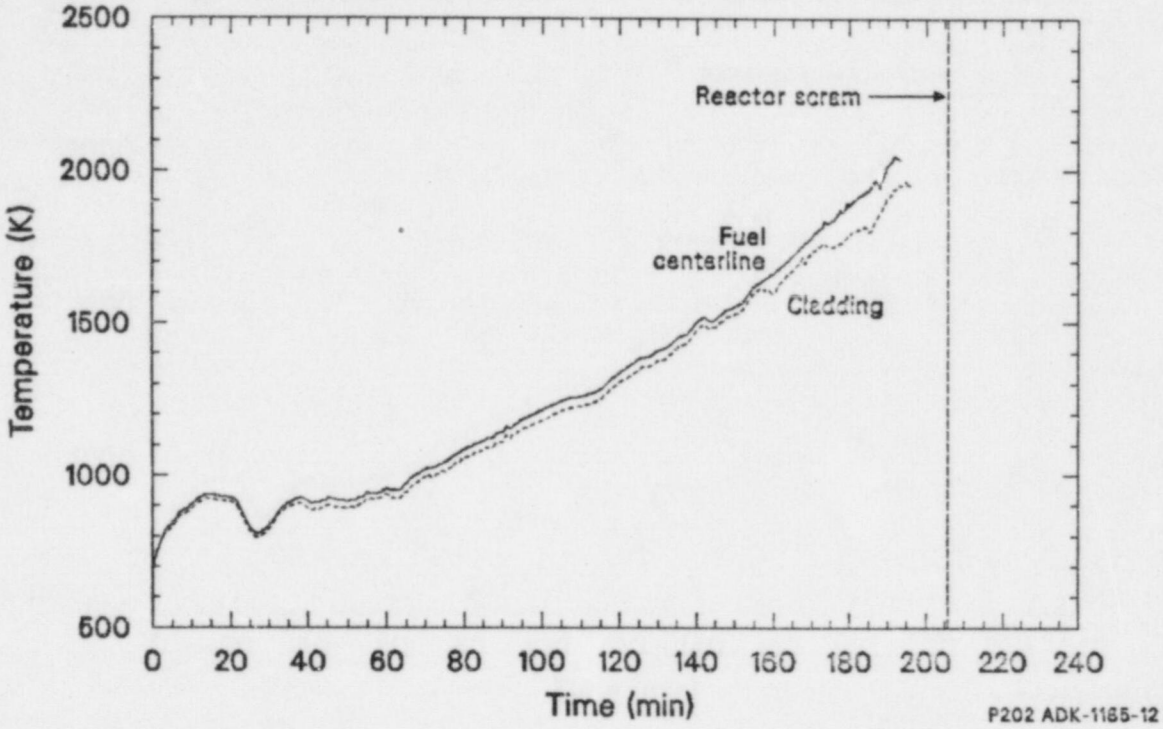

Figure 15. Radially averaged thermocouple measurements of cladding and fuel centerline temperatures at 0.70-m elevation.

Table 3. Bundle nuclear power and temperature rates of change

Time (min)	Event	Bundle Nuclear Power[a] Power (kW)	Bundle Nuclear Power[a] Increase Rate (W/s)	Temperature Increase Rate (K/s) 0.35 m Elevation	Temperature Increase Rate (K/s) 0.50 m Elevation	Temperature Increase Rate (K/s) 0.70 m Elevation
54.7	End of steady-state power hold	39.0	3.9	0.20[b]	0.08	0.10
115.4	5% flow reduction for 15 min	53.2	6.8	0.12	0.12	0.12
141.0 143.5	Power hold for DARS data transfer	63.7	6.8	0.10	0.11	0.12
156.5	5% flow reduction for 10 min	69.0	9.7	0.13	0.15	0.15
184.0	Shroud inner liner failure	85.0	—	—	—	—

a. Changes in reactor power ramp rate occurred at 128 min (20 kW/min to 40 kW/min), 161 min (40 kW/min to 50 kW/min) and 185 min (50 kW/min to 60 kW/min).

b. Temperature ramp commenced at 100 min when coolant level reduced below 0.35 m elevation.

In a high temperature steam environment such as the Scoping Test, there were several possible failure mechanisms for the thermocouples (see Appendix B). The formation of secondary, or virtual junctions was highly probable as the thermocouple leads were routed down the fuel rod through high temperature regions. It was observed that the 0.50-m and 0.70-m elevation thermocouples produced the most virtual junctions. The relocated junctions of the upper level thermocouples consistently indicated temperature rise-rates of about 10 K/s in the final minutes prior to reactor scram.

An understanding of the thermal behavior of the fuel bundle in the period when reliable thermocouple data was no longer available is important in assessing severe fuel damage computer model predictions and in the interpretation of the fission product release data. As part of the postirradiation examination, estimates of temperature were deduced for seven bundle cross sections from the observed fuel behavior. Peak fuel temperatures are estimated to have increased by ∿1000 K during the final 6 min of the test. The posttest bundle studies are described in detail in Appendix E and summarized in later subsections.

4.6 Coolant Temperatures

The measured inlet coolant temperatures were presented in Subsection 4.2 as part of the boundary conditions. Figure 16 shows the average steam temperature profile at the 0.50-m and 0.91-m elevations, and within the fallback barrier. The deviation from the mean value of the individual thermocouples distributed between the fuel rods throughout the bundle is provided in Figure 17. As with the cladding thermocouples, the measured saturation temperature, and associated agreement between thermocouples, at the 0.50-m elevation provides confidence in the two-phase/steam interface profile derived from the fission chamber data. The steam thermocouple measurements generally showed larger radial variations than those within the fuel rods, but again indicated no specific trends. The average steam temperature within the bundle at the 0.50-m elevation was ∿200 K less than the cladding temperature at the same elevation at the time when the two-phase/steam interface was at about 0.35 m. This difference decreased to about 100 K prior to shroud failure and when the radial variation was less than 50 K. The maximum measured steam temperature was at the 0.91 m elevation and for the first 60 min of the transient there appeared to be no temperature decrease into the fallback barrier. It should be noted that the shroud insulation extended up to the elevation of the steam exit line in order to reduce heat losses. Up until ∿140 min, when the 0.91-m elevation thermocouples became unreliable, an apparent temperature drop developed between the top of the fuel bundle and the fallback barrier that increased to ∿200 K. The 1.11-m elevation thermocouples were located at the base of the fallback barrier, with the 1.19-m elevation thermocouples being within the fallback barrier near the steam outlet line. The deviation from the mean plot shows that the 1.19 m thermocouples were generally recording higher temperatures than the 1.11 m thermocouples. Although this may simply reflect the overall uncertainty of the measurements, it is feasible that the effect results from flow conditions set up within the fallback barrier or the oxidation discussed in Subsection 4.9.

Figure 18 shows the measured exit steamline temperatures (1.5 and 1.8 m). These were considered valid throughout the transient. A significant period of time was required for these locations to achieve temperatures above saturation. At about 90 min into the transient both temperature recordings show a temporary decrease, amounting to about 60 K at 1.5 m and 30 K at 1.8 m. The thermocouples within the fallback barrier showed a similar but much smaller reduction, while those at lower elevations in the test bundle indicated no such response. The timing of the measured temperature reductions above the bundle is coincident with the period of fuel rod rupture. Commencing at about 135 min is a more significant period of cooling with rapid temperature drops up to 300 K. Figure 19 overlays the steamline temperatures and the separator pressure during this period. The sensitivities of the test train pressure transducers were not sufficient to establish the behavior of the control system. The two pressure drops in separator pressure of up to 170 kPa are associated with 50 kPa increases in the bypass-minus-bundle differential pressure and there is evidence of enhanced steam flow as a result of temporary increases in bundle-minus-separator differential pressure. Such temperature decreases as indicated by the 1.5 m and 1.8 m steamline thermocouples would generally be associated with suspension of flow or condensation. In the time between these temperature fluctuations, and the temperature reductions at 90 min, it is of interest to note that the 1.5 m location was

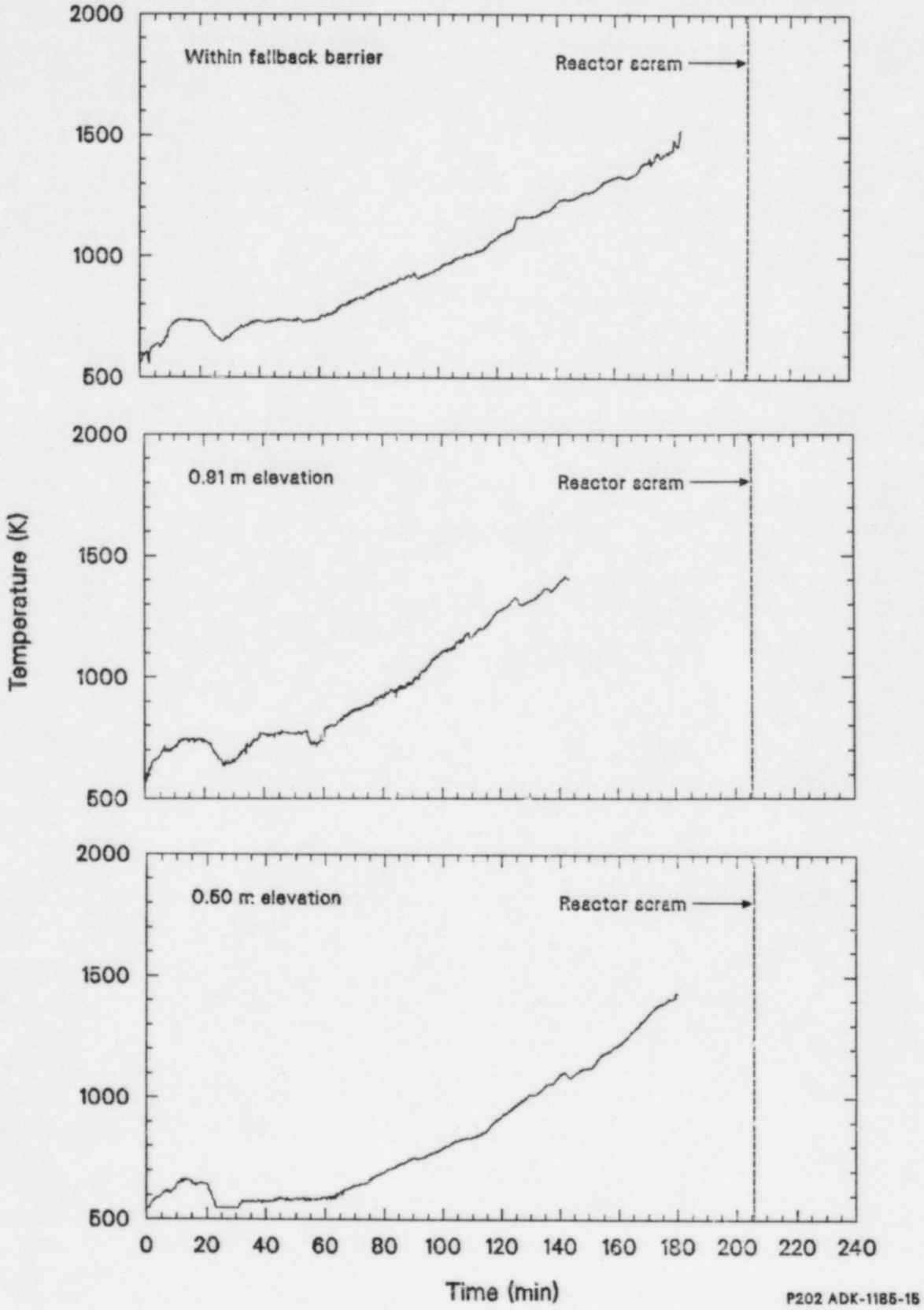

Figure 16. Radially averaged thermocouple measurements of steam temperature.

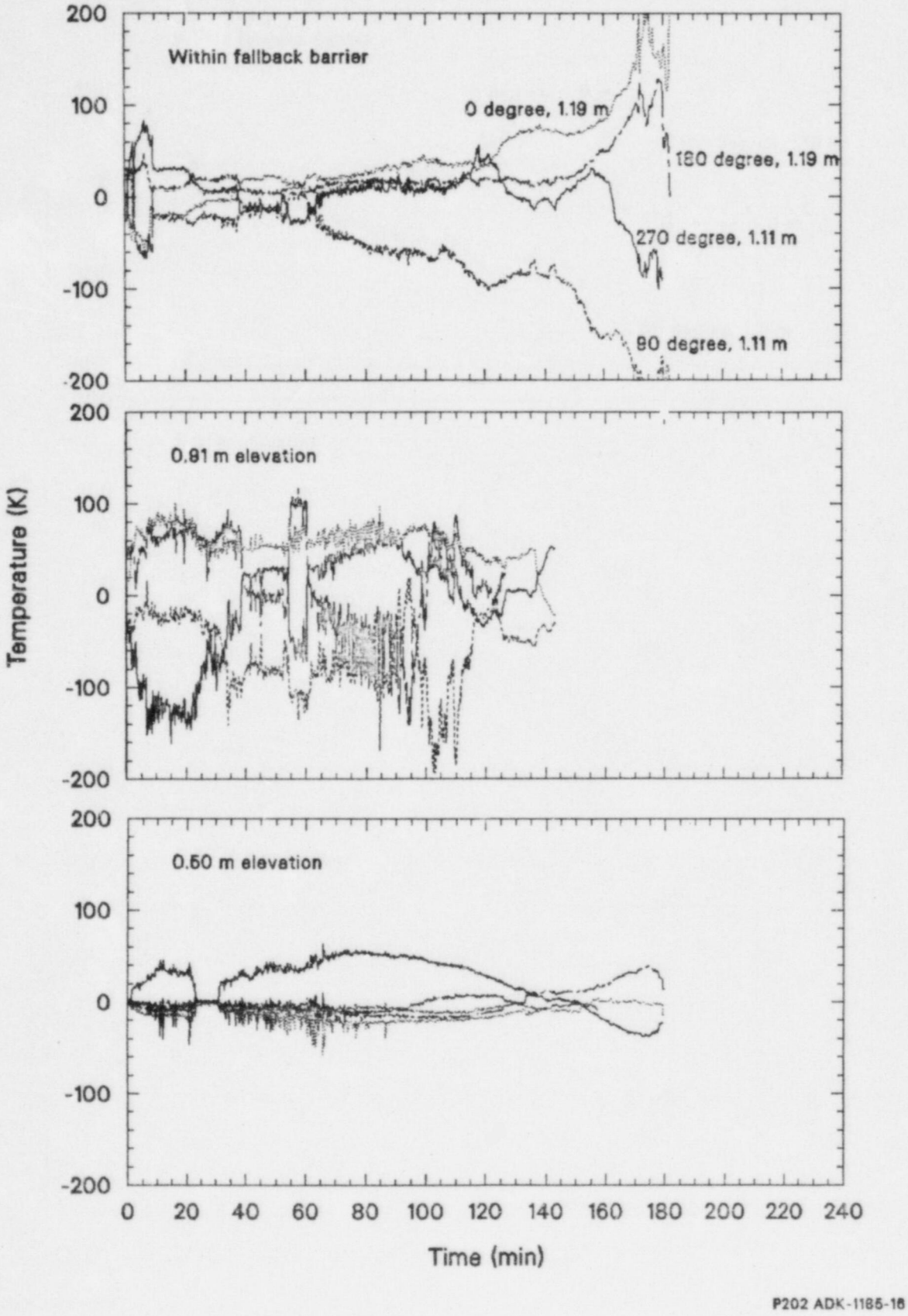

Figure 17. Deviation of thermocouple measurements from average steam temperatures.

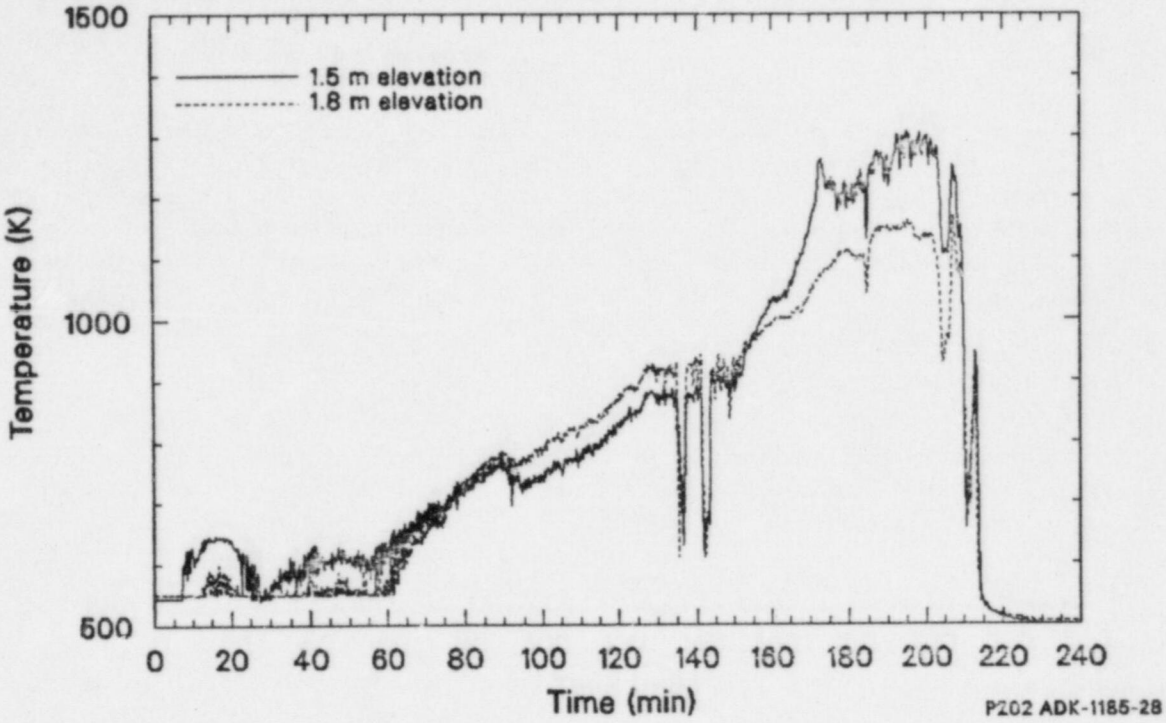

Figure 18. Steamline wall temperatures.

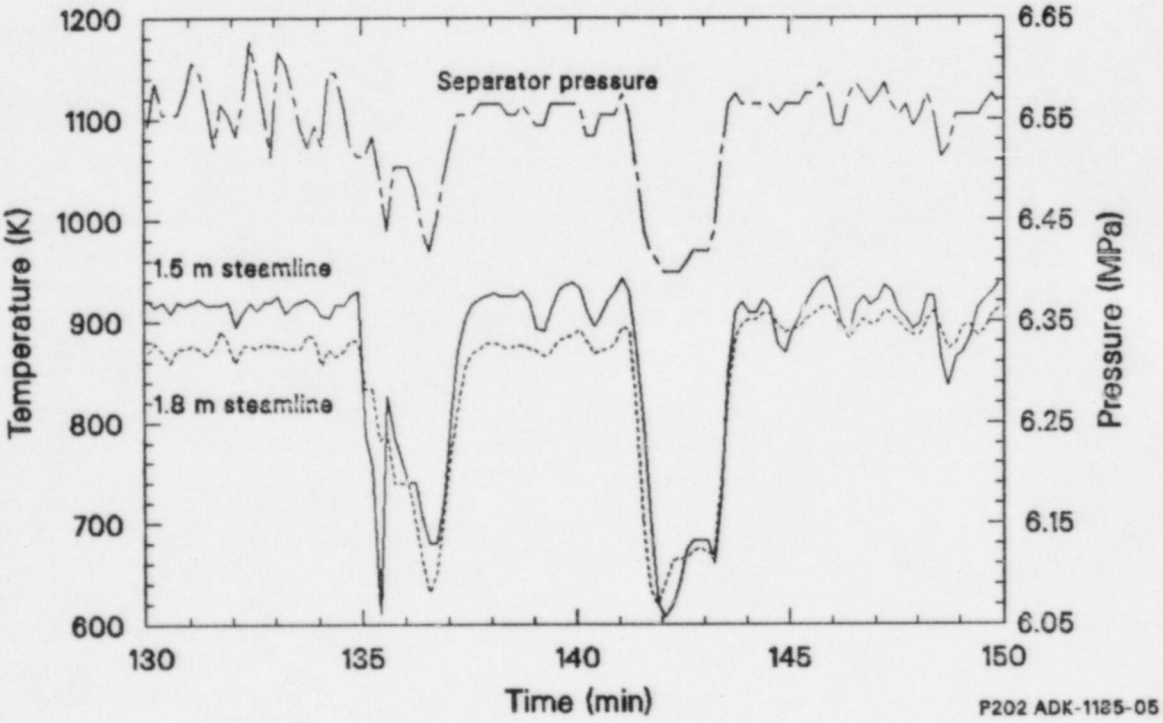

Figure 19. Overlay of steamline temperatures and separator pressure between 130 and 150 min.

apparently ∿50 K less than at the 1.8 m location. During the final high temperature phase this portion of the steamline showed the expected gradient, with a maximum decrease from fallback barrier to standpipe of about 500 K/m.

As a result of the failure of the shroud inner liner at 184 min, described in detail in the following subsection, both steamline thermocouples recorded temporary decreases of ∿60 K. About 3 min before reactor scram, with the 1.5-m location at 1280 K and the 1.8-m location at 1140 K, the steamline temperature declined ∿200 K. This was sustained for 1 to 2 min, with recovery close to the original temperatures ∿1 min after scram. The relationship between this behavior and the conditions within the bundle and fission product detection system is discussed in Subsection 4.10.

4.7 Shroud Behavior

The construction of the shroud assembly surrounding the test bundle was outlined in Subsection 2.3 and illustrated in Figure 3. The qualified thermocouple data from the shroud inner-, mid-, and outer-walls measured during the transient are presented in Figures 20 to 22. The inner and outer shroud temperature data is considered reliable as the thermocouples were actually attached to the insulation side of the inner liner wall, and the bypass side of the outer cylindrical shroud wall, respectively. However, the mid-shroud thermocouples, which were simply embedded into the fiberboard insulation through the contact pressure of the saddle, have two major related uncertainties. Without any permanent attachment, the radial location of the thermocouple could not be guaranteed, and the large radial gradient through the insulation resulted in significant errors. In addition, it was possible for the thermocouples to be in direct contact with the high density strengthening tubes and would therefore measure unrepresentatively high temperatures. The large spread in the mid-shroud results shown in Figure 21 demonstrates the measurement problems.

The first noteworthy observation from the shroud thermocouple data is that temperatures near saturation were recorded at the 0.7 m elevation during the initial phase of the transient, when the two-phase/steam interface level was below 0.5 m. Both the inner and mid-shroud thermocouples at the 90-degree orientation stayed reasonably constant for the first 30 min, while the 270-degree thermocouples showed an increase in temperature before returning to values near saturation. This effect did not occur with the equivalent elevation cladding thermocouples and it is postulated that condensation of the steam at the top of the test bundle accumulated on the slightly cooler inner liner wall. The apparent temperature drop between the top of the bundle and the fallback barrier reported in the previous subsection may also be the result of condensation. However, because of the relatively high flow rate in the Scoping Test the problem was not as severe as in the SFD 1-1 test, where an additional significant reflux power was required.

The insulation region of the shroud was pressurized with argon and controlled at about 0.34 MPa below the bundle pressure. The 0.76-mm thick inner zircaloy liner, subjected to the high temperature oxidizing steam environment, was breached at ∿184 min into the transient. The volume available to the steam was significantly increased and the steam immediately penetrated the porous zirconia fiberboard insulator. The radial penetration of the steam increased the measured temperatures at the mid-shroud in the upper elevations and the outer shroud at all elevations. The shroud thermocouple measurements for this period are shown in Figures 23 to 25. The data has all been assigned qualified status apart from the inner shroud 0.70 m thermocouple at 270-degrees after 182.3 min and the mid-shroud 0.70 m 180-degree thermocouple after 184.6 min. The heat transfer to the bypass coolant temporarily increased by about 30%, as measured by the differential temperature thermocouples shown in Figure 26. An additional, unquantified, indication of the increased heat transfer was provided by the change in the insulation resistance between the wire and sheath of the melt-through detectors (Figure 27).

The bundle pressure transducer, with its sense tube at -0.30 m, was not sensitive enough to record any pressure change at the time of shroud failure. However, the pressure in the separator showed a temporary increase of ∿14 kPa (Figure 28) as a consequence of the bypass-minus-bundle pressure control system detecting bundle depressurization at the time of the inner liner breach. The reduced pressure appears to have been sufficient to increase the coolant vaporization rate and consequently reduce the coolant level. Figure 29

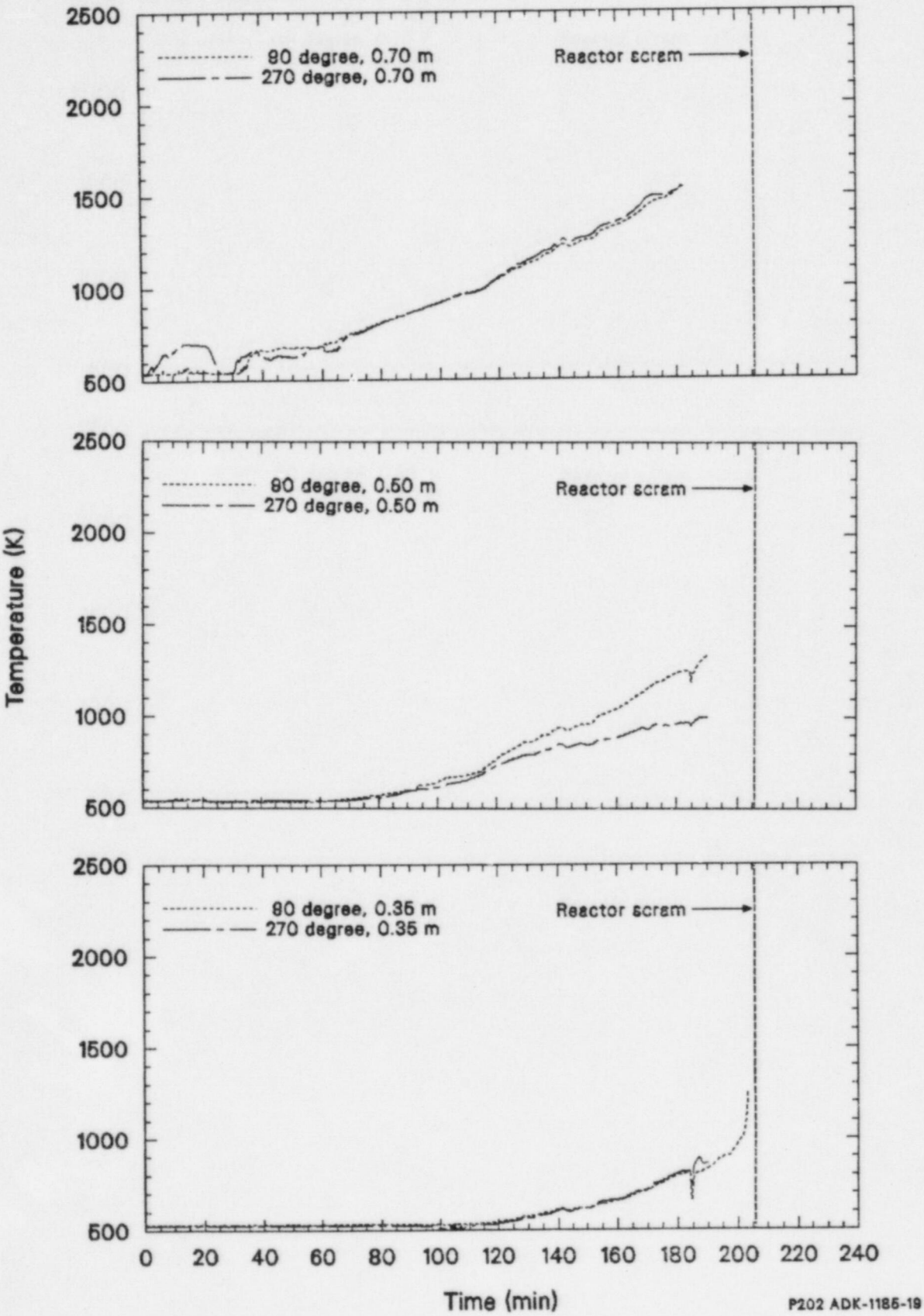

Figure 20. Thermocouple measurements of inner-shroud liner temperatures.

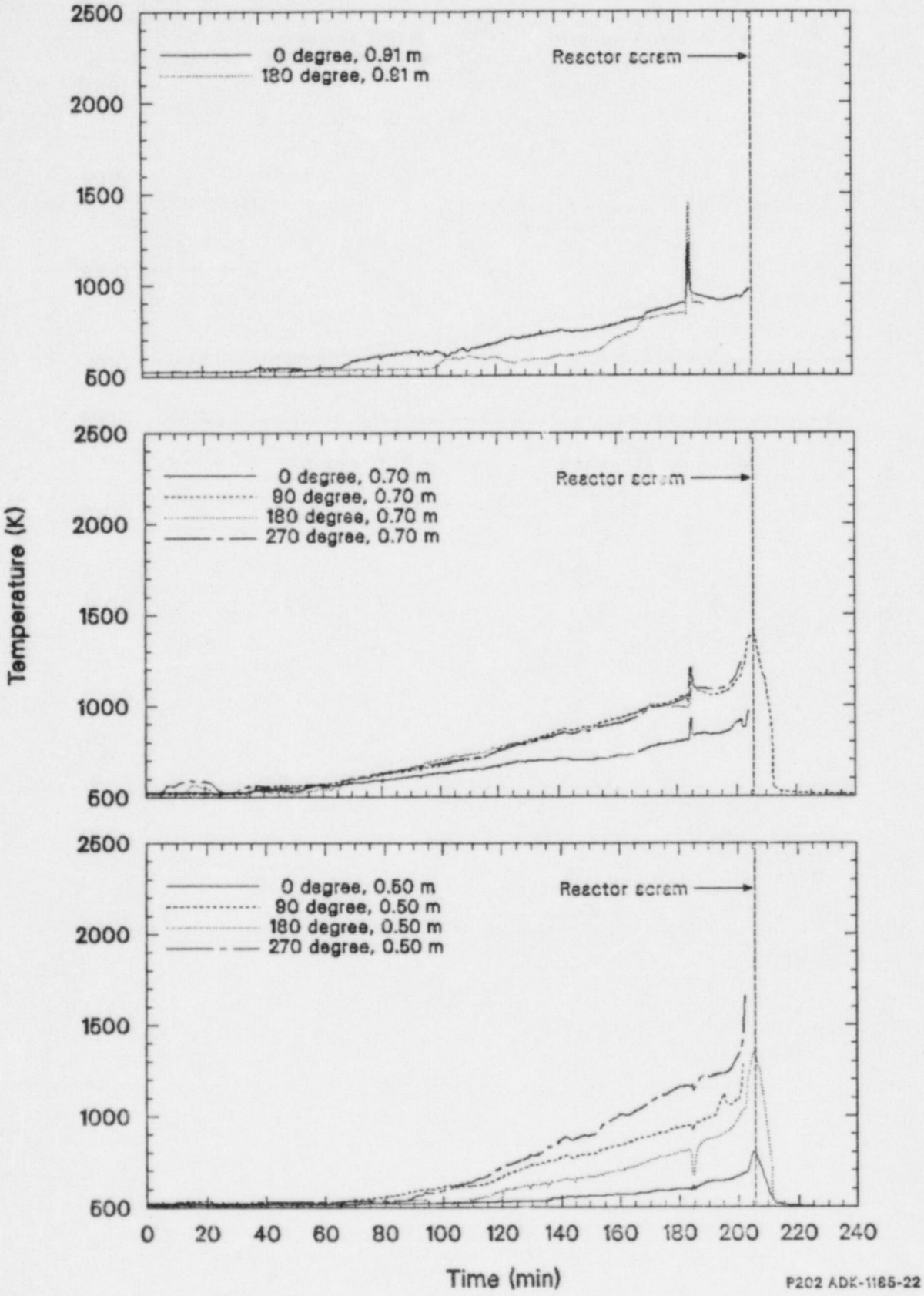

Figure 21. Thermocouple measurements of mid-shroud temperatures.

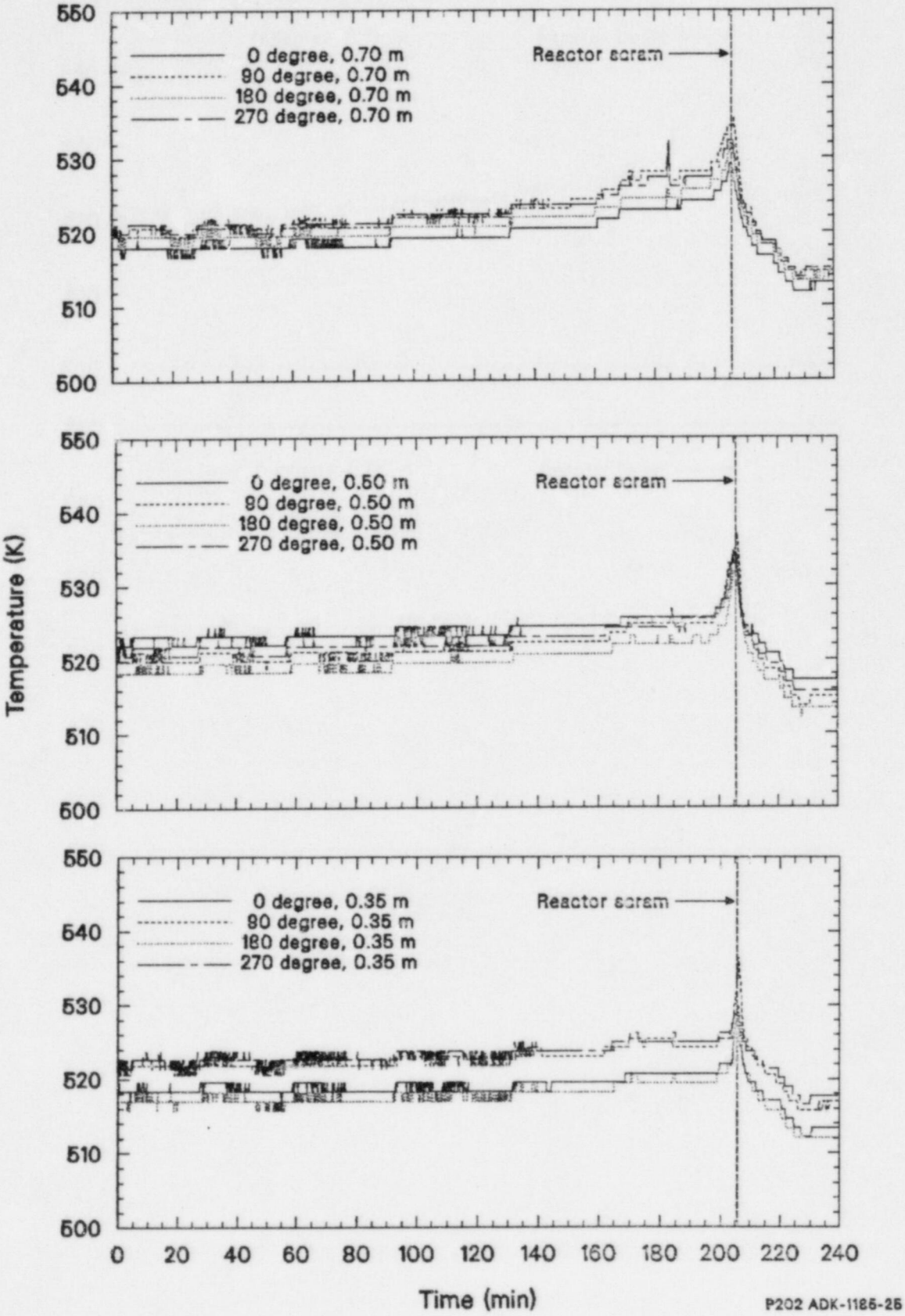

Figure 22. Thermocouple measurements of outer-shroud temperatures.

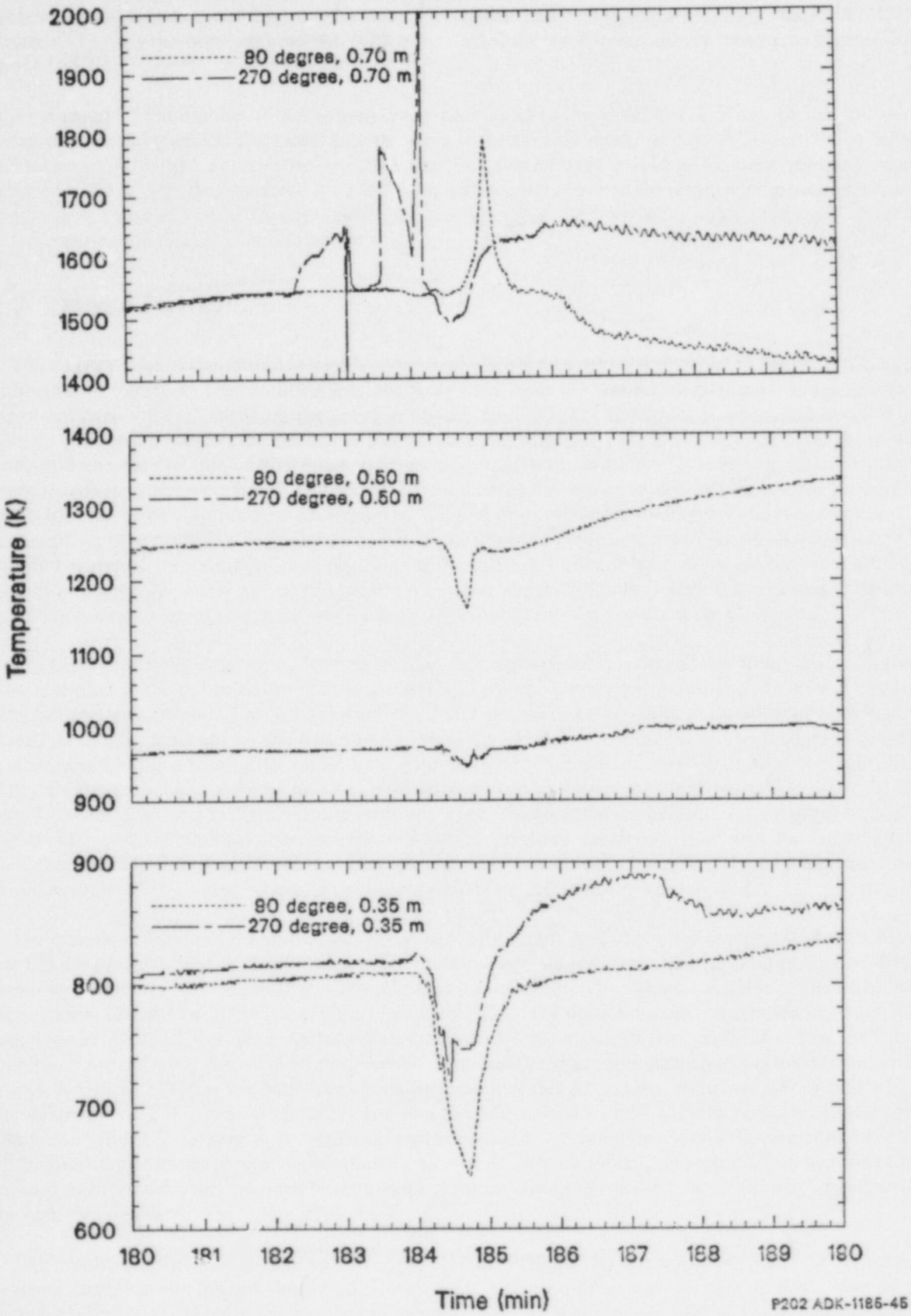

Figure 23. Inner-shroud thermocouple measurements at time of shroud failure.

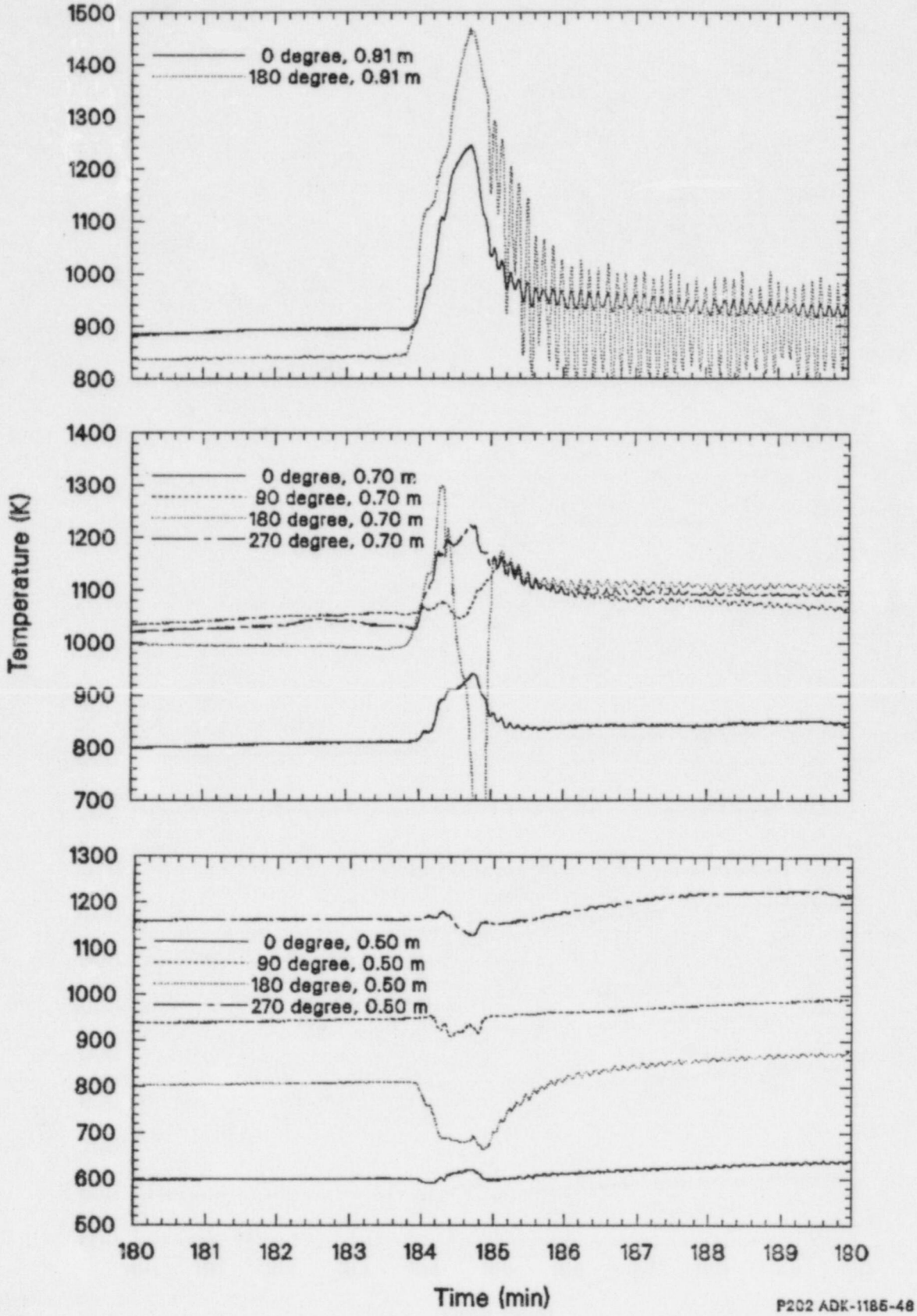

Figure 24. Mid-shroud thermocouple measurements at time of shroud failure.

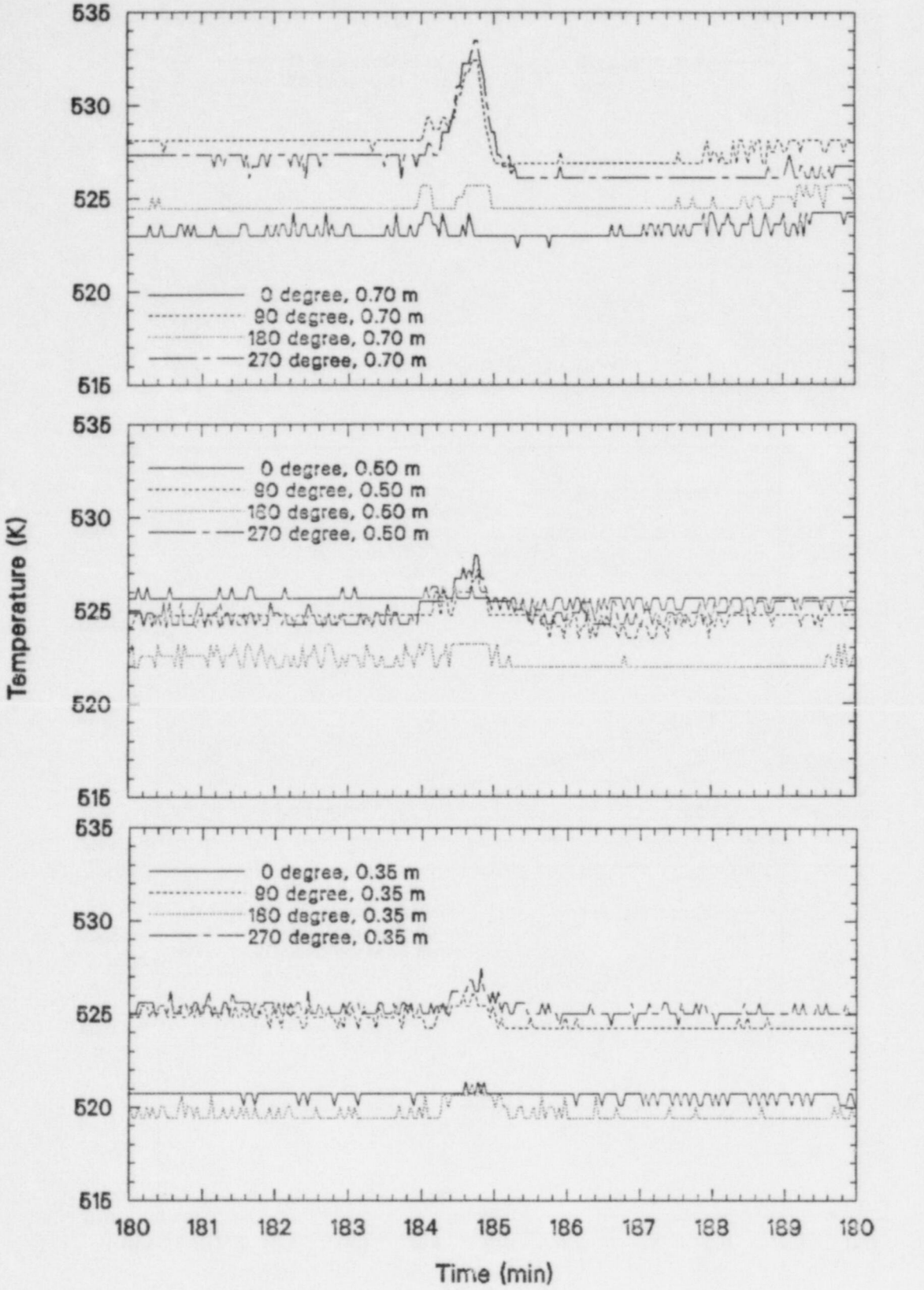

Figure 25. Outer-shroud thermocouple measurements at time of shroud failure.

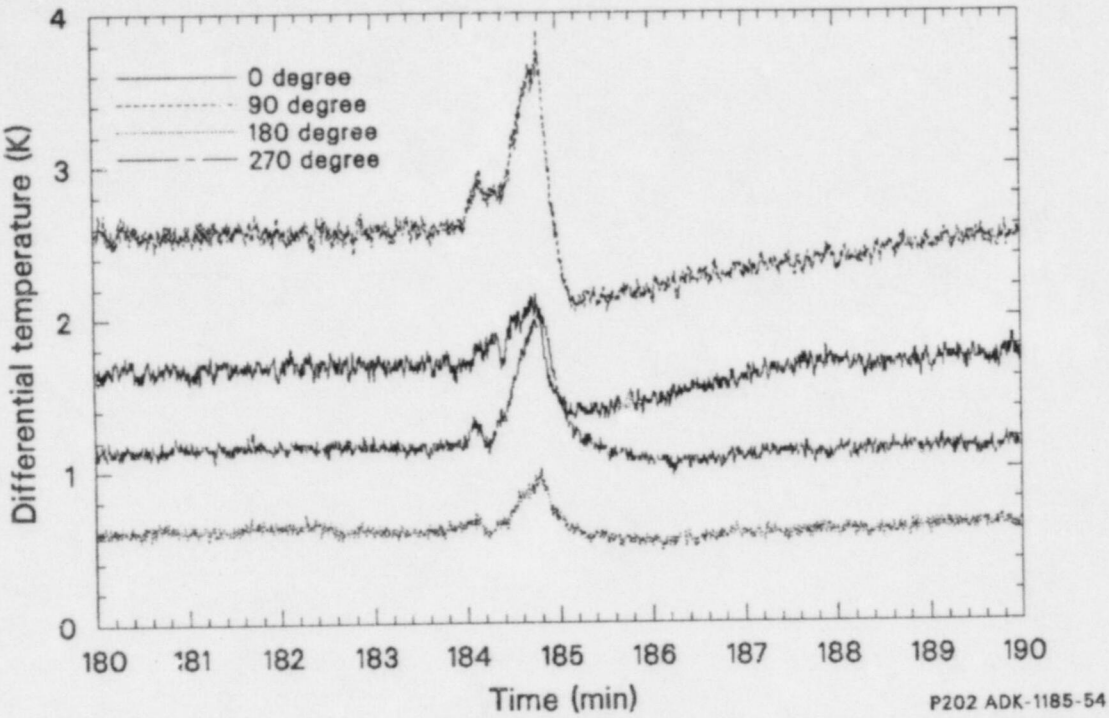

Figure 26. The differential temperature in the bypass coolant at time of shroud failure.

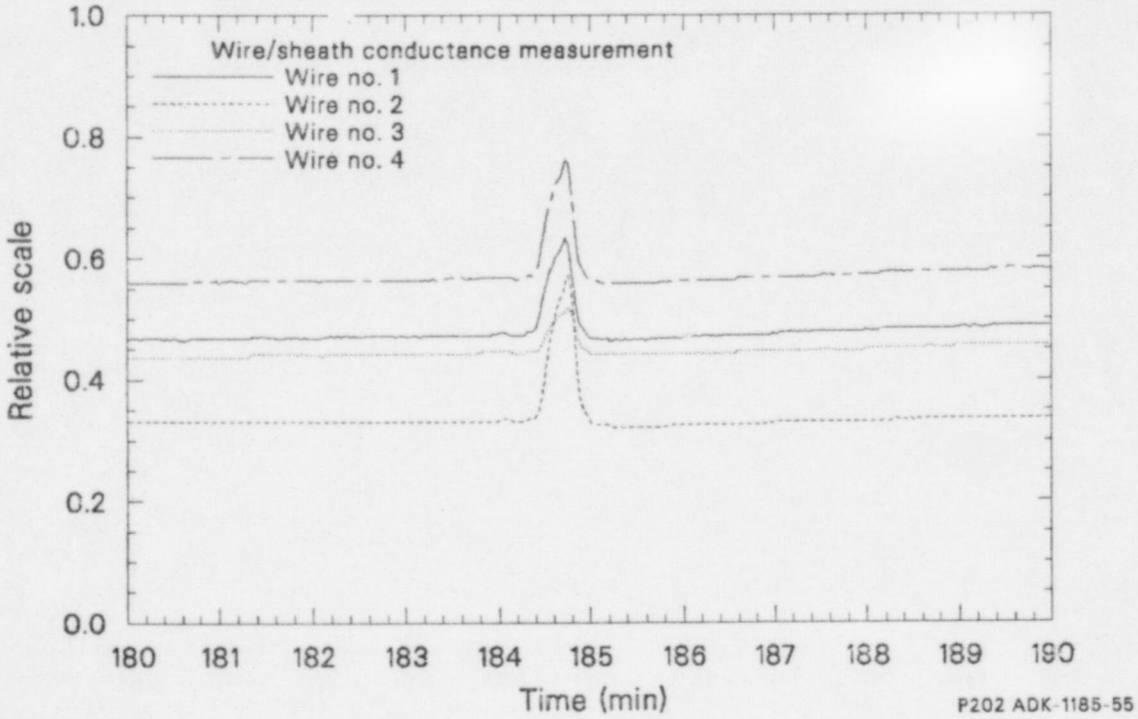

Figure 27. The melt-through detector output at time of shroud failure.

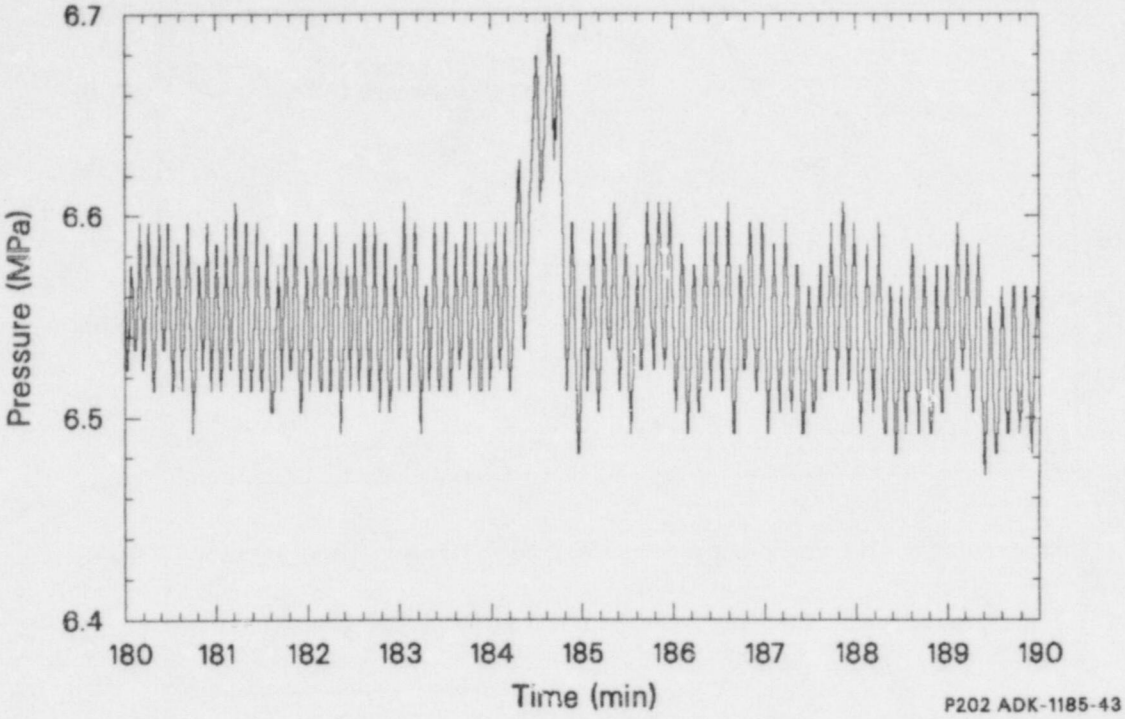

Figure 28. The separator pressure at time of shroud failure.

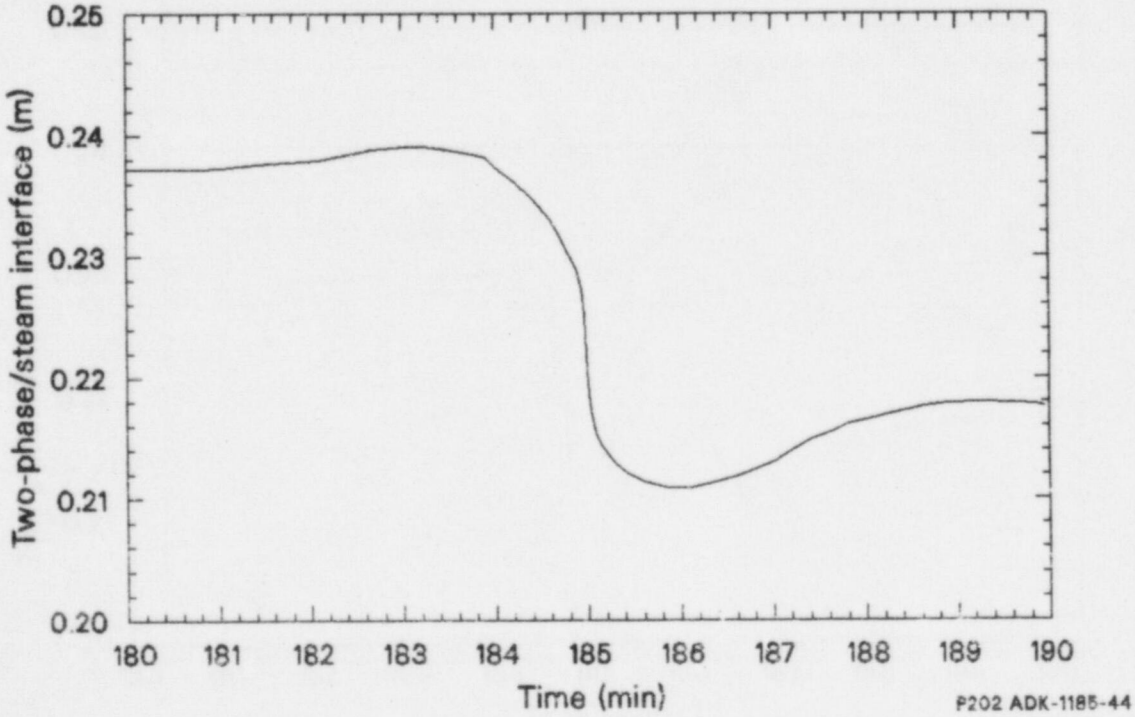

Figure 29. The two-phase/steam interface level at time of shroud failure.

shows the reduction in the two-phase/steam interface elevation deduced from the test train fission chamber data. Based on theoretical considerations the nearly 0.03 m decrease is difficult to explain. However, a cooling throughout the bundle is consistent with the level change and associated increased steam flow. During this phase the signals from the fission chambers located above the two-phase/steam interface elevation at 270 degrees followed the bundle nuclear power ramp. However, the 90-degree fission chambers signals exhibited a significant increase upon failure of the shroud inner liner, as can be seen from the normalized ratios plotted in Figure 30. The increase is attributed to a possible preferential flow of the additional steam generated on depressurization, and the associated enhanced neutron moderation.

Based on the data presented in the previous figures the following observations related to the breach of the shroud inner liner are made. The failure probably occurred at an upper elevation, the thermocouples being directly engulfed by the steam from the top of the test bundle. The steam rapidly penetrated the insulator, increasing the temperature recorded by the mid-shroud thermocouple at 0.70 m by about 200 K and twice that value at 0.91 m (Figure 24). The 0.70-m inner shroud thermocouple at an orientation of 270 degrees (Figure 23) may have provided the first indication of deterioration of the zircaloy liner at ∿182.4 min. However, the subsequent behavior of the thermocouple makes the data unreliable, even though the values appear reasonable by about 185 min. The first most positive indication of actual inner liner breach was the mid-shroud temperature increase recorded by the 180-degree 0.70-m and 0.91-m thermocouples at about 183.8 min. A temperature decrease was recorded by the mid-shroud 0.50-m thermocouple at about 183.9 min, also orientated at 180 degrees. The remaining mid-shroud thermocouples all responded shortly afterwards at around 184 min. The inner shroud temperature at the 0.35-m elevation also changed at 184 min (Figure 23), decreasing by 100 to 150 K. However, the inner shroud temperatures at 0.50 m did not decrease until about 184.4 min and at 0.70 m did not increase until 184.6 min, which was consistent with cooling from the bottom of the bundle.

The reliable inner shroud thermocouple at 0.70 m (90-degree orientation) indicated a rapid rise commencing at about 184.6 min, some 0.8 min after the first temperature increases recorded by the upper mid-shroud thermocouples. The inner- and mid-shroud temperature increases are considered to be due to different mechanisms. Prior to shroud failure the upper inner liner is at ∿1500 K and the mid-shroud at about 860 K. As stated previously, the temperature of the insulation near the failure location rose because of the entrance of steam. The inner shroud temperature rise however, is probably due to rapid local oxidation on the inside surface of the zircaloy liner.

The fuel rod thermocouples at all elevations showed that the test bundle was cooled during the failure period (Figure 31), which was consistent with the inner and mid-shroud measurements below, and including the 0.50-m elevation. The cladding temperature decrease occurred everywhere at ∿184.4 min; in agreement with the two inner shroud thermocouples at 0.50 m but ∿0.4 min later than the equivalent two at 0.35 m. The inconsistencies between the timing of the commencement of the cooling phase in the bundle, inner liner and mid-shroud can only be attributed to the possible different competing cooling processes, i.e., the enhanced steam flow through the bundle and the flow and condensation conditions set up within the insulating region as the argon gas and steam came into contact.

The thermocouple signals generally recovered to their values prior to shroud failure by about 185.5 min. A few inner shroud thermocouples were functional when the final rapid temperature excursion commenced. The timings concur with those of the remaining cladding thermocouples reported in Subsection 4.5, indicating that the rapid rise-rate began at the 0.50-m elevation ∿2.5 min prior to the 0.35-m elevation.

4.8 Structural Changes

The first observable significant changes in the bundle integrity were fuel rod rupture and associated release of fission products. Three of the five pressure switches provided a positive signal of rod rupture; 2B at 97.5 min, 3E at 99.5 min and 2B at 104.3 min. Only one of the fuel rod pressure transducers (Rod 3D) followed the internal rod pressure during the transient and indicated rod failure at ∿96 min. The maximum indicated cladding temperature (i.e., at the 0.70-m elevation) during the period of instrumented rod failure ranged from ∿1150 to 1200 K.

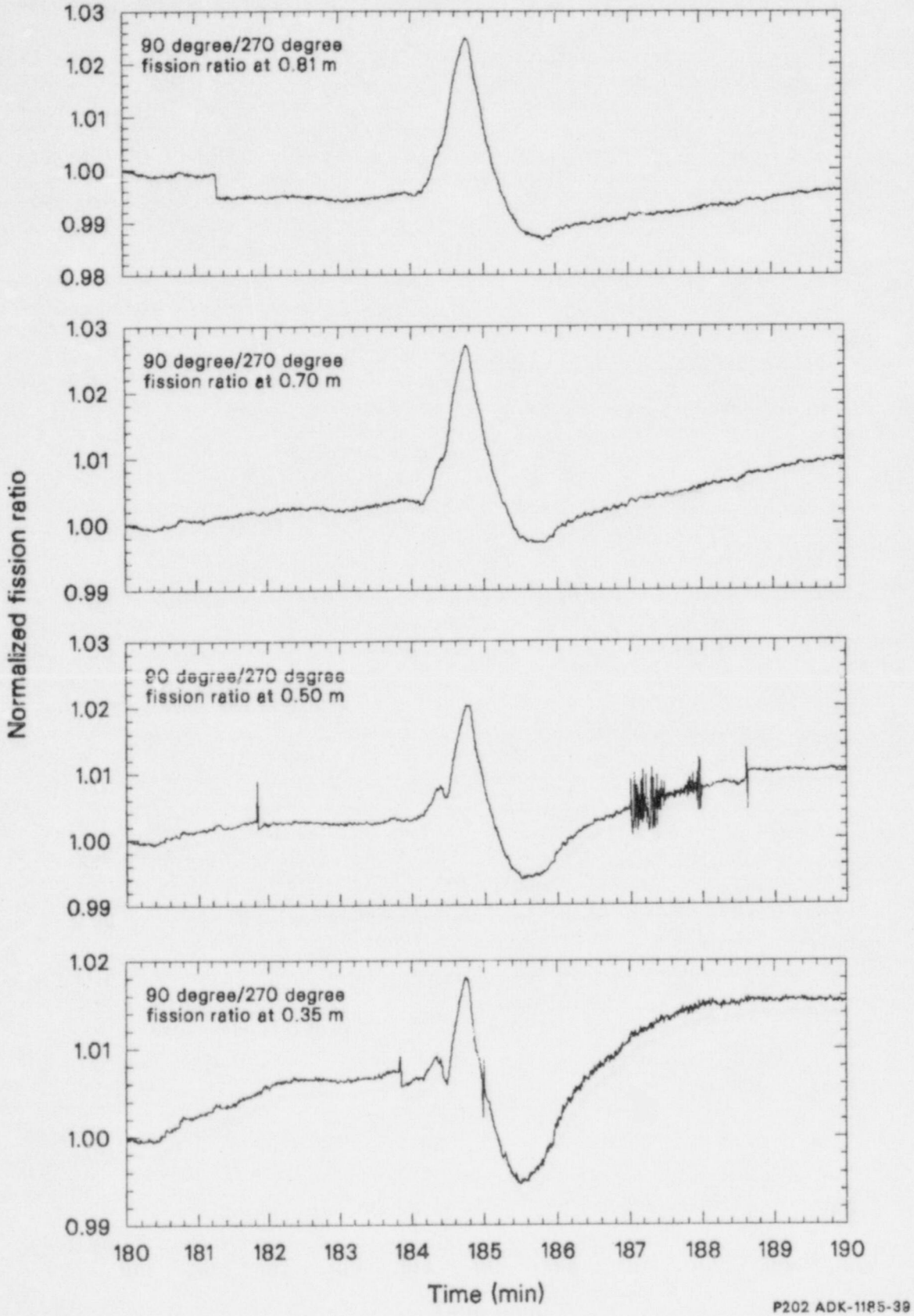

Figure 30. Responses of fission chambers at time of shroud failure.

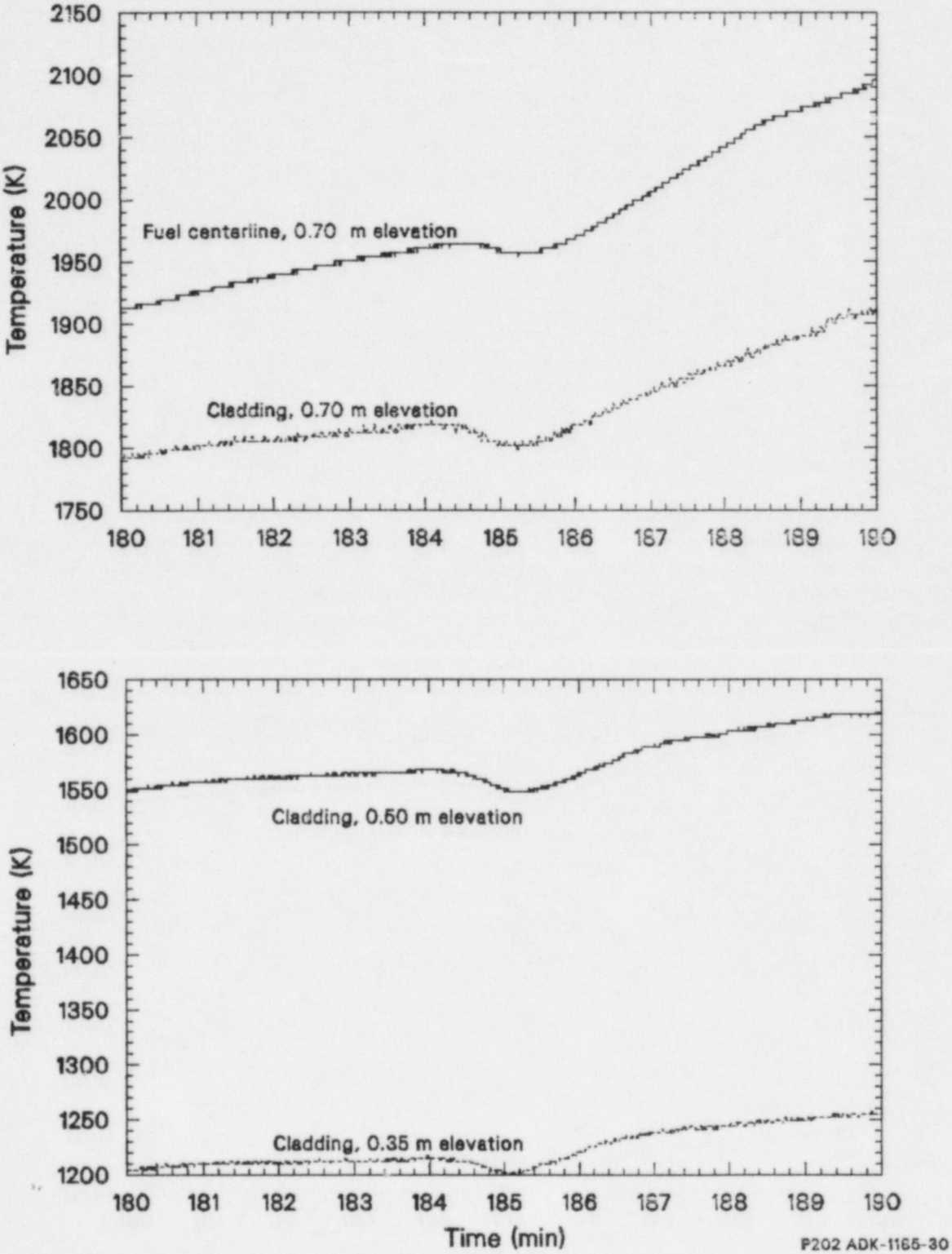

Figure 31. Rod 3D thermocouple response at time of shroud failure.

A further indication of fuel rod rupture was the increase in ion chamber signal resulting from the released fission products being swept down the outlet steamline. An overlay of the ion chamber gross radiation measurement, the internal pressure of Rod 3D, and the pressure switch signals is presented in Figure 32. No correction has been made for the estimated few second transit time between the fuel bundle and the ion chamber. Based on the large peak in the ion chamber signal, a failure period between 84 and 104 min was estimated, with corresponding peak cladding temperatures of 1100 K and 1200 K, respectively. The four internal rod pressure devices indicated failure in the latter part of the ion chamber response curve. This later failure of the instrumented rods is probably a consequence of the gas fill volume additional to that in the standard rods and located in the coolant region below the test bundle (see Appendix A). Of the 32 rods within the bundle, 13 were instrumented and had gas fill volumes approximately double that of the standard fuel rods.

Transient material behavior within the test bundle and shroud region was analyzed and interpreted using four techniques; the test train fission chamber signals, axial gross gamma scanning, neutron radiography and destructive cross-sectional examinations (metallography and elemental composition determinations). An attempt to determine the extent of material relocation was also made by measuring the pressure drop from the bundle inlet to the bundle outlet before and after the transient. A summary of the techniques and the conclusions of the analyses are provided in the following subsections. A complete description of postirradiation examination sequence, and presentation of related results, is given in Appendix E.

4.8.1 Assessment of Material Motion From Fission Chamber Data. In addition to their primary purpose of determining the coolant level in the bundle, the signals from the array of 12 fission chambers mounted on the test train were used to provide an assessment of material motion. However, since the sensitivity of individual chambers to material movement as a function of quantity and proximity has not been addressed, interpretation regarding the onset of liquefaction and material relocation remain qualitative. Reactor physics calculations, performed to aid the interpretation of the fission chamber signals, demonstrated that the fission rate would decrease due to flux spectrum hardening with an increase in fuel concentration. Thus, loss of material from a region resulted in an increase in the thermal neutron flux due to

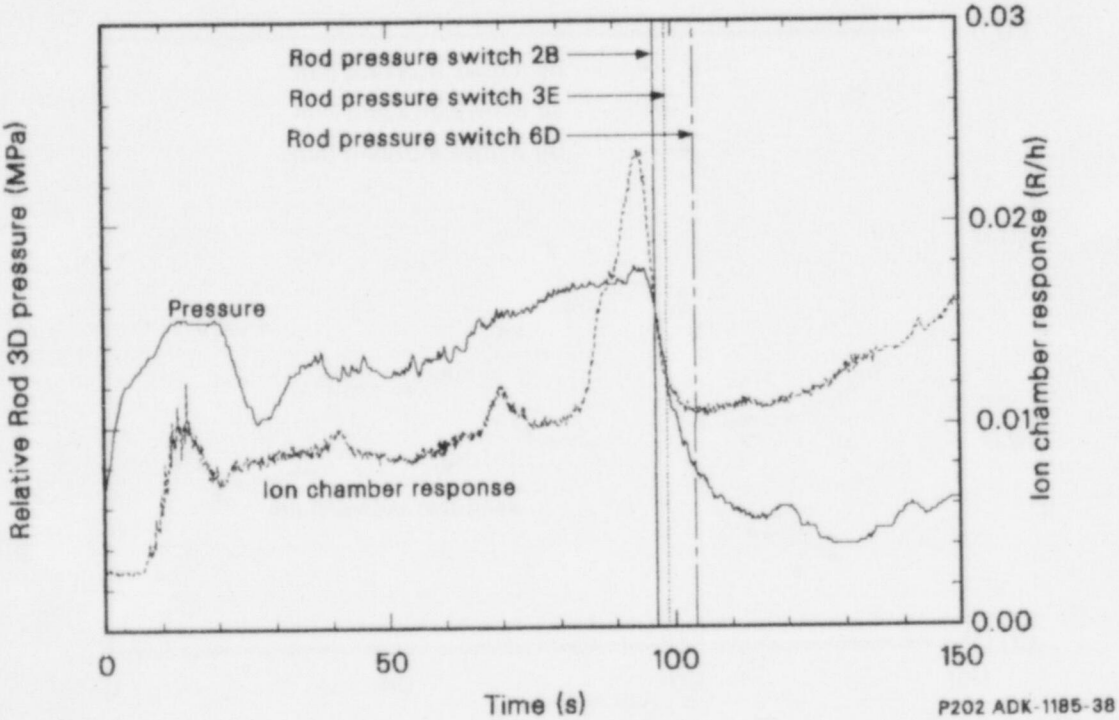

Figure 32. Fuel rod rupture indicators.

reduced absorption, and a decrease in the thermal flux in those regions where the material relocated. It should be noted that the interpretation of the neutron detector signals prior to the reactor physics analyses were based upon contrary assumptions.[7]

The power-normalized upper elevation fission chamber signals, removed from the influence of the bulk coolant, showed small variations commencing prior to 200 min. A lack of consistency between pairs of chambers at the same elevation complicated the evaluation, with opposite trends apparently indicating radial shifting of the fuel bundle. Significant fuel motion was not detected until the final minutes of the high temperature transient. Figure 33 shows the data recorded from all 12 fission chambers during the final 100 s

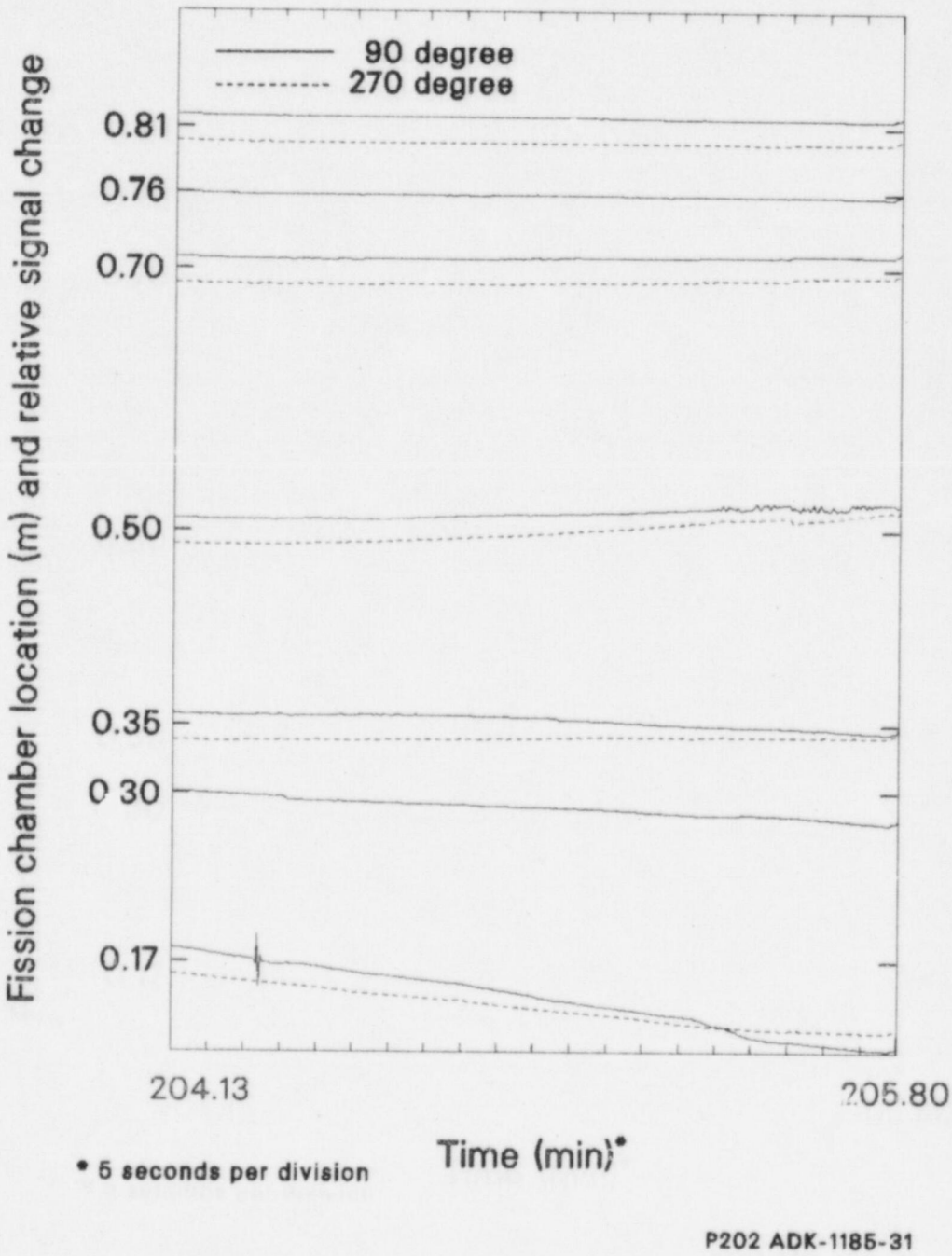

Figure 33. Test train fission chamber signals for the period 100 s prior to reactor scram.

prior to reactor scram. During this period the bundle power was effectively constant and the two-phase/steam interface level was below the bottom chamber, because the signals were not exhibiting the characteristic fluctuations of boiling water. Thus, deviations in the power normalized signals must be attributed to phenomena other than a changing coolant level. The observed slowly varying deviations are considered to be associated with the movement of the (U,Zr,O) melt. The most significant melt depletion occurred at the 0.50-m elevation, with smaller depletions being detected at the 0.70-m elevation. The majority of the melt accumulated at the bottom elevation, with smaller accumulations indicated by the fission chambers at the 0.30- and 0.35-m locations.

4.8.2 Material Relocation Based Upon Gross Gamma Scanning and Neutron Radiography. The axial power distribution within the in-pile tube was determined from the flux wire gamma scans described in Appendix B. Because of the long, high power, preirradiation history, relative to the transient period, the measured flux distribution represented the water-filled power profile and confirmed reactor physics predictions.[12]

For a period of two months following the transient, and prior to any major handling during postirradiation examinations, the test bundle was maintained in a vertical position and transferred from the PBF reactor for a gross gamma scan. The nonspectral gamma intensity profile, measured along the axis of the test bundle, largely represented the distribution of long-lived radionuclides with sufficiently high gamma energies to penetrate the bundle and test train sidewalls. These fission products were generally bound to the fuel, with lesser amounts contained in once-molten material and deposits on structural surfaces (see Appendix F).

The axial power distribution that dictated the pretransient fission product generation profile is shown in Figure 34, along with the posttest gross gamma scan. The exact test train location corresponding to the upper end of the gross gamma plot could not be positively established due to an imprecise scan speed. It was assumed to be equivalent to the top of the fuel pellet stack, identified in the neutron radiographs to be at 1.03 m (discussed in last paragraph of this subsection). On the basis of this comparison between the pretransient profile and the posttest gamma scan, the extent of the fuel movement was estimated.

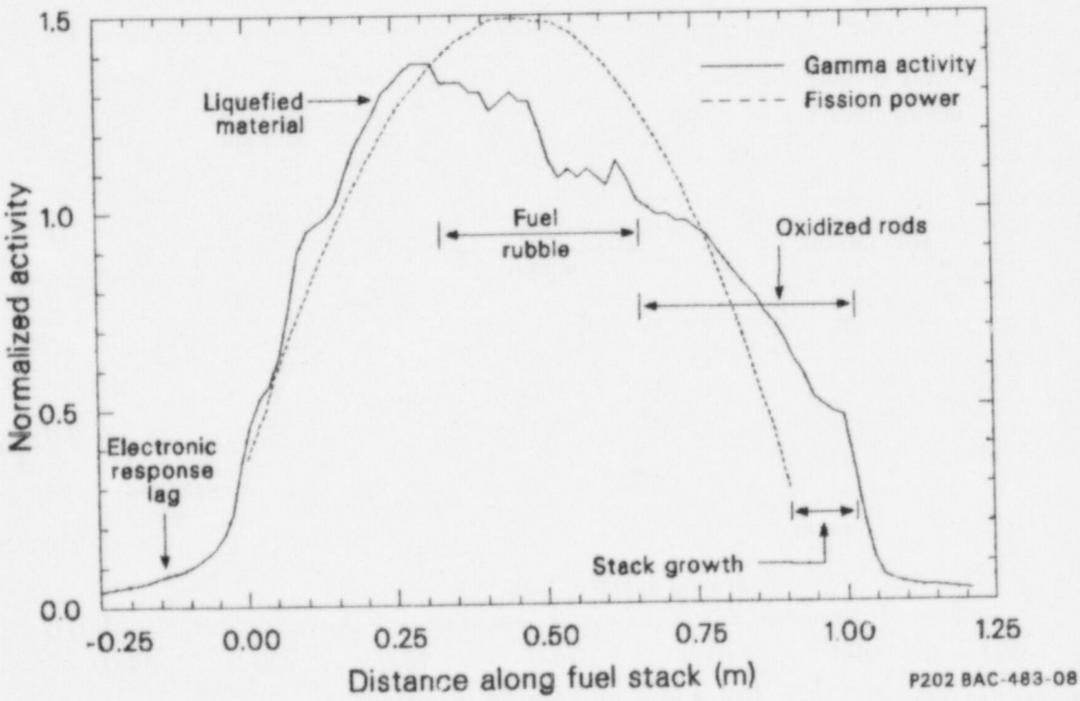

Figure 34. Normalized axial gross gamma activity and bundle fission power.

Approximately 2% of the fuel moved downward to the region between 0 and 0.31 m, 10% of the fuel moved away from the region between 0.31 m and 0.76 m and 8% of the fuel moved upward to the region above 0.76 m.

Following the gross gamma scan the bundle was transferred horizontally to a hot cell facility for drying, and then shipped to the Argonne National Laboratory-West (ANL-W). Neutron radiography, a nondestructive examination technique, was performed in a vertical position in the Hot Fuel Examination Facility at ANL-W to determine the posttest geometry. The bundle was positioned to allow radiography over seven axial sections. The procedure is described fully in Reference 9. The full-length neutron radiographs for 180 and 270 degrees are shown in Figure 35(a-c).

The lower portion of the bundle contained instrumentation leads, the bottom fuel rod insulation pellets and end caps, and the tie plate. The fuel rods remained intact in this region, with no observed molten material or debris, below the bottom grid spacer (centered at 0.05 m above the base of the fuel stack). The rod stubs extended up to an elevation of 0.198 m, with considerable molten material above the spacer grid. Above the rod stubs a large cylindrical mass formed (0.07-m diameter), consisting of fuel pellets bound together with previously liquid material. Above the cylindrical mass was a debris bed of fairly uniform consistency. The debris consisted primarily of fuel at least one-fourth pellet size and large pieces of oxidized cladding. In addition, fuel rod segments are visible at the upper end of the debris bed indicating less extensive embrittlement and handling damage. The middle and upper grid spacers are not visible in the neutrographs, evidently due to melting and intermixing. The tops of the fuel pellet columns were 0.115 m above their original location, with resultant prominent gaps between debris portions.

4.8.3 Material Relocation and Identification Determined by Metallography and Elemental Spectroscopy. After neutron radiography, the SFD-ST bundle was returned to the hot cell for epoxying, slicing of cross sections, and optical metallography. (See Appendix E and Reference 10.) Sectioning elevations were determined from the neutron radiographs and from closely spaced tomographic reconstructions, as discussed in Reference 9. In addition, twenty small diameter samples were core-drilled at positions of key metallographic interest for elemental composition determinations by scanning electron microscopy/energy-dispersive x-ray spectroscopy (SEM/EDS) and scanning Auger spectroscopy (SAS). Appendix E describes metallurgical terms and evaluation techniques, and presents the previously unreported elemental composition data in detail. In conjunction, the investigations permitted estimates of peak temperature ranges, phenomenological investigations of bundle material interactions, and approximate determinations of relative test times at which various thermochemical processes occurred.

Extensive metallography was performed on seven bundle cross sections, with supporting elemental spectroscopic determinations at five elevations. Phenomenological findings and estimated peak temperature ranges for each cross section are summarized below. A thorough description of the methodology and interpretation is given in Appendix E. For the purpose of the following summary, sufficient background information is provided by the temperature reference points listed in Figure 36 and the phase diagram illustrating fuel liquefaction by molten cladding (Figure 37).

The relative area of discrete materials within each metallographic cross section was measured. The participation of the shroud inner liner and insulation in the bundle behavior necessitated area fraction estimates relative to the area within the saddles. In the as-built geometry, the UO_2 fuel occupied 19.9% of the intersaddle area, the cladding 6.3%, and the liner and insulation 31.2%, leaving a flow area of 42.6%. In the following descriptions of the cross sections, references are made to photographs found in Appendix E.

0.055 m (Figure E-10). Since the bottom of the bundle was protected by coolant throughout the transient, this elevation contained a full fuel rod array and intact insulation region, plus the bottom spacer grid. Approximately 5% of the intersaddle area was filled by a multiphase, high oxygen (U,Zr,O) melt that was initially metallic. Another 1% was metallic melt that was mostly oxygen-stabilized alpha-zircaloy [α-Zr(O)] with some dissolved Inconel and uranium. These (U,Zr,O) melts did not contact cladding and fuel at this elevation, and therefore no equiaxed UO_2 grain growth was induced by heat transfer from the melts.

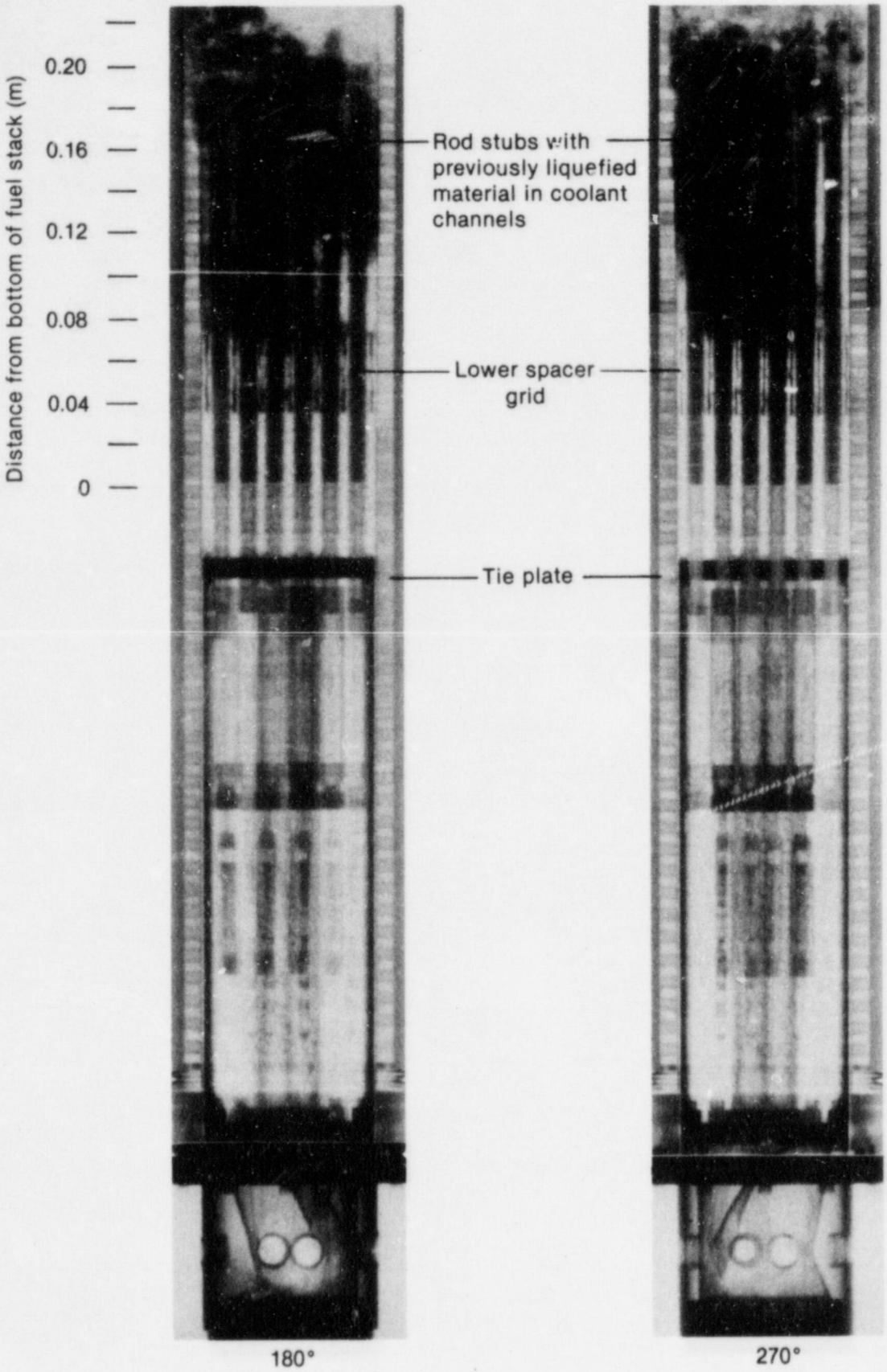

Figure 35(a). Radiograph of the bottom portion of the SFD-ST fuel bundle.

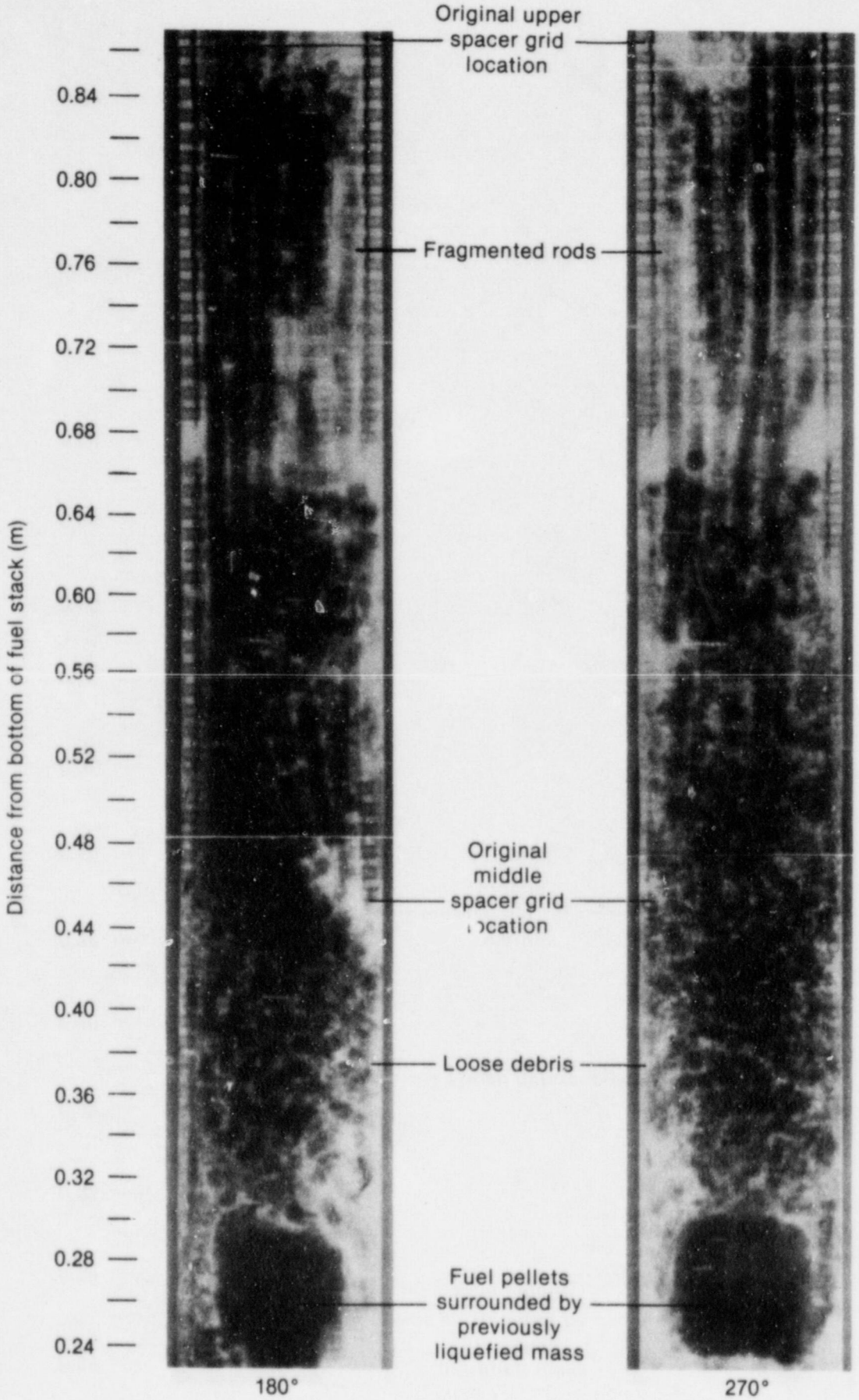

Figure 35(b). Radiograph of the middle portion of the SFD-ST fuel bundle.

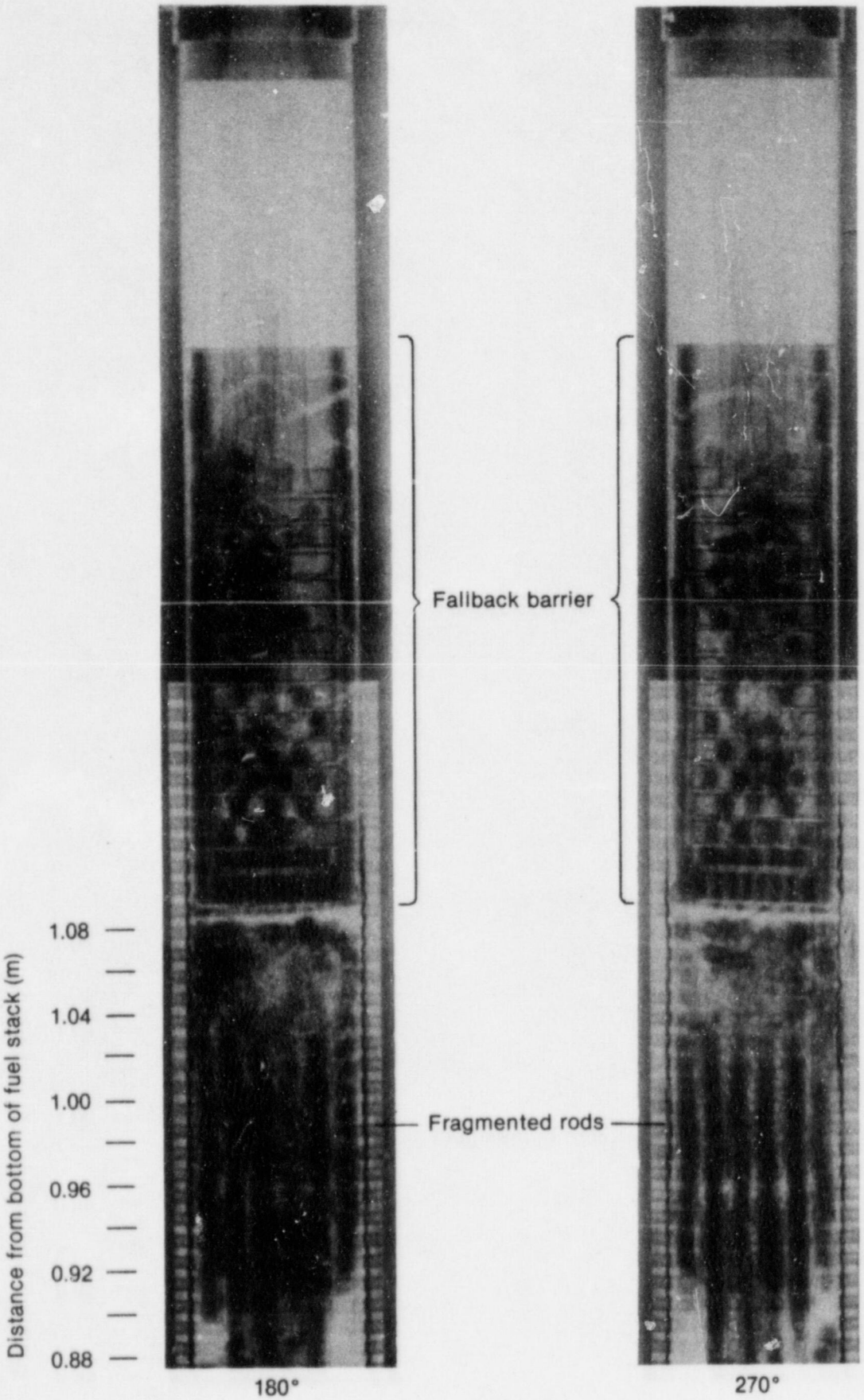

Figure 35(c). Radiograph of the top portion of the SFD-ST fuel bundle.

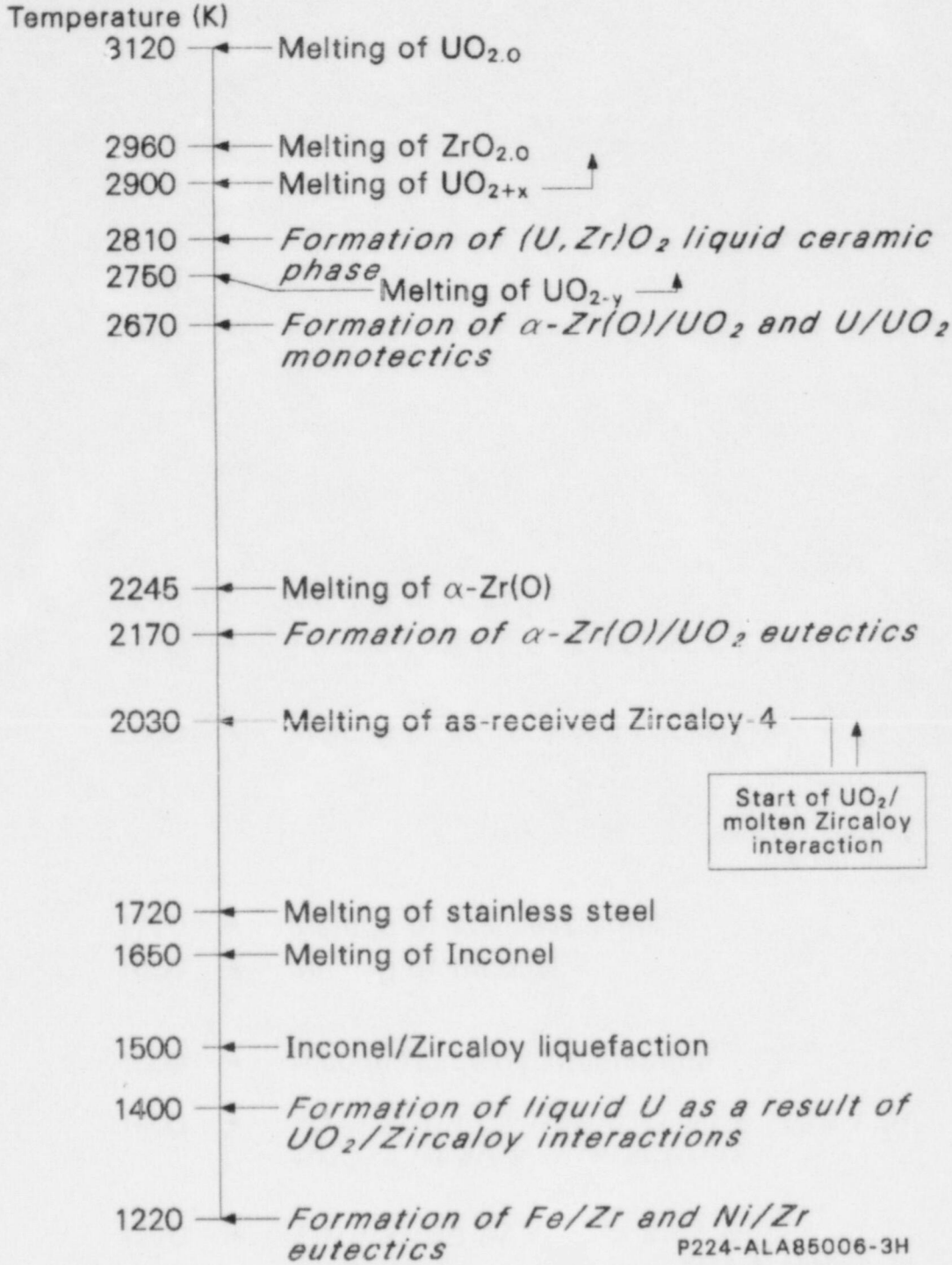

Figure 36. Metallurgical temperature reference points.

Both (U,Zr,O) melts achieved peak temperatures above 2245 K, the α-Zr(O) melting point, at some stage in their evolutions. The multiple phases in the oxidized melt suggested that it was a heterogeneous, partially metallic melt upon arrival at 0.055 m. As shown by Figure 37, this melt was probably a slurry of (U,Zr) O_{2-x} solids in L_1 [mostly molten α-Zr(O)] at a temperature of at least 2173 K before solidifying and oxidizing. The L_1 liquid phase is typically high in zirconium and low in oxygen. The L_2 liquid phase has typically high uranium, high oxygen concentrations. The metallic melt was still well

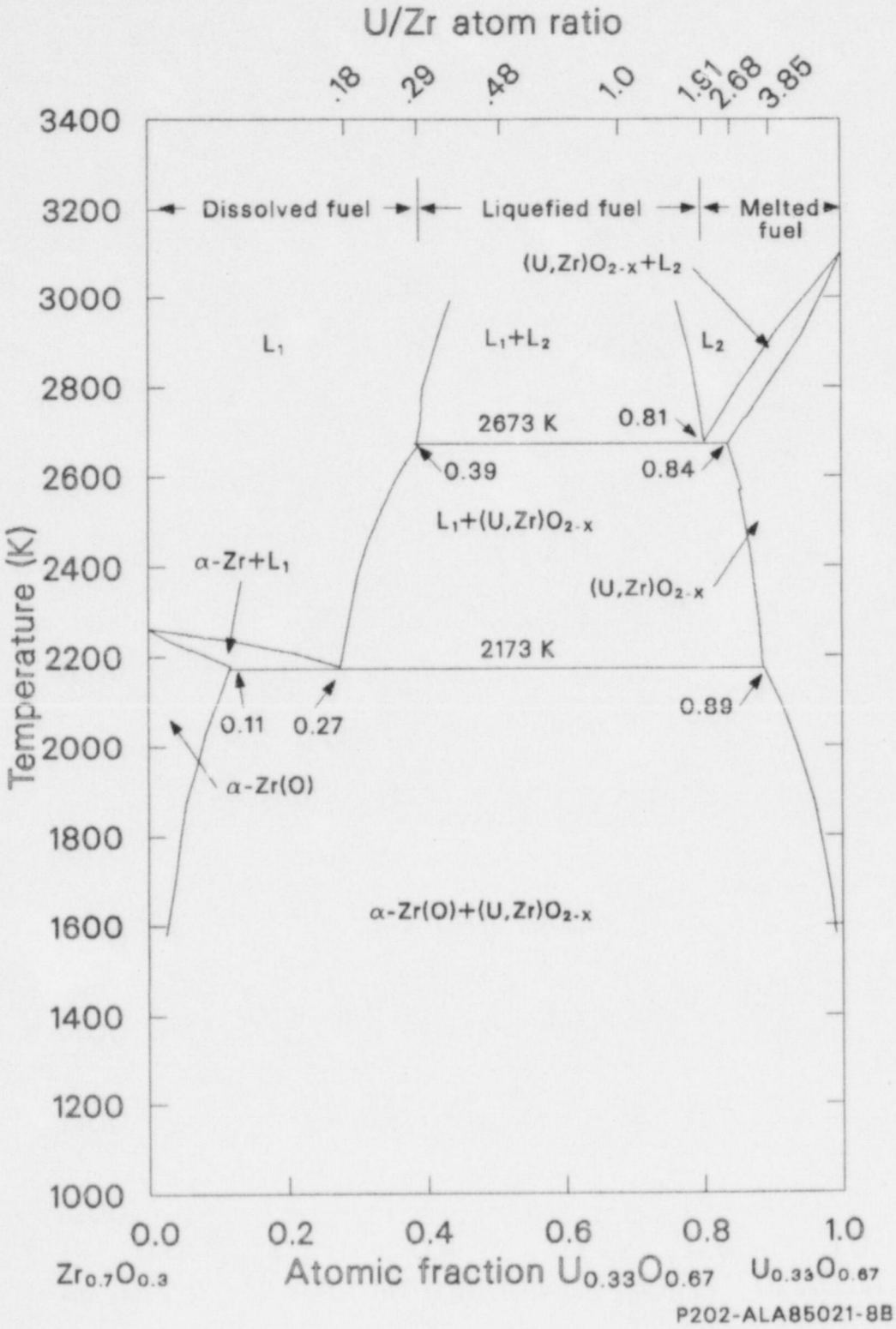

Figure 37. Quasi-binary α-Zr(O)-UO_2 phase diagram.

above 1650 K upon arrival, because localized grid regions were melted by contact rather than by forming a low melting point Zr/Inconel mixture.[15] (See Figure 36.) The metallic melt seems to have slumped later than the oxidized melt, after the coolant level had apparently decreased farther, to account for the much greater metallic melt/spacer grid interactions.

0.145 m (Figure E-11). This complex cross section contained four primary materials: melt-covered fuel pellets (11.7%); intact fuel pellets (4.0%); multiphase oxidized melt (20.6%, including porosity and cracks); and a Zr-rich metallic melt (10.4%). The damaged pellets were attacked on peripheral surfaces and along a few major internal cracks. Significant inward migration of Zr occurred, implying α-Zr(O)/UO_2 eutectic formation and local fuel temperatures above 2170 K. Minor UO_2 grain growth was observed, but with little consistency in final sizes. The intact pellets show no indications of equiaxed grain growth, even along peripheral surfaces contacted by a metallic melt that seeped into pellet-cladding gaps.

The oxidized melt contained more uranium than Zr (on an atomic basis) and was primarily liquefied fuel. It slumped to 0.145 m as a partially metallic (U,Zr,O) material, after beginning as a high temperature metallic melt (>>2245 K) and acquiring uranium and oxygen by pellet dissolution and oxygen by steam oxidation on the way down. However, this melt was not completely oxidized upon arrival, as it reduced both fuel and previously oxidized cladding before solidifying. The composition upon arrival cannot be precisely deduced, but Figure 37 indicates that the temperature was above 2173 K and could possibly have been above 2673 K. Because melt contact did not cause ZrO_2 melting, an upper bound of 2960 K can be established here.

The bulk metallic melt is primarily α-Zr(O), so its temperature before solidifying at this elevation was at least 2245 K. Appreciable dissolved Inconel and uranium were found within this material, though the uranium concentration was much lower than inside the oxidized melt as a result of relatively little fuel pellet dissolution. The metallic melt displayed very high neutron attenuation when radiographed, which cannot be explained by the Ni and U content, and strongly suggests large amounts of dissolved hydrogen acting as a moderator. ZrH_2 precipitates were not observed, evidently due to rapid cooling of the metallic melt. The hydrogen absorption most likely occurred during a temporary steam flow reduction and is discussed in Subsection 4.10.

0.170 m (Figure E-12). Only two unreacted fuel pellets are present in this cross section. Globules of (U,Zr) alloy in the prior β-Zr cladding around these pellets indicate fuel-cladding reactions and local temperatures of $\sim$1775 K. Multiphase oxidized melt occupies 38.4% of the intersaddle area, including large pores. This melt is similar in metallographic appearance to the U-rich oxidized melt at 0.145 m, but it was evidently hotter and lower in oxygen upon arrival, because pellet liquefaction and oxidized cladding dissolution were further advanced at this elevation. Fuel pellets occupy 13.9% of the area and oxidized cladding fills only 0.9%. No signs of ZrO_2 melting were found, so the melt temperature was below 2960 K. More equiaxed UO_2 grain growth was observed adjacent to the oxidized melt at 0.170 m than at 0.145 m, but final fuel grain dimensions ranged widely (10 to 50 μm) at individual positions.

Metallic melt occupies 2.9% of the intersaddle area. It was found at widely separated positions on the 180-degree side of the bundle, and penetrated shrinkage pores in the oxidized melt and gaps between oxidized melt and fuel pellets. A significant amount solidified ($\sim$2245 K) along the 225-degree side of the oxidized melt mass. This spatial distribution suggests that this material was the same as the bulk metallic melt at 0.145 m, and that much of it flowed around the oxidized melt mass before collecting underneath with metallic rivulets that drained through open pores. The metallic melt distributions at 0.145 and 0.170 m jointly indicate that the U-rich oxidized melt had solidified in place by the time the metallic melt slumped to this bundle region.

0.245 m (Figure E-13) About 36.8% of the area, including porosity, was oxidized melt (mostly liquefied fuel), with very minor amounts of metallic melt trapped inside oxidized melt porosity. The solidified U-rich melt contains two oxidized phases at room temperature, but was partially metallic upon arrival because pellets were typically attacked by reduction (i.e. melt absorption of oxygen) and molten Zr penetration. Previously oxidized cladding was probably dissolved by the same process, but ZrO_2 melting cannot be excluded at 0.245 m since no cladding remnants survived. The oxidized melt pulled away from fuel pellets during cooldown shrinkage in some cases, but remained firmly bonded to UO_2 at other locations, implying local differences in fuel wetting.

Melt composition samples (Appendix E) from the 0.245-m elevation show 2 to 3 times as many uranium atoms as zirconium atoms. Figure 37 indicates that the melt was L_2 (i.e. mainly *melted* fuel) at a temperature above 2673 K during slumping. Subsequent cooling upon contacting the two-phase/steam interface evidently converted the L_2 into a viscous two-phase slurry of $(U,Zr)O_{2-x}$ solids in Zr-rich L_1 (2173 K < T < 2673 K), with oxidation-resistant Ni trapped inside the minor L_1 phase. The slurry was then oxidized by steam to form a two-phase mixture of $(U,Zr)O_2$ and ZrO_2, where the rounded Ni ingots in the minor ZrO_2 phase suggest that the oxidation was completed while the L_1 remained liquid above 2173 K. Had the L_1 cooled below 2173 K before oxidizing, solid α-Zr(O) would probably have emerged before the Ni segregated into discrete inclusions.

Appendix E details one case where a local melt may have slumped to 0.245 m as a molten single-phase ceramic (>2810 K; see Figure E-23), melting much of a coated fuel pellet with some melting point depression from substantial Fe penetration (~10 at.%), instead of inward Zr diffusion and conspicuous fuel reduction. The melt temperature was likely near 3000 K, but no benchmarks exist for this apparent Fe/U/O eutectic behavior at high temperatures. None of the fuel pellets at 0.245 m displayed densification zones where sintering porosity disappeared by incipient fuel melting (as at the 0.915 m-elevation).

The UO_2 area fraction was estimated at 14.5%, but this value includes considerable melt that penetrated virtually every pellet crack open at the time. Fuel pellets at 0.245 m also show greater average diameter reductions than those at lower bundle elevations. Furthermore, significant UO_2 grain growth was commonly observed. Sizes generally ranged from 10 to 20 μm inside pellets, and from 15 to 50 μm along melts. A few pellets displayed 70 to 80 μm grains isolated among as-fabricated 10-μm grains across their entire diameters. Equiaxed grain growth is meaningful as an overall indicator of high temperatures, but the wide size ranges at individual positions preclude accurate comparisons to established correlations.

0.270 m (Figure E-14). This cross section was cut near the top of the solidified melt region and appeared very similar to 0.245 m. The two-phase oxidized melt occupied 40.7% of the area, including ~7% porosity. Rounded metallic inclusions, presumably high in Ni, were found throughout, indicating minimum melt temperatures of 2673 K. Previously oxidized cladding was completely dissolved, as at 0.245 m. The 17.6% UO_2 area fraction again included many melt-filled cracks. No fuel densification zones were observed, so the melt temperature did not exceed the fuel melting point after slumping to this elevation.

The major difference from the sample at 0.245 m was that several pellets along the cross-sectional periphery contained grains that exhibited a second phase during etched metallography. This microstructure is displayed in Figure 38(a), whereas Figure 38(b) provides the fuel microstructure more common at 0.245 m and within the cross-sectional interior at 0.270 m. The anomalous material was tentatively identified during metallography as U_4O_9 precipitates in a UO_2 matrix. Since no SAS measurements of oxygen concentration were made here, the phase make-up remains speculative. Assuming that fuel oxidation is responsible for the two fuel phases, the oxygen uptake probably occurred during reflood initiation, when steam flow was routed around the solidified melt and generally only contacted peripheral pellets.

Fuel grain growth was often evident at this elevation. Internal pellet grains ranged between 10 and 40 μm, while sizes next to melt regions were from 10 to 100 μm. However, little consistency in sizes was found on individual photomicrographs. The greatest uniformity in equiaxed grain growth was observed in peripheral pellets that presumably were slightly oxidized.

0.495 m (Figure E-16). This elevation is through the central bundle region, which was highly embrittled during the transient and where the most damage occurred to the insulation region. Only five fuel pellets resemble their original size, so appreciable fuel liquefaction and subsequent fragmentation of pellet remnants took place at 0.495 m. Approximately 15.9% of the area is filled by UO_2, but this percentage includes melts coated on pellet peripheries, melt-filled pellet cracks, and some porous fuel liquefied by melt intrusion (~2% total). Large differences in pellet diameter reductions were observed.

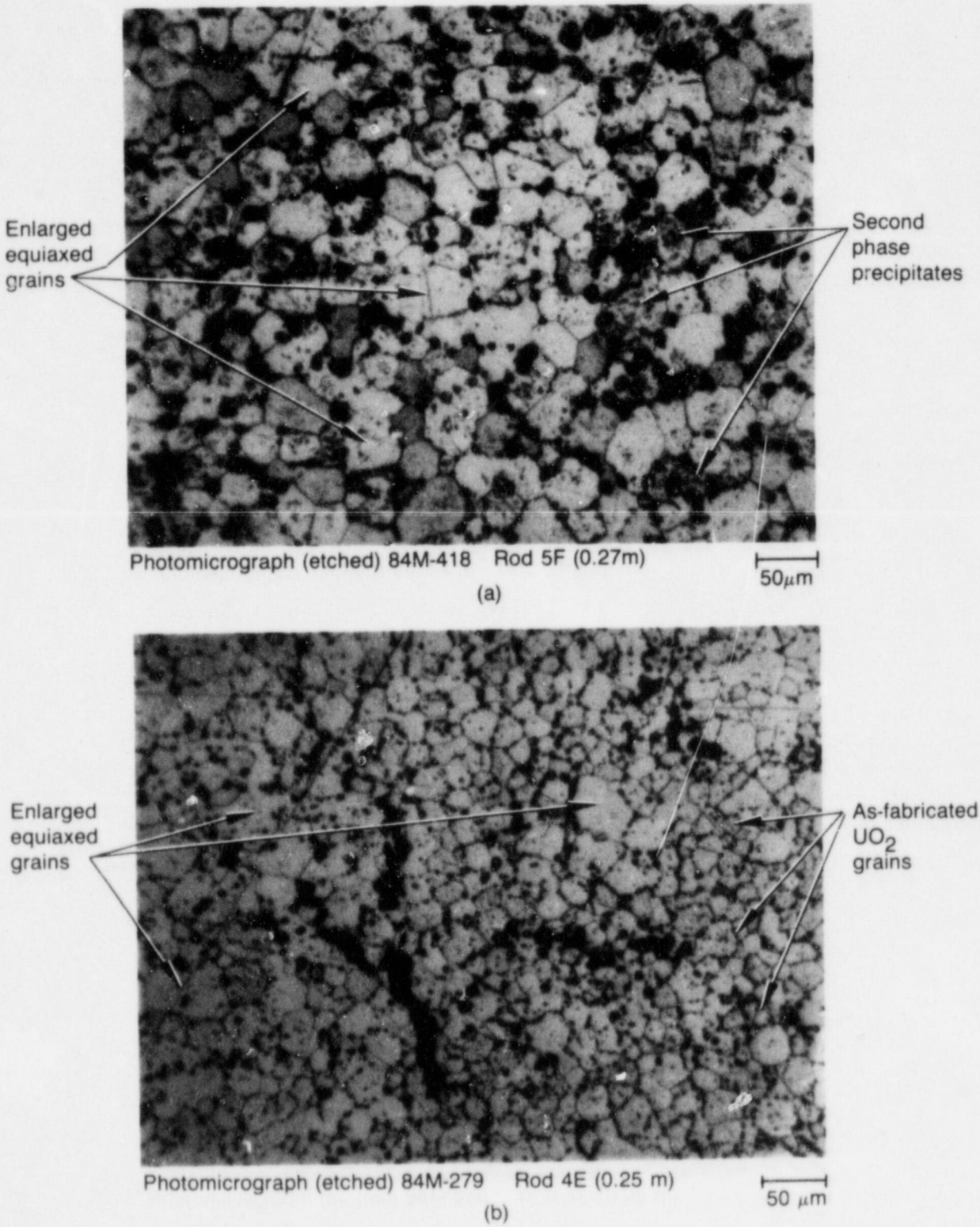

Figure 38. Comparison between (a) lightly oxidized fuel microstructure along peripheral regions of the 0.270 m cross section and (b) conventional microstructure typical at both 0.245 and 0.270 m cross sections.

Although the central bundle region was the source of most of the solidified melt mass found at lower elevations, oxidized cladding (some ballooned) can still be recognized around several pellets. This suggests that the bulk metallic melts (most subsequently oxidized) formed between fuel and cladding inside shells of ZrO_2. After temporary confinement, the melts dissolved thin ZrO_2 portions and slumped along exterior cladding surfaces, leaving the ZrO_2 shells behind. In addition, some previously metallic melts slumped along fuel-cladding gaps before solidifying at this elevation, so both relocation processes could be important.

The internal rod melts contained too much dissolved Inconel and the external melts too much dissolved uranium to have originated at 0.495 m. Observed Ni did not segregate into ingots, so oxidation was completed after solidification. Melt compositions are primarily two-phase mixtures of $(U,Zr)O_2$ (mostly liquefied fuel) and ZrO_2, and oxidation occurred by steam flow through shrinkage pores and cracks that opened during cooldown. As at lower elevations, these initially metallic melts attacked both UO_2 and ZrO_2 by reduction. Melt temperatures were likely quite hot upon arrival, but precise ranges are uncertain because solidification was apparently induced prematurely by cooldown. Temperatures of the melts that originated here, and flowed through this elevation earlier in the transient, were probably significantly higher (>2673 K), judging by the extensive fuel liquefaction that occurred.

As discussed in Appendix E, the one composition sample at 0.495 m from which SAS measurements were obtained indicated hyperstoichiometric uranium oxides ($UO_{2.3}$ to $UO_{2.9}$) both inside a fuel pellet and with adjacent uranium-bearing melts. Both materials did not etch as readily as fuel and melts below 0.495 m. Fuel oxidation may have been responsible for this microstructure. As shown in Figure 3C, this microstructure (common at 0.495 m) may be characterized by two conspicuous fuel phases, occasional large grains (>100 μm), and porosity that interlinked to form microcrack networks during cooldown. These networks exposed roughly 20% of the grain boundary surface area and their formation suggests both reduced grain boundary adhesion and large pore mobilities. These networks are found distant from melt-filled cracks, and are therefore not clearly associated with fuel reduction by the initially metallic melts.

0.915 m (Figure E-18). This elevation matches the original top of the pellet columns, but it is actually beneath 0.115 m of fuel and the upper spacer grid as a consequence of the upward bundle movement that probably occurred during reflood. (See Subsection 4.10.) Much of the bundle geometry survived, due to good lateral support from the relatively intact insulation and inner liner at this elevation. UO_2 pellets account for 14.8% of the area between the saddles, but roughly 2% represents melt-filled pellet cracks, melts coated on pellet peripheries, and porous fuel melted by reactions with molten cladding. Approximately 6.4% of the area is occupied by curlicued, once-molten remnants of ballooned cladding that mixed with molten Inconel and liquefied fuel. The presence of uranium in these cladding remnants confirms fuel pellet liquefaction above this elevation.

As at the 0.495 m elevation, pellet diameter reductions varied widely. Oxidized cladding is conspicuous around many pellets, again suggesting that melts formed in pellet-cladding gaps were temporarily confined by ZrO_2 shells. However, internal melts at this elevation contained Inconel constituents and external melts contained uranium, so some exchange occurred above 0.915 m. Melts were initially metallic and dissolved both UO_2 and ZrO_2 by reduction, as elsewhere. Despite the substantial concentrations of Inconel ingredients within the melts, no Ni-rich inclusions segregated. Therefore, these melts were oxidized after solidification by steam flow through shrinkage pores and cracks that formed upon cooldown.

The melt temperature definitely exceeded the fuel melting point (3120 K for $UO_{2.0}$; see Figure E-24) at one isolated position. Sample 19Q results presented in Appendix E confirm that at least one fuel densification zone formed by heat transfer from the nearby (U,Zr,O) melt, since this region was free of detectable impurities. The densification zone was bordered by a porous pellet region that contains considerable Zr and Inconel ingredients. Thus, while the porosity was apparently related to chemical effects and melt shrinkage, this porous region was above the fuel melting point to account for incipient fuel melting in the adjacent densification zone. Fuel melting could also have occurred in other pellets

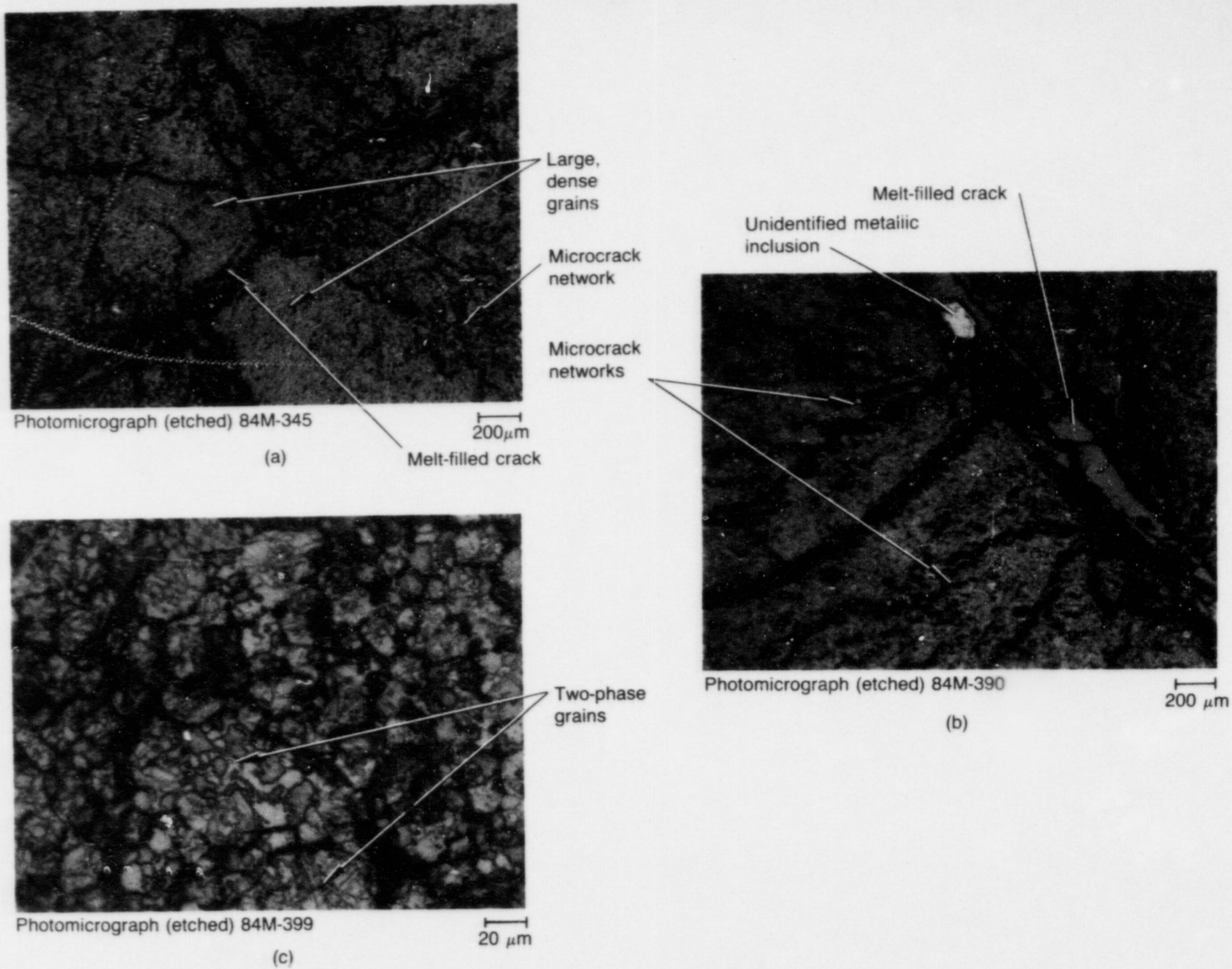

Figure 39. Two-phase, hyperstoichiometric fuel microstructures at 0.495 m: (a) pellet center, Object 2; (b) pellet center, Object 6; (c) pellet edge, Object 2.

that displayed porous regions, but no similar densification zones survived. High melt temperatures are also supported by elemental composition results, revealing U/Zr atomic ratios of 3 or greater (see Figure 37).

Oxygen concentrations were measured on two samples and both showed hyperstoichiometric uranium oxides ($UO_{2.3}$ to $UO_{2.7}$) in fuel pellets and in U-bearing melts. Solid pellet microstructures and grain sizes (50 to 100 μm) were very similar to those in Figure 39, although little etched metallography was performed at 0.915 m to positively confirm the existence of two fuel phases. Thus, fuel at this elevation appears to have been oxidized as at 0.495 m.

Results from the examinations discussed above are summarized in Table 4. Melt temperatures were estimated on the basis of interactions after arrival at each elevation. Area fractions of bundle materials have been totalled to provide an estimate of the flow area at each elevation (last column of Table 4) as an indication of overall flow blockage.

Table 4. Inter-saddle area percentages of materials and estimated temperatures

Elevation (m)	% UO_2[a]	% Cladding (Undissolved)	% Metallic[b] Melt	% Oxidized Melt[b,c]	% Insulation and Liner	% Flow Area
As-built	19.9	6.3	0.0	0.0	31.2	42.6
0.055	19.9 (nominal)	6.3 (nominal)	~1	~5	31.2 (nominal)	36.6
	$T << 2000$ K	$T < 1245$ K	$T \sim 2170$ K	$T \sim 2170$ K		
0.145	15.7	3.2	9.9	20.6	17.5	33.1
	$T \gtrsim 2170$ K	$T \sim 2250$ K	$T \sim 2170$ K	$2170\text{ K} \lesssim T < 2960$ K		
0.170	13.9	0.9	2.9	38.4	12.2	31.7
	$T \gtrsim 2170$ K	$T < 2960$ K	$T \sim 2170$ K	$2170\text{ K} \lesssim T < 2960$ K		
0.245	14.5	0.0	~0	36.8	12.1	36.6
	$2670\text{ K} \lesssim T \lesssim 3000$ K			$2670\text{ K} < T \lesssim 3000$ K		
0.270	17.6	0.0	~0	40.7	7.7	34.0
	$2670\text{ K} \lesssim T \lesssim 3000$ K			$2670\text{ K} < T \lesssim 3000$ K		
0.495	15.9	2.4	0.0	~2[d]	49.2	32.5
	$2670\text{ K} \lesssim T \lesssim 3000$ K	$T < 2960$ K		$2670\text{ K} < T \lesssim 3000$ K		
0.915	14.8	6.4	0.0	~2[d]	10.9	67.9
	$2670\text{ K} \lesssim T \lesssim 3000$ K	$T < 2960$ K		$2670\text{ K} < T \lesssim 3000$ K		

a. Fuel temperature estimated only along surfaces exposed to melts, except at 0.055 m where no equiaxed grain growth was observed.

b. Melt temperatures estimated upon arrival at elevation shown.

c. Includes shrinkage pores and cracks.

d. Oxidized melt percentage included in UO_2 value.

Figure 40 illustrates a best estimate of the general temperature behavior of the fuel bundle during the transient. A ten axial node SCDAP calculation (Section 6) that agreed closely with the fuel rod thermocouple measurements up to 200 min, allowed the peak and axially-averaged fuel temperature to be derived up to that time. The shaded area, indicating an uncertainty range, is based on the measured temperature deviation (Subsection 4.5) and the dependence on SCDAP. The peak end-of-test temperatures derived from the PIE were assumed to have occurred at reactor scram. Thermocouples outside the test bundle provided additional data and indicated when the bundle was finally cooled to saturation temperature. A simple interpolation, with large associated uncertainties of ± 200 K on the peak fuel temperatures, provide a general impression of the postulated final high temperature phase of the transient.

4.8.4 Determination of Flow Restriction From Bundle Pressure Drop Measurement. Measurements of the coolant pressure drop from the bundle inlet (-0.30-m elevation) to the bundle outlet (1.77-m elevation) were made before and after the high temperature transient to determine if material redistribution had increased the coolant pressure drop appreciably. The posttest coolant flow rate was limited to a maximum of 0.033 L/s to prevent fluidization and sweeping of the fuel debris into the PBF loop. The results of the pressure drop measurements are shown in Figure 41. The insensitivity of the posttest pressure drop measurement to flow rate indicates that the measurements are not meaningful, possibly due to unbalanced liquid in the two sense lines.

4.9 Hydrogen Production

Hydrogen generation in a LWR severe accident is important because it may significantly affect the primary coolant thermal hydrodynamics, and fission product transport chemistry and deposition. In addition, it may mix with air in the containment and produce a combustible mixture. The hydrogen released from the test train during the SFD-ST was measured as a function of time by a thermal conductivity analyzer described in Appendix D.

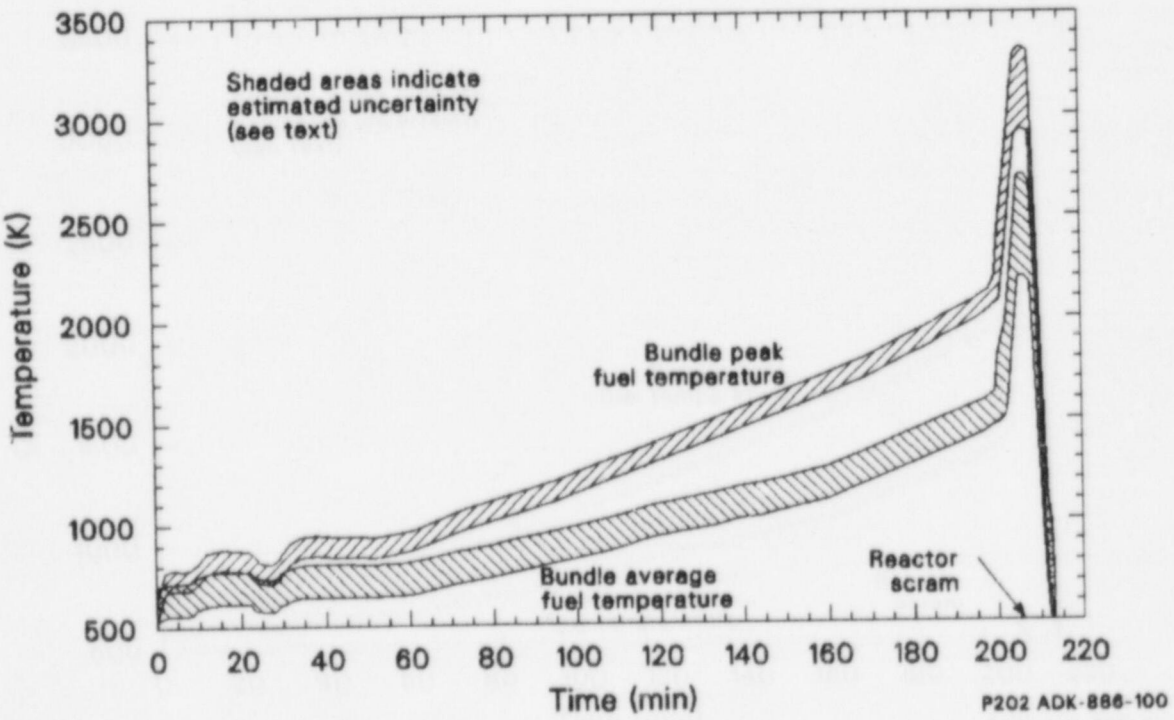

Figure 40. Graphical reconstruction of the postulated fuel temperature history during the Scoping Test transient.

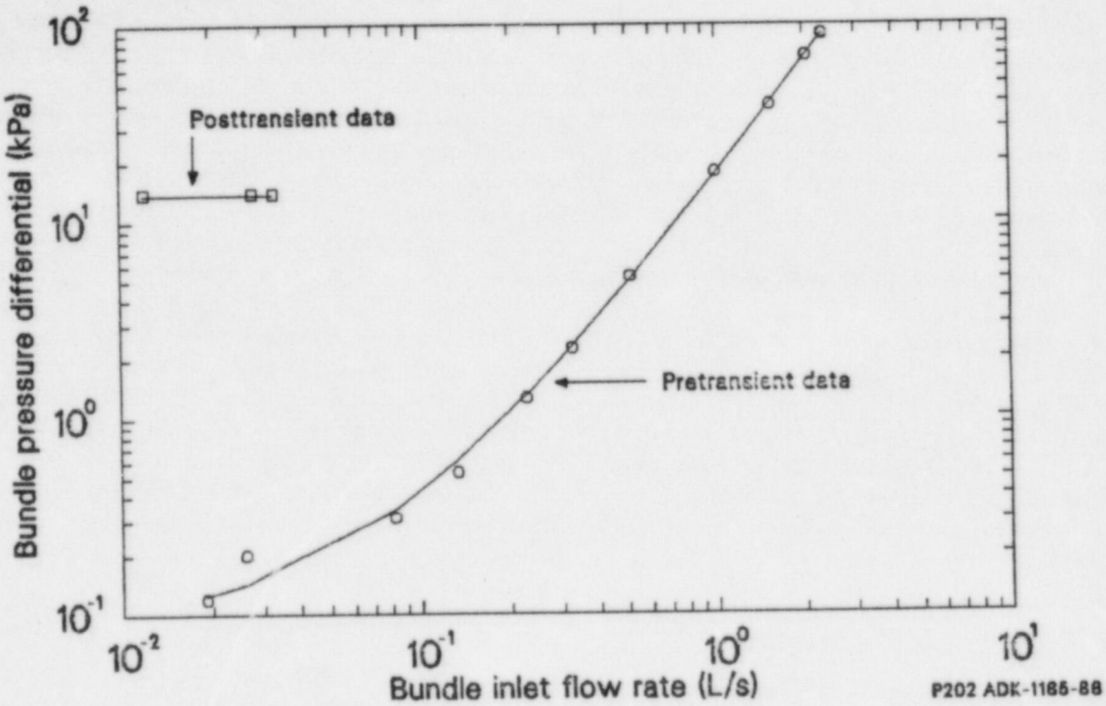

Figure 41. Bundle differential pressure versus inlet flow rate measured before and after transient.

The mass flow rate of hydrogen released from the test train, adjusted for the transit time to the hydrogen monitor is shown as a function of time in Figure 42. The applied transit times, ranging from 1.4 to 11.3 min during the test period, were as derived during the initial test interpretation and the validity of these estimates is discussed in Section 5. The plot shows a large spike in the hydrogen release rate corresponding to the rapid zircaloy oxidation during the final phase of the transient. There are significant uncertainties in the transit time during this period (up to 3 min) and therefore exact correlation of hydrogen generation and fuel bundle behavior was not possible. However, hydrogen generation after reactor scram is feasible because it took several minutes to cool and fully reflood the bundle. Thus, hydrogen continued to be emitted by a combination of postscram zircaloy oxidation, escape from melts and dead spaces, and formation of hyperstoichiometric uranium oxides. In addition, some hydrogen was expected to experience long transport times due to mixing and prolonged residence in the separator. Integration of the mass release rate provided the cumulative hydrogen mass release curve as a function of time shown in Figure 43, with a total value of 375 g. However, for reasons discussed in Appendix D the uncertainty on this integral value is estimated to be at least ± 140 g.

There were several components in the test train that had the potential to oxidize and release hydrogen during the transient, the most important of which were the saddle, the inner liner, the lead carriers, the fuel rod cladding and end caps, the fallback barrier, and the fuel and molten (U,Zr,O) material. The extent of oxidation for the various components was estimated from the postirradiation examination and is described below.

The saddle was examined at the nine metallographic cross sections and no saddle oxidation was observed at any of these elevations. However, significant oxidation of the inner liner was observed. Table 5 presents the thickness measurements of the ZrO_2 and α-Zr layers on the inner liner. To provide an estimate of the quantity of hydrogen that resulted from oxidation of the inner liner, the local thickness measurements were used to ascribe representative average values over defined axial regions (Table 6). The equivalent Zr mass, for both the α-Zr and ZrO_2 layers, was calculated from the average thicknesses, region lengths and Zr density of 6550 kg/m^3. It was assumed that there was no volume increase in the formation of the α-layer. Based on atomic mass and 300 K density values, a theoretical volume expansion coefficient of 1.525 was used to describe the oxide layer thickness growth. The assumption that the thickness growth accounted for

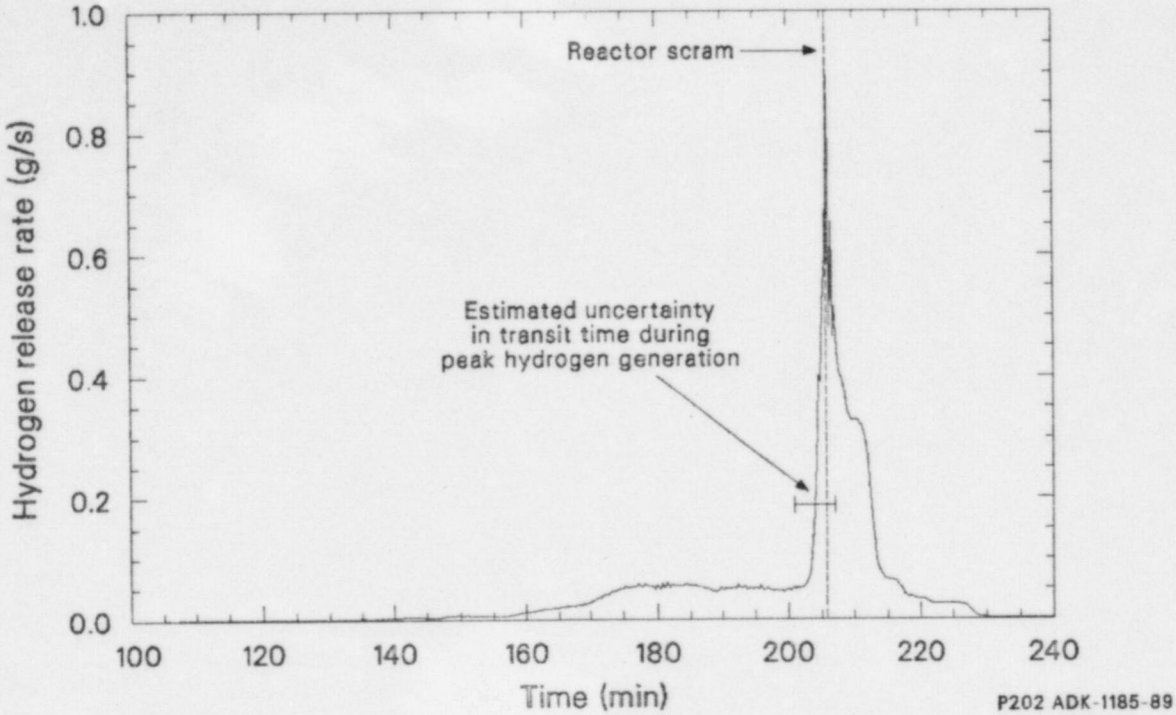

Figure 42. Measured on-line hydrogen release rate.

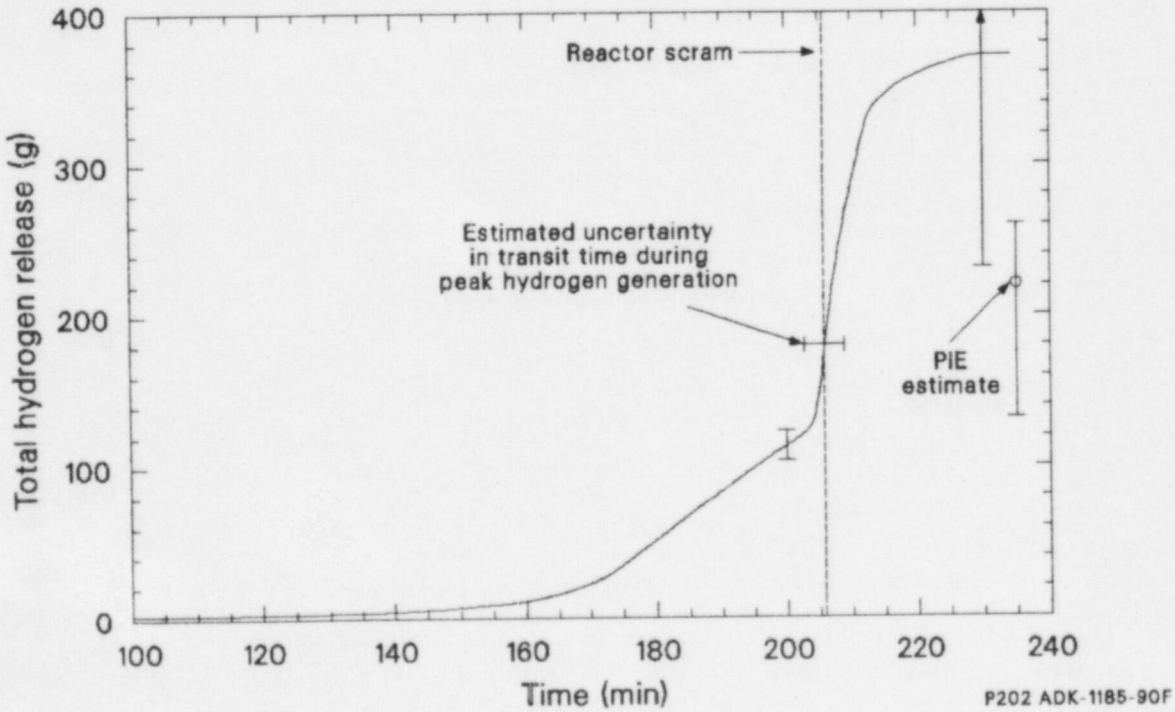

Figure 43. Comparison of integrated on-line hydrogen release and postirradiation examination estimate.

Table 5. Inner liner oxidation

Elevation (m)	Location (Degrees)	Oxide Thickness (μm)	Alpha Thickness (μm)
0.145	300	30 inner	20 inner
0.170	330 near 3A	40 inner 20 outer	90 inner 90 outer
	150 near 5F	1162 (complete oxidation)	—
0.245	290	250 inner 250 outer	470 center
	300	100 inner 100 outer	130 inner 130 outer
0.270	No Liner	—	—
0.495	No Liner	—	—
0.915	180	600 inner 400 outer	200 center

Table 6. Inner liner hydrogen generation

Elevation (m)	Total[a] Average α-Layer Thickness (μm)	α-Layer H_2 Production (g)	Total[a] Average Oxide Layer Thickness (μm)	Oxide Layer H_2 Production (g)	Total H_2 Production (g)
0.0 to 0.055	0	0.0	0	0.0	0.0
0.055 to 0.145	20	0.03	30	0.14	0.17
0.145 to 0.245	60	0.10	795	4.25	4.35
0.245 to 0.825	365	3.69	350	10.84	14.53
0.825 to 1.179[b]	200	1.24	1000	18.91	20.15
				Total	39.20

a. Combined inner and outer layer thicknesses, radially and axially averaged over given elevation range.

b. Elevation of the bottom of the steamline within the fallback barrier.

the total volume expansion introduced negligible error for the component dimensions considered. The hydrogen mass was derived from the equivalent Zr mass values using conversion factors of 0.00947 kg H_2/kg Zr for oxygen stabilized alpha zirconium and 0.04420 kg H_2/kg Zr for ZrO_2. The estimated hydrogen generation is summarized in Table 6. The liner provided a total of 39 g of hydrogen, which is 53% of the maximum possible from this source. An additional 4 g of hydrogen was estimated to be produced by oxidation of the two lead carriers.

The amount of cladding oxidation, and the subsequent hydrogen generation, were estimated in a similar manner to that for the inner liner. Table 7 presents the oxide and oxygen stabilized alpha layer thicknesses measured at specific locations. Large gradients existed in the amount of oxidation, even at a given cross section. However, based on gross assumptions on the average amount of oxidation over axial segments of the bundle, an approximate value for the total hydrogen generation from the cladding was obtained (Table 8). The estimated total hydrogen production from the cladding amounted to 112 g, 72% of the possible maximum.

There was no significant oxidation of the cladding at the bottom of the fuel rods as it was below the single-phase/steam interface for the major part of the high temperature transient. However, complete oxidation of upper region cladding occurred. It was therefore assumed that the bottom end caps did not oxidize and the top end caps completely oxidized, resulting in an additional 12 g of hydrogen.

The amount of oxidation of the components in the fallback barrier was estimated by metallographic examination of selected samples of the spheres, trays, and inner liner. About 25% of the zircaloy components in the fallback barrier, up to the elevation of the steamline, were oxidized to ZrO_2, resulting in an additional 5 g of hydrogen.

The amount of hydrogen that could have been generated by oxidation of the fuel was extremely difficult to determine with any degree of accuracy. The estimate was dependent on the actual amount of hyperstoichiometric fuel in the bundle and the average extent of oxidation, both of which could not be inferred from examination of a very limited number of fuel pellets. In order to provide an upper limit it was assumed that two-thirds of the fuel oxidized to $UO_{2.6}$, which would generate 48 g of hydrogen.

Table 9 presents the maximum possible hydrogen generation based on complete oxidation of the available zirconium, and the postirradiation examination results. The total hydrogen generation value of 220 g (+40 g, -88 g) consists of 172 ± 40 g from the oxidation of zirconium components and an upper limit of 48 g from the oxidation of fuel. Although this PIE estimate is significantly below the 375 g measured with the thermal conductivity analyzer, it is at the lower bound of that measurement as shown in Figure 43. It should be noted that integration of the mass release curve during the first 200 min, prior to the hydrogen peak and significant fuel oxidation, provided a reliable value of 113 ± 10 g that compared with the posttest analysis predictions (Subsection 6.2).

4.10 The Final High Temperature Phase

The final high temperature phase of the transient, where peak bundle temperatures increased by about 1000 K, must be examined in the context of the changing test boundary conditions during this period. It is of interest to note that the posttest SCDAP analysis does not predict a rapid temperature excursion during the final minutes of the test without the indicated bundle coolant flow reduction. The following subsections use the on-line instrumentation and PIE results to establish a best estimate scenario for the interrelated phenomena occurring during the final phase of the transient.

4.10.1 On-line Instrument Response. Figure 44 shows the differential pressure over the bundle length, the separator pressure and the inlet flow rate from just after shroud failure until completion of the rapid cooldown phase. The differential bundle pressure, measured between -0.30 m and 1.77 m, steadily increased following shroud failure until about 203 min. The differential then decreased during the next minute before increasing again by about 200 kPa up until reactor scram. The inlet flow rate and separator pressure appear constant for the first 10 min following shroud failure. The gradual increase in differential pressure may be

Table 7. Cladding oxidation

Elevation (m)	Fuel Rod Designation	Location (Degrees)	Oxidation Thickness (μm)
0.055	3C	225	50 OD (alpha and oxide)
	2D	45	0
	4D	80	0
	2B	—	0
0.145	4A	300	20 OD (oxide)
		135	10 OD (oxide)
		300	60 OD (oxide on melt)
		—	50 OD (alpha and oxide on cladding)
	4B		0
	5A	180	140 OD (alpha and oxide)
	2A	90	150 OD (oxide)
		—	50 OD (alpha)
	6C	45	60 OD (oxide double layer)
		—	60 OD (alpha)
	6B	135	30 OD (oxide)
		—	30 OD (alpha)
0.170	3A	270	30 OD (oxide)
		—	140 OD (alpha)
		0	190 OD (oxide, no beta)
	2A	45	40 OD (oxide)
		—	30 OD (alpha)
		225	30 OD (oxide)
		—	30 OD (alpha)
	1B	180	140 OD (alpha and oxide)
		270	30 OD (oxide)
		—	40 OD (alpha)
		0	30 OD (alpha and oxide)
0.270	1B	180	600 (complete oxidation, outer layer spalled)
	4D	—	(Fuel oxidized, U_4O_9)
0.495	Object 1	—	600 (complete oxidation, outer layer spalled)
	Object 3	180	910 (complete oxidation)
	Object 6	260	910 (complete oxidation)
	Object 2	280	910 (complete oxidation, U_4O_9 in fuel)
	Object 12	90	340 OD (oxide)
		—	720 OD (alpha)
0.915	2C	90	910 (complete oxidation)

Table 8. Cladding hydrogen generation

Elevation (m)	Average[a] α-Layer Thickness (μm)	α-Layer H_2 Production (g)	Average[a] Oxide Layer Thickness (μm)	Oxide Layer H_2 Production (g)	Total H_2 Production (g)
-0.026[b] to 0.055	0	0.0	0	0.0	0.0
0.055 to 0.170	50	0.34	40	0.83	1.17
0.170 to 0.270	40	0.23	40	0.72	0.95
0.270 to 0.982[c]	Negligible	0.0	910	109.63	109.63
				Total	111.75

a. Radially and axially averaged layer thickness over given elevation range.

b. Elevation of the cladding bottom.

c. Elevation of the cladding top.

Table 9. PIE estimate of total hydrogen generation

Source	Hydrogen Generation (g) Upper Limit	PIE Estimate
Cladding	155	112
Upper end caps	12	12
Lower end caps[a]	21	0
Shroud inner liner[b]	73	39
Lead carriers	6	4
Shroud saddle[b]	593	0
Fallback barrier[c]	22	5
Total Zirconium	882	172 ± 40 g
Fuel[d]	—	48^{+0}_{-48}
Total Zirconium plus fuel	—	220^{+40}_{-88}

a. Based on the standard fuel rod end caps.

b. Based on the region between the bottom fuel and bottom steamline elevations.

c. Portion of fallback barrier up to the elevation of the steamline.

d. Estimate based on two-thirds of bundle oxidized to $UO_{2.6}$ and considered as a maximum value.

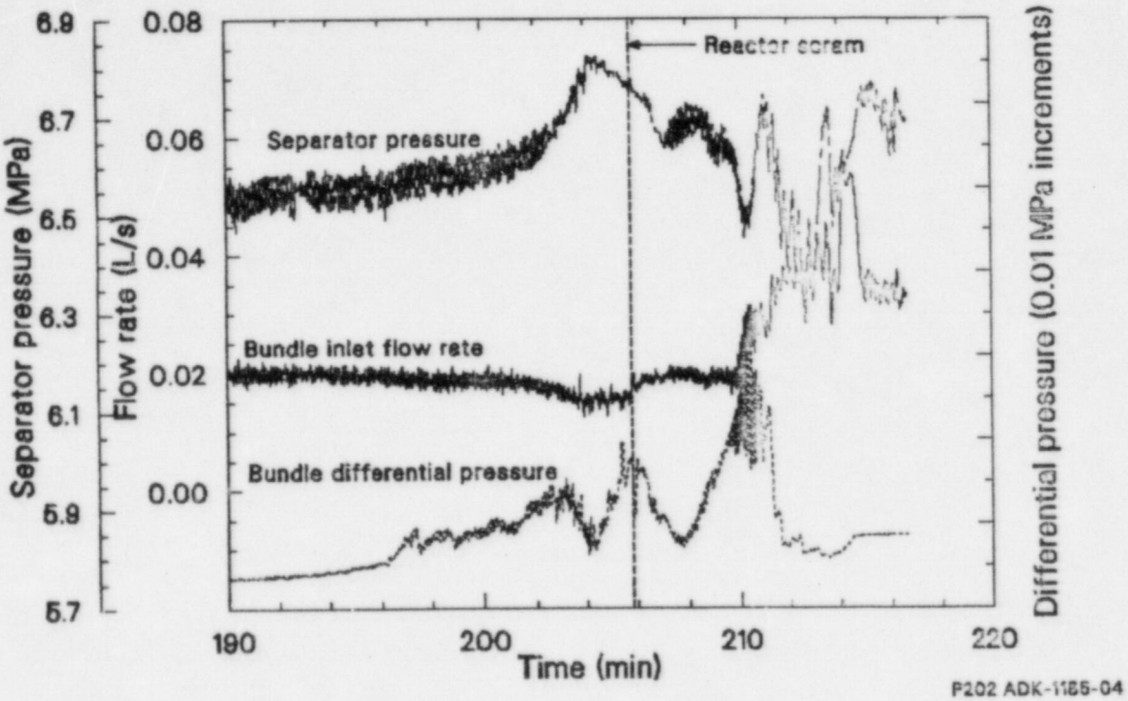

Figure 44. Bundle differential pressure, inlet flow rate and separator pressure during final phase of transient.

attributed to development of flow restriction and this aspect is discussed further in the following subsection. However, it should be noted that detection of melt relocation by the fission chambers did not occur until later, as described in Subsection 4.8.1.

In the Scoping Test the inlet flow rate was dependent on the pressure difference between the bundle and separator. Commencing about 195 min the separator pressure showed an increase of 260 kPa, while the inlet flow rate decreased from about 0.02 to 0.015 L/s. The pressure control instrumentation was operating on a small positive (< 15 kPa) bypass-minus-bundle pressure differential in order to maintain a constant bundle pressure, which translated to a positive bundle-minus-separator pressure of between 185 and 225 kPa for most of the transient. The bypass-minus-bundle and bypass-minus-separator differential pressures (recorded on a strip chart throughout the transient) both indicated negative values during a short period at around the time of reactor scram.

Based on the assumption that the magnitudes of the differentials are correct, the absolute separator pressure has been taken as the reference measurement and the bundle pressure adjusted relatively at 190 min. Figure 45 illustrates the possibility that the separator pressure was greater than the bundle pressure from about 3 min prior to reactor scram until 1 min after scram. As shown in Figure 44, the bundle differential pressure decreased between 203 and 204 min, while the separator pressure was increasing and the inlet flow was decreasing. The differential pressure decrease was possibly a result of the increasing separator backpressure through the steamline. The 260 kPa rise in the separator pressure may have forced the gas pressure above the bundle to approach the inlet pressure, with the high backpressure suppressing steam flow. It was not possible from the differential pressure measurement to estimate the extent of such a steam flow reduction due to uncertainty in the liquid densities in the upper and lower sense lines.

Coincident with the period of negative differential pressures (bypass-minus-bundle and bypass-minus-separator) was a 200 K decline in the steamline temperatures, which was sustained for over a minute before recovery close to the original temperatures about 1 min after scram (Figure 46). The temperature recorded by the thermocouple attached to the outside wall of the steamline between the standpipe and gas samples (DARS 237) also exhibited a significant decrease at this time. Such behavior is indicative of a reduced, and possibly stagnant, flow in the steamline.

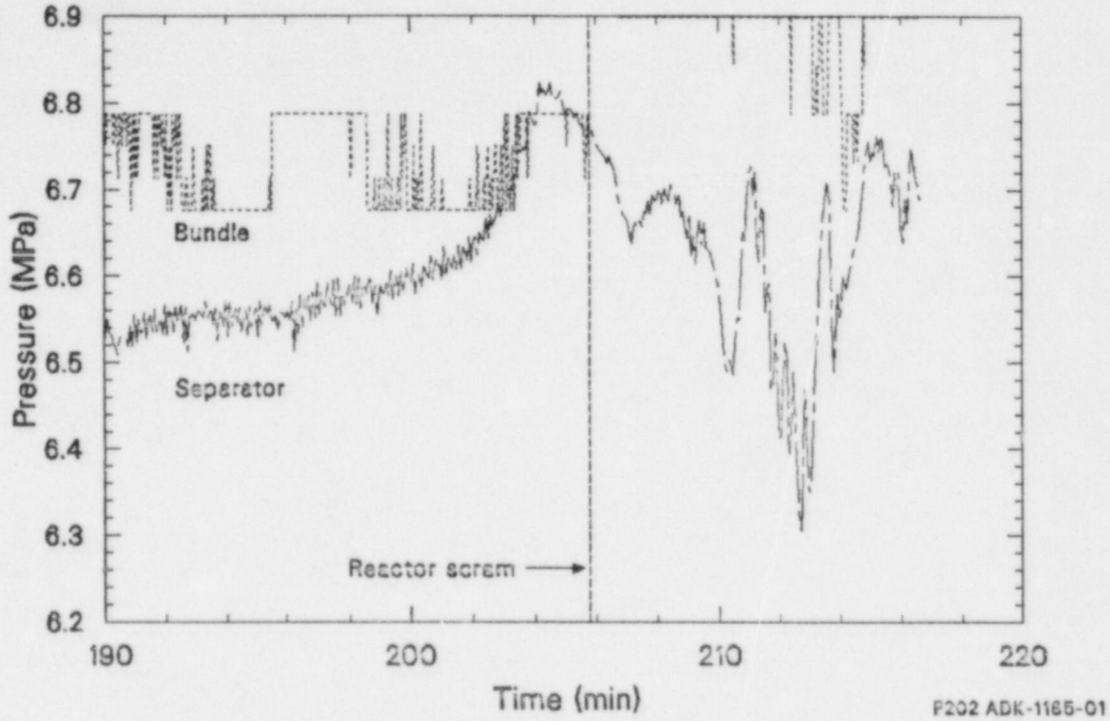

Figure 45. Bundle pressure measurement, normalized at 190 min with measured differentials to separator pressure measurement, during final phase of transient.

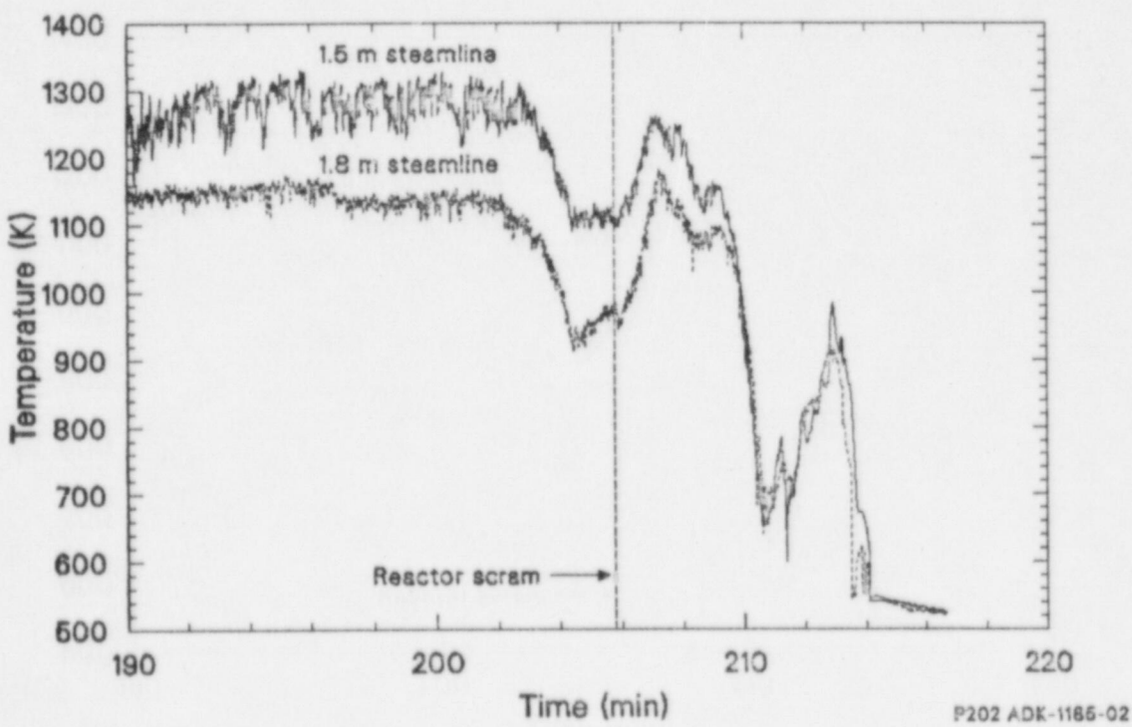

Figure 46. Steamline temperatures during final phase of transient.

Additional evidence of a flow reduction was provided by the flowmeter in the separator liquid exit line. It was necessary to average the measured data over 1 min time intervals to eliminate rapid wide range fluctuations resulting from the level controller. Figure 47 provides a comparison of the separator outlet flow rate and the bundle inlet flow rate. The ∿6 g/s discrepancy recorded throughout most of the test was discussed in Subsection 4.2. During the final minutes of the transient the difference increased to about 12 g/s, part of which can be attributed to the high production of hydrogen at this time. However, the quantity of hydrogen generated after 200 min required about 1.5 kg of water, significantly less than the apparent loss of water. Although it cannot be confidently stated that there was near zero steam flow for the period around reactor scram, there was undoubtably a very significant reduction in the flow through the fission product detection system. It should be noted that in Subsection 4.2, leakage from loose braze joints on three of the four inlet coolant lines to the bypass was discounted on the basis of the small positive bypass-minus-bundle differential pressure maintained throughout most of the transient. However, as described above, the strip chart recording indicated a negative differential pressure from ∿203 to 208 min. A leak during this period would have resulted in a flow reduction even greater than the 25% indicated by the inlet flowmeter.

The inlet flow reduction, decline in the two-phase/steam interface, and the rapid increase in zircaloy oxidation and temperature during the final phase of the transient were all strongly interrelated, with positive feedback effects. The exact sequence of events cannot be confidently defined on the basis of the on-line instrumentation. As a result, it is clearly difficult to positively establish whether the high temperatures achieved during the final minutes of the Scoping Test were a consequence of the unplanned flow rate reduction. The calculational predictions for this phase of the test are discussed in Subsection 6.2.

Immediately following reactor scram, pressure pulses were recorded by the bundle and bypass pressure transducers. During the initial interpretation the pulses were tentatively attributed to hot debris or melt material dropping into the water in the lower plenum region. A detailed examination of the 100 Hz data, with 500 points per second, was performed and concluded that the pulses were more likely to be electrical noise than the result of physical phenomena occurring in the fuel bundle. For this reason the pressure data from these two transducers has been categorized as failed for the 1 min period following reactor scram.

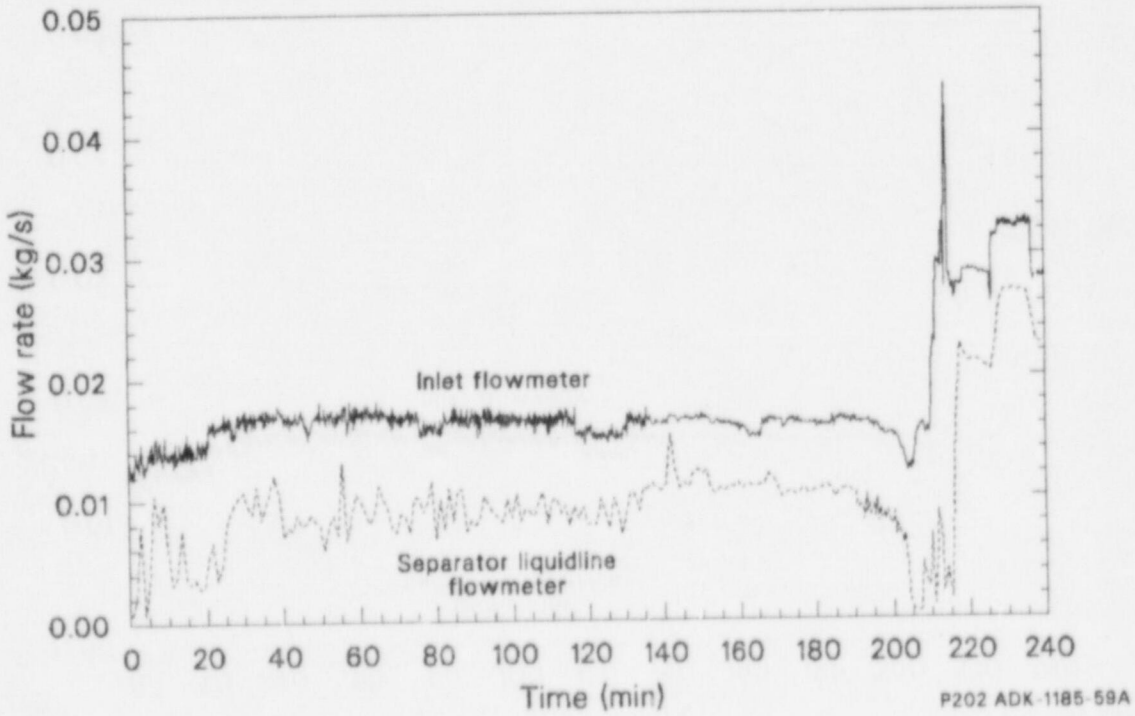

Figure 47. Comparison of the measured inlet flow rate and separator outlet flow rate.

4.10.2 Best-Estimate Bundle Scenario. Postirradiation examination of the SFD-ST bundle region provided additional insights on the later portions of the transient. These posttest findings have been correlated to certain trends in on-line instrument responses and permitted tentative conclusions on the influence of the time-varying transient conditions on the high temperature fuel behavior. The PIE results discussed in Subsection 4.8.3, and detailed in Appendix E, are briefly summarized in the following sequence:

1. Zircaloy cladding oxidized rapidly late in the transient, heating up bundle regions not covered by coolant.

2. Accelerated cladding oxidation was accompanied by the melting of unoxidized zircaloy (>2030 K), followed by incipient UO_2 fuel dissolution (>2170 K) as superheated Zr-rich melt began to slump downward. To account for the large concentrations of UO_2 that went into solution, bulk melt temperatures typically exceeded 2673 K (approaching 3100 K in some instances). This high temperature U-rich liquid (L_2 on Figure 37), also acquired oxygen by reacting with steam and ZrO_2 during its downward relocation.

3. Slumping of the oxidizing U-rich melt was halted on contact with the two-phase/steam interface at about the 0.1 m to 0.2 m elevation. Heat loss to the coolant apparently first transformed the bulk (U,Zr,O) melt into a viscous slurry of $(U,Zr)O_{2-x}$ solids in molten alpha-zircaloy (L_1 on Figure 37) between 2173 and 2673 K. Limited melt interactions with fuel rod stubs continued until bulk melt solidification (∿2173 K) occurred through a combination of cooling and oxidation.

4. Accumulation of the oxidized (U,Zr,O) melt was followed by formation and slumping of a metallic melt that was identified as mostly once-molten cladding with small amounts of dissolved fuel and Inconel spacer grid constituents. However, based on the radiographs, considerable hydrogen was also postulated to be present. The metallic melt poorly wetted UO_2 pellets while slumping. It was both highly superheated and low in viscosity, as it not only flowed around the solidified oxidized melt (225-degree orientation; see Figures E-11 and E-12, Appendix E), but also through the oxidized melt pores formed during cooling and along rod stubs where the melt had separated during cooldown shrinkage (Figures E-12 and E-13, Appendix E). Metallic melt solidified by heat loss to the coolant beneath the oxidized melt mass and, to a lesser degree, within oxidized melt passages. (See Figures A-14 through A-20 of Reference 9.)

5. An undetermined amount of fuel was oxidized beyond $UO_{2.00}$ during cooldown and resulted in a two-phase fuel microstructure (Figure 39). Fuel oxidation apparently reduced grain boundary adhesion and helped to form microcrack networks that were commonly observed in fuel pellets above the solidified melt region. In addition, a diagonal fracture occurred across embrittled cladding along the solidified melt base during the cooldown and reflood phase. Most of the bundle was lifted into the fallback barrier, where upper bundle segments were forced against intact insulation. Intermediate bundle regions evidently slid downward by varying amounts during posttest handling, forming the prominent gaps observed in the neutron radiographs (Figure 35).

The above observations from the postirradiation examination of the test bundle have been combined with the on-line instrument responses to provide the following interpretation of the final phase of the test at successive time intervals.

196-200 minutes. Determinations of bundle behavior during this interval are relatively uncertain, because structural changes early in the high temperature test phase were obscured by later thermochemical reactions and bulk relocation processes. However, Figure 40 indicates that fuel rod temperatures (∿2100 K peak, ∿1500 K average) were increasing at a low rate. Hydrogen production (Figure 42) was slow and steady over this period. Nevertheless, Figure 44 shows a distinct increase in bundle differential pressure, starting at 196 min, while the coolant level (Figure 12) was decreasing and effectively lowering the differential pressure. Zirconium/Inconel interactions occur at about 1500 K[15] and, based on Figures 40 and 44, accumulations of low melting point zircaloy/Inconel mixtures can be postulated at one or both of the upper grid elevations,

inducing minor local restrictions to steam flow. The configuration of this mixture may have resembled the curlicued remnants from ballooned cladding/spacer grid interactions that were discovered at the 0.915-m elevation (Figure E-18, Appendix E).

200-203 minutes. As discussed in Subsection 4.10.1, the inlet flow decrease at about 200 min (Figure 44) resulted in less heat removal from the bundle and permitted escalation in zircaloy oxidation and bundle temperature. Hydrogen generation increased substantially after 203 min (Figure 42) but, as outlined in Subsection 4.9, there are significant uncertainties in the transit time during this period.

Since the coolant inlet flow and level were both decreasing during this period, the differential pressure increase is attributed to a gradual loss of flow area in fuel rod coolant channels from slumping of oxidizing (U,Zr,O) melt and its initial accumulation near the coolant level (0.1 to 0.2 m). Widespread melt formation, incipient fuel liquefaction, and bulk downward relocation are expected to have commenced by 202 min, because rapid zircaloy oxidation would induce cladding melting by both direct heat conduction and radiant heat transfer.

203-206 minutes. As described in the previous subsection, there is evidence that at about 203 min a significant reduction in flow commenced. This may have produced a hydrogen-rich environment within the bundle by ∿205 min suitable for the formation of the observed low-oxygen, high-hydrogen metallic melt. The small amount of UO_2 dissolved in the metallic melt, by comparison to the U-rich oxidized melt, is due primarily to poor wetting of UO_2 pellets while the metallic melt was slumping. The poor wetting characteristics of the superheated metallic melt are attributed to negligible steam oxidation, since molten cladding does not wet UO_2 particularly well until it has been oxidized to α-Zr(O).[16] Therefore, the metallic melt slumped in a steam-deficient environment, and absorbed hydrogen instead of reacting with steam and fuel like the oxidized melt.

Although the time of metallic melt formation cannot be deduced exactly, the rise in steamline temperature at reactor scram (Figure 48) indicates increasing steam flow and therefore the metallic melt had probably slumped shortly prior to this time. Steam flow was fully reestablished about 1 min after scram (see next subsection). As previously discussed, the metallic melt encountered a solidified oxidized melt mass when it reached the lower bundle region, with some metallic melt solidifying within oxidized melt shrinkage features (Figure 49). Since the oxidized melt was mainly liquefied fuel, liquefaction by molten cladding and bulk melt accumulation had essentially ceased before metallic melt slumping.

206-211 minutes. The PIE results indicated that little unoxidized cladding remained within the upper two-thirds of the fuel bundle after slump of the metallic melt. Upon removal of the main source of bundle heating through scram of the reactor, residual cladding melting and fuel liquefaction above the bulk melt mass terminated. However, minor UO_2-melt reactions may have continued within the mass. Early reflood coolant was probably transformed into steam by the large solidified melt region and therefore thermal shock to the embrittled upper bundle regions was minimized. The rise in steamline temperature and the spike in ion chamber output (Figure 48) indicate that steam flow was fully reestablished by 207 min.

Figure 44 shows a sharp decrease in separator pressure after 210 min, matched by a sudden increase in coolant inlet flow to 0.03 L/s. This flow surge evidently induced a diagonal fracture across embrittled cladding along the solidified melt base, as can be observed in Figure 49. The fracture was followed by a hydraulic lift of the upper five-sixths of the bundle until it impacted the fixed base of the fallback barrier. The lifted bundle portion weighed nearly 17.5 kg. The differential pressure acting on the solidified melt base at 210 min was at least 40 kPa. Based on this differential pressure, and the cross-sectional area within the liner, over 24 kg of lift has been estimated. This leaves nearly 7 kg to overcome lateral friction and to account for the small portion of the cross-sectional area that was not blocked by rod stubs and solidified melt. The hydraulic lift impact apparently fractured some embrittled fuel rods and also the barrier container, the ZrO_2 steam inlet tube, and fuel rod upper plenums, leaving upper end caps at right angles to their original orientations, as can be seen in Figure 35(c). Upper bundle segments were wedged beneath the fallback barrier against the relatively intact ZrO_2 insulation. Lower segments are believed to have moved downward to varying extents during posttest handling.

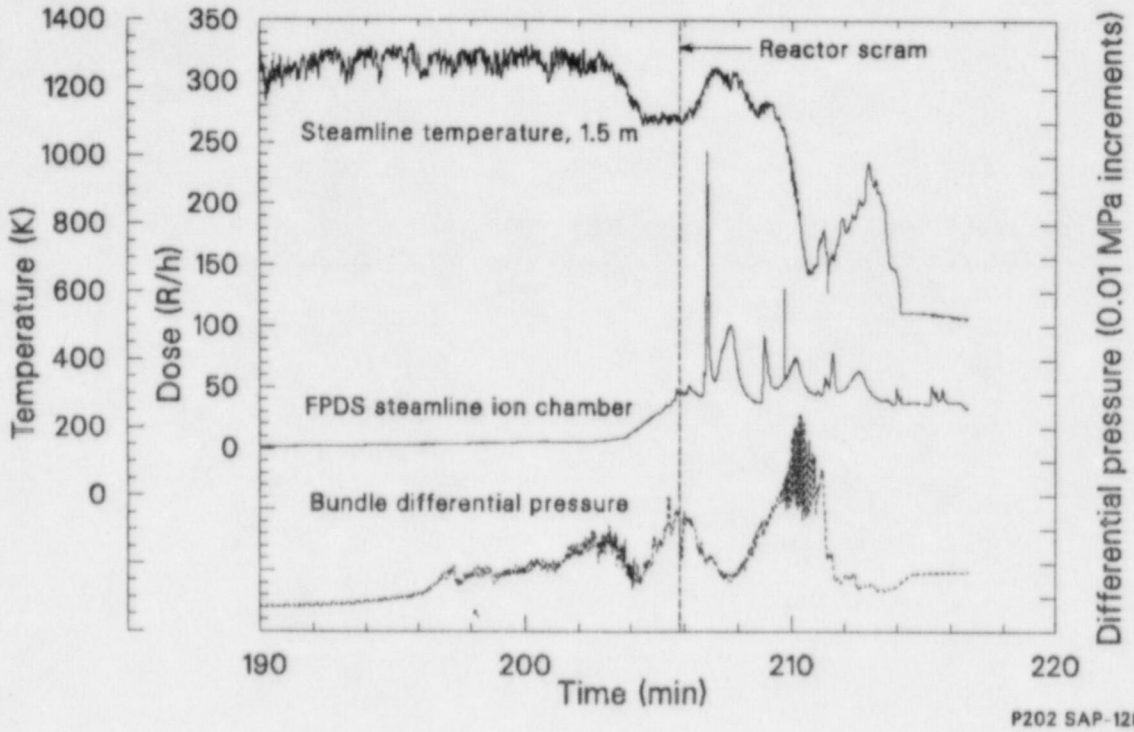

Figure 48. Overlay of steamline temperatures, gross gamma activity and bundle differential pressure during final phase of transient.

211-214 minutes. After the elevated portions of the bundle were wedged in place, coolant pressure was able evidently to wash out flow paths around the solidified melt mass and rod fragments through the extensively damaged insulation at the new elevation. Neutron tomographs confirm that insulation maintained its integrity at the original elevation of the flow restriction between 0.10- and 0.18-m elevations, whereas the insulation region was almost totally removed between 0.20 and 0.30 m.[9]

According to Figure 48, the bundle configuration stabilized shortly after 211 min. A minor differential pressure increase is shown at about 214 min, accompanied by a rapid fall in steamline temperature. However, Figure 44 demonstrates that these effects were caused by an inlet flow increase to 0.06 L/s that was related to a drop in separator pressure. The steamline temperatures in Figure 46 show that saturation conditions (556 K) were reached by 214 min.

Three elemental composition samples from the upper three-fourths of the bundle examined by SAS all showed hyperstoichiometric uranium oxides. The exact timing of the fuel oxidation cannot be established other than that it probably occurred during the cooldown phase (Appendix E). However, a recent calculation indicates that UO_2 can be oxidized beyond $UO_{2.2}$ in high pressure steam, but without a significant presence of hydrogen.[17] Substantial hydrogen release from the bundle is indicated in Figure 42 for the period after 211 min. However, as discussed in Section 4.9, there are significant uncertainties, both in timing and magnitude, associated with this measurement during the final phase of the test. The UO_2 was still at sufficient elevated temperatures to allow inward diffusion of oxygen after 211 min, with hydrogen being transported efficiently from the bundle.

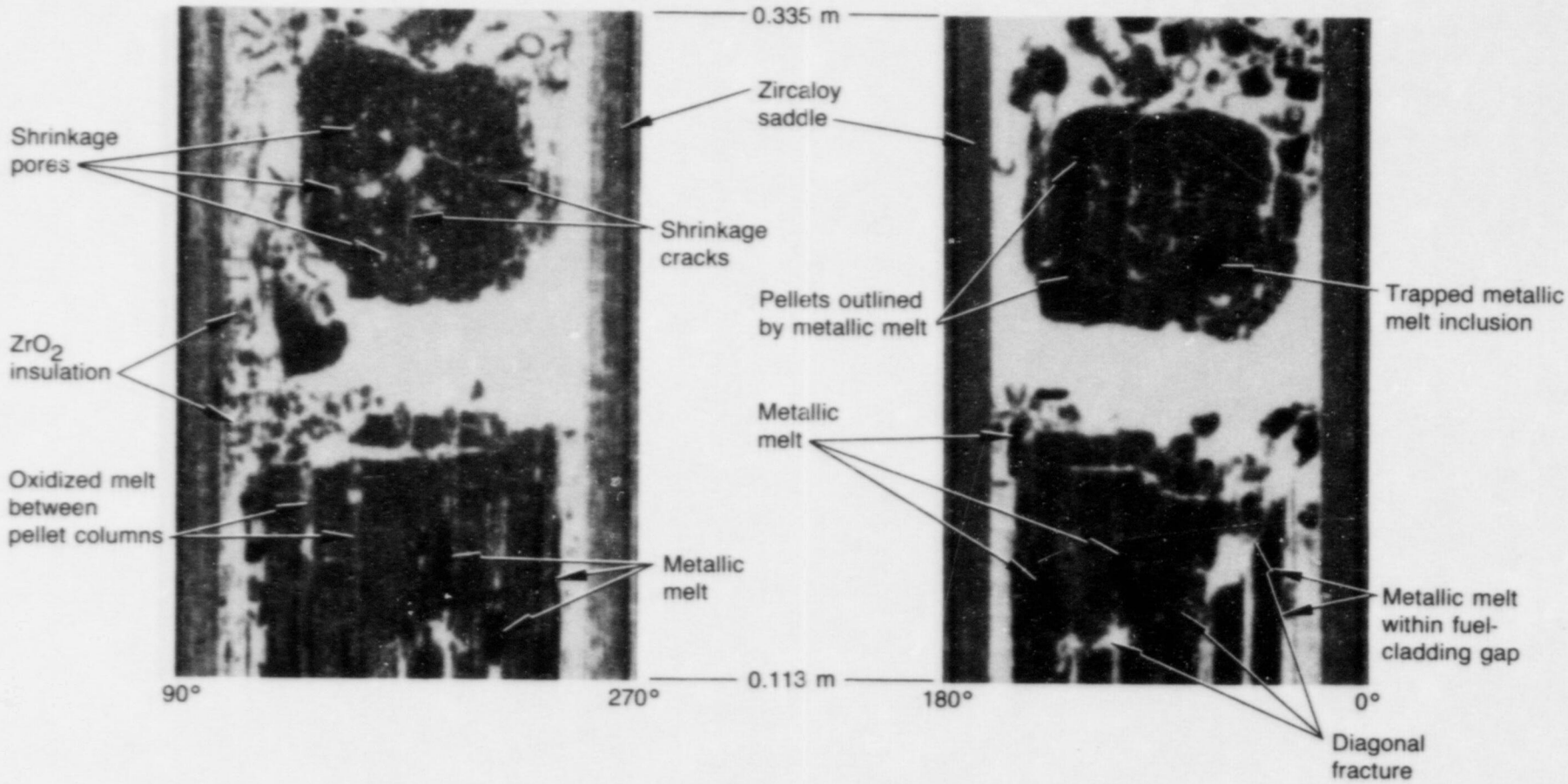

Figure 49. Axial tomographs at contrasting orientations between 0.113 m and 0.335 m.

5. FISSION PRODUCT BEHAVIOR

5.1 Overview

A comprehensive report that describes most of the fission product behavior information derived from the SFD-ST has been prepared.[11] The salient features are summarized in the following subsections, together with additional information from the postirradiation examination, SCDAP calculations, and a reassessment of tellurium behavior.

Fission product release during the SFD-ST can best be characterized with reference to the on-line gross radiation measurement of the effluent line. Figure 50 shows, to a first approximation, the integral fission product release from the test bundle as a function of time throughout the transient. This effective release has been divided into six phases, each with associated peak fuel temperatures and integral percentage release relative to the total measured up to about one hour after reactor scram. However, it is important to note that transport effects not accounted for in this analysis (discussed in a subsequent subsection) prevented precise correlation of the on-line fission product measurements to fuel behavior. The gap release and low temperature (<1700 K) diffusion phases amount to only 0.15% of the total at 270 min. High temperature diffusion, between peak fuel temperatures of 1700 and 2100 K, accounts for about 4%. Fuel liquefaction prior to reactor scram increased the release to 10%, with an additional unquantified contribution from liquefaction during the cooldown phase. The total amount of fuel liquefied during the Scoping Test was estimated to be 15 ± 3%. Assuming this originated from the center maximum power region of the bundle (i.e., maximum inventory), and that all fission products were released upon liquefaction, an upper limit of about 20% from this mechanism can be established. During the ∿8 min cooldown and reflood period, major release occurred due to a combination of processes including continued liquefaction, fuel oxidation, grain growth/separation, and formation of shrinkage cracks within porous prior-molten regions. By the time the bundle had been reflooded, and cooled to saturation temperature, 54% of the integral activity had been recorded. However, due to transit time uncertainties (Subsection 5.4), it is probable that a fraction of the cooldown contribution was released from the fuel during the high temperature liquefaction phase. The flushing process continued to extract further fission products from the bundle for several hours, in addition to resuspending species deposited within the system.

The measured iodine release fraction was 0.51 ± 0.08, the cesium and tellurium release fractions were 0.32 ± 0.05 and 0.40 ± 0.07 respectively, the barium release was about 0.01, and very small release fractions (10^{-4} - 10^{-6}) of low volatile fission products Ru, Sr, Nb, and Ce were detected downstream of the bundle. The integral noble gas release was not measured directly because the sampling apparatus was defective. However, integration of the spectrometer measurements of noble gas isotopes yielded an approximate average value of 0.5. The isotopic inventory calculations used to determine the release fractions are described in Reference 18. All volatile fission products released, except tellurium, were transported efficiently in the high velocity, steam-rich effluent stream. One fourth of the released tellurium was found irreversibly deposited on steamline walls, one-half in the liquidline particle filter, and the remaining one-fourth in the collection tank liquid.

The trace irradiation of the fuel used in the SFD-ST (91 MWd/T) was identified as the principal reason for the low release rates noted during heatup. Liquefaction of UO_2 by molten zircaloy at high temperature and fuel rod fracturing were initially identified as the principal reasons for the large release rates during cooldown and reflood. New information provided in this report has identified other possible reasons for the large releases. Reduced grain boundary adhesion in hyperstoichiometric fuel apparently aided microcrack formation during cooldown, which permitted gradual washout of fission products that accumulated at fuel grain boundaries. It also appears that some fission products were temporarily trapped inside closed melt porosity and were not freed until shrinkage cracks interlinked the pores and allowed coolant access.

Previous analysis[11] showed that low concentrations of fission products in the steam and hydrogen effluent would result in the formation of HI, CsOH, and H_2Te as the dominant chemical forms of the volatile fission

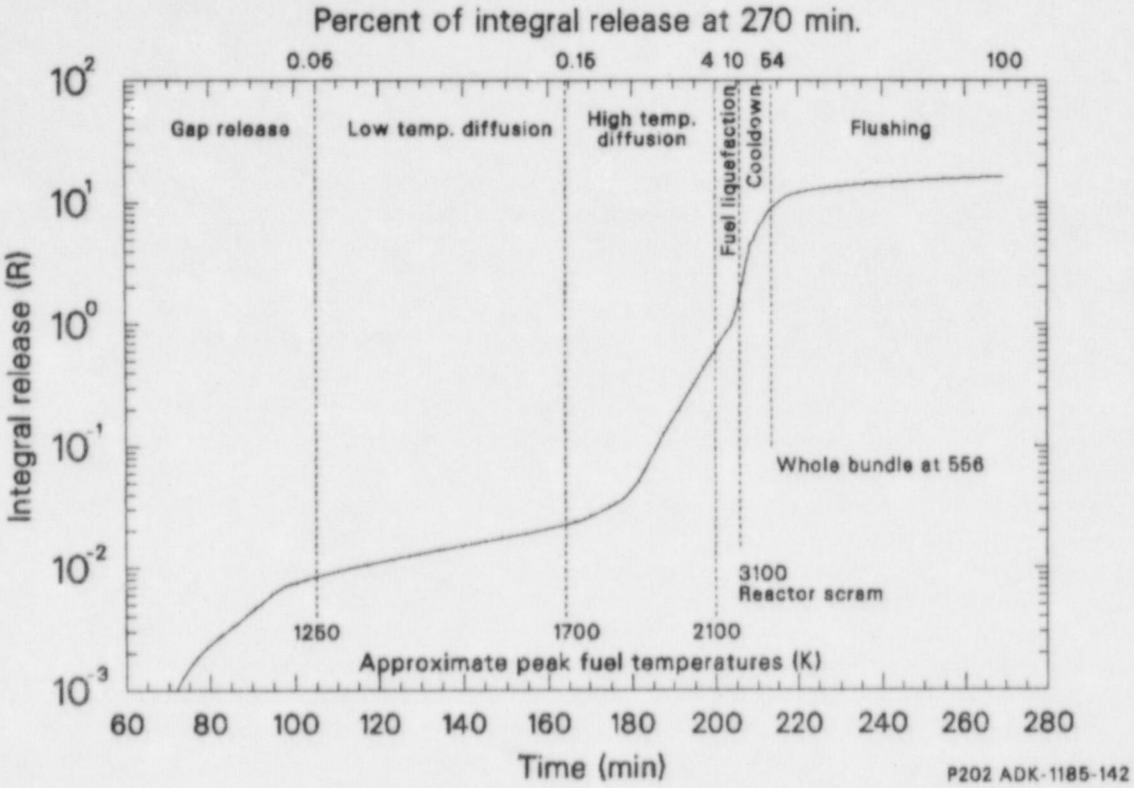

Figure 50. Overview of fission product release during SFD-ST based on ion-chamber gross activity measurement.

products. More recent analysis including a greater number of potential reaction species has identified SnTe as another probable form of tellurium. The tellurium behavior is discussed in some detail in Subsection 5.6.

Transport of fission products from the test bundle to the condenser was efficient during most of the test because transport times were short (~1-3 s) in this section of the system and condensation of volatile fission product vapors was prevented by high steamline wall temperatures. During cooldown and reflood, vapors condensed to aerosols that were carried downstream initially in gas and finally in the reflood liquid.

5.2 Fission Product Transit Time From Fuel Bundle to Detectors

The original fission product behavior analysis[11] relied upon a simplified model calculation using the inlet flowmeter data to estimate transit times from the fuel bundle to the various detectors. The model presumed that fission products, released into the sampling system, were transported through the various volumes in times dependent on the inlet flow modified only by thermal effects.

The evaluation of events in the SFD-ST, described in Section 4, necessitated a reexamination of the calculated transit times and the previously postulated fission product release correlations. To assess the significance of the assumed steam flow, the transit time calculations were essentially repeated using steam flow rates determined from the separator liquidline exit flowmeter. The calculation was again primarily based on the assumption of steady state conditions in the effluent lines such that the coolant density remained constant in time at any particular point in the system. However, density modifications were made in that portion of the line from the condenser to the separator based on the hydrogen content of the transported fluid, assuming the hydrogen and coolant were well mixed.

A major concern in the analysis was the possibility of steam condensation in the line prior to the condenser. The only available thermocouple measurement in this portion of the steamline (DARS 237)

indicated a temperature about 200 K below saturation throughout the transient. However, on the basis of the specified insulation around the ∿30 m of steamline between the bundle exit and condenser, and the measured exit temperatures, it was calculated that the gas temperatures should have been above steam saturation. The regions between the mid-bundle and separator, and the associated volumes, temperatures and densities are given in Table 10. The gas flow rate into the separator was taken as the sum of the constant nitrogen flow (0.74 g/s) and the on-line hydrogen measurement described in Subsection 4.9.

In addition to the calculations described above, an independent assessment of the transit times was provided using the spectral data from the on-line spectrometers. Each spectrum accumulated during the SFD-ST contained data from noble gas isotopes with half-lives ranging from a few minutes to a few hours. From the ratio of short- to long-lived noble gas activities in each spectrum, the decay time since release of the noble gas material from the test fuel was determined as described in Appendix G. This time, termed the average age of the material, is analogous to the calculated transit time, but does not depend on assumptions concerning plug or mixed flow and includes the effect of any unmodelled holdup or mixing. The calculation of the average age was performed for the time period of primary interest, from about 190 min until reactor scram.

The transit times to the gas and unfiltered liquid detectors, calculated using the inlet and outlet flowmeters, are plotted as a function of the test time in Figure 51. The difference between the two sets of calculations demonstrates the significant influence of the assumed flow conditions and participating volumes.

Figure 52 provides comparisons of the transit times derived from the flowmeter data and the fission product average age method for each of the three detectors. The large uncertainties associated with all three sets of age calculations, indicated by the error bars, should be noted. The gasline detector age data points are closest to the inlet flowmeter calculation until about 197 min, after which time the data tends to agree better with the outlet flowmeter values. The unfiltered liquidline age estimates are generally between the two flowmeter calculations. The filtered liquidline age estimates appear to confirm a general overestimation observed in Reference 11 in the transit times calculated using the inlet flowmeter.

The activities measured throughout the transient by the two liquidline detectors, corrected for transit times estimated using the inlet flowmeter, showed an average timing difference of 6.2 min during the heatup phase. The discrepancy was attributed to the inability to satisfactorily model the flow characteristics in the filter between the two detectors. The timing of the filtered liquidline activities was therefore adjusted by a constant 6.2 min in order to overlay the equivalent unfiltered values during the heatup phase. The filtered liquidline detector was the only spectrometer operational throughout the transient and is crucial in understanding fission product release during the important final high temperature phase, where peak temperatures increased by ∿1000 K.

Table 10. Transit time calculation parameters

Region	Volume (L)	Temperature (K)	Density (kg/m^3)
Mid-Bundle	2.00	1500	9.9
Fallback Barrier	0.47	1220	12.4
Line in Test Train	0.06	840	18.6
Standpipe	0.06	600	30.2
Steamline	1.95	560	36.2
Condenser to Separator	1.31	340	982.0
Separator to unfiltered liquid detector	2.35	340	982.0
Separator to gas detector	1.31	300	—

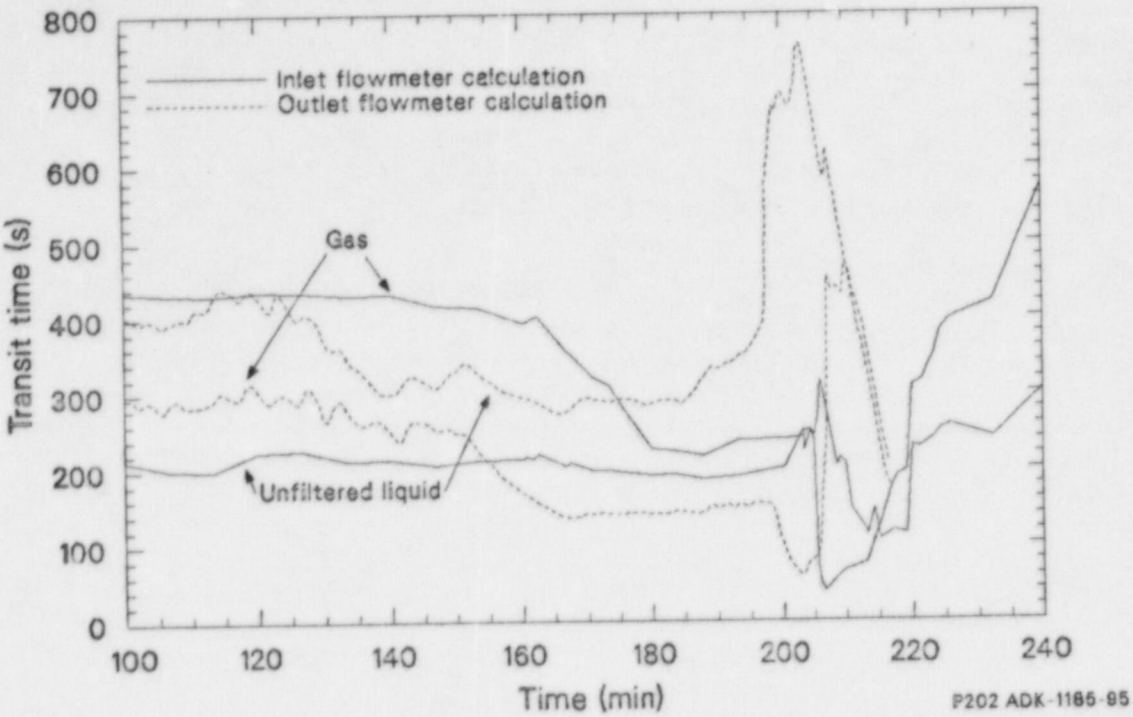

Figure 51. Calculated transit time from fuel bundle to gasline and unfiltered liquidline spectrometers as a function of test time.

For the purpose of the remaining discussion the applied transit times are based on the inlet flowmeter calculation and the additional 6.2 min offset for the filtered liquidline detector values. This is consistent with the data presented in the fission product behavior report.[11] To demonstrate the satisfactory relative consistency of the calculated transit times to the various detectors, typical examples of the measured activities are overlayed in Figure 53 for the period between 150 and 250 min. Noble gas isotopes have been used to illustrate the measured fission product release because these species are not complicated by deposition processes. The validity of the inlet flowmeter calculation, particularly during the final high temperature phase, will be considered further in Subsection 5.4.

5.3 Isotopic Fission Product Release

The three gamma spectrometers accumulated a total of 675 spectra during the transient and postscram phases of the test. Operational problems were encountered at the spectrometer control computer at 204 min, that affected the acquisition of data by the gasline and unfiltered liquidline spectrometers. Due to the transit time, this problem occurred before the enhanced fission product release during the final high temperature phase and resulted in a loss of 13 min of data. Although the liquidline spectrometer located downstream of the filter operated properly during the entire data acquisition period, 45 s of spectral data were not usable because of excessive count rates.

Analysis of the on-line spectral data was highly complex, involving several processing steps and computer programs. Details of the data processing techniques are presented in Appendix A of Reference 11. The processed data provided isotopic identifications, concentration profiles and activity flow rates. The principal focus of the results was the determination of effective release rate coefficients for the various fission product volatility groups during the heatup phase of the SFD-ST.

Analysis of each spectrum provides concentrations in microcuries per cubic centimeter for each detected nuclide. Approximately 100 different isotopes were identified in the SFD-ST spectra and are presented in

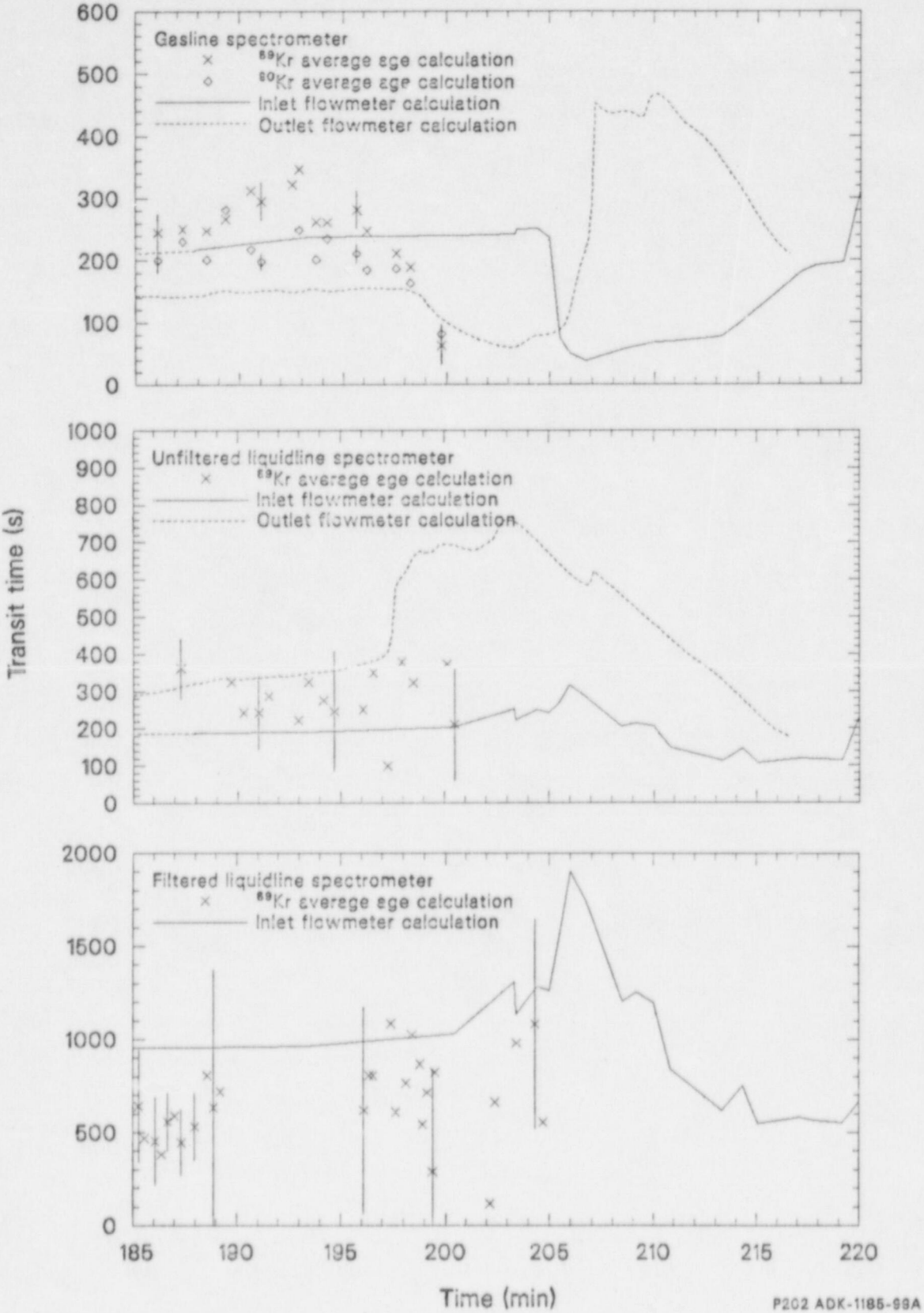

Figure 52. Comparison of the various estimates of transit time from fuel bundle to the three spectrometers as a function of test time.

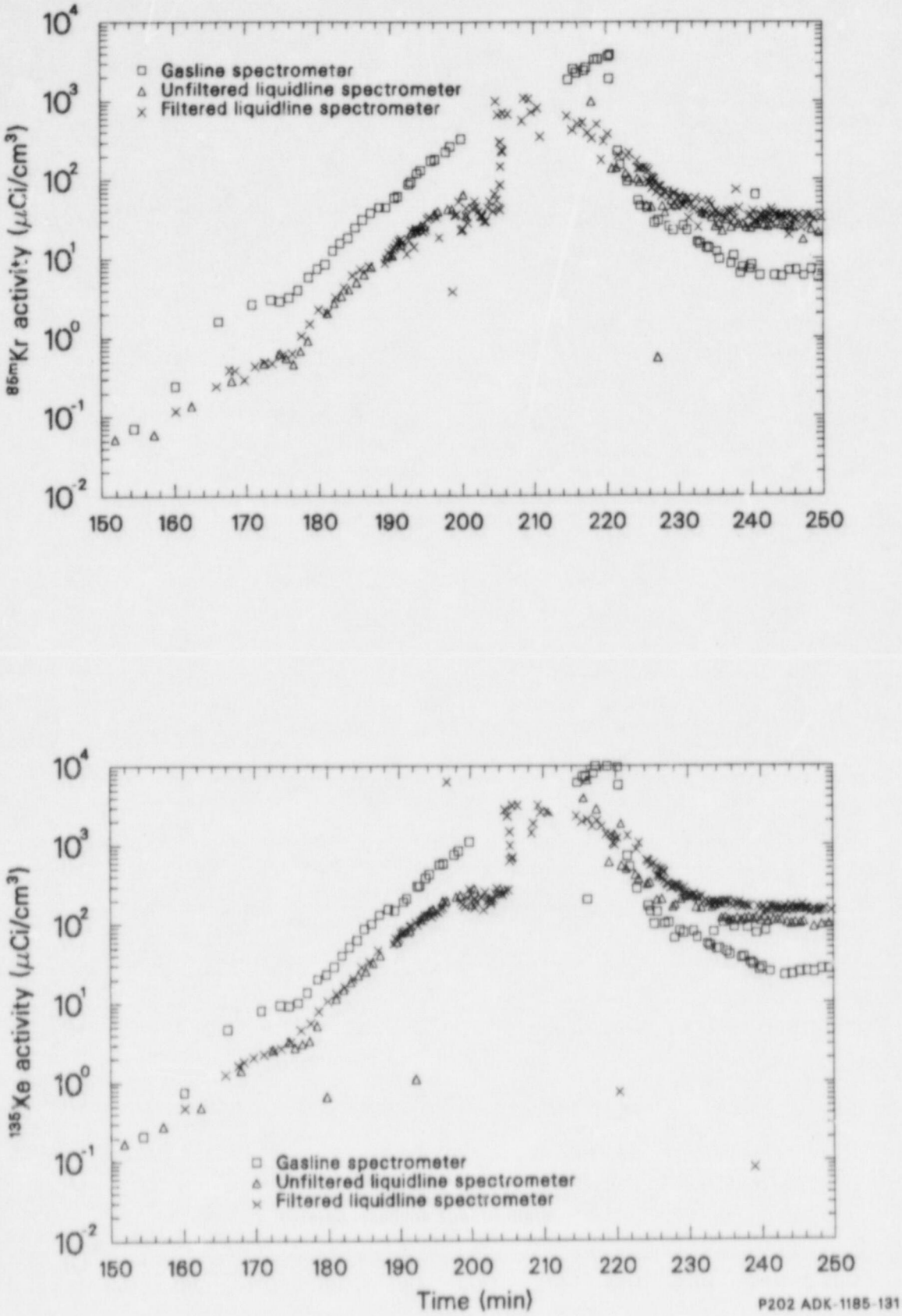

Figure 53. Overlays of typical noble gas data recorded by the three spectrometers as a function of test time.

Reference 11. Figure 54 is an example of the concentration history data accumulated for ^{131}I at the liquid detector located downstream of the particle filter. Activity flow rates at each detector location were calculated from the measured concentrations and estimated volumetric flow rates. Figure 55 shows the ^{131}I data activity flow rate as determined from the concentration presented in Figure 54 and the transit times calculated using the inlet flowmeter data with the 6.2 min offset.

A family of effective release rate constants was developed for the heatup portion of the transient. The constants were determined by a technique that employed calculation of predicted activity flow rates, comparison to measured activity flow rates and iteration until predicted values agreed with the measurements. The effective release rate coefficients that were found to best describe the measured fission product data are shown in Figure 56. The elemental group structure used in the analysis was based on the NUREG-0772[19] grouping, but revised on the basis of the observed behavior in the SFD-ST.

The effective release rate coefficient (K_{eff}) is defined as the fraction of the bundle inventory observed per minute at the detector location. The units and applications of K_{eff} are similar to the NUREG-0772 release rate coefficients for fission product release from fuel. However, it is important to note the SFD-ST measured K_{eff} values include effects of test conditions, transport, and detectability.

While the representation of release rates versus time is relatively unambiguous, the choice of a representative temperature scale for plotting the release data is not straightforward. The SFD-ST fuel bundle exhibited axial and radial variations in temperature, and axial and radial power profiles that resulted in significant local variations in fission product inventory throughout the bundle. Consequently, a model to compute an inventory for the entire bundle and then present fractional releases versus a single fuel temperature is inherently inaccurate. Nevertheless, the maximum error expected from such a simplification is less than one order of magnitude. Plotting the effective release rate constants versus the peak fuel temperature provides correlations to temperature dependent phenomena such as cladding breach, zircaloy oxidation, zircaloy melting and fuel liquefaction, which contribute to rate constant changes. Correlation of release rate enhancements with zircaloy oxidation and/or liquefaction is facilitated if the effective release rate coefficients are plotted on a temperature scale that indicates onset of these events in bundle. A best estimate of the peak fuel temperature during the transient was established from the composite of the thermocouple and PIE data, together with the SCDAP analysis (Subsection 4.8.3, Figure 40). The effective release rates as a function of these peak temperatures are presented in Figure 57.

Sweeping of the gap inventory from the bundle dominated fission gas release for nearly 45 min, until the bundle attained a peak temperature of 1500 to 1600 K. Diffusional release from the fuel matrix then started to dominate, as indicated by increasing effective release rate coefficients. The effective release rate coefficients continue to increase exponentially until the peak fuel temperature reaches about 1950 K, when a pronounced levelling is noted. This relative flattening of the release rate curves may be due to relocation of material within the bundle, to the absorption of fusion heat upon zircaloy melting, or to a change in the fission product inventory/fuel morphology relationship. However, it is also possible that the behavior is not a true bundle phenomenon but a consequence of the thermal-hydraulic conditions within the system as discussed in the following subsection. For this reason the effective release rate coefficients have not been correlated to peak temperatures above 2100 K in Figure 57.

The release rate values developed from the SFD-ST data are perturbed by various transport effects. The effective release rate coefficients (K_{eff}) measured for the noble gas isotopes may have been perturbed by holdup in the fuel-cladding gap or stagnation in the transport system, but they were not complicated by deposition processes. To assess the potential magnitude of the release and transport effects, the noble gas effective release rates are compared with the release rates of NUREG-0772, which form the basis for the CORSOR[20] model. To account for local variations in bundle temperature and fission product inventory, the NUREG-0772 release rate constants were applied to a model of the fuel bundle having ten axial nodes. The fuel temperature at each node was taken from the best estimate SCDAP calculations described in Section 6. The fission product inventory was distributed among the axial nodes according to the PBF axial power profile for a flooded bundle. The noble gas release rate from the total bundle at a given time was calculated by applying the noble gas release rate constant from NUREG-0772 appropriate for the temperature of each

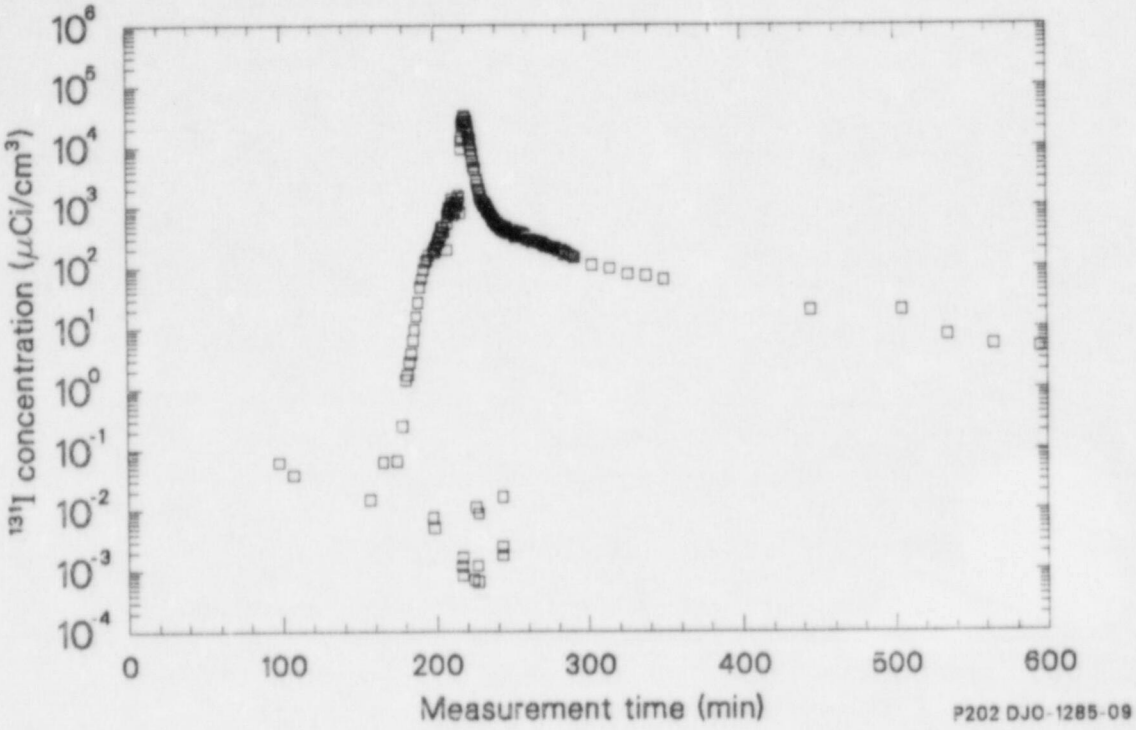

Figure 54. Concentration data for ^{131}I accumulated by filtered liquidline spectrometer as a function of measurement time.

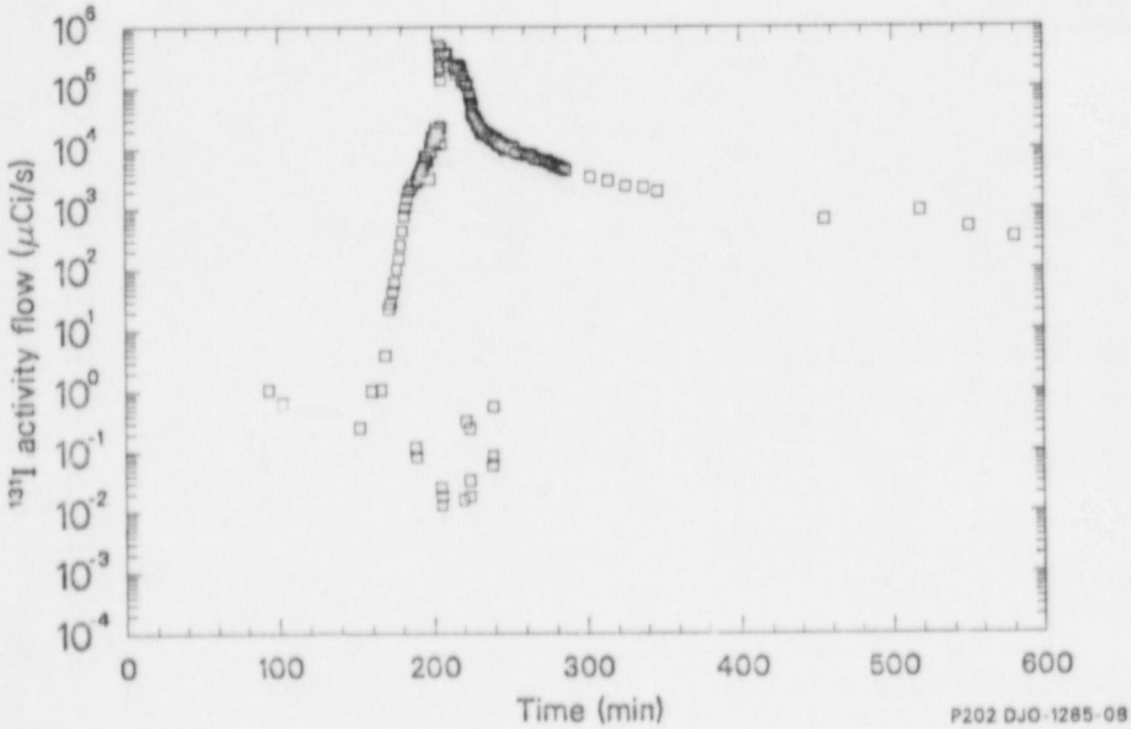

Figure 55. Activity flow rate for ^{131}I from filtered liquidline spectrometer as a function of test time.

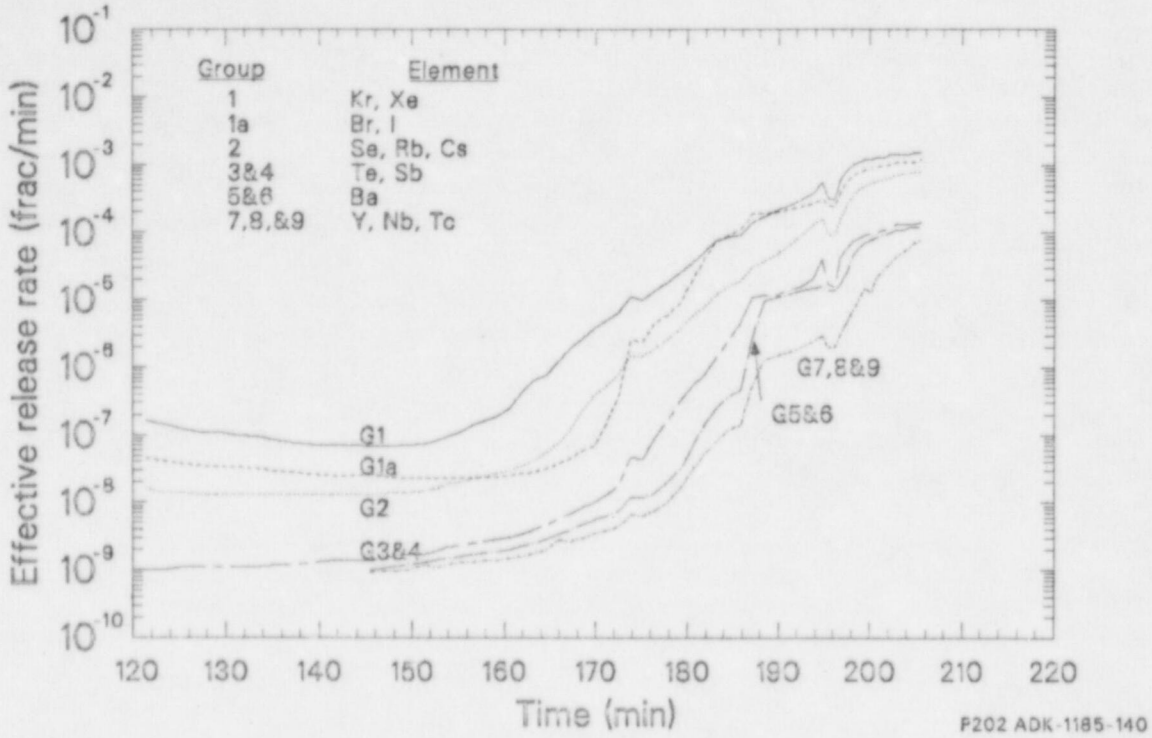

Figure 56. SFD-ST effective release rate coefficients as a function of test time.

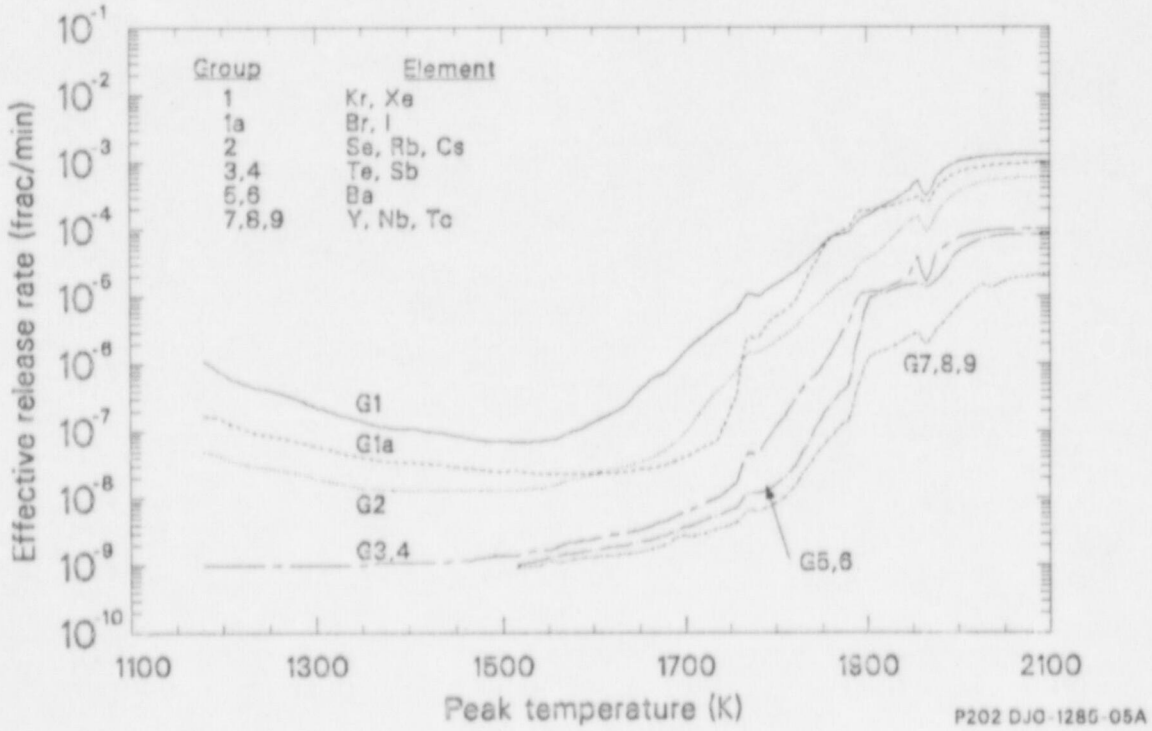

Figure 57. SFD-ST effective release rate coefficients as a function of peak temperature.

node to the nodal fission gas inventory and summing the response of all ten nodes. The result of this analysis method is a curve of average bundle response versus time based on NUREG-0772 predictions that can be compared with the measured values up to 200 min. This comparison, with associated errors, is presented in Figure 58. The measured release rate curve is over three orders of magnitude below the NUREG-0772 prediction at low temperatures during the heatup phase, decreasing to about one order of magnitude at 200 min when the peak and average bundle temperatures were about 2100 K and 1500 K, respectively. The low burnup of the SFD-ST fuel, where open porosity and release paths had not developed, was the probable major reason for the lower release rates.

5.4 Fission Product Release During the Final High Temperature Phase

The final high temperature phase of the transient, when peak fuel temperatures increased from about 2100 K to fuel melting temperatures of up to 3120 K, was discussed in Subsection 4.10. The implications of the possible events on the measured fission product release are described here.

The FPDS incorporated four gross gamma detectors, one NaI(Tl) detector at each of the three spectrometer locations and an ion chamber located on the steam effluent line at the condenser inlet. Unfortunately, the NaI(Tl) detectors were not sufficiently shielded and therefore followed the general Cubicle 13 background until the count rate saturated. However, the ion chamber responded to the steamline radiation levels. Figure 59 shows the responses of the three NaI(Tl) detectors up until saturation and the gross ion chamber. Little fission product release was noted prior to 185 min, when peak and average bundle temperatures were about 1900 K and 1400 K, respectively.

Delayed neutrons emitted from fission products transported to Cubicle 13 generated capture gamma-rays through interactions with the cadmium shielding around the detectors. Figure 60 is a relative intensity profile constructed from the three spectrometer measurements of the ^{114}Cd 558 keV capture gamma-ray. The

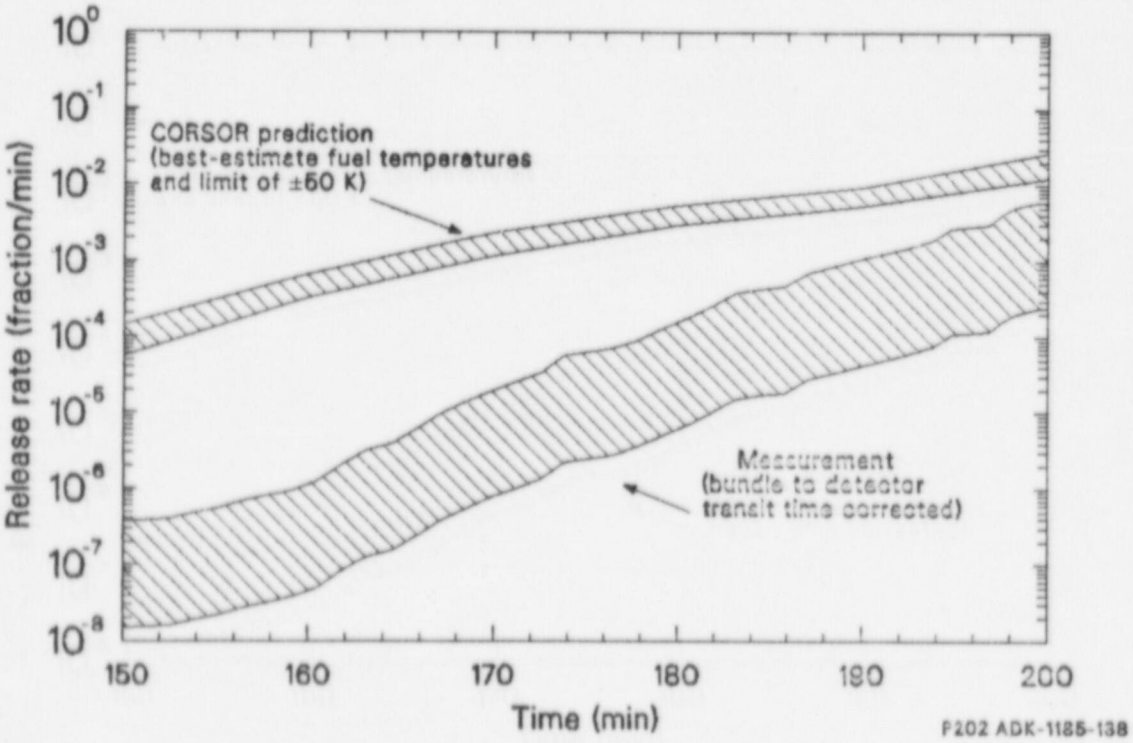

Figure 58. Measured and predicted noble gas release rates as a function of test time.

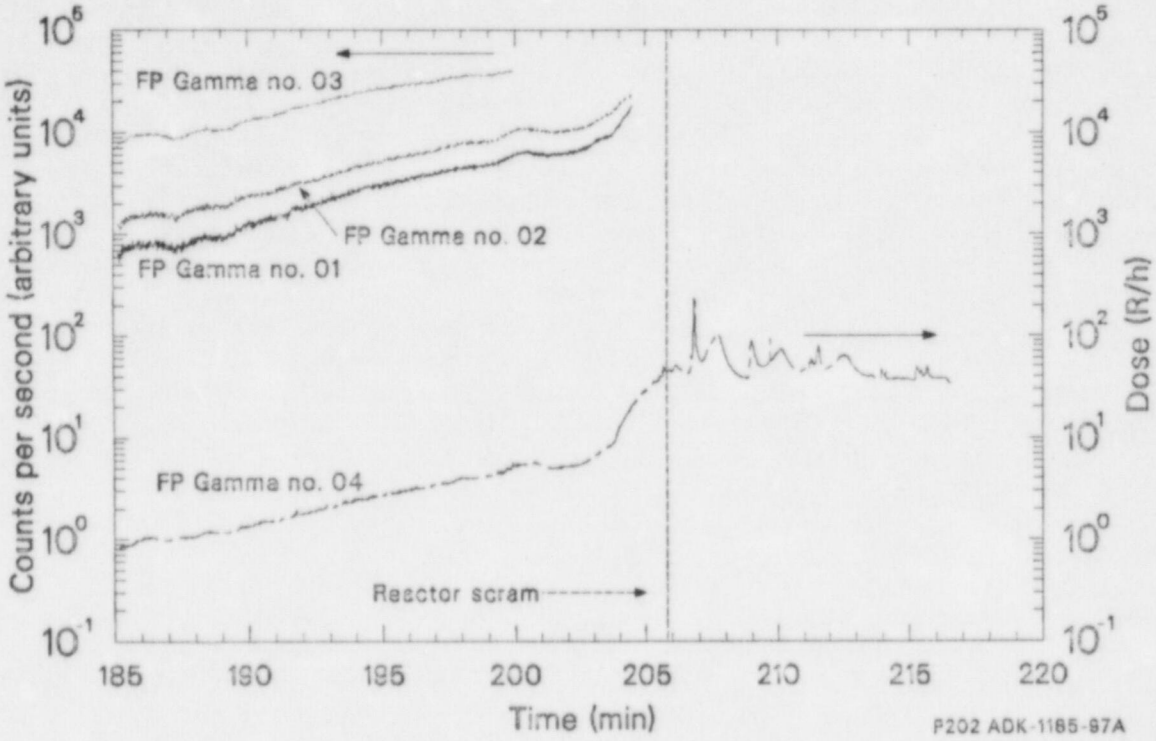

Figure 59. Response of the gross gamma detectors.

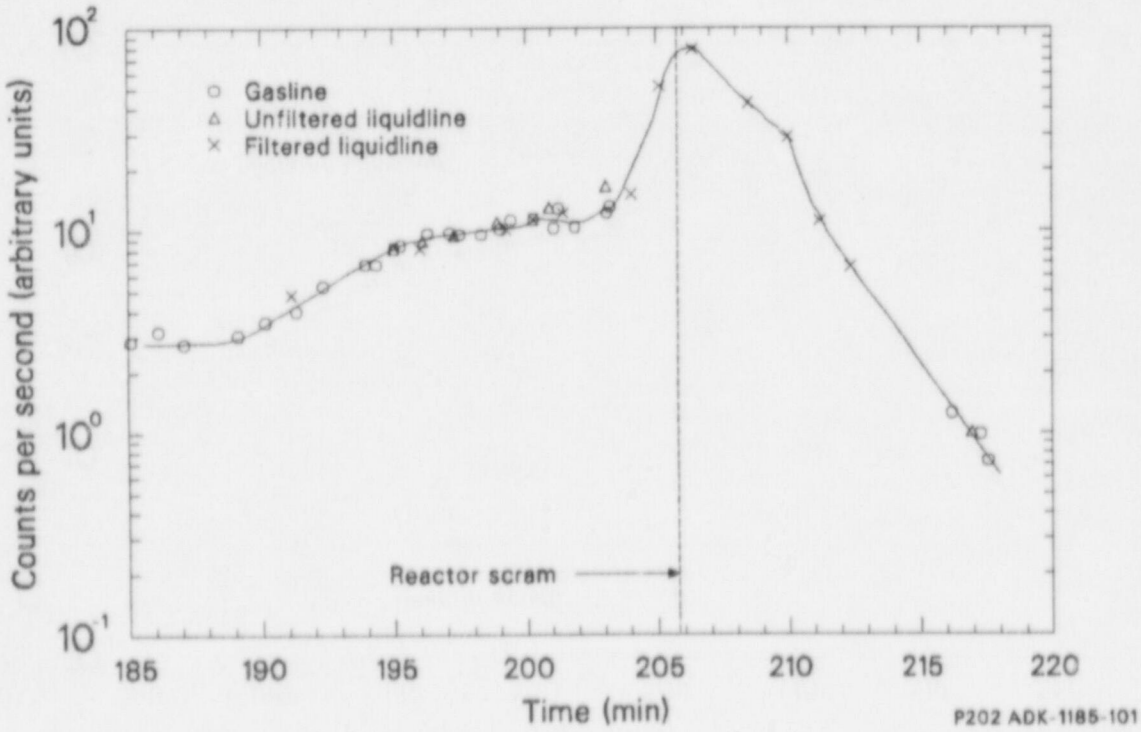

Figure 60. Effective delayed neutron measurement.

transport time from the bundle to Cubicle 13 and the gross ion chamber under high flow conditions was estimated to be 1-3 s and therefore no corrections have been applied to the plots in Figures 59 and 60. Selected noble gas activities measured by the filtered liquidline detector, and transit time corrected as described in Subsection 5.2, are provided for the same time period (Figures 61 and 62).

From about 200 min to 202.5 min, when bundle temperatures are believed to have been increasing rapidly, nearly constant values were recorded by the gross gamma detectors (Figure 59) and deduced for the effective delayed neutron measurement (Figure 60). The filtered liquidline spectrometer results (Figures 61 and 62) indicate a period of constant fission product activity extending from about 200 min to 205 min, followed by an order of magnitude step increase. As demonstrated by the various transit time calculations (Figure 52) the release times of fission products are very uncertain after 200 min. The measured order of magnitude increase in effluent activity that appears to occur at about the time of reactor scram (Figures 61 and 62) may be somewhat misleading because of the uncertainty in the transit time. The large releases probably commenced gradually several minutes prior to scram as indicated by the ion chamber measurement (Figure 59). Nevertheless, on the basis of the inlet flowmeter transit time calculations, which are generally supported by the age estimates, the majority of the fission product release occurred during the cooldown and reflood phase. The mechanisms responsible for this release are not certain, but some possible phenomena have been identified and investigated.

Insights into the timing of events during the final phase of the test were provided by the posttest metallurgical examination of the bundle. It was postulated in Subsection 4.10 that dissolution of fuel by molten cladding ended at about 205 min and allowed oxidized melt to slump and accumulate prior to scram. The amount of fuel liquefied after scram was small and the total liquefaction throughout the transient was about 15% of the initial pellet volume. Thus, liquefaction of fuel by molten zircaloy cannot alone explain the large measured cooldown release. Reduced flow through the bundle contributed to delayed detection of released fission products. It is also probable that some fission products were temporarily held within molten material, gradually emerging by liquid-state diffusion, gas bubble migration, and steam/water flow through interlinked pores and shrinkage cracks. Reversible fission product deposition on structural surfaces (especially during low flow) and later resuspension also contributed to the delayed release from the bundle.

In Subsection 4.10 it was suggested that the observed steam oxidation of UO_2 occurred during after 211 min following the peak zircaloy oxidation and hydrogen generation period, and before single phase liquid was flowing in the steamline. The amount of fuel affected by this phenomenon cannot be estimated from the existing data base and its precise impact on the fission product release is not known. However, as discussed in Subsection 4.8, hyperstoichiometric fuel appears to be associated with diminished grain boundary adhesion and formation of microcrack networks that would permit fission product release from nonliquefied fuel during cooldown.

5.5 Total Fission Product Release

Both the collection tank and the knockout drum received effluent during the test, and reference to the collection tank contents refers to the sum of these two sources. The analyses performed on the collection tank contents, coupled with analyses of the steamline and filter contents, define the total measured release fraction for the detected nuclides. Table 11 presents this information by major component. No data are presented for the fission gas nuclides because the collection tank gas space sampling system did not function properly. Estimates of the total noble gas release were made from on-line measurements and comparisons to other volatile radionuclide releases. The total bundle release fractions given in Table 11 were determined from the various sample measurements and extrapolation to account for unmeasured sources (e.g. irreversible plateout on piping surfaces that were not examined).

Of the nuclides listed, only tellurium was found in larger fractions in the steamline and filter debris than it was in the collection tank liquid. A detailed description of the off-line fission product results, is provided in Reference 8.

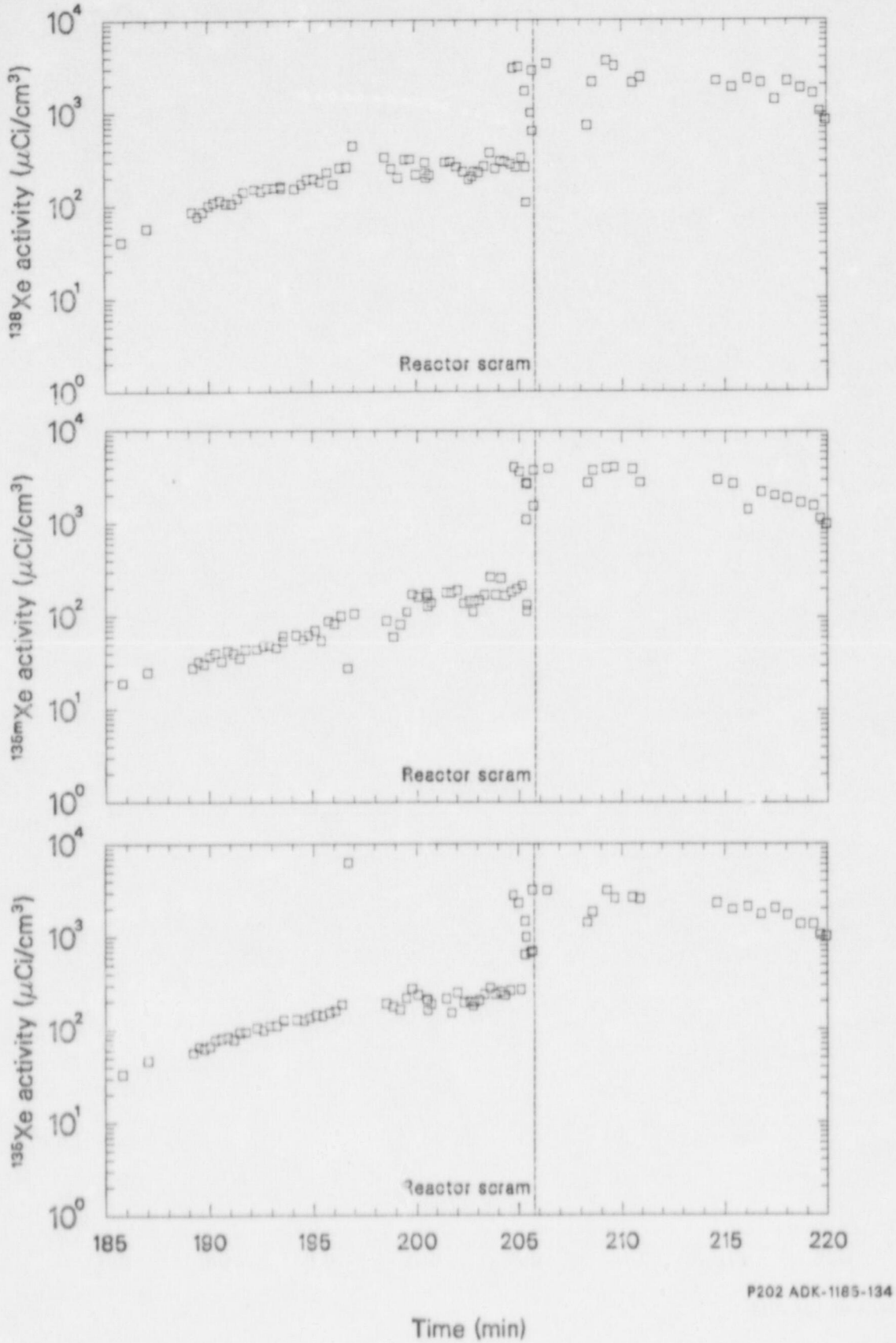

Figure 61. Activity of typical Xe isotopes measured by the filtered liquidline spectrometer as a function of test time.

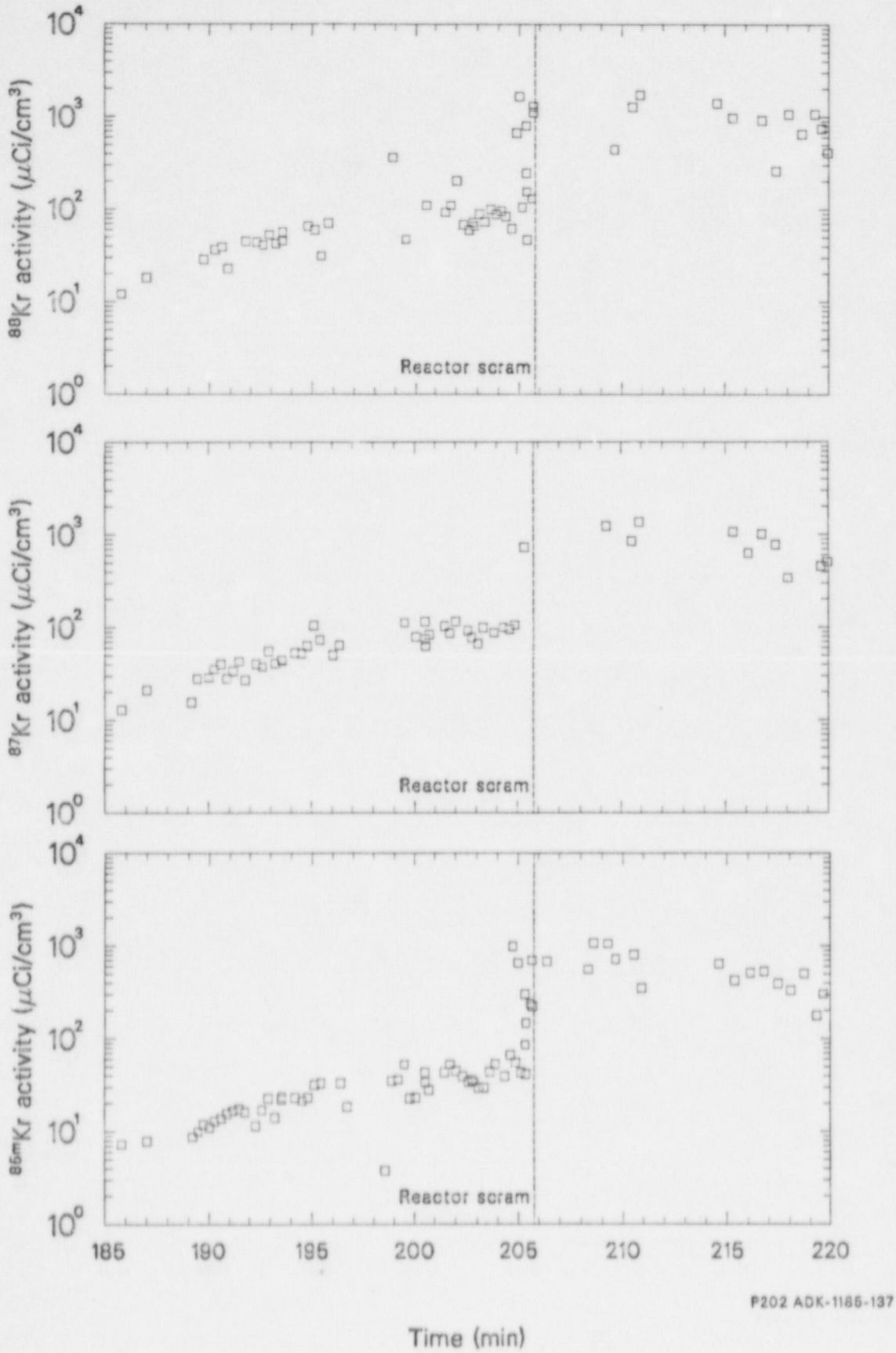

Figure 62. Activity of typical Kr isotopes measured by the filtered liquidline spectrometer as a function of test time.

Table 11. Measured isotopic release as fraction of total bundle inventory

Isotopes	Component[a] Irreversible Steamline Deposition (50%)	Steamline Grab Samples (15%)	Liquidline Filter (25%)	Collection Tank[b] (17%)	PBF Loop Water (15%)	Total
^{90}Sr	—	—	1.6×10^{-5}	—	—	$1.6 \pm 0.4 \times 10^{-5}$
^{95}Nb	6.4×10^{-6}	—	3.3×10^{-6}	—	—	$9.7 \pm 3.3 \times 10^{-6}$
^{103}Ru	6.6×10^{-5}	—	5.8×10^{-5}	1.7×10^{-4}	—	$2.9 \pm 0.5 \times 10^{-4}$
^{113}Sn[c]	5.6 mCi	—	2.3 mCi	—	—	7.9 ± 2.9 mCi
^{129m}Te	10.2×10^{-2}	7.6×10^{-5}	19.6×10^{-2}	9.8×10^{-2}	—	$4.0 \pm 0.7 \times 10^{-1}$
^{131}I	5.3×10^{-4}	3.6×10^{-4}	8.3×10^{-3}	49.4×10^{-2}	5.0×10^{-3}	$5.1 \pm 0.8 \times 10^{-1}$
^{136}Cs	—	—	2.5×10^{-2}	32.2×10^{-2}	—	$3.5 \pm 0.6 \times 10^{-1}$
^{137}Cs	1.6×10^{-3}	2.3×10^{-4}	1.6×10^{-2}	27.8×10^{-2}	8.0×10^{-4}	$3.0 \pm 0.5 \times 10^{-1}$
^{140}Ba	1.2×10^{-3}	5.7×10^{-7}	1.0×10^{-3}	8.7×10^{-3}	6.7×10^{-5}	$1.1 \pm 0.2 \times 10^{-2}$
^{141}Ce	—	—	2.2×10^{-6}	—	—	$2.2 \pm 0.6 \times 10^{-6}$

a. Value in brackets for each component is estimated uncertainty at one standard deviation confidence level.

b. These data include both collection tank and knockout drum contents.

c. Activation product.

The uncertainties on the measured fission product releases from the bundle, quoted at one standard deviation (1σ) confidence level, were dependent on the uncertainties in the various components used to calculate the final values in Table 11. The fractional uncertainty on each component was determined by combining, in quadrature sum, the fractional uncertainties of the various terms used in the calculation. For example, the liquid volume of the collection tank was measured to ± 10%; the sample volume was known to ± 1%; the radioisotope content of the sample was determined from the gamma spectrum analysis within ± 10%; the accuracy of the ORIGEN2 calculated bundle inventory was dominated by the uncertainty in the input bundle power history of ± 10%. When combined, these values yielded the ± 17% uncertainty on the collection tank component shown in Table 11. The uncertainties in the other components were estimated similarly, and found to be ± 50% for the steamlines, ± 15% for the steam samples, ± 25% for the filter content, and ± 15% for the PBF loop water. The uncertainty in the total release fraction was determined by combining, in quadrature sum, the individual numerical uncertainties of each component. Except for the case of tellurium, the uncertainties in the collection tank component dominated the total release fraction uncertainty.

As a check on the measured collection tank content the total release of ^{131}I to the collection tank was computed by integration of the curve in Figure 55. By this method the integral ^{131}I release was 389 Ci, corresponding to a release fraction of 0.43 of the estimated bundle inventory. This agrees closely with the release of 0.51 ± 0.08(1σ) determined posttest and provides confidence in the error analysis. Integral releases were not computed using this technique for elements other than iodine.

5.6 Tellurium Behavior

The behavior of tellurium during the SFD-ST is particularly noteworthy. Large fractions of the bundle inventory of ^{129m}Te were found in the effluent downstream of the bundle.[8] The total bundle release fraction of 0.40 ± 0.07 was distributed between the filter debris (0.2), the collection tank liquid (0.1), and irreversible deposition on steamline surfaces (0.1). It has been proposed that tellurium is highly reactive with metallic zircaloy and may be held up during severe accidents by formation of tellurides. Zircaloy is 98% zirconium and 1.5% tin, therefore ZrTe and SnTe formation are probable. It is believed that during oxidation of zircaloy, tin telluride and tellurium compounds are concentrated in the unoxidized zircaloy so that vaporization is enhanced. Zircaloy oxidation in the SFD-ST was extensive and is therefore valuable in studying the behavior of tellurium. End state tellurium data from the test generally support the theory, and thermo-chemical equilibrium calculations based on the SFD-ST conditions predict SnTe when tin is available and H_2Te formation if tin is not available. However, Te and TeO are also possible forms of vapor species at high temperatures.

A thermoequilibrium analysis was performed with the SOLGASMIX[21] code for the five component (Te-O-H-Sn-Zr) system. The range of parameters used in the study is given in Table 12. The H/O and Te/H_2O mole ratios are based on known test conditions, while the Sn/Zr ratio was based on volatility considerations (i.e., normal boiling points Te = 1263 K, Sn = 2873 K, Zr = 4673 K), and the Te/Sn ratio was varied to assess both a tin rich and tin deficient environment.

Calculational results are presented in Figure 63 for the principal Te-bearing species (i.e., Te, Te_2, H_2Te, TeO, TeOH, and SnTe). Figure 63(a) presents calculational results for a low Te/Sn ratio (0.1) and Figure 63(b) illustrates the strong temperature dependence of tellurium compound formation when the Te/Sn ratio is 10. It is first noted that for the tin rich environments (Te/Sn = 0.1) essentially all Te is predicted to exist as SnTe, with no contribution from other species, such as Te_2 and H_2Te. For tellurium rich environments at a Te/Sn ratio of 10, Te combines with Sn at 1500 K to its limit of ∼10%, the remaining ∼90% Te being in the forms of H_2Te and Te. This analysis was limited to a single Sn/Zr ratio of 10. For lower ratios, some zirconium species may also be predicted (e.g. $ZrTe_2$ or $ZrTe_3$). However, the lower vapor pressure of zirconium relative to tin suggests that low Sn/Zr ratios are not probable.

This analysis indicates that tin-telluride formation can have a pronounced effect on Te release behavior. Although positive identification of SnTe compounds has yet to be determined from sample analysis of the PBF-SFD test debris, indirect evidence supports such compound formation. Analysis of test debris samples trapped in both the SFD-ST steamline and filter indicated the likely presence of TeO_2, Te^{-2}, and metallic

Table 12. Parameters for Te-O-H-Sn-Zr thermoequilibrium analysis

Parameter	Values
Steam temperature (K):	2500, 1500, 1300, 1000, 500
Pressure (MPa):	7.0
H/O mole ratio:	2.06
Te/H_2O mole ratio:	10^{-9}
Te/Sn mole ratio:	0.1; 10.0
Sn/Zr mole ratio:	10

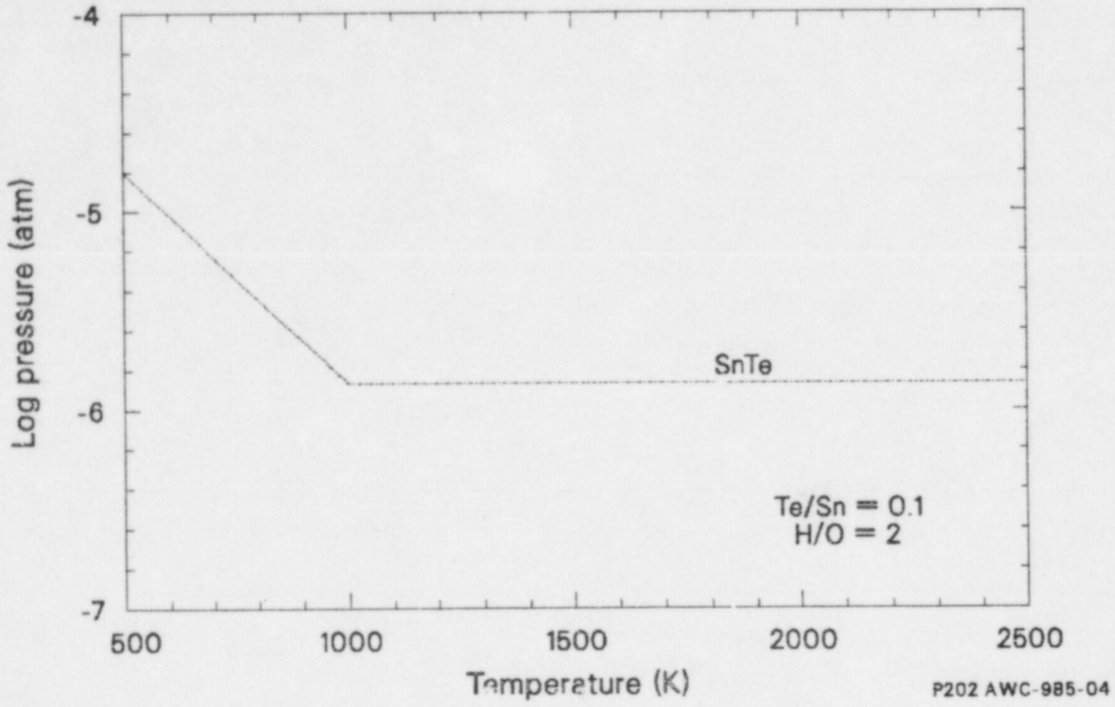

(b)

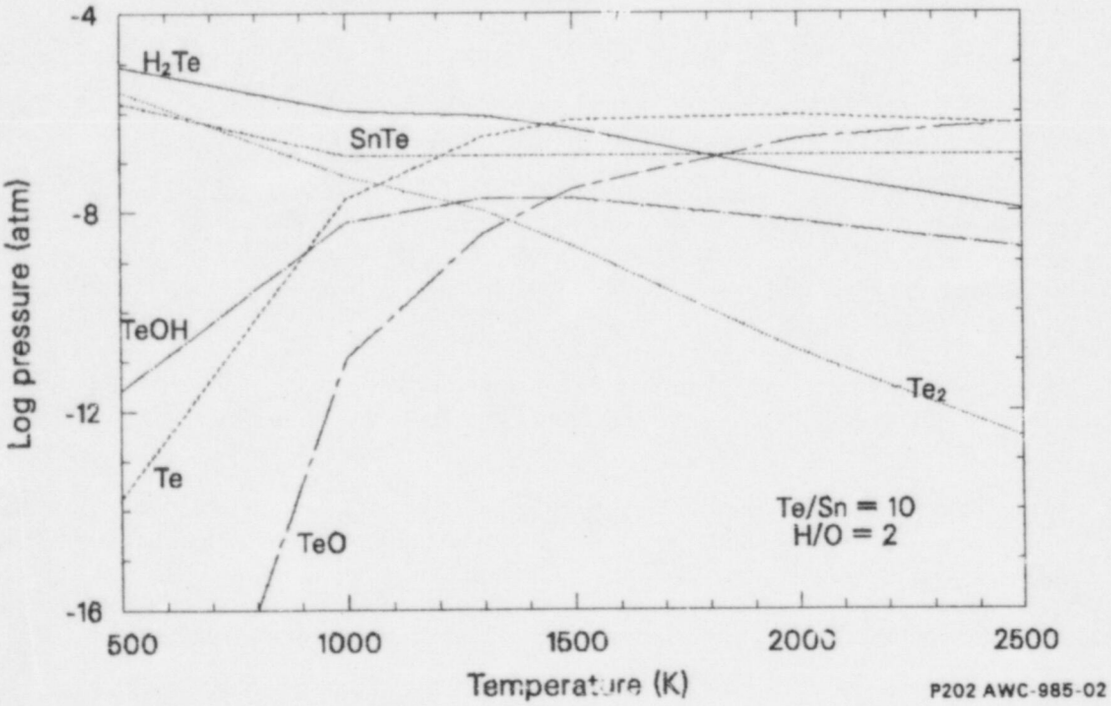

(a)

Figure 63. Predicted partial pressures of volatile Te species at high temperatures for the Te-O-H-Sn-Zr system.

tellurides[8]. Emission spectroscopy of the filter debris indicated 9 to 14 wt% of tin, and radiochemical analysis of the debris identified significant levels of ^{113}Sn and ^{129m}Te. The fact that a significant fraction of the debris was composed of Sn together with Te suggests SnTe compound formation.

The transport and deposition measurements from the SFD-ST suggest the likely presence of both SnTe and H_2Te. Of the released tellurium (40% of bundle inventory), half was collected as particulate in the liquidline filter. Since SnTe is not very soluble in water, the collected particulate was probably SnTe. The other half of the released tellurium was split evenly between tellurium found in the collection tank liquid and insoluble, deposited tellurium on steamline surfaces. Both H_2Te and SnTe would be expected to deposit on surfaces, but only H_2Te is likely to react with the stainless steel steamline wall. SnTe would form a film, with bonding that is a function of the condition (clean or covered with salts) of the wall surface. Very fine particles of SnTe and soluble reaction products of H_2Te would have been washed to the collection tank, with larger particles of SnTe collected in the filter.

This analysis suggests that tellurium chemical forms other than just SnTe existed during the SFD-ST. The Te/Sn ratio in the trace irradiated bundle is expected to be closer to 0.1 than 10. However, the observed behavior is consistent with the thermo-chemical equilibrium analysis presented in Figure 63(b) which suggests that H_2Te, TeO and Te could be formed as well as SnTe.

5.7 Retained Fission Products

Ten samples were extracted from the bundle cross sections for estimating posttest retention of ^{90}Sr, ^{95}Nb (daughter product of ^{95}Zr), ^{106}Ru, ^{125}Sb, ^{137}Cs, and ^{144}Ce. The samples consisted of two types: small cylinders core-drilled from five isolated bundle positions, and thin layers ground off five bundle cross sections. Fifteen samples were also taken from the fallback barrier to investigate fission product deposition just above the bundle. Appendix F contains detailed discussions on sample locations, analytical methods, measured fission product concentrations, and whole-bundle inventory extrapolations. Related information on sample compositions, temperature determinations and transient fuel behavior processes are presented in Subsection 4.10 with supporting detail in Appendix E.

Retention fractions measured in the core-drilled samples are given in Table 13, which contains the following noteworthy findings:

1. Sample 4F, from a fuel pellet that was neither penetrated by molten cladding nor heated above 2000 K, released an appreciable portion of its ^{125}Sb inventory. Antimony also deposited irreversibly in relatively large amounts on Sample 19S (oxidized zircaloy). Since ^{125}Sb was not detected in significant quantities beyond the base of the fallback barrier, it can be concluded that this isotope migrated only short distances.

2. Sample 19T, taken from a molten fuel region that attained a peak temperature of ~3000 K, revealed smaller retentions than the intact pellet Sample 4F for all species except ^{90}Sr. The largest indicated releases are noted for ^{137}Cs and ^{106}Ru.

3. Samples 4H and 4D taken from prior molten regions yield large retention fractions (greater than unity in most cases) for ^{90}Sr, ^{95}Nb and ^{144}Ce. The molten material was originally located at upper elevations in the test bundle and flowed down past higher inventory regions to solidify at the 0.15 m location. Normalizing fission product retention values to the inventory calculated for the 0.15 m elevation biases these values high. However, the high values may also indicate greater solubility of certain fission products in the molten materials. There were significant differences between the large retentions of ^{90}Sr, ^{95}Nb, and ^{144}Ce as compared to ^{106}Ru and ^{137}Cs in these samples. This behavior tends to indicate that Ru and Cs were very volatile (and/or very insoluble) under these conditions, whereas Sr, Zr, and Ce remained soluble in the (U,Zr,O) melts and became trapped as the melt solidified.

Table 13. Retention fractions in core-drilled samples[a]

Sample (Elevation) Morphology	4F (0.15 m) Intact Fuel Pellet	4H[b] (0.15 m) Oxidized Liquefied Fuel	4D[b] (0.15 m) Metallic Melt	19T (0.92 m) Molten Fuel	19S (0.92 m) Oxidized Zircaloy
Temperature	<2000 K	>2700 K	>2250 K	~3000 K	
Fission Product					
^{90}Sr	0.10[c] ± 0.02	1.50 ± 0.32	2.14 ± 0.45	0.80 ± 0.16	0.62 ± 0.12
^{95}Nb[d]	0.74 ± 0.13	1.22 ± 0.26	0.99 ± 0.21	0.67 ± 0.14	1.20 ± 0.24
^{106}Ru	1.00 ± 0.19	0.05 ± 0.02	0.54 ± 0.11	0.59 ± 0.12	0.82 ± 0.18
^{125}Sb	0.60 ± 0.11	0.25 ± 0.06	1.13 ± 0.24	0.44 ± 0.09	31.0[e] ± 6.2
^{137}Cs	0.98 ± 0.19	0.06 ± 0.02	0.18 ± 0.04	0.53 ± 0.10	0.37 ± 0.08
^{144}Ce	1.05 ± 0.20	1.45 ± 0.31	1.93 ± 0.41	0.74 ± 0.14	0.83 ± 0.16

a. Fission product concentrations normalized to ^{235}U measured within each sample and divided by ORIGEN2 calculated inventories for bundle elevations shown. Uncertainty values include terms for counting statistics, ^{235}U measurements, radial and axial position imprecisions, ORIGEN2 inventory uncertainties and local neutron flux determinations. Approximate elemental compositions for samples

4F: 67 at.% O, 33 at.% U
4H: 66 at.% O, 18 at.% U, 14 at.% Zr, 2 at.% Fe + Ni + Cr
4D: 29 at.% O, 5 at.% U, 56 at.% Zr, 6 at.% Ni, 4 at.% Fe
19T: 66 at.% O, 25 at.% U, 6 at.% Zr, 2 at.% Ni, 1 at.% Fe + Cr
19S: 67 at.% O, 33 at.% Zr, plus minor amounts of Ni and Fe.

b. Values reflect downward melt relocation from higher elevations. Original elevations of dissolved fuel are not known, so inventory corrections cannot be applied.

c. Suspect value, probable measurement error.

d. Mostly ^{95}Zr during the SFD-ST transient.

e. Pronounced deposition.

4. The metallic melt Sample 4D contained higher fractions of most of the measured species than the oxidized liquefied fuel sample 4H. Since the metallic melt evolved later than the oxidized liquefied fuel (see Subsection 4.10.2), the higher fission product concentrations may be due to absorption of fission products as the metallic melt flowed down over surfaces with previously deposited fission products. The greatest differences are noted for ^{106}Ru and ^{125}Sb, which may indicate that these species formed volatile oxides (e.g., RuO_2 and Sb_2O_3) and were released in greater percentages as the liquefied fuel oxidized.

Fuel retention fractions determined from the ground fission product samples are presented in Table 14. The five widely spaced bundle elevations represented: (a) rod stubs near the bundle base (0.055 m), (b) melt-covered rod segments (0.145 m), (c) pellets partially dissolved by molten cladding (0.245 m), (d) embrittled rod fragments over the central bundle region (0.495 m), and (e) upper rod remnants retaining some original bundle geometry (0.915 m). The 0.145-m and 0.245-m cross sections contained larger area fractions of slumped melt than UO_2 pellets, so the assumption could not be made that all fission products measured were retained by fuel. Instead, the melt-retained fission products were estimated by extrapolating

results from core drilled Samples 4D and 4H, and then subtracting these values from the STM-4 and -8 sample results to produce pellet bound concentrations. Except where noted, uncertainties in local retention fractions were estimated to be within ± 30% relative to the total sample content.

Strontium retention is lower than expected at all elevations shown in Table 14. Unlike the other five radionuclides, ^{90}Sr could not be conveniently gamma counted and required chemical separation and calibrated beta counting. Since leaching efficiencies may have been poor for strontium, unknown biases were introduced into the ^{90}Sr results.

Table 14 generally shows higher fission product releases for fuel pellets that were exposed to high transient temperatures, suggesting that solid state diffusion was a dominant release mechanism. While this was perhaps true for ^{137}Cs, ^{125}Sb, and ^{106}Ru, the other three nuclides are thought to be more stable in a UO_2 matrix. Thus, other release mechanisms (e.g., chemical attack or oxidation) may have affected fuel pellets above 0.055 m. Metallic melt interactions absorbed sufficient oxygen from the fuel to create UO_{2-x} at some locations during the high temperature test phase. This local reduction process may have also altered chemical forms of certain fission products, such as changing stable CeO_2 to more volatile CeO.[22] Hydrogen penetration may have formed fission product hydroxides and hydrides, with unknown consequences on volatility and release from these samples. Retention values at the 0.495-and 0.915-m elevations for Ru, Sb, and Cs may reflect postscram formation of hyperstoichiometric fuel, where release of fission products collected at fuel grain boundaries was evidently permitted by microcrack networks.

The importance of the above solid state release mechanisms is further demonstrated by comparing STM-19 solid pellet retention values to those from core-drilled molten fuel Sample 19T (both extracted at 0.915 m). STM-19 shows higher apparent retentions for ^{125}Sb (surface deposition) and for ^{95}Nb but retention values are nearly identical for ^{106}Ru, ^{137}Cs, and ^{144}Ce. Therefore, fuel melting does not seem to have been a prominent release mechanism for these six fission products as 19T retention values would have been significantly lower than STM-19. Fuel melting cannot be disregarded for other species, especially noble gas isotopes.

As detailed in Appendix F, ground sample measurements were extrapolated on the basis of gross fuel morphology in an attempt to generate whole-bundle posttest inventories. Melt-retained fission products were also factored into these calculations for overall mass balance purposes, with results plotted in histogram form in Figures F-8 through F-13 (Appendix F). The weighted-average retention fractions produced are approximately 0.5 for ^{90}Sr, 0.7 for ^{95}Nb, 0.5 for ^{106}Ru, 0.7 for ^{125}Sb, 0.5 for ^{137}Cs, and 0.6 for ^{144}Ce. Uncertainties for these fractions cannot be legitimately calculated, because having only one sample per morphologically different region permits no estimates of regional retention uniformity, accuracy of extrapolations or assessments of the background level in local retention determinations. The uncertainty, however, must be large and improvement can only be realized through analysis of more samples.

The above whole-bundle retention extrapolations are not supported by the release fractions presented in Subsection 5.5 (Table 11), with the exception of the 0.30 to 0.35 fractional releases indicated for ^{137}Cs and ^{136}Cs, respectively. Furthermore, Table F-7 (Appendix F) reveals that ^{95}Nb, ^{106}Ru, ^{125}Sb, and ^{144}Ce were not detected in appreciable amounts within the fallback barrier. Major mass balance discrepancies may thus exist for all species but ^{137}Cs, though large uncertainties in the bundle retention values could account for most of the missing ^{90}Sr, ^{95}Nb, ^{106}Ru, ^{125}Sb and ^{144}Ce.

As discussed in Appendix F, some deposition of ^{95}Zr, ^{106}Ru, ^{125}Sb, and ^{144}Ce did occur on the base of the fallback barrier and, to a lesser extent, on the bottom of the ZrO_2 steam inlet tube. This deposition was associated with the presence of white scale on ZrO_2 surfaces. This material was not studied directly, so the scale composition and fission product concentrations are not known. Moreover, the total amount of scale was not determined on the barrier base, or on upper fuel rod end caps and other oxidized surfaces between the fuel column and fallback barrier. Since large portions of the bundle were not analyzed for retained fission products, undiscovered concentrations of fission products may exist that have not been accounted for in the bundle retention data. In the absence of additional information from the bundle and fallback barrier, a reliable fission product balance has not been possible.

Table 14. Fission product fuel retention fractions estimated from ground samples[a]

Cross Section (Elevation)	STM-2 (0.055 m)	STM-4[b] (0.145 m)		STM-8[b] (0.245 m)	STM-13 (0.495 m)	STM-19 (0.915 m)
Morphology	Intact	25% Intact	75% Reacted	Reacted[c]	Reacted	Reacted
Fission Product						
^{90}Sr	0.83 ± 0.20	0.10[d] ± 0.02	0.18[e] ± 0.22	0.34[e] ± 0.17	0.41 ± 0.11	0.56 ± 0.18
^{95}Nb[f]	0.95 ± 0.24	0.74 ± 0.13	0.91 ± 0.27	0.78 ± 0.39	0.58 ± 0.17	0.87 ± 0.27
^{106}Ru	1.03 ± 0.25	1.00 ± 0.19	0.73 ± 0.21	1.00[g] ± 0.50	0.43 ± 0.12	0.52 ± 0.16
^{125}Sb	0.83 ± 0.20	0.60 ± 0.11	0.65 ± 0.20	0.44 ± 0.22	0.66 ± 0.20	0.92[h] ± 0.29
^{137}Cs	0.98 ± 0.24	0.98 ± 0.19	0.60 ± 0.18	0.65 ± 0.33	0.54 ± 0.15	0.54 ± 0.16
^{144}Ce	1.00 ± 0.24	1.05 ± 0.20	0.16[e] ± 0.20	0.51 ± 0.26	0.48 ± 0.14	0.71 ± 0.22

a. Fission product concentrations measured in cross-sectional grindings were normalized to ground layer thickness and UO_2 area fractions and then divided by ORIGEN2 predictions for each bundle elevation. Values include any fission products deposited in bundle region. Uncertainty values include counting statistics, UO_2 area fraction measurements, ground thickness nonuniformities, elevation imprecisions, ORIGEN2 inventory uncertainties, and local neutron flux determinations.

b. Fission products estimated within melt area fractions were subtracted from overall measurements.

c. Uncertainties coarsely estimated at ±50% relative, due to large melt area fraction and lack of core-drilled samples at this elevation.

d. Suspect value, probable measurement error.

e. Value probably low due to extrapolation errors from 4D and 4H samples.

f. Daughter of ^{95}Zr.

g. Value probably too large, due to underestimation of ^{106}Ru content in oxidized melt.

h. Reflects deposition on upper structural surfaces.

6. POSTTEST ANALYSIS

6.1 Overview

The ability to predict the course of events in a reactor core undergoing a severe accident is a major objective of the USNRC Severe Accident Research Program. Computer codes have been developed to simulate major phenomena such as the fuel temperature response, cladding ballooning and oxidation, meltdown and the release of fission products. Experimental programs, such as the PBF SFD series, provide valuable benchmarks for code assessment purposes. Additionally, the codes proved to be important aids in the interpretation of experimental data.

Analysis of the SFD-ST was performed with the Severe Core Damage Analysis Package (SCDAP)[23] and the mechanistic fission product release code FASTGRASS.[24-26] Appendix H provides brief descriptions of the models within SCDAP and the input data simulation of the Scoping Test. Subsection 6.2 describes the results of the two key SCDAP calculations performed during this study, namely a reference calculation using the derived posttest best-estimate input data and a sensitivity calculation where the input boundary conditions were adjusted within known uncertainties to achieve agreement with the main reliable measured parameters. The complete input and output data for the two calculations are included as Appendix H microfiche, attached to the back cover of this report. FASTGRASS predictions are compared with the fission product release measurements in Subsection 6.3.

6.2 SCDAP Calculations and Comparisons

Some general points should be noted with regard to the calculational results and the reported comparisons with the experimental data. The relatively uniform radial temperature distribution within the test bundle permitted the average results from thermocouples at similar locations (see Section 4) to be compared with the SCDAP predictions. The calculated fuel rod temperature distribution also showed little radial variation and therefore the middle ring of twelve rods (SCDAP Component 2) was taken as representative for the comparisons. Since the SCDAP axial node elevations did not coincide precisely with the thermocouple locations, as illustrated in Figure H-2, Appendix H, comparisons were made using a simple linear interpolation of the nodes above and below the thermocouple elevations at 0.35 and 0.70 m was performed. The 0.5029-m node was sufficiently close to the 0.50-m thermocouples. The interpolation is reasonable except when the nodes being used are on different sides of the two-phase/steam interface. The simple interpolation procedure will unrealistically result in two step changes in temperature, as will be evident in the 0.35-m elevation cladding temperatures presented in the next subsection. It will also be observed in these calculations that as the coolant interface crosses a node, SCDAP also predicts a rapid temperature increase at the upper elevations. This is a consequence of the step temperature rise resulting from dry-out as the interface plane crosses a calculational node, and axial interpolation with a limited nodalization.

6.2.1 The Reference Calculation. Figure 64 compares the measured and calculated two-phase/steam interface elevation throughout the high temperature transient. The level is overpredicted by over 0.1 m during the initial phase reducing during the boil-down to about 0.05 m. This high level has a significant influence on the predicted temperatures within the bundle, particularly at the lower elevations during the initial phase. Figure 65 presents the cladding temperature comparisons at the three elevations. The apparent agreement in temperature rise on dry-out at the 0.35-m elevation is a consequence of the nodal interpolation described above. The rapid temperature rise-rates at ~100 and 150 min are due to the coolant interface crossing the 0.41 and 0.32-m nodes, respectively. Agreement between the measured temperature rise on dry-out and the 0.41-m node crossing is indicative of the level being high by 0.06 m. The predicted saturation temperature for the initial 60 min at the 0.50-m elevation again results from the overprediction of the coolant level. Following this period there is an ~100 K underprediction of temperature until dry-out of the 0.32-m node at about 150 min results in a significant increase in temperature and satisfactory agreement up until thermocouple failure. The same overall trend can be observed at the 0.70-m elevation, both in the cladding temperature and

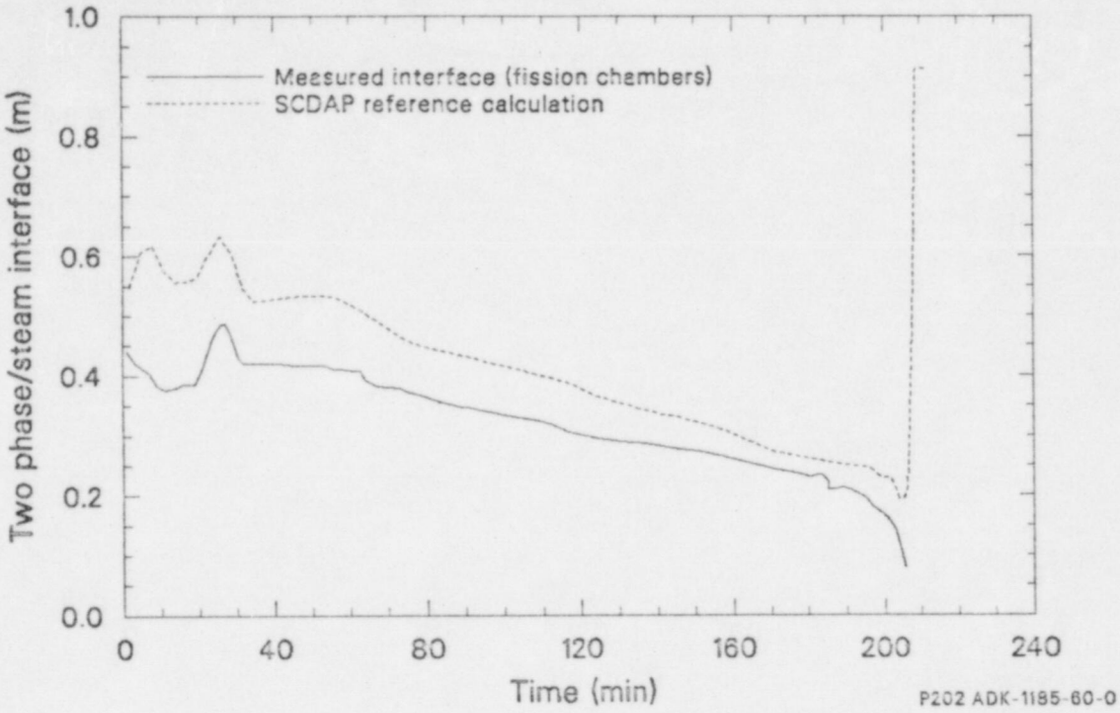

Figure 64. Comparison of the measured and reference calculation two-phase/steam interface elevation.

the fuel centerline temperature (Figure 66). After about 200 min the SCDAP calculated temperature shows at all elevations a rapid rise in temperature but with maximum values up to 700 K less than those achieved in the test. The low temperatures are consistent with an underprediction of the extent of oxidation discussed in the next subsection.

The measured and predicted steam temperature during the transient at the 0.50-m elevation are compared in Figure 67; the measured steam temperature at the 0.91-m elevation is compared with the top calculational node (0.87 m) in Figure 68. The temperature difference between the measured cladding surface and steam thermocouple values was not reproduced in the calculation resulting in a very significant underprediction of the steam temperature. This is discussed in Subsection 6.2.2.

Comparisons of the measured and predicted shroud inner liner temperatures are presented in Figure 69. The general underprediction is consistent with that of the steam temperatures but not as great, with the calculated difference between the inner liner and steam temperature being lower than measured. As discussed in Subsection 4.7, the mid-shroud thermocouple data was not considered reliable and therefore no comparison with calculation has been presented. The measured and calculated outer shroud temperature histories are given in Figure 70. Although the calculation predicts the correct general trend, the results are significantly higher at the upper elevation during the second half of the transient.

The rate of heat loss to the bypass coolant is an important boundary condition, derived from the experimental data as described in Subsection 4.3. SCDAP computes the power loss through the shroud, which is effectively equivalent to the measured heat loss to the bypass coolant. However, the measured temperature rise in the bypass was over a length greater than the bundle length that was modelled in SCDAP and therefore included slight additional gamma heating from the shroud. Furthermore, the SCDAP model does not include the direct nuclear heating component in the bypass coolant. The calculated rate of heat loss through the shroud was adjusted to account for these differences and the comparison with the measured value in the bypass coolant is presented in Figure 71. Although the general agreement appears reasonable the discrepancy of 0.7 kW during the initial steady state calibration period is significant in terms of the overall

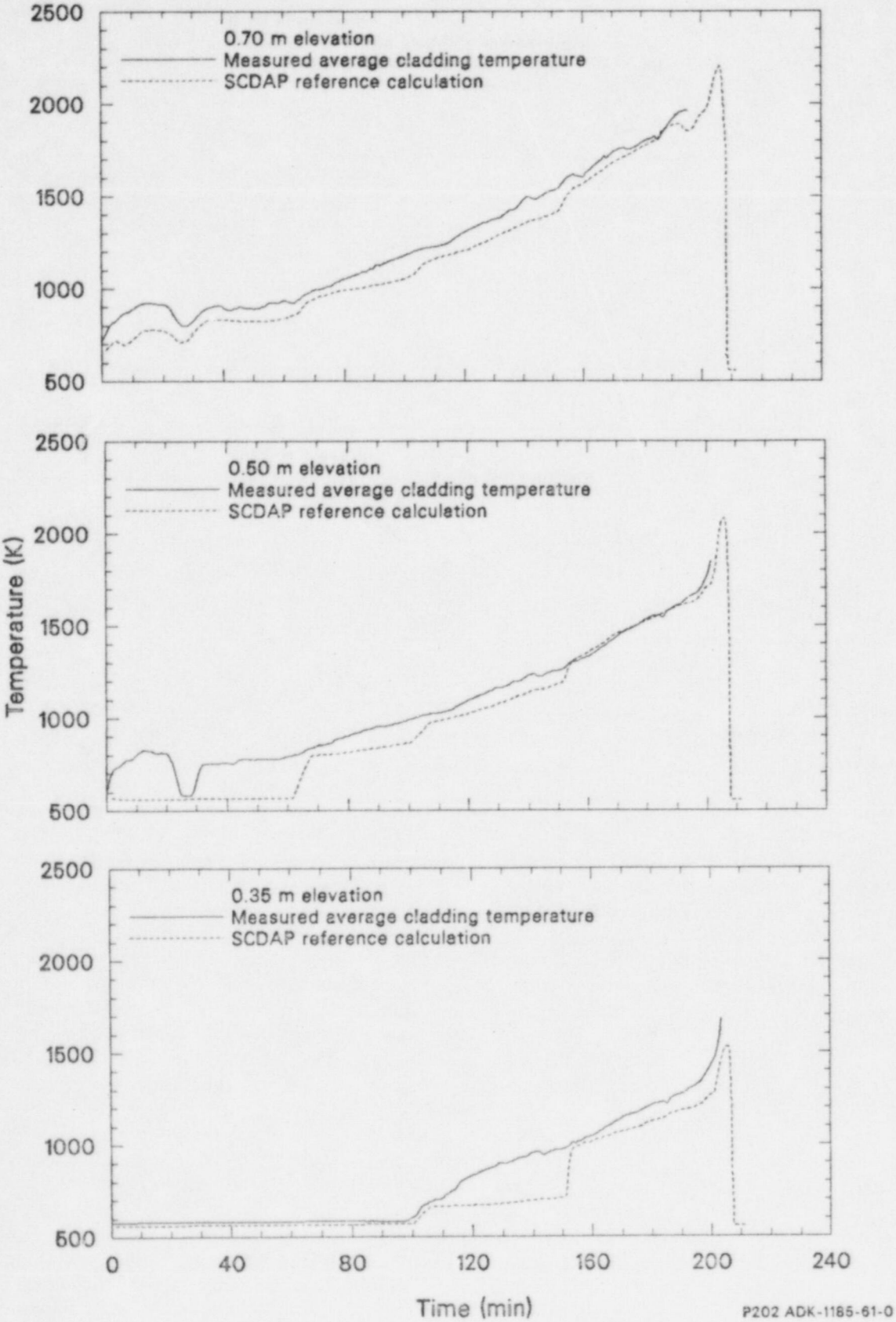

Figure 65. Comparison of the measured and reference calculation cladding temperatures.

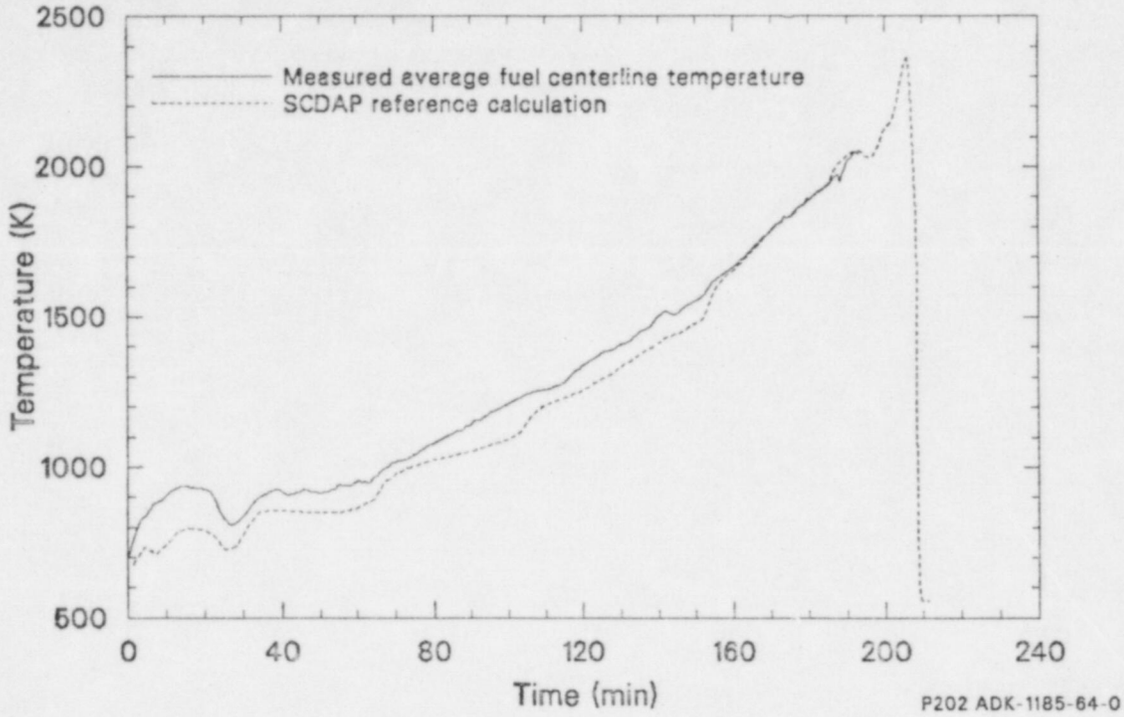

Figure 66. Comparison of the measured and reference calculation fuel centerline temperatures at 0.7-m elevation.

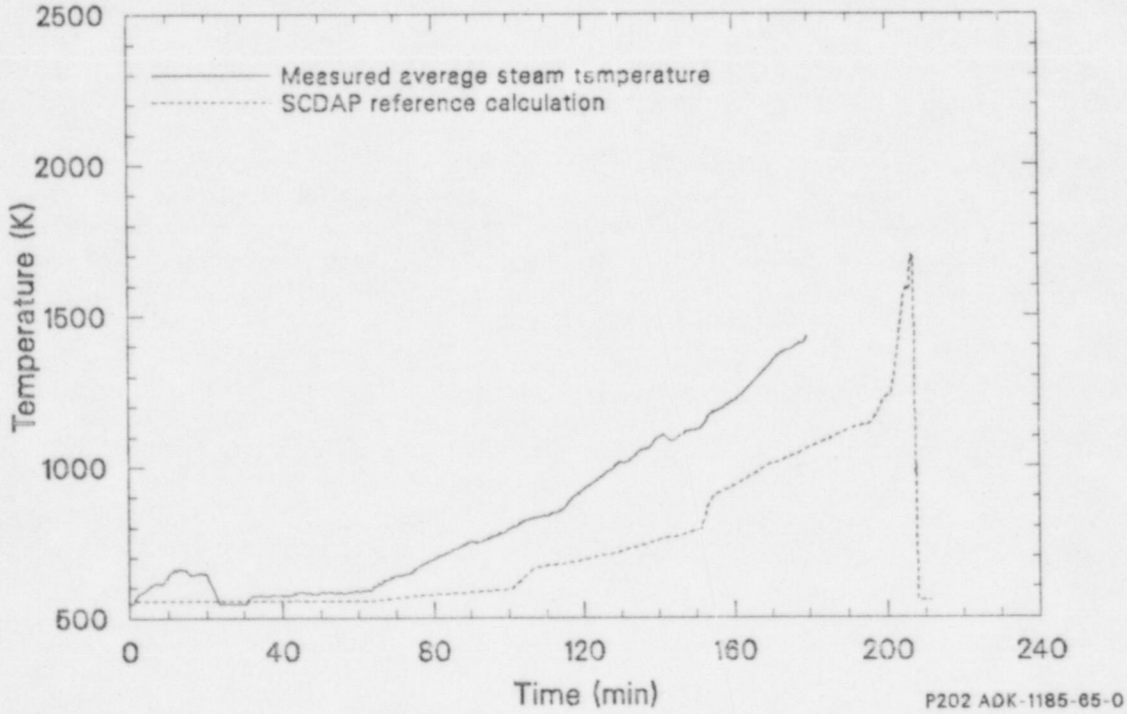

Figure 67. Comparison of the measured and reference calculation steam temperatures at 0.50-m elevation.

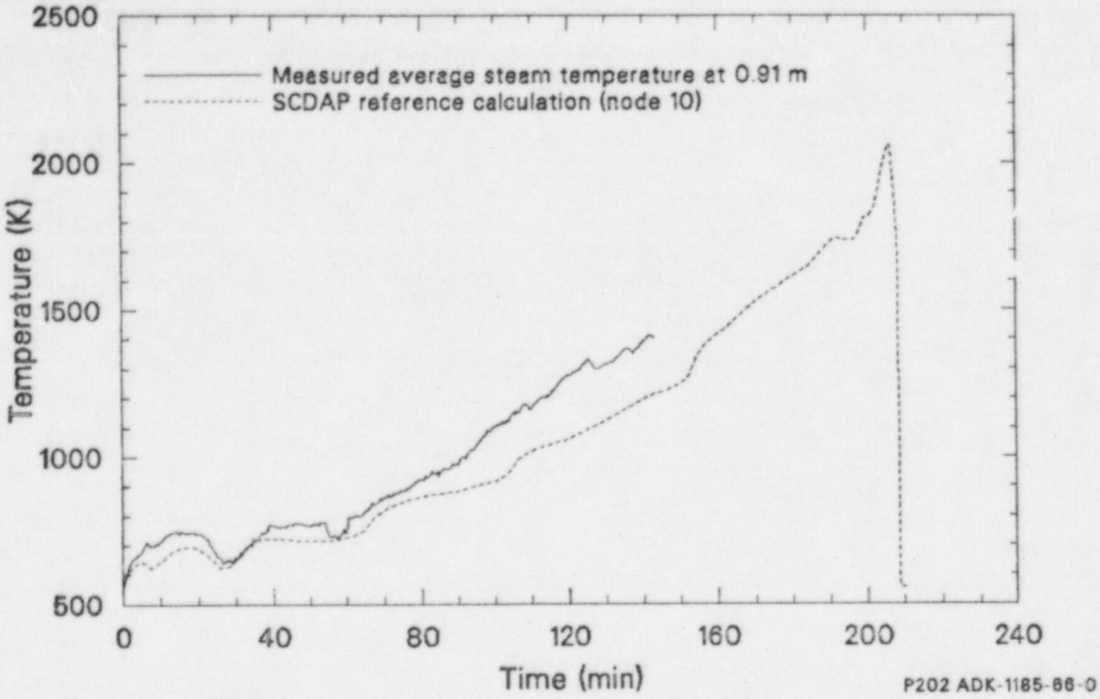

Figure 68. Comparison of the measured and reference calculation steam temperatures at top of the fuel bundle.

energy balance. However, the experimental rate of heat loss has a large associated uncertainty resulting from the temperature difference measurement, with the deviation from the mean value being about twice the 20% discrepancy.

The final transient event compared with the SCDAP reference calculation is the rupture of fuel rod cladding. As described in Appendix A, the instrumented rods were extended at the bottom to accommodate thermocouple transition pieces and pressure devices. These extensions significantly increased the total helium fill gas volume of 6.55 cm^3 in the standard fuel rod to between 12.9 cm^3 and 14.2 cm^3, depending on the particular instrumented rod. In order to compare the failure times indicated by the rod pressure devices, the instrumented rods were modelled in the SCDAP calculation. The input plenum void volume is defined in Subsection 2.1 of Appendix H as the total fill volume of the rod with the exclusion of the gap volume between the fuel outer surface and cladding inner surface. The plenum void volume thus includes both the upper and lower plenum volumes and the fuel pellets end dish and chamber volumes. SCDAP treats this entire volume as an upper plenum region, assigning a temperature equal to the upper node coolant temperature plus 6 K.

As discussed in Subsection 4.8 the instrumented rods showed cladding failure between 96.0 and 104.3 min into the transient, at maximum indicated temperatures between ~1150 and 1200 K. The SCDAP reference calculation predicted failures in the three components at Node 9 between 76.3 min and 84.0 min at temperatures approaching 1000 K. These earlier failure times at lower temperatures are consistent with a higher predicted pressure within the rods resulting from the treatment of the major fill volume as an upper plenum region. The reliability of the ballooning and rupture model is discussed further in the next subsection.

6.2.2 Sensitivity Calculations

Preliminary Evaluations. There have been several independent SCDAP analyses of the Scoping Test performed at the INEL and other laboratories[27]. The calculations were performed with earlier versions of the code and input data derived from the preliminary interpretation of the test. However, it is of interest to

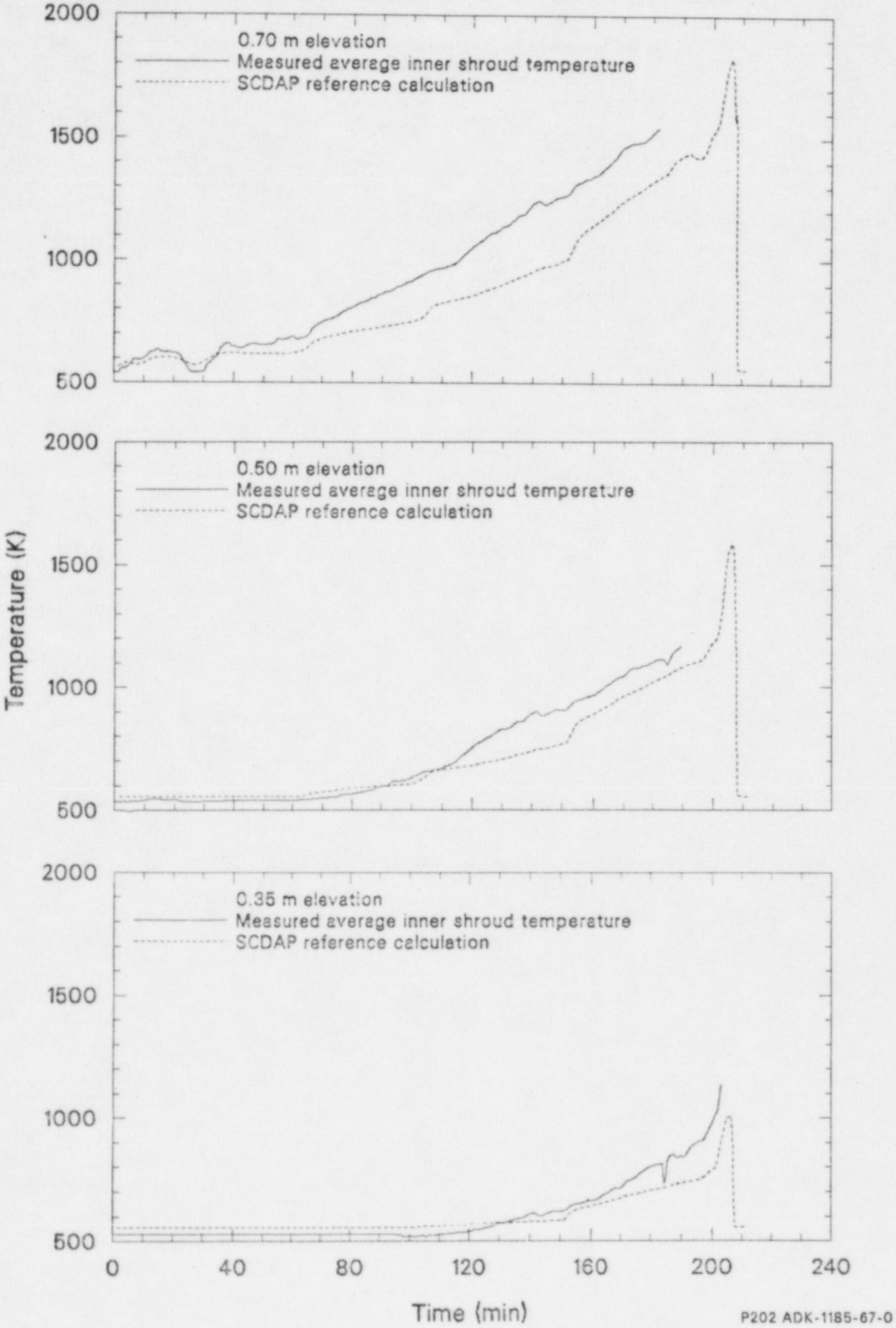

Figure 69. Comparison of the measured and reference calculation inner shroud temperatures.

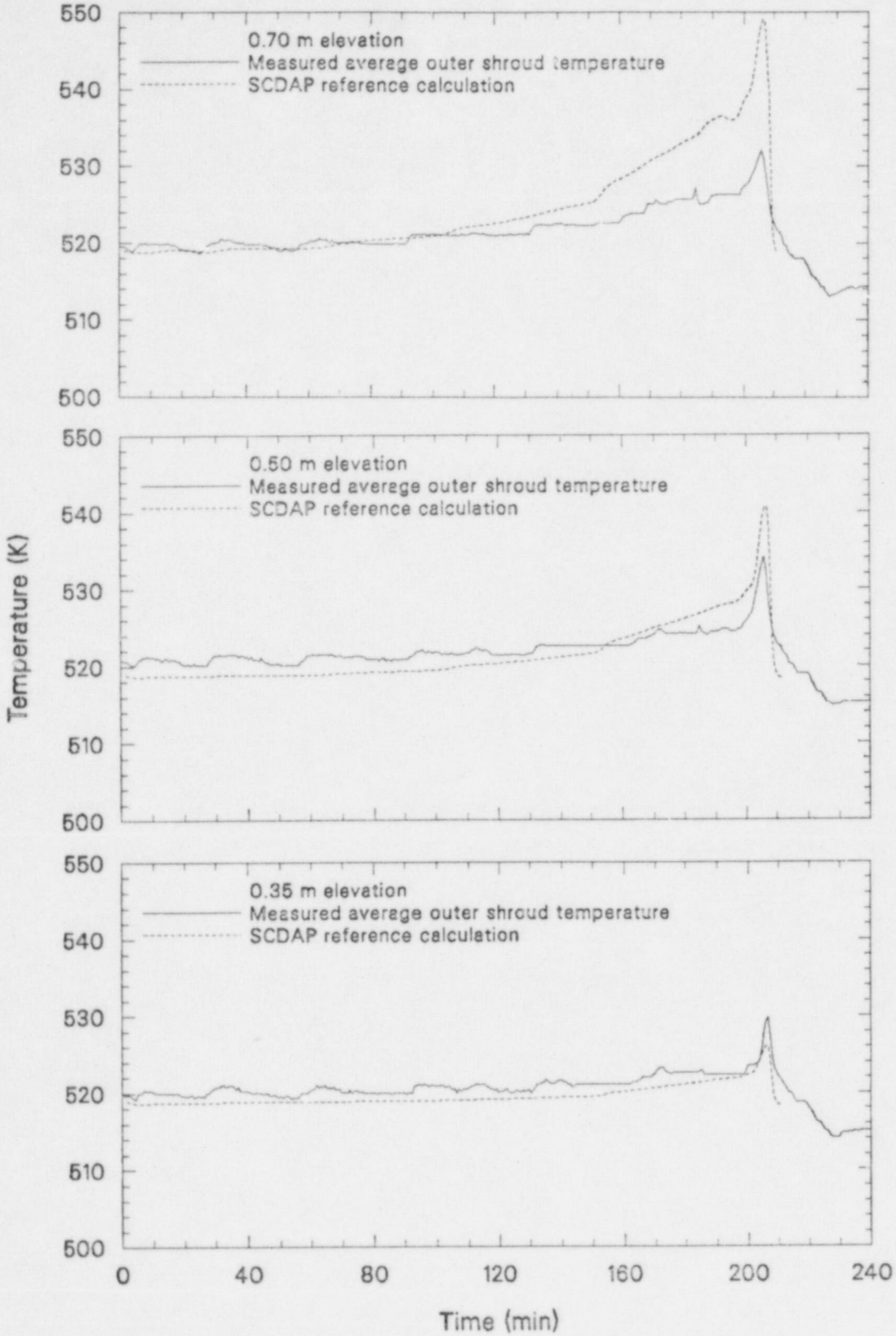

P202 ADK-1185-70-0

Figure 70. Comparison of the measured and reference calculation outer shroud temperatures.

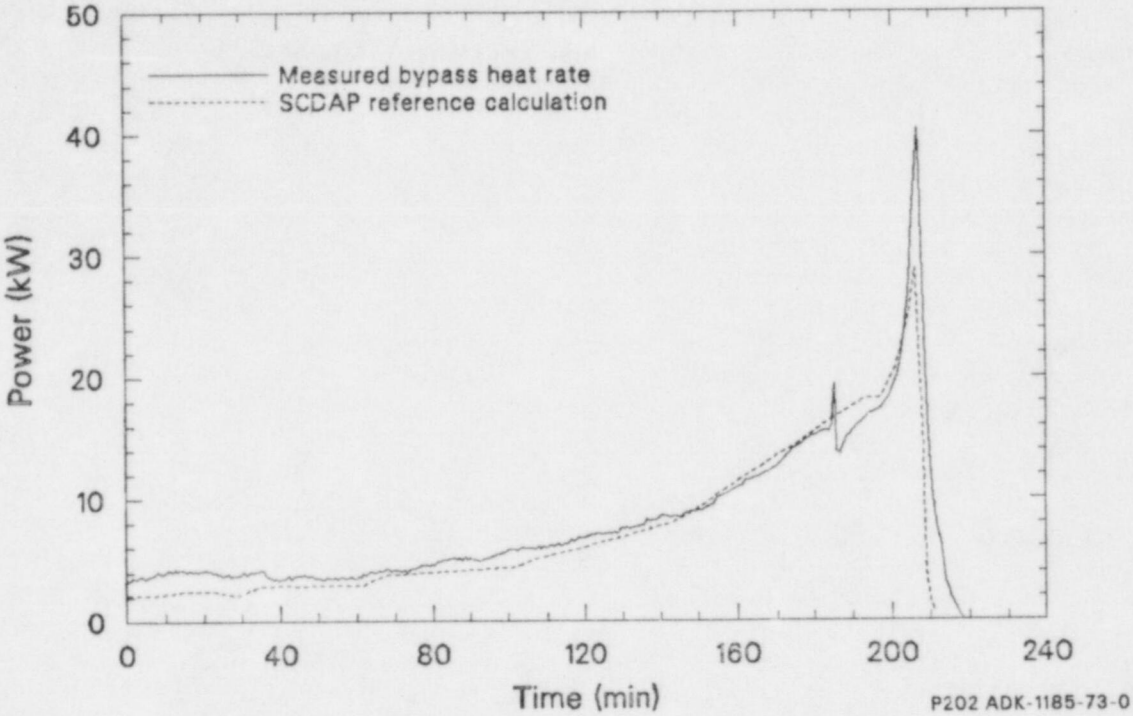

Figure 71. Comparison of the measured and reference calculation bypass coolant heat rate.

note general similarities with the current Version 18 reference calculation in that the two-phase/steam coolant elevation was overpredicted throughout the transient, with the final virtual dry-out and associated extreme temperatures and major material relocation not being reproduced.

Following the reference case, a series of SCDAP calculations was performed to assess the impact on the predicted bundle behavior of the various input values. The input parameters with uncertainties sufficient to severely influence the outcome of the calculation are the absolute power and its spatial distribution, the coolant inlet flow rate and the conductivity of the shroud insulation. Calculations were judged by their ability to simulate the reliable transient data, such as the coolant level and cladding temperatures.

As outlined in Subsection 4.2, the thermal conductivity of the shroud insulator was determined prior to the test from laboratory-measured values and a theoretical interpretation for the composite ZrO_2 fiberboard and strengthening tubes. The reference calculation was repeated with these values, and temperature predictions within the test bundle and shroud were generally in better agreement with the thermocouple data than the posttest adjusted conductivity reference calculation. However, the predicted heat loss to the bypass was a factor of two less than the values derived from the mean differential thermocouple data, although at the lower limit of the experimental uncertainties. The neutron radiograph, showed a general compaction of the fiberboard which, if it occurred throughout the high temperature transient, would have resulted in an apparent increase in thermal conductivity. Thus, the effective conductivity calculated using the measured temperature drop across the insulator and the heat flux through the shroud, was input to the two major calculations presented here. These derived values result in reasonable agreement with the measured axially-averaged heat loss through the shroud. The large axial temperature distribution in the bundle, and an increase in thermal conductivity of 0.0016 W/(m·K) per unit K, generally resulted in unsatisfactory temperature predictions at the shroud boundary. However, axial compensation in the heat transfer through the insulation provided reasonable agreement with the measured axially-averaged heat loss to the bypass.

The uncertainties associated with the derived absolute bundle nuclear power are discussed in Appendix C. Hand checks of the overall energy balance during the initial steady state phase provided confidence in the

SCDAP calculation and indicated that condensation was not a significant problem in the Scoping Test. However, a sensitivity calculation was performed to establish the consequence of a 3% increase in the overall bundle nuclear power. The maximum changes in the coolant level and cladding temperatures throughout the transient were about -0.01 m and +30 K, respectively.

The failure to reproduce the boildown two-phase level during the transient provided an indication that the axial power distribution may be in error. As outlined in Subsection 2.3 of Appendix H, the SCDAP calculation used the automatic spatial power distribution option, with the necessary input constants and relationships being derived from reactor physics calculations. The only reactor physics calculation of an axial power distribution relevant to the SFD-ST boildown had an average coolant density of 215.5 kg m^{-3} (see Appendix C). This is compared in Figure 72 with the SCDAP reference calculation profile and provides confidence in the automatic spatial power procedure. The figure also shows the test train fission chamber distribution measured at the equivalent coolant elevation. A comparison of the reactor physics water filled bundle power shape and the fission chamber measurements showed excellent agreement, indicating reliable experimental data and sensitivity corrections. However, the agreement for the one-third water filled bundle is somewhat surprising as it would be expected that the approximately cosine PBF axial power distribution would strongly influence the signal from fission chambers located outside the shroud. The measured distribution, and apparent agreement with reactor physics calculation, could be a consequence of the assumption that the sensitivity of the fission chambers remained unchanged during the boildown. On the assumption that 50% of the fission chamber signal was a result of neutrons from the reactor, the imposed cosine power shape was extracted from the measured distribution. The SCDAP relationship between the relative power and coolant density was redefined to provide agreement with the measured axial distribution modified to be more representative of the bundle. The resultant distribution is also shown in Figure 72. With a greater proportion of the bundle power in the coolant region the predicted two-phase/steam elevation compared much more favorably with the measured values throughout the transient.

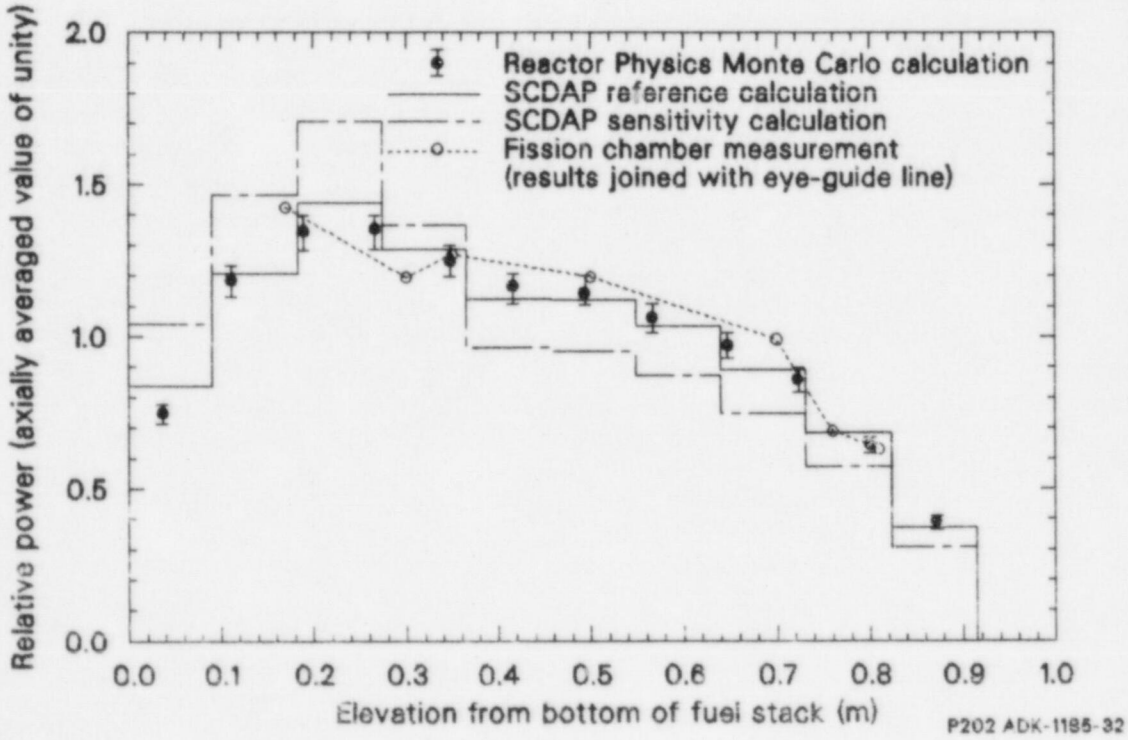

Figure 72. Comparison of the measured and calculated axial power distribution for average coolant density of 215.5 kg m^{-3}.

A similar improvement in the two-phase/steam elevation was achieved by reducing the coolant inlet flow rate in the reference calculation by 13%. However, unlike the axial power distribution input adjustment, the flow rate reduction resulted in a significant overprediction in the fuel rod temperatures throughout the transient.

As noted in the reference calculation description the small measured temperature difference between the cladding surface and the steam is not reproduced in the calculation, resulting in a very significant underprediction of the steam temperature. The influence of providing additional power to the bundle in the adjusted axial power calculation was assessed by increasing the inlet coolant enthalpy to correspond with 550 K rather than 520 K. The degree of subcooling of inlet coolant was therefore reduced, which effectively provided an additional 2 kW to heat the bundle and provided a general improvement in predicted bundle temperatures.

Final Sensitivity Calculation. The remaining part of this section presents the results of a final sensitivity calculation incorporating two of the input modifications described above. The changes, relative to the reference case, provided an inlet coolant enthalpy corresponding to 550 K and adjusted axial power profile.

The measured and calculated coolant elevation (Figure 73) and fuel rod temperatures (Figure 74) show good agreement from the steady state period into the second half of the transient. The ensuing underprediction of the coolant elevation by about 0.02 m, with a corresponding overprediction in fuel rod temperature and apparent improvement in the steam temperature, (Figures 75 and 76), are indicative of the additional effective bundle power. The measured temperature difference between the cladding surface and steam at the 0.50-m elevation was about 200 K when the two-phase/steam interface was ~0.15 m below the thermocouples, reducing to about 100 K when the interface was ~0.25 m below the thermocouples. Both the reference and sensitivity calculations showed an increase in temperature difference from ~200 to 400 K during the same period. The larger heat transfer coefficient suggested by the experimental results has previously been noted. The simplified thermal hydraulics model in SCDAP computes the convective heat transfer coefficient for single-phase vapor from the maximum of a turbulent natural convection correlation

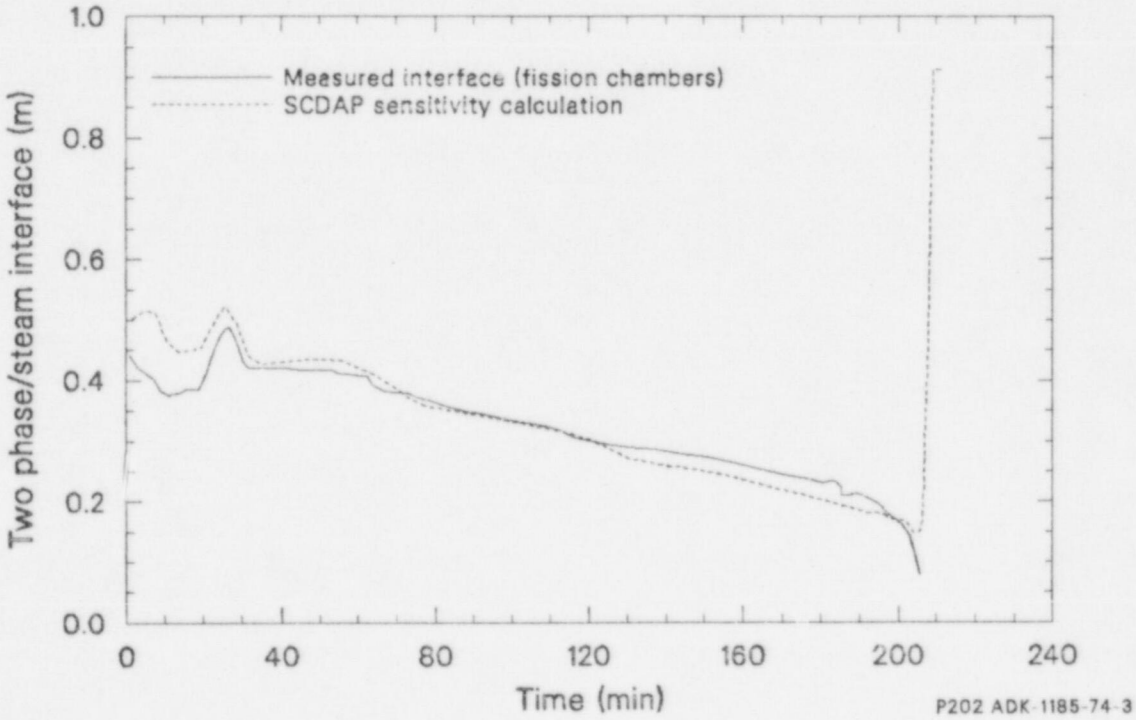

Figure 73. Comparison of the measured and sensitivity calculation two-phase/steam interface elevation.

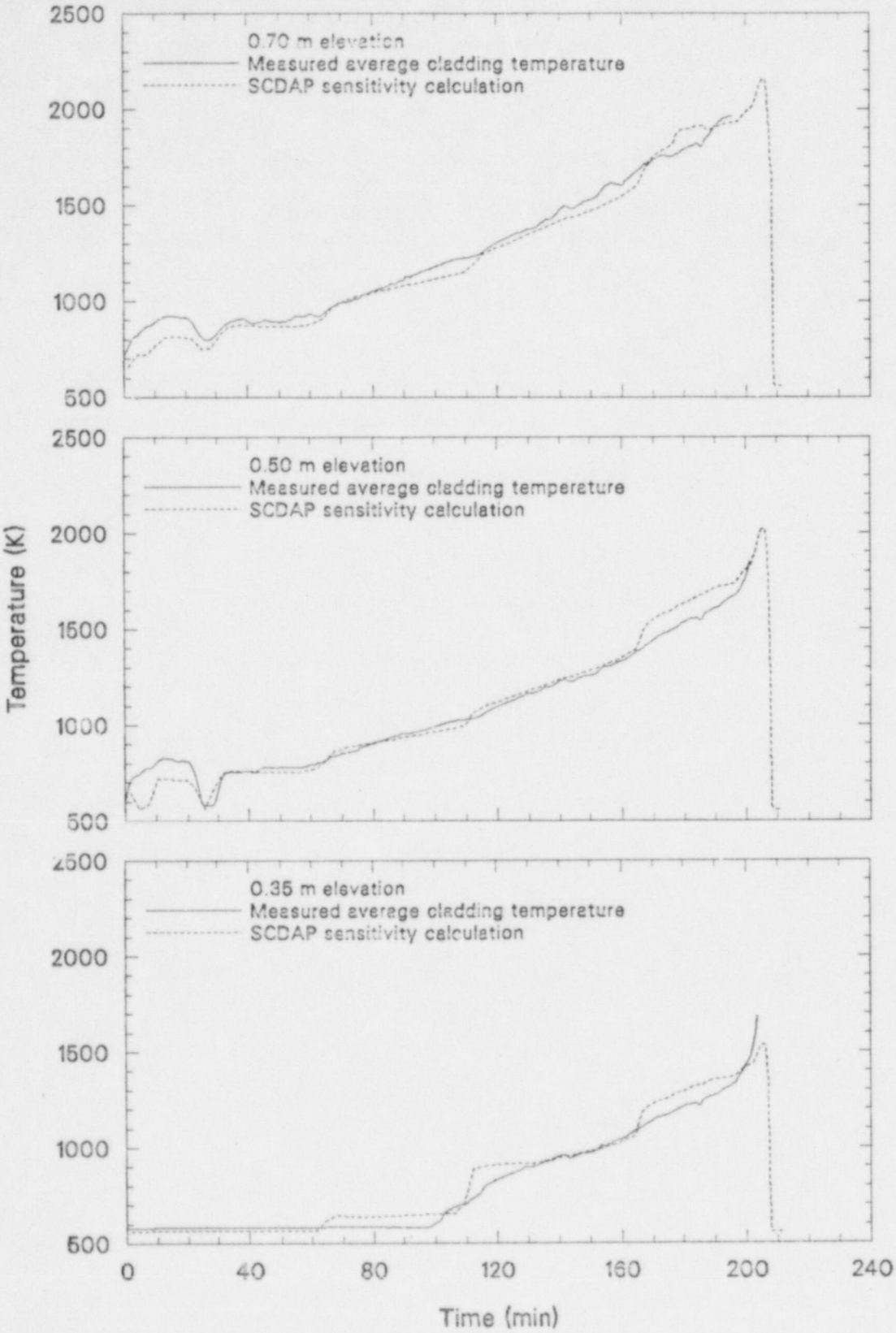

P202 ADK-1185-75-3

Figure 74. Comparison of the measured and sensitivity calculation cladding temperatures.

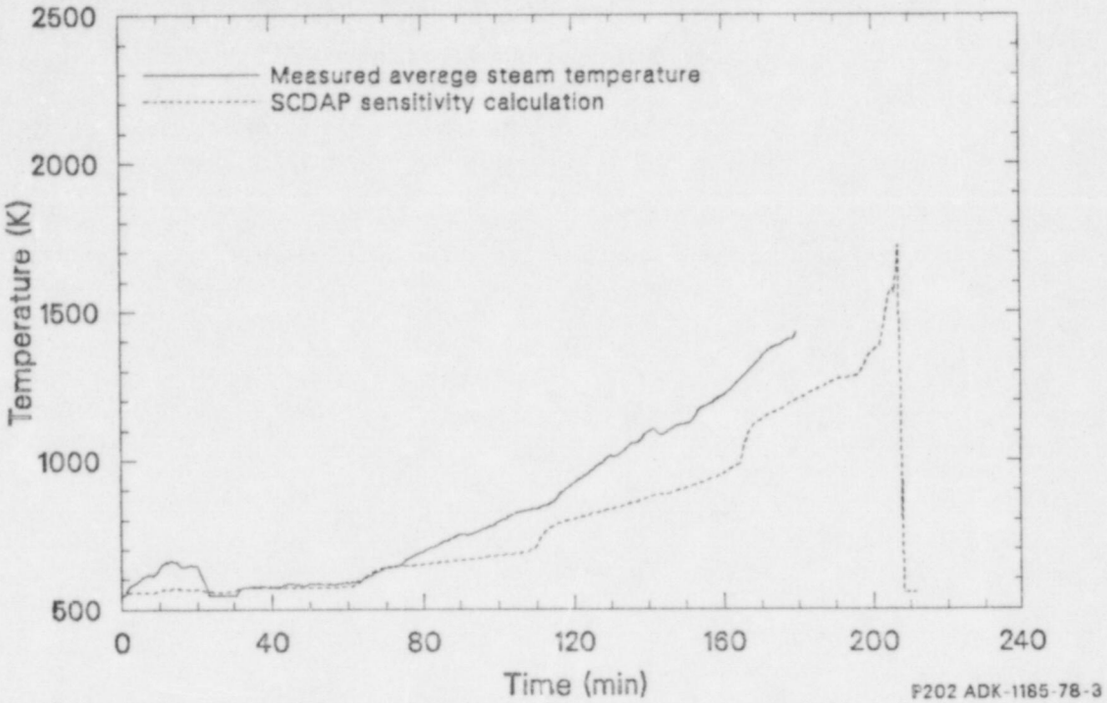

Figure 75. Comparison of the measured and sensitivity calculation steam temperatures at 0.50-m elevation.

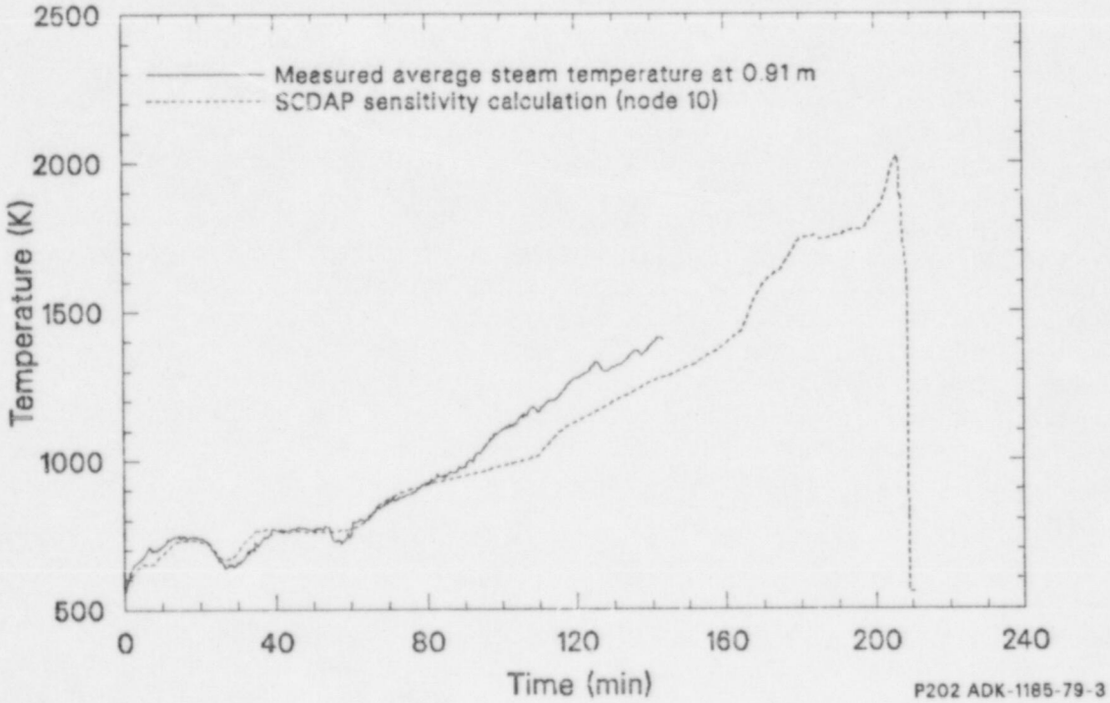

Figure 76. Comparison of the measured and sensitivity calculation steam temperatures at top of the fuel bundle.

and the Dittus-Boelter forced convection correlation. At the high temperatures, where the largest discrepancy exists, radiation is the dominant heat transfer mechanism and the theoretical convective coefficient required an increase of 70% to achieve agreement with measurement. Since such an increase must be considered unrealistic, it is considered that the steam probes were reading high for reasons yet unexplained. Radiation heat transfer from the fuel rod surfaces to the thermocouple shields, and from the shields to the thermocouples, could have resulted in higher apparent steam temperatures.

The reference case prediction of fuel rod failure was discussed in Subsection 6.2.1. Component 1 in the sensitivity calculation ballooned, and subsequently ruptured, in a manner similar to the three components in the reference case, i.e., Node 9 at 76.7 min into the transient at a temperature of ∿1000 K and pressure of about 12 MPa. However, anomalous behavior was predicted for the other two components, with ballooning occurring some 10 min earlier at Node 5 at temperatures ∿800 K and considerably lower than the peak Node 9 temperature. It should be noted that unrealistic ballooning has been reported for earlier calculations.[27] Eventual failure of Components 2 and 3 occurred at 113 to 114 min, at a temperature of 1240 K and pressure of about 14 MPa.

Considering only the rods that appear to balloon and rupture in a reasonable way, the conjecture in Subsection 6.2.1 was that the earlier predicted failure times and lower temperatures resulted from the large instrumented rod lower extension fill volume being treated as an upper plenum region. The sensitivity calculation was therefore repeated with the standard fuel rods modelled but produced virtually identical results.

Figures 77 and 78 compare the measured and predicted inner shroud and outer shroud temperature profiles respectively. Figure 79 presents the heat loss to the bypass derived from the measured data and the equivalent SCDAP values. The effect of the additional 2 kW on the shroud temperatures, and the heat loss through the shroud can be seen by comparison with the reference case. However, the general relative trends are the same in both calculations, where the heat loss to the bypass appears to be reasonably predicted but the shroud temperature comparisons deteriorate with increasing elevation. The underprediction at the inner shroud and overprediction at the outer shroud is particularly significant and indicative of the input shroud conductivity.

Although the calculated fuel rod temperatures appear acceptable for approximately the first 200 min of the test, the prediction of complete oxidation of the cladding at the top four nodes between 180 to 198 min may be the reason the final period is simulated unsatisfactorily, i.e., insufficient unoxidized zircaloy to allow triggering of high temperatures and dryout of the bundle. A further consequence of the extent of the upper elevation oxidation, in both the reference and sensitivity calculation, is that liquefaction is not predicted to occur.

The total zircaloy oxidation hydrogen production from the reference and sensitivity calculations were 77 g and 81 g, respectively. The values are significantly less than the PIE estimate of 172 ± 40 g presented in Subsection 4.9. However, as previously outlined, the final minutes of the test were not well simulated and it is therefore of more value to extract a comparison for the initial 200 min. As described in Subsection 4.9, integration of the hydrogen analyzer mass release curve for this period provided a value of 113 ± 10 g. The equivalent prediction from the sensitivity calculation is 74 g, with 71 g generated from oxidation of the cladding and 3 g from the shroud inner liner. Although a comparison of the measured and predicted generation rate is provided in Figure 80, it is important to note that not all sources of hydrogen are modelled in the SCDAP calculations.

More informative comparisons of the experimental hydrogen values and the SCDAP predictions are provided in Table 15. The first column of numbers identifies the quantities of hydrogen associated with complete oxidation of the zirconium components that were accessible to steam, and the second column lists the equivalent PIE estimates. The on-line analyzer measurement for the initial 200 min of the transient provided the total value in the next column, with the equivalent SCDAP prediction in the final column. In

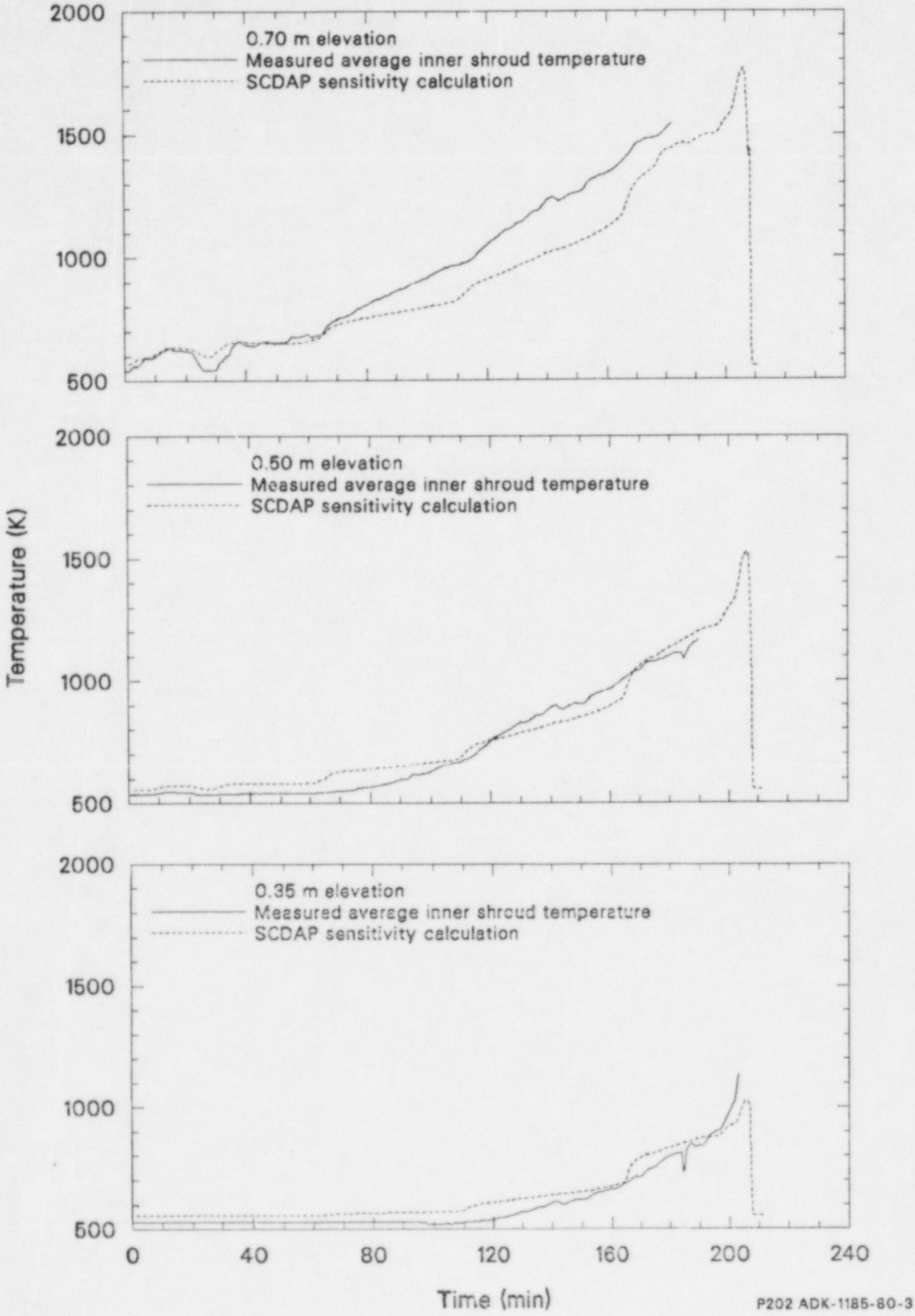

Figure 77. Comparison of the measured and sensitivity calculation inner shroud temperatures.

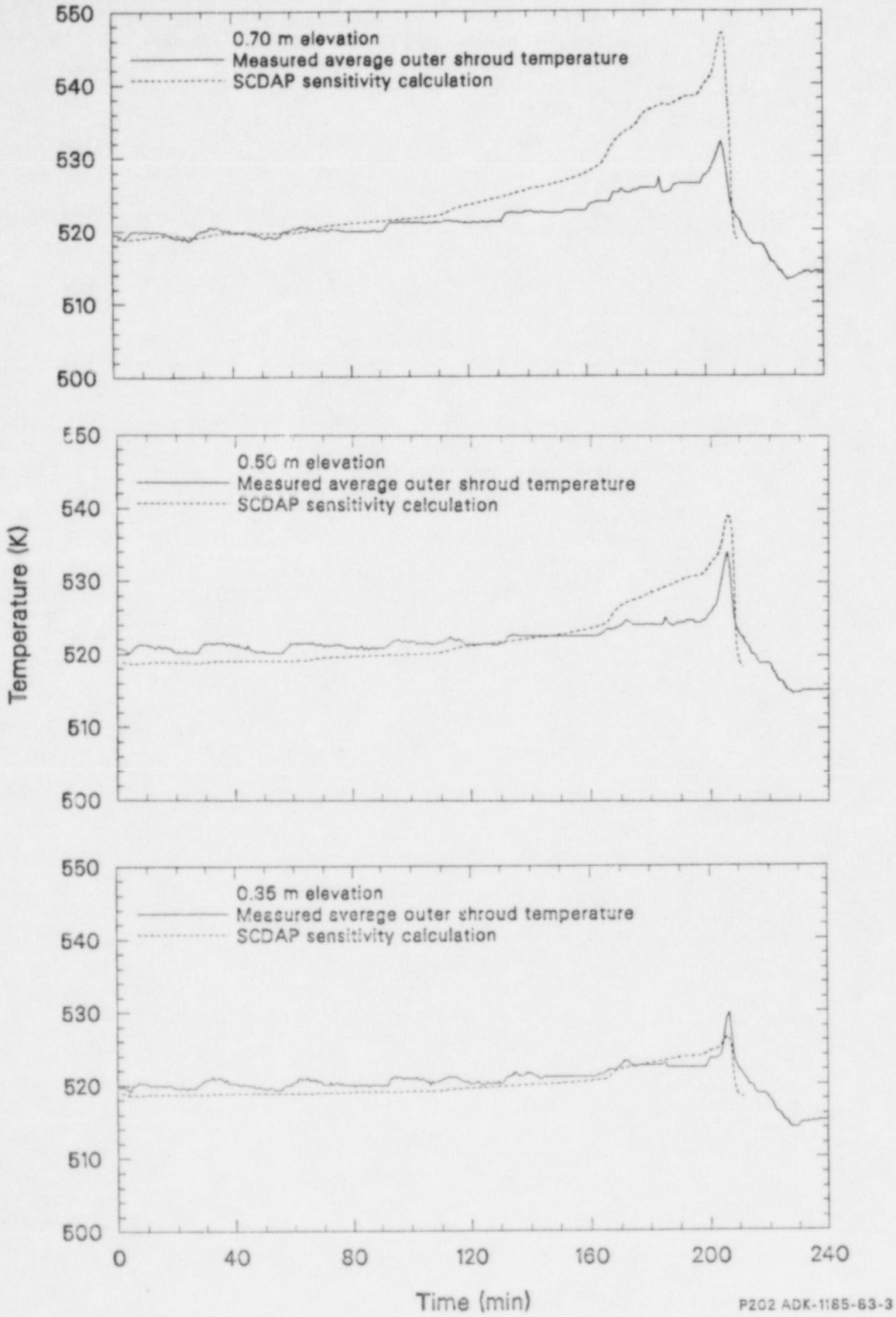

Figure 78. Comparison of the measured and sensitivity calculation outer shroud temperatures.

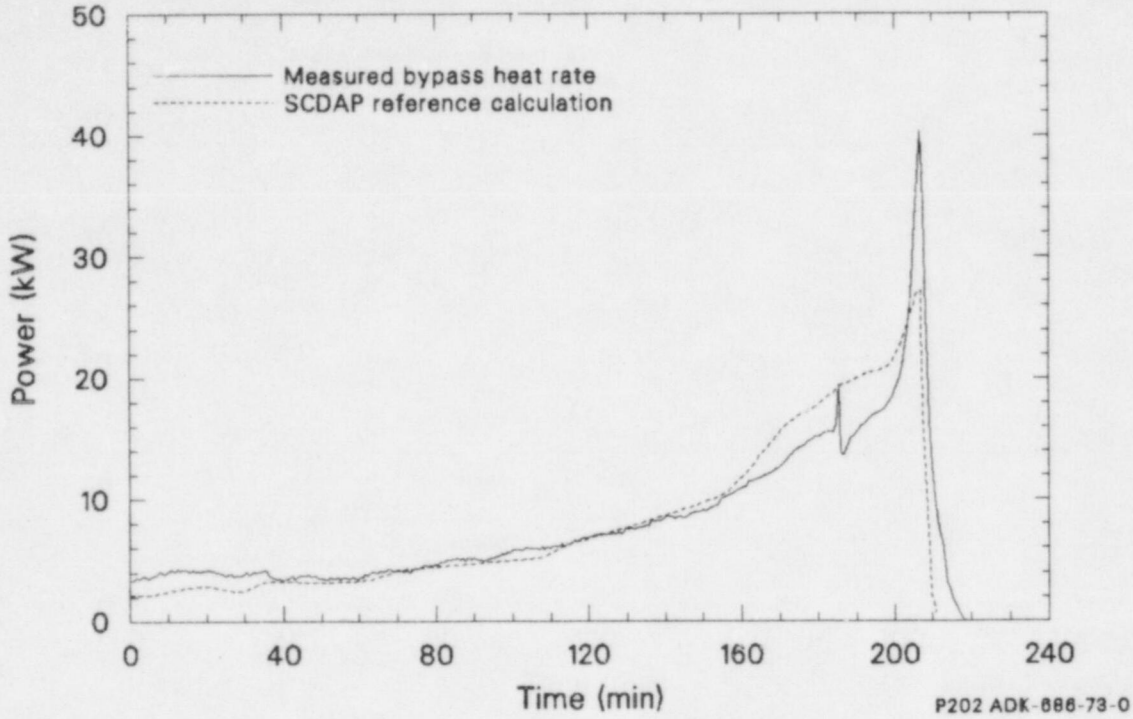

Figure 79. Comparison of the measured and sensitivity calculation bypass coolant heat rate.

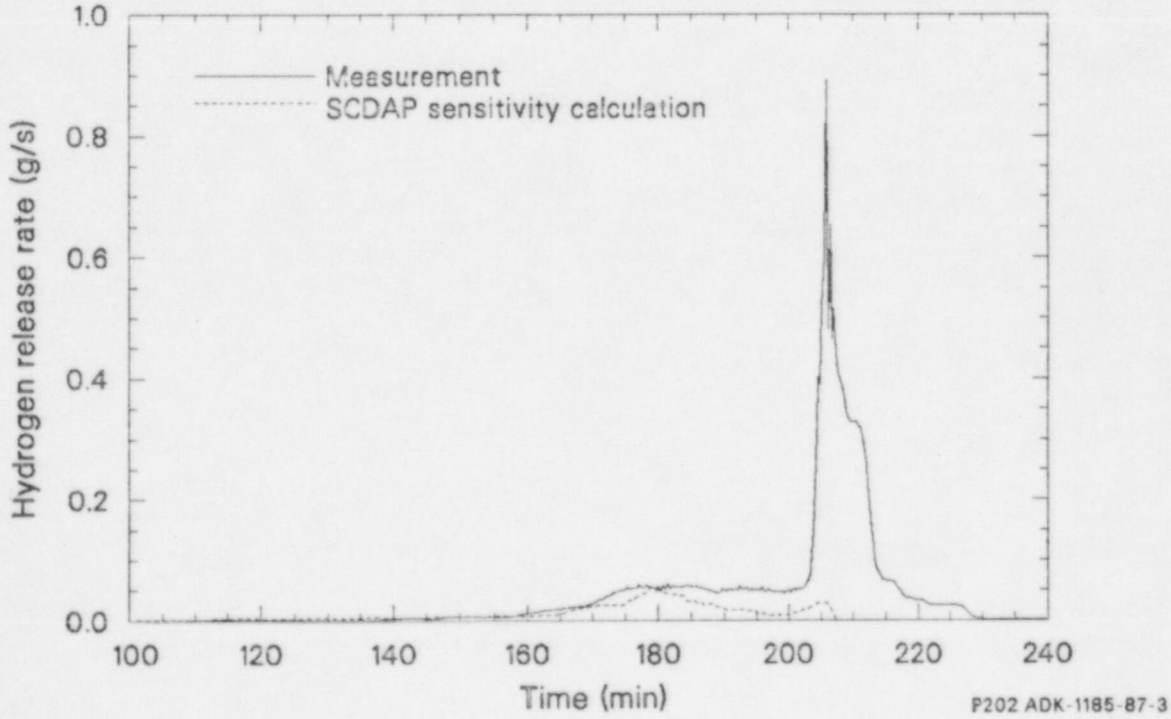

Figure 80. Comparison of the measured and sensitivity calculation hydrogen release rate.

Table 15. Comparison of measured and predicted hydrogen generation

Source of Zirconium[a]	Hydrogen Generation (g) PIE Estimate	On-Line Estimate (0-200 min)[b]	SCDAP Prediction (0-200 min)	SCDAP Prediction Corrected for Regions Not Modelled (0-200 min)
Cladding[c]	112	(73)	71[e]	78
Upper end caps	12	(8)	Not modelled	8
Lower end caps	0	(0)	Not modelled	0
Shroud inner liner[d]	39	(26)	3[e]	21
Lead carriers	4	(3)	Not modelled	3
Shroud saddle	0	(0)	Not modelled	0
Fallback barrier[f]	5	(3)	Not modelled	3
Total	172 ± 40	113 ± 10	74	113

a. See Table 9 for further details.

b. Total only measured (see text). Values in brackets = PIE component estimates x 113/172.

c. Actual cladding length = 1.0074 m. SCDAP cladding length = 0.9144 m.

d. PIE estimate length = 1.179 m. SCDAP liner length = 0.9144 m.

e. One surface and regions above 0.9144 m not modelled by SCDAP.

f. Portion of fallback barrier up to the elevation of the steamline.

order to provide a quantitative discussion of the difference between measurement and calculation, approximate *measurement* values, have been estimated for the individual components. It has been assumed that the bundle oxidized at the same rate throughout and, although not rigorously correct, the PIE component estimates have been scaled by the ratio of the 200 min total to the test total (i.e., 113 g/172 g) to give the bracketed values in Table 15. Zircaloy regions above the top of the fuel stack were not modelled in the SCDAP calculation. The predictions would therefore be expected to underestimate the hydrogen generation by approximately 28 g at 200 min. In addition, oxidation of the lead carriers, inside surface of the cladding, and outside surface of the shroud inner liner are also not modelled by the code. Due to the complete oxidation of the upper 70% of the cladding, the single sided oxidation model for this component did not appear as a major limitation in the Scoping Test analysis. However, PIE quantified extensive oxidation of the liner surface adjacent to the shroud insulation (Subsection 4.9) which was approximately equal to that of the inner surface.

Correcting the SCDAP prediction for the additional 28 g of hydrogen produced by zircaloy regions above the fuel stack elevation, the 3 g due to the lead carriers, and the approximately 8 g associated with the outside surface of the inner liner, increases the 74 g to 113 g. Although in agreement with the 200 min measured value, it should be noted in the final column of Table 15 that the cladding hydrogen production is overpredicted by 5 g, with a compensating underprediction for the liner. An important consequence of the SCDAP modelling limitations is the missing heat generation associated with oxidation.

6.2.3 Summary. The SCDAP analysis of the SFD-ST performed to date has demonstrated where the code performs satisfactorily and where some limitations exist, and provided useful insights into the possible course of events during the test. However, it is also apparent that a full assessment of the code with this test alone is not possible due to uncertainties in boundary conditions and experimental data.

The input parameters with the greatest uncertainties have been examined in separate sensitivity calculations. A combination of errors is obviously equally probable and, although difficult due to the interdependence of the boundary conditions, an iterative procedure could possibly provide a predicted bundle history consistent with the test results. The major issues that would require additional calculations to improve interpretation of the Scoping Test, and possibly better simulate the transient, are discussed below.

1. There is evidence that the flow rate measured by the inlet flowmeter, and input to these calculations, is in error (Section 4). A reduction in flow, with the appropriate decrease in bundle nuclear power, may result in satisfactory temperature predictions without the complete early oxidation of the upper bundle region.

2. A sensitivity calculation performed with SCDAP demonstrated that the predicted rapid rise in temperature at ~200 min was due to the measured inlet flow rate reduction at this time. If the postulated leakage from bundle to bypass during the final minutes of the test (Subsection 4.10) was modelled in terms of a more severe reduction in flow rate, the observed coolant level reduction, rapid oxidation of the lower portion of the bundle, and associated higher temperatures may be better simulated.

3. The overprediction in the two-phase/steam interface throughout the transient, and the corresponding influence on bundle temperatures, could be avoided by using the SCDAP option to input the time-dependent coolant elevation.

4. The inclusion of additional power, particularly in the shroud region, to simulate the oxidation energy missing due to the SCDAP model.

5. Adjustment of the shroud insulator conductivity to simulate steam penetration of the insulation upon inner liner failure and breakdown of the composite material during the final phase.

6.3 Fission Product Release Model Calculations

SCDAP Version 18 incorporates the PARAGRASS fission product release model PAR30228. However, during the Scoping Test analysis the reliability of the coupled code fuel release predictions were brought into question (Section 3, Appendix H) and have not therefore been reported. An investigation into the cause of the problem was not undertaken as an updated intact rod fission product release model, based on the FASTGRASS-VFP code, was being incorporated into SCDAP to replace PAR30228. FASTGRASS[24-26] is a mechanistic computer code for predicting fission gas and volatile behavior in UO_2 fuel during steady state and transient conditions. Models are included to assess the effects of fission product generation, atomic migration, bubble nucleation and re-solution, bubble migration and coalescence, channel formation on grain faces, interlinking on grain edges, and microcracking on both the distribution of fission products within the fuel and on the amount released. The code considers noble gases (Xr, Kr) and volatile species, with integral release models for the release and chemistry of Cs, I and Te.

Calculations of the Scoping Test with FASTGRASS have been previously reported, where the importance of the grain growth/sweeping process on the morphology characteristics and attendant release behavior from the fuel was demonstrated. Hyperstoichiometric fuel, oxidized to $UO_{2.6}$, was feasible during the rapid cooldown phase of the Scoping Test and characteristic microstructures were tentatively identified (Subsection 4.8.3). Varying degrees of grain growth were observed, from the as-fabricated 10 μm grains to 100 μm grains, although no systematic microstructure examination was performed to quantify fuel grain sizes throughout the bundle. The hyperstoichiometric correlations in the FASTGRASS model were adjusted to fit the data from the ORNL-HI tests. There are insufficient data to allow comparison of the extent of fuel oxidation and grain growth in these tests and the Scoping Test.

In order to provide a best-estimate code prediction of fission product release, the SCDAP spatial (10 node) and time dependent temperature histories were input to the current version of FASTGRASS. On the basis of

the SCDAP reference calculation histories, and allowing oxidation to occur throughout the fuel, release rates were calculated and compared with measurement (Figure 81). The predictions early in the transient are lower than previously calculated, mainly due to modelling changes. The discrepancy between calculation and experiment during this phase of the test may be due to an additional release mechanism such as rapid grain boundary diffusion, which at low temperatures would increase the release rates. However, the fractional release at these low temperatures was $<<1\%$ of the total. Following this period, and prior to when temperatures become ill defined at 200 min into the transient, the release rates were reasonably predicted. The temperatures for the final 6 min of the test were based on the PIE results rather than the SCDAP predictions. At 200 min it was assumed that the temperature of each node increased from its calculated value to the peak temperatures at the end of the test given in Table 16. Also provided are the observed grain sizes and FASTGRASS predictions of grain growth, where the initial grain size in all nodes was 10 μm. The wide variation in observed end-of-test grain sizes at given metallographic cross-sectional elevations (discussed in Subsection 4.8.3) and the large discrepancies with predictions, are not reflected in the early release rate predictions as a consequence of the modelled release being dominated by the initial doubling in grain size. However, the differences between the predicted and observed grain growth, and the resultant associated boundary dimensions, may prove very significant in the modelling of the major release mechanism observed at the end of the Scoping Test.

On the basis of liquefaction/dissolution occurring in 15% of the fuel (Appendix F), which increased predicted release rates by about an order of magnitude above 2400 K, and the assumption that all grain boundaries eventually become connected to free surfaces, fractional releases were predicted for the Scoping Test. The predicted integral releases are compared with the measured values in Table 17.

Although the release rates up to 200 min into the transient were reasonably predicted, the overwhelming fraction of fission products were released after this time. Fuel fracturing was originally postulated as the major mechanism for interconnecting boundaries in the Scoping Test but, as described in Appendix F, quench induced grain boundary shattering was not observed in the metallographic cross sections, although oxidation related microcracking exposed roughly 20% of the grain boundary surface area over much of the upper bundle. It must therefore be emphasized that, at present, there is no definite physical or chemical basis for the apparent agreement between the Scoping Test fission product measurements and the FASTGRASS predictions of integral release.

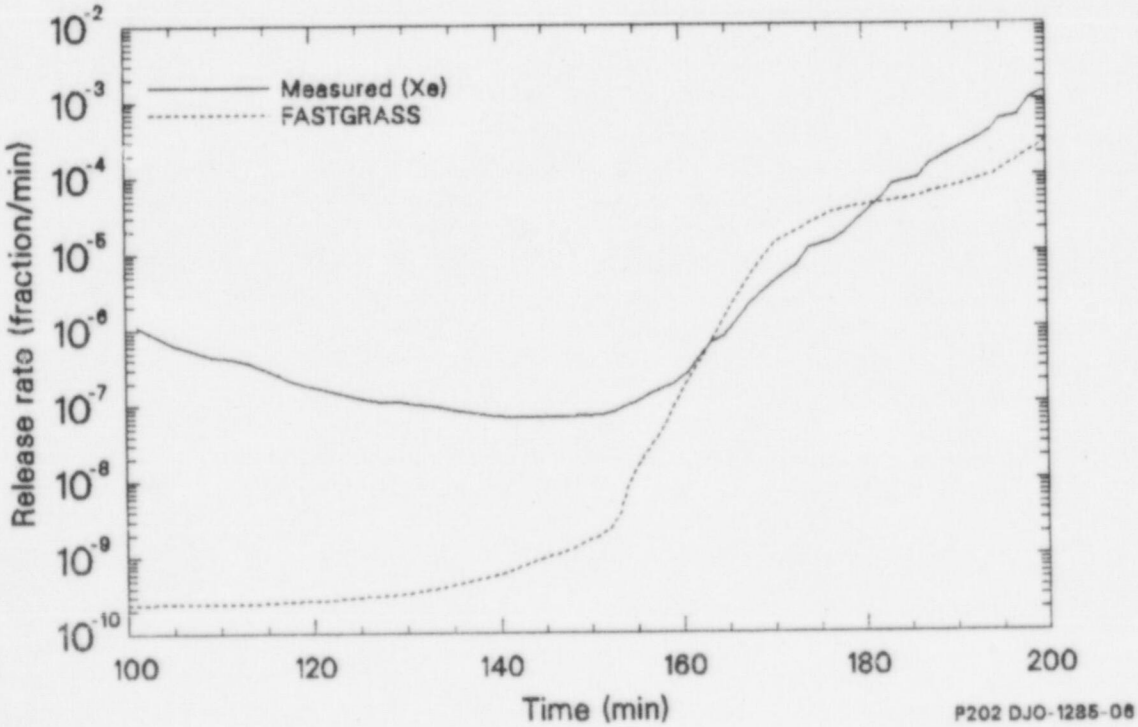

Figure 81. Comparison of the measured and predicted noble gas release rates.

Table 16. Comparison of predicted and observed fuel grain size

Axial Node Number	Axial Node Elevation (m)	FASTGRASS Input Peak Temperature (K)	FASTGRASS Predicted Grain Size (μm)	Metalographic Cross Section Elevation (m)	Approximate Observed Grain Size (μm)
10	0.8687	2190	15.8	0.915	50-100
9	0.7772	2456	19.4	—	—
8	0.6858	3013	42.7	—	—
7	0.5944	2678	26.9	—	—
6	0.5029	2407	16.2	0.495	50-100
5	0.4115	2003	10.8	—	—
4	0.3200	1904	10	0.270	10-100
3	0.2286	1805	10	0.245	10-80
2	0.1372	1604	10	0.170	10-50
1	0.0457	1243	10	0.055	10

Table 17. Comparison of measured and predicted fractional fission product release

	Fraction Released	
Fission Product	FASTGRASS	Measured
Xe	0.46	~0.5
Cs	0.46	0.32
I	0.48	0.51
Te	0.48	0.40

7. SUMMARY

The Scoping Test has proved invaluable in providing the experience necessary to perform large-scale in-pile severe fuel damage experiments. It influenced subsequent test procedures and instrumentation requirements, both in PBF and other facilities, and provided guidance to the posttest examinations and analyses of these tests.

Data collected on-line and posttest bundle examination have yielded complementary data, allowing the course of events during the test to be reconstructed to a large extent. During the high temperature transient phase from 55 to 200 min, the coolant level decreased from about 0.42 to 0.17 m. Fuel rod cladding temperatures increased from saturation (556 K) to a peak of ∿2000 K at a rate of 0.10 to 0.15 K/s and with the generation of 113 ± 10 g of hydrogen.

At ∿200 min into the transient, the bundle thermocouples indicated large increases in the temperature rise-rate. Posttest examination of the fuel bundle showed that peak temperatures reached fuel melting values of ∿3000 K. During this final phase there were redistributions of (U,Zr,O) melts, a large increase in the hydrogen production rate, significant changes in the separator pressure, a coolant level decrease to about 0.10 m and an indicated reduction in the bundle inlet flow rate of about 25%. The inlet flow reduction, decline in the two-phase/steam interface level, and the rapid increase in zircaloy oxidation and temperature during the final minutes of the transient were all strongly interrelated, with positive feedback effects. The exact sequence of events could not be positively established, but it is probable that the high temperatures and melt relocation achieved during the Scoping Test were a direct consequence of the unplanned reduction in the bundle inlet flow rate.

The overall technical objective of the SFD-ST was to contribute to the understanding of LWR fuel bundle dynamics, and the related hydrogen generation and fission product behavior, during a high temperature transient. The following subsections assess the Scoping Test in terms of the information that the experiment provided, and where it will assist severe accident regulatory policy decisions through: (a) confirmation or development of empirical and deterministic models, (b) indicating limitations in the current data base.

7.1 Hydraulic and Thermal Behavior

As the first LWR fuel bundle experiment of its kind, the Scoping Test provided valuable data with which to evaluate the Severe Core Damage Analysis Package (SCDAP). Despite uncertainties in some of the measured parameters, particularly those related to input boundary conditions, the analysis provided a general confirmation of thermal-hydraulic models in SCDAP Version 18. The main points are summarized in the following paragraphs.

The measured inlet flow was about 16 g/s throughout most of the high temperature transient. The flowmeter on the liquidline from the separator indicated an outlet flow over 30% lower. The lack of positive independent data to explain the apparent discrepancy resulted in an uncertainty in the bundle flow rate that impacted both the thermal-hydraulic analysis (i.e. input flow rate and power to SCDAP) and the estimated effluent transport time from the bundle to the various detectors.

Four radially symmetric pairs of differential thermocouples located in the bypass channel measured a large range of temperature increases in the bypass coolant (±50% spread on the mean value). The analysis boundary condition based on the resultant derived heat loss through the shroud, and the associated thermal conductivity of the insulating region, was therefore ill-defined. Inner and outer shroud temperature data were considered reliable as the thermocouples were actually attached to the insulation side of the inner liner wall, and the bypass side of the outer cylindrical shroud wall, respectively. Poor SCDAP predictions of the inner and outer shroud temperatures were indicative of the inappropriate value of the input shroud conductivity.

A reliable measurement (± 0.02 m) of the two-phase/steam interface elevation throughout the transient was derived from the test train fission chamber data. The reference SCDAP calculation overpredicted the level by 0.10 m during the initial phase, reducing during the boildown to about 0.05 m. The discrepancy may be attributable to errors in the input boundary conditions, and in particular the theoretically predicted axial power profile.

The fuel rods were well instrumented with thermocouples and provided accurate spatial and time dependent temperature data, up to values of about 2000 K. The maximum deviation of individual measurements from the radially averaged temperature profile at a given elevation was about ± 50 K, with no evidence of any general radial temperature gradient. The reference SCDAP calculation underpredicted ($\sim$100 K) both cladding and fuel centerline thermocouple measurements, again possibly due to errors in the boundary conditions.

The steam thermocouple measurements generally showed larger radial variations than those within the fuel rods, but again indicated no specific trends. The measured temperature difference between cladding and steam at about the mid-bundle elevation was 200 K when the two-phase/steam interface was $\sim$0.15 m below the thermocouples, reducing to about 100 K when the interface was $\sim$0.25 m below the thermocouples. The SCDAP calculations showed an increase in temperature difference from typically about 200 to 400 K during the same period. Radiation heat transfer from the fuel rod surfaces to the thermocouple shields, and from the shields to the thermocouples, may have resulted in higher apparent steam temperatures.

Fuel rod and steam thermocouples failed at temperatures below about 2000 and 1400 K, respectively. Peak temperatures within the fuel bundle were estimated from posttest examination on the basis of metallurgical phase distributions and elemental composition differences. Thermocouples outside the test bundle provided additional information, and indicated when the bundle was cooled to saturation temperature. The final high temperature and cooldown phases, where peak temperatures of $\sim$2100 K (200 min) increased to fuel melting by the end of the transient (206 min) before being cooled to saturation temperature (214 min), were not well represented by the SCDAP calculation. A useful evaluation of the code in the final high temperature severe fuel damage regime could not be performed due to major uncertainties in the steam generation rate and shroud behavior.

7.2 Bundle Structural Changes

The first observable significant change in bundle integrity was fuel rod rupture and the associated release of fission products, which occurred over a 20 min period at maximum cladding temperatures of $\sim$1100 to 1200 K. The ballooning and rupture model in SCDAP predicted cladding failure outside this temperature range. In the final sensitivity calculation, rupture of one component representing the central four rods occurred at a temperature of 1000 K, with the remaining components failing about 37 min later at 1240 K.

The major structural changes that took place during the final high temperature phase were not predicted by the SCDAP calculations. This was due largely to boundary conditions but also phenomena outside the scope of the SCDAP models. The main experimental observations are summarized in the following paragraphs.

The gradual increase in the bundle differential pressure when cladding temperatures were significantly below the zircaloy melting point (2030 K), and the widespread presence of Inconel constituents in both U-rich and Zr-rich solidified melts, suggested that cladding interactions with middle or upper spacer grids may have been important in initiating fuel liquefaction and melt relocation processes. However, direct evidence was obscured by later interactions.

Porous pellet regions, indicating peak temperatures near fuel melting, were found to contain substantial Zr cladding and Inconel grid constituents. Therefore, pellet liquefaction was chemically assisted and the porosity was probably associated with melt shrinkage. Melting of stoichiometric UO_2 (3120 K) could have occurred at many bundle elevations without leaving definite traces, due to subsequent melt interactions.

However, at least one conspicuous densification zone survived that indicated incipient fuel melting without chemical alterations. The highest fuel temperatures almost certainly occurred adjacent to melts, with pellet interiors remaining considerably cooler from the strong temperature gradients across melt-fuel interfaces. These gradients, and large local variations in UO_2 grains sizes, limit the applicability of isothermal grain growth correlations.

Molten cladding typically attacked UO_2 and ZrO_2 by reduction, often dynamically while slumping or while penetrating cracks. Some oxygen uptake also occurred by direct reactions with steam. Bulk oxidized melt generally arrived at the lower bundle region in a partially oxidized condition, and typically continued to react with fuel rods until solidification occurred or complete oxidation was achieved. High liquefied fuel concentrations measured in oxidized melt samples indicated temperatures greater than 2673 K.

A metallic melt formed late in the slumping sequence and relocated downward without dissolving significant quantities of fuel. This was apparently because of low viscosity and poor wetting caused by a lack of steam oxidation. Instead, it may have absorbed some of the hydrogen gas, as indicated by the high neutron attenuation during radiography. The metallic melt reacted with the previously solidified bulk oxidized melt at approximately the time of reactor scram.

The dominant mechanism for altering the bundle geometry was the formation and slumping of high temperature Zr-rich melts, accompanied by liquefaction of ~15% of the original fuel volume. Bundle geometry was extensively disrupted due to steam embrittlement over the central bundle region.

An upward fuel stack displacement of over 0.11 m, creating several axial gaps in the bundle, was observed in the neutron radiographs. The stack elongation was postulated to have occurred at 210 min (4 min after scram) when sufficient differential pressure across the solidified once-molten mass induced a diagonal bundle fracture along the melt base (0.10- to 0.17-m elevations). Most of the bundle was then lifted until it impacted the fixed fallback barrier. Upper bundle segments were permanently forced against intact insulation, while intermediate segments slid downward by varying amounts during posttest handling. The observed lift of the fuel stack was considered to be the result of flow blockage and was largely regarded as an analysis complication. However, flow channel blockage by melt accumulation does have general implications on severe reactor accidents.

The signals from the array of 12 fission chambers mounted on the test train were used to provide a qualitative assessment of material motion. Slowly varying deviations during the minute prior to reactor scram were interpreted as movement of fuel bearing melt. The most significant melt depletion occurred at the 0.50-m elevation, with smaller depletions being detected at the 0.70-m elevation. The majority of melt accumulated at the bottom elevation (0.17 m), with smaller accumulations indicated by the fission chambers at the 0.30-m and 0.35-m locations.

The extent of fuel relocation was estimated from a posttest gamma intensity profile. Approximately 2% of the fuel moved downward to the region between 0 and 0.31 m, 10% of the fuel moved away from the region between 0.31 m and 0.76 m and 8% of the fuel moved upward to the region above 0.76 m.

A qualitative assessment of the posttest bundle geometry was provided by tomographic reconstruction from multi-angle radiographs. The approximate area fractions of UO_2, Zr-rich metallic melt and U-rich oxidized melt (mostly liquefied fuel) were derived by planimetry from macrophotographs of the seven metallographic cross sections. The intact geometry inter-saddle flow area of 43% was estimated to have reduced to between 32% and 37% from the lower six metallographic cross sections (0.055 m to 0.495 m). The flow area at the upper cross section location of 0.915 m was found to be about double the intact value.

7.3 Oxidation and Hydrogen Generation

The on-line thermal conductivity analyzer provided a time-dependent measurement of hydrogen release from the test train. Integration of the first 200 min of data provided a reliable hydrogen generation value of

113 ± 10 g. However, the uncertainty in the analyzer measurement, equivalent to 140 g during the peak hydrogen production at the end of the test, and the possibility of inadequate mixing of hydrogen and the nitrogen control gas when sudden changes in flow occurred, made the total hydrogen estimate of 375 g questionable. The experimental uncertainties, both in the absolute value and timing of hydrogen release (i.e. transit time corrections), have resulted in limited correlation of oxidation and bundle behavior in the temperature range 2000 to 3000 K.

Postirradiation examination of the test bundle and shroud zirconium oxide thicknesses resulted in a hydrogen generation estimate of 172 ± 40 g. The examination also indicated the presence of hyperstoichiometric uranium oxides both inside fuel pellets and within adjacent uranium bearing melts. An upper limit estimate, based on two-thirds of the fuel oxidized to $UO_{2.6}$, provided a possible additional 48 g of hydrogen.

The thermal behavior of the test bundle was reasonably simulated by SCDAP for the first 200 min of the transient. The predicted hydrogen generation was 74 g for this period, in comparison with 113 ± 10 g measured. The lower predicted value was attributed to zirconium regions not modelled by the code. PIE quantified the extent of this oxidation (regions above the upper fuel elevation, the lead carriers, inside surface of the cladding, and outside surface of the shroud inner liner) which was estimated to account for the discrepancy. A consequence of these limitations in the SCDAP model is the missing heat generation associated with oxidation.

7.4 Fission Product Behavior

Fission product release from the bundle during the SFD-ST could be approximately characterized in six phases. However, transport effects not accounted for in the analysis complicated attempts to relate the experimental data to fuel release. The gap release and low temperature (peak fuel temperature ϵ 1700 K) diffusion phases amounted to only 0.15% of the integral activity measured up to about one hour after reactor scram. High temperature diffusion, between peak fuel temperatures of 1700 and 2100 K, accounted for about 4%. Fuel liquefaction prior to reactor scram increased the release to 10%, with an additional unquantified contribution from liquefaction during the cooldown phase. The total amount of fuel liquefied was estimated to be 15%, which results in an upper limit of 20% fission product release from this mechanism.

During the ~8 min cooldown and reflood period, major release occurred due to a combination of the continued liquefaction, fuel oxidation, grain growth/separation and formation of shrinkage cracks within porous prior molten regions. By the time the bundle had been reflooded and cooled to saturation temperature, 54% of the total activity (relative to about one hour after scram) had been recorded. However, due to transit time uncertainties, it is probable that a fraction of the cooldown contribution was released from the fuel during the high temperature liquefaction phase. The flushing process continued to extract further fission products from the bundle in addition to resuspending species deposited within the system. The primary fission product behavior for the Scoping Test, described both in this report and Reference 11, is summarized in Table 18.

The release rate values developed from the SFD-ST data are perturbed by various transport effects. The effective release rate coefficients measured for the noble gas isotopes may have been perturbed by holdup in the fuel-cladding gap or stagnation in the transport system, but they were not complicated by deposition processes. The measured noble gas release rate as a function of time was over three orders of magnitude below that predicted using NUREG-0772 constants (correctly applied to account for local variations in bundle temperature and fission product inventory) at low temperatures, decreasing to about one order of magnitude when peak and average bundle temperatures were about 2100 K and 1500 K, respectively. The low burnup of the SFD-ST fuel, where open porosity and release paths had not developed, was the probable major reason for the lower release rates. Due to uncertainties in the transit time from the test bundle to the spectrometers, effective release rate coefficients were not correlated to peak temperatures above 2100 K.

Table 18. Summary of primary fission product behavior for the SFD-ST

Fission Product Species	Bundle Release Characteristics	Fission Product/ Steam-Hydrogen Chemistry	Transport/Deposition Characteristics	Bundle Retained Fission Product Characteristics	Fallback Barrier Retention	Fission Product Mass balance
Noble gases (Xe, Kr)	0.5 release of total inventory. Value not measured directly, estimated from spectrometer data. < 1% release below 1700 K. > 90% of release is due to combination of related effects of high temperature (> 2100 K) diffusion, fuel liquefaction, fuel oxidation, grain growth/separation and shrinkage crack formation.	Inert.	Primarily follows gas flowpath.	Not detected because of procedure.	Not expected.	No mass balance possible.
Iodine (I)	0.51 ± 0.08 release of total inventory. Release as atomic-iodine predicted. < 1% release below 1700 K. > 90% of release is due to combination of related effects of high temperature (> 2100 K) diffusion, fuel liquefaction, fuel oxidation, grain growth/separation and shrinkage crack formation.	Postulated that HI (~80%) and I (~20%) are primary vapor species in high temperature bundle region due to low I concentration and steam-rich test environment. Postulated that HI and CsOH reacted to form CsI due to cooldown during transport through effluent system. CsI condensation in steamline and condenser with subsequent washout postulated.	Postulated that HI and I transported as vapors from bundle to cooler regions. Postulated that cooldown during transport through off-gasing system resulted in transformation of HI and CsOH to CsI. Postulated that CsI condensed in condenser. Iodine followed liquid flowpath beyond condenser, probably in form of soluble CsI. Measured Iodine partition factor; liquid/gas ~200.	Not detected. Inability to detect ^{129}I in fairly intact pellet indicated error in measurement procedure.	Not measured.	No mass balance possible.
Cesium (Cs)	0.32 ± 0.05 release of total inventory. < 1% release below 1700 K. > 90% of release is due to combination of related effects of high temperature (> 2100 K) diffusion, fuel liquefaction, fuel oxidation, grain growth/ separation and shrinkage crack formation.	Postulated that CsOH (99%) is the primary vapor species in the high temperature bundle region. Partial CsOH transformation (~10%) to CsI during effluent cooldown postulated.	Partial condensation of CsOH predicted in steamline portion of the collection system and washout of condensate after bundle reflood.	^{137}Cs 0.53 Unquantifiable uncertainty in extrapolating sample data to whole bundle value.	^{137}Cs 0.003	Mass balance achieved within the uncertainties.
Tellurium (Te)	0.40 ± 0.07 release of total inventory. Little end-state Te sequestering by Zr due to highly oxidizing test condition. Enhanced release upon zircaloy oxidation.	Postulated that SnTe and H_2Te are dominant forms of vapor species. Te and TeO also possible forms at high temperature.	60-90% of Te reaching filter was measured on filter.	Not detected due to excessive decay.	Small amounts.	No mass balance possible.
Barium (Ba)	~0.01 release of total Ba inventory.	—	Deposits on steamline walls and possibly on aerosols; limited washout of deposits.	No measurement due to excessive decay.	No measurement due to excessive decay.	No mass balance possible.
Strontium (Sr) Ruthenium (Ru) Cerium (Ce)	< 0.001 release measured.	—	Deposits on steamline walls and possibly on aerosols; limited washout of deposits.	^{90}Sr 0.53 ^{95}Nb 0.73 ^{106}Ru 0.51 ^{125}Sb 0.66 ^{144}Ce 0.61 Unquantifiable uncertainties in extrapolating sample data to whole bundle values.	^{90}Sr No data ^{95}Nb 0.004 ^{106}Ru 0.006 ^{125}Sb 0.032 ^{144}Ce 0.0001	Possible low bias in the fallback barrier sampling. Additional short distance migration and ex-bundle deposition postulated.

The measured iodine release fraction was 0.51 ± 0.08, the cesium and tellurium release fractions were 0.32 ± 0.05 and 0.40 ± 0.07 respectively, the barium release was about 0.01, and very small release fractions (10^{-4} - 10^{-6}) of low volatile fission products Ru, Sr, Nb, and Ce were detected downstream of the bundle. The integral noble gas release was not measured directly because the sampling apparatus was defective. However, integration of the spectrometer measurements of noble gas isotopes yielded an approximate average value of 0.5. All volatile fission products released, except tellurium, were transported efficiently in the high velocity, steam rich effluent stream. One-fourth of the released tellurium was found irreversibly deposited on steamline walls, one-half in the liquidline particle filter, and the remaining one-fourth in the collection tank liquid.

Retained fission product estimates indicated appreciable releases of ^{90}Sr, ^{95}Zr, ^{106}Ru, ^{125}Sb, ^{137}Cs, and ^{144}Ce from fuel pellets that remained solid. Likely phenomena contributing to solid fuel releases of all fission products are prescram formation of UO_{2-x} by reaction of solid fuel with molten cladding and postscram formation of hyperstoichiometric fuel ($\sim UO_{2.6}$). Hydrogen penetration of fuel pellets during the steam flow reduction may also have created highly volatile chemical forms of certain fission products. However, the ostensibly nonvolatile fission products (^{90}Sr, ^{106}Ru, ^{144}Ce, etc.) that were released evidently migrated only short distances before irreversibly depositing, as they were not detected downstream of the bundle in significant quantities.

SCDAP spatial and time dependent temperature histories were input to the fission product release code FASTGRASS. Release rates were underpredicted by several orders of magnitude during the early low temperature phase (peak temperatures <1700 K) of the transient, but this accounted for $<<1\%$ of the total fractional release. Following this period, and prior to when temperatures became ill-defined at 200 min, the release rates were reasonably predicted. On the basis of liquefaction/dissolution occurring in 15% of the fuel bundle, which increased predicted release rates by about an order of magnitude above 2400 K, and the assumption that all grain boundaries eventually become connected to free surfaces, fractional releases were in general agreement with the measurements (FASTGRASS/measured for Xe was 0.46/0.5; Cs 0.46/0.32; I 0.48/0.51, Te 0.48/0.40). The mechanism for separating fuel grains has not been positively identified, although there was evidence of microcrack networks associated with fuel oxidation.

7.5 Conclusion

The data from this analysis of the Scoping Test are being combined with those from the subsequent three tests performed in PBF, other integral and separate-effects experiments, and the TMI-2 core examination. A substantial data base related to severe fuel damage, melt progression, hydrogen generation and fission product behavior is becoming established. The identification of key phenomena and processes, and a consistent interpretation of the data from all the available sources, will greatly assist the development and validation of accident analysis models. This will permit more reliable, plant-specific, probabilistic risk assessment and will be instrumental in the development of regulatory policy on severe accidents.

8. REFERENCES

1. M. Rogovin (Director of NRC Special Inquiry Group Three Mile Island), *A Report to the Commissioners and to the Public*, NUREG/CR-1250, 1980.

2. J. T. Larking and M. A. Cunningham, *Nuclear Power Plant Severe Accident Research Plan*, NUREG/CR-0900, January 1983.

3. P. E.MacDonald, B. J. Buescher, R. R. Hobbins, R. K. McCardell, and G. E. Gruen, "PBF Severe Fuel Damage Program: Results and Comparison to Analysis," *Proceedings of the International Meeting on Light Water Reactor Severe Accident Evaluation, Cambridge, Massachusetts, August 28-September 1, 1983.*

4. P. E. MacDonald, C. L. Nalezny, and R. K. McCardell, "Severe Fuel Damage Test 1-1 Results," *Transactions of the American Nuclear Society 46*, 1984, pp. 478-479.

5. R. W. Miller, R. K. McCardell, and P. Kuan, "Severe Fuel Damage Test 1-3 in the Power Burst Facility," *Transactions of the American Nuclear Society 49*, 1985, p. 249.

6. Z. R. Martinson and R. W. Miller, "SFD 1-4 Test Results with Irradiated Fuel and Control Rods," *Transactions of the American Nuclear Society 50*, 1985, p. 319.

7. R. D. Crowe and R. W. Albrecht, *Interpretation of Neutron Detector Signals During the PBF Severe Fuel Damage Scoping Test*, to be issued.

8. K. Vinjamuri and D. J. Osetek, *Results of the Severe Fuel Damage Scoping Test Effluent System Sample Analyses*, to be issued.

9. B. A. Cook, P. A. Kalish, and D. M. Tow, *Posttest Examination of SFD Scoping Test Bundle Geometry*, to be issued.

10. P. Hofmann, *Metallographic Examination of the Severe Fuel Damage Scoping Test (SFD-ST) Fuel Rod Bundle Cross Sections*, to be issued.

11. A. W. Cronenberg, J. K. Hartwell, D. L. Hagrman, and D. J. Osetek, *Fission Product Behavior During the PBF Severe Fuel Damage Scoping Test*, to be issued.

12. J. D. Abrashoff, *Reactor Physics Analysis for the Phase I Severe Fuel Damage Experiments in the Power Burst Facility*, EG&G Internal Document, EGG-PHYS-5550, October 1981.

13. F. W. Dittus and L. M. K. Boelter, "Heat Transfer in Automobile Radiators of the Tubular Type," *University of California Publication, 2*, 1930, pp. 443-461.

14. K. J. Therp, *Instrument Schedule and Calibration Data for SFD-ST Test Train*, EG&G Internal Document, KCT-65-82, July 1982.

15. B. Daniel, A. L. Nichols and J. A. H. Simpson, *The Liquefaction of Alloys Identified with Structural Material in a PWR Core: Zircaloy, Inconel-600 and 304 Stainless Steel*, AEEW-M2250, 1985.

16. P. Nikolopoulos et al., "Determination of the Interfacial Energy and Work of Adhesion in the UO_2/Zircaloy-4 Diffusion Couple," *Journal of Nuclear Materials, 124*, 1984, pp. 106-113.

17. D. R. Olander, *Oxidation of UO_2 by High Pressure Steam*, LBL-20531, Department of Nuclear Engineering, Lawrence Berkeley Laboratory, Submitted for publication in November 1985.

18. B. G. Schnitzler, EG&G internal letter to D. L. Hagrman, "SFD-ST and SFD 1-1 Isotopic Distributions," BG7-7-84, June 14, 1984.

19. U.S. Nuclear Regulatory Commission, *Technical Bases for Estimating Fission Product Behavior During LWR Accidents*, NUREG/CR-0772, June 1981.

20. M. R. Kuhlman, et al., *CORSOR User's Manual*, NUREG/CR-4173, 1985.

21. T. M. Besmann, *SOLGASMIX-PX, A Computer Program to Calculate Equilibrium Relationships in Complex Chemical Systems*, ORNL/TM-5775, Oak Ridge National Laboratory, 1977.

22. R. P. Wichner and R. D. Spence, "A Chemical Equilibrium Estimate of the Aerosols Produced in an Overheated Light Water Reactor Core," *Nuclear Technology, 70*, September 1985.

23. C. M. Allison, E. R. Carlson, and R. H. Smith, "SCDAP: A Computer Code for Analyzing Light Water Reactor Severe Core Damage," *Proceedings of the International Meeting on Light Water Reactor Severe Accident Evaluation, Cambridge, Massachusetts, August 28-September 1, 1983*.

24. J. Rest, "Volatile Fission-Product Source Term Evaluation using the FASTGRASS Computer Code," *Proceedings of the International Meeting on Thermal Reactor Safety, Chicago, Illinois, August 29-September 2, 1982*, pp. 111-121.

25. J. Rest, "Evaluation of Volatile and Gaseous Fission Product Behavior in Water Reactor Fuel Under Normal and Severe Core Accident Conditions," *Nuclear Technology, 61*, 1983, pp. 33-48.

26. J. Rest, "The Mechanistic Prediction of Xenon, Iodine, and Cesium Release from LWR Fuel Under Degraded-Core Accident Conditions," *ANS Topical Meeting on Fission Product Behavior and Source Term Research, Snowbird, Utah, July 15-19, 1984*.

27. J. N. Lillington, *Analysis of the PBF Severe Fuel Damage Scoping Test Using SCDAP*, AEEW-R1757, October 1984.

APPENDIX A

FUEL ROD CHARACTERISTICS

APPENDIX A

FUEL ROD CHARACTERISTICS

The nominal design characteristics for the standard fuel rods in the SFD-ST bundle are provided in Table A-1. Based on these values the total UO_2 fuel mass and zircaloy mass is 16.2 kg and 4.5 kg respectively. However, only 19 of the 32 rods in the bundle were standard rods and the design of the remaining 13 instrumented rods introduced notable differences to the nominal characteristics. Instrument access to the rods was through modified bottom end plugs, which were extended to accommodate thermocouple transition pieces and the pressure devices. The extensions significantly increased the total fill gas volumes to between 12.9 cm^3 and 14.2 cm^3, depending on the particular instrumented rod. The 10 rods containing thermocouples had small additional fill gas volumes resulting from oversized lead access channels in the fuel pellets. The lead access channels also reduced slightly the fuel mass in each of the thermocouple instrumented rods.

The fuel bundle was assembled using three Inconel grid spacers to maintain a typical PWR fuel rod pitch of 12.75 $\pm$ 0.25 mm. An overall view of the SFD-ST test train was given in Section 2.2, Figure 2, of the main text. Figure A-1 provides a more detailed schematic of the test bundle within the shroud, and the associated inlet and outlet regions.

Table A-1. Nominal design characteristics for standard fuel rod in the SFD-ST

Parameter	Value
Fuel:	
Material	UO_2 sintered pellets
Density	95% theoretical density(TD = 10980 kg/m^3)
Enrichment	6.2 wt% U-235 in total U
Pellet OD	8.268 mm
Pellet length	9.525 mm
Fuel stack length	0.9144 m
Pellet end dish (2)	1.51% of pellet cylindrical volume
Pellet rims	0.57% of pellet cylindrical volume
UO_2 fuel mass	0.50625 kg per rod
Cladding:	
Material	ASTM B353, Grade RA-2 (zircaloy-4 tubing)
Tube OD	9.627 mm
Tube wall thickness	0.597 mm
Tube ID	8.433 mm
Fuel Rod:	
Spring material	Inconel X-750
Spring load on fuel stack	22.2 - 66.7 N
Filler gas	Helium
Fill gas volume	6.55 cm^3
Plenum volume above fuel	2.79 cm^3
Initial gas pressure (STP)	3.8 MPa
Diametral gap	0.165 mm
Insulator pellet material	Al_2O_3

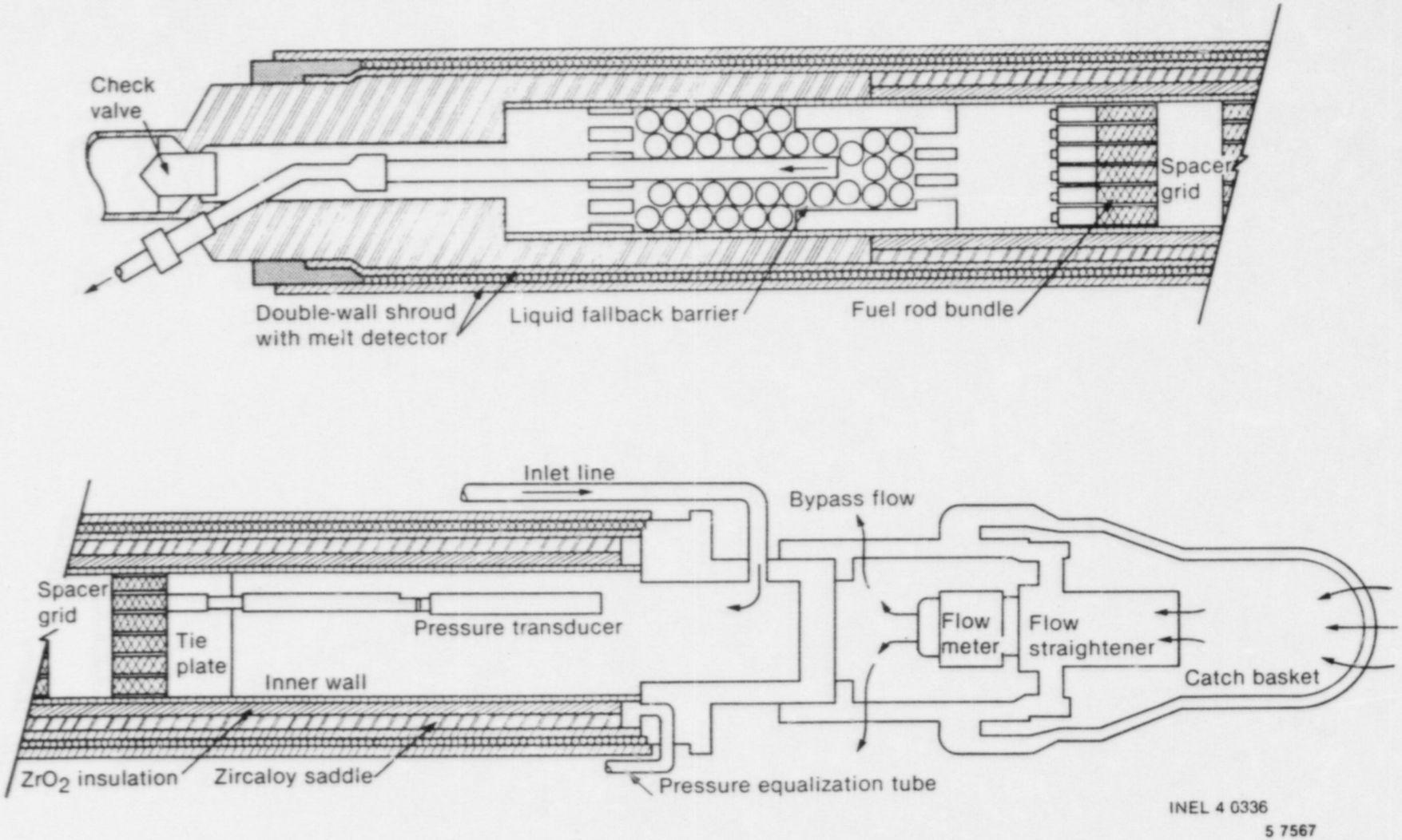

Figure A-1. SFD-ST test train schematic.

APPENDIX B

INSTRUMENT LOCATION, TESTING, AND PERFORMANCE

APPENDIX B

INSTRUMENT LOCATION, TESTING, AND PERFORMANCE

1. INTRODUCTION

Detailed tables and diagrams, identifying each instrument and categorizing performance, are provided in this appendix. Also included are descriptions of the pretransient checks, posttest data qualification procedures, and overall instrument performance.

2. INSTRUMENT LOCATION

The instruments associated with the SFD-ST are listed in Table B-1, with the exception of the two pressure transducers that failed prior to the installation of the test train and the temperature profile detectors, from which no data were obtained. The table summarizes the measurement quantity and the instrument type, location, and identifier. The identifier is a descriptive label that includes information about the instrument type and location. Also associated with each instrument, and given in Table B-1, is the PBF Data Acquisition and Reduction System (DARS) parameter number. This number has been used to locate instruments on a series of schematics (shown in square brackets): Figures B-1 to B-3 identify the instrumentation at 10 elevations (level 1 through 10), Figure B-4 is an overall view of the test train, Figure B-5 shows the test train coolant and pressure control system and Figure B-6 shows the Fission Product Detection System.

3. INSTRUMENT CHECKS

The initial set-up and test procedures for the experiment instrumentation were detailed in the Data Acquisition Specification (DAS). This document (see also Appendix I, Subsection 2.2) identifies the amplifiers to be used, gain settings, zero offsets, instrument ranges, patch panel connections and associated DARS parameter numbers. Transducer calibration coefficients were developed and checked for use in the DARS directory as outlined in the Transducer Report (Appendix I, Subsection 2.3). For those instruments that were not calibrated, coefficients were determined on the basis of laboratory calibration data. Some of the coefficients were adjusted as a result of in situ calibration or special experiment requirements.

The various check phases of the system are summarized in the following six subsections.

3.1 Initial System Check.

After the installation of the test train, and completion of the instrumentation-DARS interconnections, the procedures listed below were carried out.

1. Millivolt readings were taken from each sensor where applicable

2. The sensor was disconnected from the input patch panel and, with a millivolt input, readings were taken at

   a. The low level amplifier output (millivolts)

   b. The DARS input (counts)

   c. The DARS output (Engineering Units)

3. The various readings were compared against calculated outputs, and if discrepancies were found appropriate corrective action was taken.

3.2 DARS Precalibration

Each DARS channel was calibrated prior to the beginning of the test by voltage insertion at the electronic input. The magnitude, frequency, sign or wave form of the test signal was representative of the transducer output for that channel. The calibration performed immediately prior to the test is termed the *precalibration*. The test data were evaluated during the data qualification process, for zero offset or gain error introduced by the electronics, based on this pretest calibration.

3.3 Cold Hydro Pressure Verification

With the loop piping at approximately ambient temperature, the pressure was varied in 10% steps to 15.53 MPa and returned in the same manner. At each of these steps millivolt readings from the pressure transducers were taken at the test train and plant instrumentation system interface and in the control room. These were compared to verify proper operation.

3.4 Auto Calibration

Prior to each heatup, a system auto-calibration was performed. By remote control from the control room, the front end of the DARS was instructed (channel by channel) to disconnect itself from the transducer, read five voltage steps provided by a highly accurate programmable direct current source, then calculate second order regression coefficients to correct all future readings to what they would be were the system totally free of gain and drift.

3.5 Heatup

This phase of the test raised the system from ambient pressure and temperature to system operating conditions and a 2.2 L/s coolant flow. The pressure transducers were corrected over the range of the heatup to correspond to the SYS PRES Ashcroft gauge. At the end of heatup, under assumed isothermal conditions, all test train thermocouples were adjusted to the mean temperature. After this was performed, all thermocouples read within 5 K of each other. Also during heatup, the test train flowmeters were intercalibrated.

3.6 Nuclear Instrumentation Verification

Nuclear operation was commenced, and the system ramped to, and held at, a 4 MW power level to provide verification of nuclear instrumentation and a check of correct differential thermocouple connections.

4. DATA QUALIFICATION CATEGORIES AND PROCESS

The classification of Engineering Unit data was made by assignment of data to defined categories during particular test intervals. The assignment was made first by determining which data were not to be reviewed and would be left unqualified. These data are retained in raw form on computer tapes and are not presented in this report. The remaining data were assigned categories on the basis of documented methods, procedures, and guidelines. Category assignment was made through examination of single channel test data in Engineering Units. The examination process determined whether the measurement channel output represented the expected, predicted or required response. As a result of examination, one or more of the categories defined below were assigned by the Data Integrity Review Committee (DIRC) to each measurement as a function of time.

1. Qualified Engineering Unit Data (Q)

2. Trend Data (T)

3. Failed Instrument Data (F).

4.1 Qualified Data

Data assigned a *Qualified* status by the DIRC met all the following criteria:

1. Engineering Unit conversion equations had been applied

2. Data acquisition system calibrations had been applied

3. All identifiable and verifiable systematic errors had been removed

4. Uncertainty limits were established for the 95% confidence level including

   a. All calibration uncertainties

   b. Systematic and random uncertainties because of the effects on perturbations of the phenomena

   c. Uncertainties due to the application of any models

   d. Uncertainties in the measurement channels and DARS

5. Some useful information was contained in the data.

4.2 Trend Data

Trend data have been verified (by DIRC with input from appropriate analysts and data integrity specialists) to represent the relative changes in the phenomenon but do not necessarily represent the absolute level in the phenomenon measured because

1. Instrument calibrations did not adequately represent the environment that the transducer measured

2. The calibration and performance of the data acquisition system were suspect but known errors had been eliminated

3. Uncertainty limits could not be adequately quantified

4. Transducer performance was suspect but thought to be relatively correct

5. Environmental effects could not be adequately compensated.

These data have met the following criteria:

1. Instrument and data acquisition calibrations had been applied

2. Unreasonable points had been removed

3. Data had been filtered by appropriate anti-aliasing filtering.

4.3 Failed Instrument Data

Data were considered *Failed* by DIRC for one or more of the following reasons:

1. Data did not meet the requirements of any other data classification categories
2. Useful information was irretrievable from data
3. There was a component failure in the measurement channel or in the data acquisition system
4. Inadequate rejection of extraneous noise, transients, or frequencies
5. Loss of synchronization and data channel continuity
6. Enigmas in the data.

4.4. Methods For Evaluating Uncertainties

A transducer and associated signal conditioning electronics introduce uncertainty into a measurement. To establish validity of experiments and their correlation to analytical models, performance and accuracy of the test instrumentation and data recording system must be demonstrated. Uncertainties in instrument accuracy propagate through the experimental data to the evaluation of the analytical models and overall program results.

A measurement channel included the transducer, signal conditioning, and data acquisition and reduction system (DARS). The form of uncertainty presented may be either tabular, representing the uncertainty values for a particular operating condition, or graphical, with uncertainty versus input signal from which the user can determine the uncertainty for any value within the useful range of the transducer. The uncertainty values in either Engineering Units or percent of reading, were determined from

$$U = \left[B^2 + t_{95}\, S^2\right]^{1/2} \qquad \text{(B-1)}$$

where

U = uncertainty

B = total channel systematic error (bias)

S = total channel random error (precision index)

t_{95} = two-tailed Student t factor for 95% confidence level (2 σ).

The t_{95} factor was determined from a Student t table and the degrees of freedom associated with random error measurement. The bias, B, is the root-sum-square (RSS) of all the elemental biases in the measurement channel. Likewise, the precision index is the RSS of all the elemental precision indexes in the measurement channel.

Test-independent uncertainty analyses of PBF measurement systems have been performed. The methodology used in the analysis of the uncertainties was based on standard statistical practices that were applied in evaluating the constant and variable portions of both the bias and random error components of each measurement channel. The individual error components were then combined to produce a total measurement channel uncertainty.

When a measurement channel was analyzed for test-independent measurement uncertainty, that uncertainty applied to a representative assembly of specific types of channel components rather than a specific component. If an individual component was replaced by a component of the same type, the uncertainty of the measurement channel remained unchanged.

The data qualification procedure, performed by the PBF Data Integrity Review Committee (DIRC), served to identify some of the significant test-dependent uncertainties such as instrument mounting effects, two-phase flow regimes, and transient measurements. In some cases, additional or special calibrations, multiple instrumentation, and additional engineering calculations resulted in significantly lower uncertainty estimates than those found in the uncertainty analyses. These test-dependent considerations have been factored into the total uncertainty values presented for each measurement.

4.5 Presentation of the Qualified Data

Table B-2 provides a complete summary of the qualification categories for each measurement. A complete set of plots of the data is presented in the final appendix of this report (Appendix J) and these supercede all previously released data. Qualified and Trend data appear as solid and dashed lines, respectively, on the plots. In cases where part of the data have been classified as Failed there are no plot lines. The Qualified data presented in Appendix J contain error bars representing the 95% confidence level (2σ). Data plots presented in the body of this report are from the same source but do not show the uncertainties.

4.6 Summary of Instrument Performance

4.6.1 Thermocouples. The test train and coolant control system were instrumented with over 80 thermocouples. The steam, internal cladding, and shroud thermocouples all had zircaloy sheaths and W/Re thermal elements (Type C). The zircaloy sheaths, however, were of three types: pure zircaloy, zircaloy with an oxidized inside layer, and zircaloy with a tantalum inner liner. The responses of the various sheath types, and the influence of different locations, are summarized graphically in Figure B-7, where the temperature at which the data became erratic or of questionable accuracy is indicated. The steam probes with pure zircaloy sheaths averaged 1355 K, whereas the same type of thermocouple in the shroud insulation averaged 1223 K before becoming erratic. These results are consistent with laboratory tests in which freely suspended thermocouples (steam probes) operated successfully at consistently higher temperatures than thermocouples fastened to a zircaloy substrate (shroud insulation saddles).

The zircaloy sheath with the oxidized inner layer did not appear to function better than the pure zircaloy sheath. The sheath with the tantalum liner was superior to the other types in both the shroud and fuel applications, where it measured average temperatures of 1531 and 2020 K, respectively, before becoming erratic.

Figure B-8 provides a more detailed comparison of the performance of each of the cladding inside surface thermocouples, indicating the temperatures at which they were considered failed. It can be seen that thermocouples with the tantalum lined sheath in general performed better than the devices with the ZrO_2 inner coating. It will also be observed that the rate of temperature rise appears to have a significant influence on the thermocouples performance, higher failure temperatures occurring with the faster rise rates.

The performance of the fuel centerline W/Re thermocouples with Mo/Re sheaths was about the same as that of the zircaloy-sheathed, tantalum-lined, thermocouples. Both types operated properly to temperatures above 2000 K.

4.6.2 Pressure Switches and Transducers. There were five pressure switches mounted in the fuel rods. These devices should have been *cocked* by the rod internal pressure when it reached values above 7.5 MPa

during the transient and then should have *released* when the rods failed and the rod internal pressure decreased to the system pressure. Three of the five devices (in Rods 6D, 3E, and 2B) worked properly, and recorded rod failure.

Of the five internal fuel rod pressure transducers, two failed before the test train was installed in the PBF. Of the remaining three, only the transducer in Rod 3D approximately followed the rod internal pressure as it changed with power and temperature and indicated failure at the same time as the pressure switches. All of the differential pressure transducers appeared to work properly. The three system pressure transducers all operated properly.

4.6.3 Fission Chamber System. The 12 fission chambers and the corresponding special signal conditioning instruments operated properly throughout the experiment. In addition to the digital data that were recorded, analog data were recorded from single fission chambers at 0.81, 0.70, 0.35, and 0.17 m above the bottom of the fuel stack. From these analog data it was possible to determine the steam-water/steam and the steam-water/water interfaces as they moved past these fission chambers. These devices also provided information on two-phase flow velocities and directions early in the transient, and possible fuel movement late in the transient.

4.6.4 Turbine Flowmeters. Two turbine flowmeters were installed in the test train. One flowmeter was installed at the bottom of the train and was used to measure the bypass flow rate past the outer wall of the shroud. A second flowmeter was installed in the outlet of the test train to measure the flow out of the test bundle and through the check valve during the high-flow, preconditioning phases of the test. These flowmeters remained operational throughout the test. Two turbine flowmeters (high- and low-flow capacity) were also installed in the experiment cooling line that supplied inlet flow to the test bundle. The high-flow flowmeter failed during preconditioning and the flow through the bundle was measured using the outlet flowmeter on the test train.

4.6.5 Bundle Temperature Profile Detectors. Both of the devices, intended to measure the axial movement of selected temperature fronts along the bundle, failed near the beginning of the transient. No data were obtained from these detectors.

4.6.6 Shroud Melt-Through Detector. The shroud melt-through detector, designed to indicate melt-through of the outer wall of the shroud assembly, operated properly throughout the experiment and detected both the inner shroud liner failure and the high temperature bundle operation near the end of the transient. The detector indicated that melt-through of the outer shroud wall did not occur.

4.6.7 Flux Wires. Two aluminum-cobalt alloy flux wires were axially mounted on the outer shroud wall, one at 0-degrees and one at 180-degrees. The axial power profile within the in-pile tube was determined from the flux wire gamma scans. The flux wires could not be extracted from their sheaths and were therefore removed as units from the test train. The wires and tubings were cut into ~25-mm long sections and analyzed by gamma-ray spectroscopy techniques to obtain the ^{60}Co activity. Since the sections were not identical in length the results were expressed in terms of activity per unit weight.

4.6.8 Fission Product Detection System (FPDS). The principal objectives of the FPDS during the SFD-ST were to investigate the overall operating performance of the system, identify any problem areas with reference to future tests, and obtain as much useful fission product data as possible. The objectives were met, and a few design changes were identified that improved FPDS performance for the following tests.

The system was operated by two computers at different locations, and as a result collimator control and grab sample timing were troublesome. A single, consolidated FPDS control station in the PBF control room was eventually installed.

Background radiation measurements taken during the high-power preconditioning phase of the test indicated that several radioactive gaseous isotopes were present in the environment of the germanium detectors.

The radioactive gas was leaking into the detector enclosures, causing a degradation in the signal-to-background ratio. A clean air purge of the enclosures was established following high-power preconditioning to help prevent contamination of the detectors during the remainder of the test. A reduction in the measured count rate of fission gas isotopes was noted during the subsequent 4 h, low power fuel conditioning phase. Background count rates taken during preconditioning were markedly different for each of the three spectrometers. The gasline spectrometer displayed a count rate nearly double that of the unfiltered liquidline spectrometer. The filtered liquidline spectrometer indicated the highest background count rate of the three detectors. The effectiveness of the shielding was different for each of the detectors due to the different geometry and arrangement in the room which housed the FPDS (Cubicle 13). The gasline spectrometer was nearest the PBF core and had a 200 mm outside shield wall. The filtered liquidline spectrometer was most distant from the PBF core and had a 100 mm outside shield wall with several conduit penetrations. The unfiltered liquidline spectrometer was in the center of the enclosure and, thus, had the greatest effective shield thickness. The spectrometers with greater background count rates had greater uncertainty in results and detection sensitivity.

Fission product activity in the sample lines during the transient greatly exceeded levels experienced during PBF tests prior to the SFD program. The germanium detectors recorded count rates exceeding 10^5 cps. The combination of fast electronics and variable collimators allowed the acquisition of valid, high-resolution spectra even when the sample line dose-rates were of the order of 100 R/h. A review of the spectrometer data indicated that sample intensities twice those encountered during the SFD-ST are within the performance margin of the FPDS.

The collimators were periodically closed during the test to assess signal-to-background ratios. Background counts were excessive at times when Cubicle 13 radiation levels were high.

Approximately 45 s of data were lost by the filtered liquid spectrometer due to excessive dead-time at wide collimator settings. Approximately 13 min of data were lost by the gas and unfiltered liquid spectrometers partly due to slow, manual operation of the remote spectrometer computers.

The gross radiation monitors in the FPDS gave mixed results during the SFD-ST. The ion chamber response was very useful, whereas the NaI and delayed neutron detectors seemed to indicate only general Cubicle 13 radiation levels.

Six steam and six liquid grab samples were taken during the test but selection of sample times was difficult. There was also a problem in determining the location of the sampling sequences resulting in samples being taken twice.

4.6.9 Overall Performance. Table B-3 presents a summary of the test train instrument performance during the high-temperature transient. Failure of an instrument has been defined as the inability of the device to produce usable data or when the data were erratic or of questionable accuracy. The partial failures listed in the table indicate that these instruments failed below their expected peak operating range, but that usable data were obtained up to the failure time.

Table B-1. SFD-ST instrument identification

Measurement	Instrument	Location	Rod Number	Identifier	DARS Parameter Number
Clad surface temperature	Thermocouple Type C	Interior clad wall	—	—	
		0.35 m, 045°	4B	CLADTEMPbb045b35B4	235
		0.35 m, 045°	6B	CLADTEMPbb045b35B6	236
		0.35 m, 045°	2C	CLADTEMPbb045b35C2	247
		0.35 m, 135°	4C	CLADTEMPbb135b35C4	249
		0.35 m, 135°	3D	CLADTEMPbb135b35D3	250
		0.35 m, 045°	5E	CLADTEMPbb045b35E5	251
		0.35 m, 045°	3F	CLADTEMPbb045b35F3	239
		0.50 m, 315°	3A	CLADTEMPbb315b50A3	240
		0.50 m, 135°	3A	CLADTEMPbb135b50A3	241
		0.50 m, 270°	4B	CLADTEMPbb270b50B4	242
		0.50 m, 180°	6B	CLADTEMPbb180b50B6	243
		0.50 m, 270°	2C	CLADTEMPbb270b50C2	244
		0.50 m, 000°	4C	CLADTEMPbb000b50C4	245
		0.50 m, 000°	3D	CLADTEMPbb000b50D3	246
		0.50 m, 045°	1E	CLADTEMPbb045b50E1	67
		0.50 m, 225°	1E	CLADTEMPbb225b50E1	68
		0.50 m, 135°	5E	CLADTEMPbb135b50E5	69
		0.50 m, 135°	3F	CLADTEMPbb135b50F3	70
		0.70 m, 180°	4B	CLADTEMPbb180b70B4	57
		0.70 m, 270°	6B	CLADTEMPbb270b70B6	58
		0.70 m, 180°	2C	CLADTEMPbb180b70C2	59
		0.70 m, 225°	4C	CLADTEMPbb225b70C4	60
		0.70 m, 225°	3D	CLADTEMPbb225b70D3	61
		0.70 m, 270°	5E	CLADTEMPbb270b70E5	63
		0.70 m, 270°	3F	CLADTEMPbb270b70F3	64
Shroud temperature outer wall	Thermocouple Type K	-0.31 m, 090°	—	SHRDTEMPbbOUT09031	196
		-0.31 m, 270°	—	SHRDTEMPbbOUT27031	207
		0.35 m, 000°	—	SHRDTEMPbb0UT00035	65
		0.35 m, 090°	—	SHRDTEMPbb0UT09035	213
		0.35 m, 180°	—	SHRDTEMPbb0UT18035	214
		0.35 m, 270°	—	SHRDTEMPbb0UT27035	215
		0.50 m, 000°	—	SHRDTEMPbb0UT00050	227
		0.50 m, 090°	—	SHRDTEMPbb0UT09050	80
		0.50 m, 180°	—	SHRDTEMPbb0UT18050	81
		0.50 m, 270°	—	SHRDTEMPbb0UT27050	82
		0.70 m, 000°	—	SHRDTEMPbb0UT00070	83
		0.70 m, 090°	—	SHRDTEMPbb0UT09070	84
		0.70 m, 180°	—	SHRDTEMPbb0UT18070	85
		0.70 m, 270°	—	SHRDTEMPbb0UT27070	86
Steam temperature	Thermocouple Type C	0.50 m, 5A-315°	—	STEAMTMPbbA5315b50	97
		0.50 m, 4D-315°	—	STEAMTMPbbD4315b50	98
		0.50 m, 1D-45°	—	STEAMTMPbbD1045b50	99
		0.50 m, 2E-45°	—	STEAMTMPbbE2045b50	100
		0.50 m, 6E-225°	—	STEAMTMPbbE6225b50	101
		0.91 m, 5A-135°	—	STEAMTMPbbA5135b91	102
		0.91 m, 1B-225°	—	STEAMTMPbbB1225b91	103
		0.91 m, 4C-225°	—	STEAMTMPbbC4225b91	104
		0.91 m, 5E-315°	—	STEAMTMPbbE5315b91	105
		0.91 m, 4F-315°	—	STEAMTMPbbF4315b91	106
		1.11 m, BR-270°	—	STEAMTMPbbBR270111	117
		1.11 m, BR-90°	—	STEAMTMPbbBR090111	118
		1.19 m, BR-000°	—	STEAMTMPbbBR000131[a]	71
		1.19 m, BR-180°	—	STEAMTMPbbBR180131[a]	72

Table B-1. (continued)

Measurement	Instrument	Location	Rod Number	Identifier	DARS Parameter Number
Steam line wall temperature	Thermocouple	1.5 m	—	STMLINEbbbWLTMP150	73
		1.8 m	—	STMLINEbbbWLTMP180	74
Rod pressure sensors	Thermocouple Type K and pressure switch	Fuel rod bottom	2B	RODPRESSbbSWITCHB2	75
			6B	RODPRESSbbSWITCHB6	76
			4C	RODPRESSbbSWITCHC4	87
			6D	RODPRESSbbSWITCHD6	88
			3E	RODPRESSbbSWITCHE3	89
Fuel centerline temperature	Thermocouple Type C	0.70 m	3A	FUELTEMPbbCLb70bA3	90
			4B	FUELTEMPbbCLb70bB4	91
			3C	FUELTEMPbbCLb70bC3	92
			3D	FUELTEMPbbCLb70bD3	93
			1E	FUELTEMPbbCLb70bE1	94
			5E	FUELTEMPbbCLb70bE5	95
Shroud temperature inner liner wall	Thermocouple Type C	0.35 m, 90°	—	SHRDTEMPbbIN090b35	96
		0.35 m, 270°	—	SHRDTEMPbbIN270b35	107
		0.50 m, 90°	—	SHRDTEMPbbIN090b50	108
		0.50 m, 270°	—	SHRDTEMPbbIN270b50	109
		0.70 m, 90°	—	SHRDTEMPbbIN090b70	110
		0.70 m, 270°	—	SHRDTEMPbbIN270b70	111
Shroud temperature between insulation and saddle regions	Thermocouple Type C	0.50 m, 0°	—	SHRDTEMPbbMID00050	112
		0.50 m, 90°	—	SHRDTEMPbbMID09050	113
		0.50 m, 180°	—	SHRDTEMPbbMID18050	114
		0.50 m, 270°	—	SHRDTEMPbbMID27050	115
		0.70 m, 0°	—	SHRDTEMPbbMID00070	116
		0.70 m, 90°	—	SHRDTEMPbbMID09070	127
		0.70 m, 180°	—	SHRDTEMPbbMID18070	128
		0.70 m, 270°	—	SHRDTEMPbbMID27070	129
		0.91 m, 0°	—	SHRDTEMPbbMID00091	130
		0.91 m, 180°	—	SHRDTEMPbbMID18091	131
Bundle coolant flow	Flowmeter (Low)	Plant	—	FLOWRATEbbFT1014PT	9137
Bundle coolant flow	Flowmeter (High)	Plant	—	FLOWRATEbbFT1013PT	11
Rod plenum pressure	Pressure transducer	Fuel rod bottom	3A	RODbPRESbbbbbbbbA3	13
			3D	RODbPRESbbbbbbbbD3	14
			5E	RODbPRESbbbbbbbbE5	15
Bundle pressure	Pressure transducer	Lower test train, Sense tube -0.3 m	—	SYSPRESbb69EGbLTT	41
Bypass pressure	Pressure transducer	Outside reactor, Sense tube 0.5 m	—	SYSPRESbb17bbbbbb	42
Bundle pressure differential	Differential pressure transducer	-0.3 m to 1.77 m	—	DIFbPRESbbNO2bbbTT	50
Fuel rod power profile	Flux wire Al - CO	Outer wall of shroud at 0° and 180°	—	FLUXWIREbbbbbb000	—
			—	FLUXWIREbbbbbb180	—
Bundle inlet coolant temperature	Thermocouple Type K	-0.305 m, 135°	—	INLTTEMPbb135bbb31	119
		-0.305 m, 315°	—	INLTTEMPbb315bbb31	173

Table B-1. (continued)

Measurement	Instrument	Location	Rod Number	Identifier	DARS Parameter Number
Bypass coolant temperature	Thermocouple Type K	-0.31 m, 0°	—	BYPbTEMPbb000bb-31	120
		-0.31 m, 90°	—	BYPbTEMPbb090bb-31	121
		-0.31 m, 180°	—	BYPbTEMPbb180bb-31	122
		-0.31 m, 270°	—	BYPbTEMPbb270bb-31	124
		-0.91 m, 0°	—	BYPbTEMPbb000bbb91	125
		-0.91 m, 90°	—	BYPbTEMPbbu90bbb91	49
		-0.91 m, 180°	—	BYPbTEMPbb180bbb91	253
		-0.91 m, 270°	—	BYPbTEMPbb270bbb91	256
Bypass coolant differential temperature	Differential thermocouple Type K	Lower legs at -0.31 m	—	—	
		Upper legs at +0.91 m	—	—	
		0°	—	DELbTEMPbbBYPbb000	43
		90°	—	DELbTEMPbbBYPbb090	44
		180°	—	DELbTEMPbbBYPbb180	45
		270°	—	DELbTEMPbbBYPbb270	46
Bypass coolant volumetric flow rate	Flowmeter	Lower test train	—	FLOW RATEbbBYPASS	170
Bundle coolant volumetric flow rate	Flowmeter	Upper test train	—	FLOW RATEbbBUNDLE	171
Neutron flux	Fission chambers	0.17 m, 90°	—	FISSCHAMbb090bDC17	141
		0.17 m, 270°	—	FISSCHAMbb270bDC17	142
		0.30 m, 90°	—	FISSCHAMbb090bDC30	143
		0.35 m, 90°	—	FISSCHAMbb090bDC35	133
		0.35 m, 270°	—	FISSCHAMbb270bDC35	134
		0.50 m, 90°	—	FISSCHAMbb090bDC50	135
		0.50 m, 270°	—	FISSCHAMbb270bDC50	147
		0.70 m, 90°	—	FISSCHAMbb090bDC70	148
		0.70 m, 270°	—	FISSCHAMbb270bDC70	149
		0.76 m, 90°	—	FISSCHAMbb090bDC76	151
		0.81 m, 90°	—	FISSCHAMbb090bDC81	152
		0.81 m, 270°	—	FISSCHAMbb270bDC81	153
Neutron flux	Fission chamber	0.17 m, 90°	—	FISSCHAMbb090bAC17	29
		0.17 m, 270°	—	FISSCHAMbb270bAC17	36
		0.30 m, 90°	—	FISSCHAMbb090bAC30	30
		0.35 m, 90°	—	FISSCHAMbb090bAC35	31
		0.35 m, 270°	—	FISSCHAMbb270bAC35	37
		0.50 m, 90°	—	FISSCHAMbb090bAC50	32
		0.50 m, 270°	—	FISSCHAMbb270bAC50	38
		0.70 m, 90°	—	FISSCHAMbb090bAC70	33
		0.70 m, 270°	—	FISSCHAMbb270bAC70	39
		0.76 m, 90°	—	FISSCHAMbb090bAC76	34
		0.81 m, 90°	—	FISSCHAMbb090bAC81	35
		0.81 m, 270°	—	FISSCHAMbb270bAC81	40
Reactor power NMS-3	Ion chamber	Plant	—	REACbPOWbbNMS-03PT	53
Reactor power NMS-4	Ion chamber	Plant	—	REACbPOWbbNMS-04PT	34
Reactor power PPS-1	Ion chamber	Plant	—	REACbPOWbbPPS-01PT	55
Reactor power PPS-2	Ion chamber	Plant	—	REACbPOWbbPPS-02PT	56
Reactor power TR-1	Ion chamber	Plant	—	REACbPOWbbTR-1bbPT	155
Reactor power TR-2	Ion chamber	Plant	—	REACbPOWbbTR-2bbPT	156
System pressure	PXD	Plant	—	SYSbPRESbbHEISEbPT	187
Loop flow	Flowmeter	Plant	—	LOOPbFLObbFRC-10PT	188
Gross gamma rate	No. 1 detector	FPDS	—	FPbGAMMAbbbbNo.b01	199

Table B-1. (continued)

Measurement	Instrument	Location	Rod Number	Identifier	DARS Parameter Number
Gross gamma rate	No. 2 detector	FPDS	—	FPbGAMMAbbbbNo.b02	200
Gross gamma rate	No. 3 detector	FPDS	—	FPbGAMMAbbbbNo.b03	201
Ion chamber	No. 4 detector	FPDS	—	FPbGAMMAbbbbNo.b04	255
Delayed neutron rate	Neutron detector	FPDS	—	FPbNEUTbbbbbNo.b01	195
Hydrogen concentration	H_2 Detector	FPDS	—	FPbHYDRbbbCONCENTb	219
Inlet line temperature	Thermocouple	FPDS	—	FPbTEMPbbbTE13-8PT	237
Condenser outlet fluid temperature	Thermocouple	FPDS	—	FPbTEMPbbbTE1329PT	238
Separation vessel pressure	PXD	FPDS	—	FPbPRESSbbPT13-42	175
Filter bypass pressure	Differential pressure transducer	FPDS	—	DIFFPRESSbbDP13-66	254
Separation vessel liquid flow	Flowmeter	FPDS	—	FPbFLOWbbbFT13-69	220
Collection vessel liquid level	Diff PXD	FPDS	—	BLOWbLEVbbLIT17bPT	167
Collection vessel pressure	PXD	FPDS	—	BLOWPRESbbPT12bbPT	169
Steam sample actuation	Limit switch	FPDS	—	FPbGASbbbbSAMPLE01	—
			—	FPbGASbbbbSAMPLE02	—
			—	FPbGASbbbbSAMPLE03	—
			—	FPbGASbbbbSAMPLE04	—
			—	FPbGASbbbbSAMPLE05	—
			—	FPbGASbbbbSAMPLE06	—
Liquid sample actuation	Limit switch	FPDS	—	FBbLIQDbbbSAMPLE01	—
			—	FBbLIQDbbbSAMPLE02	—
			—	FBbLIQDbbbSAMPLE03	—
			—	FBbLIQDbbbSAMPLE04	—
			—	FBbLIQDbbbSAMPLE05	—
			—	FBbLIQDbbbSAMPLE06	—
Shroud melt through	Melt detector	Outer shroud wall	—	SHRDMELTbbTHRUWW01	5
			—	SHRDMELTbbTHRUWS01	126
			—	SHRDMELTbbTHRUWW02	7
			—	SHRDMELTbbTHRUWS02	6
			—	SHRDMELTbbTHRUWW03	174
			—	SHRDMELTbbTHRUWS03	10
			—	SHRDMELTbbTHRUWW04	226
			—	SHRDMELTbbTHRUWS04	225
Instrumented spool piece flow	Flowmeter	Spool piece	—	ICSVFLOWbbFE05SPIC	1
Instrumented spool piece temperature	RTD	Spool piece	—	ICSSTEMPbbTE20SPIC	2
Instrumented spool piece pressure	Pressure	Spool piece	—	ICPRESSWbbPE09SPIC	3
Reactor heat exchanger differential temperature	Differential thermocouple	Plant	—	PFHXRDTbbbHXDTPT	123
Reactor coolant flow rate	Flowmeter	Plant	—	REARFLOWbbPRIMFLOW	79

a. Level identifier 131 incorrect; actual level of 1.19 m.

Table B-2. SFD-ST qualification categories

DARS PARAMETER NUMBER	INSTRUMENT IDENTIFIER	QUALIFICATION	START TIME	STOP TIME
1	ICSVFLOWFE05SPIC	QUALIFIED	10/13 00:07: 0.0	10/29 10:20: 0.0
2	ICSSTEMPTE20SPIC	QUALIFIED	10/13 00:07: 0.0	10/29 02:50: 0.0
		QUALIFIED	10/29 02:50: 0.0	10/29 10:20: 0.0
3	ICPRESSWPE09SPIC	TREND	10/13 00:07: 0.0	10/29 10:20: 0.0
5	SHRDMELTTHRUWW01	TREND	10/28 16:50: 0.0	10/29 02:50: 0.0
6	SHRDMELTTHRUWS02	TREND	10/28 16:50: 0.0	10/29 02:50: 0.0
7	SHRDMELTTHRUWW02	TREND	10/28 16:50: 0.0	10/29 02:50: 0.0
9	FLOWRATEFT1014PT	QUALIFIED	10/28 16:50: 0.0	10/29 02:50: 0.0
10	SHRDMELTTHRUWS03	TREND	10/28 16:50: 0.0	10/29 02:50: 0.0
11	FLOWRATEFT1013PT	QUALIFIED	10/13 00:07: 0.0	10/13 13:00: 0.0
		FAILED	10/13 13:00: 0.0	10/22 00:00: 0.0
		QUALIFIED	10/27 04:47: 0.0	10/28 16:50: 0.0
		QUALIFIED	10/29 02:50: 0.0	10/29 10:20: 0.0
13	ROD PRES A3	FAILED	10/28 16:50: 0.0	10/29 02:50: 0.0
14	ROD PRES D3	TREND	10/28 16:50: 0.0	10/29 02:50: 0.0
15	ROD PRES E5	FAILED	10/28 16:50: 0.0	10/29 02:50: 0.0
29	FISSCHAM090 AC17	TREND	10/28 23:00: 0.0	10/29 02:50: 0.0
30	FISSCHAM090 AC30	TREND	10/28 23:00: 0.0	10/29 02:50: 0.0
31	FISSCHAM090 AC35	TREND	10/28 23:00: 0.0	10/29 02:50: 0.0
32	FISSCHAM090 AC50	TREND	10/28 23:00: 0.0	10/29 02:50: 0.0
33	FISSCHAM090 AC70	TREND	10/28 23:00: 0.0	10/29 02:50: 0.0
34	FISSCHAM090 AC76	TREND	10/28 23:00: 0.0	10/29 02:50: 0.0
35	FISSCHAM090 AC81	TREND	10/28 23:00: 0.0	10/29 02:50: 0.0
36	FISSCHAM270 AC17	TREND	10/28 23:00: 0.0	10/29 02:50: 0.0
37	FISSCHAM270 AC35	TREND	10/28 23:00: 0.0	10/29 02:50: 0.0
38	FISSCHAM270 AC50	TREND	10/28 23:00: 0.0	10/29 02:50: 0.0
39	FISSCHAM270 AC70	TREND	10/28 23:00: 0.0	10/29 02:50: 0.0
40	FISSCHAM270 AC81	TREND	10/28 23:00: 0.0	10/29 02:50: 0.0
41	SYS PRES69EG LTT	QUALIFIED	10/13 00:07: 0.0	10/29 02:25:47.7
		FAILED	10/29 02:25:47.7	10/29 02:26:47.0
		QUALIFIED	10/29 02:26:47.0	10/29 10:20: 0.0
42	SYS PRES17	QUALIFIED	10/13 00:07: 0.0	10/29 02:25:47.7
		FAILED	10/29 02:25:47.7	10/29 02:26:47.0
		QUALIFIED	10/29 02:26:47.0	10/29 10:20: 0.0
43	DEL TEMPBYP 000	QUALIFIED	10/28 16:50: 0.0	10/29 02:50: 0.0
44	DEL TEMPBYP 090	QUALIFIED	10/28 16:50: 0.0	10/29 02:50: 0.0

Table B-2. (continued)

DARS PARAMETER NUMBER	INSTRUMENT IDENTIFIER	QUALIFICATION	START TIME	STOP TIME
45	DEL TEMPBYP 180	QUALIFIED	10/28 16:50: 0.0	10/29 02:50: 0.0
46	DEL TEMPBYP 270	QUALIFIED	10/28 16:50: 0.0	10/29 02:50: 0.0
49	BYP TEMP090 91	QUALIFIED	10/28 16:50: 0.0	10/29 10:20: 0.0
50	DIF PRESNO2 TT	QUALIFIED	10/13 00:07: 0.0	10/29 10:20: 0.0
53	REAC POWNMS-03PT	QUALIFIED	10/28 23:00: 0.0	10/29 02:50: 0.0
54	REAC POWNMS-04PT	QUALIFIED	10/28 23:00: 0.0	10/29 02:50: 0.0
55	REAC POWPPS-01PT	QUALIFIED	10/13 00:07: 0.0	10/29 10:20: 0.0
56	REAC POWPPS-02PT	QUALIFIED	10/13 00:07: 0.0	10/29 10:20: 0.0
57	CLADTEMP180 70B4	FAILED	10/13 00:07: 0.0	10/29 02:50: 0.0
58	CLADTEMP270 70B6	QUALIFIED	10/13 00:07: 0.0	10/29 01:33: 1.0
		TREND	10/29 01:33: 1.0	10/29 02:50: 0.0
59	CLADTEMP180 70C2	QUALIFIED	10/13 00:07: 0.0	10/29 01:41:11.0
		TREND	10/29 01:41:11.0	10/29 02:50: 0.0
60	CLADTEMP225 70C4	FAILED	10/13 00:07: 0.0	10/29 10:20: 0.0
61	CLADTEMP225 70D3	QUALIFIED	10/13 00:07: 0.0	10/29 02:16: 4.0
		TREND	10/29 02:16: 4.0	10/29 02:26:32.0
		FAILED	10/29 02:26:32.0	10/29 02:50: 0.0
63	CLADTEMP270 70E5	QUALIFIED	10/13 00:07: 0.0	10/29 01:33: 1.0
		TREND	10/29 01:33: 1.0	10/29 02:17:39.0
		FAILED	10/29 02:17:39.0	10/29 02:26: 7.0
		TREND	10/29 02:26: 7.0	10/29 02:50: 0.0
64	CLADTEMP270 70F3	QUALIFIED	10/13 00:07: 0.0	10/29 01:20:20.0
		FAILED	10/29 01:20:20.0	10/29 01:25:50.0
		TREND	10/29 01:25:50.0	10/29 02:50: 0.0
65	SHRDTEMPOUT00035	QUALIFIED	10/13 00:07: 0.0	10/29 10:20: 0.0
67	CLADTEMP045 50E1	QUALIFIED	10/13 00:07: 0.0	10/29 02:21:40.0
		FAILED	10/29 02:21:40.0	10/29 02:50: 0.0
68	CLADTEMP225 50E1	QUALIFIED	10/13 00:07: 0.0	10/29 02:22: 0.0
		FAILED	10/29 02:22: 0.0	10/29 02:29:10.0
		TREND	10/29 02:29:10.0	10/29 02:50: 0.0
69	CLADTEMP135 50E5	QUALIFIED	10/13 00:07: 0.0	10/29 02:11:40.0
		TREND	10/29 02:11:40.0	10/29 02:50: 0.0
70	CLADTEMP135 50F3	QUALIFIED	10/13 00:07: 0.0	10/29 01:35: 9.0
		TREND	10/29 01:35: 9.0	10/29 02:50: 0.0
71	STEAMTMPBR000131	QUALIFIED	10/13 00:07: 0.0	10/29 02:02:30.0
		FAILED	10/29 02:02:30.0	10/29 02:35: 0.0
		TREND	10/29 02:35: 0.0	10/29 10:20: 0.0
72	STEAMTMPBR180131	QUALIFIED	10/13 00:07: 0.0	10/29 02:04:52.0
		FAILED	10/29 02:04:52.0	10/29 02:17:50.0
		TREND	10/29 02:17:50.0	10/29 10:20: 0.0
73	STMLINE WLTMP150	QUALIFIED	10/28 16:50: 0.0	10/29 02:50: 0.0

Table B-2. (continued)

DARS PARAMETER NUMBER	INSTRUMENT IDENTIFIER	QUALIFICATION	START TIME	STOP TIME
74	STMLINE WLTMP180	QUALIFIED	10/28 16:50: 0.0	10/29 02:50: 0.0
75	RODPRESSSWTCH B2	TREND	10/28 16:50: 0.0	10/29 02:50: 0.0
76	RODPRESSSWTCH B6	FAILED	10/28 16:50: 0.0	10/29 02:50: 0.0
79	REARFLOWPRIMFLOW	QUALIFIED	10/13 00:07: 0.0	10/29 10:20: 0.0
80	SHRDTEMPOUT09050	QUALIFIED	10/13 00:07: 0.0	10/29 02:50: 0.0
		QUALIFIED	10/29 02:50: 0.0	10/29 10:20: 0.0
81	SHRDTEMPOUT18050	QUALIFIED	10/13 00:07: 0.0	10/15 15:25:34.0
		QUALIFIED	10/15 18:37: 0.0	10/16 14:35: 0.0
		QUALIFIED	10/16 16:15: 0.0	10/29 02:50: 0.0
		QUALIFIED	10/29 02:50: 0.0	10/29 10:20: 0.0
82	SHRDTEMPOUT27050	QUALIFIED	10/13 00:07: 0.0	10/15 15:25:34.0
		QUALIFIED	10/15 17:13:40.0	10/29 02:50: 0.0
		QUALIFIED	10/29 02:50: 0.0	10/29 10:20: 0.0
83	SHRDTEMPOUT00070	QUALIFIED	10/13 00:07: 0.0	10/15 15:25:34.0
		QUALIFIED	10/15 17:13:40.0	10/29 02:50: 0.0
		QUALIFIED	10/29 02:50: 0.0	10/29 10:20: 0.0
84	SHRDTEMPOUT09070	QUALIFIED	10/13 00:07: 0.0	10/15 15:25:34.0
		QUALIFIED	10/15 17:13:40.0	10/29 02:50: 0.0
		QUALIFIED	10/29 02:50: 0.0	10/29 10:20: 0.0
85	SHRDTEMPOUT18070	QUALIFIED	10/13 00:07: 0.0	10/15 15:25:34.0
		QUALIFIED	10/15 17:13:40.0	10/29 02:50: 0.0
		QUALIFIED	10/29 02:50: 0.0	10/29 10:20: 0.0
86	SHRDTEMPOUT27070	QUALIFIED	10/13 00:07: 0.0	10/15 15:25:34.0
		QUALIFIED	10/15 17:13:40.0	10/29 02:50: 0.0
		QUALIFIED	10/29 02:50: 0.0	10/29 10:20: 0.0
87	RODPRESSSWTCH C4	FAILED	10/28 16:50: 0.0	10/29 02:50: 0.0
88	RODPRESSSWTCH D6	TREND	10/28 16:50: 0.0	10/29 02:50: 0.0
89	RODPRESSSWTCH E3	TREND	10/28 16:50: 0.0	10/29 02:50: 0.0
90	FUELTEMPCL 70 A3	QUALIFIED	10/13 00:07: 0.0	10/29 02:16: 4.0
		TREND	10/29 02:16: 4.0	10/29 02:50: 0.0
91	FUELTEMPCL 70 B4	QUALIFIED	10/13 00:07: 0.0	10/15 15:25:30.0
		QUALIFIED	10/15 17:13:50.0	10/29 02:13:12.0
		FAILED	10/29 02:13:12.0	10/29 02:50: 0.0
92	FUELTEMPCL 70 C3	QUALIFIED	10/13 00:07: 0.0	10/15 15:25:30.0
		QUALIFIED	10/15 17:13:50.0	10/29 01:45:15.0
		TREND	10/29 01:45:15.0	10/29 02:22:55.0
		FAILED	10/29 02:22:55.0	10/29 02:50: 0.0
93	FUELTEMPCL 70 D3	QUALIFIED	10/13 00:07: 0.0	10/15 15:25:30.0
		QUALIFIED	10/15 17:13:50.0	10/29 02:15: 0.0
		FAILED	10/29 02:15: 0.0	10/29 02:50: 0.0
94	FUELTEMPCL 70 E1	QUALIFIED	10/13 00:07: 0.0	10/15 15:25:30.0
		QUALIFIED	10/15 17:13:50.0	10/29 02:06:29.0
		TREND	10/29 02:06:29.0	10/29 02:50: 0.0

Table B-2. (continued)

DARS PARAMETER NUMBER	INSTRUMENT IDENTIFIER	QUALIFICATION	START TIME	STOP TIME
95	FUELTEMPCL 70 E5	QUALIFIED	10/13 00:07: 0.0	10/15 15:25:30.0
		QUALIFIED	10/15 17:13:50.0	10/29 02:18: 0.0
		FAILED	10/29 02:18: 0.0	10/29 02:50: 0.0
96	SHRDTEMPIN090 35	QUALIFIED	10/13 00:07: 0.0	10/15 15:25:30.0
		QUALIFIED	10/15 17:13:50.0	10/29 02:23:25.0
		FAILED	10/29 02:23:25.0	10/29 10:20: 0.0
97	STEAMTMPA5315 50	QUALIFIED	10/13 00:07: 0.0	10/15 15:25:30.0
		QUALIFIED	10/15 17:13:50.0	10/29 01:59:10.0
		TREND	10/29 01:59:10.0	10/29 02:23: 0.0
		FAILED	10/29 02:23: 0.0	10/29 10:20: 0.0
98	STEAMTMPD4315 50	QUALIFIED	10/13 00:07: 0.0	10/15 15:25:30.0
		QUALIFIED	10/15 17:13:50.0	10/29 01:13:20.0
		TREND	10/29 01:13:20.0	10/29 02:26:20.0
		FAILED	10/29 02:26:20.0	10/29 10:20: 0.0
99	STEAMTMPD1045 50	QUALIFIED	10/13 00:07: 0.0	10/15 15:25:30.0
		QUALIFIED	10/15 17:13:50.0	10/29 02:12:30.0
		TREND	10/29 02:12:30.0	10/29 02:16:40.0
		FAILED	10/29 02:16:40.0	10/29 10:20: 0.0
100	STEAMTMPE2045 50	QUALIFIED	10/13 00:07: 0.0	10/15 15:25:30.0
		QUALIFIED	10/15 17:13:50.0	10/29 02:00: 0.0
		TREND	10/29 02:00: 0.0	10/29 02:22:20.0
		FAILED	10/29 02:22:20.0	10/29 10:20: 0.0
101	STEAMTMPE6225 50	QUALIFIED	10/13 00:07: 0.0	10/15 15:25:30.0
		QUALIFIED	10/15 17:13:50.0	10/29 01:38:20.0
		TREND	10/29 01:38:20.0	10/29 02:25: 0.0
		FAILED	10/29 02:25: 0.0	10/29 10:20: 0.0
102	STEAMTMPA5135 91	QUALIFIED	10/13 00:07: 0.0	10/15 15:25:30.0
		QUALIFIED	10/15 17:13:50.0	10/29 01:33: 0.0
		FAILED	10/29 01:33: 0.0	10/29 02:26: 3.0
		FAILED	10/29 02:26: 3.0	10/29 10:20: 0.0
103	STEAMTMPB1225 91	QUALIFIED	10/13 00:07: 0.0	10/15 15:25:30.0
		QUALIFIED	10/15 17:13:50.0	10/29 01:24: 0.0
		FAILED	10/29 01:24: 0.0	10/29 02:26:30.0
		TREND	10/29 02:26:30.0	10/29 10:20: 0.0
104	STEAMTMPC4225 91	QUALIFIED	10/13 00:07: 0.0	10/15 15:25:30.0
		QUALIFIED	10/15 17:13:50.0	10/29 01:29:10.0
		FAILED	10/29 01:29:10.0	10/29 02:26:30.0
		TREND	10/29 02:26:30.0	10/29 10:20: 0.0
105	STEAMTMPE5315 91	QUALIFIED	10/13 00:07: 0.0	10/15 15:25:30.0
		QUALIFIED	10/15 17:13:50.0	10/29 01:07: 6.0
		FAILED	10/29 01:07: 6.0	10/29 01:11:30.0
		TREND	10/29 01:11:30.0	10/29 01:31:40.0
		FAILED	10/29 01:31:40.0	10/29 10:20: 0.0
106	STEAMTMPF4315 91	QUALIFIED	10/13 00:07: 0.0	10/15 15:25:30.0
		QUALIFIED	10/15 17:13:50.0	10/29 00:34:10.0
		FAILED	10/29 00:34:10.0	10/29 02:26:30.0
		FAILED	10/29 02:26:30.0	10/29 10:20: 0.0
107	SHRDTEMPIN270 35	QUALIFIED	10/13 00:07: 0.0	10/15 15:25:30.0
		QUALIFIED	10/15 17:13:50.0	10/29 02:10: 0.0
		TREND	10/29 02:10: 0.0	10/29 02:20:25.0
		FAILED	10/29 02:20:25.0	10/29 10:20: 0.0

Table B-2. (continued)

DARS PARAMETER NUMBER	INSTRUMENT IDENTIFIER	QUALIFICATION	START TIME	STOP TIME
108	SHRDTEMPIN090 50	QUALIFIED	10/13 00:07: 0.0	10/15 15:25:30.0
		QUALIFIED	10/15 17:13:50.0	10/29 02:19:10.0
		TREND	10/29 02:19:10.0	10/29 10:20: 0.0
109	SHRDTEMPIN270 50	QUALIFIED	10/13 00:07: 0.0	10/15 15:25:30.0
		QUALIFIED	10/15 17:13:50.0	10/29 02:04:10.0
		FAILED	10/29 02:04:10.0	10/29 10:20: 0.0
110	SHRDTEMPIN090 70	QUALIFIED	10/13 00:07: 0.0	10/15 15:25:30.0
		QUALIFIED	10/15 17:13:50.0	10/29 02:03: 0.0
		TREND	10/29 02:03: 0.0	10/29 02:22: 2.0
		FAILED	10/29 02:22: 2.0	10/29 10:20: 0.0
111	SHRDTEMPIN270 70	QUALIFIED	10/13 00:07: 0.0	10/15 15:25:30.0
		QUALIFIED	10/15 17:13:50.0	10/29 01:58:52.0
		TREND	10/29 01:58:52.0	10/29 02:20: 0.0
		FAILED	10/29 02:20: 0.0	10/29 10:20: 0.0
112	SHRDTEMPMID00050	QUALIFIED	10/13 00:07: 0.0	10/15 15:25:30.0
		QUALIFIED	10/15 17:13:50.0	10/29 02:50: 0.0
		QUALIFIED	10/29 02:50: 0.0	10/29 10:20: 0.0
113	SHRDTEMPMID09050	QUALIFIED	10/13 00:07: 0.0	10/15 15:25:30.0
		QUALIFIED	10/15 17:13:50.0	10/29 02:21:40.0
		TREND	10/29 02:21:40.0	10/29 10:20: 0.0
114	SHRDTEMPMID18050	QUALIFIED	10/13 00:07: 0.0	10/15 15:25:30.0
		QUALIFIED	10/15 17:13:50.0	10/29 02:50: 0.0
		QUALIFIED	10/29 02:50: 0.0	10/29 10:20: 0.0
115	SHRDTEMPMID27050	QUALIFIED	10/13 00:07: 0.0	10/15 15:25:30.0
		QUALIFIED	10/15 17:13:50.0	10/29 02:22:20.0
		TREND	10/29 02:22:20.0	10/29 10:20: 0.0
116	SHRDTEMPMID00070	QUALIFIED	10/13 00:07: 0.0	10/15 15:25:30.0
		QUALIFIED	10/15 17:13:50.0	10/29 02:24:10.0
		TREND	10/29 02:24:10.0	10/29 10:20: 0.0
117	STEAMTMPBR270111	QUALIFIED	10/13 00:07: 0.0	10/15 15:25:30.0
		QUALIFIED	10/15 17:13:50.0	10/29 02:00: 0.0
		FAILED	10/29 02:00: 0.0	10/29 02:30:30.0
		TREND	10/29 02:30:30.0	10/29 10:20: 0.0
118	STEAMTMPBR090111	QUALIFIED	10/13 00:07: 0.0	10/15 15:25:30.0
		QUALIFIED	10/15 17:13:50.0	10/29 02:04:30.0
		FAILED	10/29 02:04:30.0	10/29 02:06:30.0
		FAILED	10/29 02:06:30.0	10/29 10:20: 0.0
119	INLTTEMP135 31	QUALIFIED	10/13 00:07: 0.0	10/15 15:25:30.0
		QUALIFIED	10/15 17:13:50.0	10/29 02:50: 0.0
120	BYP TEMP000 -31	QUALIFIED	10/13 00:07: 0.0	10/15 15:25:30.0
		QUALIFIED	10/15 17:13:50.0	10/29 02:50: 0.0
		QUALIFIED	10/29 02:50: 0.0	10/29 10:20: 0.0
121	BYP TEMP090 -31	QUALIFIED	10/13 00:07: 0.0	10/15 15:25:30.0
		QUALIFIED	10/15 17:13:50.0	10/29 02:50: 0.0
		QUALIFIED	10/29 02:50: 0.0	10/29 10:20: 0.0
122	BYP TEMP180 -31	QUALIFIED	10/13 00:07: 0.0	10/15 15:25:30.0
		QUALIFIED	10/15 17:13:50.0	10/29 02:50: 0.0
		QUALIFIED	10/29 02:50: 0.0	10/29 10:20: 0.0

Table B-2. (continued)

DARS PARAMETER NUMBER	INSTRUMENT IDENTIFIER	QUALIFICATION	START TIME	STOP TIME
123	PFHXRDT HXDTPT	QUALIFIED	10/13 00:07: 0.0	10/15 15:25:30.0
		QUALIFIED	10/15 17:13:50.0	10/17 08:18: 0.0
124	BYP TEMP270 -31	QUALIFIED	10/28 16:50: 0.0	10/15 15:25:30.0
		QUALIFIED	10/15 17:13:50.0	10/29 10:20: 0.0
125	BYP TEMP000 91	QUALIFIED	10/28 16:50: 0.0	10/29 02:50: 0.0
		QUALIFIED	10/29 02:50: 0.0	10/29 10:20: 0.0
126	SHRDMELTTHRUWS01	TREND	10/28 16:50: 0.0	10/29 02:50: 0.0
127	SHRDTEMPMID09070	QUALIFIED	10/13 00:07: 0.0	10/15 15:25:30.0
		QUALIFIED	10/15 17:13:50.0	10/29 02:50: 0.0
		QUALIFIED	10/29 02:50: 0.0	10/29 10:20: 0.0
128	SHRDTEMPMID18070	QUALIFIED	10/13 00:07: 0.0	10/15 15:25:30.0
		QUALIFIED	10/15 17:13:50.0	10/29 02:04:35.0
		FAILED	10/29 02:04:35.0	10/29 10:20: 0.0
129	SHRDTEMPMID27070	QUALIFIED	10/13 00:07: 0.0	10/15 15:25:30.0
		QUALIFIED	10/15 17:13:50.0	10/29 02:21:40.0
		TREND	10/29 02:21:40.0	10/29 10:20: 0.0
130	SHRDTEMPMID00091	QUALIFIED	10/13 00:07: 0.0	10/15 15:25:30.0
		QUALIFIED	10/15 17:13:50.0	10/29 02:25: 0.0
		TREND	10/29 02:25: 0.0	10/29 10:20: 0.0
131	SHRDTEMPMID18091	QUALIFIED	10/13 00:07: 0.0	10/15 15:25:30.0
		QUALIFIED	10/15 17:13:50.0	10/29 02:50: 0.0
		QUALIFIED	10/29 02:50: 0.0	10/29 10:20: 0.0
133	FISSCHAM090 DC35	TREND	10/13 00:07: 0.0	10/15 15:25:30.0
		TREND	10/15 17:13:50.0	10/28 23:00: 0.0
		QUALIFIED	10/28 23:00: 0.0	10/29 02:50: 0.0
134	FISSCHAM270 DC35	TREND	10/13 00:07: 0.0	10/15 15:25:30.0
		TREND	10/15 17:13:50.0	10/28 23:00: 0.0
		QUALIFIED	10/28 23:00: 0.0	10/29 02:50: 0.0
135	FISSCHAM090 DC50	TREND	10/13 00:07: 0.0	10/15 15:25:30.0
		TREND	10/15 17:13:50.0	10/28 23:00: 0.0
		QUALIFIED	10/28 23:00: 0.0	10/29 02:50: 0.0
141	FISSCHAM090 DC17	TREND	10/13 00:07: 0.0	10/15 15:25:30.0
		TREND	10/15 17:13:50.0	10/28 23:00: 0.0
		QUALIFIED	10/28 23:00: 0.0	10/29 02:50: 0.0
142	FISSCHAM270 DC17	TREND	10/13 00:07: 0.0	10/28 19:59: 0.0
		FAILED	10/28 19:59: 0.0	10/28 20:13: 0.0
		TREND	10/28 20:13: 0.0	10/28 23:00: 0.0
		QUALIFIED	10/28 23:00: 0.0	10/29 02:50: 0.0
143	FISSCHAM090 DC30	TREND	10/13 00:07: 0.0	10/28 23:00: 0.0
		QUALIFIED	10/28 23:00: 0.0	10/29 02:50: 0.0
147	FISSCHAM270 DC50	TREND	10/13 00:07: 0.0	10/28 23:00: 0.0
		QUALIFIED	10/28 23:00: 0.0	10/29 02:50: 0.0
148	FISSCHAM090 DC70	TREND	10/13 00:07: 0.0	10/28 19:59: 0.0
		FAILED	10/28 19:59: 0.0	10/28 20:13: 0.0
		TREND	10/28 20:13: 0.0	10/29 23:00: 0.0
		QUALIFIED	10/29 23:00: 0.0	10/29 02:50: 0.0

Table B-2. (continued)

DARS PARAMETER NUMBER	INSTRUMENT IDENTIFIER	QUALIFICATION	START TIME	STOP TIME
149	FISSCHAM270 DC70	TREND	10/13 00:07: 0.0	10/28 23:00: 0.0
		QUALIFIED	10/28 23:00: 0.0	10/29 02:50: 0.0
151	FISSCHAM090 DC76	TREND	10/13 00:07: 0.0	10/28 19:59: 0.0
		FAILED	10/28 19:59: 0.0	10/28 22:24: 0.0
		TREND	10/28 22:24: 0.0	10/28 23:00: 0.0
		QUALIFIED	10/28 23:00: 0.0	10/29 02:50: 0.0
152	FISSCHAM090 DC81	TREND	10/13 00:07: 0.0	10/28 19:59: 0.0
		FAILED	10/28 19:59: 0.0	10/28 20:13: 0.0
		TREND	10/28 20:13: 0.0	10/28 23:00: 0.0
		QUALIFIED	10/28 23:00: 0.0	10/29 02:50: 0.0
153	FISSCHAM270 DC81	TREND	01/01 00:00: 0.0	10/28 23:00: 0.0
		QUALIFIED	10/28 23:00: 0.0	10/29 02:50: 0.0
155	REAC POWTR-1 PT	QUALIFIED	10/28 16:50: 0.0	10/29 02:50: 0.0
156	REAC POWTR-2 PT	FAILED	10/28 16:50: 0.0	10/29 02:50: 0.0
167	BLOW LEVLIT17 PT	FAILED	10/28 16:50: 0.0	10/29 02:50: 0.0
169	BLOWPRESPT12 PT	QUALIFIED	10/28 16:50: 0.0	10/29 02:50: 0.0
170	FLOWRATEBYPASS	QUALIFIED	10/13 00:07: 0.0	10/29 02:50: 0.0
171	FLOWRATEBUNDLE	QUALIFIED	10/28 16:50: 0.0	10/29 02:50: 0.0
173	INLTTEMP315 31	FAILED	10/13 00:07: 0.0	10/29 10:20: 0.0
174	SHRDMELTTHRUWW03	TREND	10/28 16:50: 0.0	10/29 02:50: 0.0
175	FP PRESSPT13-42	QUALIFIED	10/28 16:50: 0.0	10/29 10:20: 0.0
187	SYS PRESHEISE PT	QUALIFIED	10/13 00:07: 0.0	10/29 10:20: 0.0
188	LOOP FLOFRC-10PT	QUALIFIED	10/13 00:07: 0.0	10/29 10:20: 0.0
195	FP NEUT NO. 01	TREND	10/28 16:50: 0.0	10/29 10:20: 0.0
196	SHRDTEMPOUT09031	FAILED	10/13 00:07: 0.0	10/29 02:50: 0.0
		FAILED	10/29 02:50: 0.0	10/29 10:20: 0.0
199	FP GAMMANO.01	TREND	10/28 16:50: 0.0	10/29 10:20: 0.0
200	FP GAMMANO.02	TREND	10/28 16:50: 0.0	10/29 10:20: 0.0
201	FP GAMMANO.03	TREND	10/28 16:50: 0.0	10/29 10:20: 0.0
207	SHRDTEMPOUT27031	FAILED	10/13 00:07: 0.0	10/29 02:50: 0.0
		FAILED	10/29 02:50: 0.0	10/29 10:20: 0.0
213	SHRDTEMPOUT09035	QUALIFIED	10/13 00:07: 0.0	10/29 02:50: 0.0
		QUALIFIED	10/29 02:50: 0.0	10/29 10:20: 0.0
214	SHRDTEMPOUT18035	QUALIFIED	10/13 00:07: 0.0	10/29 02:50: 0.0
		QUALIFIED	10/29 02:50: 0.0	10/29 10:20: 0.0
215	SHRDTEMPOUT27035	QUALIFIED	10/13 00:07: 0.0	10/29 02:50: 0.0
		QUALIFIED	10/29 02:50: 0.0	10/29 10:20: 0.0
219	FP HYDR CONCENT	QUALIFIED	10/28 16:50: 0.0	10/29 10:20: 0.0

Table B-2. (continued)

DARS PARAMETER NUMBER	INSTRUMENT IDENTIFIER	QUALIFICATION	START TIME	STOP TIME
220	FP FLOW FT13-69	TREND	10/28 16:50: 0.0	10/29 10:20: 0.0
225	SHRDMELTTHRUWS04	TREND	10/28 16:50: 0.0	10/29 02:50: 0.0
226	SHRDMELTTHRUWW04	TREND	10/28 16:50: 0.0	10/29 02:50: 0.0
227	SHRDTEMPOUT00050	QUALIFIED	10/13 00:07: 0.0	10/29 02:50: 0.0
		QUALIFIED	10/29 02:50: 0.0	10/29 10:20: 0.0
235	CLADTEMP045 35B4	FAILED	10/13 00:07: 0.0	10/29 02:50: 0.0
236	CLADTEMP045 35B6	QUALIFIED	10/13 00:07: 0.0	10/29 02:23:50.0
		TREND	10/29 02:23:50.0	10/29 02:50: 0.0
237	FP TEMP TE13-8PT	TREND	10/28 16:50: 0.0	10/29 10:20: 0.0
238	FP TEMP TE1329PT	TREND	10/28 16:50: 0.0	10/29 10:20: 0.0
239	CLADTEMP045 35F3	QUALIFIED	10/13 00:07: 0.0	10/29 01:53:20.0
		TREND	10/29 01:53:20.0	10/29 02:24:35.0
		FAILED	10/29 02:24:35.0	10/29 02:50: 0.0
240	CLADTEMP315 50A3	QUALIFIED	10/13 00:07: 0.0	10/29 02:21:40.0
		FAILED	10/29 02:21:40.0	10/29 02:25:50.0
		TREND	10/29 02:25:50.0	10/29 02:50: 0.0
241	CLADTEMP135 50A3	QUALIFIED	10/13 00:07: 0.0	10/29 02:16:40.0
		TREND	10/29 02:16:40.0	10/29 02:22:40.0
		FAILED	10/29 02:22:40.0	10/29 02:25:50.0
		TREND	10/29 02:25:50.0	10/29 02:50: 0.0
242	CLADTEMP270 50B4	FAILED	10/13 00:07: 0.0	10/29 02:50: 0.0
243	CLADTEMP180 50B6	QUALIFIED	10/13 00:07: 0.0	10/29 02:14:35.0
		FAILED	10/29 02:14:35.0	10/29 02:26:15.0
		TREND	10/29 02:26:15.0	10/29 02:50: 0.0
244	CLADTEMP270 50C2	QUALIFIED	10/13 00:07: 0.0	10/29 02:13:40.0
		FAILED	10/29 02:13:40.0	10/29 02:25:30.0
		TREND	10/29 02:25:30.0	10/29 02:50: 0.0
245	CLADTEMP000 50C4	QUALIFIED	10/13 00:07: 0.0	10/29 02:07: 0.0
		TREND	10/29 02:07: 0.0	10/29 02:23:40.0
		FAILED	10/29 02:23:40.0	10/29 02:26:15.0
		TREND	10/29 02:26:15.0	10/29 02:50: 0.0
246	CLADTEMP000 50D3	QUALIFIED	10/13 00:07: 0.0	10/29 02:18:20.0
		TREND	10/29 02:18:20.0	10/29 02:50: 0.0
247	CLADTEMP045 35C2	QUALIFIED	10/13 00:07: 0.0	10/29 02:23:30.0
		FAILED	10/29 02:23:30.0	10/29 02:25:30.0
		TREND	10/29 02:25:30.0	10/29 02:50: 0.0
249	CLADTEMP135 35C4	QUALIFIED	10/13 00:07: 0.0	10/29 02:24:10.0
		FAILED	10/29 02:24:10.0	10/29 02:26: 5.0
		TREND	10/29 02:26: 5.0	10/29 02:50: 0.0
250	CLADTEMP135 35D3	QUALIFIED	10/13 00:07: 0.0	10/29 02:23:30.0
		FAILED	10/29 02:23:30.0	10/29 02:50: 0.0
251	CLADTEMP045 35E5	QUALIFIED	10/13 00:07: 0.0	10/29 02:16:40.0
		TREND	10/29 02:16:40.0	10/29 02:23:20.0
		FAILED	10/29 02:23:20.0	10/29 02:50: 0.0

Table B-2. (continued)

DARS PARAMETER NUMBER	INSTRUMENT IDENTIFIER	QUALIFICATION	START TIME	STOP TIME
253	BYP TEMP180 91	QUALIFIED	10/28 16:50: 0.0	10/29 10:20: 0.0
254	DIFFPRESDP13-66	QUALIFIED	10/28 16:50: 0.0	10/29 10:20: 0.0
255	FPGAMMA NO. 04	TREND	10/28 16:50: 0.0	10/29 10:20: 0.0
256	BYP TEMP270 91	QUALIFIED	10/28 16:50: 0.0	10/29 10:20: 0.0

Table B-3. Summary of test train instrument response

Instrument	Total Number	Partial Failures	Complete Failures[a]
Rod pressure switches	5	—	2
Rod pressure transducers	5	—	4[b]
System pressure transducers	3	—	—
Fission chambers	12	—	—
Flowmeters	2	—	—
Bundle temperature profile detector	2	—	2
Melt-through detector	1	—	—
Cladding thermocouples	25	9	5
Fuel centerline thermocouples	6	6	—
Shroud liner and insulation thermocouples	16	11	1
Steam thermocouples	16	11	—
Low temperature thermocouples	16	—	—

a. No usable data or erratic or questionable data.

b. Two of the transducers failed before installation of test train.

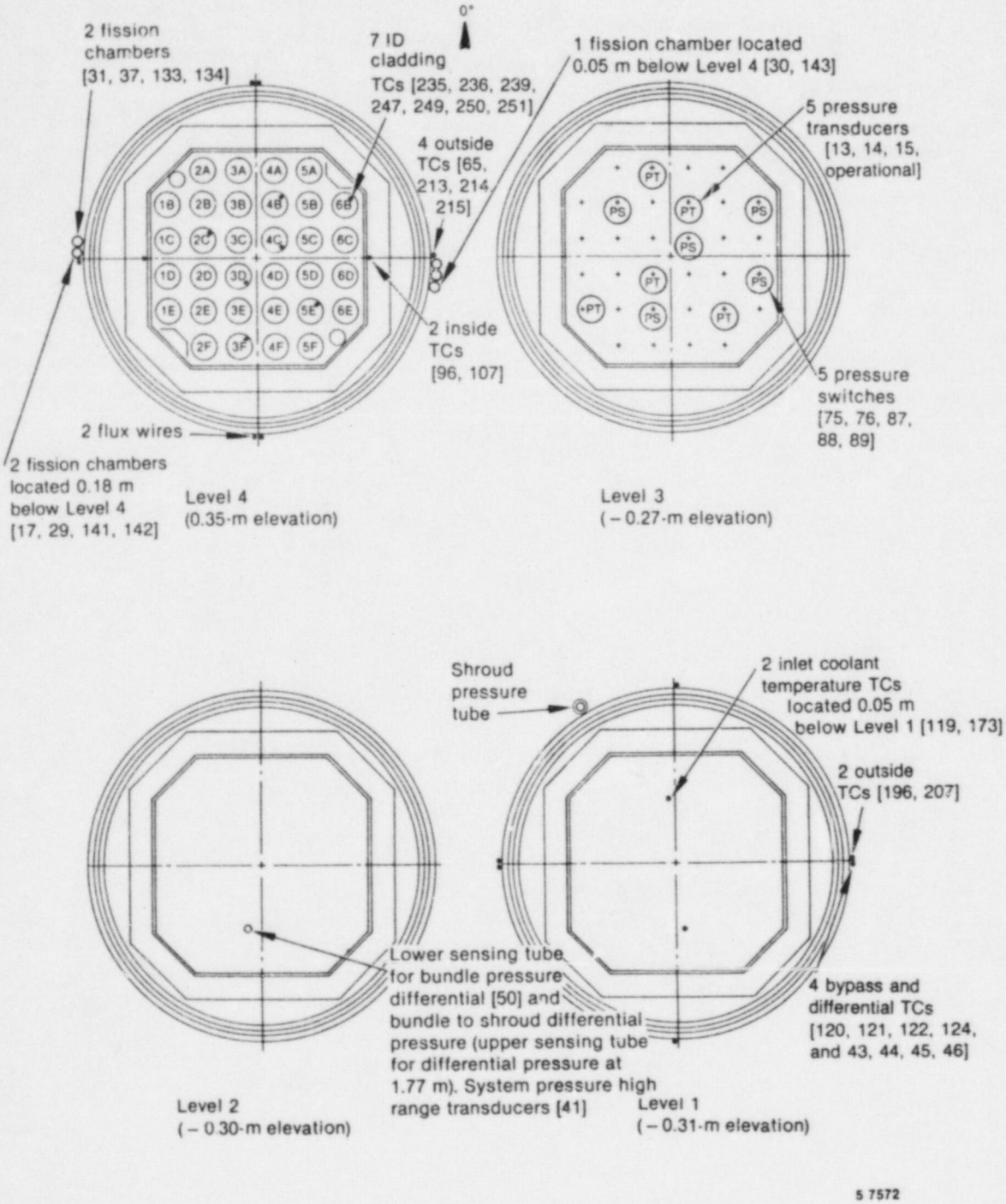

Figure B-1. Cross section of shroud and test bundle (levels 1-4) (DARS parameter numbers in square brackets).

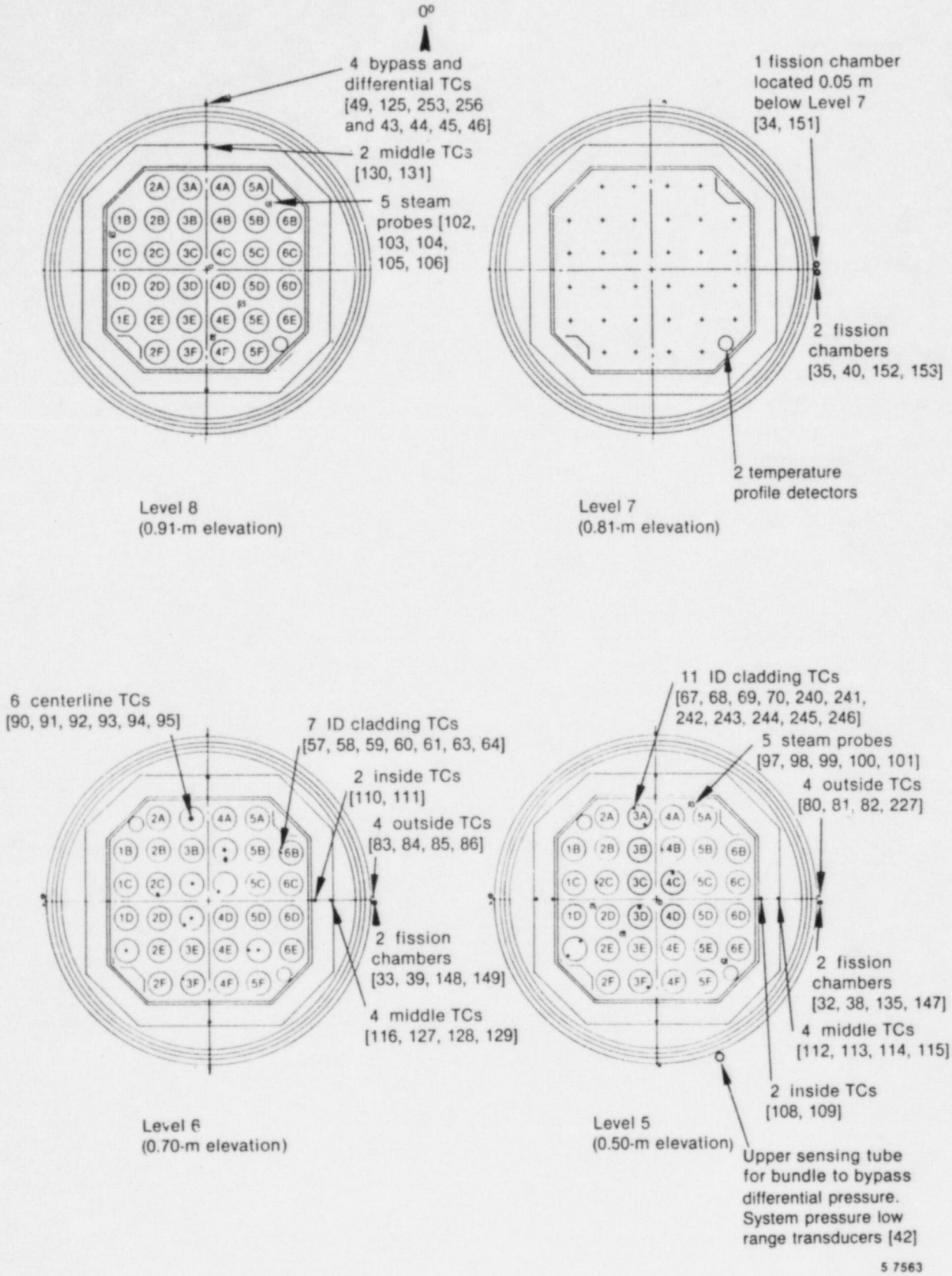

Figure B-2. Cross section of shroud and test bundle (levels 5-8) (DARS parameter numbers in square brackets.)

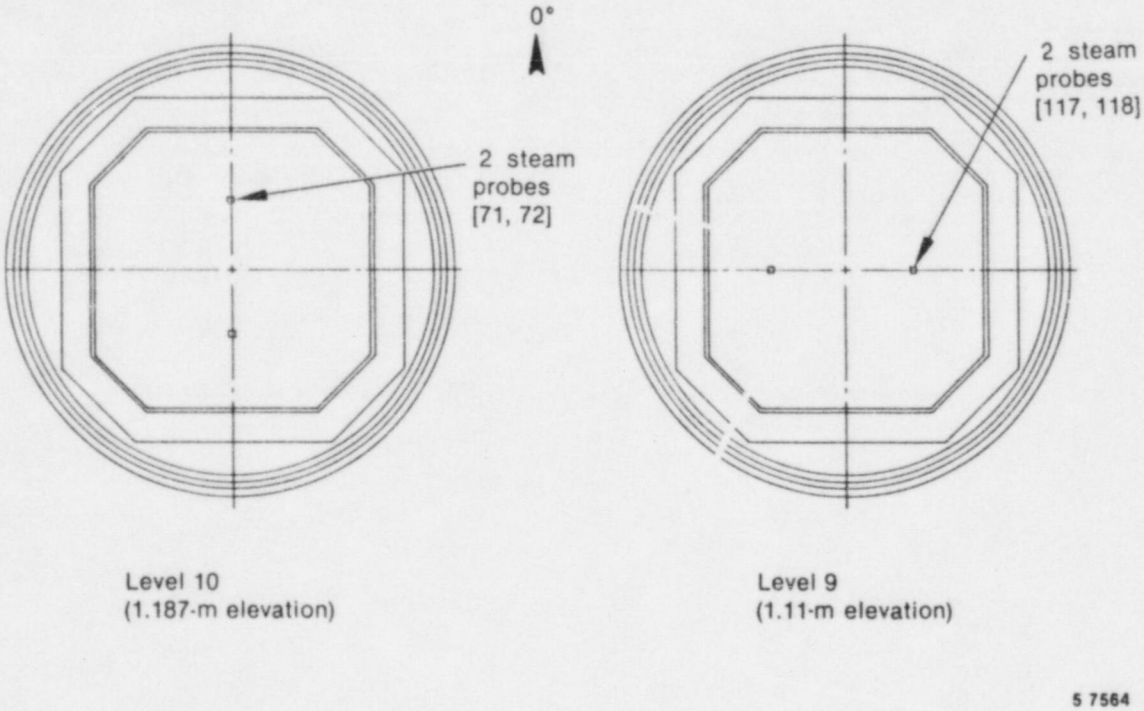

Figure B-3. Cross section of shroud and test bundle (levels 9 and 10) (DARS parameter numbers in square brackets).

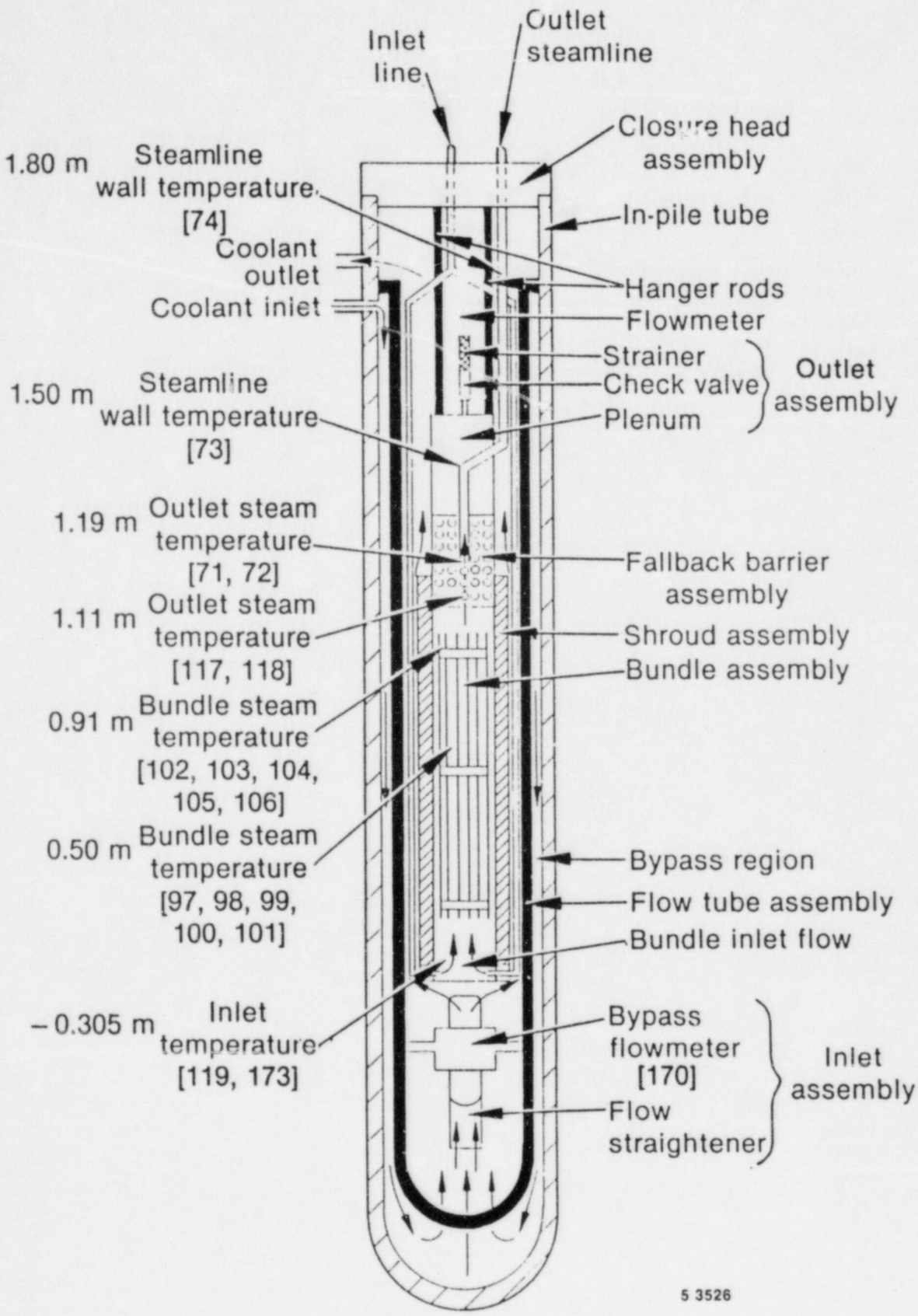

Figure B-4. Elevation view of SFD-ST test train (DARS parameter numbers in square brackets).

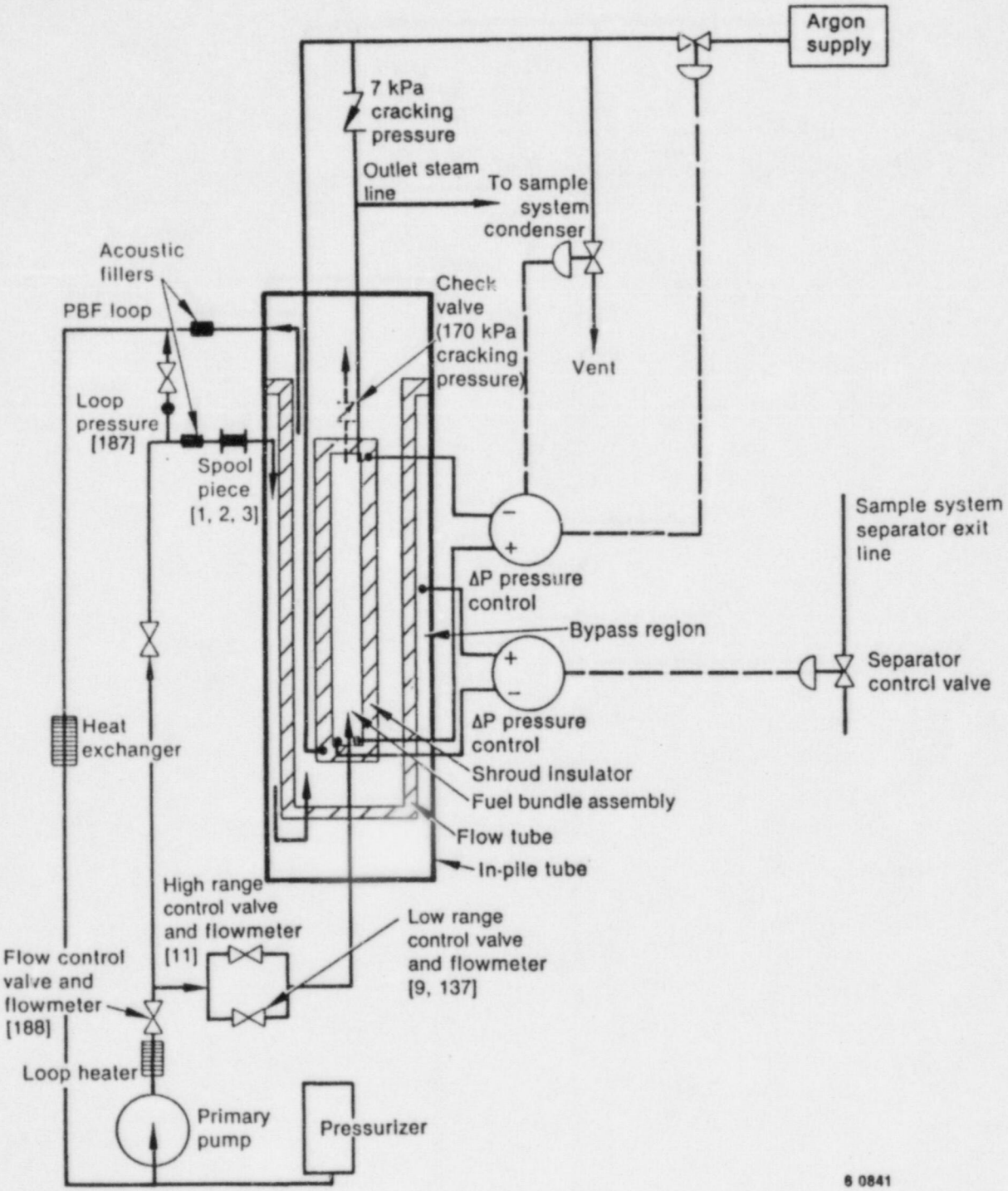

Figure B-5. Schematic of the test train coolant and pressure control system (DARS parameter numbers in square brackets).

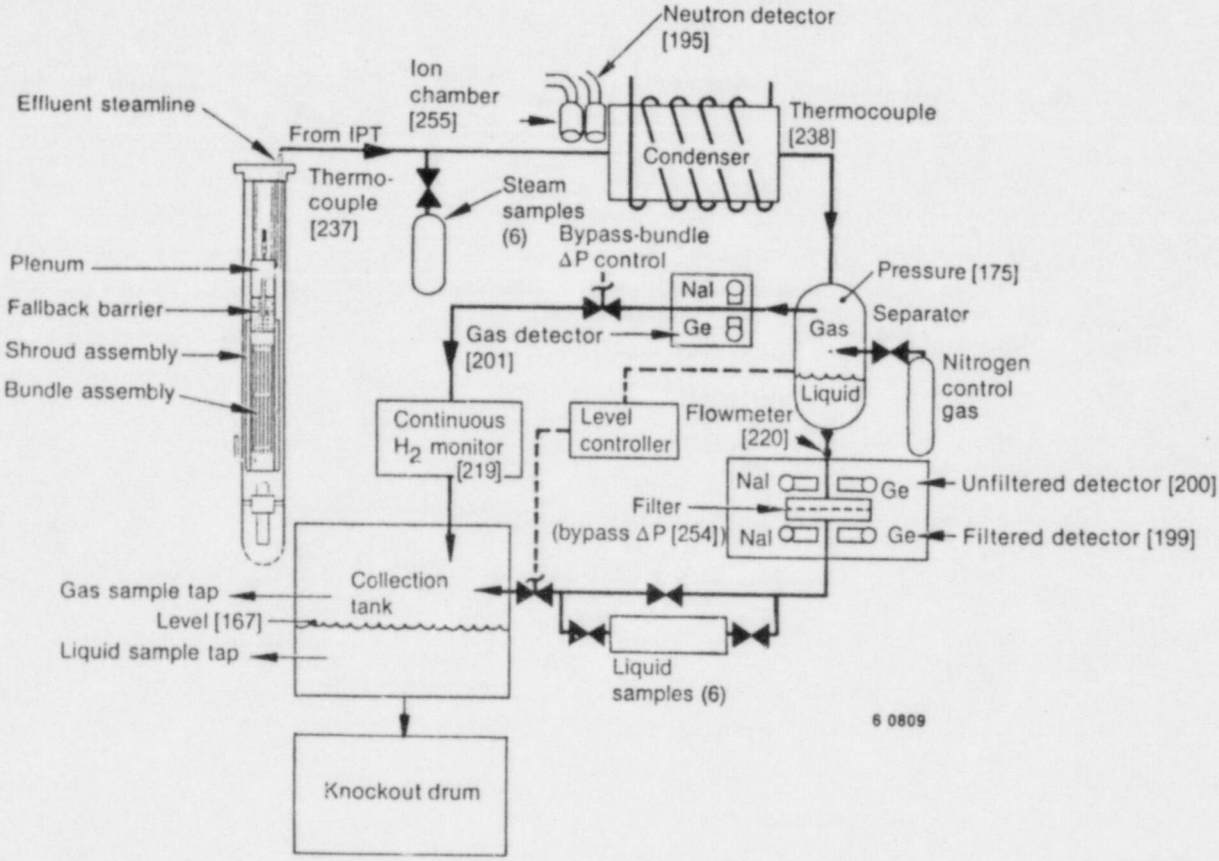

Figure B-6. Schematic of the effluent sampling and monitoring system (DARS parameter numbers in square brackets).

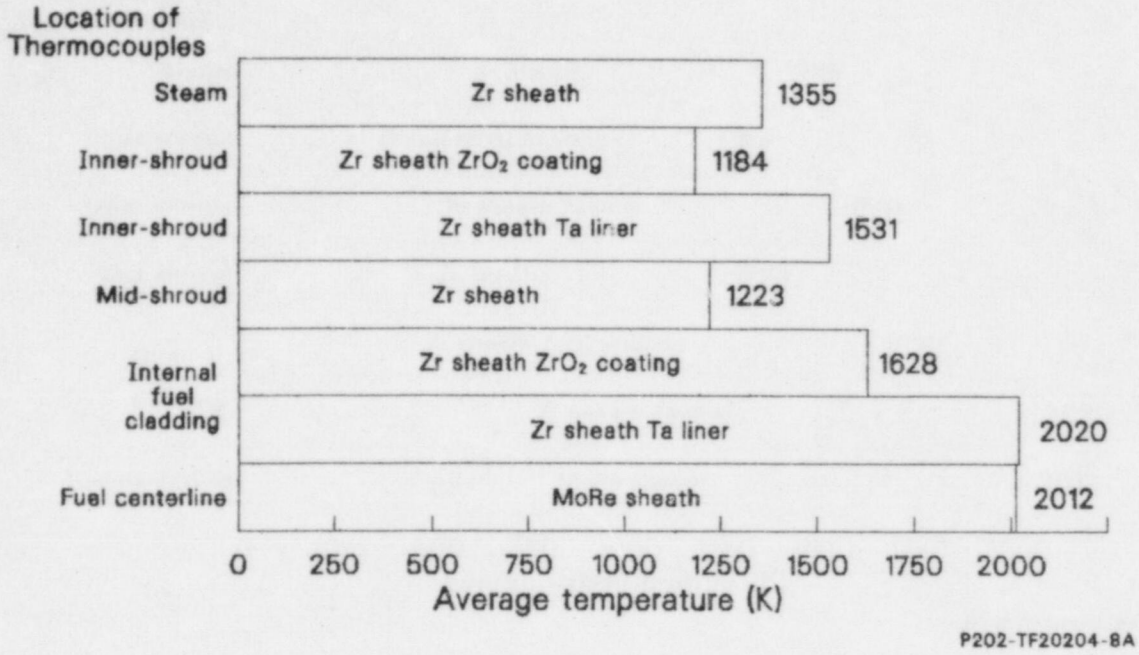

Figure B-7. Comparison of Type C thermocouple average peak temperature performance.

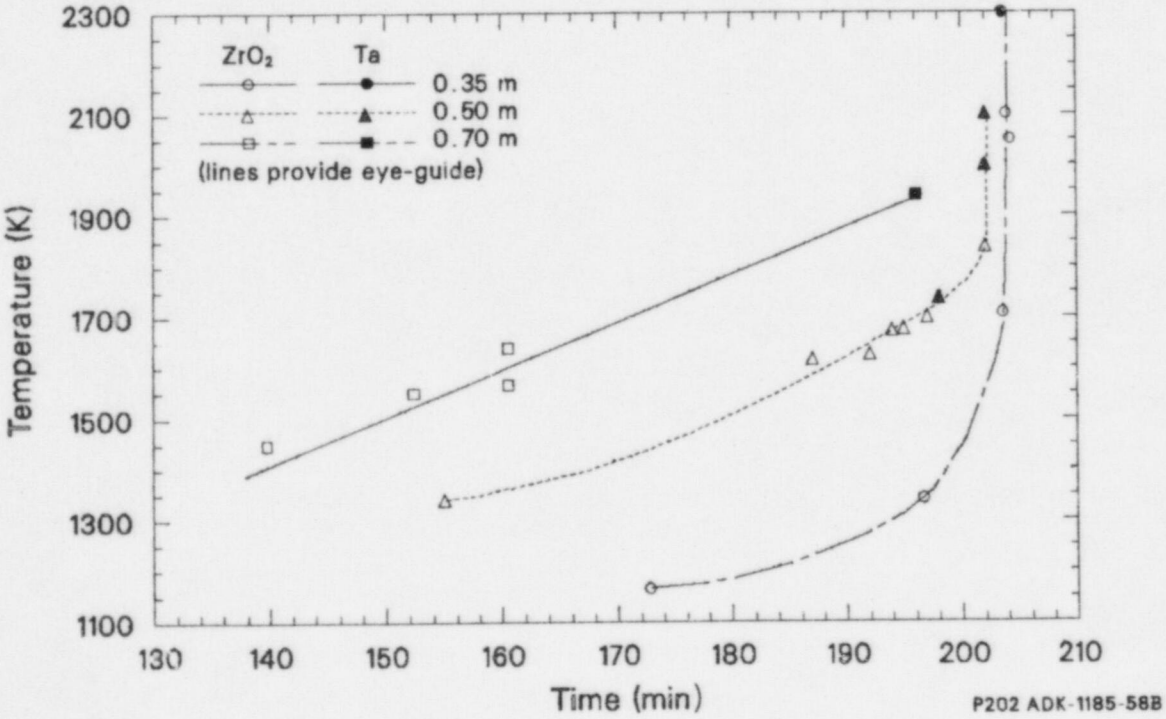

Figure B-8. Comparison of Ta-lined and ZrO_2-coated zircaloy-sheathed cladding thermocouples performance.

APPENDIX C

TEST TRAIN POWER SOURCES AND CALIBRATION

APPENDIX C

TEST TRAIN POWER SOURCES AND CALIBRATION

1. INTRODUCTION

This appendix identifies the major individual contributions to the energy deposition within the test train and outlines the power balance resulting from the overall heat transfer process. Although the energy sources within the test bundle are primarily the fission power of the fuel rods and the energy released by the zircaloy-steam oxidation reaction, the transport of gamma-rays and fast neutrons has a significant influence on the power calibration.

2. THE MAJOR ENERGY SOURCES

The major contributions to the nuclear energy deposition within the test train components can be summarized as

$$E_b = f_b + \beta_b + \gamma_b \tag{C-1}$$

where

E_b = nuclear energy deposition within the test bundle excluding the coolant contribution

f_b = fission fragment contribution from fissions within the fuel bundle and can be considered to deposit their energy at the point of fission. This source provides 169.58 MeV/fission[C-1]

β_b = energy generated in the form of beta particles from the decay of fission fragments and again can be considered to deposit their energy at the point of fission. This source provides 6.43 MeV/fission

γ_b = energy deposition from gamma-rays produced both in the test train and reactor core. This energy is deposited in the fuel, cladding and structural materials.

$$E_{bc} = n_{bc} + \gamma_{bc} \tag{C-2}$$

where

E_{bc} = nuclear energy deposition within the bundle coolant

n_{bc} = fast neutron contribution from fissions within both the test fuel and the core

γ_{bc} = the energy deposition from gamma-rays produced both in the test train and reactor core.

$$E_s = \gamma_s \tag{C-3}$$

where

E_s = nuclear energy deposition within the shroud

γ_s = energy deposition from gamma-rays produced both in the test train and reactor core.

$$E_{bp} = n_{bp} + \gamma_{bp} \tag{C-4}$$

where

E_{bp} = nuclear energy deposition within the bypass coolant

n_{bp} = fast neutron contribution from fissions within both the test fuel and reactor core

γ_{bp} = the energy deposition from gamma-rays produced both in the test train and reactor core.

The gamma-ray source contributions referred to above are generated during fission (prompt gamma-rays), the decay of fission fragments (delayed gamma-rays), neutron capture and neutron inelastic scattering.

At a temperature above ~1100 K there is a strong exothermic reaction between the steam and zircaloy that provides an additional energy source (E_o = 6.5 MJ per kg of Zr) written as

$$Zr + 2H_2O \rightarrow ZrO_2 + 2H_2 + E_o \quad . \tag{C-5}$$

3. THE POWER BALANCE

The energy sources identified in Section 2 of this appendix and the heat transfer process result in the following overall power balance

$$E_b' + E_{bc}' + E_o' + E_s' + E_{bp}' = Q_c + Q_{bp} + Q_b + Q_s \tag{C-6}$$

where

the subscripts on the energy, E, identify the sources and the prime superscript refers to the rate of heat gain,

Q_c = rate of heat gain by the bundle coolant

Q_{bp} = rate of heat gain by the bypass coolant

Q_b = rate of internal heat gain by the fuel bundle

Q_s = rate of internal heat gain by the shroud.

The required bundle nuclear power, P_{bn}, is given by

$$P_{bn} = E_b' + E_{bc}' \quad . \tag{C-7}$$

At temperatures below the onset of oxidation and under steady state conditions, E_o', Q_b, and Q_s are zero and the bundle nuclear power can be defined by

$$P_{bn} = Q_c + Q_{bp} - E_s' - E_{bp}' \quad . \tag{C-8}$$

Thermocouples mounted above and below the test bundle and in the bypass, together with coolant flow rate and pressure measurements, allow the rate of heat gain by the bundle coolant, Q_c, and bypass coolant, Q_{bp}, to be derived. The rate of heat transfer to the bypass coolant may also be calculated with the use of the Dittus-Boelter correlation[C-2] for subcooled water at the bundle outlet. Both the gamma-ray energy deposition in the shroud and the direct nuclear energy deposition in the bypass coolant are obtainable from reactor physics calculation.

4. REACTOR PHYSICS ANALYSIS

Reactor physics calculations[C-3] were performed primarily to establish a pretest relationship between the bundle nuclear power and the overall reactor thermal power. The relationship is a function of the reactor control rod insertion, the test train pressure and temperature distribution, and the bundle coolant level. The ratio, R, of the bundle power and the reactor thermal power was calculated using

$$R = \frac{kj\ SE_n}{\nu\ P_{rt}} \text{ bundle nuclear kW per reactor thermal MW} \qquad \text{(C-9)}$$

where

k = number of neutrons produced per neutron entering the in-pile tube

j = neutron current entering the in-pile tube (n/m^2s)

S = inside surface area of the in-pile tube (m^2)

E_n = total nuclear energy deposited in the test bundle per fission in the test fuel (kJ/fission)

ν = number of neutrons produced per fission in the test fuel

P_{rt} = reactor thermal power that yields the current j (MW).

The major contributions to the total nuclear energy deposited in the bundle were identified in Equations (C-1) and (C-2). The fission fragments and beta particles deposit their kinetic energy effectively at the point of interaction and total 176.0 MeV/fission. A further 19.3 MeV/fission is recoverable in the form of heat from the fission of ^{235}U, produced largely from the prompt and delayed gamma-rays and fission neutrons. However, the transport processes of gamma-rays and neutrons results in the energy being deposited away from the fission site. The SFD test series reactor physics calculations used a value of E_n = 190.0 MeV (3.028×10^{-14} kJ) deposited per fission in the test fuel, indicating that more energy leaves the test bundle than enters from the PBF core. It should also be noted that the calculations assumed the reactor to have been operational a sufficient time for the saturation of fission-product activity.

5. BUNDLE NUCLEAR POWER CALIBRATION

The PBF reactor ion chamber monitors were calibrated under steady state conditions to provide the reactor thermal power, which, when multiplied by the reactor physics estimate of R, gave a measure of the bundle nuclear power. Four coolant conditions were modeled by the reactor physics calculations, only two of which were strictly applicable to the SFD-ST. These were a liquid full situation and a case with an average axial coolant density variation of 215.5 kg m^{-3}. During the high temperature transient period the average bundle coolant density decreased from ~360 kg m^{-3} to 150 kg m^{-3}, with an associated reduction in the ratio R of 20%. For the posttest analysis, the bundle nuclear power was derived from a steady state calibration and the test train fission chamber data, as described in Subsection 4.3 of the main text. However, the validity of the reactor physics calculations is of interest to the later SFD test analysis and so comparisons with measurement have been performed and are presented here.

The most straightforward experimental value of bundle nuclear power was obtained for a water-filled bundle under steady state conditions, with single-phase water at both the inlet and outlet. During the fuel conditioning phase, at a reactor thermal power of 11.12 MW and a control rod setting of 0.442 m, the rate of heat gain by the bundle coolant, Q_c, was derived from the measurements to be 189.8 kW. The thermal-hydraulic analysis was performed using a multirod bundle thermal power and heat loss program (BUNPOW). The program calculated from the Dittus-Boelter correlation the rate of heat transfer through

the shroud to be 0.59 kW. This resulted in a bundle nuclear power of 184.77 kW and an experimental value for the ratio R of 17.06 bundle nuclear kW per reactor thermal MW. The pretest reactor physics calculation assumed a bundle and bypass coolant temperature of 519 K, system pressure of 6.9 MPa, and a reactor control rod setting of 0.591 m. The actual test coolant conditions were very close to the prescribed values and the changes had a negligible influence on the calculated results. The predicted relationship was adjusted for the difference in control rod insertion on the basis of a 0.055% change per mm. The corrected value of 16.87 bundle nuclear kW per reactor thermal MW compares very well with the experimental value, giving a ratio of measurement to calculation of 0.99.

The second reactor physics calculation that was relevant to the SFD-ST had an average coolant density of 215.5 kg m^{-3}. On the basis of the SCDAP calculations described in Subsection 6.2 of the main text, this density corresponds to a two-phase coolant, single-phase steam level of 0.31 m. The test train fission chamber system recorded this level at a time of 117 min, when the reactor thermal power was 4.96 MW and the control rod setting 0.397 m. Figures C-1 and C-2 show the measured inlet (-0.305 m) coolant temperature, average bundle outlet steam temperature and the differential (-0.31 m and +0.91 m) temperature in the bypass coolant throughout the high temperature transient. At 117 min the rate of heat gain by the bundle coolant, Q_c, and the bypass coolant, Q_{bp}, were determined to be 49.00 kW and 6.57 kW respectively. Reactor physics calculations provided a shroud gamma-ray heating fraction of 0.431 kW per reactor thermal MW and a direct bypass coolant nuclear heating fraction of 0.329 kW per reactor thermal MW. From these fractions and the reactor thermal power $E_s' + E_{bp}'$ was calculated to be 3.77 kW. It can be seen from the steam outlet temperature plot in Figure C-1 that steady state conditions did not exist at 117 min. Therefore, the rate of internal heat gain by the bundle and shroud must be taken into account in the estimation of the bundle nuclear power. The contribution of oxidation energy was negligible at this stage and thus

$$P_{bn} = Q_c + Q_{bp} + Q_b + Q_s - E_s' - E_{bp}' \quad . \tag{C-10}$$

The total internal heat gain rate was deduced from a SCDAP calculation to be 1.23 kW, resulting in a bundle nuclear power of 53.03 kW and associated ratio R of 10.69 bundle nuclear kW per reactor thermal MW. The reactor physics prediction, corrected to the appropriate control rod setting of 0.397 m, was 9.96 bundle nuclear kW per reactor thermal MW, giving a ratio of measurement to calculation of 0.93.

The dependence on a SCDAP calculation to provide an estimate of the internal heat gain in order to derive the bundle nuclear power is undesirable. The approach adopted, as described in Subsection 4.3 of the main text, was to utilize a steady state determination of the bundle power to normalize the integrated axial fission distribution measured throughout the transient by the chambers mounted outside the shroud. The transient bundle nuclear power history, presented in Figure 11 of Subsection 4.3, is plotted against reactor power in Figure C-3. At the reactor thermal power of 4.96 MW the bundle nuclear power of 54.07 kW gives a value for R of 10.90 bundle nuclear kW power per reactor thermal MW. The value is 2% greater than that attained with the transient calibration described above, with a measured to calculated ratio of 0.91.

As stated at the beginning of this section, four coolant conditions were modeled in the reactor physics calculations. The predicted ratios of the reactor thermal power to the bundle nuclear power are plotted in Reference C-3 as a function of the average coolant density. The equivalent experimental relationship was derived from the data presented in Figure C-3, adjusted to the constant control rod insertion assumed for the reactor physics calculations, and the associated average coolant density that was deduced from the SCDAP correlation of density and coolant level. Comparison of prediction and measurement throughout the whole transient phase showed a systematic underestimate of the calculated bundle to reactor power ratio, increasing from 6% to 12% over the period. It is of interest to note, on the basis of comparisons for earlier tests in PBF with LWR fuel rods,[C-3] that such an underestimate appears typical. Confidence in the calculated relationship is of particular interest to the subsequent tests in the SFD test series, where it may not be feasible to use experimental calibrations of the kind described above.

The uncertainty in the measured bundle power profile can be considered to consist of two components: that associated with the calibration used to normalize the relative fission chamber curve and the assumption the curve is representative of the bundle nuclear power throughout the whole transient. The integrated fission

chamber data and the thermal-hydraulic measurements used to derive the calibration factor include both systematic and random uncertainties. During the 39 kW calibration the maximum measured deviation from the mean bypass differential temperature was equivalent to an uncertainty in the power to the bypass of 1.5 kW (i.e., 4% of the total power). However, the standard deviation on the mean of the four steady state evaluations of the calibration factor (ratio of the thermal-hydraulic derived power to the integrated fission data) was 2%. The thermal-hydraulic power calibration at steady state required a calculated correction to account for the nuclear heating in the bypass coolant. A pessimistic 25% error in the correction would introduce a 2% change in the calibration factor. The additional systematic uncertainties in the measurements result in an overall estimated uncertainty on the bundle nuclear power during the steady state hold of $\pm 10\%$.

The suitability of the power profile derived from the fission chamber data has been assessed using both measurement and the reactor physics calculations. The analysis of the bundle nuclear power performed independent of the fission chamber data agreed to within 2% of the profile value at 117 min. Similar direct comparisons later in the transient cannot be performed due to the increasing significance of the oxidation energy. A degree of confidence in the adequacy of the fission profile for the final 88 min is provided by the constant difference in relation to the reactor physics prediction from 117 min to $\sim$185 min, and which increases by only a further 2% towards the end of the transient. On the basis of the various comparisons performed through the transient phase, the maximum uncertainty in the bundle nuclear power was estimated to be about $\pm 15\%$.

It should be noted that the above analysis does not include possible major uncertainties in the coolant flow rate. The measured inlet flow rate was about 16 ± 3 g/s throughout most of the high temperature transient. The flowmeter on the liquidline from the separator was calibrated following the test and indicated an outlet flow over 30% less than the inlet flowmeter. Such a reduction would have a significant impact on the derived bundle nuclear power. However, as described in Subsection 4.2 of the main text, there were insufficient data to positively explain the apparent discrepancy and therefore the recorded bundle inlet flow was assumed representative during this analysis.

Although individual fission chambers showed a response to the relocation of fuel rod material in the final minute of the high temperature transient (see Subsection 4.8 in the main text), the analysis considers the integrated fission power to be representative of a fixed geometry bundle power. The reactor physics predictions were also based on a fixed geometry bundle. The bundle nuclear power profile for the transient is an important input parameter to the severe fuel analysis calculation using SCDAP. The present version of the code requires the volumetric power history for the model of the fuel rod bundle specified at the start of the transient. When SCDAP predicts fuel relocation the power is adjusted to account for the quantity moved from one calculational node to another.

6. REFERENCES

C-1. *American National Standard for Decay Heat Power in Light Water Reactors*, ANSI/ANS-5.1, 1979.

C-2. F. W. Dittus and L. M. K. Boelter, *Heat Transfer in Automobile Radiators of the Tubular Type*, University of California Publication, 2, 1930, pp. 443-461.

C-3. J. D. Abrashoff, *Reactor Physics Analysis for the Phase I Severe Fuel Damage Experiments in the Power Burst Facility*, EG&G Internal Document, EGG-PHYS-5550, October 1981.

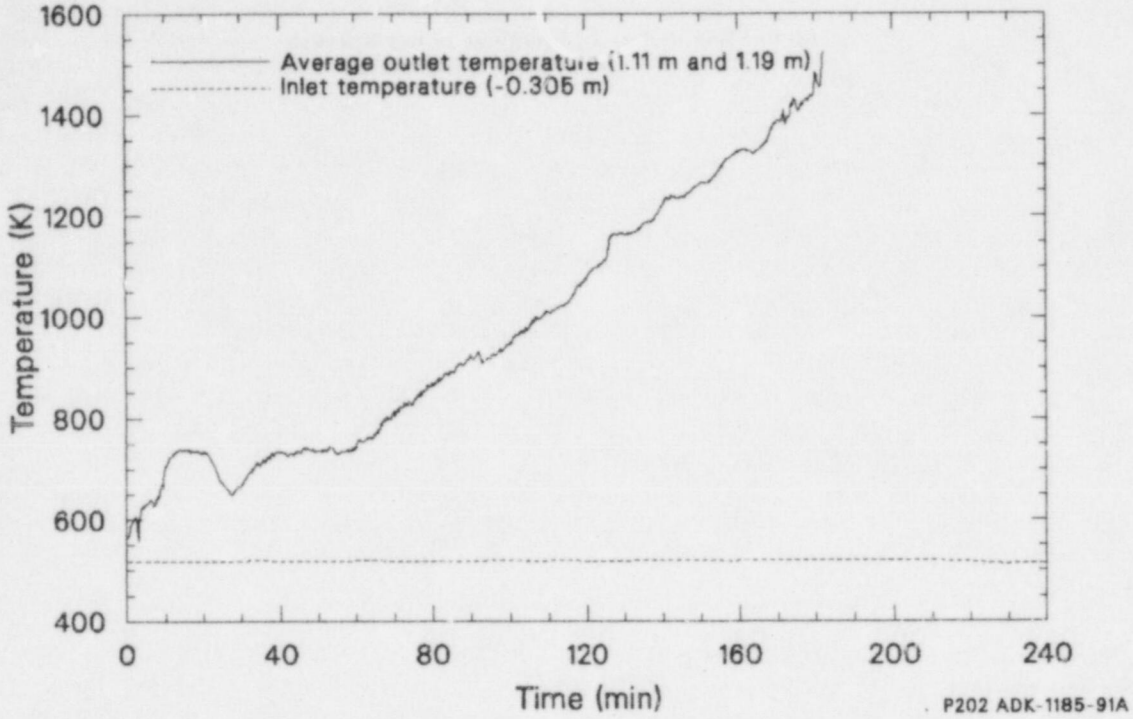

Figure C-1. Bundle inlet and outlet temperatures throughout high temperature transient.

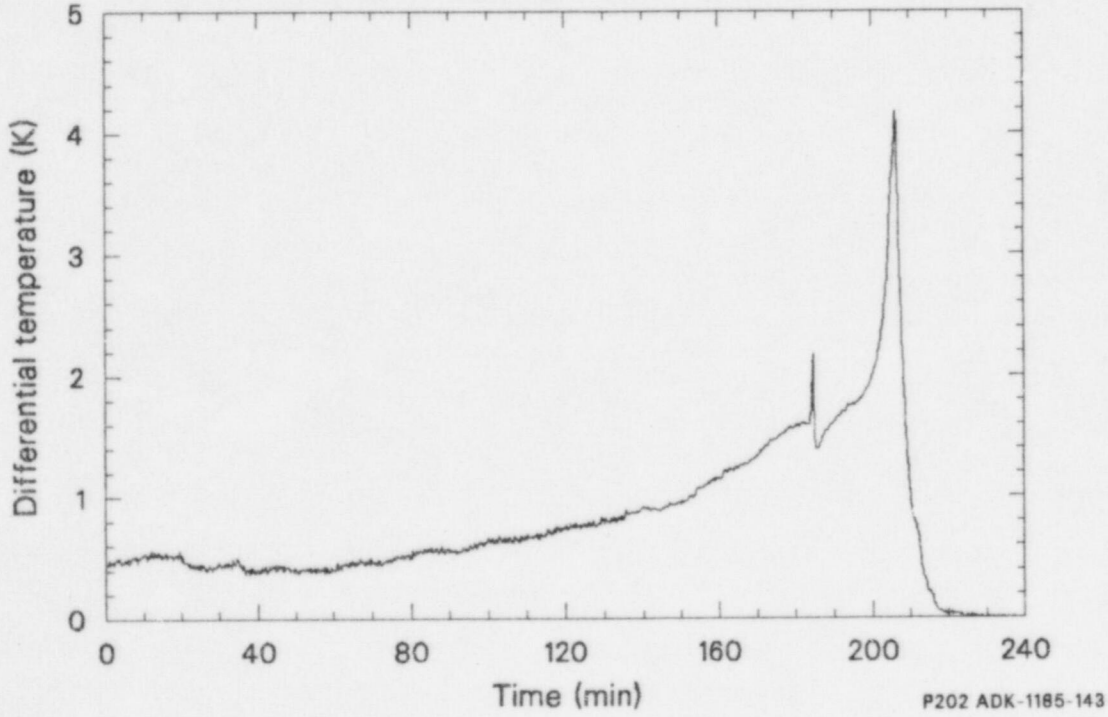

Figure C-2. Differential temperature in the bypass coolant throughout high temperature transient.

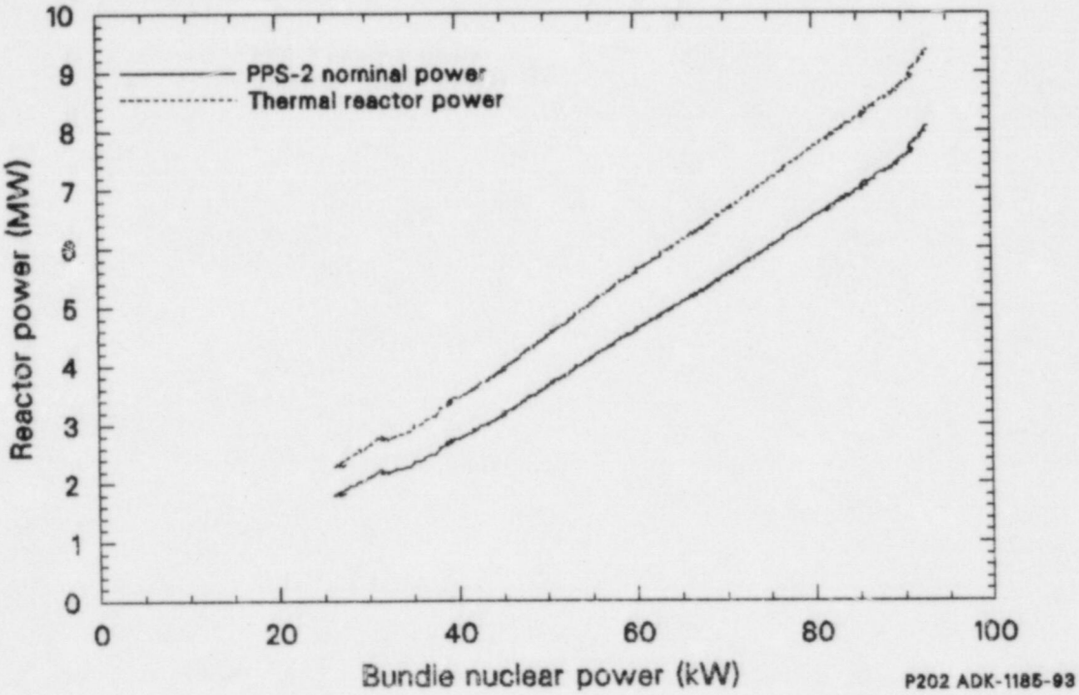

Figure C-3. Bundle nuclear power versus monitor PPS-2 nominal power and reactor thermal power.

APPENDIX D

THE HYDROGEN THERMAL CONDUCTIVITY ANALYZER MEASUREMENT

APPENDIX D

THE HYDROGEN THERMAL CONDUCTIVITY ANALYZER MEASUREMENT

The hydrogen released from the SFD-ST test train during the high temperature transient was measured by an analyzer located in the fission product detection system gasline, between the separator and collection tank, as shown in Figure B-6. The analyzer, a Beckman Model 7C, measured the thermal conductivity of the gas flowing through its detector cell.

Nitrogen carrier gas at a constant flow rate of 0.74 g/s was used to sweep hydrogen from the separator and past the analyzer. The instrument was set to read 0% conductivity for nitrogen and 100% conductivity for hydrogen. A nonlinear calibration supplied by Beckman was used to convert gas thermal conductivity to percent hydrogen.

The thermal conductivity of a gas changes with temperature and therefore the temperature through the analyzer had to be kept constant. This was accomplished with a thermostatically controlled heater that maintained a temperature of 327 K for the incoming gases. The gas flowing from the separator was sampled by a metering valve such that a flow of 200 cm^3/min was ensured through the analyzer, essentially independent of flow fluctuation through the separator during the experiment. This system eliminated the possibility of low hydrogen readings due to high flow rates through the detector.

The possible interference in the hydrogen measurement from other gases passing the detector cell was considered. Only helium from the pressurized fuel rods had a conductivity close to that of hydrogen but, with a total inventory of <2 g, had negligible effect. Upon failure of the shroud the argon pressurizing gas was released to the bundle region. The available quantity of argon, with a conductivity lower than nitrogen, was estimated to provide an apparent hydrogen signal of only a few percent.

Moisture in the gas passing through the analyzer, condensing on the filaments, could produce a noisy instrument output. However, the conditions in the separator (290 K and 6.55 MPa) promoted low humidity in the gas phase, and the relative humidity was reduced further by heating the gas to 327 K in the analyzer. Therefore, no significant influence was observed from moisture in the gas stream.

It should be noted that the hydrogen generation inferred from the measurement has an unquantifiable error resulting from the possible inadequate mixing of hydrogen and nitrogen when sudden changes in the hydrogen flow occurred.

An instrument instability uncertainty was estimated by the vendor to be $\pm 3\%$ of the indicated value. A slight drift in the zero and/or span calibration may have occurred during the three days the instrument was operating. Thus, an instrument error of $\pm 5\%$ for the test period has been assumed. However, due to the relationship between hydrogen mass flow rate and volume percent hydrogen in the gas stream exiting the separator, large errors in mass flow rate can be generated at high concentrations of hydrogen. The hydrogen analyzer measured volume percent hydrogen in nitrogen as given by

$$\% H_2 = \frac{\% H_2(L/s) \times 100}{N_2(L/s) + H_2(L/s)} \quad . \tag{D-1}$$

To convert volumetric flow rates to mass flow rates, the following relationships were used for the conditions in the separator

$$H_2(L/s) = \frac{H_2(g/s) \times 0.37(L/mole)}{2(g/mole)} \tag{D-2}$$

$$N_2(L/s) = \frac{N_2(g/s) \times 0.37(L/mole)}{28(g/mole)} \tag{D-3}$$

where 0.37 L/mole is the molar volume at the temperature and pressure conditions in the separator. Substituting Equations (D-2) and (D-3) into Equation (D-1) and solving for hydrogen mass flow rate yields

$$H_2(g/s) = \frac{\% H_2 \times N_2(g/s)}{(100 - \% H_2) \times 14} \ . \tag{D-4}$$

Since the nitrogen flow rate during the test was constant at 0.74 g/s, this equation was used to calculate the mass flow rate of hydrogen. The hydrogen release rate was integrated to obtain the total amount of hydrogen released.

The possible error in the hydrogen reading of $\pm 5\%$ had little effect on the mass flow rate of hydrogen when the percent hydrogen is low. However, when the percent hydrogen was high the $\pm 5\%$ error severely alters the denominator term $(100 - \% H_2)$ in Equation (D-4) and is equivalent to 140 g during the peak hydrogen production in the Scoping Test.

APPENDIX E

POSTIRRADIATION EXAMINATION DATA

APPENDIX E

POSTIRRADIATION EXAMINATION DATA

Examination of the SFD-ST fuel bundle was performed posttest using several techniques. This appendix summarizes the results of those examinations, which includes gross gamma scanning, neutron radiography, neutron tomography, sectioning and metallography, scanning electron microscopy/energy-dispersive x-ray spectroscopy (SEM/EDS), and scanning Auger spectroscopy (SAS). The detailed gross gamma scan, neutron radiographic, neutron tomographic, and initial sectioning results are reported in Reference E-1 The detailed metallographic examination results are described in Reference E-2. However, SEM/EDS and SAS results have not been previously published and are therefore presented here in comprehensive detail.

1. GROSS GAMMA SCANNING

The SFD-ST fuel assembly was transferred vertically from the PBF reactor to an adjacent canal and gross (nonspectral) gamma scanned to qualitatively determine the axial fuel distribution before handling motions during disassembly and prior to tipping for horizontal transport. This operation was performed by elevating the test train with an overhead crane in front of a stationary collimator and shielded ion chamber. Despite some slight variations in crane speed and a signal strength reduction because of a collimator leak during repeat scans, a valid gamma intensity profile was obtained, the major features of which were later confirmed by neutron radiography.

The desired information regarding the fuel distribution could be extracted from the gamma profile because most gamma-rays sufficiently energetic to reach the detector after nearly two months of decay originated from nonvolatile radionuclides generally bound to the UO_2 fuel. However, since the axial fuel distribution is convoluted with the cosine-shaped PBF flux profile, the data on fuel relocation had to be obtained by comparison to the fission power curve. The gamma scan and PBF flux profiles are shown in Figure E-1. The overall shape of the gamma intensity plot indicates significant downward relocation of fission product-bearing material. Approximately 0.11 m of upward fuel stack relocation is also indicated, although the specific inflection point corresponding to the stack top is somewhat uncertain because of the imprecise crane speed. Localized peaks and valleys suggest regions of relative concentration and dilution of UO_2.

The percent fuel movement was calculated by comparing the gamma profile to the PBF flux profile. Approximately 2% of the fuel moved downward to the region between 0 and 0.31 m, 10% of the fuel moved away from the region between 0.31 and 0.76 m, and 8% of the fuel moved upwards to the region above 0.76 m. It was assumed in this analysis that the gamma intensity is a linear function of the fuel mass. However, because of the PBF power profile, fuel from the lower and upper regions of the fuel bundle had less gamma intensity per fuel mass than fuel from the center region of the bundle. If fuel moved from the center of the bundle to the lower portion, it may appear that a larger amount of fuel has moved than actually occurred. It is difficult to establish the uncertainty without determining exactly the origin of relocated fuel.

2. NEUTRON RADIOGRAPHY

The SFD-ST bundle was shipped horizontally from the PBF reactor to a hot cell facility where the bundle was dried before being shipped, horizontally, to Argonne National Laboratory-West (ANL-W). Neutron radiography was performed in a vertical position in the Hot Fuel Examination Facility (HFEF) at ANL-W. The radiography facility consists of four components: a neutron source; a collimation structure to transmit, align, and shape the neutron beam; a specimen, which can be any material that attenuates neutrons; and some type of neutron imaging device. The neutron source for the HFEF radiography facility is the Neutron Radiography Reactor (NRAD), which is a tank-type, water-moderated reactor with solid fuel in a heterogeneous configuration.

During neutron radiography, the reactor was run at a steady state power of 250 kW(t). The beam port was aligned at the core-coolant interface, enabling a large percentage of epithermal neutrons to be used for radiography. The collimation structure was 16.76 m in length and the beam was shaped by a beam scraper set at a rectangular opening of 0.432 by 0.254 m. The imaging device was a foil package consisting of a 0.5-mm thick cadmium foil, to provide attenuation of thermal neutrons, and an indium foil to absorb epithermal (1.45-eV) neutrons. The foils were pressed together, inserted into an aluminum cassette, and vacuum sealed.

The Cd-In foil package was exposed for a 50-min period. The indium foil was removed and pressed tightly against a piece of Kodak T x-ray film in the vacuum film cassette overnight allowing the radioactive indium foil to decay over ∿12 half-lives, and thereby satisfactorily exposing the film. After processing this film, the resulting radiograph corresponded to a negative image of material structure within the bundle This information was then analyzed with a microdensitometer and the data tapes sent to EG&G Idaho for tomographic image reconstruction (see Section 3 of this appendix).

Successive radiographs were taken of the bundle for a more complete characterization of the material within. The bundle was remotely repositioned to allow radiography in seven axial positions, two of which were radiographed at multiple angles for tomography. Rotation of the bundle was performed in 2.4-degree increments in the clockwise direction (viewing the bundle from the top).

The fuel rods were aligned in rows at elevations where rod-like geometry was maintained. This is evident at both the 180 and 270 degree orientations, as shown, in Figures E-2 (a), (b), and (c). The bottom of the bundle contains instrumentation leads, the bottom end caps, the tie plate, and bottom insulation pellets in each rod. The fuel rods remained intact and no molten material or debris is observed below the bottom grid spacer (centered at 0.05 m above the bottom of the fuel stack). The bottom of the rod stubs extend up to 0.198 m. Molten material that moved down into the rod stub region extended from 0.072 to 0.198 m. Above the rod stubs is a large, nearly cylindrical mass, about 0.07 m in diameter, of rod segments bound together with previously liquid material. Above the mass is a debris bed of fairly uniform consistency. The debris probably consists primarily of fuel pieces about one-fourth fuel pellet size or greater, and large cladding sections. The middle grid spacer is not visible in the neutrographs. Sections of fuel rods are visible at the upper end of the debris bed (many segments lying at odd angles) and are probably highly oxidized. There is a gap in the fuel stacks just below the top grid spacer. The upper ends of the fuel rods are about 0.11 m above their original location. All of the structural components unique to the SFD test train are apparent in the neutron radiographs. A comparison between the location of the various structures in the neutron radiographs and the gross gamma scan is shown in Figure E-3.

3. NEUTRON TOMOGRAPHY

Sections of the SFD-ST bundle were examined in a nonintrusive manner by computerized tomography using multiangle neutron radiography. This inspection technique, commonly referred to as neutron tomography, provided computer-generated cross-sectional images of the test bundle. Different angular views of the bundle were acquired during neutron radiography by rotating the bundle about a fixed axis parallel to the longitudinal axis. The data were digitized, and cross-sectional images perpendicular to the axis of rotation computer-generated using a reconstruction algorithm.

Neutron tomography cross sections were generated every 8 mm over most of the 0.81 m region radiographed. In addition, axial views were generated from 0.113 to 0.335 m and from 0.435 to o.658 m at each of the rod rows for two orientations. The representative tomographs presented in Figures E-4 through E-8 are oriented such that the upward side corresponds to the side that remained up during all handling of the fuel bundle. The lower grid spacer is apparent in the 0.0635 m elevation cross section (Figure E-4), as well as some relocated previously molten relocated materials. The 0.164-m elevation (Figure E-5) shows relocation of large amounts of material around remnants of the fuel rod array. The cross section at the 0.276-m elevation (Figure E-6), is through the large molten cylinder in the bottom one-third of the bundle. An example of the debris bed at the 0.4386-m elevation is shown in Figure E-7. The ballooned cladding near the top of the bundle is apparent in Figures E-8 and E-9 at the 0.7975- and 0.8055-m elevations, respectively.

4. BUNDLE SECTIONING

The epoxy encapsulation and sectioning of the SFD-ST bundle, performed remotely in a hot cell facility, permitted a detailed examination of the chemical interaction of the materials and retained fission products in the bundle. In addition, the metallographic cross sections were compared with those generated using neutron tomography.

After evaluating three different epoxy systems, the one composed of dye-impregnated Dow Epoxy Resin 332 and Jeffamine T-403, mixed in a weight ratio of 100 to 45, respectively, was chosen as the SFD-ST bundle encapsulant. This epoxy exhibited good debris penetration and polishing characteristics and generated little heat during the curing stage. The volume of epoxy required was calculated to be $\sim$7 L based upon the assumption that the insulation region would not fill with epoxy. However, during the potting operation, 9.5 L of epoxy were necessary to fill the bundle, implying complete epoxy penetration of the insulation region and all voids. Sectioning of the bundle confirmed this result.

The sectioning saw was manufactured by Felker and included a 0.355-m-diameter by 3.17-mm-thick, diamond-embedded steel blade. The saw had a traversing table with an average manual feed rate of 0.71 mm per minute and a blade speed of $\sim$1600 rpm. Eleven 25.4-mm metallographic sections were cut and vacuum impregnated with epoxy into metallographic mounts. Analysis of these sections showed excellent penetration of the epoxy into the debris and insulation.

Nine cross sections, representative of all of the major regions in the bundle, were polished and are shown in Figures E-10 through E-18. The cross sections are located at 0.055, 0.145, 0.17, 0.245, 0.270, 0.395, 0.495, 0.825, and 0.915 m above the bottom of the fuel stack. All samples were viewed from the bottom surface, with counterclockwise orientations. However, to be consistent with the neutron tomography results, the photographs of the metallographic cross sections are reversed in this report. Therefore, all sections appear as if they were viewed from the top and all orientations are clockwise. This is not the case for the SEM and metallographic images in the next section, which were taken on bottom cross-sectional surfaces.

5. METALLURGICAL METHODS FOR ESTIMATING TEMPERATURES

The metallographic information and elemental composition distributions presented in the next section reflect several fuel damage mechanisms. These processes occurred with varying consequences depending on local temperatures, reaction durations, steam flow rates, and other transient conditions. In many cases, characteristic microstructures and other distinguishing features permitted estimates to be made of key dynamic variables, particularly temperature. The thermochemical phenomena of primary influence are introduced in this section, along with associated metallurgical terms and phase diagrams.

5.1 Zircaloy Phase Changes with Temperature

Zircaloy cladding progresses through several distinct microstructural changes with increasing temperature. The original (as-fabricated) zircaloy microstructure consists of alpha-zircaloy (α-Zr) grains elongated in the axial direction. This structure is observed with peak temperatures of <920 K. With increasing temperature, the α-Zr grains recrystallize and become equiaxed ($920 < T < 1105$ K). At about 1105 K, the transformation from α-Zr to the β-Zr phase begins. The β-Zr transforms back to α-Zr as temperatures are reduced below 1105 K. However, the microstructural appearance of the transformed β-Zr grains (referred to as *prior* β-Zr) is distinctly different from the α-Zr grains that were not exposed to temperatures >1105 K. The two-phase α + prior β-Zr mixture is observed in materials exposed to $1105 < T < 1245$ K. The temperatures at which this transformation occurs increases with increasing oxygen content in the Zr. (see Figure E-19.)

Several phenomena occur between $1245 < T < 2030$ K. As the temperature increases above 1245 K, the α-Zr transforms completely to β-Zr and then transforms back to α-Zr on cooling (prior β-Zr). The prior β-Zr structure appears as large, equiaxed grains with a characteristic α-Zr lamellar structure within each grain. Interaction of the zircaloy cladding with steam on its outside surface and UO_2 fuel on its inside surface (in the case of physical contact) becomes significant above 1245 K and substantial oxidation of the cladding occurs. Two layers are formed on the outside surface, a layer of α-Zr that has been stabilized at high temperatures because of oxygen uptake [denoted α-Zr(O)], and a layer of ZrO_2 outside the α-Zr(O) layer. The longer the cladding is exposed to temperatures >1245 K, the thicker these two layers become. The entire wall thickness can eventually transform to ZrO_2 and α-Zr(O). Frequently, there are two layers in the ZrO_2 phase. The inside layer closest to the α-Zr(O) would contain a metallic α-Zr(O) phase thus indicating that the ZrO_2 was slightly hypostoichiometric at temperature and underwent eutectoid decomposition into stoichiometric $ZrO_{2.00}$ + α-Zr(O) during cooling. This decomposition only takes place if the ZrO_2 has been at temperatures above $\sim$1760 K (Figure E-19).

If fuel-cladding contact exists, interaction of the UO_2 fuel with cladding also occurs, resulting in oxidation of the cladding from the inside surface. The internal UO_2/Zr interaction results in the formation of the following reaction layer sequence:

$$[UO_2 + U] \rightarrow [\alpha\text{-Zr(O)}_a + (U,Zr)] \rightarrow (U,Zr)\ \text{alloy} \rightarrow \alpha\text{-Zr(O)}_b$$

where

$UO_2 + U$ = UO_{2-x} at high temperatures

a = α-Zr(O) next to the fuel

b = α-Zr(O) near the center of the cladding.

These layers will then be followed by prior β-Zr $\rightarrow$ α-Zr(O) $\rightarrow$ ZrO_2 or only α-Zr(O) $\rightarrow$ ZrO_2, depending on the amount of steam oxidation from the outside. The fuel is reduced by the Zr to form metallic α-Zr(O) and elemental uranium. ZrO_2 cannot form as a result of the UO_2/Zr reaction alone. The metallic uranium does not remain at the $UO_2/\alpha\text{-Zr(O)}_a$ interface, because it tends to interact with Zr low in oxygen and diffuses into the cladding to form a (U,Zr) alloy rich in uranium. This (U,Zr) alloy lies between two α-Zr(O) layers and is liquid above $\sim$1425 K, depending on the Zr content. The α-Zr(O) layer adjacent to the fuel contains small amounts of the (U,Zr) alloy, primarily along grain boundaries, but also as small globules within the $\alpha\text{-Zr(O)}_a$ grains. The $\alpha\text{-Zr(O)}_b$ layer adjacent to the prior β-Zr contains no (U,Zr) alloy. During cooldown, hypostoichiometric UO_{2-x} decomposes into stoichiometric $UO_{2.00}$ and additional metallic uranium.

The two-phase $[\alpha\text{-Zr(O)}_a + (U,Zr)]$ layer is made up of relatively small, radially elongated α-Zr(O) grains, in comparison to the $\alpha\text{-Zr(O)}_b$ layer (and α-Zr(O) in general), which is made up of large grains. The boundary between the $[\alpha\text{-Zr(O)}_a + (U,Zr)]$ and (U,Zr) layers is distinct, but the interface between the (U,Zr) and $\alpha\text{-Zr(O)}_b$ layers can be very irregular. The formation of large (U,Zr) globules within the $\alpha\text{-Zr(O)}_b$ layers occurs only at temperatures ≥ 1775 K; at lower temperatures, small spherical particles form.

5.1.1 Interaction of UO_2 and Molten Zircaloy. The UO_2 fuel and zircaloy cladding comprise $\sim$98% of the bundle. Therefore, the interactions of these two materials with each other and with steam are the most important phenomena to be considered in evaluating bundle behavior. The zircaloy cladding can begin to melt at 2030 K, while stoichiometric UO_2 fuel does not melt until 3120 K. However, interaction of the Zr, UO_2, and steam results in materials with intermediate melting temperatures. (See Figure E-20.) The melting point of Zr increases with increasing oxygen content, with the melting temperature of oxygen-saturated α-Zr(O) being $\sim$2245 K. A eutectic interaction takes place between oxygen-saturated α-Zr(O) and UO_2 at 2173 K and a monotectic interaction at 2673 K, as shown in Figure E-21. The UO_2 and ZrO_2 form a solid solution at high temperatures, and a 50/50 mole% composition melts at $\sim$2809 K. Other low-temperature melts can form between the zircaloy cladding and Inconel spacer grids.

The key to determining the temperature ranges reached is the number, composition, and distribution of phases present in a prior molten material at room temperature. Neglecting effects of alloying elements, the observed phases should agree with the (U,Zr,O) ternary phase diagram. The ternary equilibrium phase diagrams of the (U,Zr,O) system at 1773 and 2273 K are shown in Figure E-22. Interaction between UO_2 and Zr at 2273 K results in either a single-phase homogeneous liquid, or a two-phase of (U,Zr,O) liquid and $(U,Zr)O_{2-x}$ solid (at >3.6-wt% oxygen). Upon solidifying, the homogeneous melt will decompose into two metallic components, namely an α-Zr(O) phase containing some uranium and a (U,Zr) alloy containing little or no oxygen. The heterogeneous melt also decomposes on cooldown, with the solid $(U,Zr)O_{2-x}$ particles having low Zr content decomposing into stoichiometric $(U,Zr)O_2$ and a (U,Zr) alloy, and the (U,Zr,O) liquid decomposing into α-Zr(O) and (U,Zr) alloy upon solidification.

Steam oxidation of the heterogeneous and homogeneous melts must be considered, as this affects the final microstructural appearance. If oxidation occurs after solidification, α-Zr(O) will transform to ZrO_2 and (U,Zr) alloy will transform to $(U,Zr)O_2$. Therefore, a homogeneous melt will transform from [α-Zr(O) + (U,Zr)] to [ZrO_2 + $(U,Zr)O_2$], and the two phases should be distinguishable. The same transformations will occur during oxidation of a solidified heterogenous melt, accompanied by transformation of $(U,Zr)O_{2-x}$ to $(U,Zr)O_2$.

A (U,Zr,O) melt can absorb oxygen while in the liquid state. As the oxygen content of the melt increases, the temperature required to keep the material molten also increases. A $(U,Zr)O_2$ solid solution forms if this temperature is not maintained. The ZrO_2 and UO_2 can also form a solid solution by diffusion at temperatures up to 2800 K and by mixing of molten oxides at higher temperatures. Figure E-23 shows the ZrO_2-UO_2 binary phase diagram. The minimum melting point of the solid solution occurs at about the 50/50 mol% composition, where only one phase will appear on cooldown. If this $(U,Zr)O_2$ has been molten, it will generally show structures such as large pores and irregular or nonexistent grain structure.

The amount of interaction with other materials is another indication of whether a $(U,Zr)O_2$ solid solution was initially a metallic melt. When a metallic melt contacts a ceramic material (UO_2 or ZrO_2), some dissolution will occur by reduction. A ceramic melt contacting a ceramic solid will show very little chemical interaction, although mixing will occur where a ceramic solid melts by heat transfer.

5.1.2 Inconel Grid Interactions. As described in the next section, small amounts of Ni, Fe, and Cr were commonly found in melt regions, including melts between cladding and fuel pellets due to prior reactions with Inconel spacer grids. These cladding-grid reactions can begin at ~1500 K through formation of a low melting point alloy.[E-3] Thus, cladding liquefaction and subsequent fuel dissolution may have begun relatively early at grid elevations during the SFD-ST transient. In addition, uranium was found to intermix readily with molten Inconel, and its constituents (especially Fe) often participated in pellet liquefaction by Zr-rich melts. Unfortunately, high temperature phase diagrams with appropriate reference points for these multicomponent situations do not as yet exist.

The presence of dissolved Inconel does permit melts oxidized in the liquid state to be distinguished from melts oxidized after solidification, because of the resistance of Ni to oxidation. Ni will be dispersed in a homogeneous (U,Zr,O) liquid after molten cladding-grid interactions. After sufficient fuel dissolution and steam oxidation has formed a heterogeneous melt of $(U,Zr)O_{2-x}$ solids plus L_1 (mostly molten alpha-zircaloy; see Figure E-21), the Ni will segregate with the phase containing the least oxygen. The L_1 liquid phase is typically high in zirconium, and low in oxygen. The L_2 liquid phase has typically high uranium, high oxygen concentrations. Upon complete liquid state oxidation of L_1 into ZrO_2 solids, Ni will be isolated into molten metallic ingots, often in conjunction with Sn, Mo, and other elements with low oxygen affinities. However, if the L_1 solidifies by cooling below 2173 K before complete oxidation is achieved, Ni ingots cannot form. This is even true if the solidified melt continues to oxidize to $(U,Zr)O_2$ and ZrO_2, as the diffusion rates would be too slow to permit such macroscopic Ni segregation. Similarly, if the homogeneous melt temperature exceeds 2673 K and liquefies sufficient fuel to form the U- and O-rich liquid L_2 in Figure E-21, the dissolved Ni will be dispersed in L_2. However, if the L_2 continues to oxidize above 2673 K, the Ni will be trapped in the decreasing L_2 phase as $(U, Zr,)O_{2-x}$ solids emerge, and the dispersed Ni will eventually segregate into molten Ni globules in a $(U,Zr)O_{2-x}$ matrix.

5.1.3 Fuel Grain Growth and Melting. A ceramic indicator of time at elevated temperatures is equiaxed UO_2 grain growth. Grain size correlations exist for isothermal conditions and well-defined atmospheres (pure steam, argon, etc.). However, these correlations are difficult to apply to nonequilibrium situations with rapidly changing temperatures, varying amounts of hydrogen in the steam flow, and fuel penetration by Zr and other impurities. Furthermore, high temperature melts are often found adjacent to fuel without detectable grain growth, suggesting that very large temperature gradients can occur across such boundaries. An equally significant practical problem on SFD-ST fuel was the wide range of grain sizes observed at individual positions. Thus, little quantitative information on the integrated time-at-temperature was extracted by this method.

Another indication of fresh fuel exposure to high temperatures (>2000 K) is rearrangement of sintering voids. Void mobility increases with progressively higher temperatures, and these pores tend to agglomerate at grain boundaries to lower the surface free energy of the system. Relatively large voids form between UO_2 grains from an initially random distribution of small pores within grains, but this phenomenon is also difficult to treat on a quantitative basis.

As the melting point of stoichiometric UO_2 (3120 K) is approached, individual fuel grains become essentially void-free, sharp corners on UO_2 grains become rounded, and the grains tend to separate slightly. When fuel actually melts (2900 to 3120 K, depending upon exact composition; see Figure E-24), the sintering porosity and grain boundaries disappear completely leaving an amorphous densified material. With superheating above the melting point, bubbles of vapor (UO, UO_2, and UO_3) form in the molten fuel. Eventually, the superheated fuel can take on a foamy appearance that survives cooldown to room temperatures. Without elemental composition data, this foamy structure can be confused with pores that form during cooling of O-rich (U,Zr,O) melts, where the peak temperatures of the two materials can be quite different. Most of the pore volume in oxidized (U,Zr,O) melts appears because of shrinkage, but several mechanisms could cause pore nucleation, including hydrogen gas, metal vapor, and fission gases in high burnup material.

5.1.4 Fuel Oxidation. As shown in the uranium-oxygen phase diagram provided in Figure E-24, UO_2 can absorb free oxygen or OH^- radicals at temperature, and can eventually become oxidized to UO_3. Upon cooldown, two fuel phases will generally emerge, where the phase make-up is determined by the extent of the oxidation. This phenomenon can be important to fission product behavior, because the oxidation process is typically accompanied by accelerated grain growth and higher associated fission product mobilities, as well as reduced grain boundary adhesion (desintering).

Until recently, fuel oxidation beyond $\sim UO_{2.2}$ was considered impossible in a pure steam flow. However, this understanding was based upon extrapolating data obtained at 1-atm pressure. Due in part to evidence found during SAS examinations on both SFD-ST fuel and fuel from the damaged Three Mile Island core, (discussed in next section and Reference E-4), effects of much higher pressures ($\sim$150 atm) have been incorporated in a recent thermodynamic calculation. As discussed in Reference E-5, fuel can oxidize to $\sim UO_{2.6}$ without surplus free oxygen, but only if very little hydrogen is present. These conditions existed during the cooldown phase of SFD-ST, after the period of rapid zircaloy oxidation and hydrogen generation had ceased.

6. ELEMENTAL COMPOSITION STUDIES

Twenty samples were extracted from the epoxied SFD-ST fuel bundle for scanning electron microscopy/energy-dispersive x-ray spectroscopy (SEM/EDS) and for scanning Auger spectroscopy (SAS). Detailed information was produced on the concentrations and local distributions of key elements (U, Zr, and O, plus structural material constituents) and on interactions between dissimilar bundle components during the high temperature transient. These data were primarily intended to supplement the results from metallographic investigations reported in Reference E-2. Accordingly, sample selection was governed by important phenomena (fuel liquefaction, melt solidification, etc.) and unresolved metallographic questions

(unusual microstructures and other intriguing features). A secondary objective was to identify the elemental makeup of the five core-drilled retained fission product specimens, as discussed in Appendix F.

Samples 2A and 2B were taken from the 0.055-m bundle elevation, where the 2 in the sample identifiers denotes bundle cross section STM-2. Samples 4C through 4I were extracted from cross section STM-4 (0.145 m), Samples 8J through 8N were from 0.245 m, Samples 13O and 13P were removed from 0.495 m, and Samples 19Q through 19T were taken from 0.915 m. This data base is strongly weighted toward the bottom one-third of the bundle primarily to study melt interactions in well-defined geometries, and therefore the SEM/EDS results do not represent the average posttest condition of the SFD-ST bundle. Many more samples would have been required to thoroughly describe each morphologically distinct bundle region (i.e., lower rod stubs, melt-covered pellets, central loose fragments, and upper rod segments). SAS examinations were confined to Samples 4C, 4I, 8K, 13P, 19Q, and 19R.

6.1 Sampling Methods

Each composition sample consisted of a circular wafer (5.6-mm diameter, 5.1-mm thickness) that was mounted on either an aluminum SEM stub or a stainless steel SAS shim. These wafers were sliced with a thin-sectioning saw from one-inch-long cylinders. The cylinders had earlier been remotely extracted from bundle cross sections with a diamond-tipped core drill and a conventional drill press, where the drill position was controlled by holes in templates prefabricated from cross-sectional macrophotographs (1:1 scale). Water was used as a lubricant in the drilling and slicing operations.

The composition wafers were mounted with the saw-cut faces downward in order that surfaces measured for elemental compositions corresponded very closely to those studied by metallography. The surfaces were not identical because, after completing metallography and before core-drilling the cylinders, two 25-μm layers were mechanically abraded from the STM-2, -4, -8, -13, and -19 cross sections for retained fission product determinations. (See Appendix F.) Consequently, the upper wafer surfaces were ground (as opposed to polished) and were slightly rougher than metallographic surfaces. More significantly, the grinding operation removed regions altered by metallographic etching, so the SEM/EDS and SAS findings were not compromised by chemical damage.

6.2 Analytical Techniques and Calibrations

SEM/EDS surveys were done to determine spatial distributions of elements above atomic number 10 and to semiquantitatively assay local concentrations of these elements. The measurements were performed on two different instruments at the INEL: an ISI Mini-SEM operated by Westinghouse Idaho Nuclear Co. (WINCO) and an Amray 1200B operated by EG&G Idaho, Inc. Performance of the two SEMs was very similar, except that the WINCO instrument featured a Robinson backscattered electron detector that produced much greater contrast by average atomic number on backscattered electron images. Consequently, differing metallurgical phases were far easier to distinguish with the WINCO instrument, and therefore most of the individual phase mapping was restricted to samples examined at this facility.

Both SEMs have Tracor-Northern EDS attachments (TN-2000 at EG&G and NS-880 at WINCO), with semiquantitative computer routines for spectral analyses. Both EDS devices contained lithium-drifted silicon x-ray detector crystals with beryllium windows. However, the crystals are of different vintages, sizes, and efficiencies, and displayed dissimilar performance characteristics. At WINCO, the prominent Zr peak was at 2.04 keV (Lα) and the prominent U peak was at 3.17 keV (Mα), whereas the major peaks at EG&G were at 15.8 keV for Zr (Kα) and at 13.6 keV for U (Lα). The lower efficiency WINCO detector was also much less sensitive to sample radiation. It generated EDS data without difficulty on specimens up to 10 Rad/hr (β-γ) with only a thin lead sheet and a 1-mm (diameter) collimator opening for detector shielding. However, it proved necessary to install a 1-mm thick plastic window in addition to a lead collimator on the EG&G detector for samples above 2 Rad/hr (β-γ).

The extra plastic window on the EG&G instrument also had the undesired effects of eliminating small x-ray peaks below 3 keV and of preferentially depressing lower energy peaks above this value. In practice, the greatest impact was on the Cr, Fe, and Ni Kα peaks at 5.4, 6.4 and 7.5 keV, respectively. Comparing semiquantitative results from both EDS systems on the same area of one sample revealed that EG&G values for Cr, Fe, and Ni were approximately a factor of three lower. This comparison further confirmed that EG&G U-to-Zr ratios were somewhat smaller than yielded at WINCO. Nevertheless, because EDS measurements were primarily intended for qualitative indications of elemental distributions, the different EDS detector characteristics were not a major drawback.

The biggest limitation of EDS was the inability to detect oxygen and to quantify concentrations of this element. Since these twenty samples generally consisted of varying mixtures of UO_2, ZrO_2, and oxygen-stabilized alpha zircaloy [α-Zr(O)], oxygen was typically a major sample constituent. Accordingly, the semiquantitative weight percentages produced for detected elements were biased upward by indeterminate amounts. Therefore, SAS was subsequently employed to provide accurate oxygen concentration data on six selected samples. The SAS measurements were performed on a Physical Electronics Corp. 549 spectrometer equipped with a 3-μm (minimum diameter) rastered electron beam. This apparatus also featured a computerized data acquisition system for time-averaging spectra (noise reduction) and for monitoring removal of surface contaminants by sputter-etching with argon ions. All spectra were recorded during a continuous light sputter to minimize readsorption of CO, CO_2, and H_2O gases that would have compromised accurate oxygen determinations.

Quantitative SAS necessarily required careful calibration to standards, where the electron beam size, current, voltage, and angle of incidence had to be maintained for valid results. Matching chemical form is also important in generating appropriate peak-to-atom percent conversion factors. For these samples, accurate Zr, U, and O concentrations were only achieved after separate factors were derived for metallic and oxidized areas. A UO_2/Zr interaction standard donated by the Kernforschungszentrum Karlsruhe (Federal Republic of Germany) supplied well-characterized UO_2 and α-Zr(O) regions, while an extruded ZrO_2 rod obtained from Babcock and Wilcox Co. provided a known Zr-O peak ratio for fully oxidized zircaloy. These calibration efforts produced accuracies within ± 3 at.% for major elemental constituents. The beam diameter was increased to 10 μm for a stronger signal and to reduce sensitivity to local surface topography, which can alter the angle of beam incidence and perturb quantitative results. Spectra were area-averaged over regions much larger than the electron beam size because most of the sample regions examined contained multiphase mixtures, and the poor imaging capabilities on this apparatus would not guarantee centering the beam on representative materials.

Quantitative SAS measurements were made on areas previously characterized by EDS, wherever SAS stage movements and imaging resolution allowed, to enable coarse calibrations of the semiquantitative results from both EDS systems. Although only seven SAS areas could be compared directly to each of the two EDS data sets, the following equations produce reasonably good fits to the U and Zr amounts measured by SAS (after converting atomic percentages to weight ratios). In these equations, Zr_c and U_c denote SAS-calibrated weight percentages, Zr_I and U_I represent weight percentages indicated for zirconium and uranium by the semiquantitative EDS outputs, and ΣM_I stands for the indicated sum of all minor elements detected by EDS (Fe, Ni, Cr, Sn, instrument elements, etc.).

WINCO

Samples 2A, 2B, 4C, 4D, 4E, 4F, 4I, and 19Q

$$Zr_c \cong \frac{100Zr_I}{Zr_I + 1.4U_I + \Sigma M_I}; \quad U_c \cong \frac{140U_I}{Zr_I + 1.4U_I + \Sigma M_I}.$$

EG&G

Samples 4G, 4H, 8J, 8K, 8L, 8M, 8N, 13O, 13P, 19R, 19S, and 19T

$$Zr_c \cong \frac{100Zr_I}{Zr_I + 1.8U_I + \Sigma M_I}; \quad U_c \cong \frac{180U_I}{Zr_I + 1.8U_I + \Sigma M_I}.$$

Because the EDS values on the accompanying sample figures are directly from the semiquantitative output listings, the above coupled equations must be used before comparing EDS results between samples analyzed at EG&G and WINCO. Note that both systems overestimated zirconium content at the expense of uranium, though by different extents due to the extra plastic window on the EG&G x-ray detector. Note also that these calibration equations do not yield true weight percentages in that the varying oxygen weights are unavoidably neglected. However, U_c/Zr_c ratios are independent of oxygen concentrations and therefore true U and Zr weight percentages can be calculated by proportional reduction wherever oxygen weights can be reliably estimated from metallurgically similar (etched metallography) SAS-characterized areas.

The SAS/EDS correlations further revealed that WINCO EDS values for Fe, Ni, and Cr are approximately correct, whereas EG&G transition metal quantities are far too low. These findings substantiate the previously discussed single-sample direct comparison between EDS systems, where a factor of three difference was found. Thus, weight percentages for Fe, Ni, and Cr on figures from EG&G samples should be increased by a factor of three, and indicated Zr and U values should be reduced proportionately, before the calibration formulas are applied. Unfortunately, enlarging transition metal values is not possible where plastic window attenuation diminished the Kα peaks to unquantifiable traces.

6.3 Detailed Composition Results

SEM/EDS and SAS findings from Samples 2A through 19T are presented in Figures E-25 through E-73. Data are displayed in several forms: secondary and backscattered electron images (SEM), x-ray dot maps of individual element distributions, and semiquantitative EDS and quantitative SAS listings for indicated sample regions. In limited cases, continuous SAS line scans for U, Zr, and O are shown across interfaces to indicate diffusion zone widths. Wherever possible, photomicrographs revealing associated microstructures are included for convenient comparison. The introductory figure for each sample provides a macrophotographic segment from each metallographic cross section to illustrate the local fuel bundle context. Note that the SEM/EDS examinations were performed at a 45-degree tilt angle for maximum x-ray detection, so the circular samples appear oval.

6.3.1 Sample 2A (WINCO). Thermochemical reactions between metallic cladding and Inconel[a] spacer grids are of interest in that eutectic formation between Zr and Ni, Fe, and Cr may have triggered localized cladding melting during the heat-up phase of the SFD-ST transient. Because no intact remnants of the upper two grids were discovered, this phenomenon must be investigated where melt droplets contacted the bottom grid.

One such place (between Rods 4C and 4D) is shown in Figure E-25, where sufficient heat was transferred from the adherent metallic melt to induce localized grid melting (>1650 K). Surrounding grid and cladding portions were otherwise unaltered at the 0.055-m bundle elevation, since coolant boiloff and rapid cladding oxidation did not progress this low. Considerable superheating of the melt was evident in that this droplet lost heat to both coolant and cooler materials before reaching this elevation, with sufficient heat left over to melt the grid region before solidifying. However, the melt did not wet the grid uniformly, so the isolated heat transfer may have been caused by a spring tab just above the sectioning plane. It should be noted that missing grid segments nearby occur midway between grid corners at spring tab positions. The inference can be made that melt droplets generally reached the grid by running down exterior cladding surfaces.

Local elemental compositions (neglecting oxygen) in the vicinity of the contact position are indicated by the EDS data in Figure E-26. The melt composition was found to be reasonably uniform, except near the once-molten Inconel. The melt in Area E consisted of at least two metallurgical phases, probably α-Zr(O) and (U,Zr) alloy with varying amounts of Ni, Fe, and Cr. Phase compositions were difficult to precisely

---

a. The nominal composition of Inconel 718 is 53.5 wt% Ni, 18.6 wt% Cr, 18.5 wt% Fe, 5.0 wt% Nb, 3.1 wt% Mo, 0.9 wt% Ti, and 0.4 wt% Al, plus small amounts of Co, Si, Mn, Cu, and other trace elements.[E-6] The formulation listed in Reference E-2 and E-7 is incorrect in that Ta is substituted for Nb.

resolve, because scattering of the 30-keV SEM electron beam excited x-rays from several microns around the incident beam. However, the melt evidently absorbed uranium during attack of a fuel pellet well above the 0.055-m elevation, while most of the transition metal content may be due to dissolution of the adjacent grid tab.

Distributions of the primary elements along the contact zone are displayed in Figure E-27. One noteworthy finding is that uranium migrated from the metallic melt into the molten Inconel, but Zr did not. This suggests that reactions between U and Ni, Cr, and Fe were more important here than transition metal-Zr reactions, though such behavior would not occur where only zircaloy and Inconel were in contact. In view of the prior mixing of (U,Zr,O) melt and Inconel, it is somewhat surprising that the molten Inconel constituents did not diffuse farther into the melt (i.e., that the boundaries on the Fe, Cr, and Ni x-ray images are so sharply defined.) When combined, these elemental distribution observations infer that liquid-state diffusion rates were much higher for uranium than for other species.

Formation of distinct reaction layers along the melt-Inconel interface is displayed in Figure E-28 (see Figure E-26 for precise position). Much of this micro-segregation probably occurred during cooldown, coincident with phase precipitation. Unlike uranium, which mixed readily with the Inconel ingredients, Zr penetration of the molten Inconel did not progress beyond the Zr-rich band (Point E).

6.3.2 Sample 2B (WINCO). This sample was extracted to investigate the varying extents of oxidation on separate metallic melts between Rod 2D (45 degrees) and a spacer grid junction (see Figure E-25 for exact sample position). As shown in Figure E-29, both melts are suspended from above, analogous to stalactites. The larger melt contains a thin oxide layer, while a relatively thick layer is found on the smaller melt. Both melts display pronounced dendritic microstructures.

Both of these features were tentatively identified during metallography as metallic (U,Zr,O) melts. If true, different liquefaction and solidification times could have been presumed from the variations in oxidation. However, the larger melt contains much more Ni and proportionately less Zr and uranium than the smaller melt (Figure E-30). The timing of solidification could still have been quite different in the two cases, but this cannot be deduced from the melt compositions.

Specific EDS data are presented in Figure E-31. As indicated, the smaller melt was predominately Zr. Lesser amounts of Ni, U, Sn, Fe, Cr, Re, and Ta created the complex multiphase precipitates during cooldown. By comparison, the larger melt consisted almost totally of oxidation resistant Inconel, with some dissolved U and Zr and a swirl of Mo-Re thermocouple sheathing. (The 6.9 wt.% Zr listed for Area B includes some Nb; the Lα peaks for these two elements are very difficult to resolve.) The larger melt is nearly identical to the molten grid in Sample 2A. However, unlike Sample 2A, limited Zr-Inconel mixing apparently occurred after grid liquefaction.

6.3.3 Sample 4C (WINCO). A high degree of oxidation occurred in the SFD-ST fuel bundle because of the relatively large steam flow rates during the transient. Nevertheless, a region of bulk metallic melt accumulated near the 0.145-m elevation. This material slumped toward the end of the transient and is apparently related to a temporary flow restriction measured by the bundle differential pressure transducer as discussed in the text of this report. Before cooling and solidifying, this bulk metallic melt was able to chemically react with coated fuel rod stubs.

Sample 4C illustrates many aspects of metallic melt behavior. The metallic melt reacted with a UO_2 pellet (Rod 2E) and an oxidized cladding segment (Figure E-32). Moreover, an irregularly shaped steam channel formed nearby, where steam oxidized the surface of this large pore before the melt cooled. Figure E-32 also reveals a large shrinkage crack that bisects all of these features, confirming that metallic melt reactions had ceased prior to complete cooldown.

Elemental distributions for the primary sample constituents (excepting oxygen) are displayed in Figure E-33. The boundary between the Zr-rich melt and the UO_2 pellet is distinct, especially after allowance for x-ray background conspicuous over the notch-shaped pore, inferring that melt-pellet diffusional

exchanges were in an early stage of progression when cooldown terminated reactions. The Fe x-ray image indicates some penetration of the fuel pellet by Fe, since the dots are definitely more concentrated over the fuel pellet than over the epoxied pore. By comparison, the Ni dot density is approximately the same over these two regions (i.e. only background observed), so Ni was evidently confined to the metallic melt.

Detailed EDS and SAS composition findings are presented in Figure E-34. Areas E, F, and G confirm diffusional penetration of the fuel pellet by both Zr and Fe, as well as the absence of Ni within the UO_2 matrix. Area H (SAS) was intended to be along the pellet periphery to determine the extent of UO_2 reduction, but the poor imaging capabilities on this apparatus inadvertently resulted in an overlap into the metallic melt, detecting Ni in the process. Metallic melt Areas B and D yielded nearly identical EDS values, but slightly more uranium was found in Area D by SAS. SAS imaging did not permit precisely reproducing EDS-analyzed regions. Results from both EDS and SAS are surprisingly similar for Areas A and C, where Area A began as metallic melt and Area C was ZrO_2 when the melt arrived.

The compositional similarities between Areas A and C can be largely explained by recognizing that Area A is incompletely oxidized melt while Area C is partially reduced ZrO_2. The highly magnified backscattered electron image of Area A reveals dark grains surrounded by bright material, where the darker substance must have a lower average atomic number. However, the point EDS data show higher uranium content within the darker regions, so they must contain appreciably more undetected oxygen. Therefore, the dark grains are most likely $(U,Zr)O_2$ and the bright stringers are probably (U,Zr) alloy. Small amounts of α-Zr(O) or ZrO_2 could also be present within Area A, but a third phase cannot be readily distinguished.

Area C displays a similar microstructure, with large dark regions and interspersed bright material. Although no point spectra were obtained, it is evident that the ZrO_2 was both reduced to ZrO_{2-x} and penetrated by melt intrusions upon melt arrival. During cooldown, the ZrO_{2-x} decomposed into ZrO_2 and α-Zr(O), while the (U,Zr,O) melt intrusions probably decomposed into α-Zr(O) and (U,Zr) alloy. Little or no $(U,Zr)O_2$ would be present. Thus, despite the overall similarity in elemental compositions, Areas A and C probably reflect their different evolutions in terms of metallurgical phase make-up.

Some caution must be exercised in interpreting the quantitative SAS results in Figure E-34, due to the manner in which standard calibrations were performed. Oxide sensitivity factors from UO_2 and ZrO_2 standards were applied to the U and Zr peaks from Areas A and C. However, because these areas are not completely oxidized, very minor deviations from true atom percentages should be expected. Metallic Areas B and D were analyzed using an α-Zr(O) sensitivity factor for the Zr peak and metallic factors for Ni and Fe. However, a uranium sensitivity factor appropriate for (U,Zr) alloy was not empirically derived from the Karlshruhe interaction standard and therefore the UO_2 sensitivity factor was used. As a consequence, the U values shown for Areas B and D are slightly too low. Oxide sensitivity factors were applied to the U and Zr peaks from Area H because the partial shift into the metallic melt region was not recognized at the time. Averages of oxide and metallic sensitivity factors would have been more appropriate here, and Area H SAS values may be outside the ± 3 at.% uncertainty band that validly applies to most SAS-characterized regions. It is worth noting that improving the accuracy of quantitative SAS is impractical because an exact knowledge of chemical forms would be required for each region analyzed, as well as an immense library of standard sensitivity factors.

An additional feature in Sample 4C was the presence of metallic inclusions within the fuel pellet. As indicated in Figure E-35, these small inclusions are $\sim$84 wt.% Fe and 16 wt.% Cr, which does not match any known bundle substance nor any material used in cutting, preparing, and handling the fuel bundle cross sections. The presence of parallel grinding marks confirms both that the inclusions are metallic and that they were in place before retained fission product sampling. No metallography was performed at the Sample 4C position, so no further inferences can be made.

Figure E-35 further enables coarse determinations of fuel grain sizes. The estimated range obtained from a higher magnification image was between 6 and 18 μm, with most grains between 10 and 12 μm. The nominal as-fabricated grain size is 10 μm, so little equiaxed grain growth occurred on average.

6.3.4 Sample 4D (WINCO). The 4D sample position (between Rods 2D, 2E, 3D, and 3E) was selected for assaying the fission product content of the bulk metallic melt (see Appendix F). Consequently, composition Sample 4D was primarily intended to determine the concentrations of principal elements within the companion retained fission product wafer.

The composition of this sample was expected to be reasonably uniform over its surface but, as indicated in Figure E-36, some variation in EDS results was found. This heavy element variation correlates to a texture difference, where the rougher portion probably contains more oxygen. Area B EDS values are nearly identical to metallic melt Areas B and D of Sample 4C and are probably more representative of the bulk metallic melt. The anomalous composition and texture of Area A may indicate that prior reactions occurred with a dissimilar material, possibly U-rich oxidized melt or a fuel pellet fragment, outside the sectioning plane.

Area C of Sample 4D was examined in greater detail, and results are presented in Figure E-37. The U and Ni dot maps and the point EDS values infer that these two elements are localized within the same metallurgical phase. Points 1 and 2 further suggest a second phase, with Zr as the only heavy element of significance. In addition, at least two phases are present on the etched photomicrograph taken over a nearby metallic melt region. It therefore appears that the room temperature metallic melt is composed of α-Zr(O) and (U,Zr) alloy, with transition metals concentrated with the (U,Zr) alloy. This two-phase mixture was probably homogeneous at temperature.

6.3.5 Sample 4E (WINCO). As shown in the STM-4 cross-sectional macrophotograph (Figure E-11), fuel rod stubs along the 0-degree side of the SFD-ST bundle were not covered by metallic and oxidized melts. This region serves as a baseline for evaluating effects of external melt-induced damage elsewhere at the 0.145-m elevation. In several situations, melt contact occurred over only a small portion of the cladding circumference, which enabled studying incipient external melt-cladding reactions. Sample 4E represents one such case. Figure E-38 shows that a large droplet or rivulet of metallic melt wetted Rod 4A at the 315-degree orientation. The acicular structure along the cladding exterior suggests formation of large β-Zr grains (>1245 K) and incursions of α-Zr(O), while the cladding interior may consist of small prior β-Zr grains or an α - + β-Zr two-phase mixture ($1105\ K < T < 1245\ K$). Other noteworthy features on the composite photomicrograph are steam oxidation of the oval pore surface, formation of an external melt-cladding reaction layer, and a second metallic melt between the cladding and the fuel pellet. No signs of internal melt-cladding interaction are evident. Supporting metallography revealed that the internal melt extended well beyond the azimuthal arc of external melt contact, so the two melts are not clearly related. Note also that this undamaged stub extended upward for at least another 20 mm, indicating that the internal melt must have been strongly superheated to slump this far without solidifying.

The interaction zone is displayed in greater detail in Figure E-39, along with x-ray dot maps for U and Zr. The U image reveals significant dissolved fuel concentrations within the internal and external melts, a small amount within the cladding, and the presence of fuel pellet fragments to the right of the external melt. The Zr map indicates limited penetration of the fuel pellet, as well as marked contrast between the internal melt and the cladding. The lower Zr dot density within the cladding is primarily due to more dissolved light elements (oxygen, hydrogen) than contained by the internal melt. The cladding Zr dot density is similar over the external metallic melt, which is mostly α-Zr(O) with $\sim$30 at.% oxygen. Some hydrogen was indicated by metallographic detection of circumferential ZrH_2 precipitates.

The internal cladding melt/UO_2 interface is presented at higher magnification in Figure E-40. Also included are elemental distributions for U, Ni, Fe, and Zr. The Ni, Fe, and Zr maps are shifted toward the fuel pellet. The uranium concentration is noticeably higher within the internal melt than inside the cladding. The Ni and Fe maps show about the same dot densities in the fuel and cladding, both at x-ray background levels, and thus these elements did not diffuse from the melt into the fuel to detectable extents. By comparison, Zr penetration of the UO_2 is quite conspicuous. The Zr dot density is considerably higher over the melt than the cladding, again inferring that the cladding Zr signal has been diluted by appreciable uptake of oxygen (and probably hydrogen). However, the parallel saw-cut marks confirm that the cladding is still uniformly metallic. This sample was inadvertently mounted upside-down, but examinations were not compromised.

Semiquantitative EDS findings from Sample 4E are presented in Figure E-41, where results from the external melt-cladding interface are given on the right photograph. Areas E, F, and G confirm uranium diffusion from the melt into the cladding. However, the dominant effect of the external melt was probably to heat the cladding. As reported in Reference 2, precipitation of zirconium hydrides was widespread elsewhere around the circumference of Rod 4H, but hydride precipitation was inhibited by localized heat transfer.

Area A results are exactly as expected for as-fabricated zircaloy-4, apart from the fact that considerable undetected oxygen and some hydrogen must also be present. The EDS values for Area B indicate that the internal metallic melt is essentially a mixture of (U,Zr) alloy and dissolved Inconel, where the Inconel must have originated at a spacer grid. Light and dark phases are distinctly evident within the internal melt on the backscattered electron image. With reference to points 1 and 2, this contrast is due to more uranium and less Ni, Fe, and Cr within the bright phase. Results for Areas C and D confirm earlier indications of Zr diffusion into the fuel pellet.

When combined with the Zr dot maps in preceding figures, these EDS results present an apparent contradiction with thermodynamic understandings of interactions between UO_2 fuel and Zr-rich melts. Recall that the Zr dot density is considerably higher over the internal metallic melt than over the cladding, despite volumetric melt dilution by substantial amounts of U, Ni, Fe, and Cr (30 to 35 at.% total). After allowing for dilution of the cladding Zr signal by realistic amounts of oxygen (30 at.%), and unknown amounts of ZrH_2, virtually no oxygen can be present within the internal melt or else the dot density contrast would be reversed. Nevertheless, exchanges of Zr and U have occurred between the melt and adjacent fuel without apparent oxygen absorption by the melt (without melt reduction of UO_2). Sample 4E requires precise SAS measurements of oxygen concentrations for clarification on the melt-fuel reactions.

Lastly, fuel grain sizes can be estimated from the left SEM micrograph in Figure E-41. Most grains are $\sim$10 μm in width, the nominal as-fabricated dimension. However, a few individual grains are as large as 20 μm, indicating isolated equiaxed grain growth along the pellet periphery.

6.3.6 Sample 4F (WINCO). As discussed in Appendix F, a retained fission product specimen was core-drilled from Rod 5A for an intact, unreacted fuel pellet benchmark (see Figure E-38 for location). Care was exercised to extract the central pellet portion, since metallography detected an internal metallic melt around this pellet very similar to that studied in Sample 4E. A composition sample was sliced adjacent to the RFP wafer to confirm that no inward Zr diffusion had occurred within the radial confines of the specimen. Sample 4F proved to be featureless UO_2 without any EDS indications of Zr penetration or evidence of equiaxed grain growth. Thus, there was no need to present figures and EDS results from this particular sample.

6.3.7 Sample 4G (EG&G). A small, isolated region of metallic melt was found near Rods 4D and 5D at the 0.145-m bundle elevation, as illustrated in Figure E-42. This region appeared similar to the bulk metallic melt concentrated elsewhere in this cross section, and was tentatively identified during metallography as a three-phase mixture of α-Zr(O), (U,Zr) alloy, and $(U,Zr)O_2$. Due to the unusual porosity and dendritic microstructure, a composition sample was core-drilled from this location. Comparing the backscattered electron micrograph to the photomicrograph (both at the base of Figure E-42) reveals that the porous metallic melt is largely present on only the left half of Sample 4G. This material was evidently very thin on the lower portion of the photomicrograph and was removed during grinding of the STM-4 retained fission product sample.

The predominate elements detected by EDS on Sample 4G are Zr, U, and Ni, plus significant amounts of Fe, Cr, and Re. Figure E-43 displays the distributions of the three major elements. Zr tends to be found in a mid-sample band, while uranium is concentrated on the right side. It is further evident that Ni is a key ingredient in the porous metallic melt.

Semiquantitative EDS results from various portions of Sample 4G are presented in Figure E-44. Because the EDS measurements were made at EG&G with the extra plastic window to shield the x-ray detector from

radiation, the lower energy peaks (Ni, Fe, Cr, and Re) were artificially depressed and higher energy peaks (U, Zr) exaggerated. As mentioned earlier, a factor of three increase in transition metal values should generally correct the preferential attenuation. However, this is only valid for minor constituents as the net impact of the extra detector window is less severe when low energy peaks predominate over a given area. In addition the uranium content was underestimated appreciably on this instrument in favor of Zr.

Only the upper two micrographs on Figure E-44 apply to the metallic melt, which consisted of Inconel, (U,Zr) alloy, and Re. The Inconel originated at the upper or middle spacer grid, while the Re probably came from the cladding thermocouple (Type C) inside Rod 4C. Some W is probably also present but the W Lα peak is disguised by the Ni Kβ peak and could not be resolved. The high Inconel and Re content distinguished this metallic melt from that in other regions of the STM-4 cross section.

The remaining four micrographs in Figure E-44 are varying mixtures of U, Zr, and undetected oxygen. Individuals phases could not be identified and mapped in the absence of a high contrast backscatter detector on the EG&G SEM. Consequently, few specific features can be recognized with confidence. The rightmost area is probably a fuel pellet fragment, while the Zr-rich region may be an oxidized cladding remnant. Much of the nonmetallic material was probably oxidized (U,Zr,O) melt, since metallography showed the metallic melt surrounded by oxidized melt. (See Figure E-42.)

6.3.8 Sample 4H (EG&G). This sample was the companion composition wafer to the retained fission product specimen core-drilled from the oxidized melt at the 0.145-m bundle elevation. Elemental surveys by EDS revealed a high degree of uniformity, so Sample 4H was not studied extensively. This sample (Figure E-45) was mostly uranium and undetected oxygen, with appreciable Zr. (Applying the calibration equations and assuming 66 at.% O yields 19 at.% U and 15 at.% Zr.) High magnification metallography exposed small, irregularly shaped metallic inclusions that were probably a second phase (U,Zr) alloy, but these features could not be resolved on the EG&G SEM. Random point probing along grain boundaries did not find any small areas of unusual elemental make-up, probably because oxygen content differentiated the inclusions from the bulk oxidized melt. It is clear that the oxidized melt at this elevation contained more liquefied fuel and less Zr than the bulk metallic melt.

6.3.9 Sample 4I (WINCO). Several fuel pellets surrounded by oxidized (U,Zr,O) melt in the 0.145-m cross section were also outlined with a thin layer of metallic melt. These layers seemed to be unoxidized cladding that had melted upon arrival of the oxidized melt. The widespread presence of metallic melt at this elevation indicates the possibility that metallic melt had penetrated oxidized melt porosity during its downward relocation. Sample 4I was extracted from the 315-degree orientation of Rod 4F to resolve this issue. As illustrated in Figure E-46, the metallic melt had also attacked the UO_2 along a pellet crack. Detailed inspection further revealed a remnant of external cladding ZrO_2 layer that partially separated the metallic and oxidized melts.

Figure E-46 also summarizes EDS and SAS results from major regions of Sample 4I. SAS imaging permitted exactly matching areas analyzed earlier by EDS. Areas A and B indicate fuel penetration by both Zr and Fe, but the pellet periphery (66 at.% O) did not show significant reduction (oxygen depletion) by the metallic melt. Areas C, D, and E give local metallic melt compositions. The metallic melt was mainly α-Zr(O), but Inconel constituents are present in sufficiently high concentrations to confirm slumping from a spacer grid elevation rather than melted local cladding. The metallic melt was also higher in O content than α-Zr(O), which saturates near 30 at.% O. Therefore, the metallic melt (superheated upon arrival) reacted with the oxidized melt and the ZrO_2 layer, before cooling and solidifying. Area F results demonstrate both penetration by U-bearing melt intrusions and appreciable reduction of the ZrO_2 layer (52 at.% O down from 67%) . Areas G and H illustrate that the oxidized melt is noticeably higher in U content than the metallic melt from dissolving more fuel. Furthermore, Area G infers partial reduction of the oxidized melt (58 at.% O) by the metallic melt.

Additional investigations along the pellet periphery are presented in Figure E-47. The x-ray dot maps show widespread penetration of the fuel pellet by both Zr and Fe diffusion, but the high magnification

backscattered electron image provides no evidence of equiaxed UO_2 grain growth. Most of the contrast on the two backscattered micrographs is due to topography, with raised regions appearing brighter. The local EDS values indicate that a Zr- and Fe-rich second phase exists within the fuel matrix. The continuous SAS line scans across the pellet-melt interface apparently intersected some of this second phase material at mid-length, as indicated by the U plot depression and the associated small peak in the Zr plot. However, these features are not accompanied by a significant depression on the O plot, and therefore the second phase was probably oxidized as also suggested by the 66% at.% O content of Area B. In addition, a grain of oxidized melt $(U,Zr)O_2$ is conspicuous on the right side of the line scans. The *zero level* scope traces for the three elements actually denote inelastically scattered, non-Auger secondary electrons at energies adjacent to the respective SAS peaks. This background can be influenced by topography, sample charging, and electron gun instability.

The metallic melt is displayed at high magnification in Figure E-48. The photomicrograph shows numerous oxidized melt grains within the metallic melt, confirming SAS indications in this regard. The x-ray maps and point EDS data reveal complex partitioning of the melt ingredients, with no certainty as to the exact number of metallurgical phases. However, it is clear that the metallic melt is largely composed of α-Zr(O), Inconel, and $(U,Zr)O_2$, with some (U,Zr) alloy also probable. Since the composition changed continuously during reactions with the oxidized melt and ZrO_2, the exact metallic melt make-up and temperature upon arrival is impossible to deduce.

Metallic melt attack along a fuel pellet crack is portrayed in Figure E-49. In this instance, it is interesting to contrast the behavior of the different metallic melt ingredients. Fe displayed the strongest tendency of the three transition metals to penetrate UO_2, while Ni remained within the melt and Cr showed an intermediate capacity. Both Fe and Cr were relatively more aggressive than Zr, although more Zr penetrated fuel on an absolute basis. These observations are somewhat inconsistent with thermodynamic expectations and point toward the importance of nonequilibrium kinetic considerations.

Figure E-50 depicts the results obtained from the oxidized melt in Sample 4I. This material appears to be mostly $(U,Zr)O_2$ with substantial α-Zr(O) and occasional traces of other elements. X-ray dot maps over the oxidized melt were generally featureless, with the exception of Cr that tended to segregate and possibly be accompanied by Al in a third phase. The oxidized melt is lower in uranium and higher in Zr than Sample 4H, reflecting reactions with the ZrO_2 and metallic melt at this position.

6.3.10 Sample 8J. This sample was accidentally dropped during SEM loading, fracturing it into irretrievably small fragments. Consequently, no images and composition data can be presented. Sample 8J was intended to characterize a large metallic ingot found near Rod 3D at 0.245 m. The STM-8 macrophotograph (Figure E-13) shows roughly ten major ingots, all apparently within large oxidized melt pores. Moreover, virtually all of them are located on the 270-degree side of the bundle directly above the bulk metallic melt at 0.145 m (Figure E-11). Thus, some of the metallic melt probably reached its final position by permeating the oxidized melt, enlarging and connecting some pores in the process, but also occasionally being trapped and chilled.

6.3.11 Sample 8K (EG&G). Nearly all of the fuel pellets at the 0.245-m elevation (Figure E-13) were covered by porous oxidized melt, with several pellets in advanced stages of dissolution. Fuel cracks were generally filled by melt and pellet diameters were often substantially reduced. One pertinent question is whether the oxidized melt was a molten ceramic upon arrival or initially metallic and oxidized during and after pellet attack. Reference E-2 makes a preliminary deduction of an initially metallic melt that was fully oxidized while still liquid, postulating melt temperatures in excess of 2810 K. This tentative conclusion relied upon two key metallographic observations: (a) the melt apparently reduced adjacent fuel to UO_{2-x} that decomposed during cooling to UO_2 and small uranium ingots. Subsequently, the metallic inclusions dislodged during metallographic grinding and polishing, forming larger porosity along fuel grain boundaries than can be explained by sintering void agglomeration; and (b) segregation of oxidation resistant metals (Ni, Sn, etc.) within the melt would only occur during liquid-state oxidation. Accordingly, Samples 8K, 8M, and 8N were intended to provide detailed empirical determinations on behavior of these mechanisms.

Sample 8K was extracted from the 135-degree side of Rod 4B. As can be seen in Figure E-51, this fuel pellet was roughly half dissolved, partially as a consequence of containing one fuel centerline thermocouple and three internal cladding TCs. All four TCs were Type C (W-5%Re/W-26%Re) with BeO insulation, but the centerline TC had a Re-augmented W sheath, while the cladding TCs were sheathed in zircaloy.[E-8] TC elements were not detected within Sample 8K, so their chemical influence on fuel liquefaction was probably minor. However, the hole drilled to accommodate the centerline TC certainly permitted early melt access to the pellet interior and the internal cladding TCs may have focused external melt attack at those pellet orientations.

The composite photomicrograph in Figure E-51 illustrates the primary features of interest: melt-filled pellet cracks that are distinguished by elongated shrinkage voids; fuel grains typically surrounded by relatively large voids that suggest pullout of U inclusions; and round metallic inclusions in the single-phase, oxidized (U,Zr,O) melt. Fuel grain sizes ranged from 15 to 50 μm, providing strong evidence of equiaxed grain growth. The small oxidized melt inclusions are not necessarily the same substance as the large metallic ingots on the macrophotograph insert, which also shows two of the large ingots within the confines of Sample 8K. Unfortunately, the ingot material was evidently very thin and ground away during STM-8 retained fission product sampling, the secondary electron image revealing only epoxy at the ingot positions. Figure E-51 further displays U and Zr dot maps, with Zr concentrated on the left side and U on the right. Traces of Zr were actually found within the fuel matrix, so the Zr signal over the pellet region is primarily from melt within pellet cracks rather than the inward Zr diffusion that is superficially indicated.

Detailed EDS and SAS results from Sample 8K are presented in Figure E-52. Areas A, B, and C represent the oxidized melt (primarily liquefied fuel), with Area C containing slightly more U due to its fuel proximity. All three areas were higher in U than Sample 4H, which was relatively distant from fuel pellets; these areas are also noticeably higher in Fe and Ni. Area F provided the composition of one metallic inclusion within the oxidized melt and is overwhelmingly Ni since plastic window attenuation has exaggerated the listed U and Mo concentrations. Areas D and E revealed surprisingly large Fe amounts within the fuel matrix, particularly in view of the negligible Zr penetration. Similarly, Area G depicted both Zr and Fe within the melt-filled crack, but only Fe was found in adjacent fuel.

Area D is shown at higher magnification in Figure E-53, along with a corresponding Fe dot map. Again, due to plastic window effects, the true Fe concentrations in Area D are considerably higher than listed, while the actual Zr content must be very small. The Fe x-ray image confirms point EDS indications that the Fe segregated into a second phase (possibly a U/Fe/O eutectic) that is unusual in nuclear fuel degradation experiments.

The SAS values in Figure E-52 indicate extensive oxidation on both sides of the melt-pellet interface, and both inside and outside of melt-filled cracks. A metallic sensitivity factor was required for Fe, since neither a FeO nor a Fe_2O_3 standard was available for calibration. A properly standardized Fe conversion factor would have slightly decreased the listed Fe atomic percentages, with most of the difference added to the O concentrations. Consequently, these data cannot confirm the metallographic deduction of an initially metallic melt reducing nearby UO_2. However, the proposed scenario is still viable, since both materials could have been steam-oxidized after interacting and since the Ni-rich inclusions in the oxidized melt lend credence to liquid-state oxidation. Moreover, SAS would only indicate net UO_2 reduction if the postulated U inclusions were still present, but these inclusions could have been dislodged during grinding of the fission product sample.

Despite the above qualifications, the possibility should be reconsidered that the oxidized melt was a molten ceramic upon arrival at this bundle position, with fuel liquefaction driven by heat transfer rather than melt reduction. Had the melt been initially metallic, some diffusional Zr penetration of the pellet should have occurred while the melt was absorbing O from the UO_2. Instead, Fe was the only melt ingredient to diffuse inward in significant amounts. Thermodynamic requirements dictate that such extensive Fe penetration, and formation of a Fe-rich second phase, can only happen if the Fe has already been oxidized to FeO or Fe_3O_4. Segregation of the Ni-rich inclusions would still occur within an initially ceramic melt and that the melt temperature was probably above 2810 K whether metallic or ceramic upon arrival.

6.3.12 Sample 8L (EG&G). As shown in Figure E-54, a heart-shaped pellet remnant was discovered between the insulation region and Rod 6E. As all of the fuel pellets on the 90-degree side of the bundle had already been identified, this pellet probably dropped from a higher bundle elevation, probably during posttest handling. Despite the uncertainty in its initial position, Sample 8L was extracted here to investigate two unusual features: (a) a darkened fuel appearance over two interior pellet regions; and (b) unoxidized melt within the crack that bisects the pellet.

The photomicrograph in Figure E-54 illustrates distinctly different fuel microstructures over this pellet. The darkness on the macrophotograph insert indicates some pullout of fuel grains during metallographic grinding and polishing due to diminished grain boundary adhesion. The pullout tendency correlates with a texture difference caused by larger fuel grains (20 to 25 μm here versus 10 to 15 μm elsewhere). However, the local EDS results indicate that the fuel structure differences cannot be explained by variations in heavy element concentrations.

Crack region investigations are presented in Figure E-55. The metallic melt within the crack had been tentatively identified during metallography as a homogeneous mixture of α-Zr(O) and (U,Zr) alloy. However, no Zr was actually present and Area G revealed that the metallic melt is mostly Ni and U, with minor amounts of Fe and W. Areas E and F and the Ni dot map confirm limited diffusion of melt species throughout the smoothly textured fuel adjacent to the crack. It is possible that these foreign elements within the fuel matrix inhibited the equiaxed grain growth observed just outside the crack region, but this would not explain the smooth fuel texture along the pellet periphery that showed nearly pure U on EDS. Similarly, the large-grained fuel could conceivably be oxidized with the crack region reduced by melt contact, but the apparent as-fabricated fuel microstructure along the periphery again poses a contradiction. It is noteworthy that an identical large-grained fuel region is found over the interior of pellet 6B at this elevation, but not the exterior (see Figure E-54).

6.3.13 Sample 8M (EG&G). This sample is superficially similar to Sample 8K in that a fuel pellet at 0.245 m (Rod 4E, 135 degrees) has been surrounded by oxidized melt. In both cases, no traces of cladding remained. Nevertheless, close inspection revealed significant differences in both the fuel and the melt. As indicated in Figure E-56, relatively little of the pellet has been dissolved, and a gap is conspicuous between the fuel and oxidized melt (mostly liquefied fuel) at most orientations. Fuel grain growth occurred up to 50 μm, but the occasionally large equiaxed grains are widely separated by grains of roughly as-fabricated dimensions. The pore sizes and distributions are also less suggestive of melt reduction and pullout of precipitated inclusions than Sample 8K, but inclusion pullout is very difficult to distinguish from sintering void agglomeration.

The melt contained considerable irregular porosity, very small metallic inclusions, and two conspicuous phases. The local EDS results infer that the melt probably consisted mainly of U-rich $(U,Zr)O_2$ with a smaller amount of either ZrO_2 or Zr-rich $(U,Zr)O_2$. The transition metal content was much smaller than Sample 8K, which corresponds to the tiny size of the metallic inclusions in Sample 8M and the large separation between them. Finally, there are no strong indications in Sample 8M of melt-pellet interactions. The pellet appears to have been merely coated by relatively cool oxidized melt that solidified shortly after arrival and pulled away during shrinkage. However, the melt was slightly higher in uranium content than the Sample 8K oxidized melt, and was therefore probably the end-product of fuel liquefaction at higher bundle elevations. Accordingly, the minor pellet damage at this elevation may have been produced by an earlier metallic melt that continued to slump downward before being replaced by the oxidized melt.

6.3.14 Sample 8N (EG&G). This sample (Rod 3E, 45 degrees) represents a third version of fuel pellet-oxidized melt interactions at 0.245 m. According to Figure E-57, the microstructures within the pellet and melt are nearly identical to those in Sample 8M, although the maximum fuel grain size ($\sim$35 μm) is somewhat smaller. However, the melt and fuel in Sample 8N clearly reacted before the melt solidified. The melt thoroughly penetrated the pellet crack, and strong wetting is also demonstrated by shrinkage pore formation along the crack center during cooling. In addition, melt-fuel bonding was sufficiently strong at the bottom crack corner for some fuel to be fractured during melt shrinkage. Nevertheless, the melt-fuel interaction was nowhere near as extensive as in Sample 8K.

Local EDS results from Sample 8N are displayed in Figure E-58. Areas A and D are well inside the fuel matrix and reveal no inward diffusion of melt species. Areas B, C, F, and G represent the oxidized melt, which again is mostly liquefied fuel. As with Sample 8M, the melt appears to be mostly U-rich $(U,Zr)O_2$ with a minor second phase of either ZrO_2 or Zr-rich $(U,Zr)O_2$. Only traces of transition metals are present, but Point 1 of Area G confirms that the tiny metallic inclusions are primarily oxidation-resistance Ni. Area E, which covers the lower pellet corner, shows a cluster of Ni-rich inclusions within the fuel matrix. These inclusions are reminiscent of the Fe-rich inclusions that extensively penetrated fuel in Sample 8K, although these may not be oxidized. Again, no signs of inward Zr diffusion are evident, which may indicate that the melt was substantially oxidized before slumping to the 0.245-m elevation and contacting the pellet. Due to its high uranium content, the melt was above 2673 K at some stage of its evolution, but may have cooled before reaching this position.

6.3.15 Sample 130 (EG&G). The central bundle region became severely embrittled during the test, and much of the local geometry was disrupted. Consequently, as displayed in Figure E-16, the original pellet positions can no longer be recognized. Instead, fuel rod remnants were referred to by an *object number* during metallography.

Sample 130 was extracted from the 270-degree side of Object 4, a fuel pellet located very near the geometric center of cross section STM-13 (0.495-m elevation). The macrophotograph insert in Figure E-59 shows that the left pellet side is missing and that the center has been filled by melt. The melt extends along the major pellet crack until it fills the pellet-cladding gap on the right side. Unfortunately, the core drill was offset from its intended position, so the internal pellet zone was omitted on this sample. In addition, the wafer sliced from the core-drilled cylinder was inadvertently mounted upside-down, so it was necessary to study the saw-cut surface. However, the saw blade indentations proved helpful in distinguishing different metallurgical phases and partially compensated for the lack of a high contrast backscatter detector.

The right half of Sample 130 included a bright powdery material that was present in many portions of the 0.495-m elevation. This material was tentatively identified as ZrO_2 fiberboard insulation, but the Zr dot map in Figure E-59 challenges this interpretation. Some ZrO_2 was probably involved, but it must be very dilute. One possibility is that the highly hygroscopic ZrO_2 powder absorbed atmospheric moisture before the bundle was epoxied (after neutron radiography). Even small amounts of moisture would interfere with the curing process, so the anomalous material could largely be hydrated epoxy (not detectable by EDS).

Area A of Figure E-59 is also worthy of comment. This unusual feature proved to be an ingot of nearly pure metallic uranium covered by once-molten $(U,Zr)O_2$. The mechanism by which such a large uranium ingot could be formed is not obvious.

Local EDS results and representative SEM micrographs from Sample 130 are displayed in Figure E-60. Areas C and D (as well as Area B on Figure E-59) reveal no significant penetration of melt ingredients into the fuel matrix. Fuel grain sizes are uniformly close to 10 μm, the as-fabricated dimension. Areas E and F are from the internal melt (both slightly higher in U than Zr on an atomic basis), but the higher Zr content within Area F suggests appreciable melt-cladding interaction. Area G represents the interior cladding region, where the columnar grains indicate ZrO_2 that was locally reduced and radially penetrated by metallic melt intrusions. However, Area G did not melt because Areas E, F, and G would be more uniform in composition. Areas H and I are from the exterior ZrO_2 portion that did not react with the metallic melt. The width spanned by Areas G, H, and I is very close to 600 μm, the as-fabricated cladding thickness. Area J shows that the thin external melt layer is mainly ZrO_2 with significant amounts of Inconel constituents, plus Ti from a sleeve around an internal cladding thermocouple.

Since Areas H and I are ZrO_2 and still reveal saw indentations, while UO_2 Areas C and D do not, some tentative deductions can be made on phase make-ups between the fuel and oxidized cladding. Area E exhibits considerable hardness and is probably single-phase $(U,Zr)O_2$. Area F contains two distinct phases, with greater and lesser amounts of $(U,Zr)O_2$ and ZrO_2, respectively. Area G is also a two-phase mixture, but here the dominant substance is almost certainly ZrO_2. The melt must have been only partially oxidized upon arrival and later fully oxidized to $(U,Zr)O_2$ by steam flow through shrinkage pores and cracks that required

cooling to form. That is, melt oxidation was probably completed during the cooldown phase of the test, after melt solidification occurred. Note that no round metallic inclusions segregated from this oxidized melt to indicate liquid-state oxidation, despite the presence of Ni traces. According to Figure E-20, the melt temperature was certainly above 2173 K and could have been above 2673 K to account for the high uranium content.

6.3.16 Sample 13P (EG&G). This sample was extracted between Objects 1 and 2 that were two fuel rod remnants on the 225-degree side of the 0.495-m cross section. As shown in Figure E-61, both rods had ballooned and the balloon spaces later filled with melt. In addition, melt collected between the two objects, partially dissolving oxidized cladding on both. The internal melts attacked both fuel and cladding, although locations of internal melt-cladding interaction are relatively infrequent. All materials appear highly oxidized in the composite photomicrograph. As with Sample 130, metallic inclusions are absent within oxidized melt regions.

The secondary electron image also shows cement that accidentally flowed over part of the sample during mounting. The cement peeled off most regions easily but adhered to the oxidized cladding. Nevertheless, the cement residue was easily identified on the SEM and SAS instruments and posed no difficulty during composition measurements.

SEM/EDS findings across the base of Sample 13P are given in Figure E-62. Area A is within the fuel pellet and shows limited inward diffusion of Zr. Areas B through E represent the internal melt (mostly liquefied fuel) and demonstrate high compositional uniformity. The melt evidently absorbed some uranium by direct fuel liquefaction, although it probably contained considerable uranium before slumping to this elevation. Areas F, G, and H cover the Object 2 oxidized cladding. Areas F and G reveal little cladding interaction with the internal melt. However, the uranium content of Area H indicates strong attack by the external melt. The low uranium concentration over Area I relative to Areas B through E suggests that the external melt was more metallic upon arrival, and more inclined to reduce ZrO_2 than the internal melt. The uranium content of the external melt is still appreciable and demonstrates significant fuel dissolution before slumping to this elevation and solidifying.

Results from a similar EDS traverse across the upper sample portion are displayed in Figure E-63. Short stage travel forced a 180-degree sample rotation to image this region at high magnification, so these micrographs are upside-down with respect to Figures 61, 62, and 64. Areas J and K yield external melt compositions, with Area K slightly higher in Zr from greater ZrO_2 interactions. Area L shows much more uranium penetration into the external ZrO_2 than in Area H, perhaps reflecting the larger external melt thickness on this side of the sample. Areas M and N are essentially pure ZrO_2, so virtually no mixing occurred across the internal cladding-internal melt boundary. Areas O and P are from the internal melt and, unlike Areas B through E, reveal some inhomogeneity with Area P containing somewhat more uranium. Both areas are significantly higher in uranium than Areas B through E, inferring more fuel liquefaction at this pellet orientation. Area Q is a region where melt firmly bonded to the pellet periphery, breaking off a fuel fragment during cooldown shrinkage. This melt-pellet bonding is also apparent on the U and Zr dot maps. Area R is within the fuel matrix and shows no signs of melt attack or equiaxed grain growth.

SAS findings over this same vicinity are presented in Figure E-64. SAS micrographs were not of report quality, so an inverted SEM image was used to locate SAS measurements. The continuous line scans show a broader diffusion zone across the ZrO_2-external melt boundary than across the internal melt-fuel pellet interface, with allowance for the shrinkage crack between Area J and T. Apart from Areas V and W, which are clearly ZrO_2, the remaining four areas indicate uranium oxidation beyond nominal stoichiometry. Area S values convert to nearly $UO_{2.9}$. Areas T and U contain substantial ZrO_2, but hyperstoichiometric uranium oxide is also present ($\sim UO_3$ and $\sim UO_{2.7}$, respectively). Area X even suggests some enhanced oxidation ($\sim UO_{2.3}$) of the external melt. These unexpected oxidation results are partially supported by the two-phase fuel microstructures (found during metallography of Object 2) shown at the top of Figure E-64.

The surprisingly high oxygen values measured over U-bearing portions of Sample 13P cannot be easily attributed to SAS uncertainties. The same sensitivity factors and measurement parameters were used here as

with oxidized regions of Samples 4C, 4I, and 8K, where no hyperstoichiometric U oxides were found. The ± 3 atom % uncertainty for major constituents converts approximately to ± 0.3 on O/U ratios, so anything beyond $UO_{2.3}$ is definitely hyperstoichiometric. However, where oxidation beyond $UO_{2.5}$ has occurred, minor deterioration in accuracy should be expected due to the lack of a UO_3 or U_3O_8 standard for additional calibration points to compliment the UO_2 standard. Nevertheless, improved calibration would not cause large changes in the indicated O concentrations. Precise knowledge of phase make-ups requires a technique like x-ray diffraction that is better suited to this specific objective.

These hyperstoichiometric oxide measurements cannot be explained by alterations during sample preparation. Bundle drying before neutron radiography required heating, but temperatures were monitored and restricted to within 10K of the water boiling point. Bundle epoxying also involved a thermal excursion, but not above 400K. Metallographic grinding and polishing, retained fission product sampling, and core drilling and thin sectioning of the composition wafers were always performed with copious water lubricant to preclude local heating. In addition, these activities applied to all bundle cross sections sampled and would have impacted SAS-characterized regions from the lower bundle. The sole situation unique to Sample 13P was the overflow of mounting cement, which did not adhere to most sample regions and was easily recognized by its high carbon content on the patches over the oxidized cladding.

As with Sample 130, it seems that the internal melt was initially metallic (incompletely oxidized liquefied fuel upon arrival) and that final oxidation occurred only after shrinkage voids and cracks formed to accommodate internal steam flow. Thus, the most likely interval for completion of melt oxidation is the cooldown phase of SFD-ST. The absence of small metallic inclusions in the oxidized melt signifies some solid-state oxidation, since ample Ni was present for segregation in the case of liquid-state oxidation. The melt temperature was probably above 2673 K before slumping to this elevation, to account for the large liquefied fuel content, but the temperature here could have been somewhat lower.

Oxidation of the fuel pellet periphery presumably also happened late in the test, after rapid cladding oxidation and the associated generation of hydrogen had been terminated. A recent calculation (partially prompted by these measurements) indicates that fuel can oxidize to $UO_{2.6}$ in high pressure steam, but only in the absence of appreciable amounts of hydrogen.[E-5] This thermodynamic study contradicts a widespread understanding that significant fuel oxidation is not possible beyond $\sim UO_{2.2}$ in pure steam, where results derived at 1-atm pressure were inappropriately applied to high pressure transient reactor conditions (pressures $\sim$100 atm.). Nevertheless, these SAS measurements apply only to the melts and the pellet periphery and do not necessarily imply enhanced oxidation of the pellet interior.

6.3.17 Sample 19Q (WINCO). The 0.915-m elevation cross section corresponds to the original top of the fuel pellet column. However, after melt slumping and solidification effectively blocked coolant flow, sufficient differential pressure accumulated after reactor scram to fracture the embrittled bundle along the melt base (between 0.10 and 0.17 m; see Figure E-2(a)) and to lift most of the bundle upward 0.115 m into the fullback barrier. While intermediate bundle portions slid downward varying distances during posttest handling, the upper segment was wedged in place by the shroud liner. Consequently, the STM-19 cross section is actually beneath 0.11 m of fuel and the remnants of the upper spacer grid. (See Section 4.10 of main text for further discussion.)

The STM-19 macrophotograph (Figure E-18) reveals that much of the upper bundle geometry survived the transient and subsequent handling. Many fuel pellets were partially dissolved, and curlicued remnants of ballooned cladding-Inconel grid interactions are conspicuous over the entire cross section. Several pellets further display a porous structure that suggested pure fuel melting (>3120 K) during metallographic investigations.

Sample 19Q was drilled from the 315-degree side of pellet 2D. The macrophotograph insert in Figure E-65 illustrates that this pellet includes a large wedge of porous once-molten material, where the wedge point forms the left side of the sample. The wedge region is primarily liquefied fuel mixed with molten zircaloy and Inconel, rather than the metallographic interpretation of molten stoichiometric UO_2. The original composition of the attacking melt cannot be determined, since considerable mixing probably happened after pellet liquefaction.

Area F represents the original pellet periphery and is somewhat richer in Inconel ingredients than Area E. At higher magnification, Area F exhibits a complex dendritic microstructure that includes at least two phases. Areas A, B, C, and D are from three portions of the curlicued substance and demonstrate significant nonuniformity in composition, despite the superficial similarity in appearance. The high uranium content in Areas A through D indicated appreciable melt liquefaction of upper fuel pellets before slumping to this elevation, reacting, and solidifying. The absence of discrete Ni inclusions in all six areas of Figure E-65 implies that the oxidation was completed after solidification.

Detailed studies on the solid pellet portion of Sample 19Q are presented in Figure E-66. This region was of keen interest in that a conspicuous densification zone separates the porous melt from the fuel grains inside the pellet. This densification zone was interpreted during metallography as incipient fuel melting, and here the composition measurements support the metallographic deduction. Areas D and E best represent the densified fuel and show only traces of Zr. Similarly, the fuel matrix (Area F) revealed very little Zr. Although Area C contained 2.5 at.% Zr, the liquefaction temperature still must have been very close to the fuel melting point. Areas A and B were noticeably absent of Inconel constituents and indicated that Inconel-fuel interactions were of negligible influence in the liquefaction process.

It therefore appears that the melt temperature was above the fuel melting point (between 2900 and 3120 K, depending on exact composition; see Figure E-24) and that the fuel was being liquefied by heat transfer before chemical mixing. This process was possibly accompanied by melt absorption of oxygen, creating the densification zone. Some Zr penetration of the zone boundary may have occurred after the melt cooled slightly. Again, the existence of the densification zone is essential to concluding fuel melting, because this low porosity, low impurity boundary rules out fuel liquefaction by melt reduction, large scale formation of UO_{2-x}, and subsequent penetration by melt intrusions.

As with Sample 13P, the SAS measurements in Figure E-66 indicate substantial fuel oxidation. After subtracting ZrO_2 concentrations, the SAS values convert to $\sim UO_{2.7}$ for Areas A and C, $UO_{2.5}$ for Area D, and $UO_{2.3}$ for Area F, with an uncertainty of approximately ± 0.3 on these O/U ratios. As noted earlier (Sample 13P), these ratios could be refined slightly with a UO_3 or U_3O_8 standard. The enhanced oxidation probably occurred by steam flow through the melt's shrinkage pores, which formed after melt solidification. Again, the melt could not have oxidized completely in the liquid state, or the oxidation-resistant Ni would have segregated into discrete ingots. Consequently, the relatively impermeable densification zone may have protected the pellet interior from greater oxidation.

Area F indicated hyperstoichiometric fuel and therefore the solid microstructure was probably two-phase and not as-fabricated, as identified during metallography. The porosity appeared excessive for as-fabricated fuel. In addition, the grain growth indicated on the high magnification photomicrograph is significant, although not as large as fuel melting temperatures would suggest. Thus, a strong temperature gradient probably existed across the densification zone.

6.3.18 Sample 19R (EG&G). This sample was extracted to study incipient fuel liquefaction in a relatively undamaged rod at the 0.915-m elevation (Rod 2C, 315 degrees). As indicated in Figure E-67, the cladding circumference was coated with melt and an internal melt also formed between the fuel and cladding. The composite photomicrograph (90-degree orientation) demonstrates melt penetration along a pre-existing pellet crack, with the fuel microstructure characterized by excessive porosity for as-fabricated UO_2 and grain boundaries that are not easily distinguished. This image also reveals pronounced columnar grains within the cladding and reaction layers between the cladding and the oxidized internal and external melts.

The metallographic interpretation is that the cladding was fully oxidized before contact with metallic melts and before reduction to a two-phase mixture of α-Zr(O) and ZrO_2. The internal melt bonded better to the oxidized cladding than to the fuel, although some fuel fractured away from the pellet during cooldown shrinkage. No metallic inclusions are evident within the internal and external melts, and so were apparently oxidized after solidification.

Findings from the SEM/EDS traverse across the base of Sample 19R are displayed in Figure E-68. Area A is within the fuel matrix and shows negligible Zr penetration. Area B includes both internal melt and bonded cladding, and the EDS values suggest that the melt absorbed appreciable uranium before slumping to this elevation. Area C is well inside the cladding yet still reveals considerable uranium penetration, most probably in the form of (U,Zr) alloy intrusions during melt reduction of the ZrO_2. Area D covers the cladding exterior and demonstrates inward movement of uranium and Inconel constituents from the external melt. External melt compositions are provided by Areas E and G, where the high uranium concentrations confirmed that the melt was almost one-half liquefied fuel. Area F is a region where external melt reacted with a curlicued remnant of ballooned cladding, leading to higher Zr than within most of the external melt.

Figure E-69 presents the results of another traverse across the top of the sample. The major difference is that the internal melt is noticeably thicker and better bonded to the UO_2, apparently inducing the circumferential pellet crack during cooling. Area H shows correspondingly more Zr in the adjacent fuel than Area A. Area I is all internal melt, and the uranium content (equal to Zr on an atomic basis) is clearly too high to be due solely to fuel dissolution at this elevation. The Inconel ingredients also confirm melt formation at a higher elevation, rather than direct cladding-fuel interaction. Areas J, K, and L span the cladding width, with strong evidence of melt penetration and associated ZrO_2 reduction in all three areas. External melt Area M was high in uranium and its composition was very close to Area I, inferring that the internal and external melts were joined at a higher elevation. The Ni dot map for this area shows segregation into a second phase, but no rounded metallic ingots can be distinguished on the Area M micrograph. Consequently, while the melt may have been substantially oxidized as a liquid, the oxidation was completed in the solid state.

SAS data were obtained across the cladding-internal melt-fuel interface at positions close to Areas H, I, and J, with the findings given in Figure E-70. As expected, the continuous line scans reveal a general decrease in uranium and an increase in Zr going from the fuel into the reacted cladding. However, significant problems were encountered with electron beam stability, as indicated by the major shifts in background levels. These were photographed at times different from the respective elemental traces. The electron beam stability, combined with poor imaging capabilities, created problems in the assignment of sensitivity factors to Areas O and P. Whereas oxide factors were certainly appropriate for Area N, the oxygen signal decreases considerably to the right. This decrease appears to be between Areas O and P, and therefore oxide factors were also applied to Area O. However, a second decrease is evident beyond Area P on the wide-span oxygen trace. An α-Zr(O) factor was therefore inappropriate for Area P and instead an average of the α-Zr(O) and ZrO_2 factors was applied. As explained previously, a metallic uranium factor was not empirically derived and therefore no choice could be made in this regard. In any case, the sensitivity factors for Area P were somewhat arbitrary, so listed results could be outside the ± 3 at.% uncertainty band for this specific region.

The SAS results that emerged indicated that both the fuel and internal melt were oxidized above stoichiometry, with respective O/U ratios of 2.4 and 2.5. Since the oxidized cladding was reduced earlier by the initially metallic melts, it appears that Area P was oxidized back up to nearly $(U,Zr)O_2$ while the cladding beyond Area P stayed in a reduced condition. This interpretation infers that Area P is actually in a reaction layer created by steam flow through the shrinkage pores in the internal melt. By extension, the external reaction layer in Figure E-67 is also due to steam oxidation, presumably during the cooldown phase of SFD-ST. However, these inferences are tentative and could be altered with more comprehensive SAS data across Sample 19R.

6.3.19 Sample 19S (EG&G). This sample is the companion wafer to the core-drilled specimen measured for fission product deposition on upper bundle structural surfaces. (See Appendix F.) Sample 19S was taken along the inner shroud liner at the 0.915-m elevation (135-degree corner of cross section STM-19) to avoid fuel-bearing material. In this manner, released and deposited fission products could be discriminated from those that migrated along with UO_2 and liquefied fuel.

As displayed in Figure E-71, Sample 19S contained a segment of partially oxidized shroud liner and a fragment of fully oxidized cladding, plus a ballooned cladding remnant (Area A) and two inclusions of

unusual appearance. It should be noted that the cladding fragment was epoxied at a high tilt angle relative to the sectioning plane, and therefore appears much thicker than 600 μm. The liner segment and cladding fragment showed no traces of foreign elements. However, Area A revealed some Inconel and a trace of uranium within the curlicued cladding remnant. The Area B EDS study indicated that the two inclusions were pure Fe plus an indeterminate amount of undetected oxygen. This composition does not match any bundle component and thus, the origin of this substance is unknown. Since only a trace of uranium was discovered, little fuel-bearing material was present and the adjacent wafer was well-suited for investigating fission product deposition.

6.3.20 Sample 19T (EG&G). This sample was obtained from a partially liquefied fuel pellet (Rod 4E 270 degrees) that exhibited high porosity. As with Sample 19Q, the porosity was attributed during metallography to melting of stoichiometric UO_2. However, this preliminary deduction was made without the benefit of etching to expose additional phases, and later proved to be incorrect. As illustrated in Figure E-72, the porous structure contained Zr and Ni, as well as uranium. Thus, chemical alterations and subsequent fuel liquefaction appear to have caused the porosity by melt shrinkage, rather than pure UO_2 melting. In addition, no densification zones of the sort found in Sample 19Q were discovered in Sample 19T. However, UO_2 melting cannot be discounted completely, because the observed elemental mixing could conceivably have occurred after fuel melting.

EDS results from Sample 19T are presented in Figure E-73. As indicated, the porous material is mostly uranium and undetected oxygen. However, due to preferential plastic window attenuation, the Inconel ingredients are roughly a factor of three low and the listed Zr concentration correspondingly high. Thus, this porous pellet is somewhat higher in uranium than the porous wedge in Sample 19Q. A Ni-rich second phase is conspicuous within Area B. Metallography determined that the porous melt was highly oxidized and therefore the Ni segregation implies some liquid-state oxidation. Additionally, the inference can be made that the intermixed melt was initially metallic and reduced the fuel during liquefaction, thereby lowering the melting point. Finally, since the Ni did not segregate into discrete metallic ingots, the reoxidation of the liquefied fuel was probably completed after solidification, presumably by steam flow during the cooldown phase.

Based upon the original metallographic interpretation, a companion retained fission product specimen was analyzed to investigate fission product releases at temperatures >3120 K. However, because the porous material would perhaps better be described as liquefied fuel, or a high-U version of an oxidized melt, the liquefaction temperature was probably below the melting point of stoichiometric UO_2. Nevertheless, melt-induced liquefaction dissolution better represents SFD-ST fuel damage as a whole and therefore the retained fission product information was still valuable.

6.4 Overview of Composition Results

The SFD-ST composition samples enable the following firm conclusions to be reached in conjunction with the earlier findings from metallography and neutron radiography and tomography.

1. Porous fuel pellet regions found within the upper bundle do not indicate pure UO_2 melting and temperatures in excess of 3120 K. Such regions contained considerable Zr cladding and Inconel grid constituents, which strongly imply that melt interactions reduced the fuel before liquefaction, lowering the melting point considerably.

2. Incipient fuel melting (2900 to 3120 K, depending upon exact composition) was confirmed in one sample, where the critical feature permitting this identification was a densification zone free of detectable impurities and very low in porosity from fabrication sintering.

3. Oxidized U-rich melts in the lower bundle region generally slumped as metallic (partially oxidized) liquids, that attacked UO_2 and ZrO_2 by reduction. Formation of discrete Ni-rich inclusions in most of these melts indicated that oxidation occurred before solidification was completely achieved. The higher concentrations of uranium than zirconium confirm melt temperatures of at least 2673 K.

4. Oxidized melts in the upper bundle were not completely oxidized as liquids. Ni did segregate into a second metallurgical phase, but no discrete ingots formed. Liquid-state oxidation was terminated by cooling that presumably followed reactor scram. Melt oxidation was apparently completed in the solid state by steam flow through cooling-induced shrinkage pores and cracks.

5. Steam flow oxidized pellet peripheries and U-bearing melts into hyperstoichiometric uranium oxides, at least at isolated positions within the upper bundle region. The oxidation must have occurred after rapid zircaloy oxidation, and the associated hydrogen production, was terminated. Because of the small SAS data base, no conclusions could be made on the frequency and extent of fuel oxidation during SFD-ST. However, this phenomenon may be responsible for unusual fuel microstructures (porosity, grain texture, phase distributions, and microcrack networks) widely encountered over the upper two-thirds of the bundle.

6. No hyperstoichiometric uranium oxides were measured within lower bundle regions, where melt solidification typically restricted steam access. Steam flow during the cooldown phase of SFD-ST was routed around the solidified melts or through a few coolant channels at these elevations, apparently precluding any enhanced uranium oxidation.

7. A high degree of compositional uniformity was measured within the metallic melt regions at the 0.145-m elevation (STM-4 cross section). Most of these unoxidized melts were evidently formed by the same mechanism and may be characterized by poor wetting properties and high initial superheating. The relatively high Inconel concentrations suggest that formation occurred at, or near, one of the upper two spacer grids. These metallic melts formed and slumped after the lower oxidized melts, and are probably related to a temporary flow reduction. However, metallic melt formation almost certainly occurred before coolant flow was reestablished. The strong neutron attenuation of this material, as observed in the neutron tomographs, cannot be explained by the low uranium and Ni concentrations and must be due to absorption of the hydrogen present during the period of the steam flow reduction.

8. Few (if any) indications of quench-shattered fuel were detected anywhere within the test bundle. Early reflood coolant was evidently transformed into steam by the large solidified melt region near the bundle base, so thermal shock to the embrittled upper bundle regions was minimized. However, during the reflood, a temporary overpressure beneath the solidified melt resulted in a diagonal fracture along the melt base and a pronounced upward movement of most of the bundle. Some mechanical damage to embrittled regions apparently occurred on impact with the fixed fallback barrier (see Section 4.10 of main text).

Several additional trends and tendencies also emerged during the examinations and are summarized below. However, these inferences are relatively uncertain and could be substantially revised as a result of a more comprehensive sampling.

1. Thermocouple constituents (W,Re,etc.) were not detected in most samples, so no indications were found of broad radial and azimuthal intermixing of molten bundle materials. Where such elements were detected, their influence appears to have been confined to formation of exotic precipitate structures during cooldown.

2. Significant equiaxed growth of fuel grains was encountered in many samples where melts contacted fuel. Where grain growth was observed, final grain sizes generally ranged widely in size at a given position. Consequently, grain growth correlations could not readily be applied to produce accurate estimates of times at elevated temperatures. This problem may be due to influences of elemental impurities and to strong temperature gradients across melt-fuel boundaries.

3. All internal melts (melts between fuel and cladding) contained measurably significant amounts of Inconel constituents. No indications of direct fuel-cladding interactions were discovered as they were obscured by later melt reaction. These findings suggest that reactions at spacer grid elevations may have been very important to propagating melt formation and fuel liquefaction.

4. Wide variations in UO_2 pellet penetration were encountered among metallic melt ingredients. Zr was commonly the most aggressive in attacking fuel, but Fe (in particular) occasionally displayed markedly reactive behavior. These variations were probably influenced by oxygen concentrations and melt temperatures, and may eventually provide useful benchmarks. However, these observations are somewhat inconsistent with thermodynamic considerations and may point toward important kinetic implications in modelling melt-fuel interactions.

5. In certain cases, melts appear to have been relocating downward while reacting with fuel, oxidized cladding, etc. Thus, the melt that eventually solidified at a given position may have been different in composition, temperature, viscosity, wetting, and other key dynamic parameters, from the melt responsible for the end-state damage to adjacent fuel pellets.

6. Formation, slumping, and solidification of the lower oxidized melts seemingly occurred at different times between coolant channels and over a range of temperatures and oxygen concentrations. Consequently, it is difficult to generalize melt behavior at a specific elevation. This observation is probably related to substantial differences in local peak temperatures and pellet liquefaction at upper elevations. Detailed modelling efforts would require tracing melt behavior along individual coolant channels over many bundle cross sections. Digital processing of tomographic data and/or axially oriented sectioning might be required to support such endeavors.

7. FALLBACK BARRIER

The fallback barrier was the first region through which the fuel bundle effluent passed. The effluent consisted of steam, hydrogen, and fission products. The fallback barrier was generally cooler than the fuel region itself and it was possible that the steam and fission products could have condensed. The temperature within the fallback barrier was measured by two Type C thermocouples, located at the 1.11- and 1.19-m elevations. The individual measurements are discussed in Section 4.6 of the main text. The average temperature throughout the transient is shown in Figure E-74.

Although fallback barrier component temperatures were not measured directly, several techniques were available to provide estimations. Certain material microstructure changes occur in the Zr-O system at known temperatures under equilibrium conditions. Metallographic examination therefore determined if any of these reactions took place and provided upper temperature limits.

Another method is based on oxidation kinetic correlations developed mainly by Cathcart.[E-9] This method uses the metallographically determined reaction layer thicknesses as the primary input. The correlations are expressed as a parabolic rate law of the form

$$d(CHI)/dt = \frac{1}{(CHI)} \frac{K_p^2}{2}$$

where (CHI) is the measured kinetic parameter (the thickness of the respective reaction layers in μm), t is the reaction time in seconds at the isothermal test temperature, and K_p is a proportionality constant that is equal to the square root of the diffusivity of oxygen in zircaloy, thus

$$K_p^2 = D = D^* \exp(Q/RT)$$

where D* is the diffusion coefficient (mm^2/s), Q is the activation energy or heat of activation of the reaction process (cal/mol), R is the universal gas constant (1.987 cal/mol-K), and T is the isothermal temperature (K). The correlations for the reaction layer thicknesses are usually expressed in integrated form, and is written as

$$(CHI) = K_p t^{1/2} .$$

Cathcart presented the correlations as

ZrO_2	$(CHI)_O/t^{1/2}$	=	1500.67 exp(-9031/T)
Alpha-Zr(O)	$(CHI)_O/t^{1/2}$	=	12340.99 exp(-123113/T)
ZrO_2 + Alpha-Zr(O)	$(CHI)_O/t^{1/2}$	=	8260.75 exp(-10493/T) .

Isothermal calculations applied to the entire transient are of limited use. However, if the time-temperature response is known, and it is assumed to be made up of small isothermal steps, then the final reaction layer thickness can be approximated by the sum of the individual steps. A program based on COBILD (subcode of MATPRO)[E-10] was used to estimate the peak temperatures reached by the materials. The time-temperature response of the steam probes at the 1.11- and 1.19 m elevations were input along with the measured reaction layer thicknesses. The COBILD predictions and the results of isothermal calculations are presented in Figure E-75.

8. RECOMMENDATIONS

Two observations were central to the determination of the timing of fuel behavior events, and associated fission product releases, during SFD-ST. The extraordinarily high neutron attenuation of the bulk metallic melt has been attributed to absorbed hydrogen, because of the relatively small amounts of other highly attenuating elements. Nevertheless, because the hydrogen content is critical to establishing formation of this material during the flow reduction near scram, direct measurement of the hydrogen concentration by vacuum fusion (or equivalent technique) is highly desirable. The releases of fission products after 211 min have largely been ascribed to enhanced fuel oxidation, but this deduction rests upon SAS data from only three samples in the upper three-fourths of the bundle. Moreover, these samples did not include interior pellet regions and the measurements were made without the benefit of U_3O_8 and UO_3 standards. Accordingly, unambiguous confirmation of fuel oxidation by x-ray diffraction measurements of fuel phases is recommended on representative pellets from widely separated portions of the SFD-ST bundle.

Manual planimetry for quantifying area fractions of discrete materials on cross-sectional macrophotographs and tomographs should be replaced by digital image processing, although significant development and benchmarking efforts would be required in both cases. After major algorithm improvements, high resolution tomographic composition mapping would be very valuable for generating axial profiles of UO_2, Zr-rich melts, U-rich liquefied fuel, hyperstoichiometric fuel, etc., whereas such distributions can now only be crudely estimated at best. This capability would also be helpful in selecting elevations for sectioning.

SEM/EDS and SAS are adequate for establishing occurrences of phenomena and for studying localized elemental interactions, but the data sets are cumbersome and not easily extrapolated over larger regions in quantitative fashion. Moreover, elemental spectroscopy samples are time-consuming to extract and analyze, and therefore statistically meaningful bundle coverage would be prohibitively expensive. Etched metallography provides greater coverage, but it is limited on chemical compositions. In addition it is still impractical to convert into accurate cross-sectional area fractions, and even more so into whole-bundle distributions. It is therefore necessary to investigate other techniques with potential for segregating phenomenologically different materials on a macroscopic basis, such as ultraviolet luminescence and infrared reflectance. With such information, metallography and composition sampling could be directed toward legitimately representative regions for maximum modeling benefit.

9. REFERENCES

E-1. B. A. Cook, P. A. Kalish, and D. M. Tow, *Posttest Examination of the Severe Fuel Damage Scoping Test Bundle Geometry*, to be issued.

E-2. P. Hofmann, *Metallographic Examination of the Severe Fuel Damage Scoping Test Fuel Rod Bundle Cross Sections*, to be issued.

E-3. B. Daniel, A. L. Nichols and J.A.H. Simpson, *The Liquefaction of Alloys Identified with Structural Material in a PWR Core: Zircaloy, Inconel-600 and 304 Stainless Steel*, AEEW-M2250, 1985.

E-4. D. W. Akers et al., *TMI-2 Core Debris Grab Samples-Examination and Analysis*, EG&G Internal Document, EG&G-TMI-6853, July 1985.

E-5. D. R. Olander, *Oxidation of UO_2 by High Pressure Steam*, LBL-20531, Department of Nuclear Engineering, Lawrence Berkeley Laboratory, Submitted for publication in November 1985.

E-6. The International Nickel Company, Inc., *Properties of Some Metals and Alloys (3rd Edition)*, November 1968.

E-7. K. Vinjamuri and D. J. Osetek, *Results of the Severe Fuel Damage Scoping Test Effluent System Sample Analyses*, to be issued.

E-8. B. J. Buescher et al., *Severe Fuel Damage Test Series SFD-Scoping Test Experiment Operating Specification*, EG&G Internal Document, EGG-TFBP-5912, July 1982.

E-9. J. V. Cathcart, *Quarterly Progress Report on the Zirconium Metal-Water Oxidation Kinetics Program Sponsored by the NRC Division of Reactor Safety Research for April-June 1978*, ORNL/NUREG/TM-41, August 1978.

E-10. D. L. Hagrman et al. *MATPRO-Version 11 (Revision 2) A Handbook of Materials Properties for Use in the Analysis of Light Water Reactor Fuel Rod Behavior*, NUREG/CR-0497, TREE-1280 Rev. 2, August 1981.

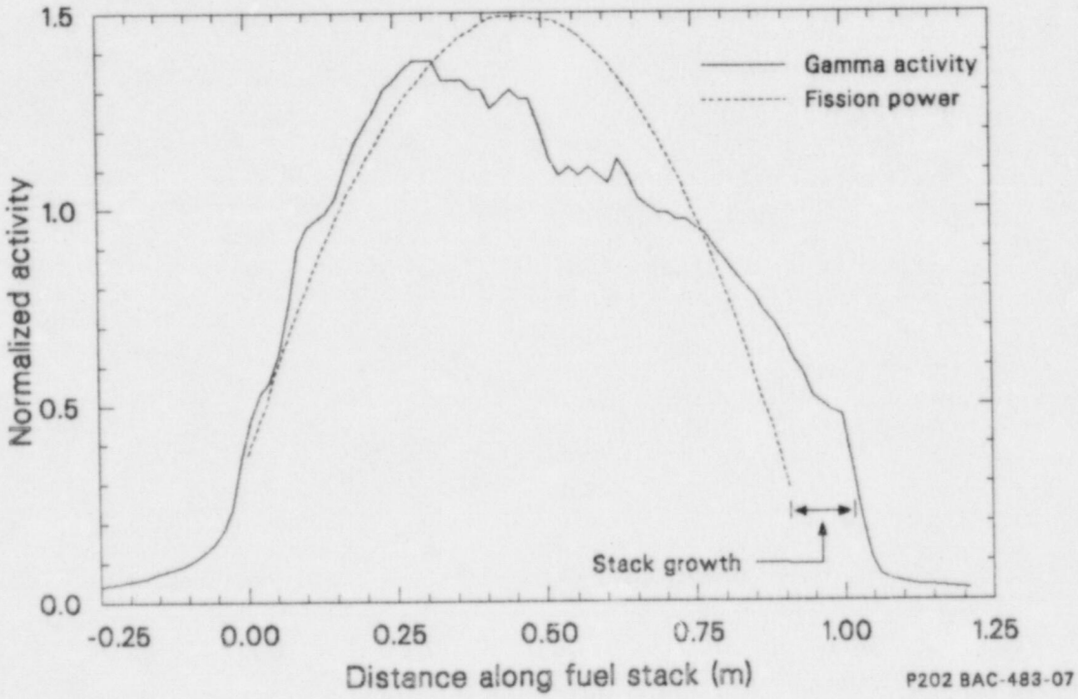

Figure E-1. Normalized axial gross gamma activity and bundle fission power.

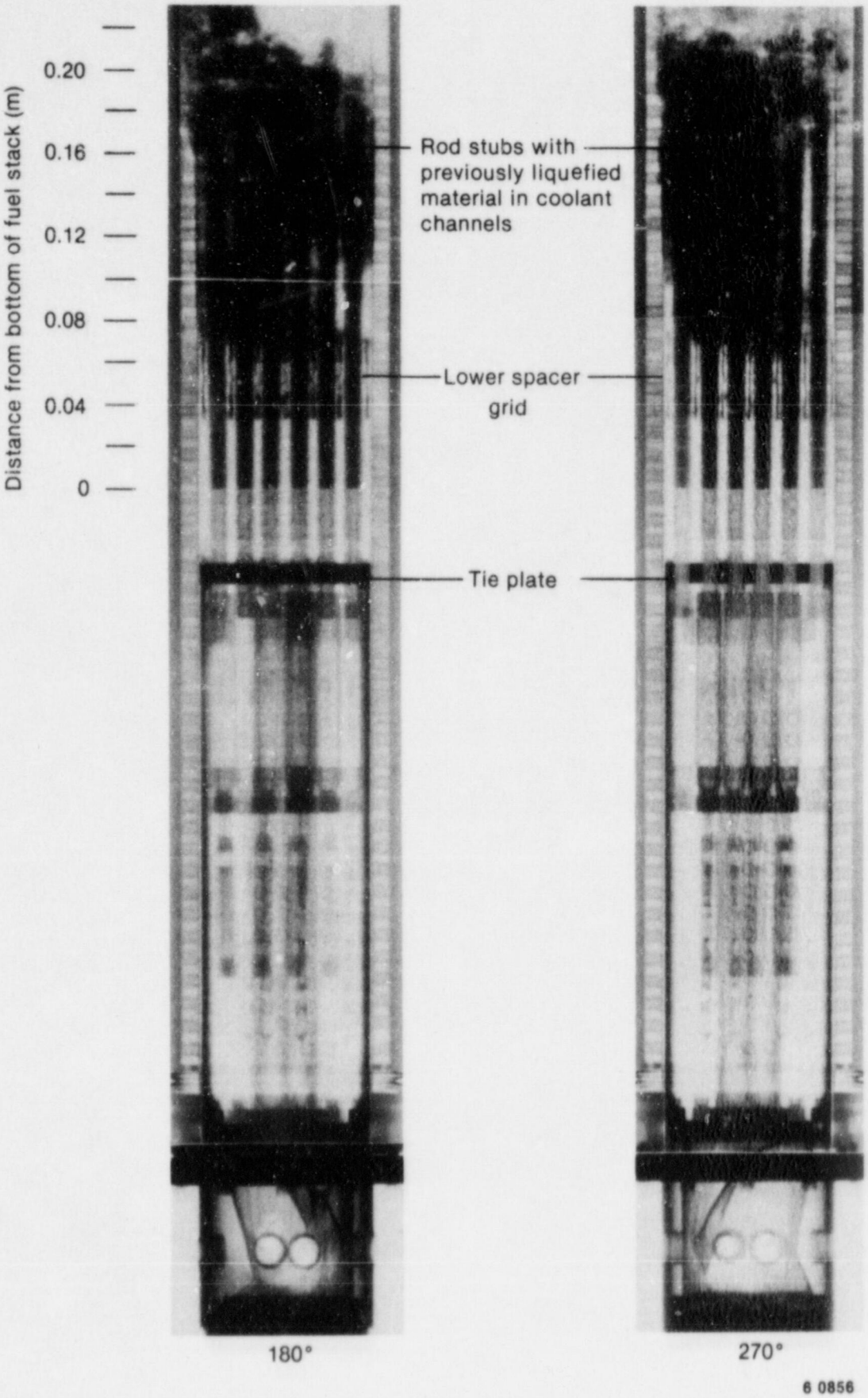

Figure E-2(a). Radiograph of the bottom portion of the SFD-ST fuel bundle.

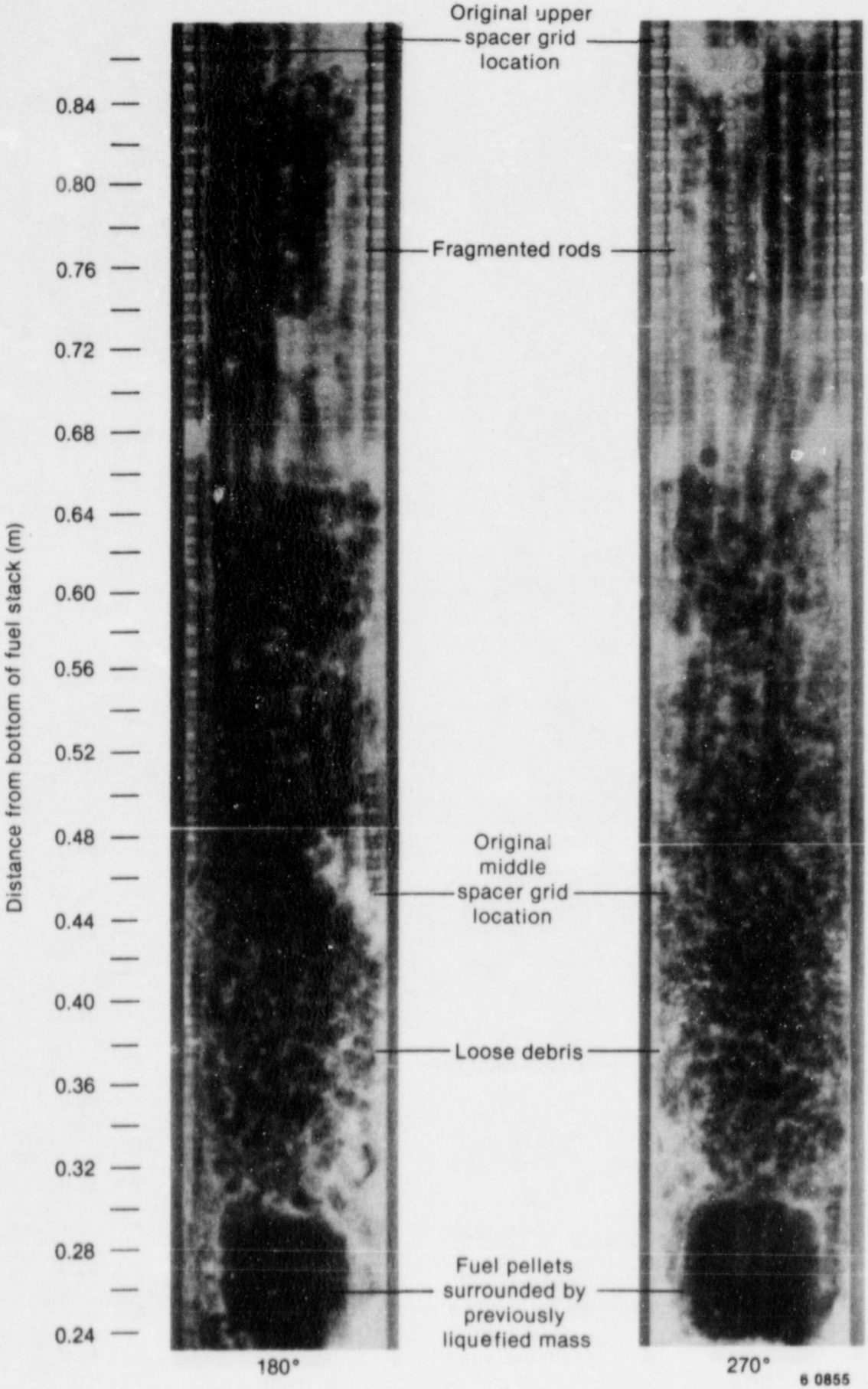

Figure E-2(b). Radiograph of the middle portion of the SFD-ST fuel bundle.

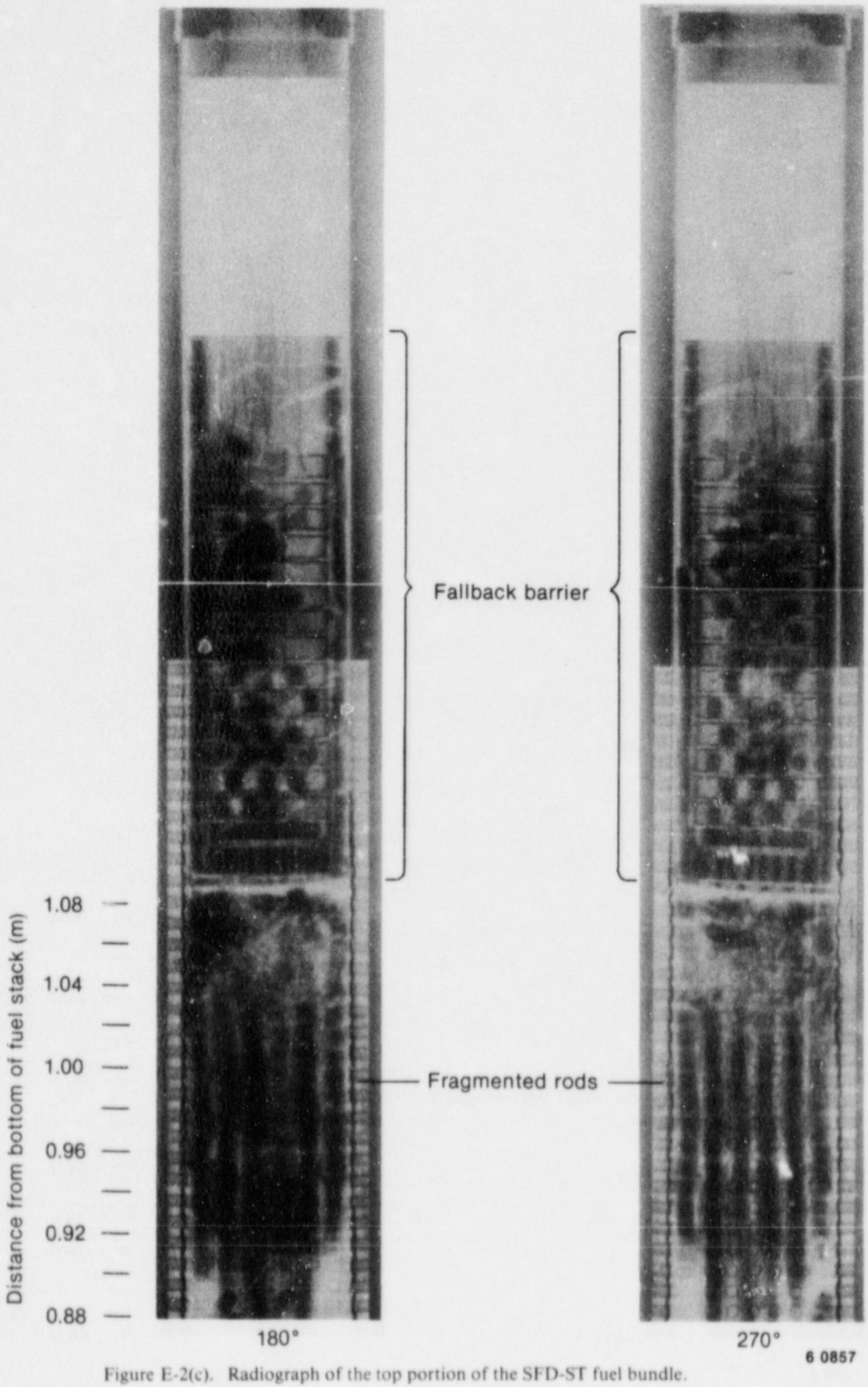

Figure E-2(c). Radiograph of the top portion of the SFD-ST fuel bundle.

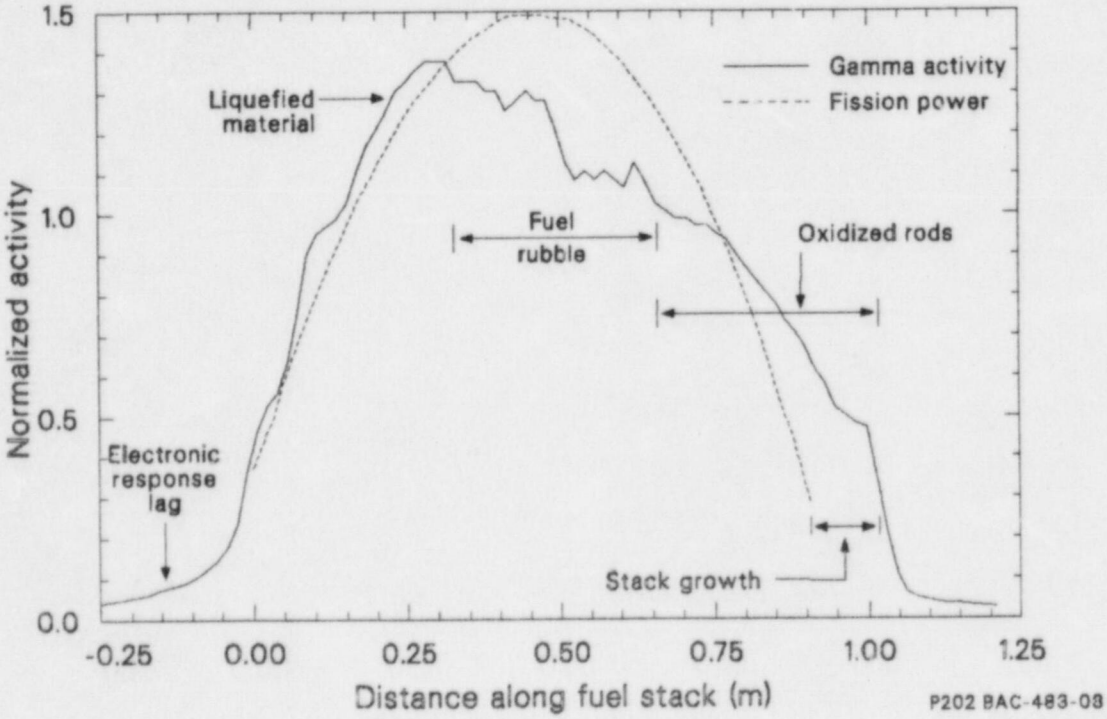

Figure E-3. Comparison of gross gamma scan and structures visible in neutron radiograph.

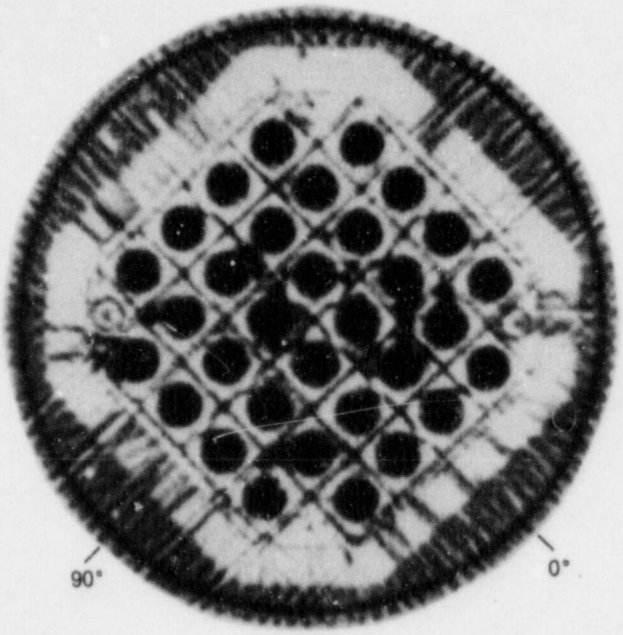

Figure E-4. Neutron tomography of SFD-ST bundle at the 0.0635-m elevation.

Figure E-5. Neutron tomography of SFD-ST bundle at the 0.1640-m elevation.

Figure E-6. Neutron tomography of SFD-ST bundle at the 0.2760-m elevation.

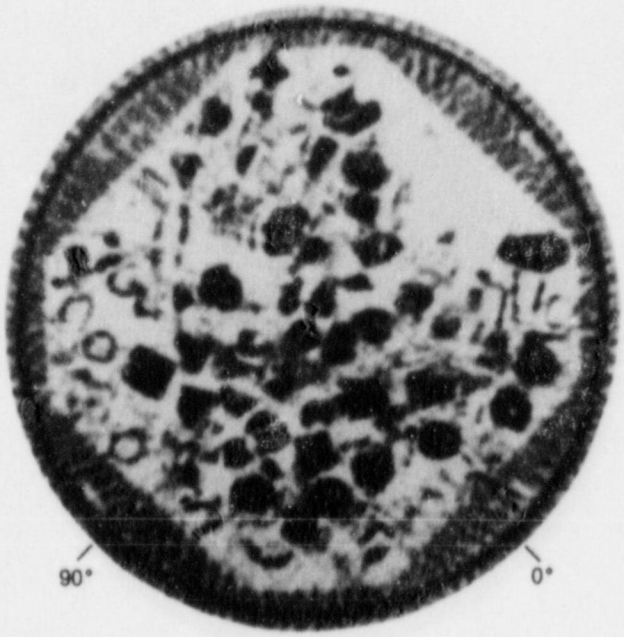

Figure E-7. Neutron tomography of SFD-ST bundle at the 0.4386-m elevation.

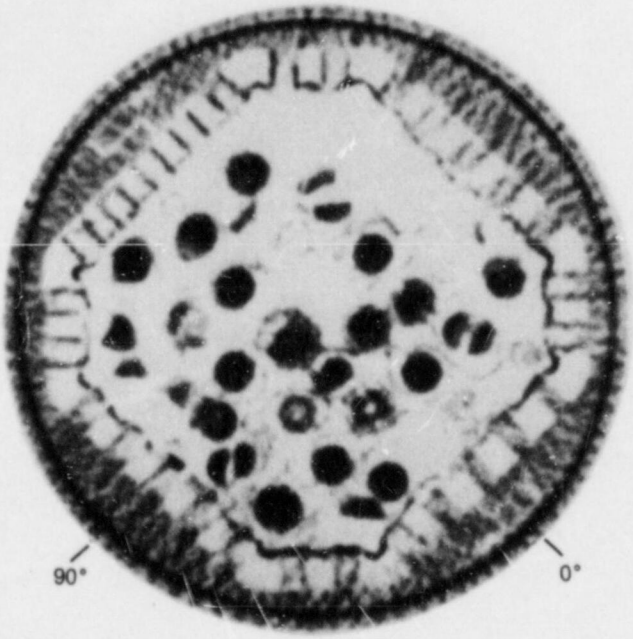

Figure E-8. Neutron tomography of SFD-ST bundle at the 0.7975-m elevation.

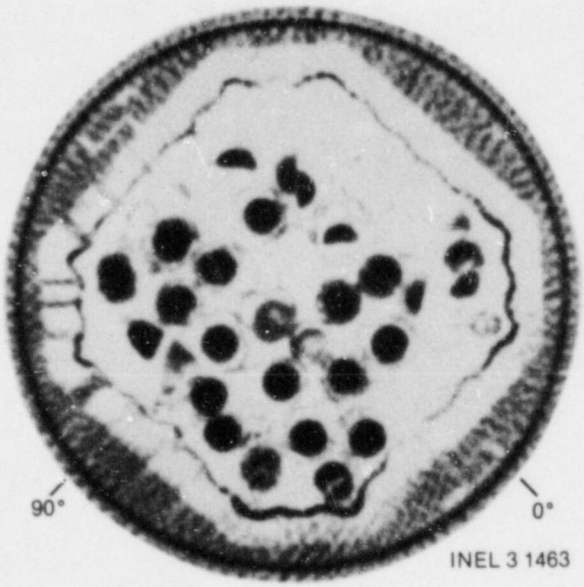

Figure E-9. Neutron tomography of SFD-ST bundle at the 0.8055-m elevation.

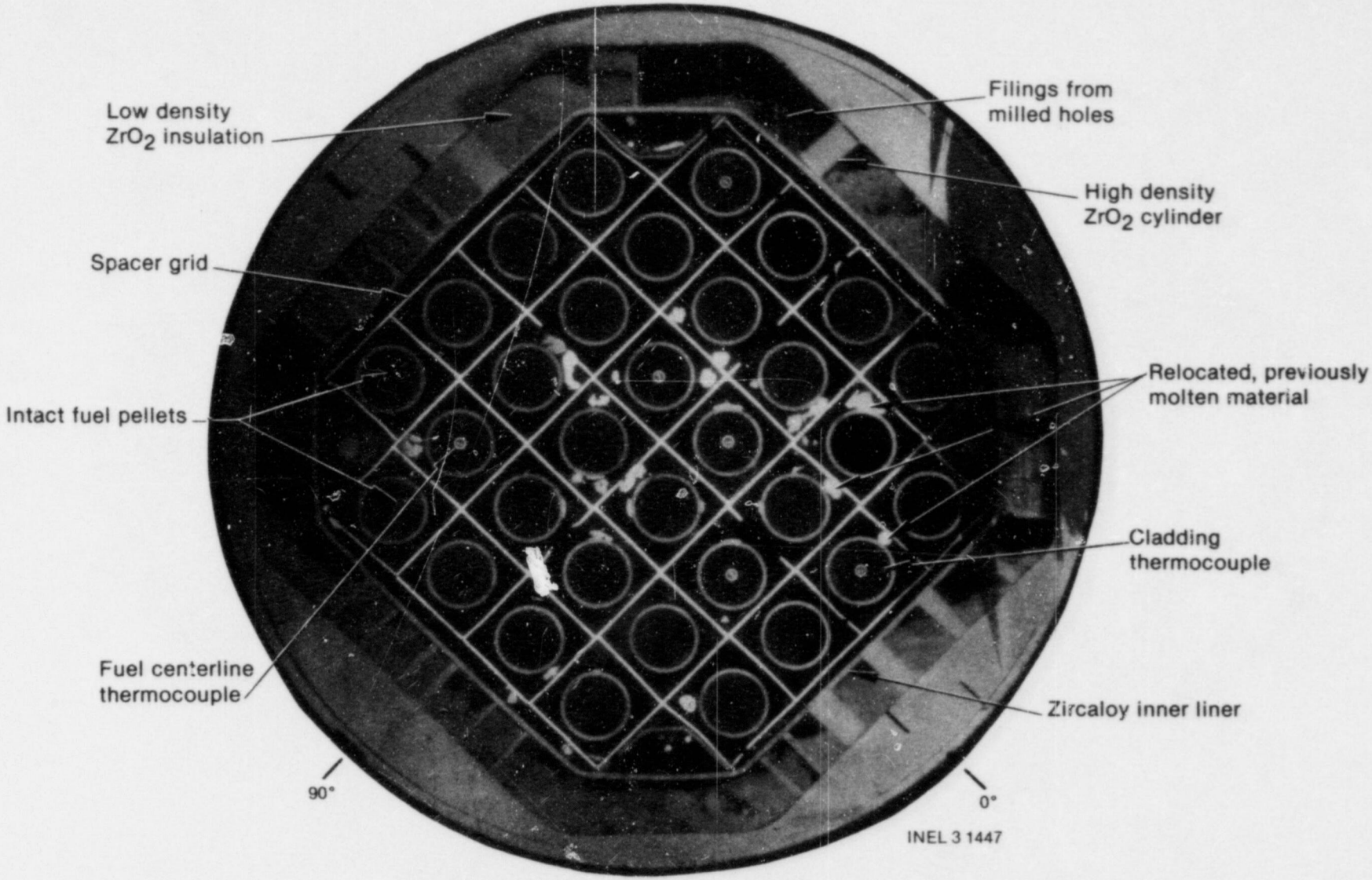

Figure E-10. Metallographic cross section of the SFD-ST bundle at the 0.055-m elevation.

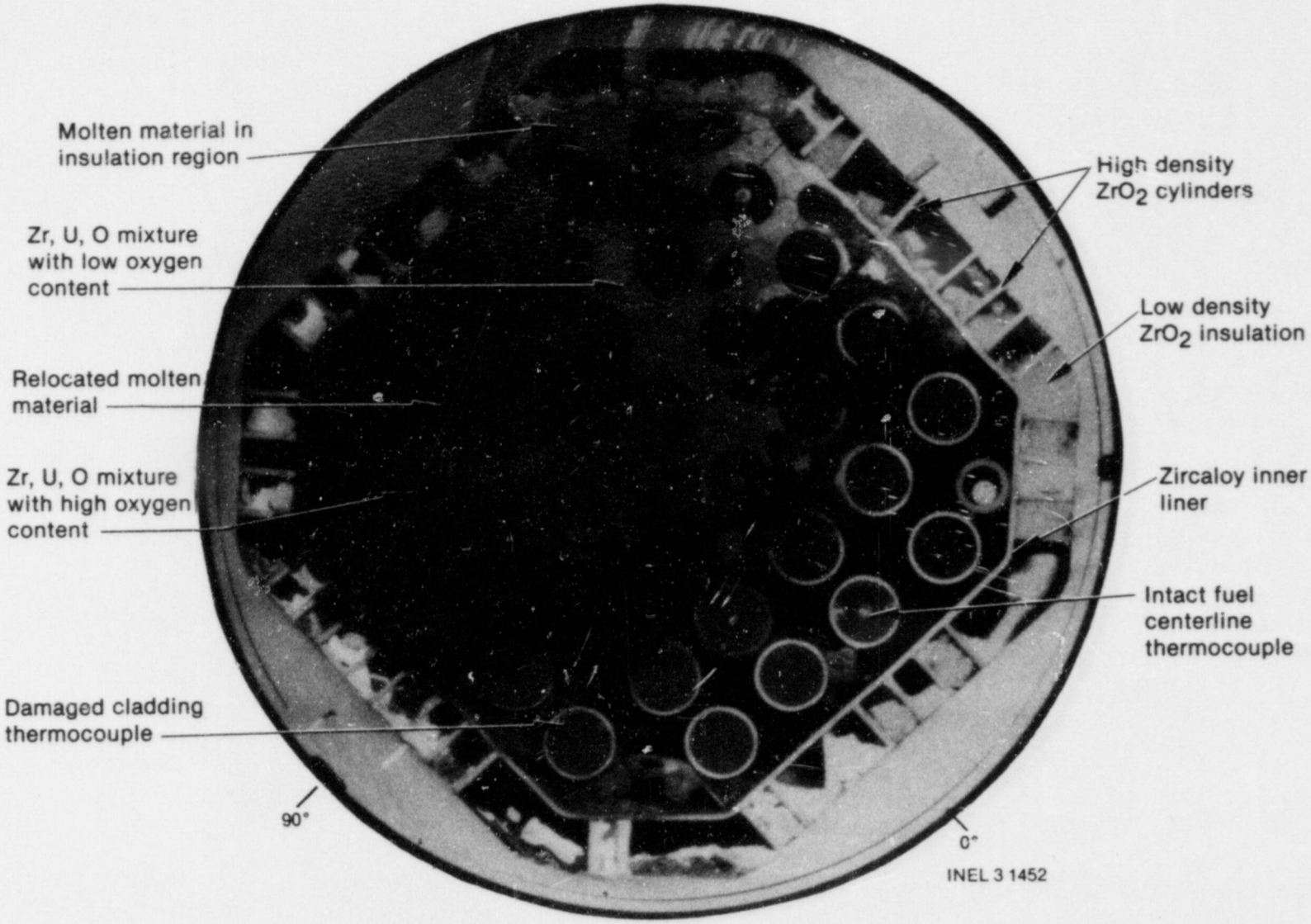

Figure E-11. Metallographic cross section of the SFD-ST bundle at the 0.145-m elevation.

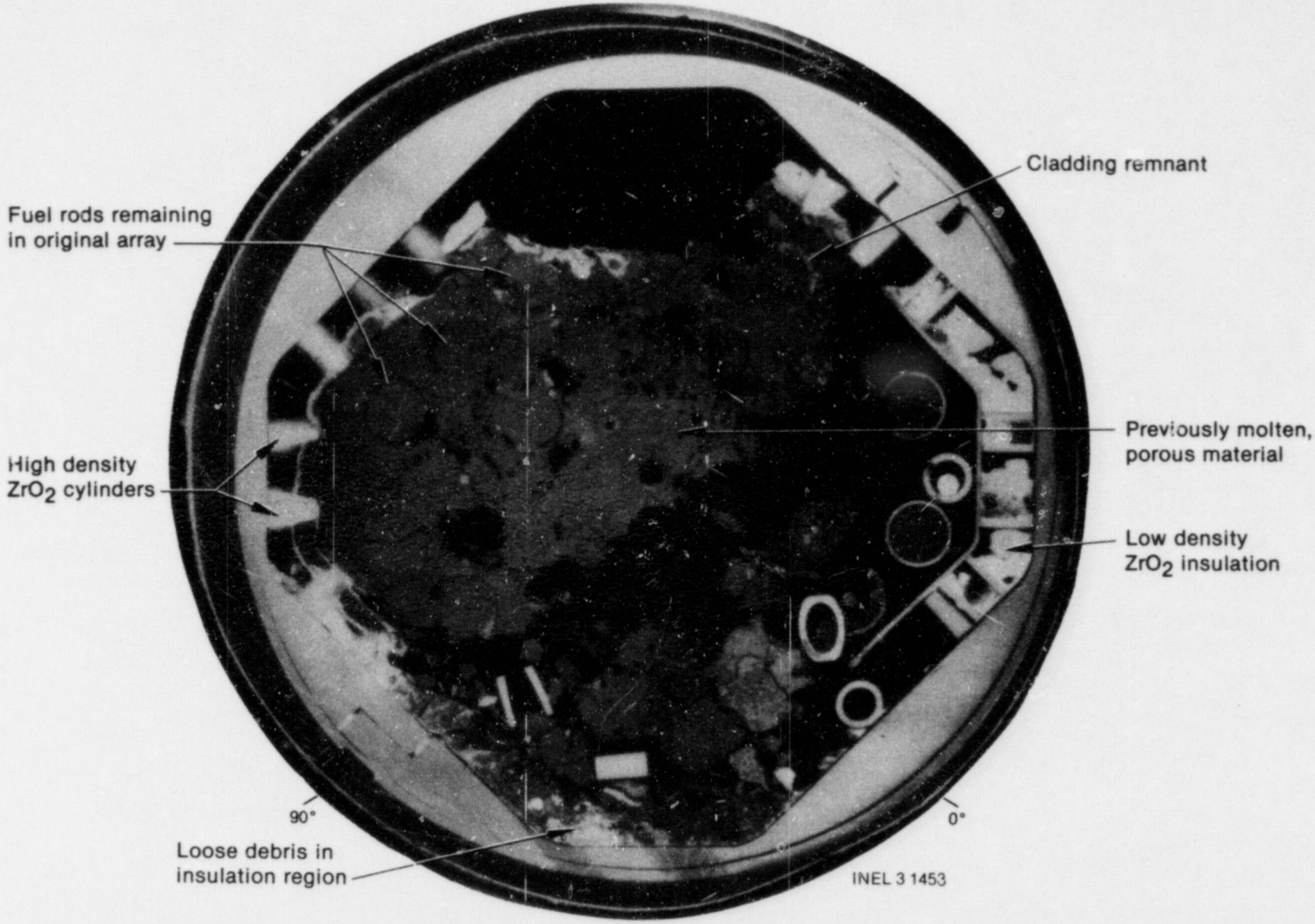

Figure E-12. Metallographic cross section of the SFD-ST bundle at the 0.170-m elevation.

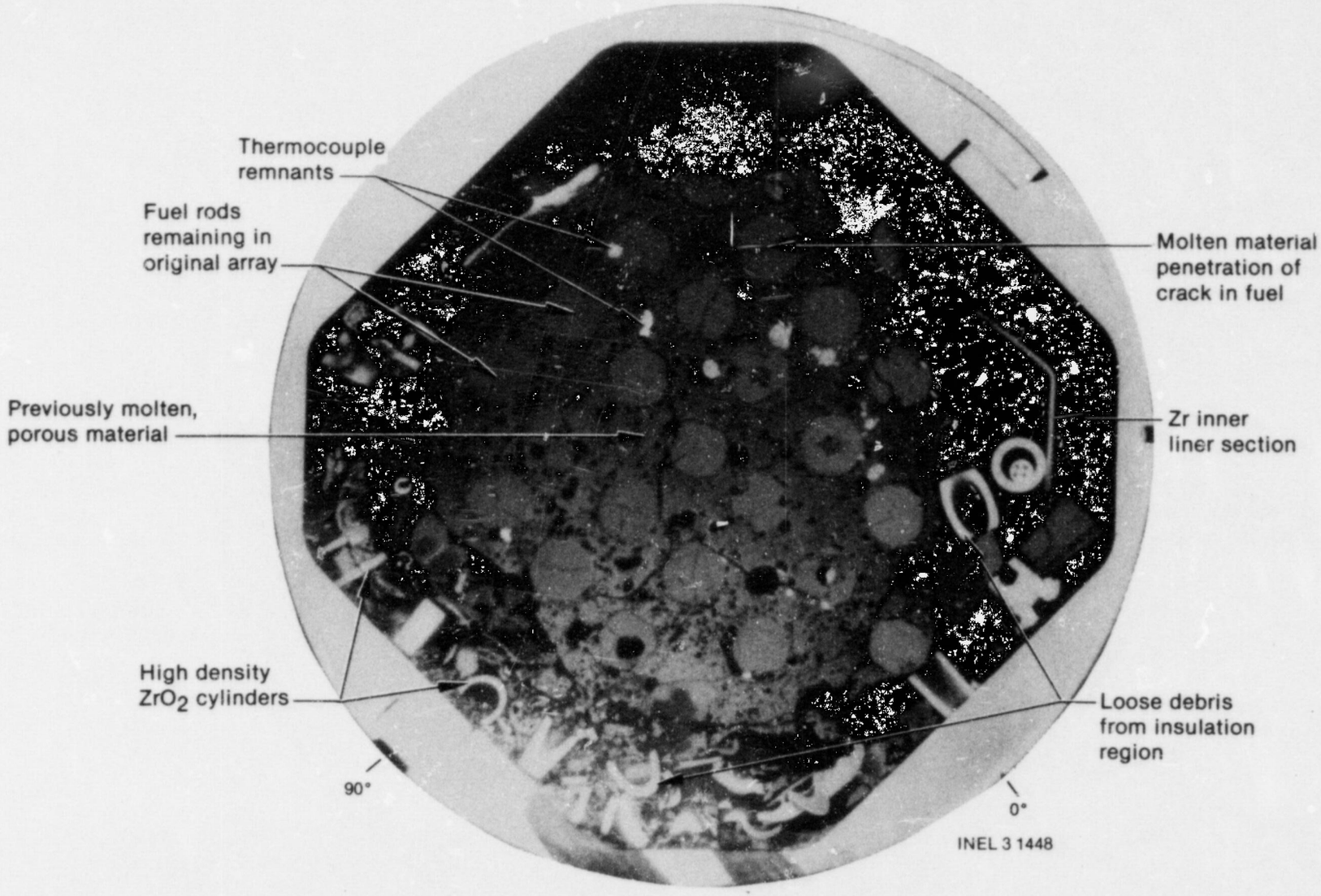

Figure E-13. Metallographic cross section of the SFD-ST bundle at the 0.245-m elevation.

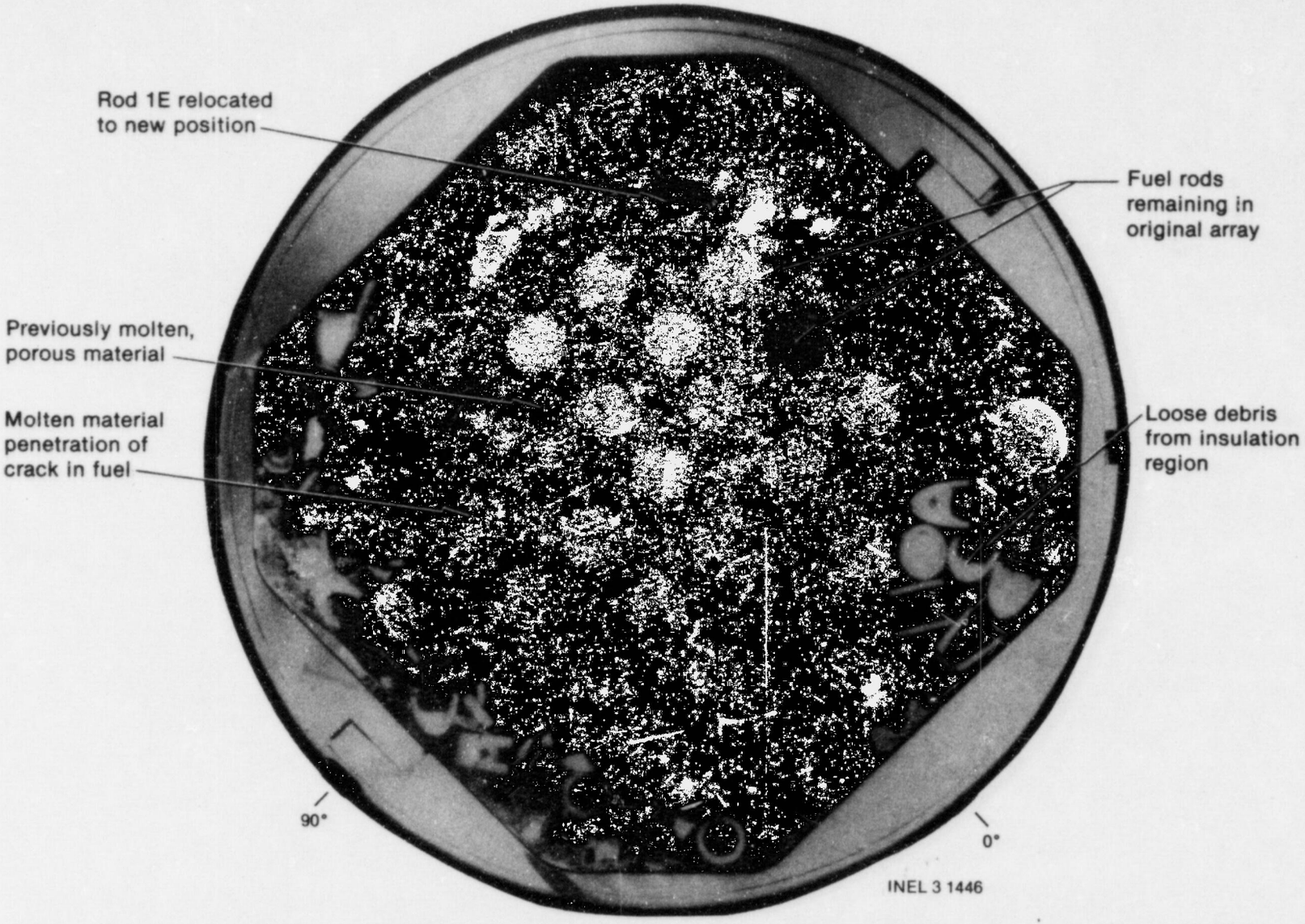

Figure E-14. Metallographic cross section of the SFD-ST bundle at the 0.270-m elevation.

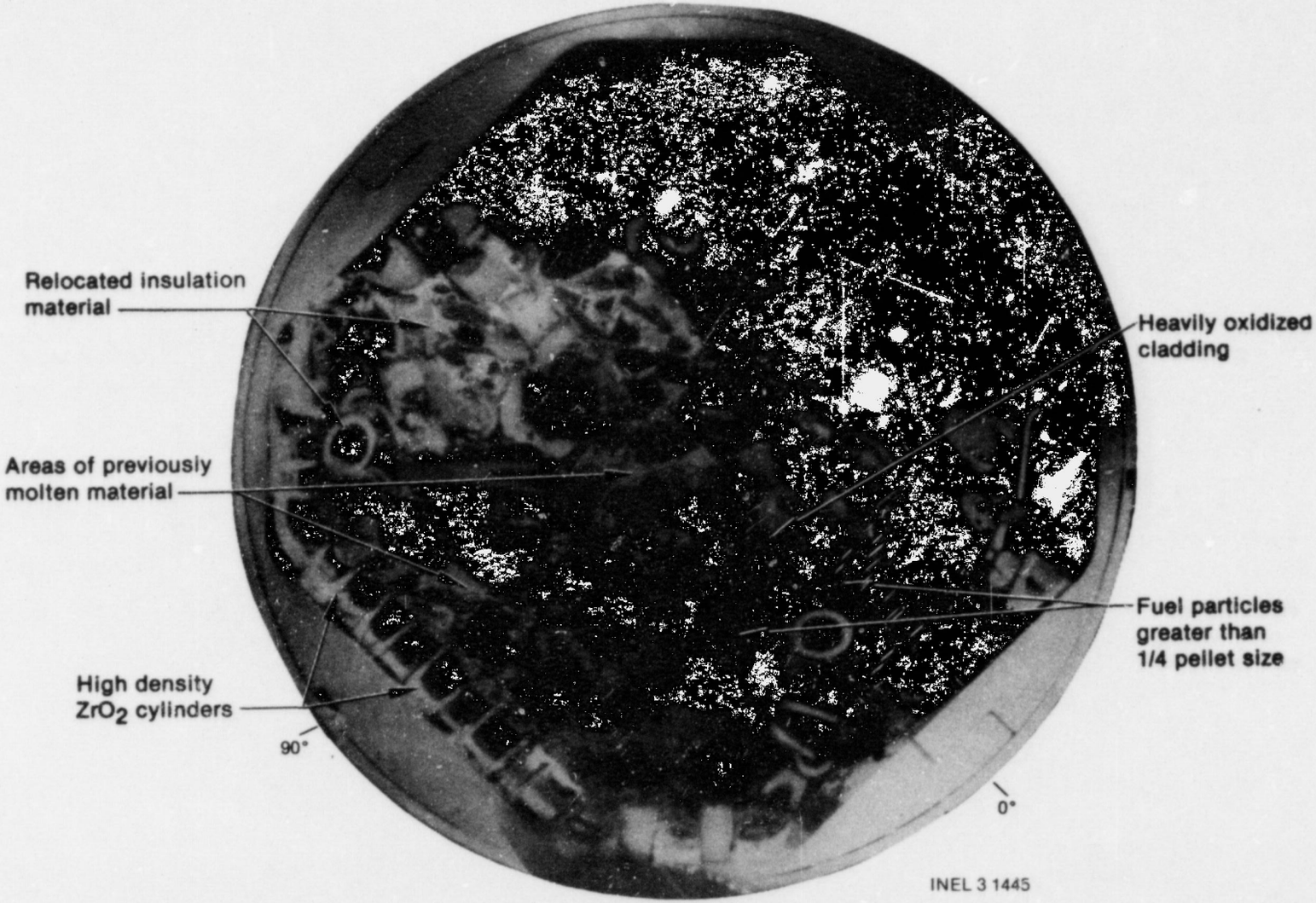

Figure E-15. Metallographic cross section of the SFD-ST bundle at the 0.395-m elevation.

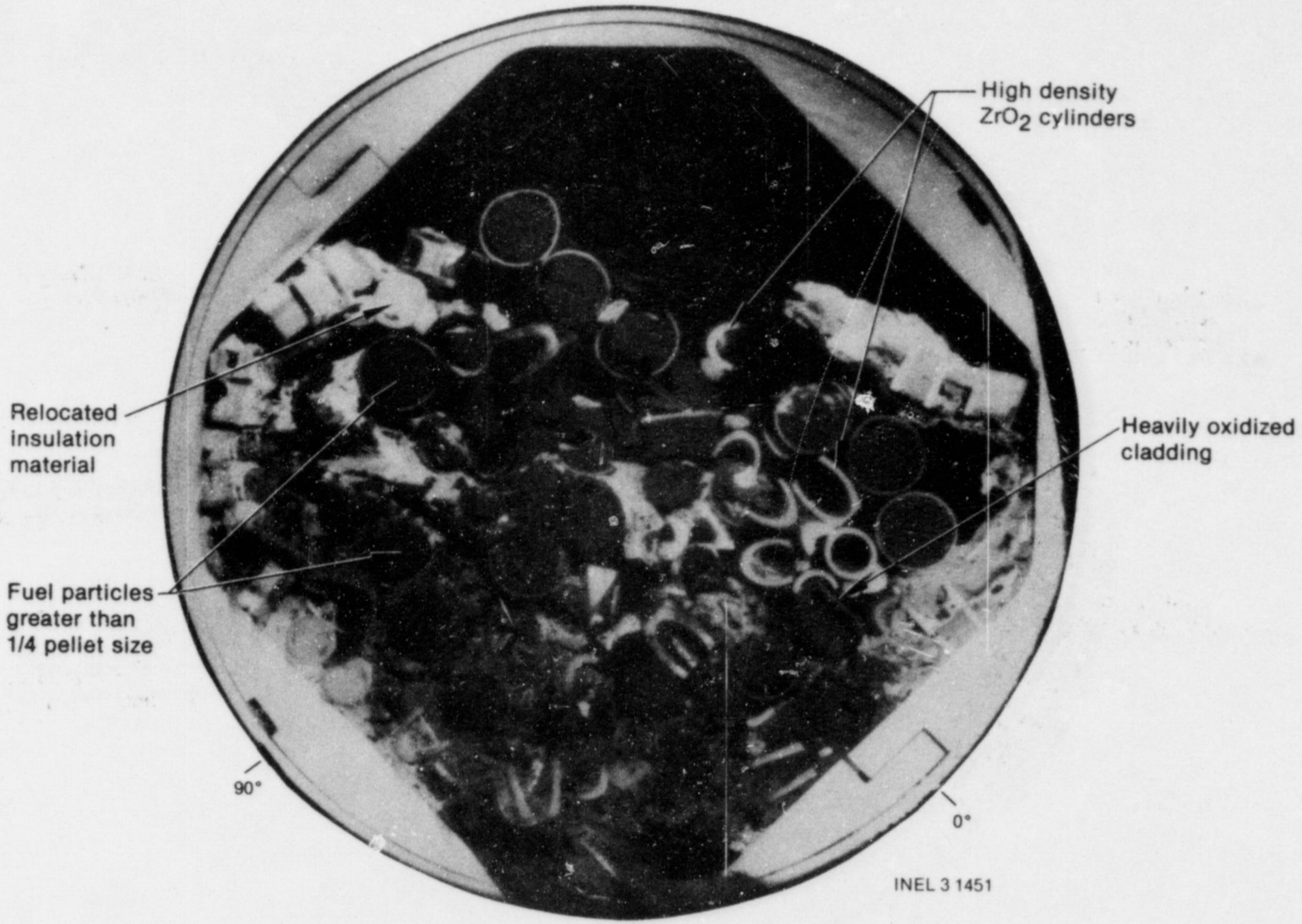

Figure E-16. Metallographic cross section of the SFD-ST bundle at the 0.495-m elevation.

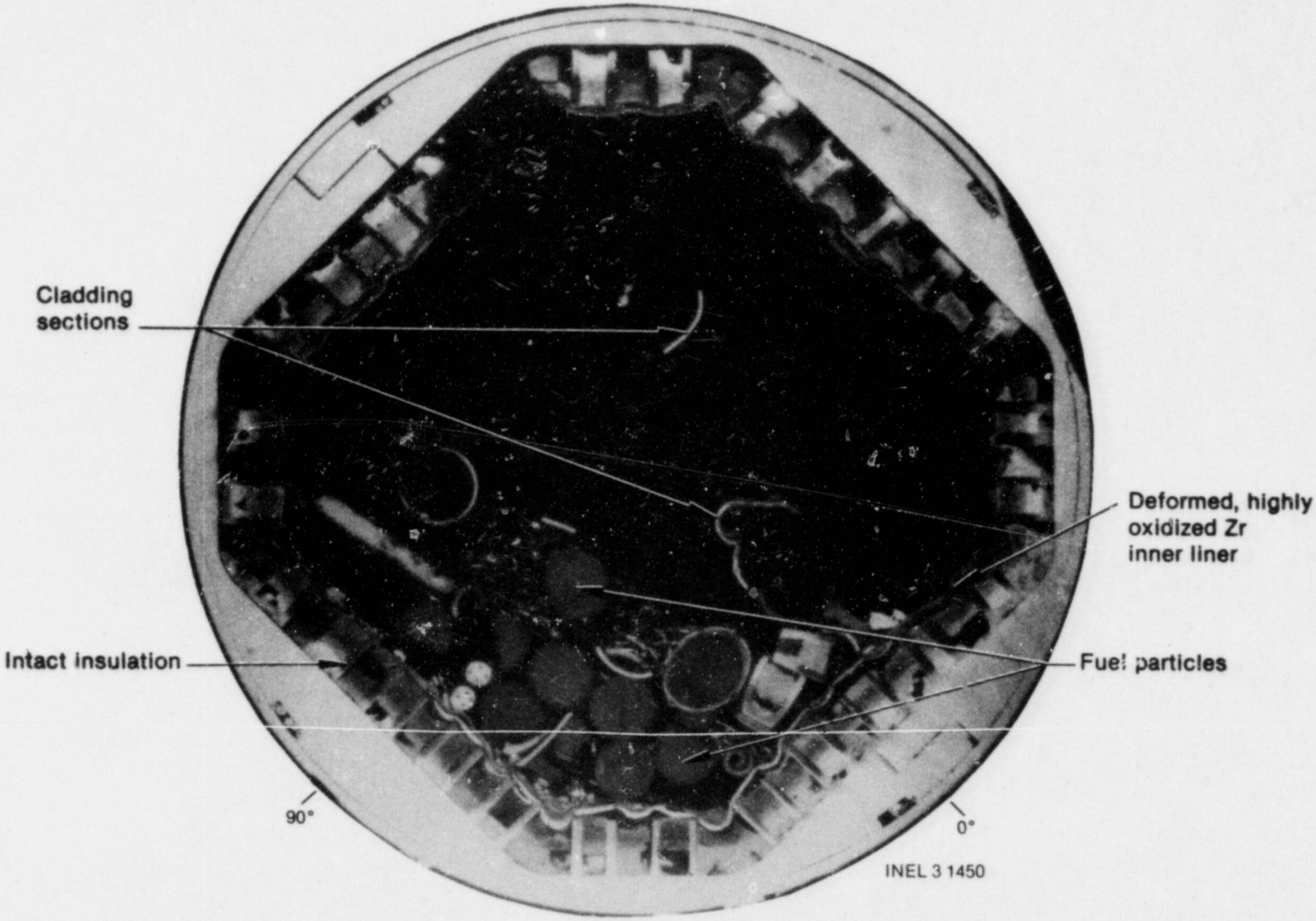

Figure E-17. Metallographic cross section of the SFD-ST bundle at the 0.825-m elevation.

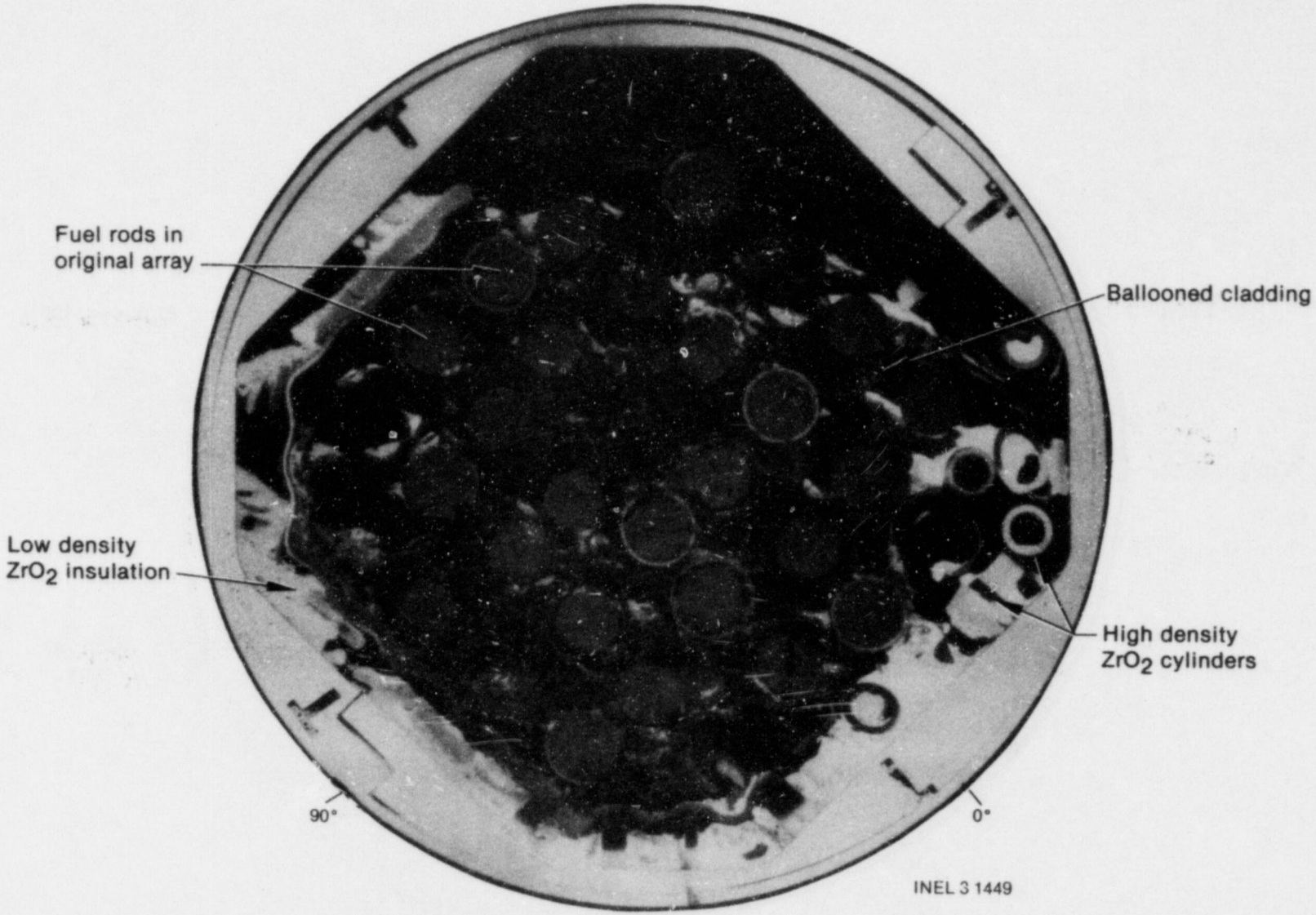

Figure E-18. Metallographic cross section of the SFD-ST bundle at the 0.915-m elevation.

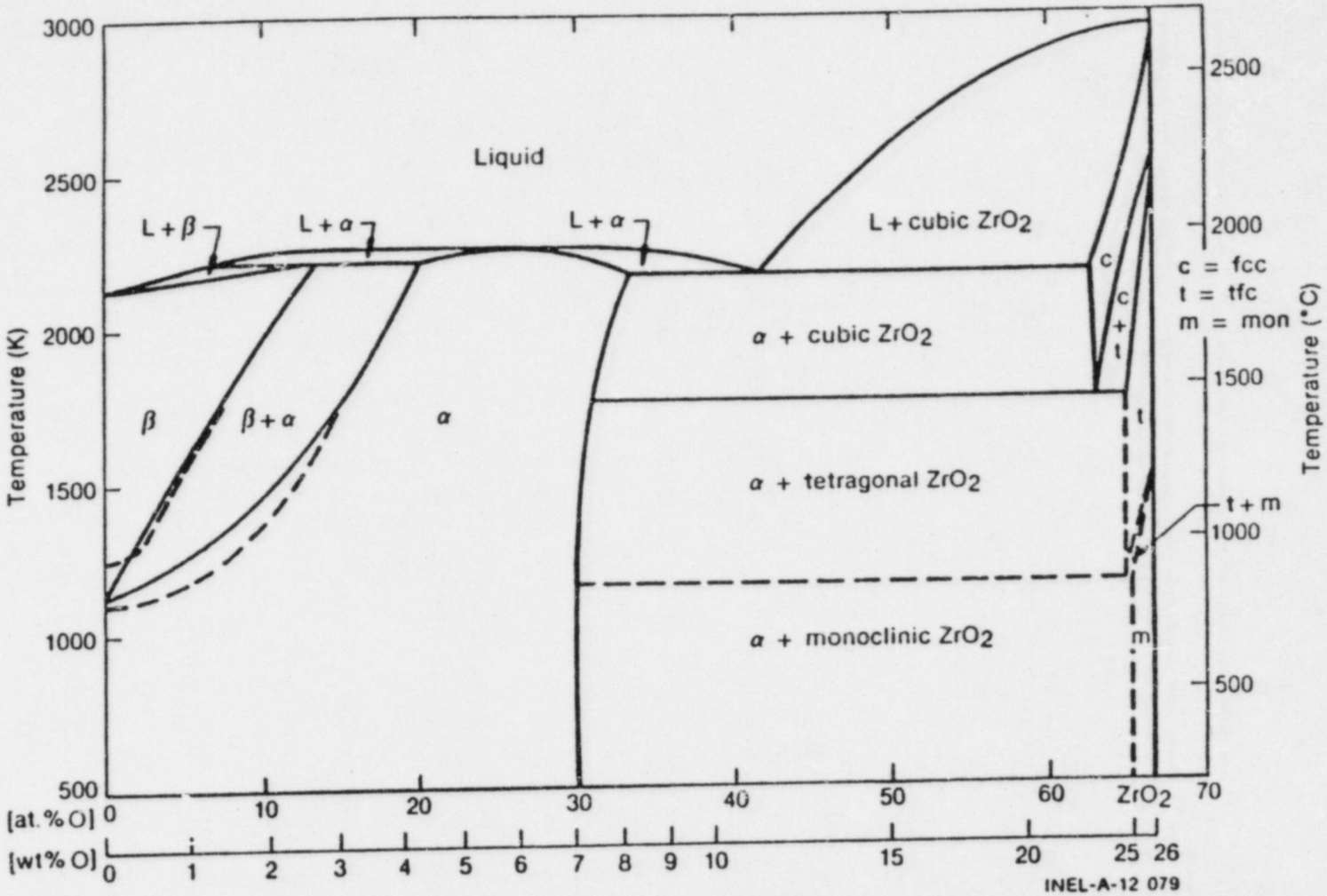

Figure E-19. Zirconium-oxygen equilibrium phase diagram.

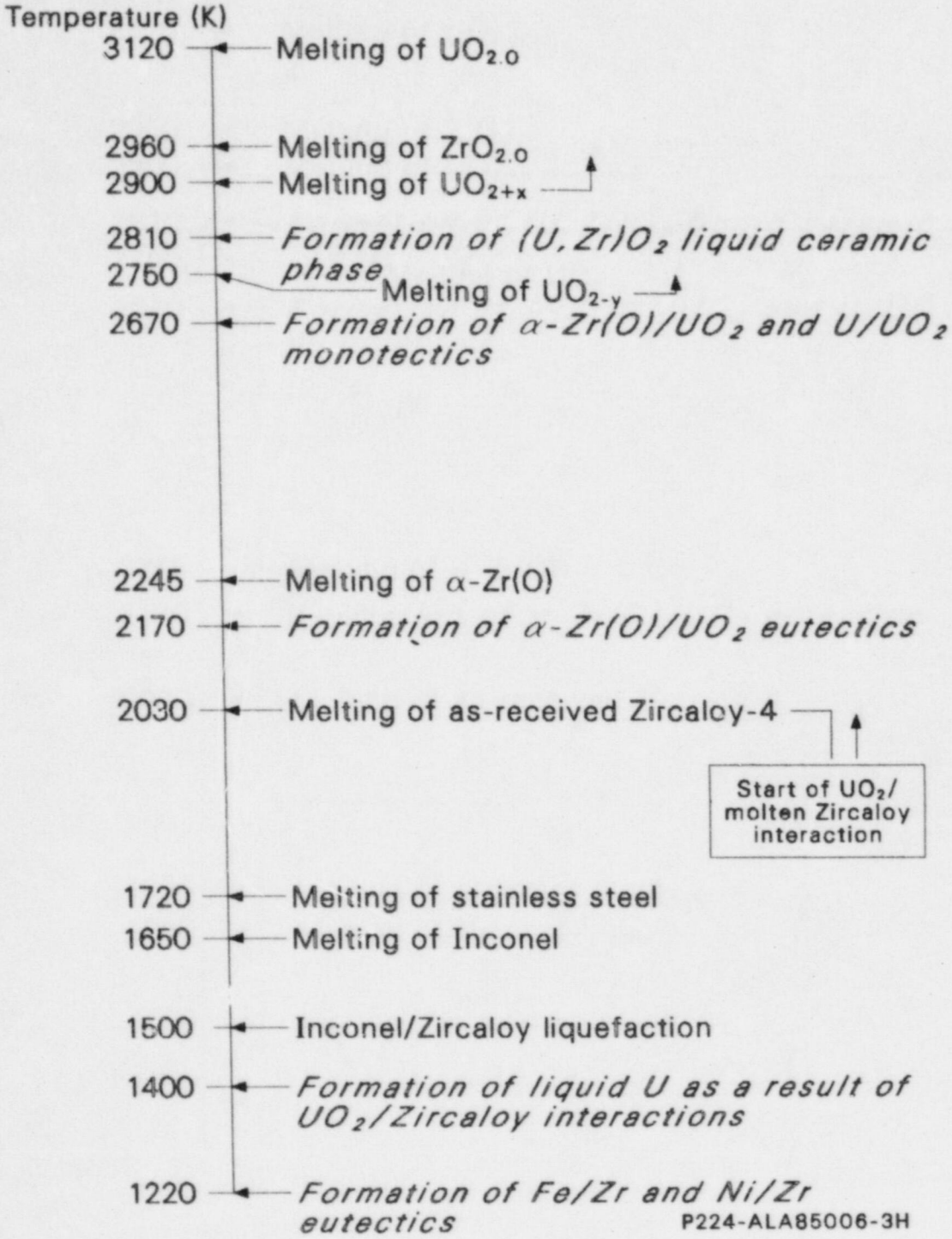

Figure E-20. Metallurgical temperature reference points.

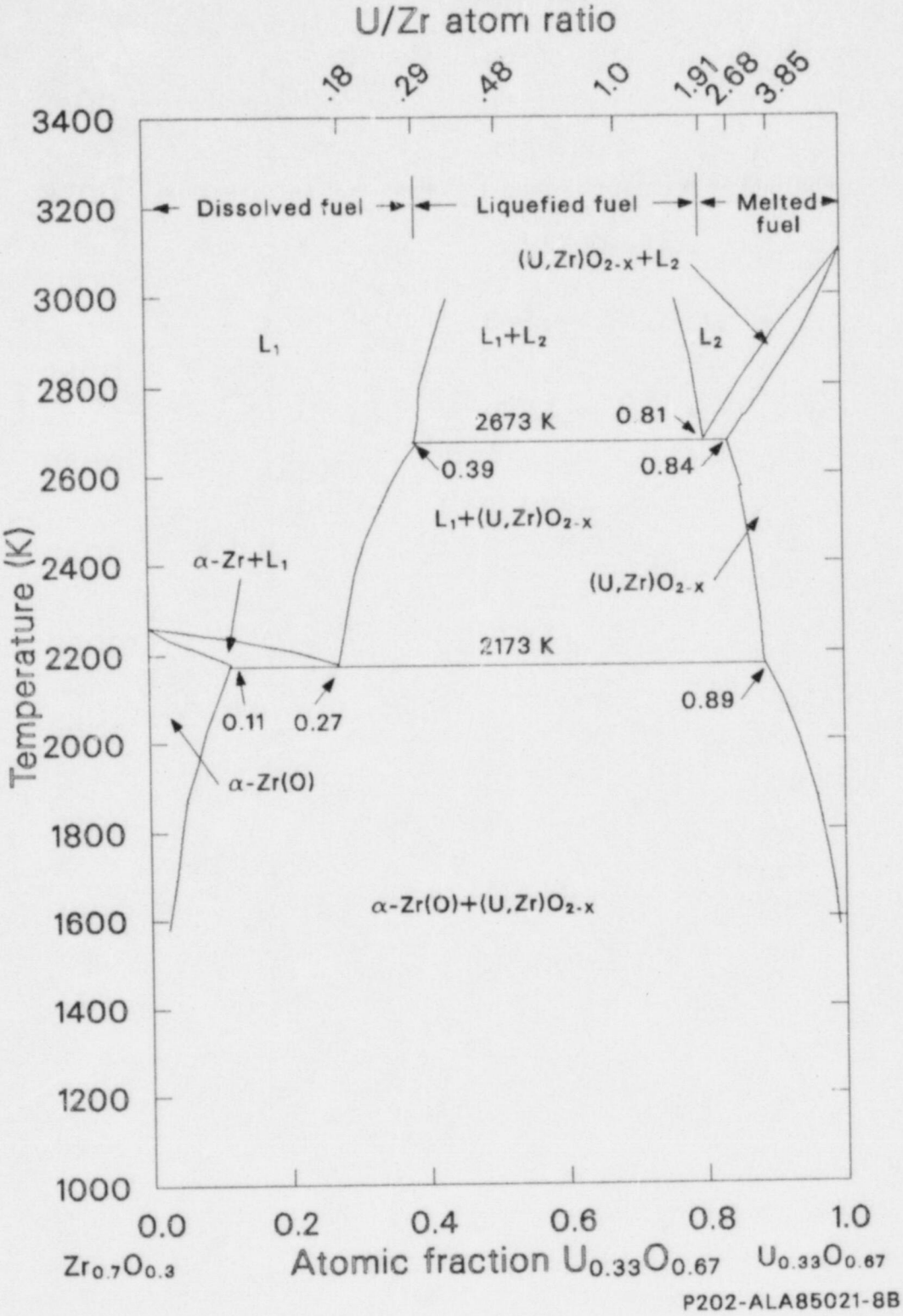

Figure E-21. Quasi-binary α-Zr(O)—UO_2 phase diagram.

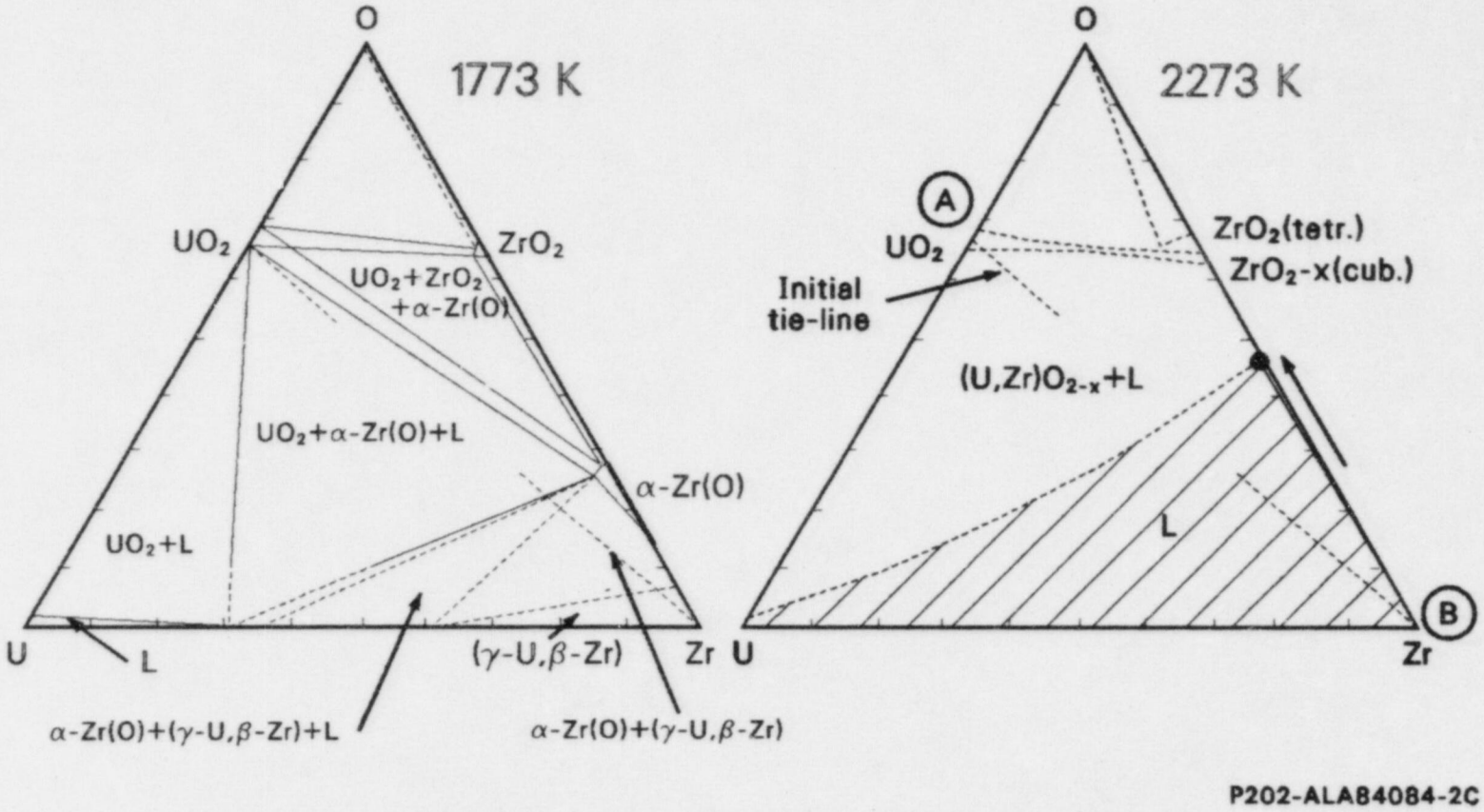

Figure E-22. U-Zr-O ternary phase diagrams for temperatures of 1773 K and 2273 K.

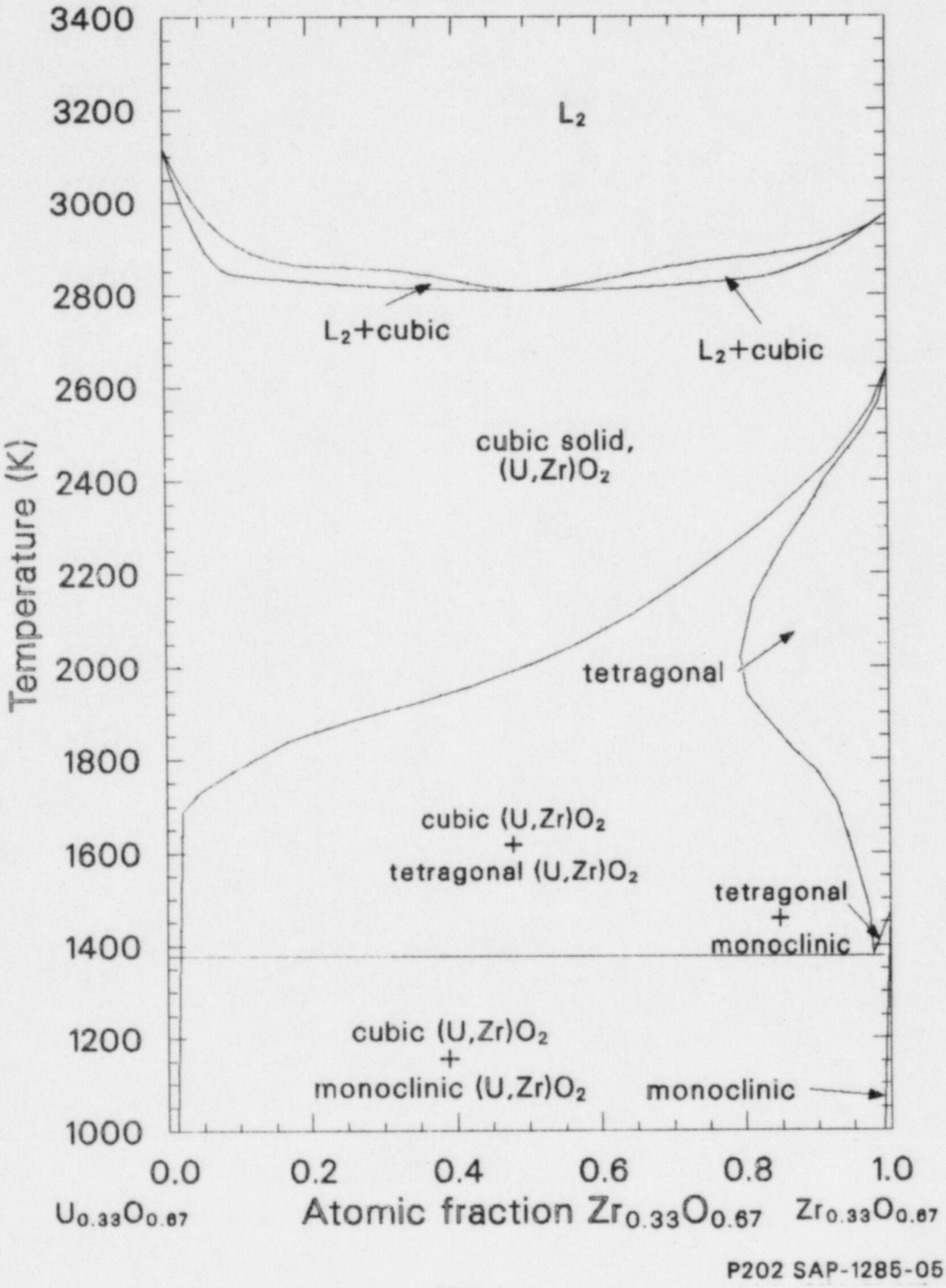

Figure E-23. UO_2-ZrO_2 binary phase diagram (solidus and liquidus curves represent preliminary data).

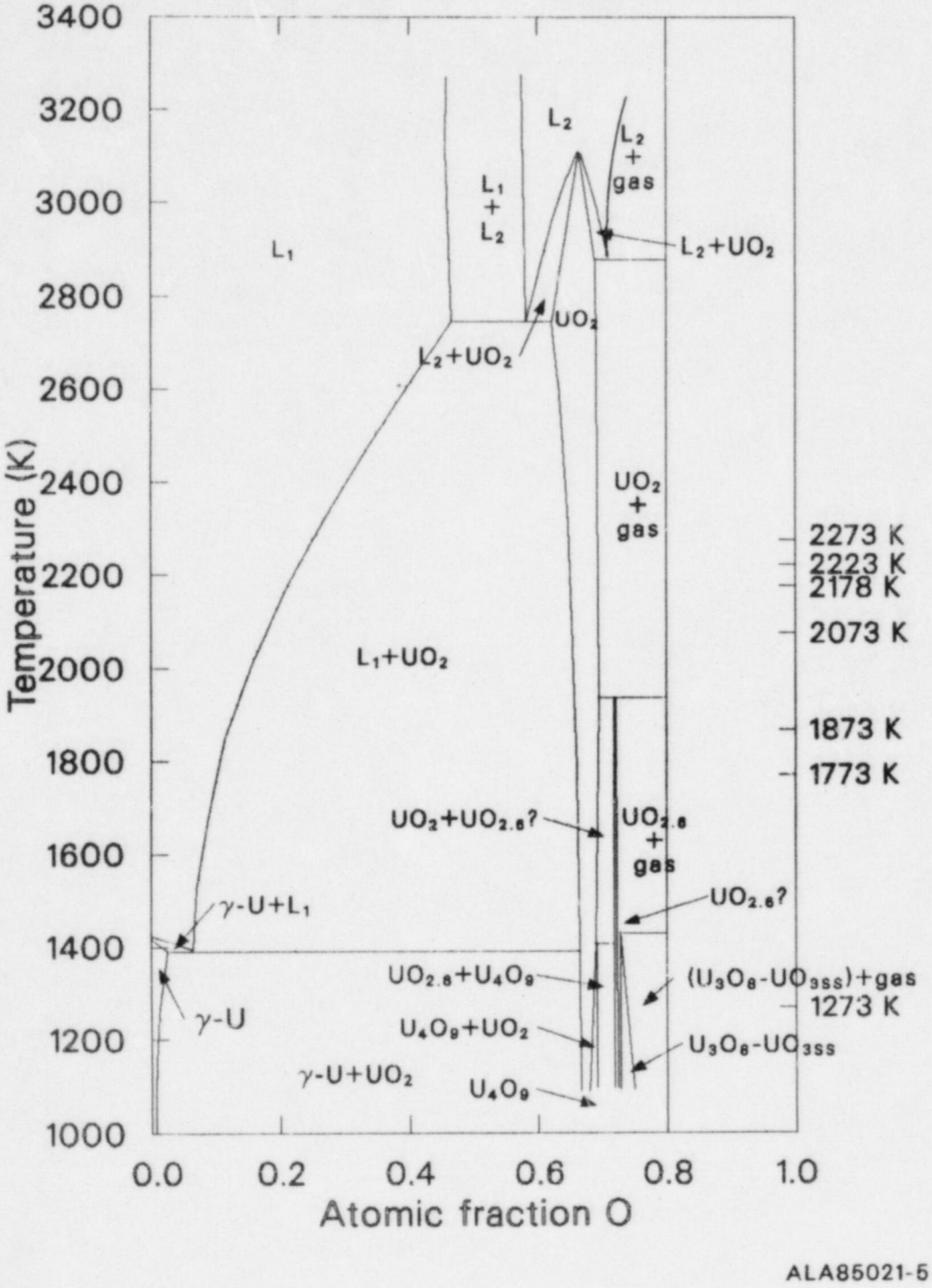

Figure E-24. Uranium-oxygen phase diagram.

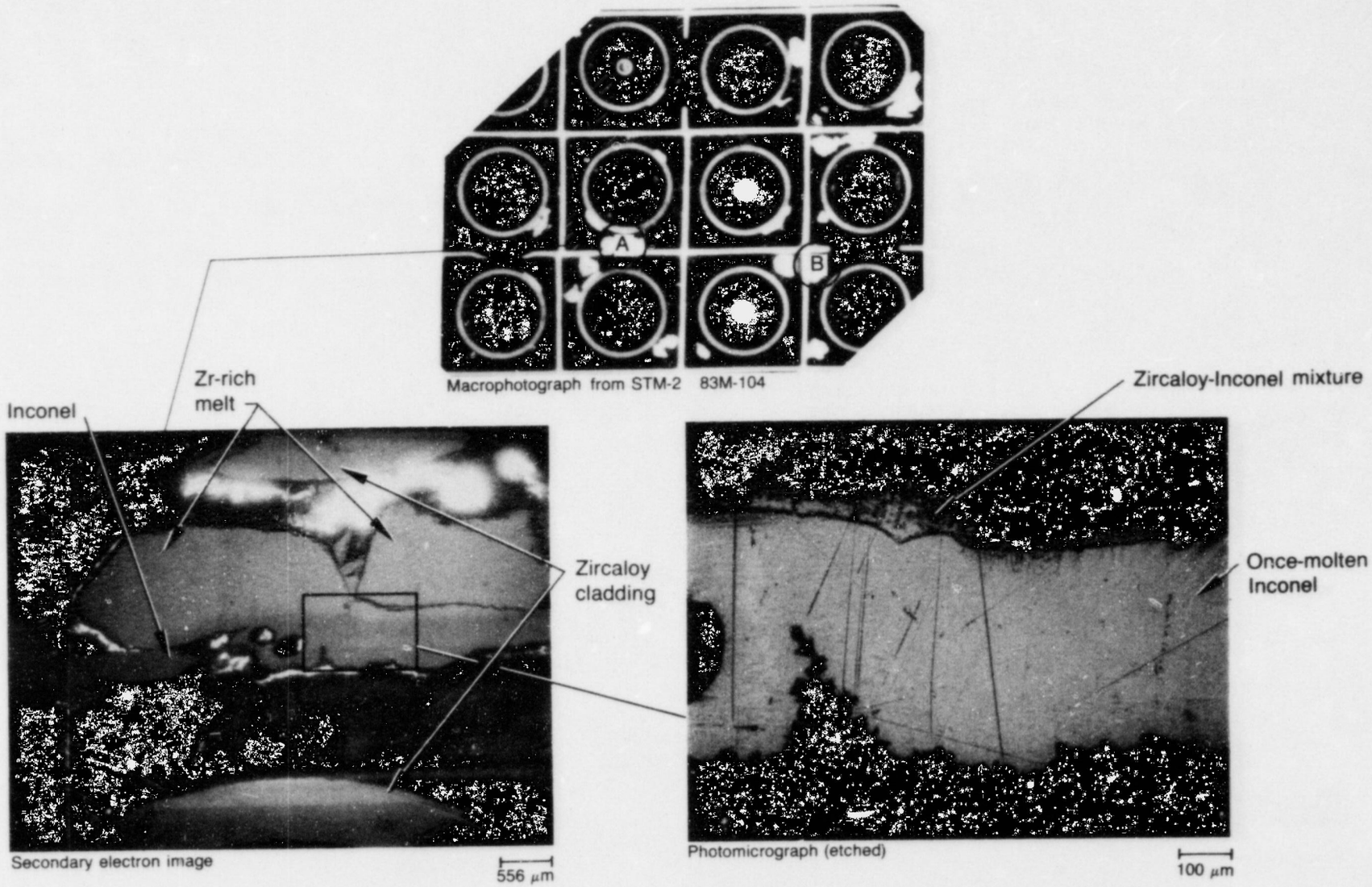

Figure E-25. Metallic melt attack of Inconel spacer grid in Sample 2A from cross section STM-2 (0.055 m).

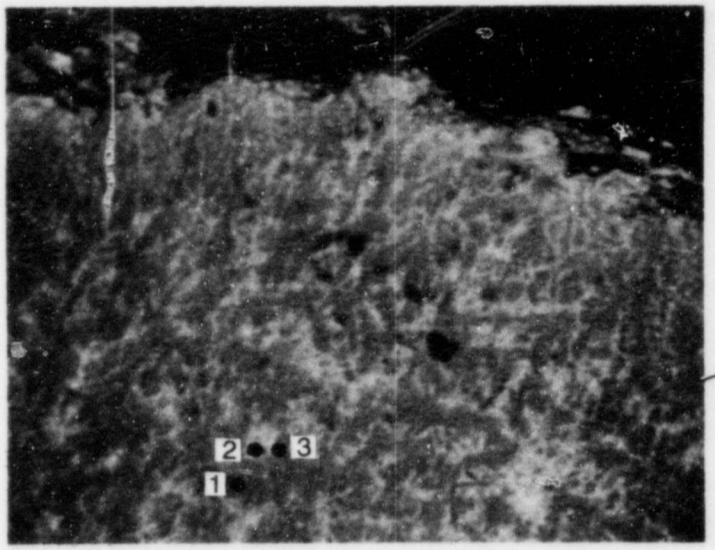

Backscattered electron image

17 μm

Change of brightness level

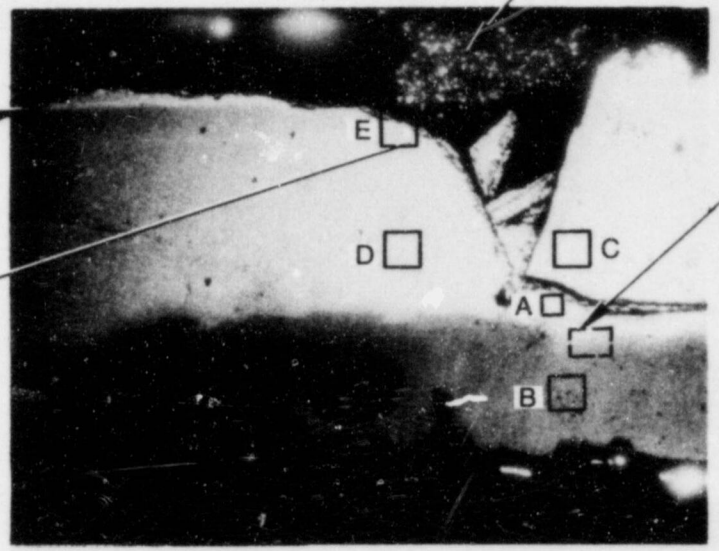

Backscattered electron image

278 μm

Area average: Zr-76.7 wt%, U-14.3 wt%, Ni-5.2 wt%, Fe-2.1 wt%, Cr-1.8 wt%
Point 1: Zr-93.5 wt%, U-5.6 wt%, Ni-1.0 wt%
Point 2: Zr-64.1 wt%, U-16.9 wt%, Ni-10.7 wt%, Fe-4.4 wt%, Cr-3.9 wt%
Point 3: Zr-57.2 wt%, U-25.8 wt%, Ni-9.5 wt. %, Fe-4.1 wt%, Cr-3.4 wt%

Area average: Zr-54.2 wt%, Ni-19.3 wt%, U-10.4 wt%, Cr-8.3 wt%, Fe-7.8 wt%
Areas A, C, D: Zr-78.0 wt%, U-12.7 wt%, Ni-5.1 wt%, Fe-2.2 wt%, Cr-2.0 wt%
Area B: Ni-53.0 wt%, Cr-19.1 wt%, Fe-18.4 wt%, Nb-5.8 wt%, U-3.7 wt%
Reaction layer average: Ni-38.0 wt%, Zr-28.1 wt% (includes some Nb), Cr-14.6 wt%, Fe-13.8 wt%, U-5.5 wt%

Figure E-26. Semiquantitative results from energy-dispersive x-ray spectroscopy on Sample 2A.

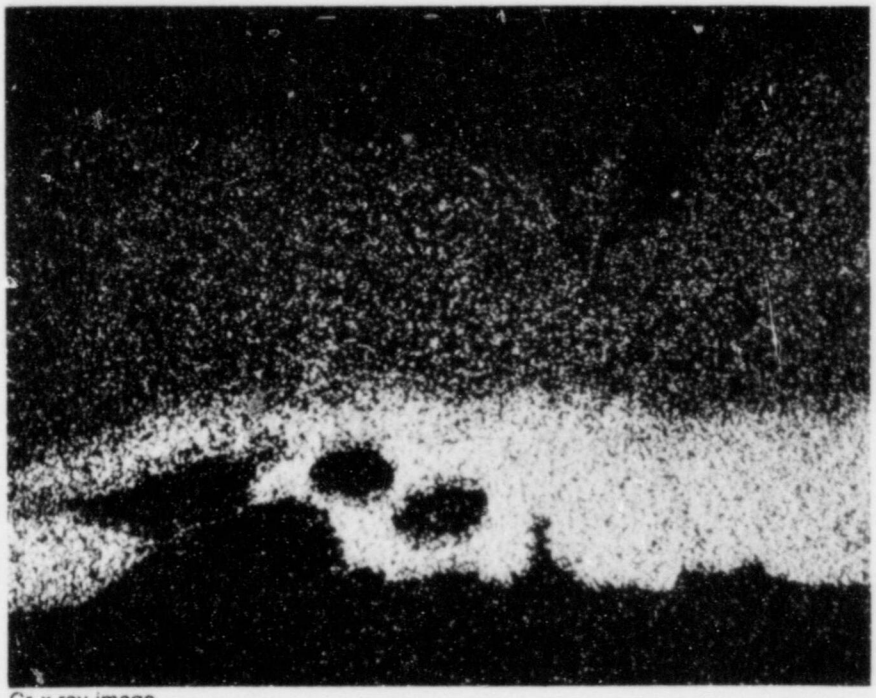

Cr x-ray image

278 μm

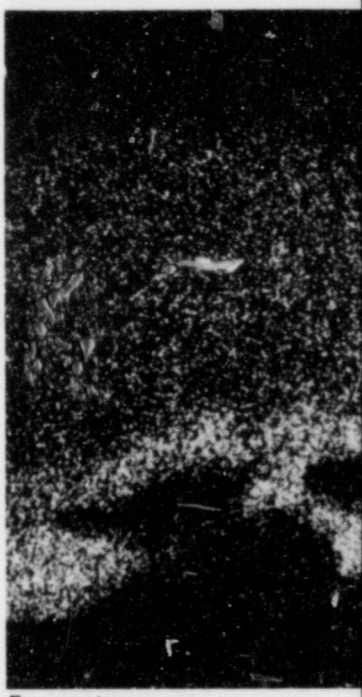

Fe x-ray image

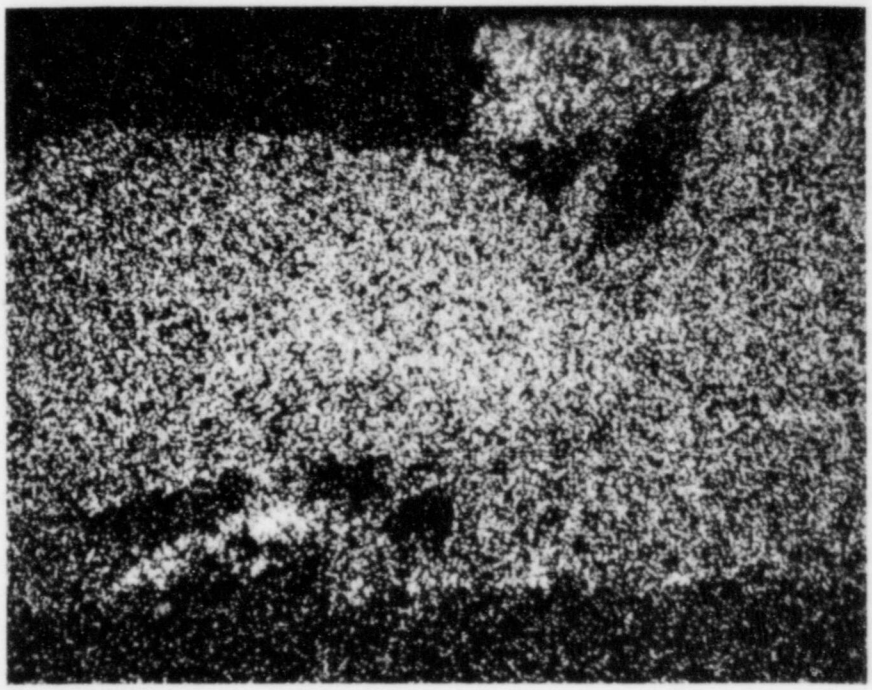

U x-ray image

278 μm

Figure E-27. Elemental distribution.

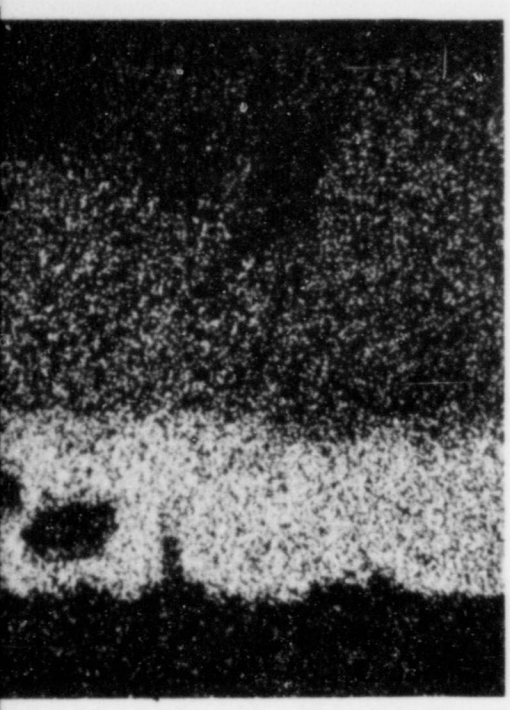

278 μm

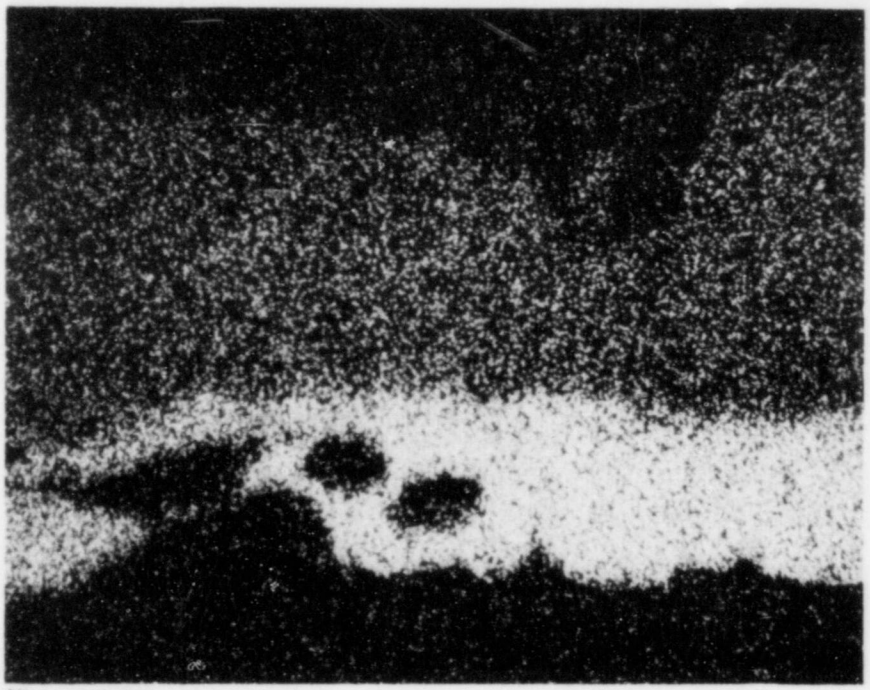

Ni x-ray image

278 μm

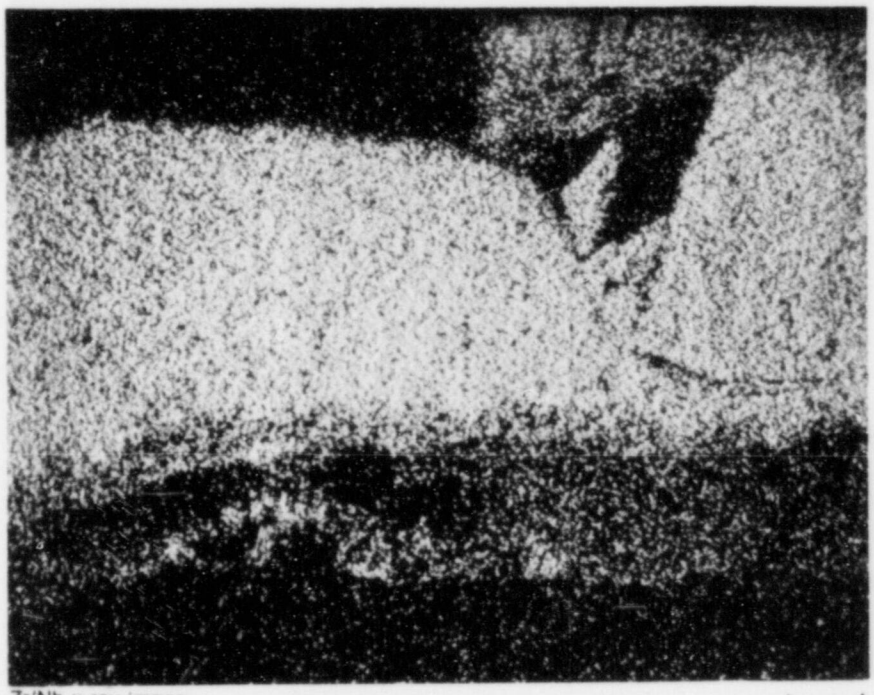

Zr/Nb x-ray image

278 μm

Nb band; no detectable Zr

TI
APERTURE
CARD

Also Available On
Aperture Card

over the melt/grid interaction region on Sample 2A.

8609300386-01

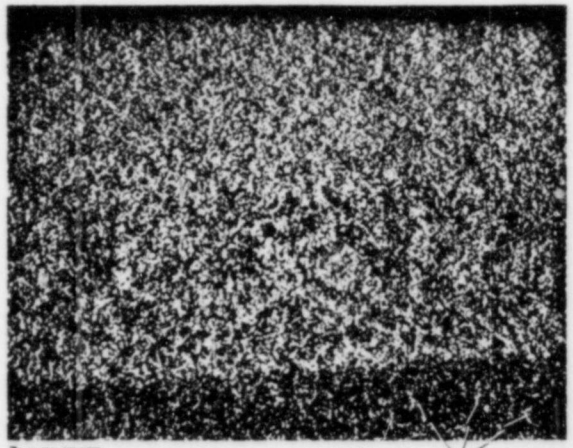

Zr x-ray image

17 μm

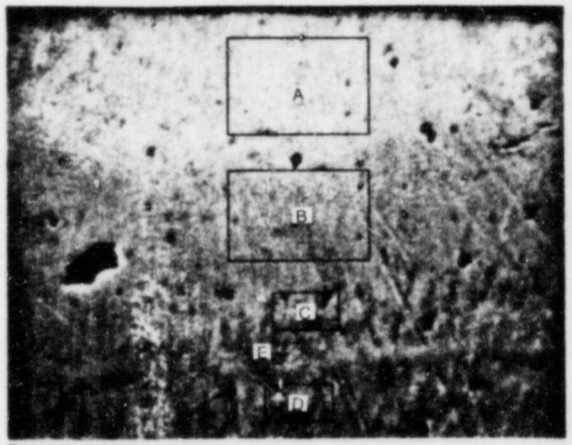

Backscattered electron image

17 μm

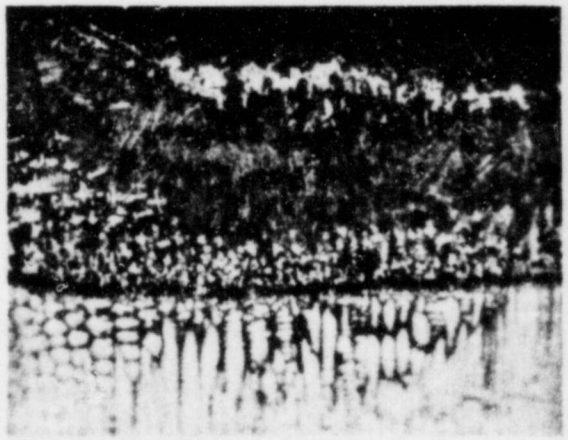

Photomicrograph (etched) 84M-306

20 μm

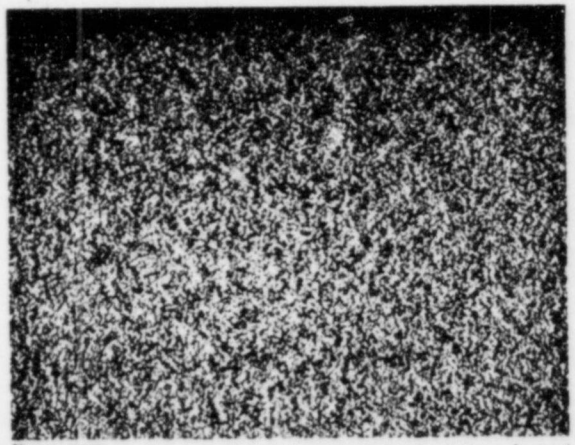

Ni x-ray image

17 μm

Area average: Ni-38.0 wt %, Zr-28.1 wt % (with some Nb), Cr-14.6 wt %, Fe-13.8 wt %, U-5.5 wt %
Area A: Zr-47.3 wt%, Ni-28.1 wt%, U-8.5 wt%, Fe-8.3 wt %, Cr-7.8 wt %
Area B: Ni-41.4 wt %, Zr-23.5 wt %, Cr-16.0 wt %, Fe-14.8 wt %, U-4.3 wt %
Area C: Ni-40.8 wt %, Zr-19.9 wt % (with some Nb), Cr-18.6 wt %, Fe-16.8 wt %, U-4.0 wt %
Area D: Ni-50.7 wt %, Cr-19.7 wt %, Fe-18.7 wt %, Nb-7.2 wt %, U-3.7 wt %
Point E: Zr-40.3 wt %, Ni-29.9 wt %, Cr-11.7 wt %, Fe-10.2 wt %, U-7.8 wt %

ATI
APERTURE
CARD

Also Available On
Aperture Card

Figure E-28. Reaction layer formation at the metallic melt/Inconel grid interface.

8609300386 -02

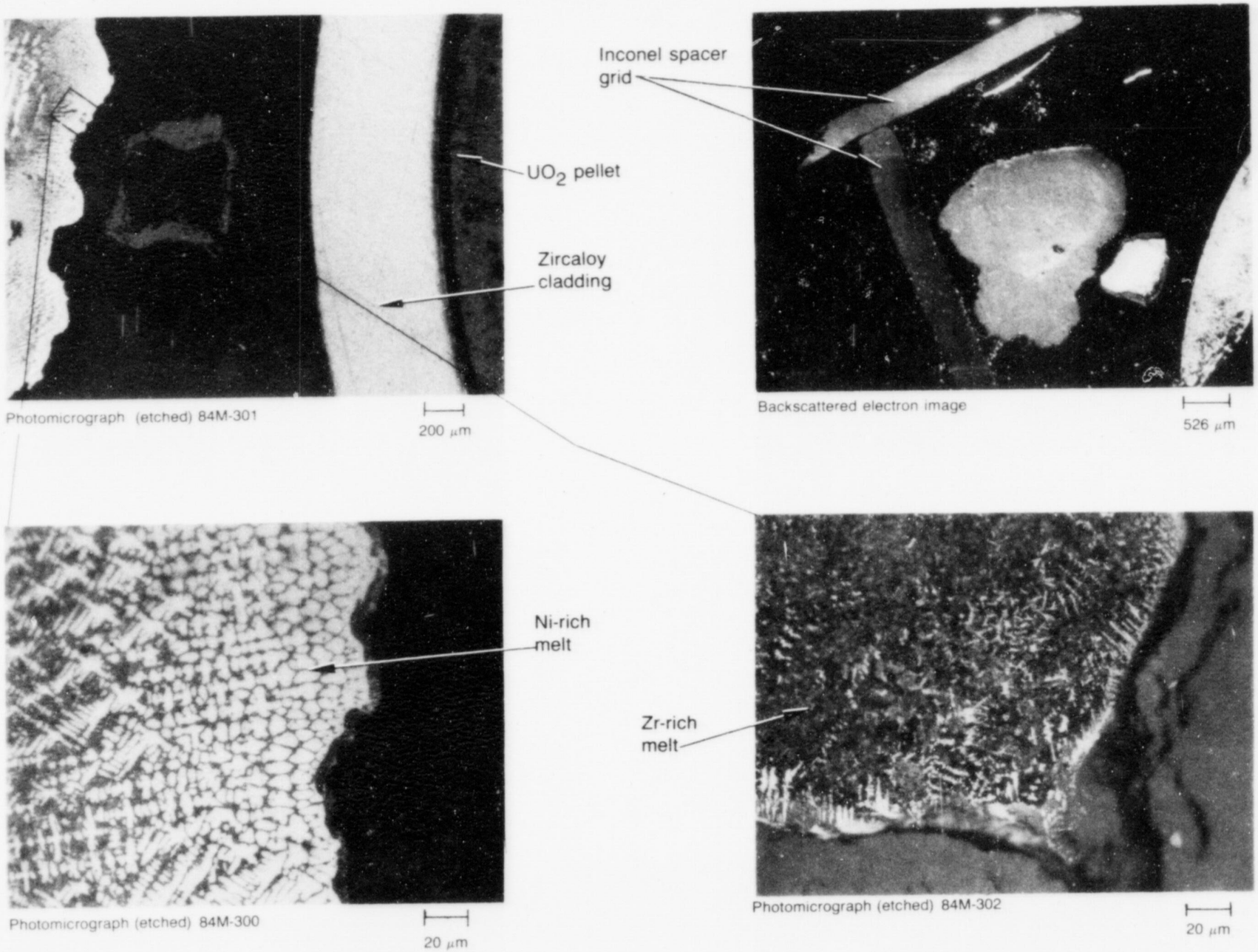

Figure E-29. Characteristic melt microstructures found in Sample 2B (0.055 m).

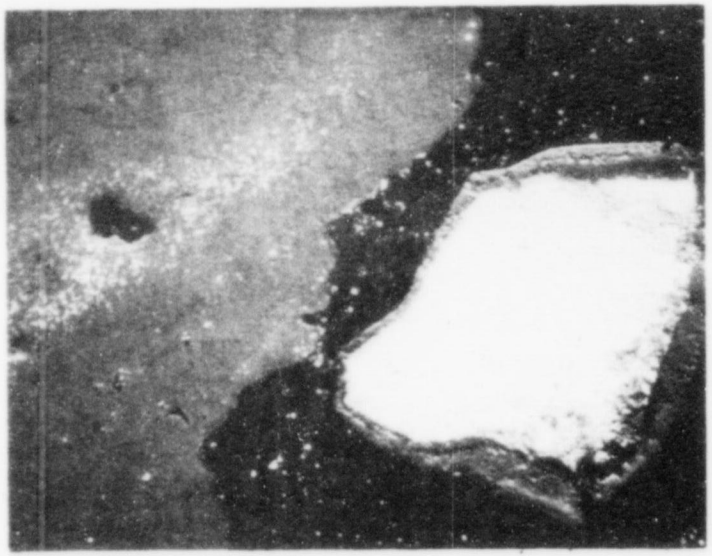

Backscattered electron image

135 μm

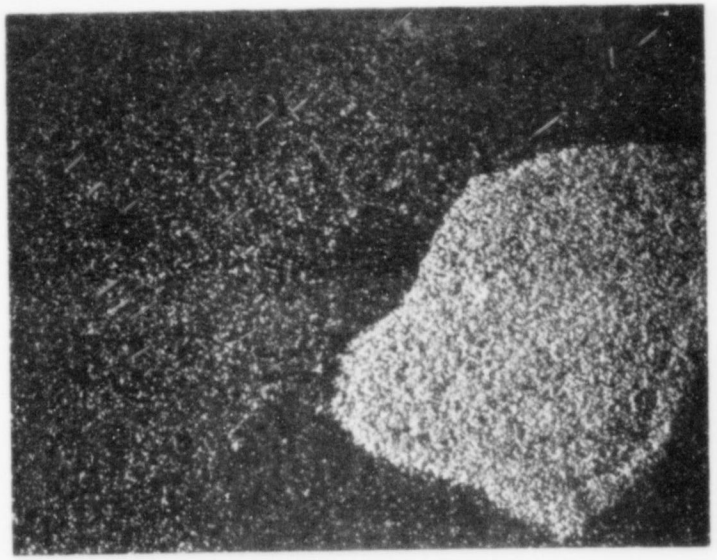

Zr x-ray image

135 μm

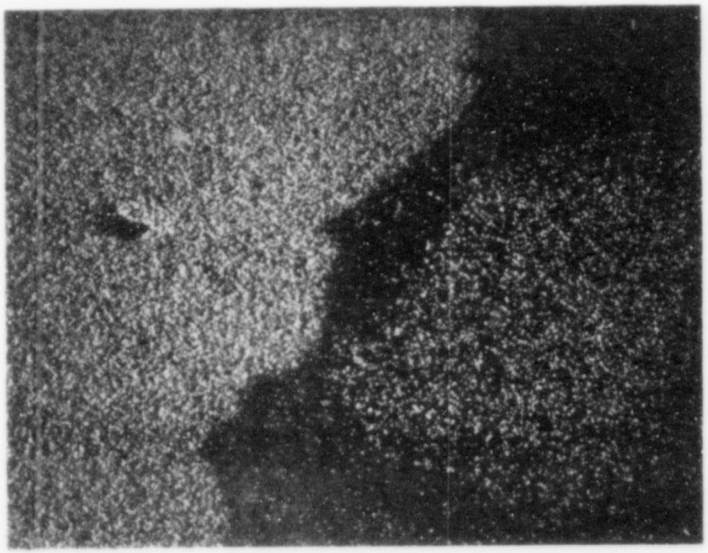

Ni x-ray image

135 μm

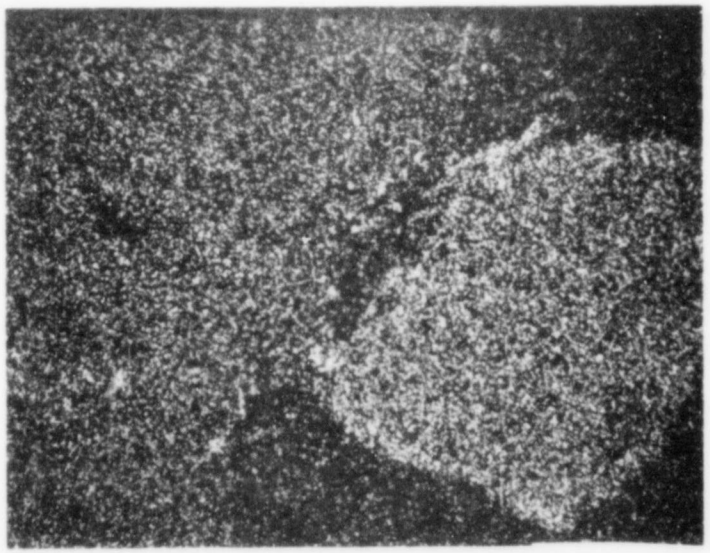

U x-ray image

135 μm

Figure E-30. Elemental distribution maps over Area A from Sample 2B.

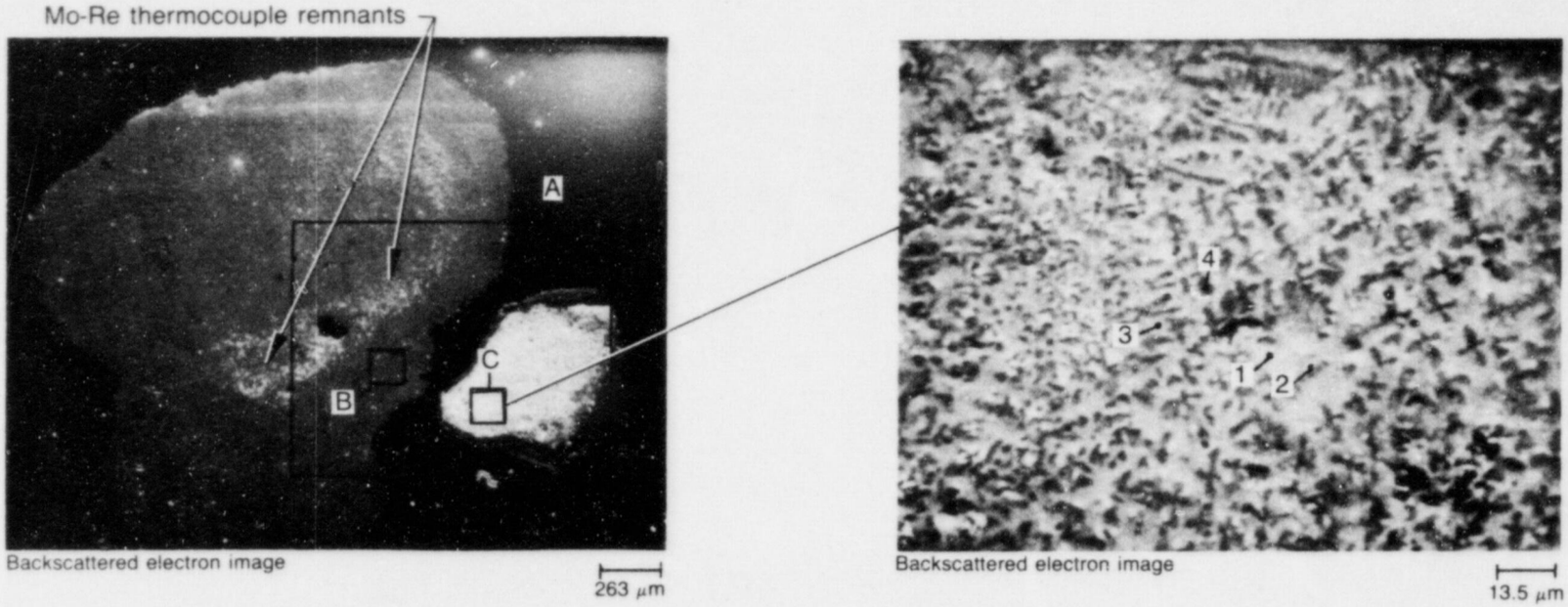

Area A: Ni-52.2 wt %, Zr-23.5 wt %, Fe-13.7 wt %, Cr-5.9 wt %, U-4.8 wt %

Area B: Ni-66.4 wt %, Fe-15.1 wt %, Zr-6.9 wt %, Cr-5.8 wt %, Mo-2.9 wt %, U-2.8 wt %

Area C: Zr-69.6 wt %, U-10.1 wt %, Ni-9.6 wt %, Ta-5.1 wt %, Fe-3.4 wt %, Cr-2.3 wt %

Point 1: Zr-63.4 wt%, Ni-13.1 wt%, U-11.7 wt%, Sn-6.4 wt%, Fe-4.1 wt%, Cr-1.5 wt%

Point 2: Zr-53.3 wt%, Re-17.5 wt%, Ta-12.8 wt%, U-4.6 wt%, Cr-4.5 wt%, Ni-4.3 wt%, Fe-3.1 wt. %

Point 3: Zr-65.6 wt%, Ni-12.1 wt%, Sn-8.5 wt%, U-7.7 wt%, Fe-4.8 wt%, Cr-1.9 wt%

Point 4: Zr-76.3 wt%, U-16.2 wt%, Ni-2.7 wt%, Ta-1.7 wt%, Re-1.3 wt%, Fe-1.2 wt%, Cr-0.7 wt. %

Figure E-31. EDS results from the two melts in Sample 2B.

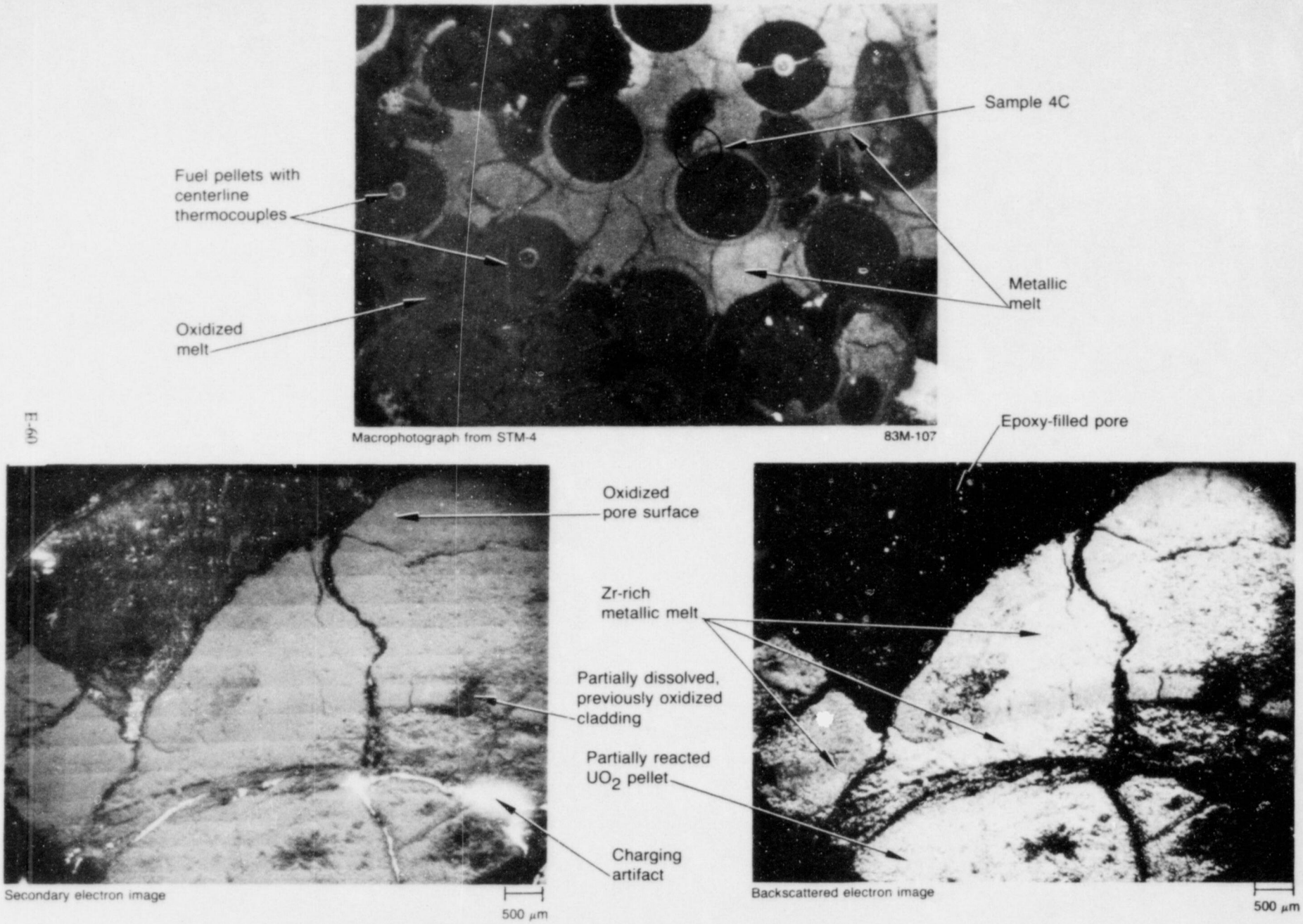

Figure E-32. Sample 4C (0.145 m) illustrating metallic melt interactions with UO_2 fuel, oxidized cladding and pore steam.

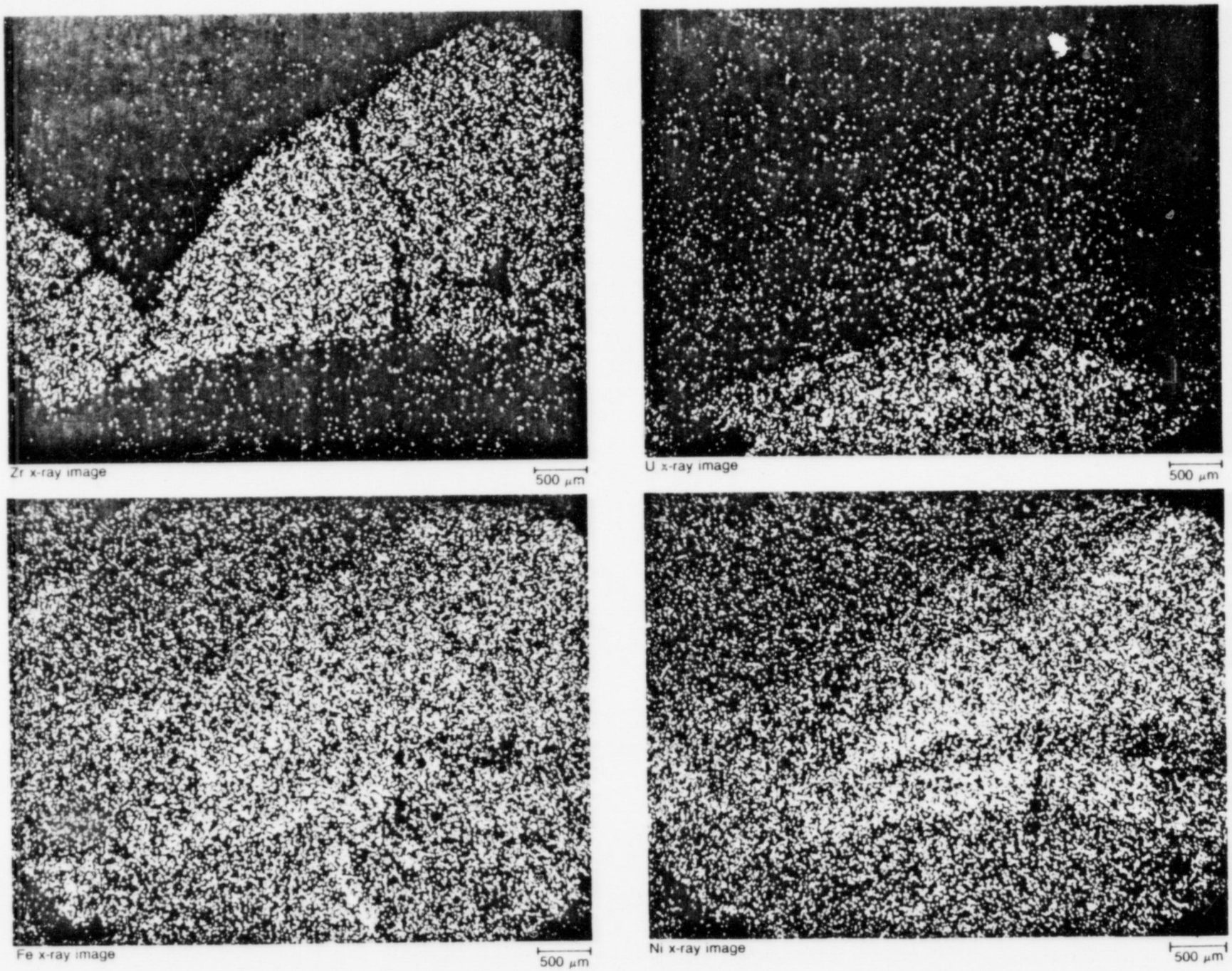

Figure E-33. Relative elemental distributions over Sample 4C.

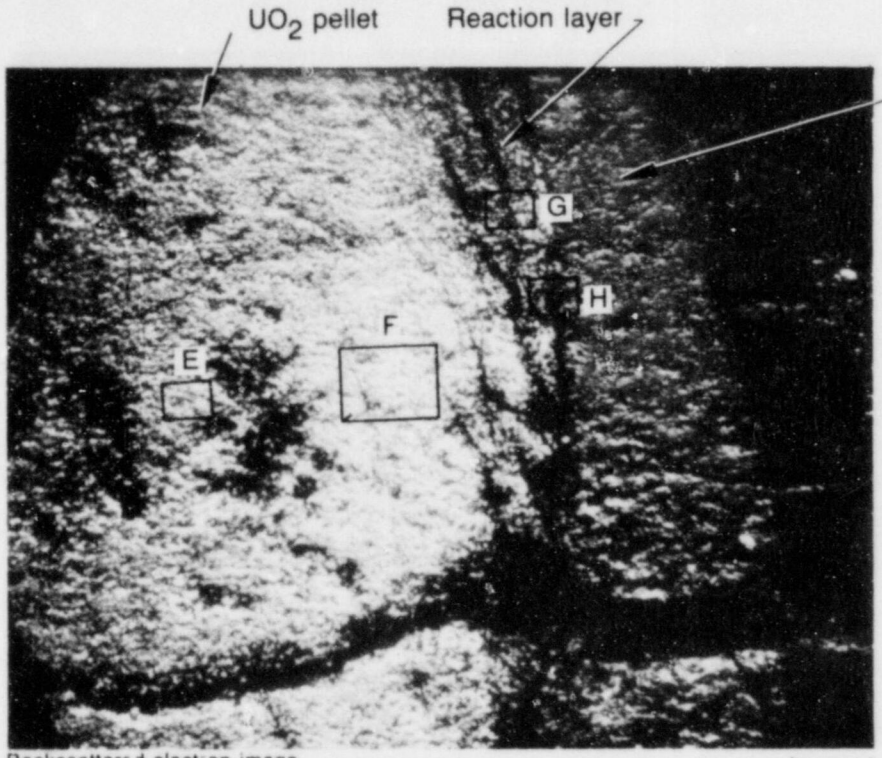

Backscattered electron image

250 μm

Area E: U-94.8 wt%, Zr-3.6 wt%, Fe-1.6 wt%
Area F: U-95.9 wt%, Zr-3.2 wt%, Fe-0.9 wt%
Area G: U-89.3 wt%, Zr-9.0 wt%, Fe-1.8 wt%

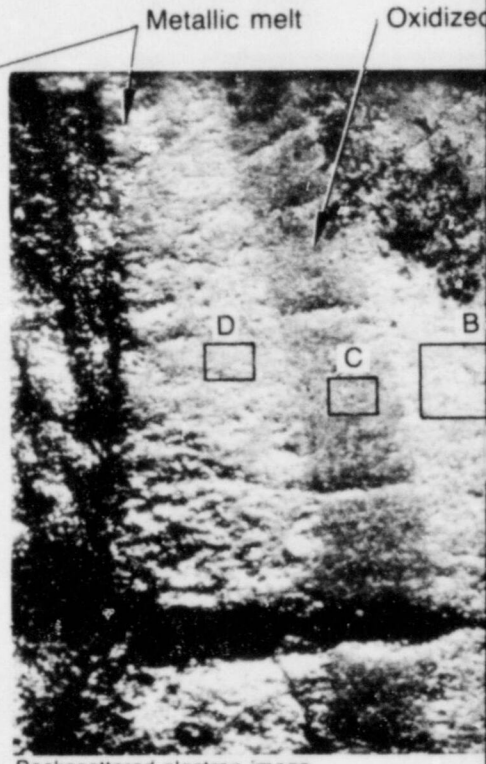

Backscattered electron image

Area A: Zr-79.6 wt%, U-18.7 wt%, Ni-1.0
Area B: Zr-74.1 wt%, U-15.4 wt%, Ni-6.1
Area C: Zr-81.5 wt%, U-16.2 wt%, Ni-1.5
Area D: Zr-72.6 wt%, U-15.4 wt%, Ni-7.4

Area A: O-60.7 at. %, Zr-34.3 at. %, U-5.0 at. %, plus some Fe and Ni
Area B: Zr-56.2 at. %, O-28.9 at. %, Ni-6.0 at. %, U-4.9 at. %, Fe-4.0 at. %
Area C: O-61.8 at. %, Zr-30.7 at. %, U-7.5 at. %, plus traces of Fe, Cr and Ni
Area D: Zr-57.2 at. %, O-30.8 at. %, U-6.5 at. %, Ni-3.5 at. %, Fe-2.0 at. %
Area H: O-50.0 at. %, Zr-37.4 at. %, U-8.1 at. %, Ni-2.0 at. %, Fe-2.0 at. %

Figure E-34. Semiquantitative EDS (wt%) and qu

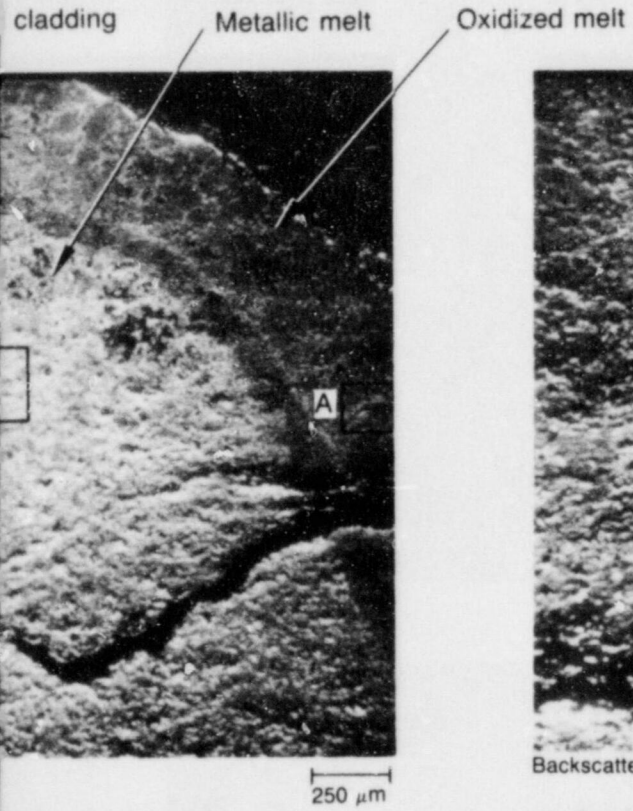

wt %, Fe-0.8 wt %,
wt %, Fe-2.9 wt %, Cr-1.6 wt %
wt %, Fe-0.8 wt %
wt %, Fe-3.0 wt %, Cr-1.6 wt %

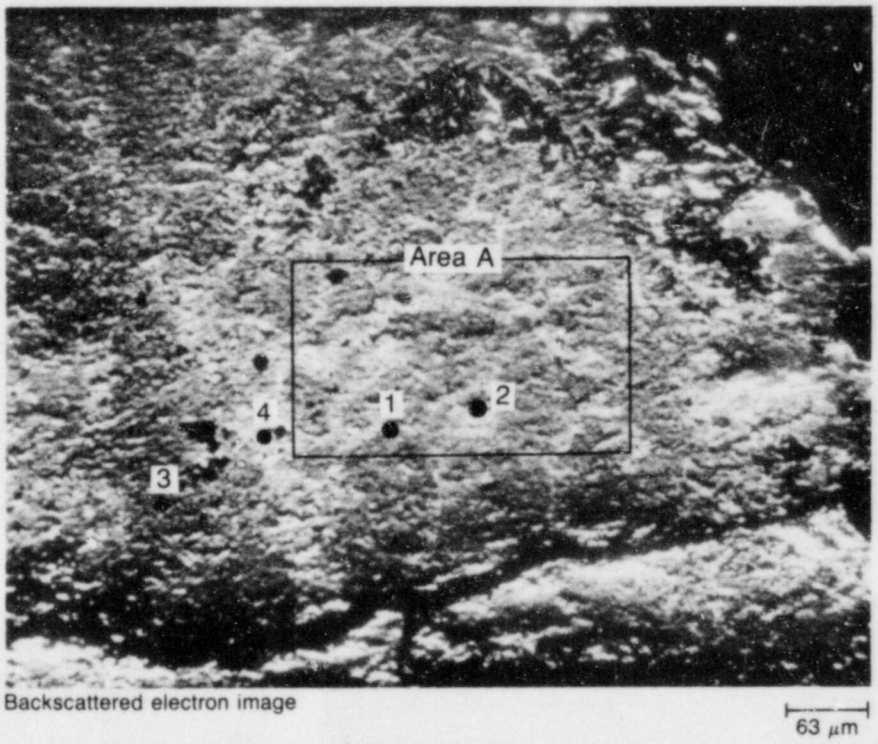

Point 1: Zr-84.2 wt %, U-15.9 wt %
Point 2: Zr-96.7 wt %, U-2.7 wt %, Ni-0.7 wt %
Point 3: Zr-76.4 wt %, U-19.7 wt %, Ni-2.8 wt %, Fe-1.1 wt %
Point 4: Zr-88.9 wt %, U-11.2 wt %

antitative SAS (at.%) results over Sample 4C.

TI
APERTURE
CARD

Also Available On
Aperture Card

8609300386-03

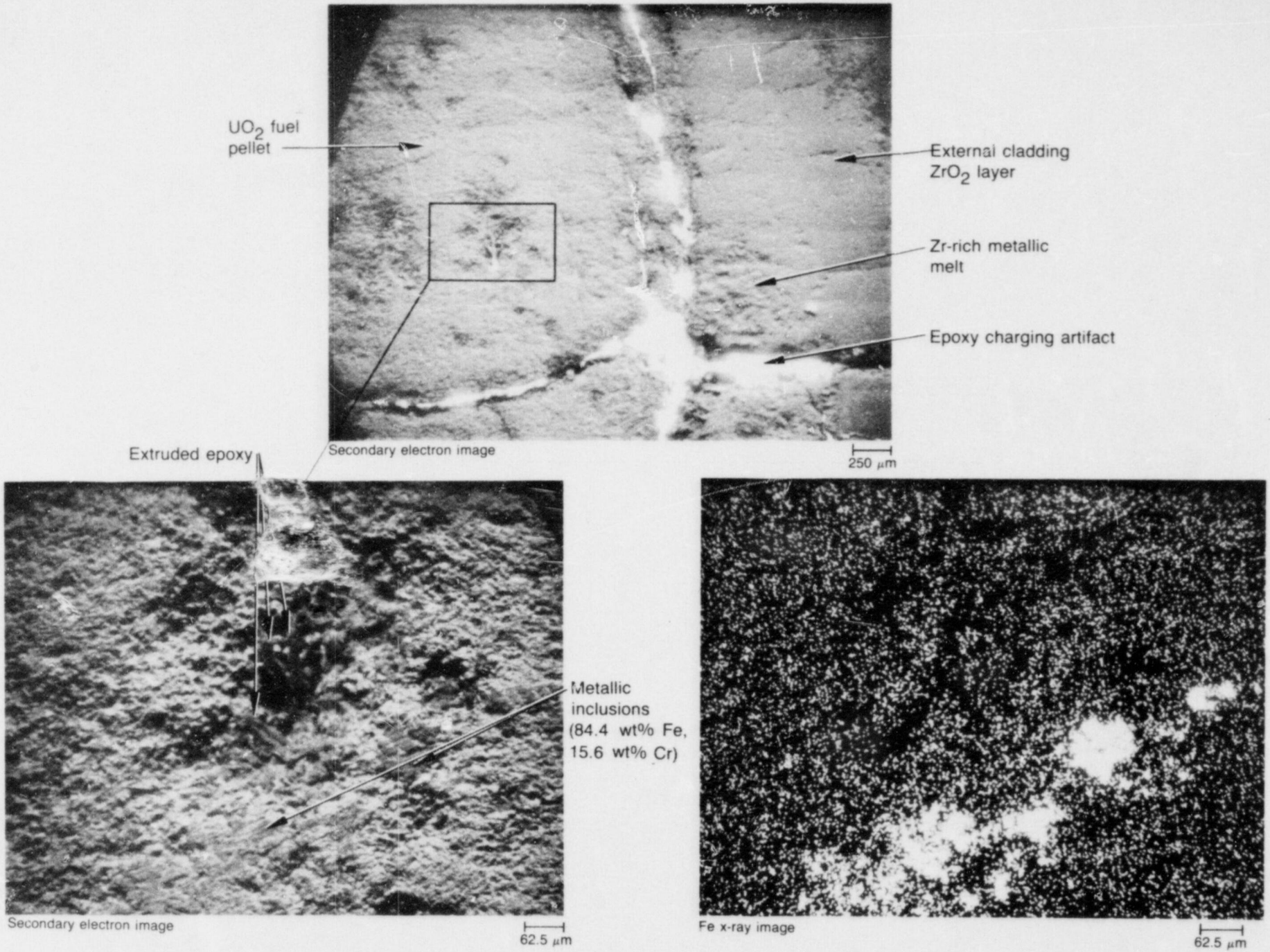

Figure E-35. SEM/EDS investigations of metallic inclusions in Sample 4C UO_2 fuel.

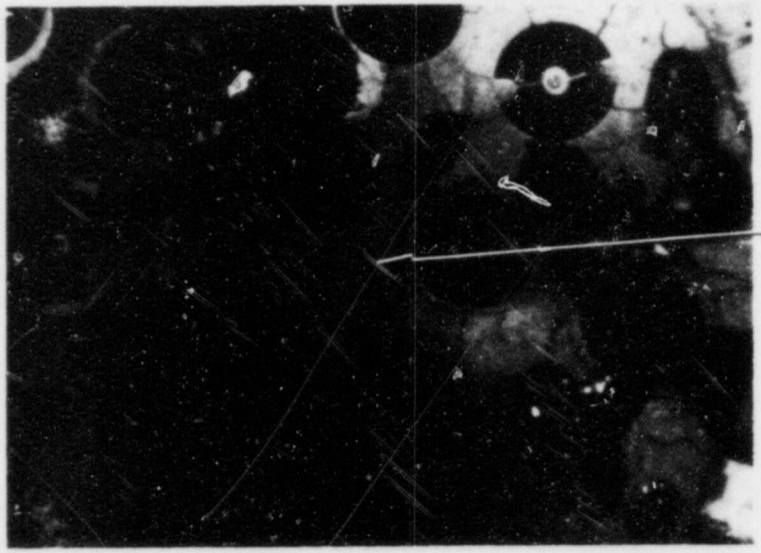

Macrophotograph from STM-4 83M-107

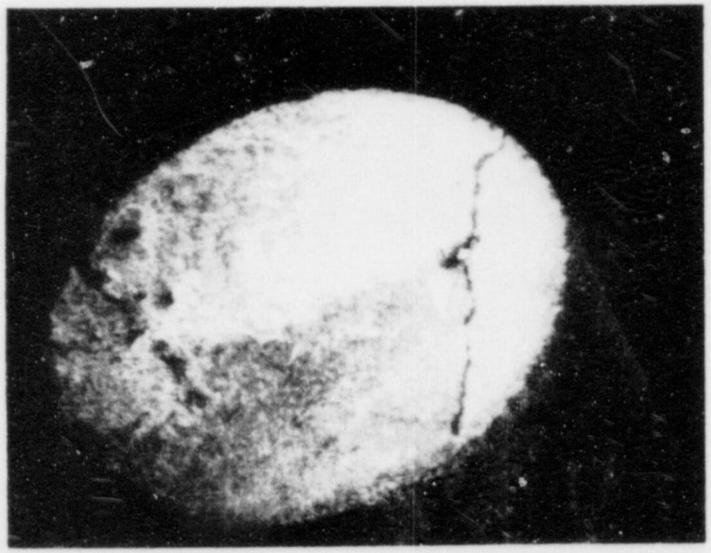

Secondary electron image

694 μm

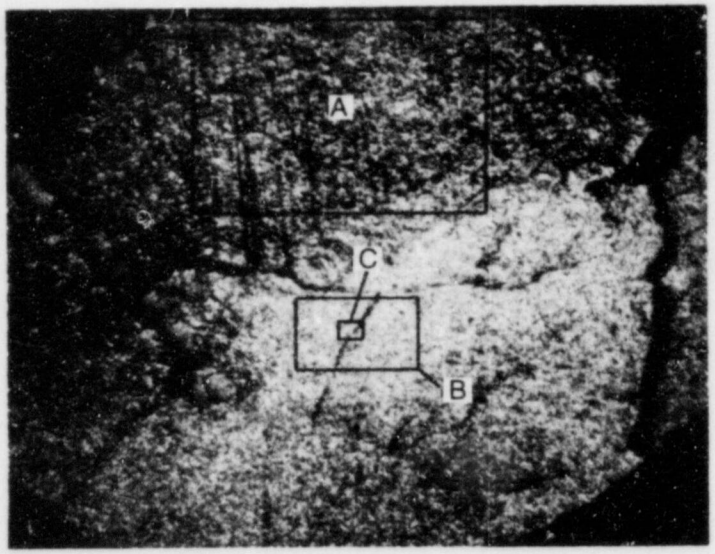

Backscattered electron image

417 μm

Sample 4D average: Zr-70.7 wt%, U-20.3 wt%, Ni-4.8 wt%, Fe-3.0 wt% Cr-1.4 wt%
Area A: Zr-68.7 wt%, U-23.4 wt%, Ni-4.4 wt%, Fe-2.4 wt%, Cr-1.3 wt%
Area B: Zr-74.2 wt%, U-16.9 wt%, Ni-5.3 wt%, Fe.2.3 wt%, Cr-1.2 wt%

Figure E-36. Composition and texture variations in metallic melt Sample 4D (0.145 m).

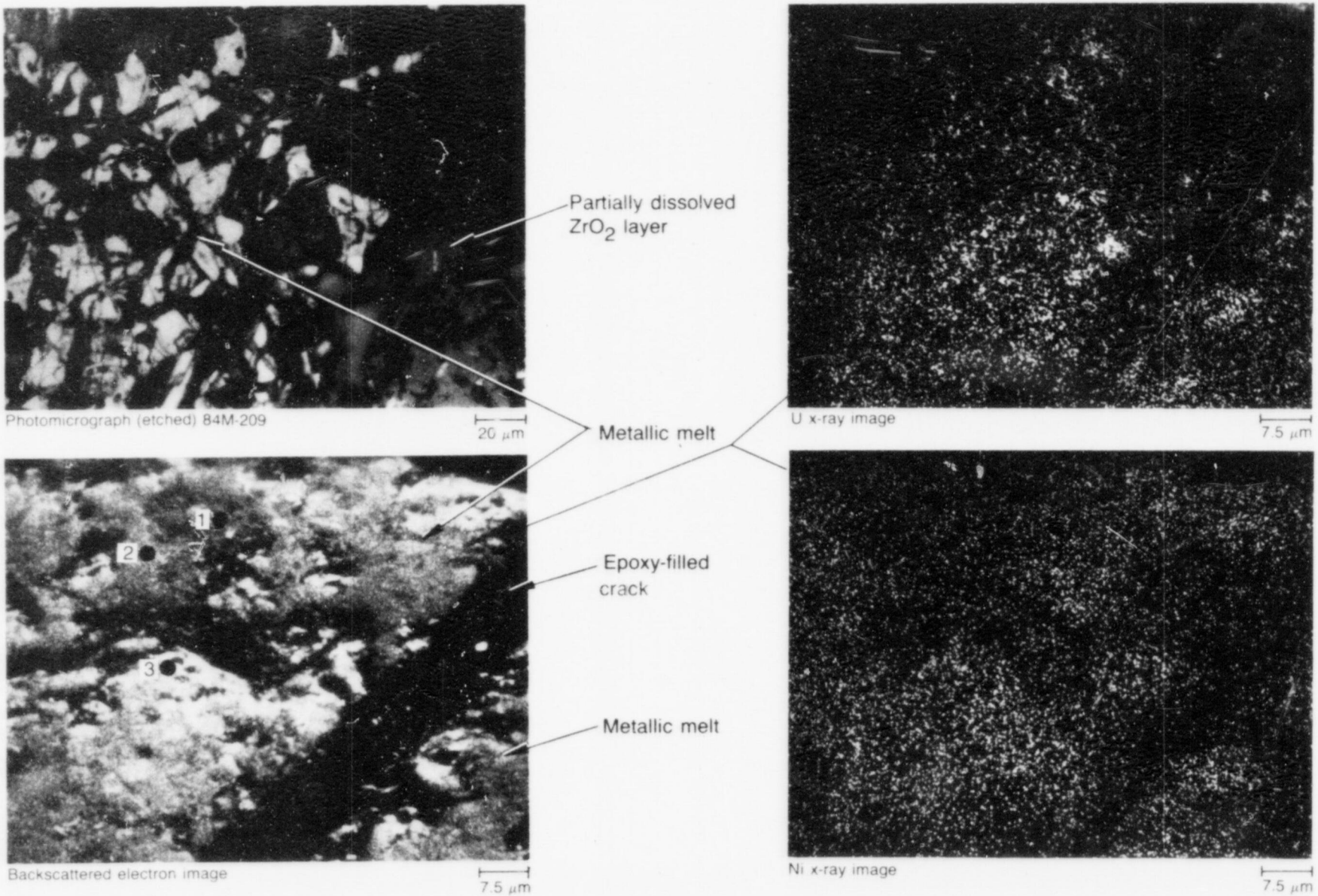

Point 1: Zr-100.0 wt%
Point 2: Zr-95.5 wt%, U-4.6 wt%
Point 3: Zr-64.0 wt%, Ni-14.5 wt%, U-11.1 wt%, Fe-6.4 wt%, Cr-4.1 wt%

Figure E-37. Typical metallic melt microstructure plus elemental composition distributions in Area C from Sample 4D.

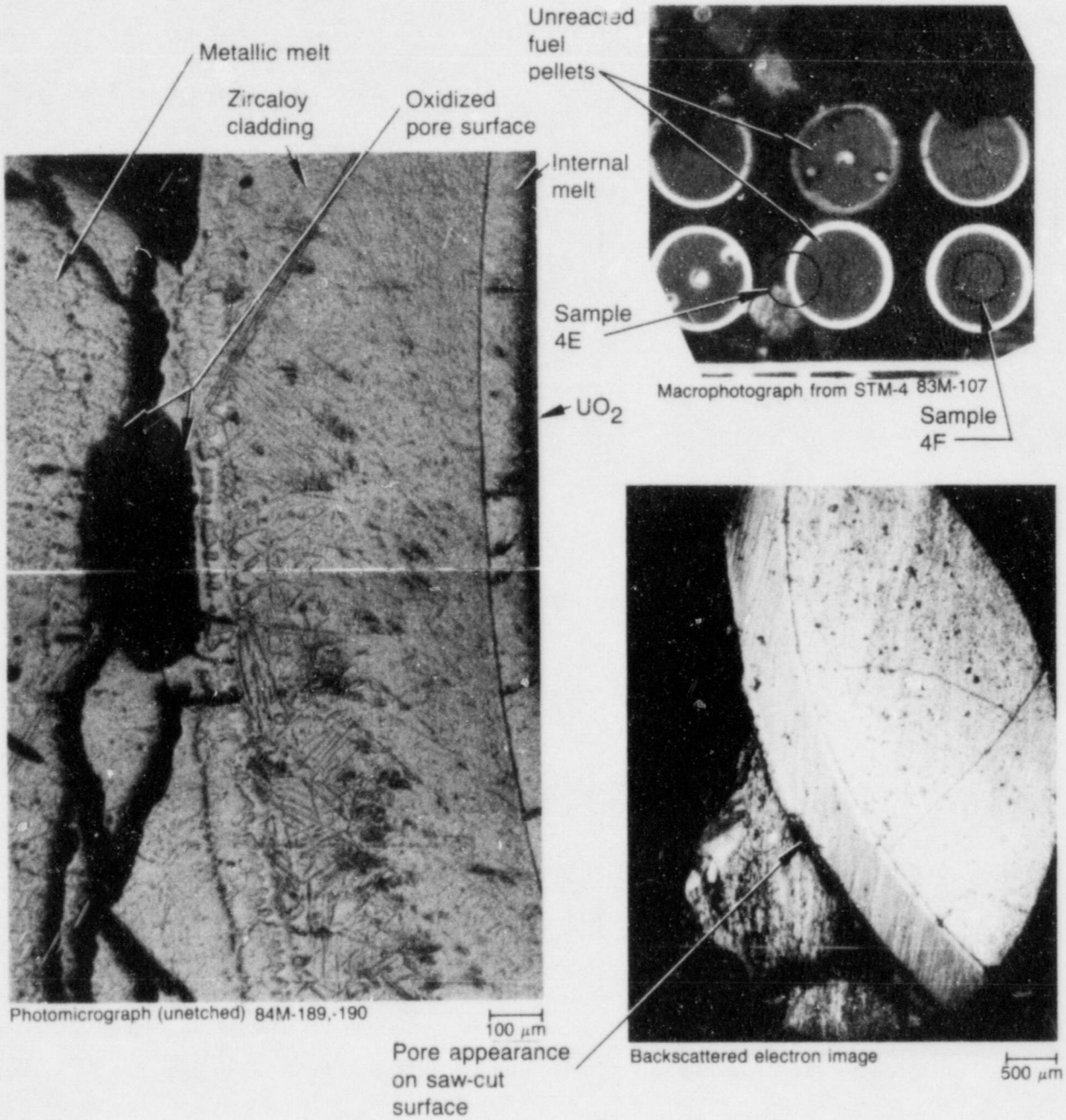

Figure E-38. Attack of cladding by exterior metallic melt and slumping of a second metallic melt between fuel and cladding on Sample 4E (0.145 m). (Saw-cut wafer surface was erroneously mounted upward, so SEM and metallographic orientations are reversed).

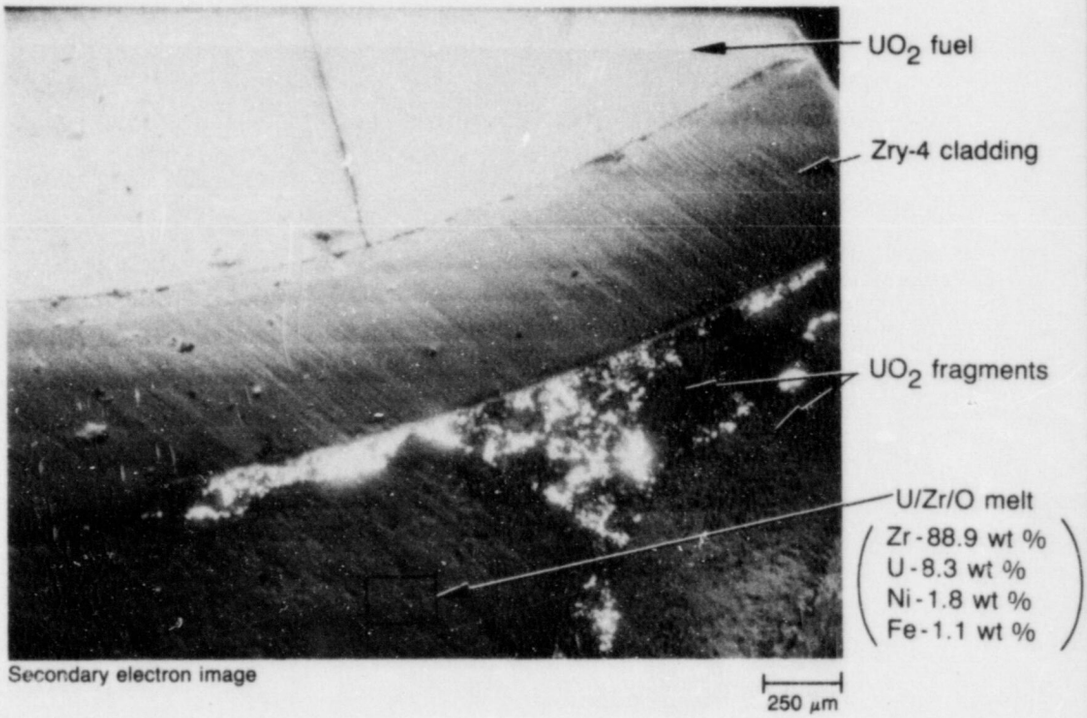

Figure E-39. Major element distributions near me

Backscattered electron image

250 μm

U x-ray image

250 μm

TI
APERTURE
CARD

Also Available On
Aperture Card

t/cladding and cladding/fuel interaction zones on Sample 4E.

8609300386-04

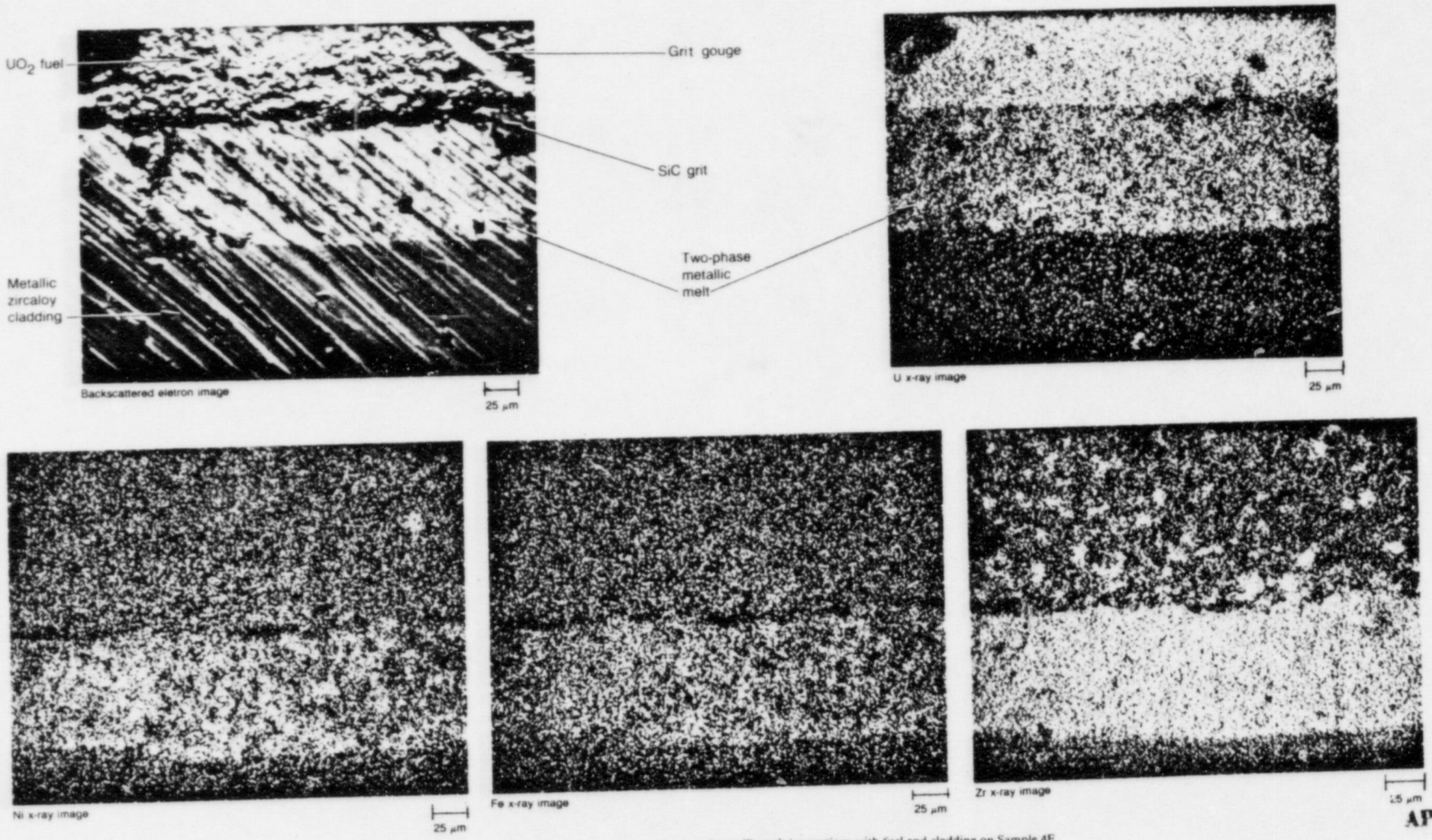

Figure E-40. High magnification elemental maps of metallic melt interactions with fuel and cladding on Sample 4E. (Note upward shift on bottom three maps with respect to upper two images.)

APERTURE CARD

Also Available On Aperture Card

8609300386-05

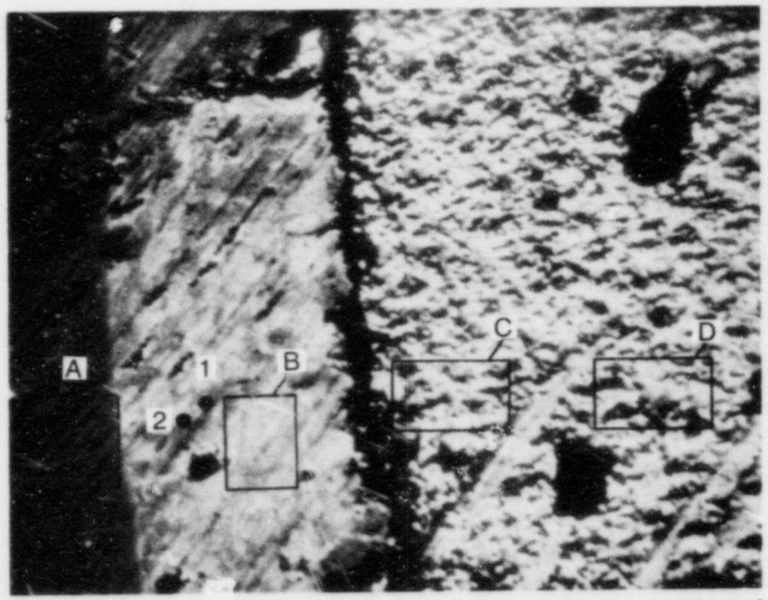

Backscattered electron image

25 μm

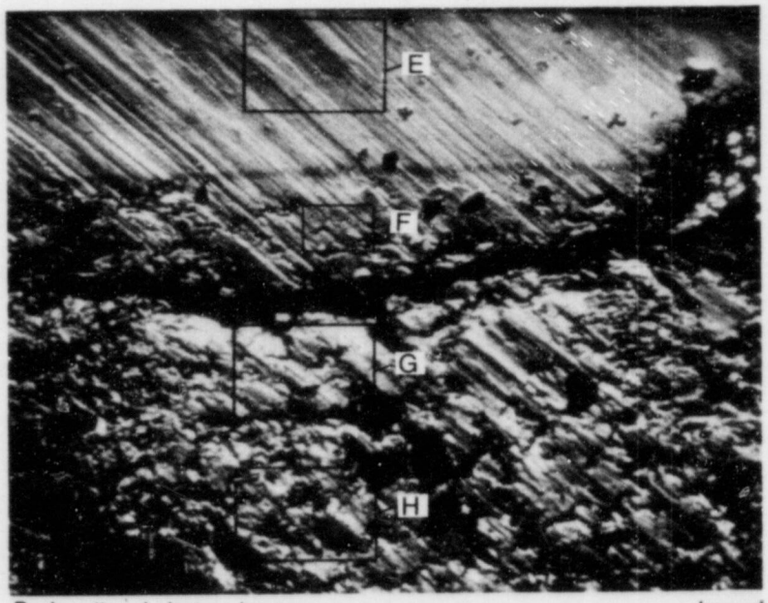

Backscattered electron image

62.5 μm

Area A: Zr-99.0 wt%, Sn-1.0 wt%
Area B: Zr-53.5 wt%, U-34.7 wt%, Ni-5.9 wt%, Fe-4.0 wt%, Cr-2.0 wt%
Area C: U-90.2 wt%, Zr-9.8 wt%
Area D: U-94.4 wt%, Zr-5.7 wt%
Point 1: Zr-50.8 wt%, U-27.9 wt%, Ni-13.2 wt% Fe-6.8 wt%, Cr-1.4 wt%
Point 2: U-49.9 wt%, Zr-48.8 wt%, Fe-0.7 wt%, Cr-0.6 wt%

Area E: Zr-96.2 wt%, U-2.3 wt%, Sn-1.5 wt%
Area F: Zr-95.9 wt%, U-3.0 wt%, Sn-1.2 wt%
Area G: Zr-91.6 wt%, U-4.9 wt%, Sn-1.6 wt%, Ni-1.1 wt%, Fe-0.8 wt%
Area H: Zr ~ 93 wt%, U ~ 4 wt%, Sn ~ 1 wt%, Ni ~ 1 wt%, Fe ~ 1 wt%
(Semiquantitative results for Area H were perturbed by a calibration drift.)

Figure E-41. Semiquantitative EDS results from internal melt/fuel reaction zone (left) and from external melt/cladding reaction zone (right) on Sample 4E.

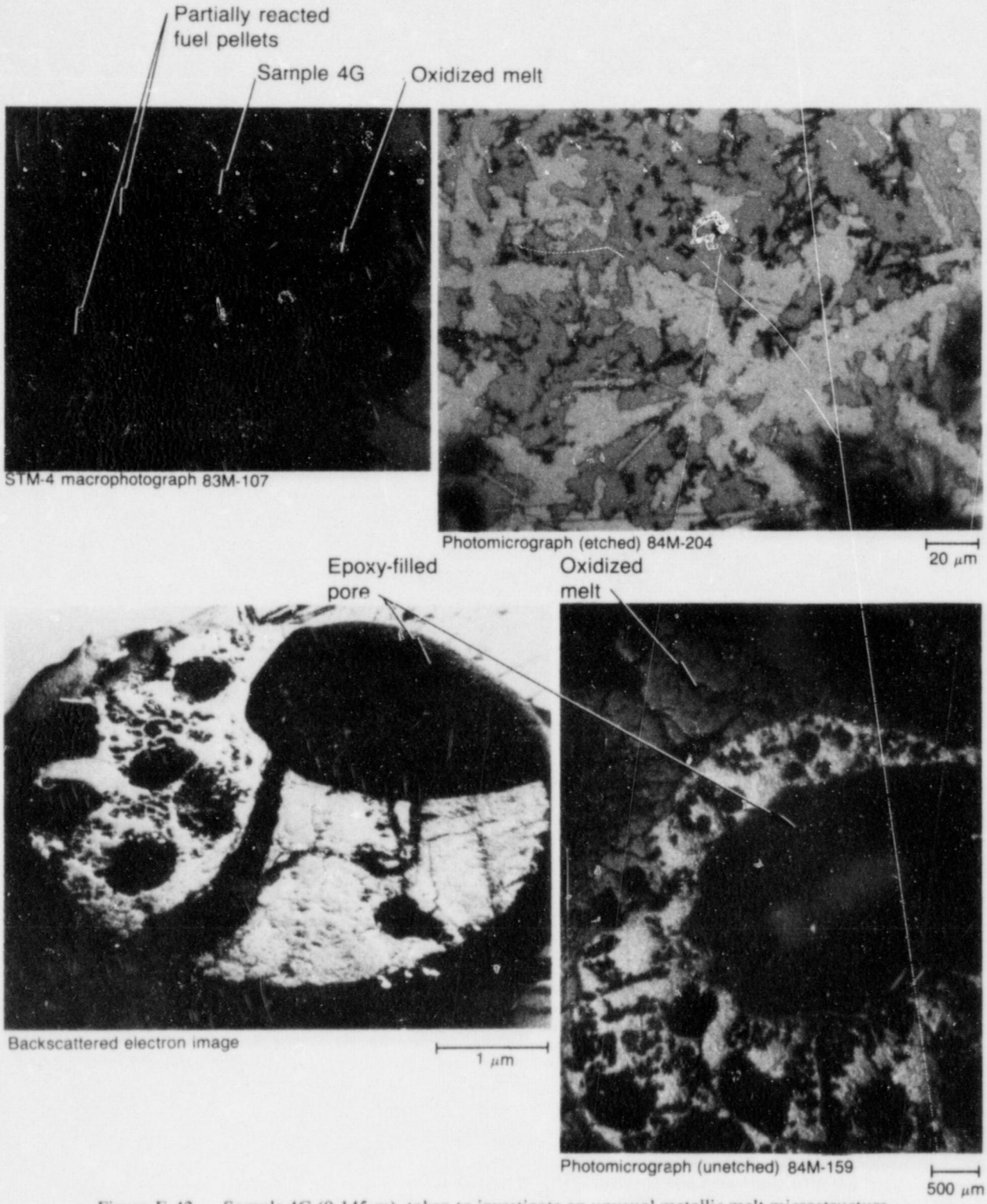

Figure E-42. Sample 4G (0.145 m), taken to investigate an unusual metallic melt microstructure.

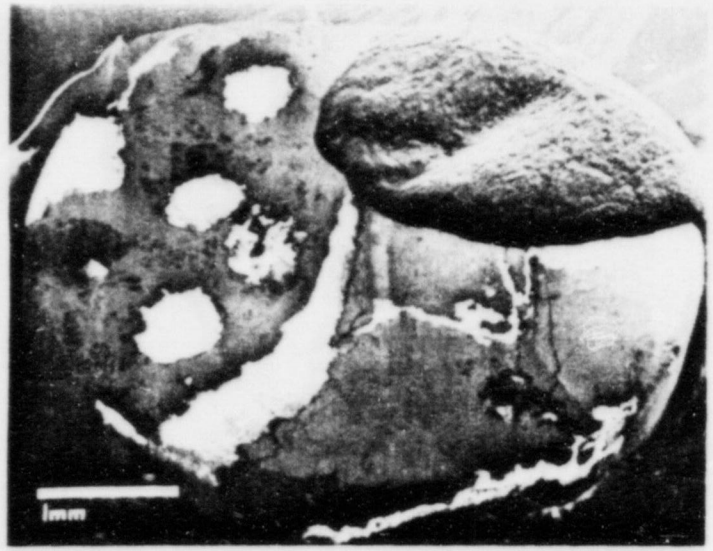

Secondary electron image

Zr x-ray image

1 mm

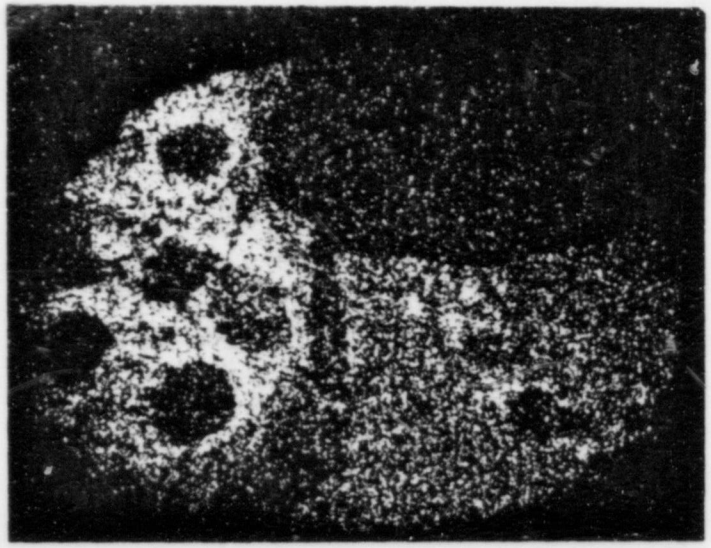

Ni x-ray image

1 mm

U x-ray image

1 mm

Figure E-43. Distributions of primary elements over Sample 4G.

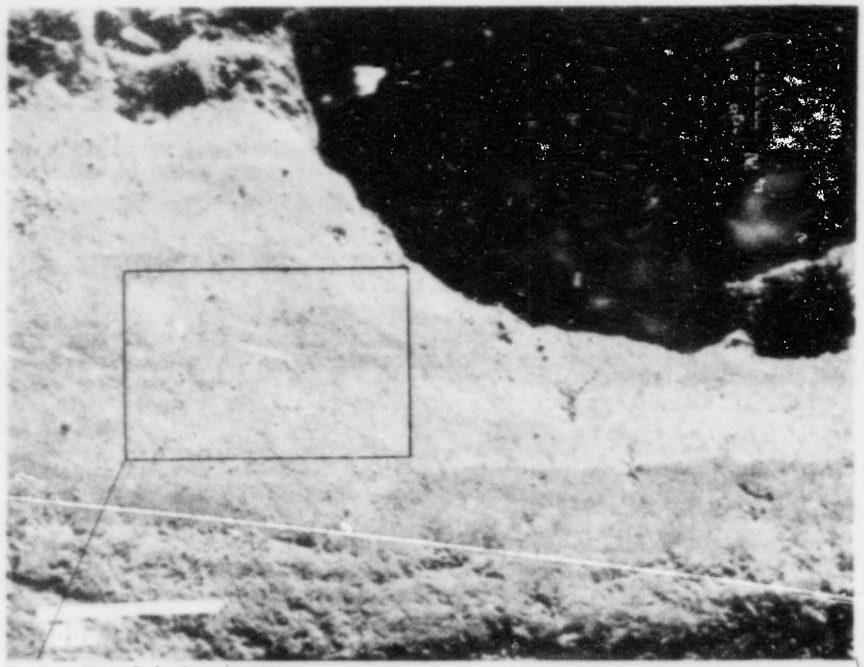

Backscattered electron image

Ni-26.9 wt %, U-25.9 wt %, Zr-18.4 wt %, Fe-11.8 wt %, Re-11.3 wt %, Cr-5.6 wt %

Backscattered electron image

U-64.4 wt %, Zr-33.6 wt %, Ni-1.4 wt %, Fe-0.4 wt %, Cr-0.2 wt %

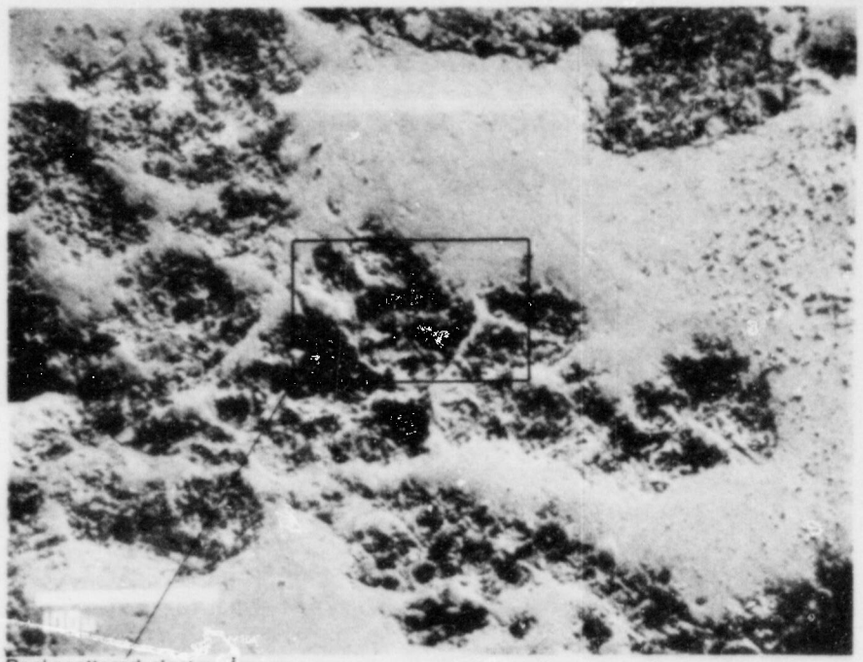

Backscattered electron image

U-44.2 wt %, Zr-26.2 wt %, Ni-14.9 wt %, Re-6.9 wt %, Fe-5.1 wt %, Cr-2.6 wt %

TI
APERTURE
CARD

Also Available On
Aperture Card

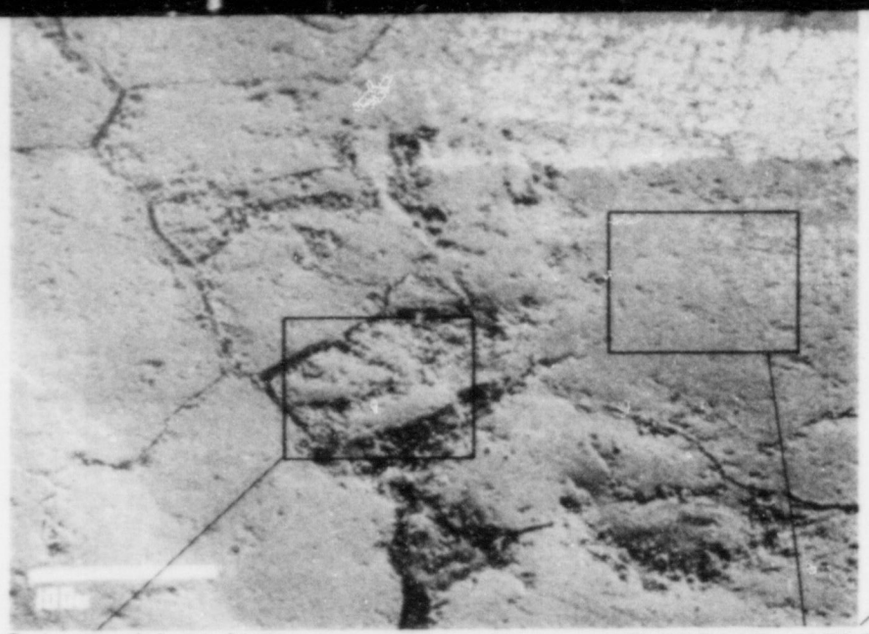

Backscattered electron image

Zr-64.7 wt %, U-33.3 wt %,
Ni-1.2 wt %, Fe-0.5 wt %, Cr-0.2 wt %

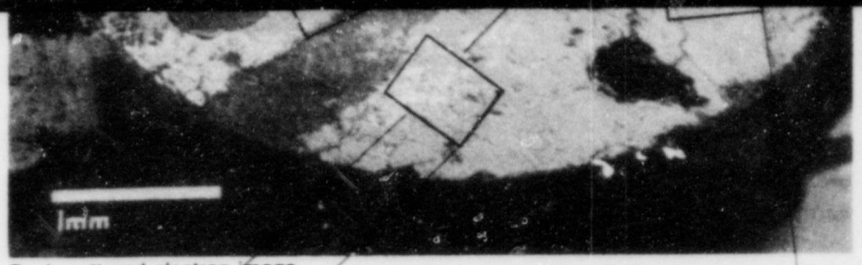

Backscattered electron image

Zr-61.5 wt %, U-33.9 wt %, Ni-3.4 wt %,
Fe-0.9 wt %, Cr-0.3 wt %,

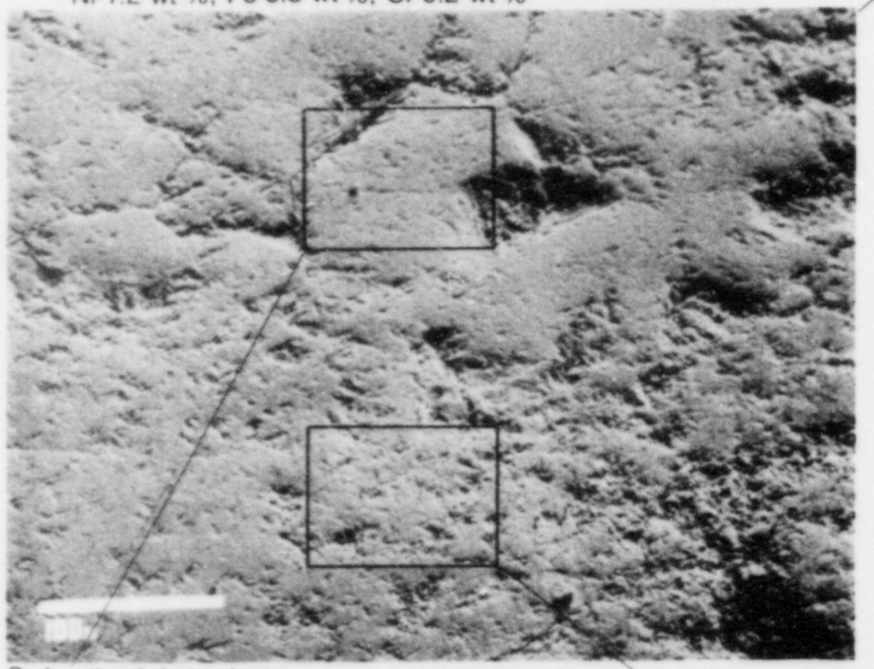

Backscattered electron image

Zr-71.3 wt %, U-28.6 wt %,

U-51.0 wt %, Zr-43.0 wt %

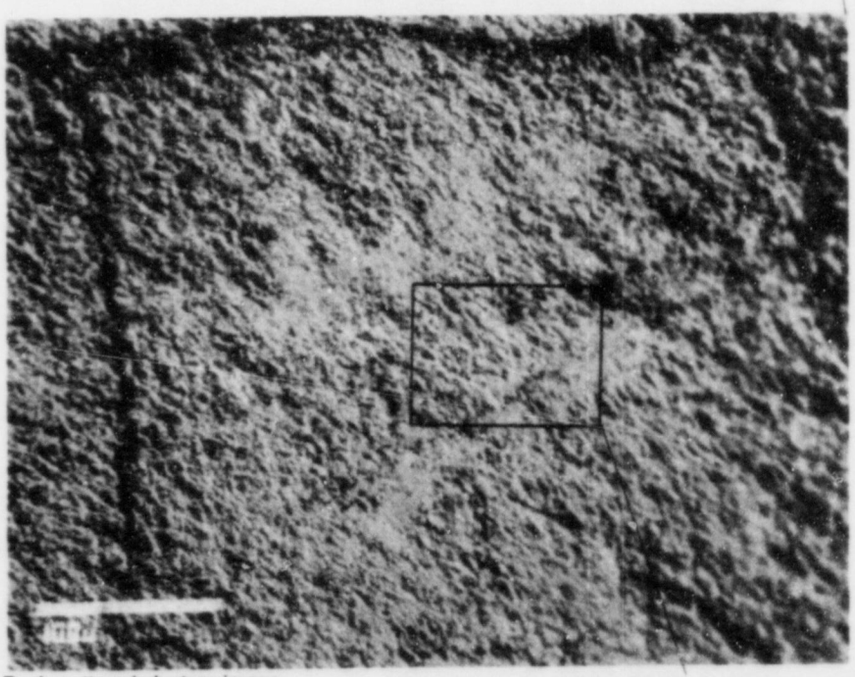

Backscattered electron image

U-96.5 wt %,
Ar-3.6 wt %

Figure E-44. Semiquantitative EDS results from Sample 4G.

90-0880300860

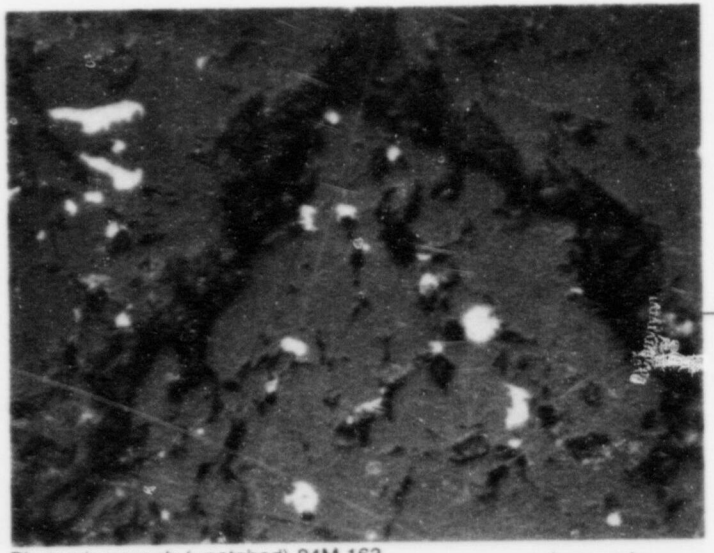

Photomicrograph (unetched) 84M-163

20 μm

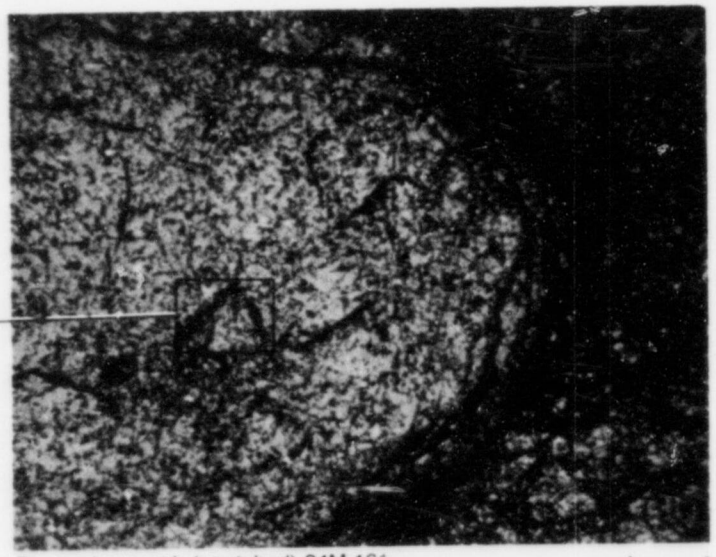

Photomicrograph (unetched) 84M-161

200 μm

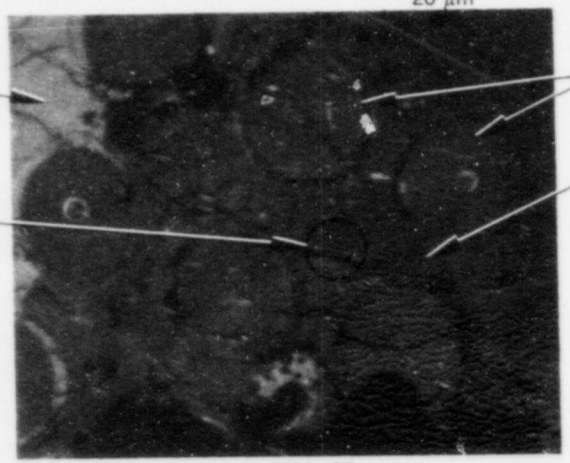

STM-4 macrophotograph 83M-107

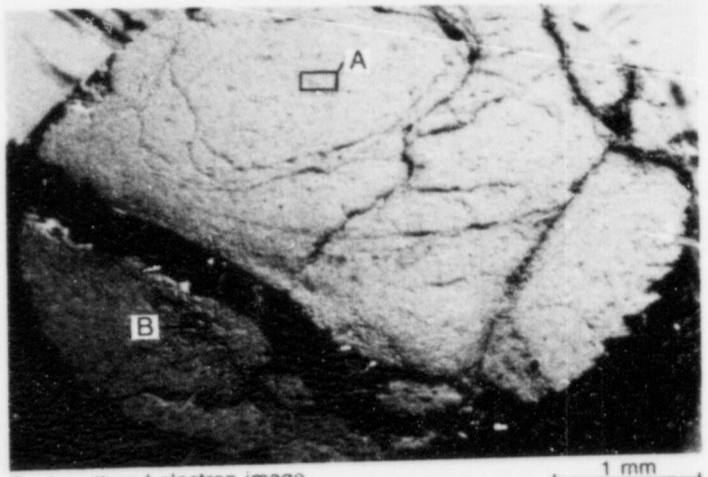

Backscattered electron image

1 mm

Area average: U-65.1 wt %, Zr-35.0 wt %, plus traces of Fe, Ni and Cr
Area A: U-63.5 wt %, Zr-36.5 wt %
Area B: U-67.6 wt %, Zr-32.4 wt %

Figure E-45. Microstructure and composition of oxidized melt Sample 4H. (0.145 m).

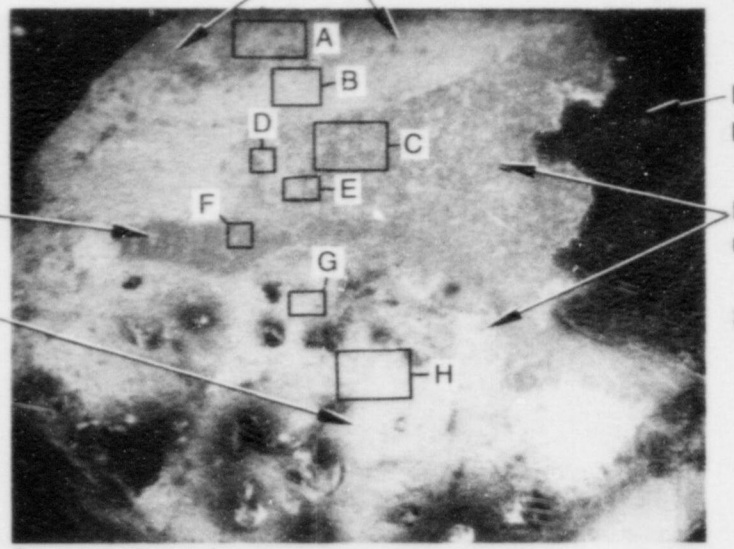

Secondary electron image

Macrophotograph from STM-4 83M-107

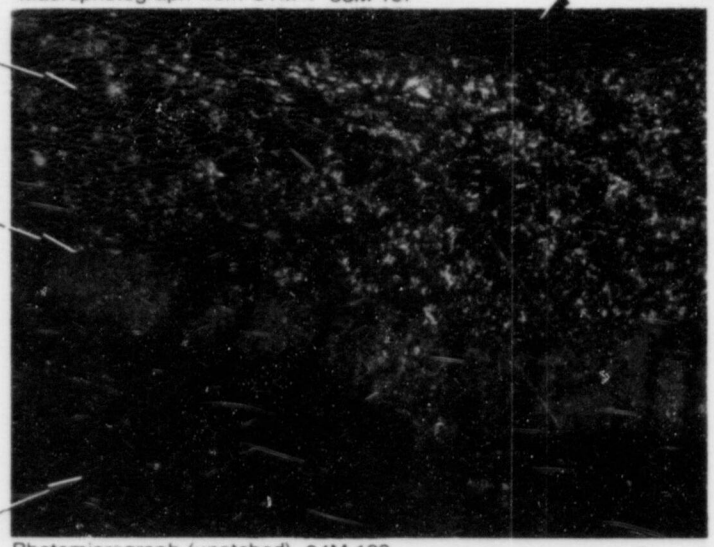

Photomicrograph (unetched) 84M-183

Area A: (EDS) U-76.1 wt%, Zr-17.2 wt%, Fe-6.7 wt%,
Area B: (EDS) U-87.2 wt%, Zr-11.1 wt%, Fe-1.7 wt%
(SAS) O-66.1 at. %, U-23.8 at. %, Zr-10.2 at. %, plus trace of Fe
Area C: (EDS) Zr-63.7 wt%, U-24.0 wt%, Ni-6.4 wt%, Fe-3.3 wt%, Cr-2.6 wt%
Area D: (SAS) Zr-48.1 at. %, O-37.0 at. %, U-5.6 at. %, Ni-5.6 at. %, Fe-3.7 at. %
Area E: (SAS) Zr-49.9 at. %, O-34.2 at. %, Ni-7.0 at. %, Fe-4.5 at. %, U-4.4 at. %
Area F: (SAS) O-51.9 at. %, Zr-39.6 at. %, U-8.5 at. %, plus traces of Ni, Fe and Cs
Area G: (EDS) U-58.4 wt%, Zr-40.3 wt%, Cr-1.4 wt%, plus traces of Fe and Ni
(SAS) O-58.1 at. %, Zr-21.5 at. %, U-13.0 at. %, Fe-3.8 at. %, Ni-3.6 at. %
Area H: (EDS) U-60.2 wt%, Zr-38.7 wt%, Cr-1.1 wt%

Figure E-46. Summary of elemental composition data from melt interaction Sample 4I (0.145 m).

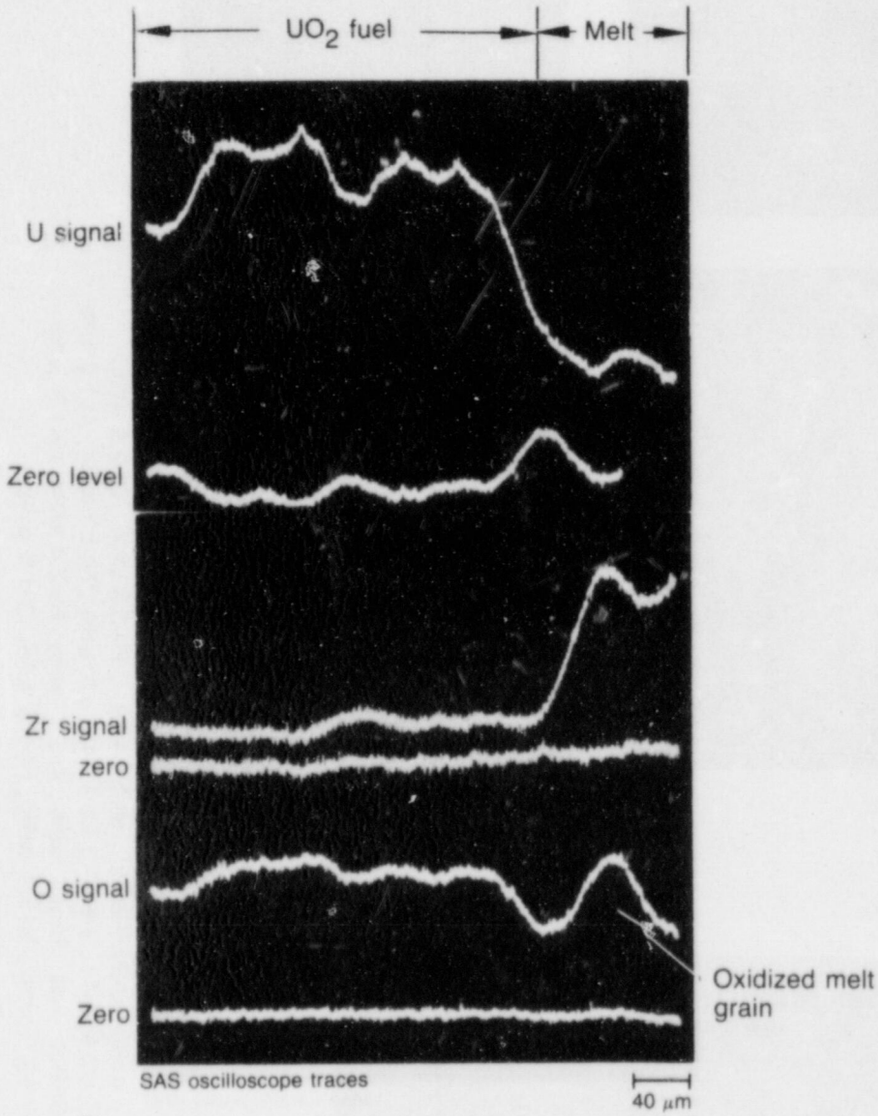

Backscattered electron image

Area average: U-76.1 wt%,
Area I: U-77.9 wt%, Zr-17.9
Area J: U-88.0 wt%, Zr-6.1
Point K: U-63.0 wt%, Zr-23.

Backscattered electron image

Metallic melt

Figure E-47. Distributions of primary elements within interface on Sample 41.

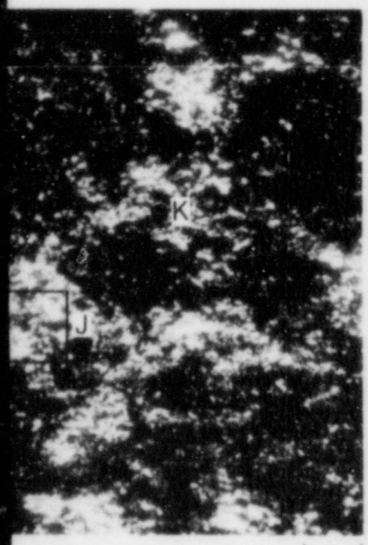

68 μm

Zr-17.2 wt%, Fe-6.7 wt %
wt %, Fe-4.3 wt%
wt %, Fe-5.0 wt%, Cr-1.0 wt%
9 wt %, Fe-12.3 wt%

227 μm

Path of U, Zr, and O line scans

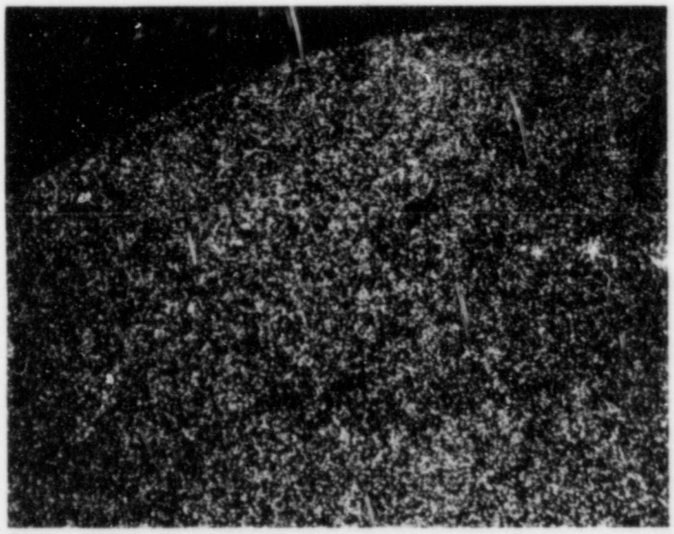

Fe x-ray image

227 μm

U x-ray image

227 μm

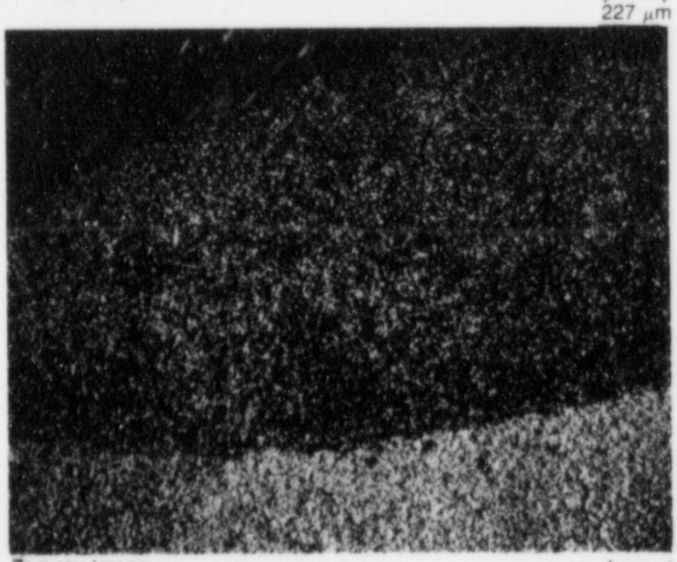

Zr x-ray image

227 μm

the partially reacted fuel and near the fuel/metallic melt

TI
APERTURE
CARD

Also Available On
Aperture Card

8609300386-07

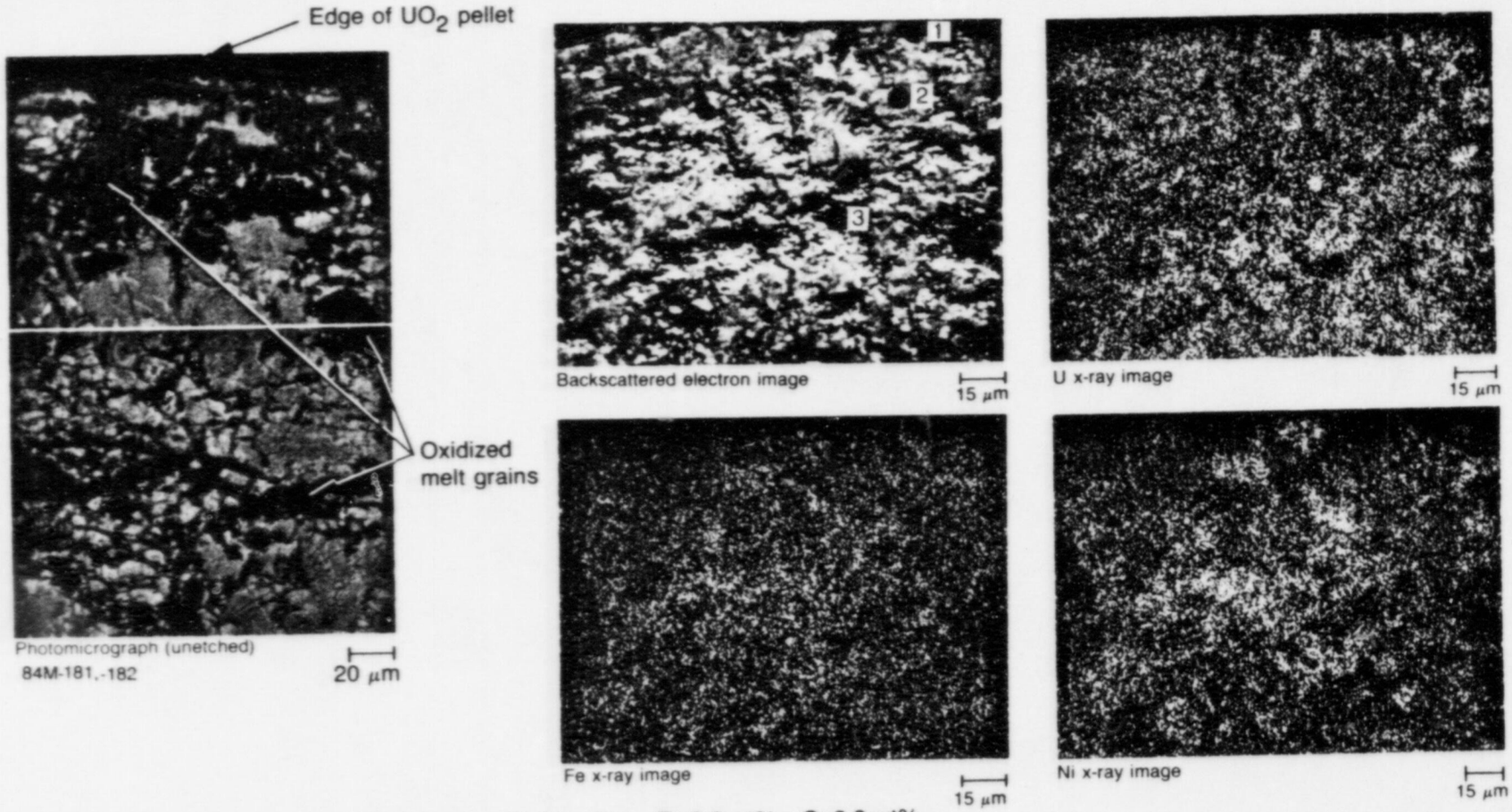

Area C average: Zr-63.7 wt% , U-24.0 wt% , Ni-6.4 wt% , Fe-3.3 wt% , Cr-2.6 wt%
Point 1: Zr-48.5 wt% , Cr-23.5 wt% , Fe-10.8 wt% , U-10.6 wt% , Ni-4.8 wt% , Al-1.9 wt%
Point 2: Zr-77.4 wt% , Sn-8.8 wt% , Ni-6.5 wt% , Al-3.7 wt% , Fe-2.4 wt% , Cr-1.3 wt%
Point 3: U-70.0 wt% , Zr-20.7 wt% , Ni-5.0 wt% , Fe-2.8 wt% , Cr-1.6 wt%

Figure E-48. Fine structure of the Zr-rich, predominately metallic melt, within Area C of Sample 41.

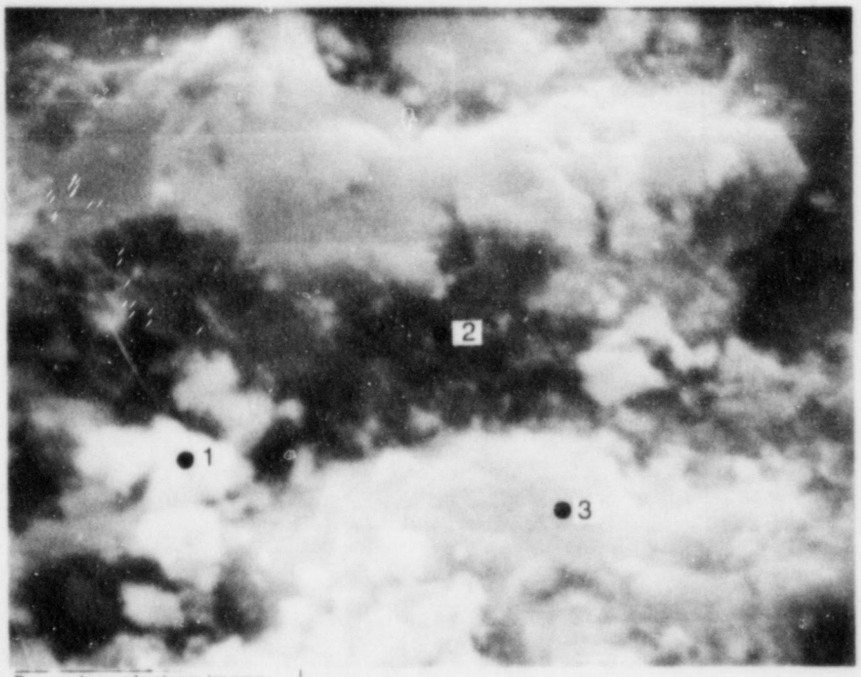

Secondary electron image

2.6 μm

Point 1: U-70.8 wt %,
Zr-24.9 wt %,
Ni-3.2 wt %,
Fe-1.1 wt %
Point 2: Zr-53.9 wt %,
Ni-36.6 wt %,
Fe-7.1 wt %,
Cr-2.4 wt %
Point 3: Zr-79.8 wt %,
Sn-8.9 wt %,
Ni-8.5 wt %,
Fe-2.1 wt %,
Cr-0.8 wt %

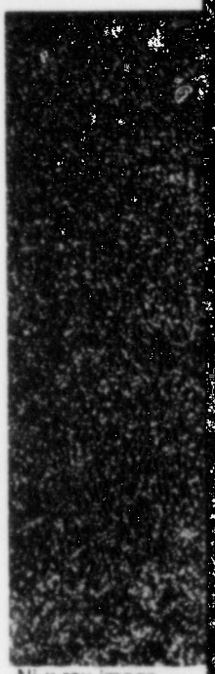

Ni x-ray image

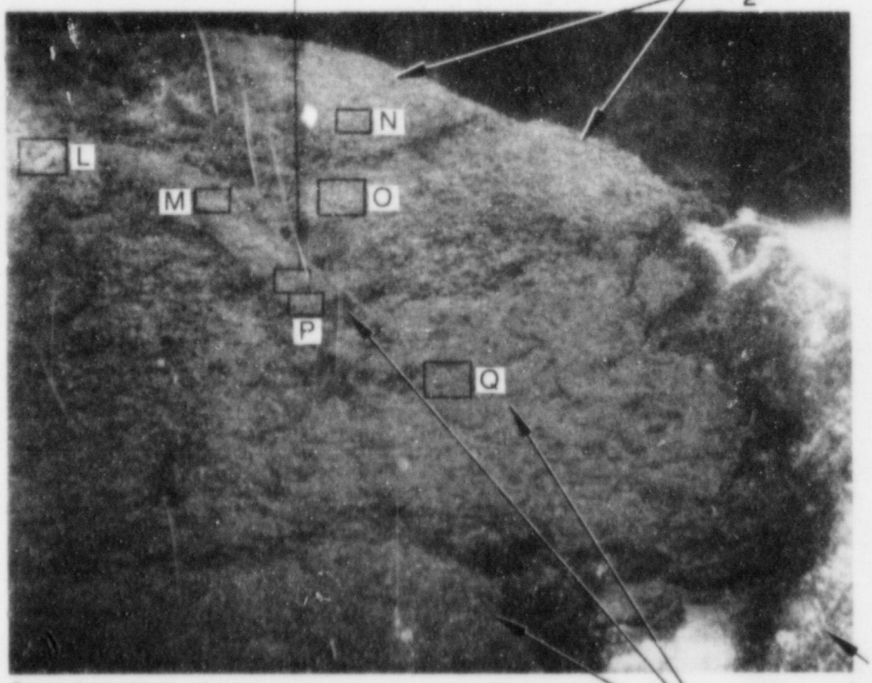

Secondary electron image

128 μm

Epoxy filled pore

Metallic melt

Area L: U-64.8 wt %,
Zr-30.4 wt %,
Fe-3.5 wt %,
Ni-1.4 wt %
Area M: Zr-61.0 wt %,
U-21.1 wt %,
Ni-9.9 wt %,
Fe-4.5 wt %,
Cr-3.4 wt %
Area N: U-100.0 wt %
Area O: U-93.0 wt %,
Zr-6.5 at. %
Fe-0.6 wt %
Area P: Zr-67.8 wt %,
Ni-11.0 wt %,
U-9.2 wt %,
Fe-5.4 wt %,
Sn-3.3 wt %,
Cr-2.6 wt %
Area Q: Zr-67.8 wt %,
U-22.5 wt %,
Ni-5.0 wt %,
Fe-2.7 wt %,
Cr-2.1 wt %

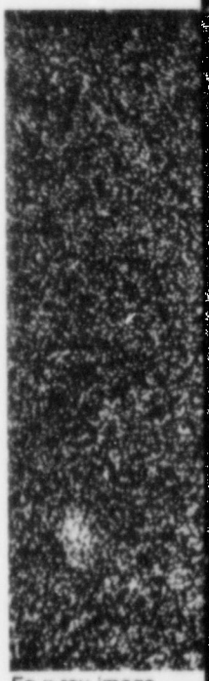

Fe x-ray image

Figure E-49. Melt penetrati

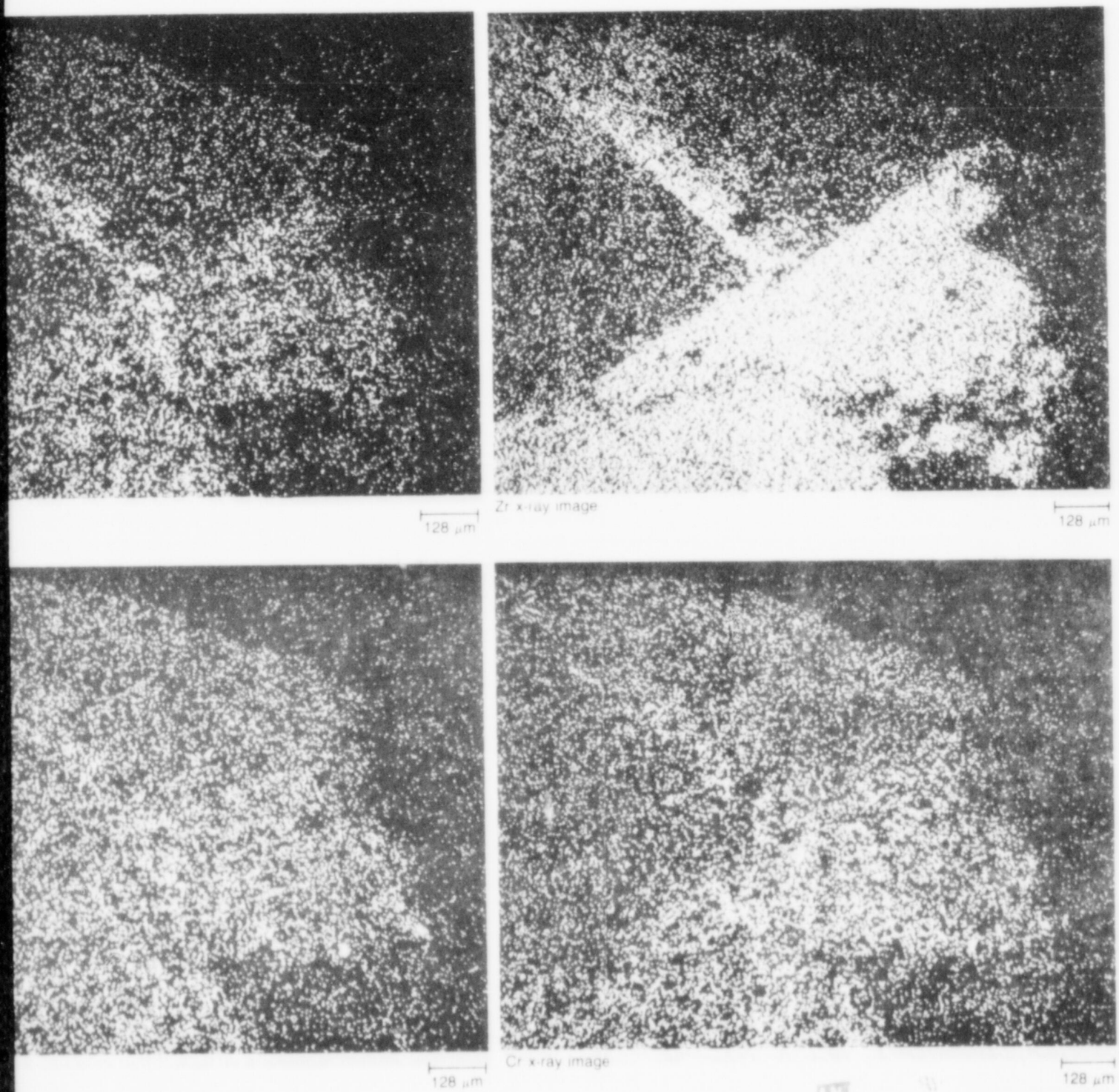

on along pellet crack in Sample 4I.

TI
APERTURE
CARD

Also Available On
Aperture Card

8609300386-08

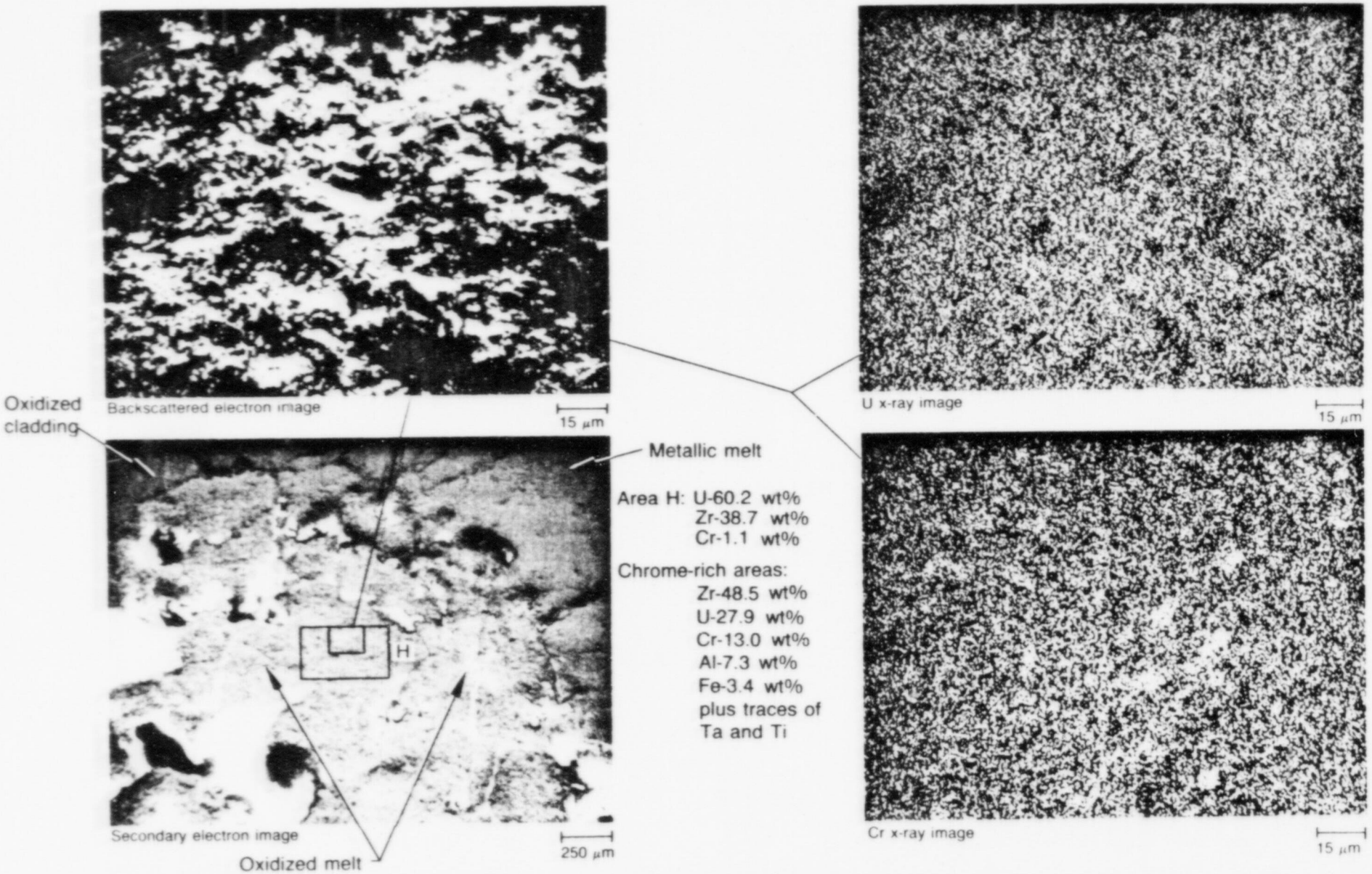

Figure E-50. Oxidized melt investigations in Sample 41.

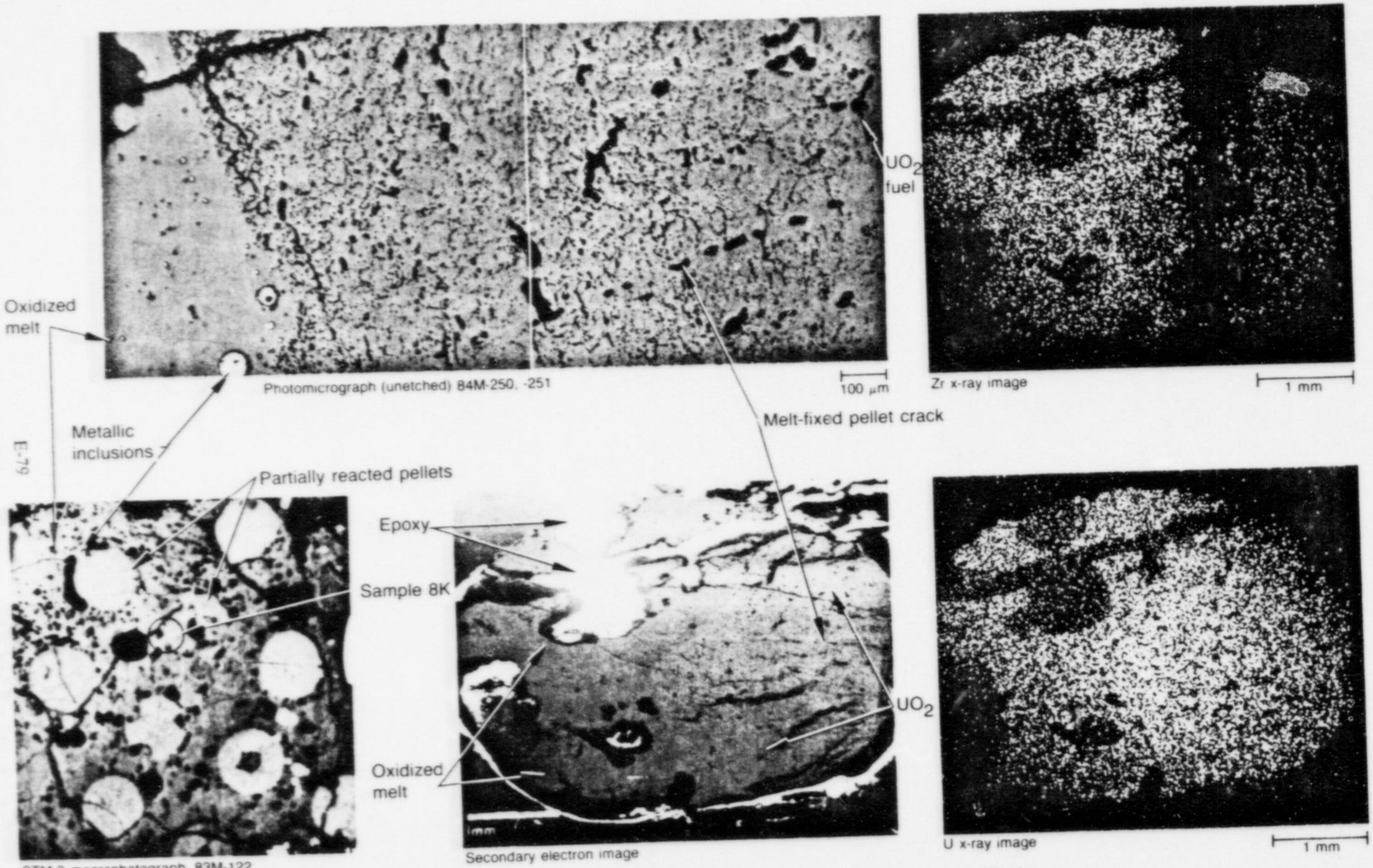

Figure E-51. Sample 8K (0.245 m), illustrating melt attack of a fuel pellet before melt solidification.

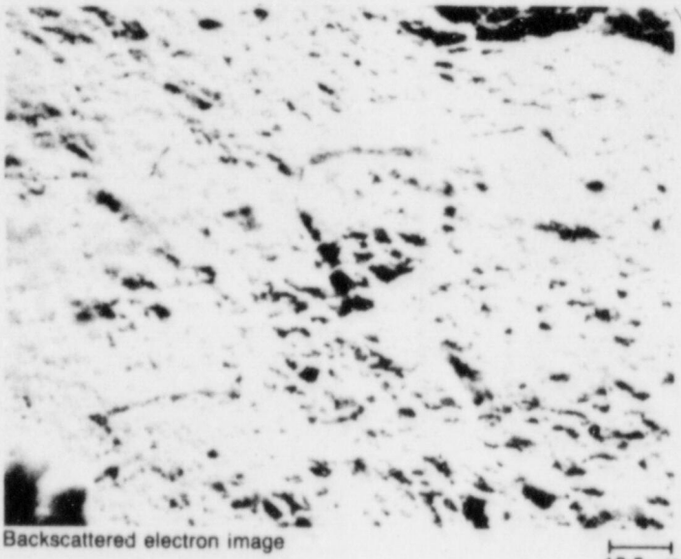

Backscattered electron image

12.5 μm

EDS: U-74.6 wt%, Zr-22.7 wt%, Fe-2.2 wt%, Ni-0.5 wt%, trace of Cr

Backscattered electron image

Inclusion (EDS): Ni-54.8 w
U-13.7 w

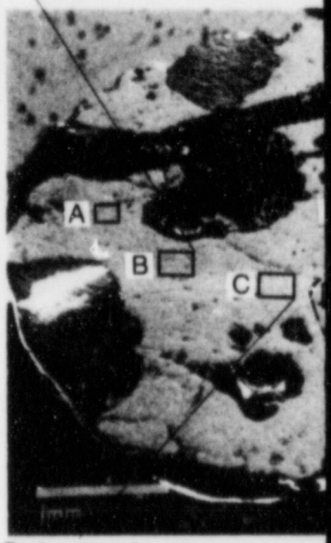

Backscattered electron image

Sample average (EDS): U-82.1 wt%, Zr-14.0
Area A (EDS): U-74.1 wt%, Zr-22.3 wt%, Fe-
Area D (EDS): U-97.7 wt%, Fe-2.4 wt%, trac
(SAS): O-64.8 at. %, U-25.2 at. %, Fe

Backscattered electron image

EDS: U-76.5 wt%, Zr-20.8 wt%, Fe-2.1 wt%, Ni-0.6 wt%, trace of Cr
SAS: O-63.3 at. %, U-19.9 at. %, Zr-9.5 at. %, Fe-7.4 at. %

Figure E-52. Summary of semiquantitative EDS (wt

TI
APERTURE
CARD

Also Available On
Aperture Card

17 μm

t %, Mo-24.5 wt %,
%, Fe-7.1 wt %

Melt-filled pellet crack

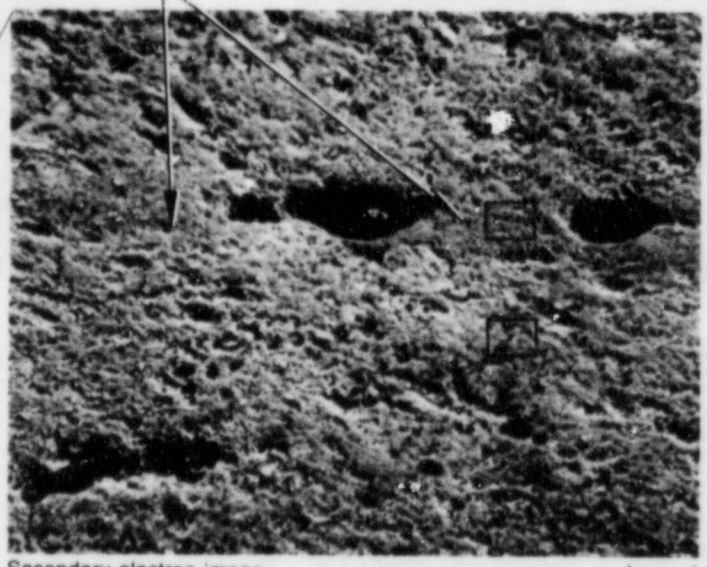

Secondary electron image

25 μm

Crack (EDS): U-80.5 wt %, Zr-16.1 wt %, Fe-3.5 wt %, trace of Ni
(SAS): O-63.5 at. %, Fe-20.7 at. %, U-13.3 at. %, Zr-2.5 at. %
Matrix (EDS): U-95.2 wt %, Fe-4.9 wt %
(SAS): O-62.9 at. %, Fe-25.4 at. %, U-11.7 at. %

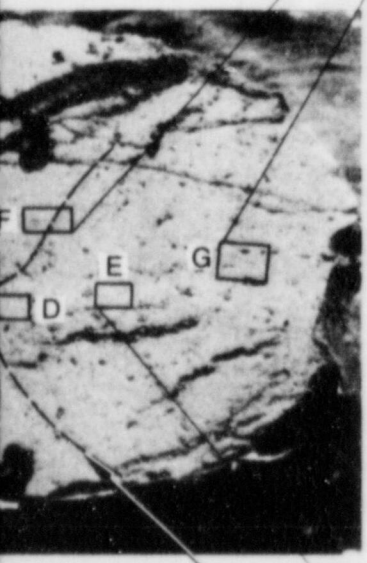

Melt-pellet
interface

wt%, Fe-3.3 wt %, Ni-0.7 wt %, trace of Cr
.0 wt %, Ni-0.6 wt %, trace of Cr
of Zr
10.0 at. %

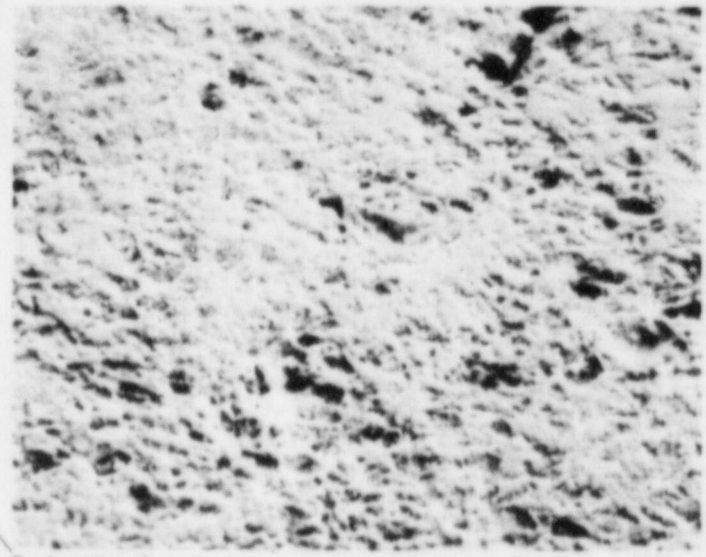

Backscattered electron image

12.5 μm

EDS: U-97.9 wt %, Fe-1.8 wt %, Ni-0.4 wt %, trace of Zr

%) and quantitative SAS (at. %) results from Sample 8K.

8609300386-09

Backscattered electron image

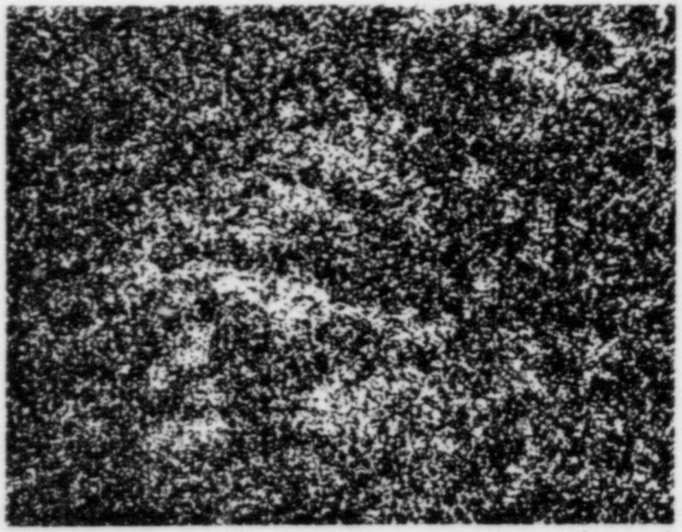

Fe x-ray image

12.5 μm

Area average (EDS): U-97.7 wt%, Fe-2.4 wt%
Point 1: U-94.5 wt%, Fe-5.6 wt%, traces of Zr and Ni
Point 2: U-86.4 wt%, Fe-13.7 wt%, traces of Zr and Ni

Figure E-53. Fe-rich phase within Area D of Sample 8K. (Possible formation of a U/Fe/O eutectic at temperature.)

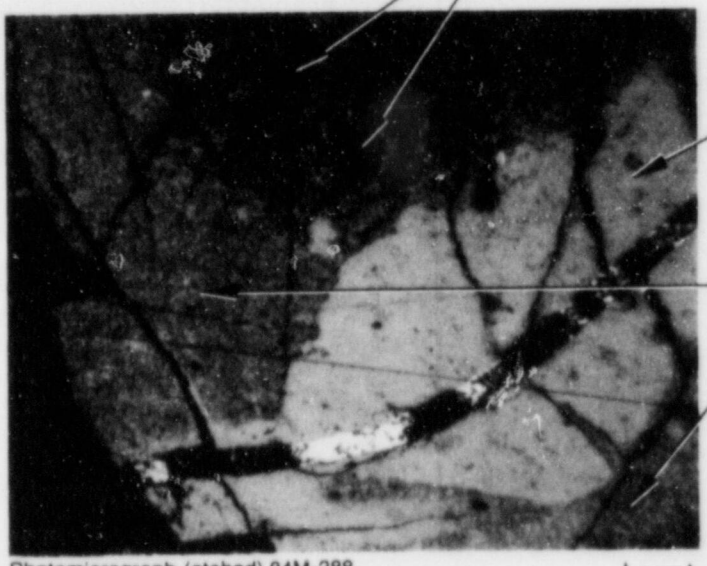

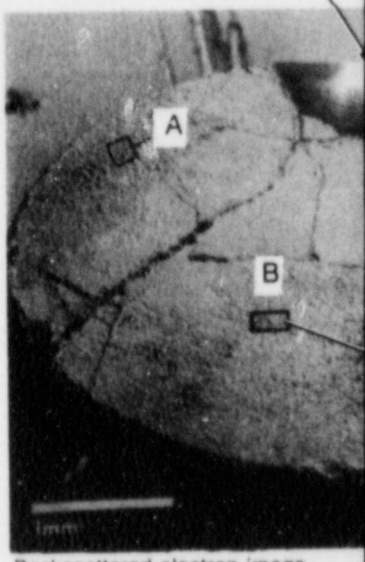

Area A (EDS): U-100.0 wt %
Area D (EDS): U-69.7 wt %

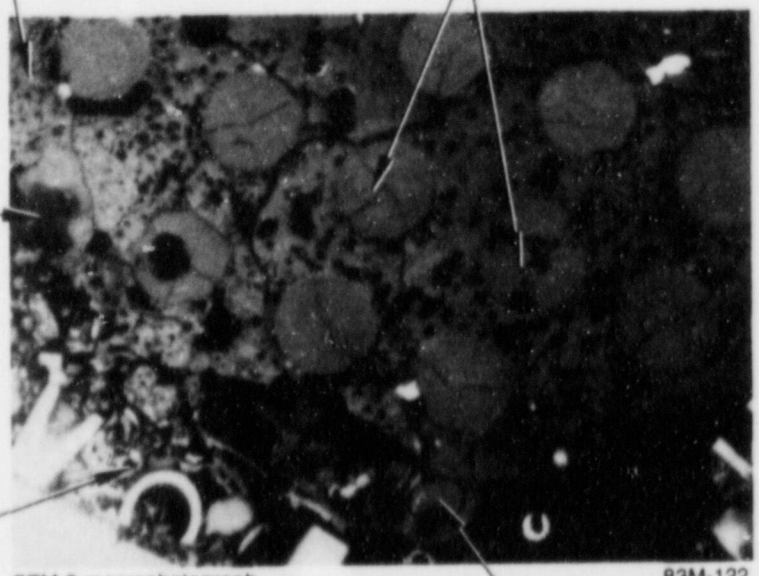

Figure E-54. Composition findings on fuel microstructures t
slumped to the 0.245-m bundle elevation.

TI
APERTURE
CARD

Also Available On
Aperture Card

Backscatterd electron image

EDS: U-100.0 wt%, traces of Zr, Fe, and Ni

17 μm

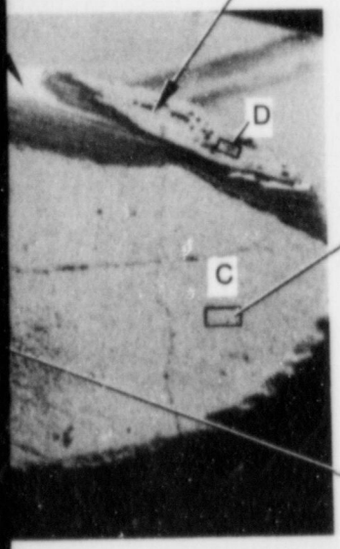

, traces of Ni, Zr, and Fe
Zr-30.4 wt%, traces of Fe, Ni and Cr

Backscattered electron image

EDS: U-100.0 wt%, traces of Zr, Fe, and Ni

h Sample 8L, extracted from a fuel pellet remnant that

8609300386-10

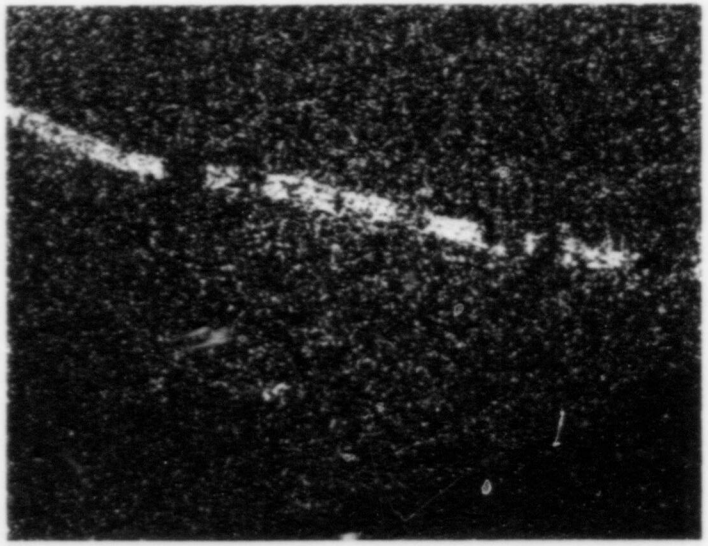

Ni x-ray image

172 μm

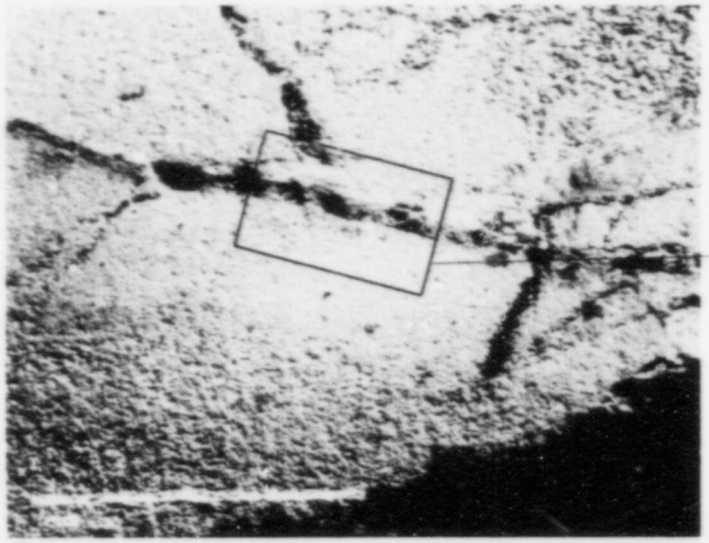

Backscattered electron image

172 μm

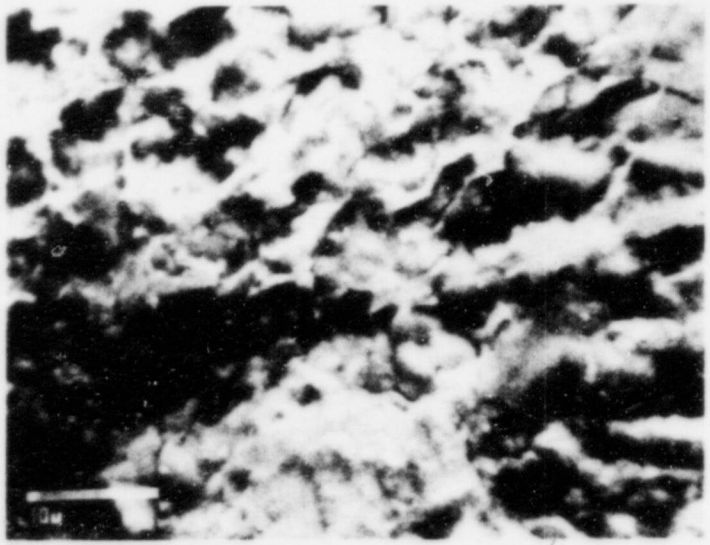

Backscattered electron image

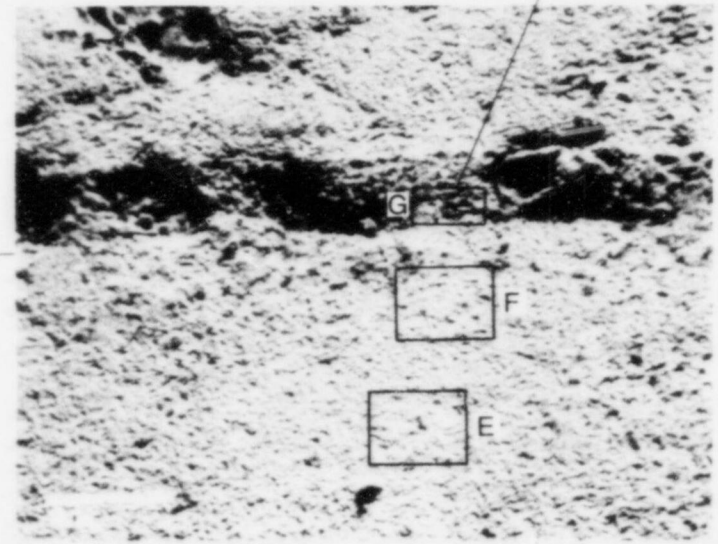

Backscattered electron image

45 μm

Area E: U-99.6 wt%, Ni-0.4 wt%, trace of Fe
Area F: U-95.6 wt%, Ni-1.8 wt%, W-1.5 wt%, Fe-1.1 wt%
Area G: U-47.7 wt%, Ni-39.5 wt%, Fe-8.6 wt%, W-4.3 wt%

Figure E-55. SEM/EDS results in melt-filled crack region of Sample 8L.

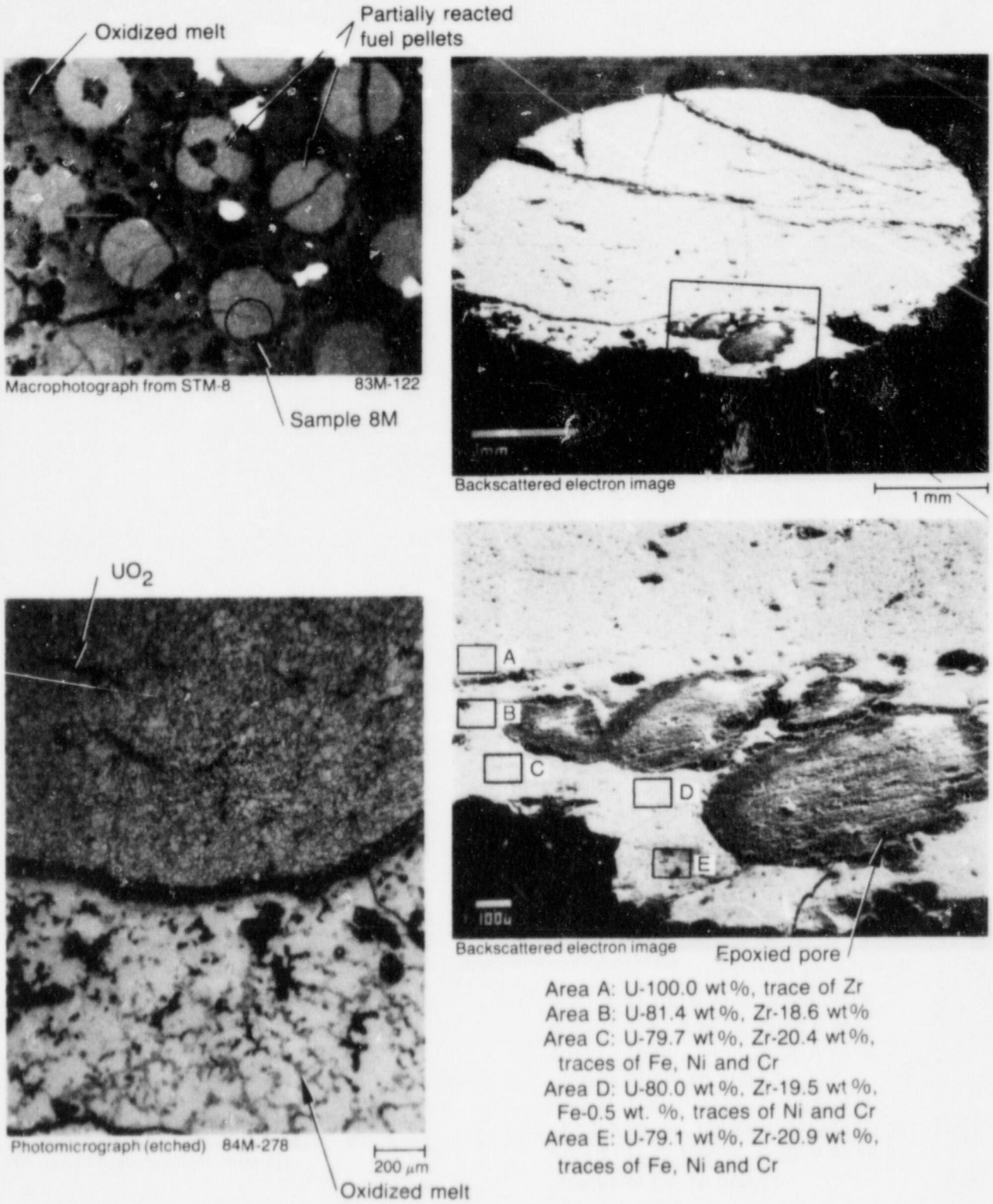

Area A: U-100.0 wt%, trace of Zr
Area B: U-81.4 wt%, Zr-18.6 wt%
Area C: U-79.7 wt%, Zr-20.4 wt%, traces of Fe, Ni and Cr
Area D: U-80.0 wt%, Zr-19.5 wt%, Fe-0.5 wt. %, traces of Ni and Cr
Area E: U-79.1 wt%, Zr-20.9 wt %, traces of Fe, Ni and Cr

Figure E-56. SEM/EDS results from coated pellet Sample 8M (0.245 m).

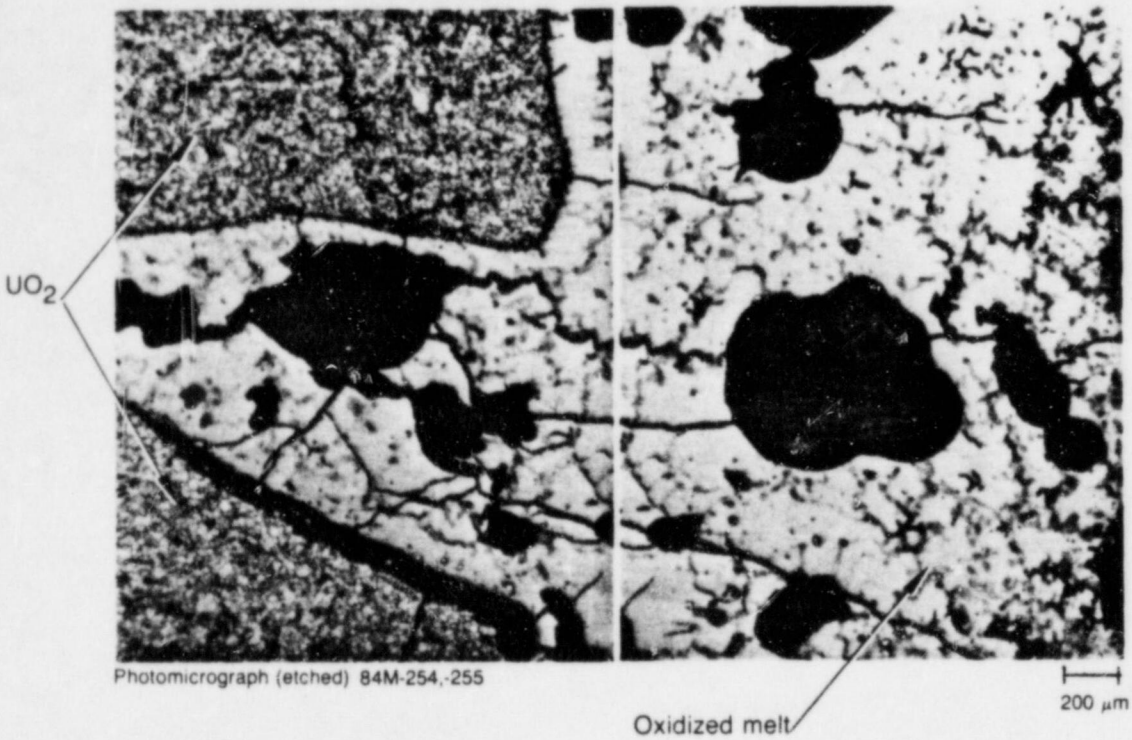

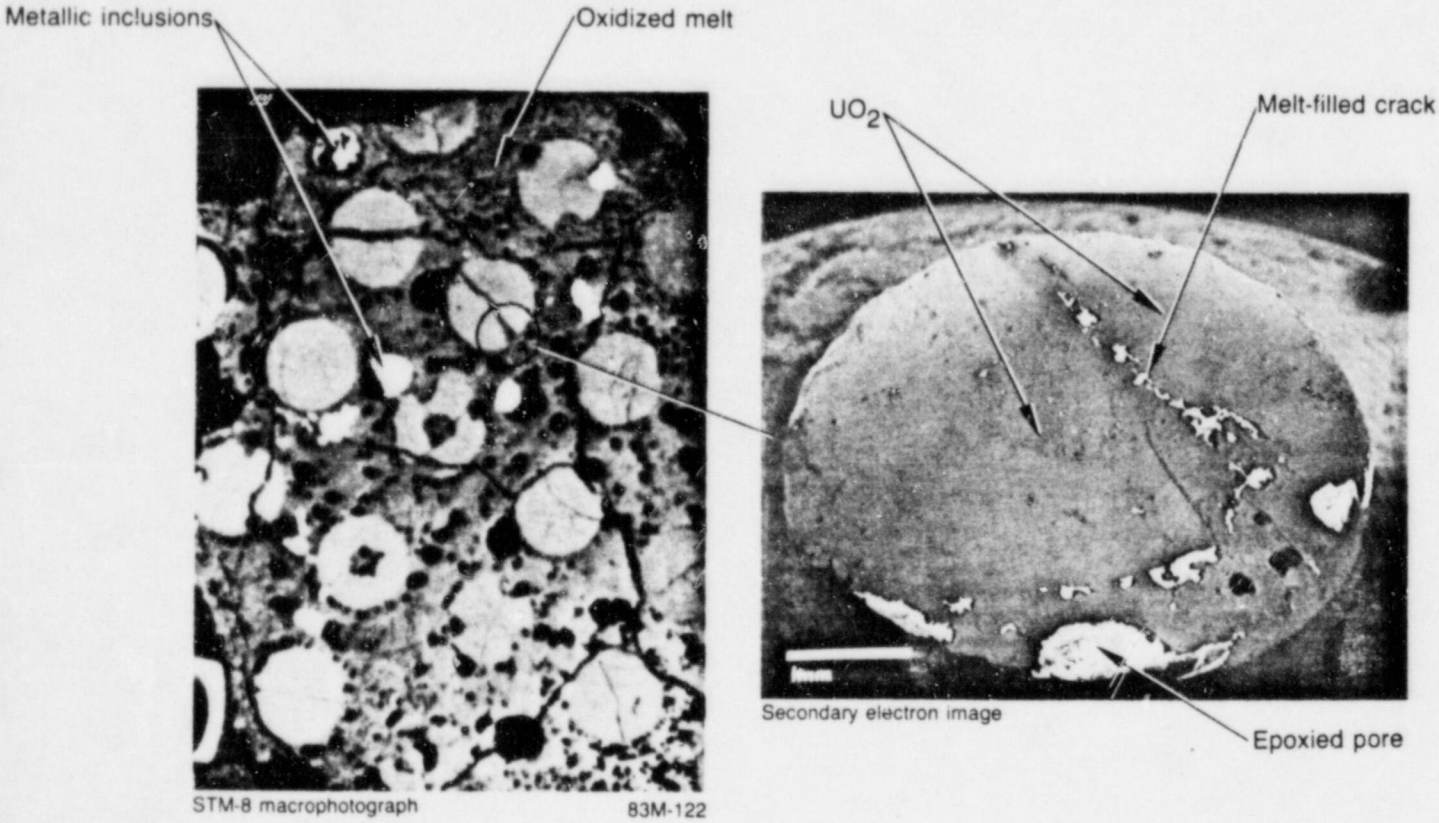

Figure E-57. Crack penetration Sample 8N (0.245 m).

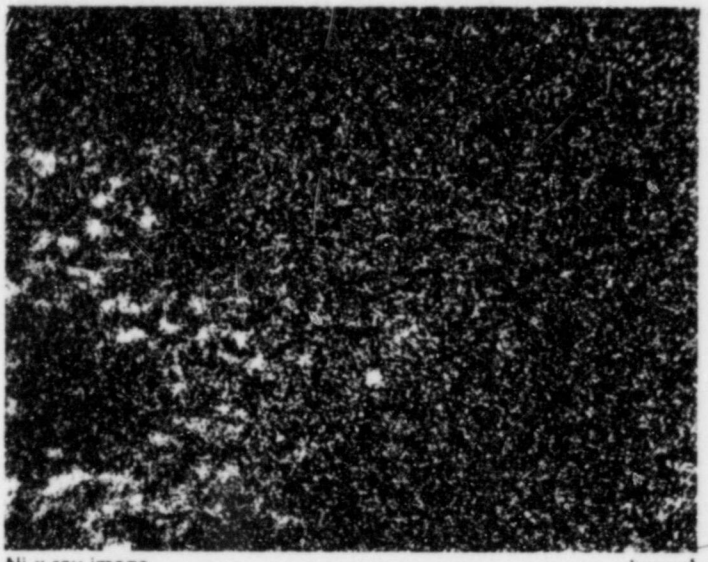

Ni x-ray image

12.5 μm

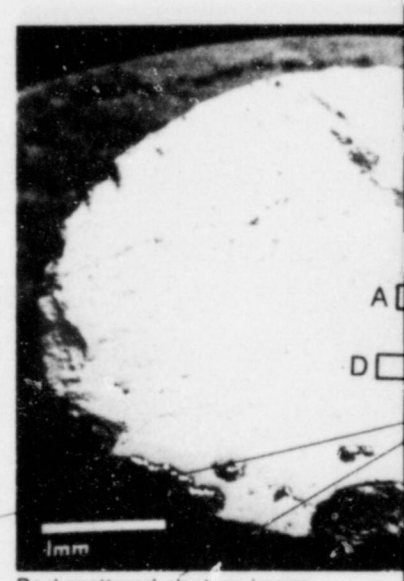

Backscattered electron image

Area A: U-100.0 wt %, trace o
Area D: U-100.0 wt %, traces
Area F: U-82.0 wt %, Zr-18.0 w

Backscattered electron image

Area E: U-98.5 wt %, Ni-1.6 wt %, traces of Zr, Fe and Cr

Backscattered electron image

Area G: U-79.6 wt %, Zr-20.4 wt %
Point 1: Ni-98.1 wt %, Fe-1.8 wt %
Point 2: U-58.6 wt %, Zr-41.4 wt %
Point 3: U-79.5 wt %, Zr-20.5 wt %

Figure E-58. SEM/EDS fi

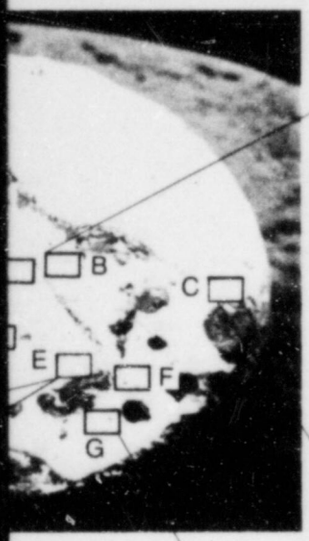

Zr
of Zr and Ni
t %, traces of Ni, Fe, and Cr

Backscattered electron image

12.5μm

Area B: U-81.1 wt %, Zr-18.9 wt%, traces of Fe and Cr

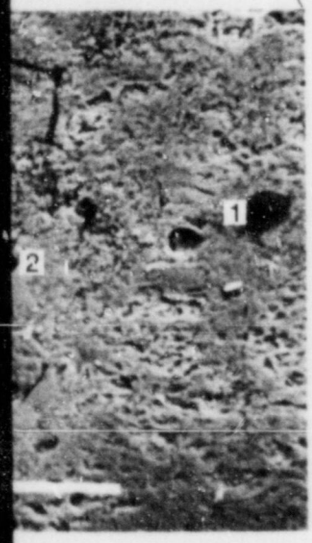

, traces of Ni, Fe and Cr
, trace of U
, trace of Fe
, trace of Fe

dings from Sample 8N.

Backscatered electron image

12.5 μm

Area C: U-77.8 wt %, Zr-22.3 wt %, traces of Fe, Cr and Ni

TI
APERTURE
CARD

Also Available On
Aperture Card

8609300386-11

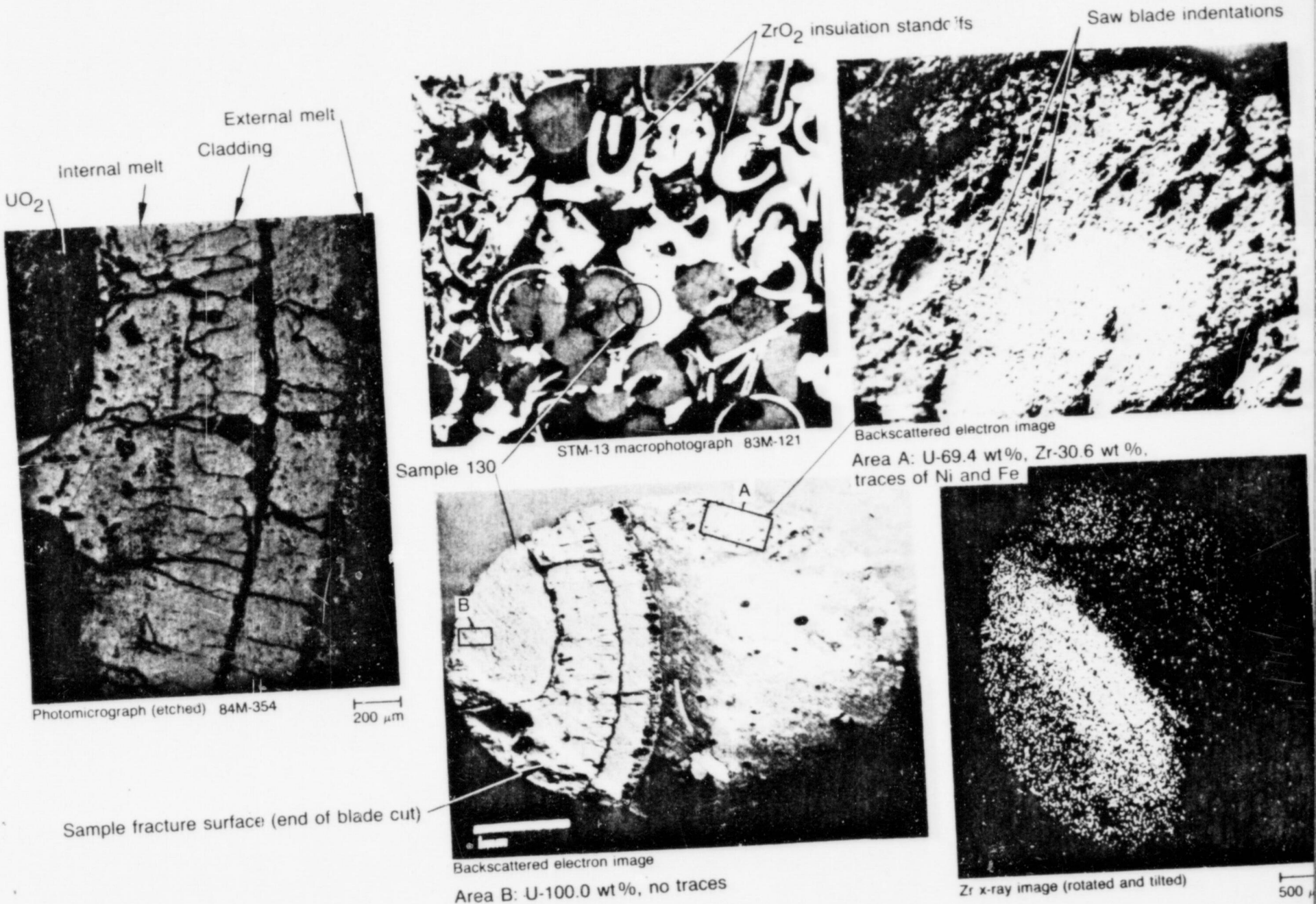

Figure E-59. Fuel liquefaction Sample 130 (0.495 m) elevation. (Saw-cut side of water was inadvertently mounted upward.)

Backscattered electron image

Area E: U-73.2 wt%,
Zr-26.8 wt%,
traces of Ni,
Fe and Cr

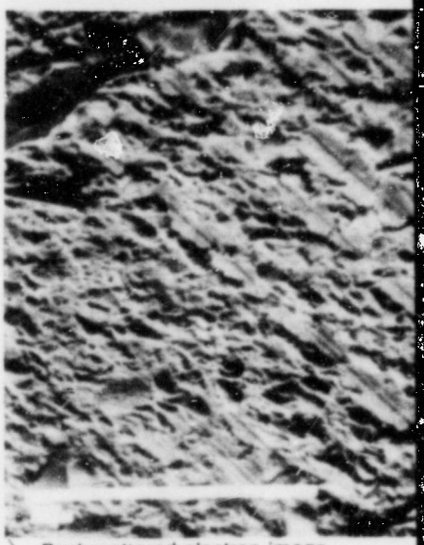

Backscattered electron image

Area F: U-63.7 wt%, Zr-
traces of Ni, Fe

Backscattered electron image

Area D: U-100.0 wt%,
trace of Zr

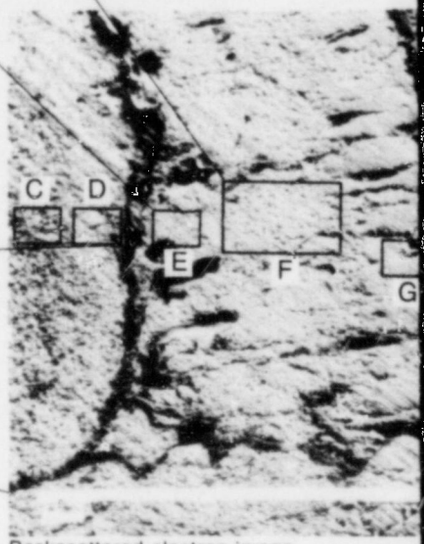

Backscattered electron image

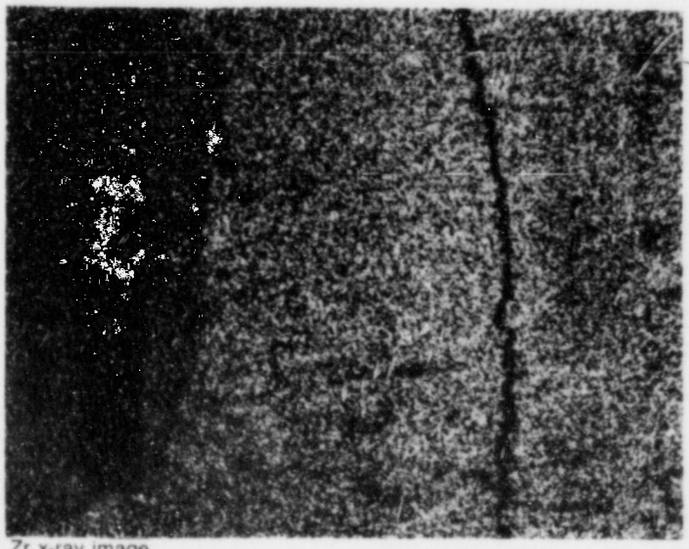

Zr x-ray image

133 μm

Area C: U-100.0 wt %, no traces
Area H: Zr-100.0 wt %, trace of U
Area I: Zr-99.8 wt %, Ti-0.4 wt %,

Figure E-60. SEM/EDS results fom fuel/melt/cla

TI
APERTURE
CARD

Also Available On
Aperture Card

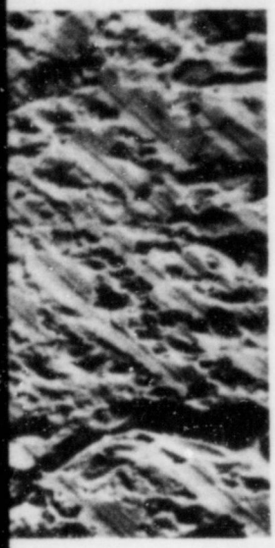

20 μm

6.3 wt %,
and Cr

Area G: Zr-68.3 wt %,
U-31.6 wt %

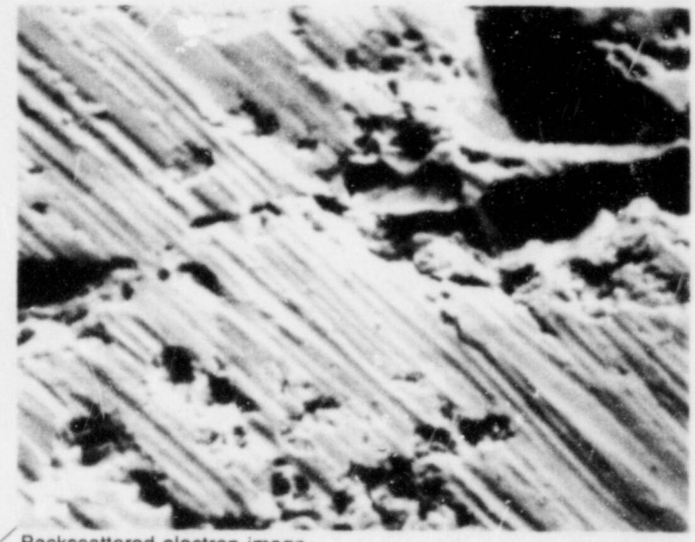

Backscattered electron image

10 μm

Area J: Zr-96.2 wt %,
Ti-1.4 wt %,
Fe-0.9 wt %,
Cr-0.9 wt %,
Ni-0.7 wt%,
trace of U

Backscattered electron image

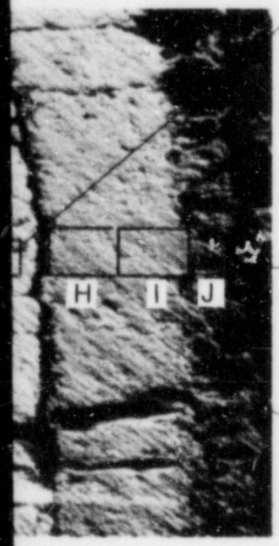

133 μm

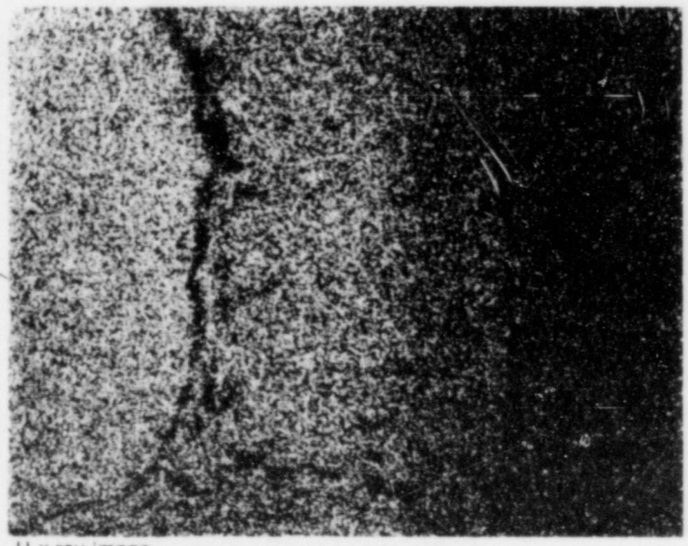

U x-ray image

133 μm

traces of U and Fe

ding interaction zone on Sample 130.

8609300386-12

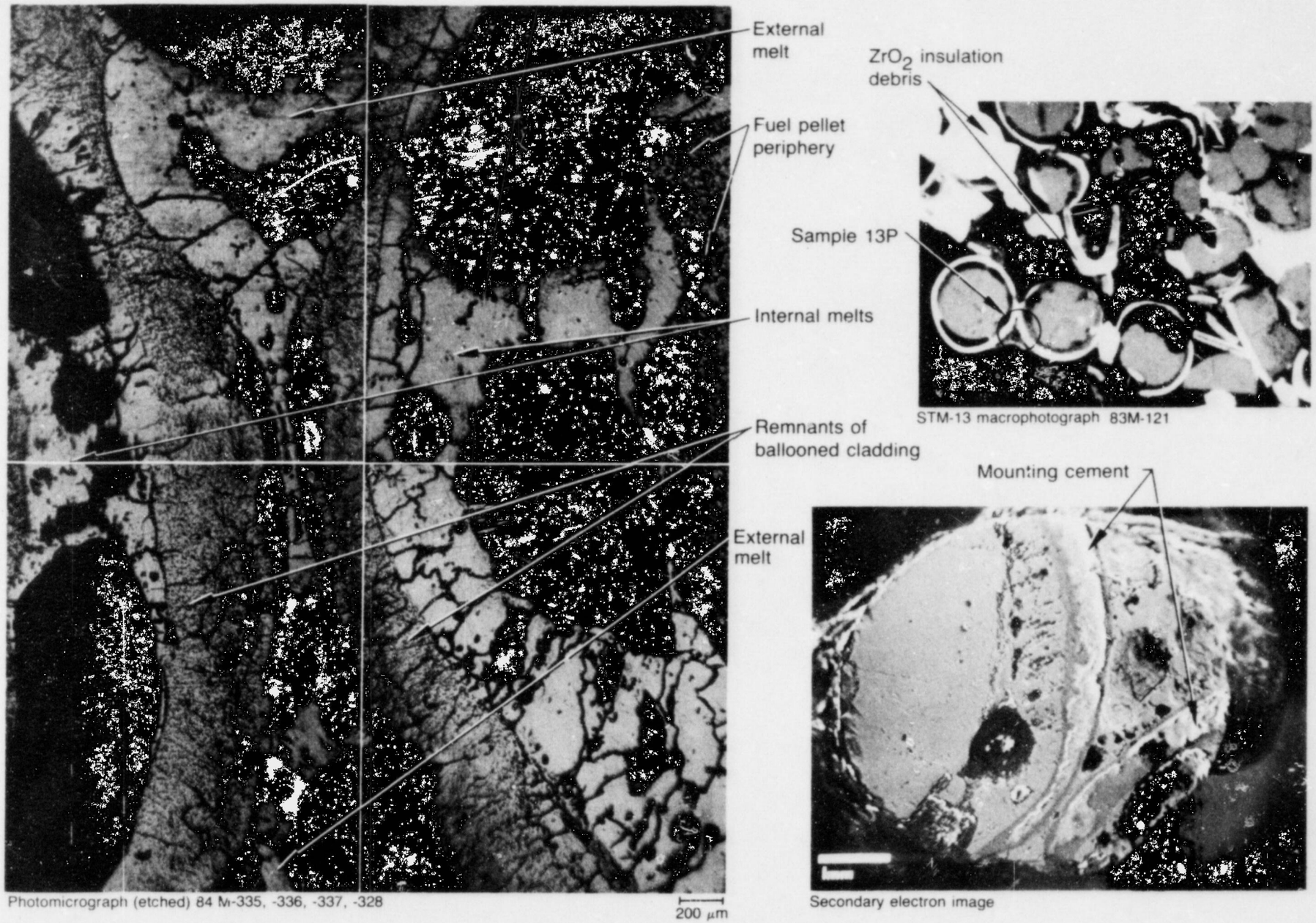

Figure E-61. Melt interaction Sample 13P (0.495 m).

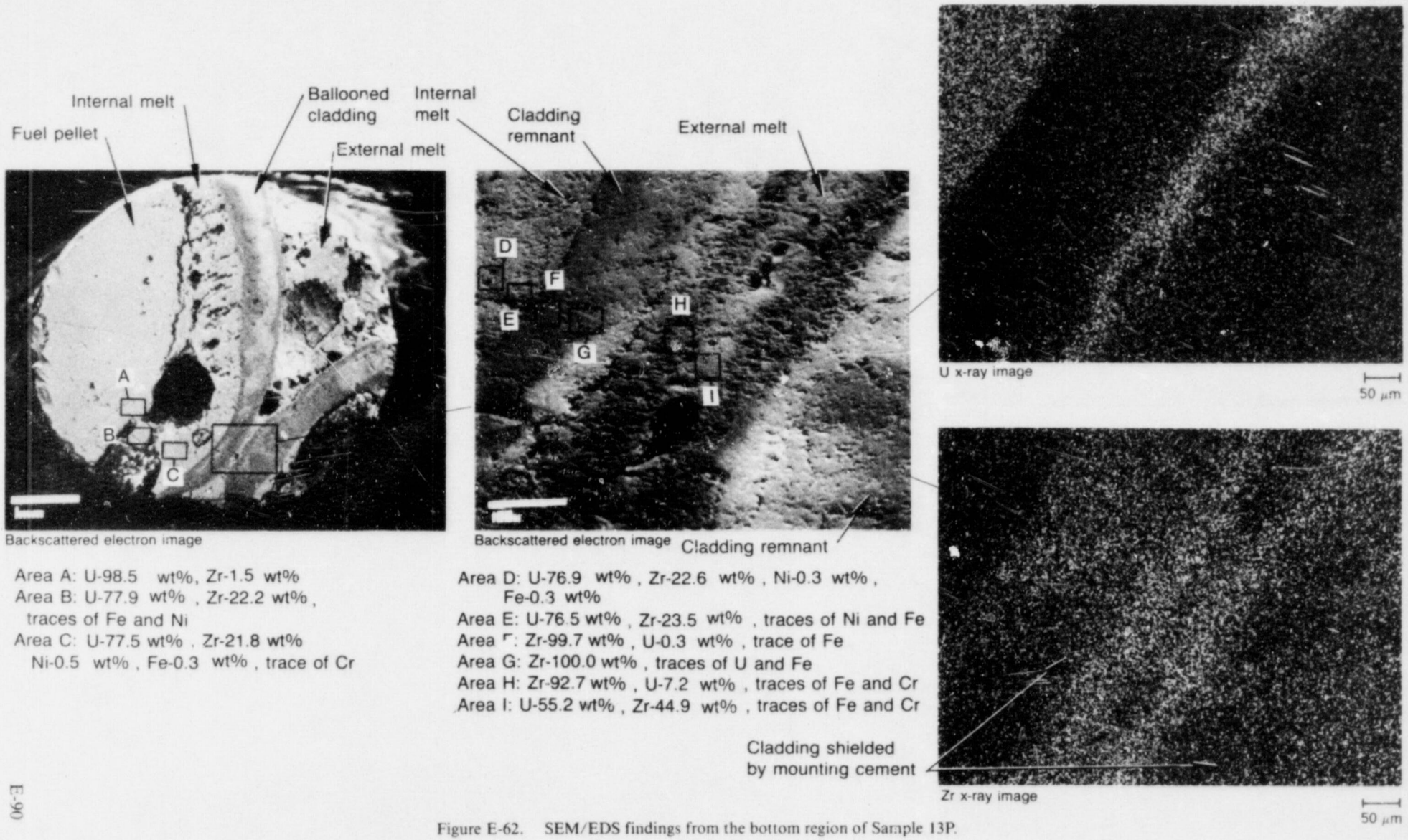

Area A: U-98.5 wt%, Zr-1.5 wt%
Area B: U-77.9 wt% , Zr-22.2 wt% , traces of Fe and Ni
Area C: U-77.5 wt% , Zr-21.8 wt% Ni-0.5 wt% , Fe-0.3 wt% , trace of Cr

Area D: U-76.9 wt% , Zr-22.6 wt% , Ni-0.3 wt% , Fe-0.3 wt%
Area E: U-76.5 wt% , Zr-23.5 wt% , traces of Ni and Fe
Area F: Zr-99.7 wt% , U-0.3 wt% , trace of Fe
Area G: Zr-100.0 wt% , traces of U and Fe
Area H: Zr-92.7 wt% , U-7.2 wt% , traces of Fe and Cr
Area I: U-55.2 wt% , Zr-44.9 wt% , traces of Fe and Cr

Figure E-62. SEM/EDS findings from the bottom region of Sample 13P.

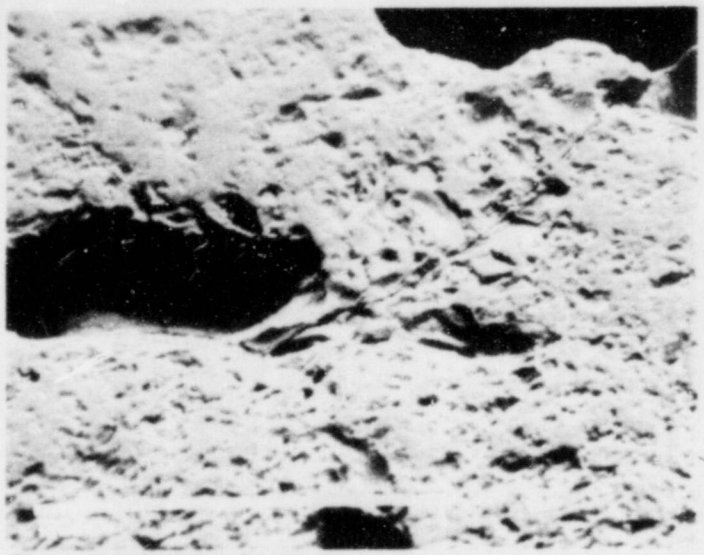

Backscattered electron image

Area O: U-73.0 wt%, Zr-27 ı wt%, traces of Fe and Ni

Backscattered electron image

Area J:
U-68.3 wt%,
Zr-31.4 wt%,
Ni-0.3 wt%,
trace of Fe

Cladding remnant

Cladding remnant

External melt

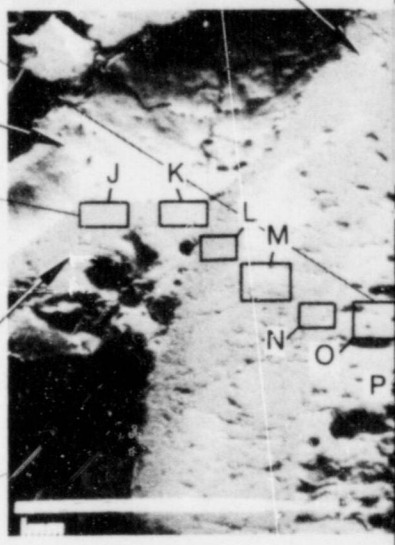

Area K: U-61.0 wt %, Zr-38.8 wt %, Ni-
Area L: Zr-75.6 wt %, U-24.0 wt %, Ni-
Area M: Zr-100.0 wt %, traces of U, Ni
Area N: Zr-100.0 wt %, traces of U, Fe
Area P: U-78.2 wt %, Zr-21.8 wt %, trac

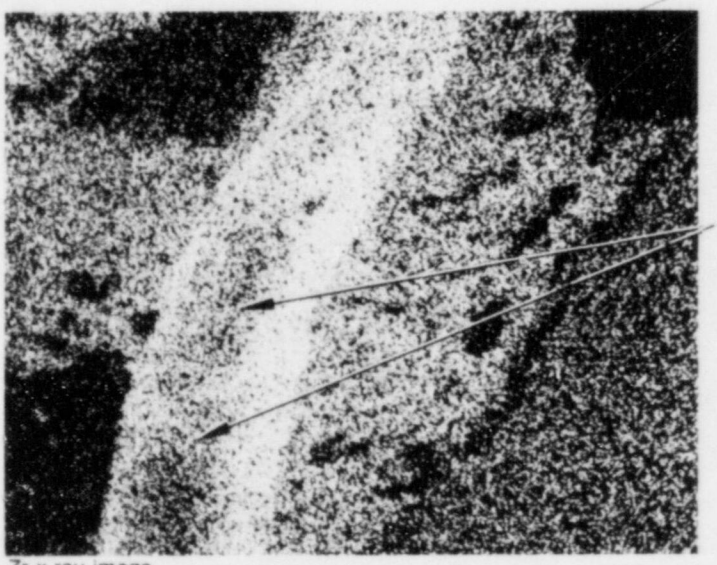

Zr x-ray image

Shielded by
mounting cement

250 μm

Figure E-63. SEM/EDS results from upper interaction
upside-down with respect to sample macropho

Area Q: U-82.6 wt %, Zr-17.5 wt %

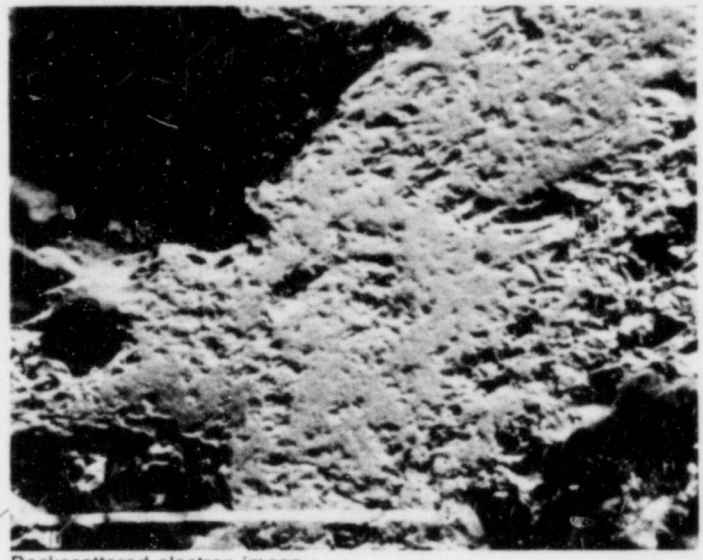

Backscattered electron image

14 μm

Internal melt

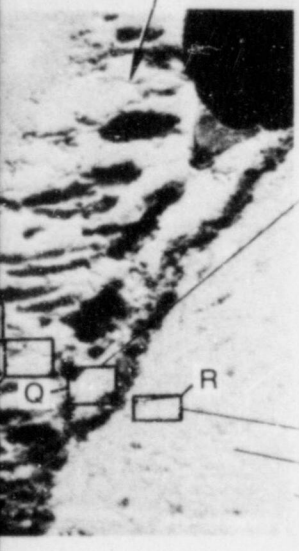

Area R:
U-100.0 wt %, trace of Zr

Backscattered electron image

Fuel pellet

.3 wt %, traces of Fe and Cr
.5 wt %, traces of Fe and Cr
Fe and Cr
and Ni
e of Fe

U x-ray image

250 μm

TI
APERTURE
CARD

Also Available On
Aperture Card

zone on Sample 13P. (Photograph orientations are
ograph.)

8609300386-13

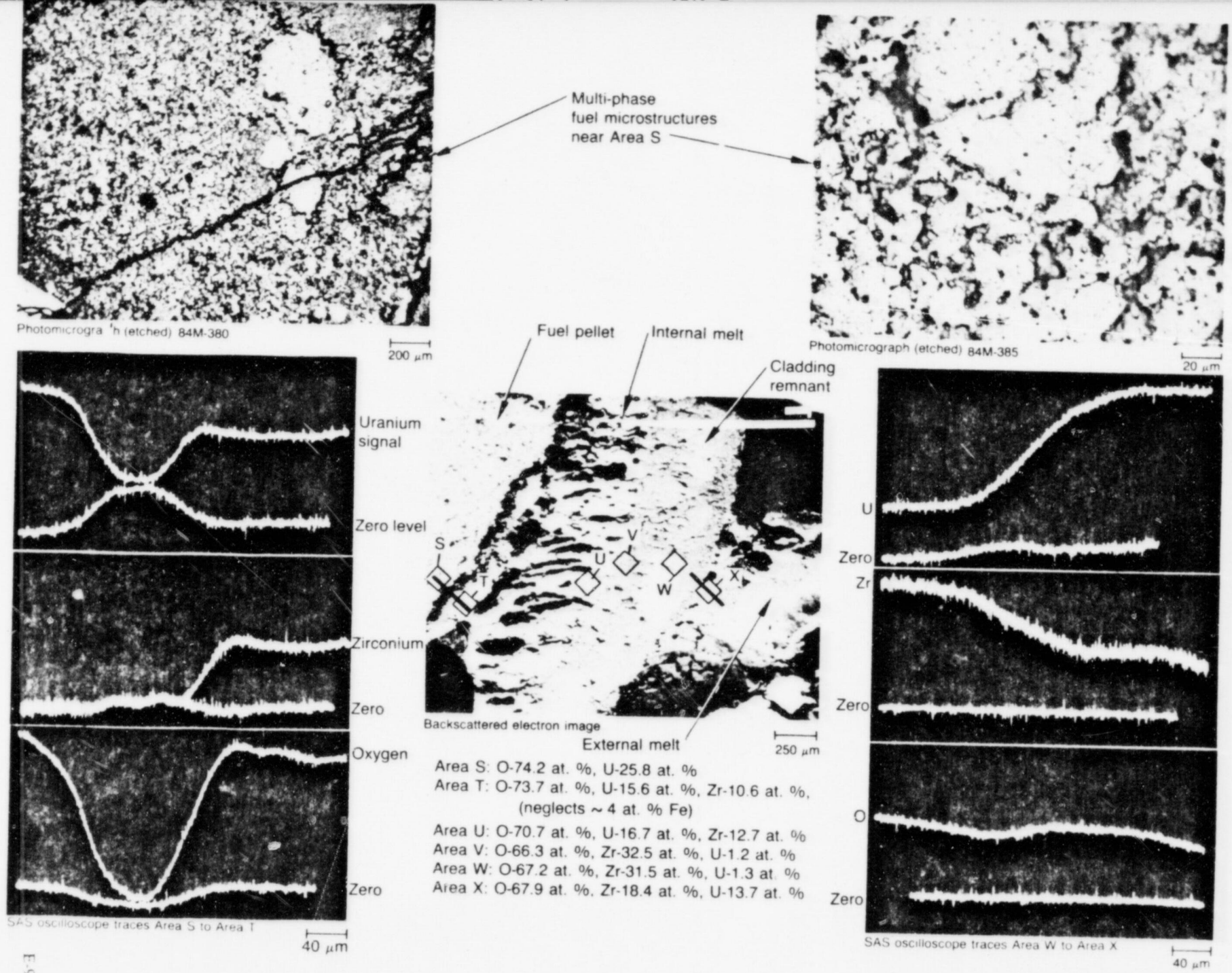

Area S: O-74.2 at. %, U-25.8 at. %
Area T: O-73.7 at. %, U-15.6 at. %, Zr-10.6 at. %,
(neglects ~ 4 at. % Fe)

Area U: O-70.7 at. %, U-16.7 at. %, Zr-12.7 at. %
Area V: O-66.3 at. %, Zr-32.5 at. %, U-1.2 at. %
Area W: O-67.2 at. %, Zr-31.5 at. %, U-1.3 at. %
Area X: O-67.9 at. %, Zr-18.4 at. %, U-13.7 at. %

Figure E-64. Quantitative SAS data from upper interaction region on Sample 13P. (Photographic orientations match sample macrophotograph.)

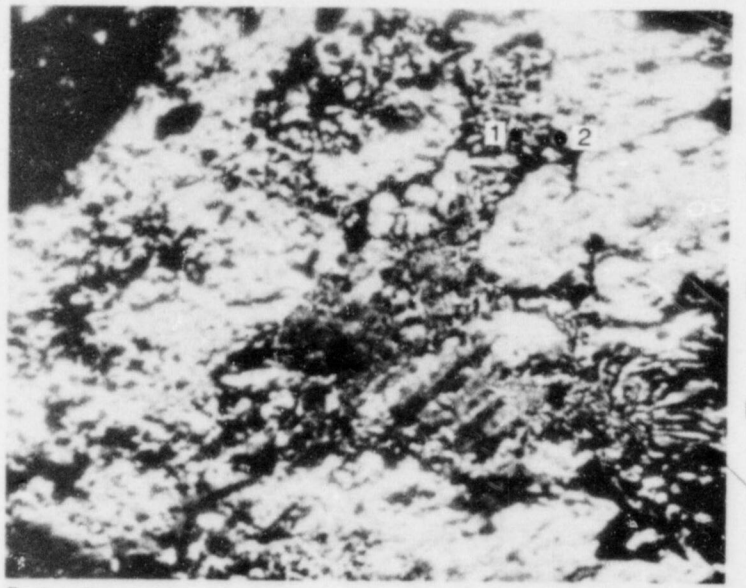

Backscattered electron image

19 μm

Area F: U-70 wt% Ni-10.9 wt%
Zr-9.5 wt% Cr-6.1 wt%
Fe-3.5 wt%

Point 1: U-59.0 wt% Cr-14.0 wt%
Zr-11.3 wt% Ni-9.8 wt%
Fe-6.0 wt%

Point 2: U-74.6 wt% Ni-10.6 wt%
Zr-9.0 wt% Fe-3.0 wt%
Cr-2.9 wt%

Partially liquefied pellet

Sample 19Q

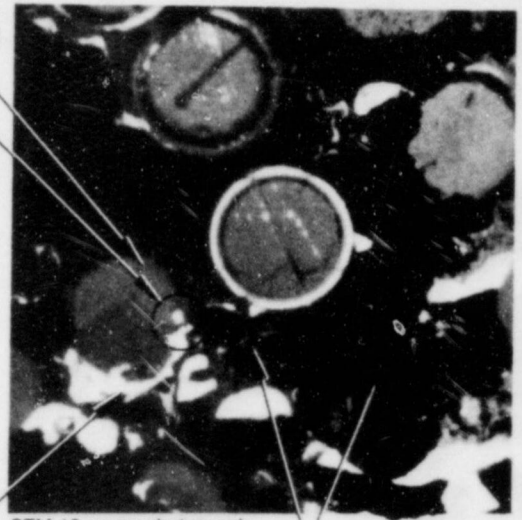

Insulation material

STM-19 macrophotograph

Reaction remnants from ballooned cladding and Inconel spacer grid

Pure U (EDS)

Area A: Zr-53.4 wt% , U-37.2 wt% , Cr-4.1 wt%, Ni-3.3 wt%, Fe-2.0 wt%
Area B: U-68.0 wt% , Zr-18.9 wt% , Ni-6.3 wt% , Cr-4.3 wt%, Fe-2.3 wt%
Area C: Zr-50.9 wt% , U-39.8 wt% , Cr-4.2 wt% , Ni-3.0 wt% , Fe-2.1 wt%
Area D: Zr-45.2 wt% , U-39.4 wt% , Cr-6.8 wt% , Ni-6.1 wt%, Fe-2.6 wt%
Area E: U-83.1 wt% , Zr-8.9 wt% , Ni-3.1 wt%, Cr-3.0 wt%, Fe-2.0

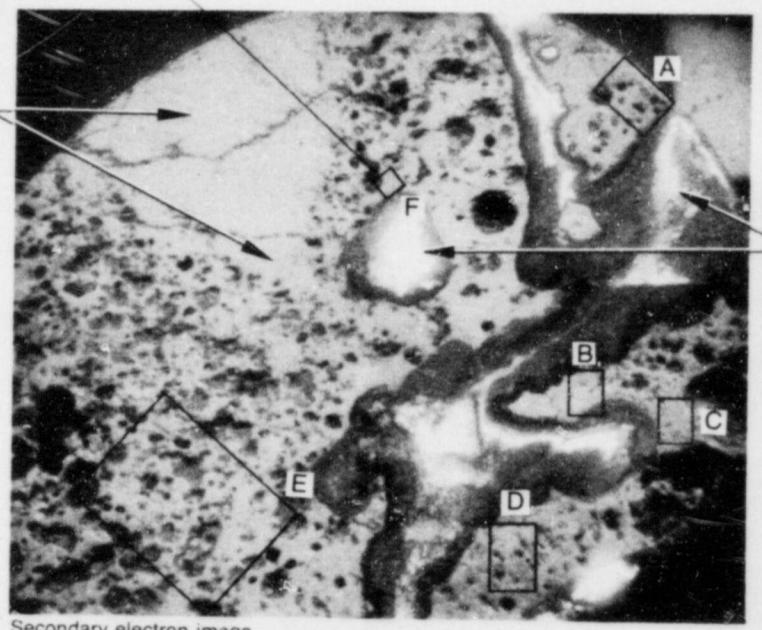

Epoxy charging artifacts

Secondary electron image

588 μm

Figure E-65. Fuel melting Sample 19Q (0.915 m).

Photomicrograph (unetched) 84M-10

200 μm

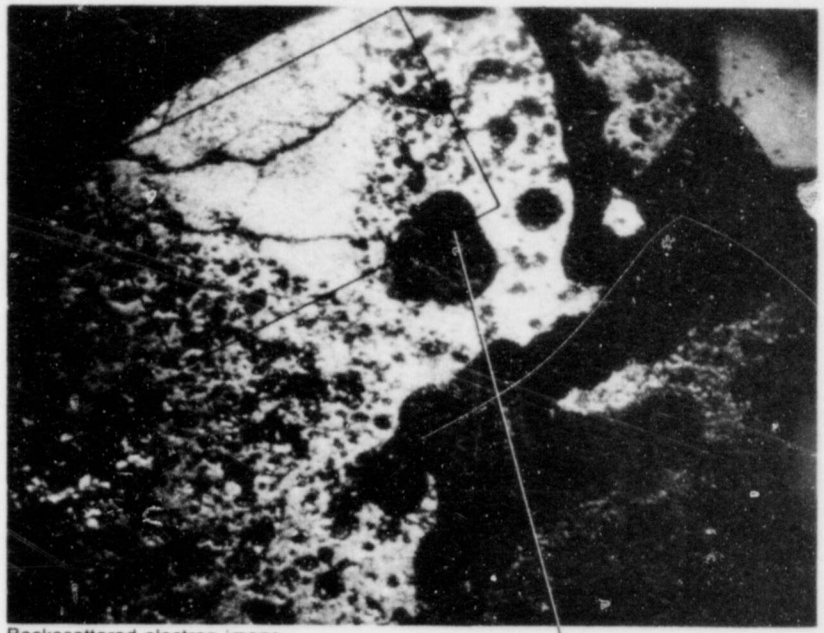

Backscattered electron image

588 μm

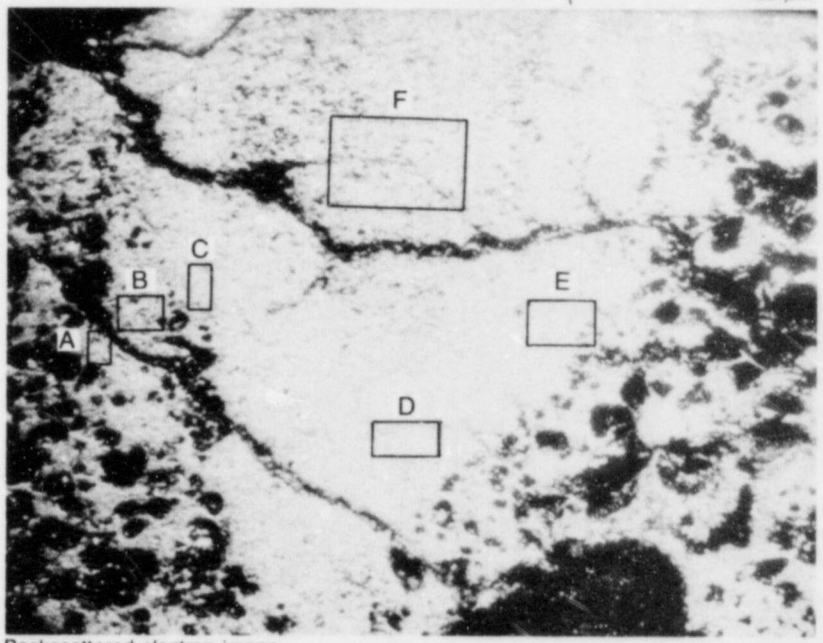

Backscattered electron image

250 μm

Area A (SAS): O-72.7 at. %, U-24.2 at. %, Zr-3.0 at. %
Area B (EDS): U-100.0 wt% , trace of Zr
Area C (SAS): O-72.2 at. %, U-25.2 at. %, Zr-2.5 at. %
Area D (SAS): O-71.6 at. %, U-28.4 at. %, trace of Zr
(EDS): U-100.0 wt% , trace of Zr
Area E (EDS): U-100.0 wt% , trace of Zr
Area F (SAS): O-69.7 at. %, U-30.3 at. %, trace of Zr
(EDS): U-98.8 wt% , Zr-1.3 wt% ,

Figure E-66. Quantitative SAS and Semiquantitative EDS results from the fuel melting region of Sample 19Q.

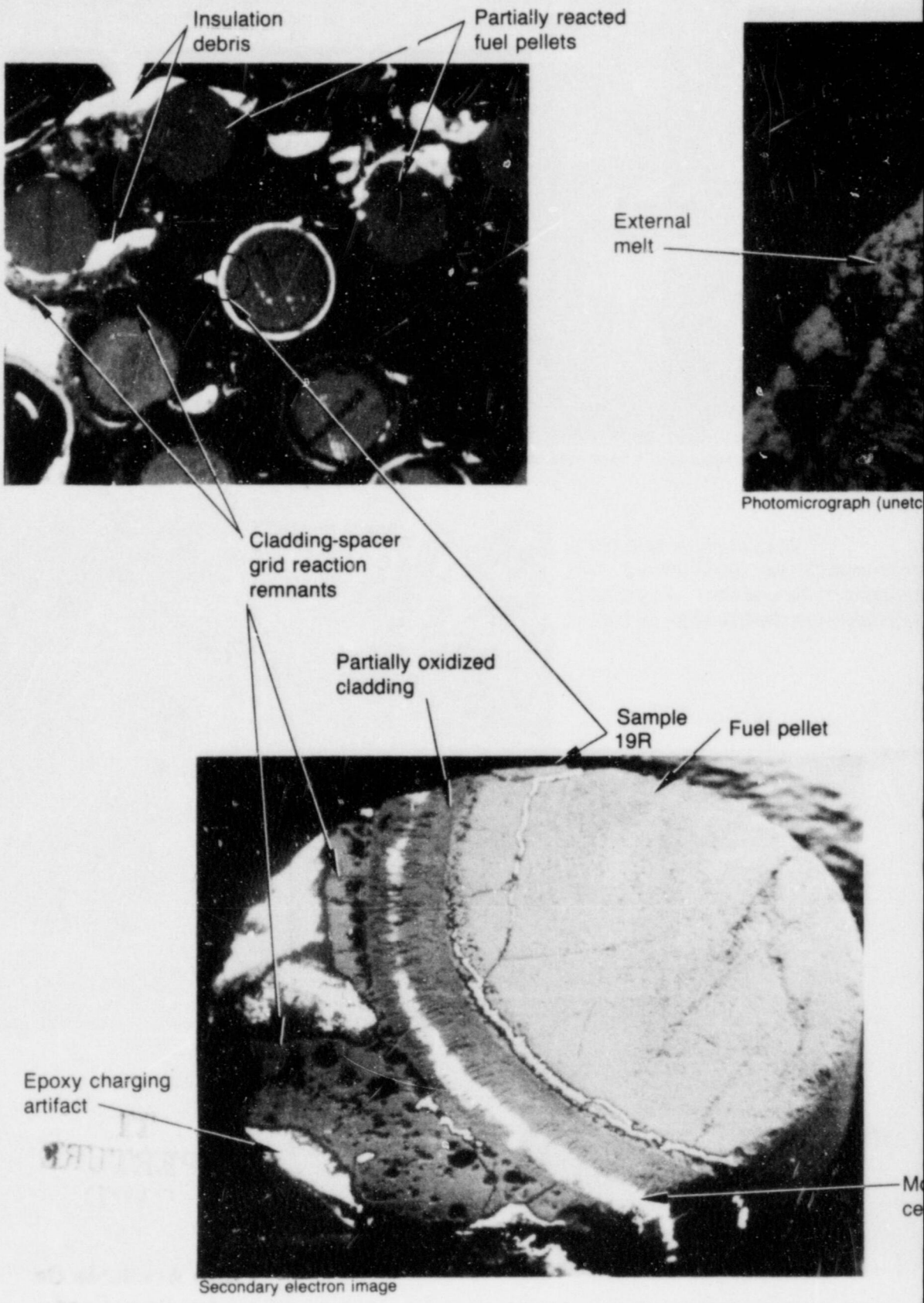

Figure E-67. Incipient fuel

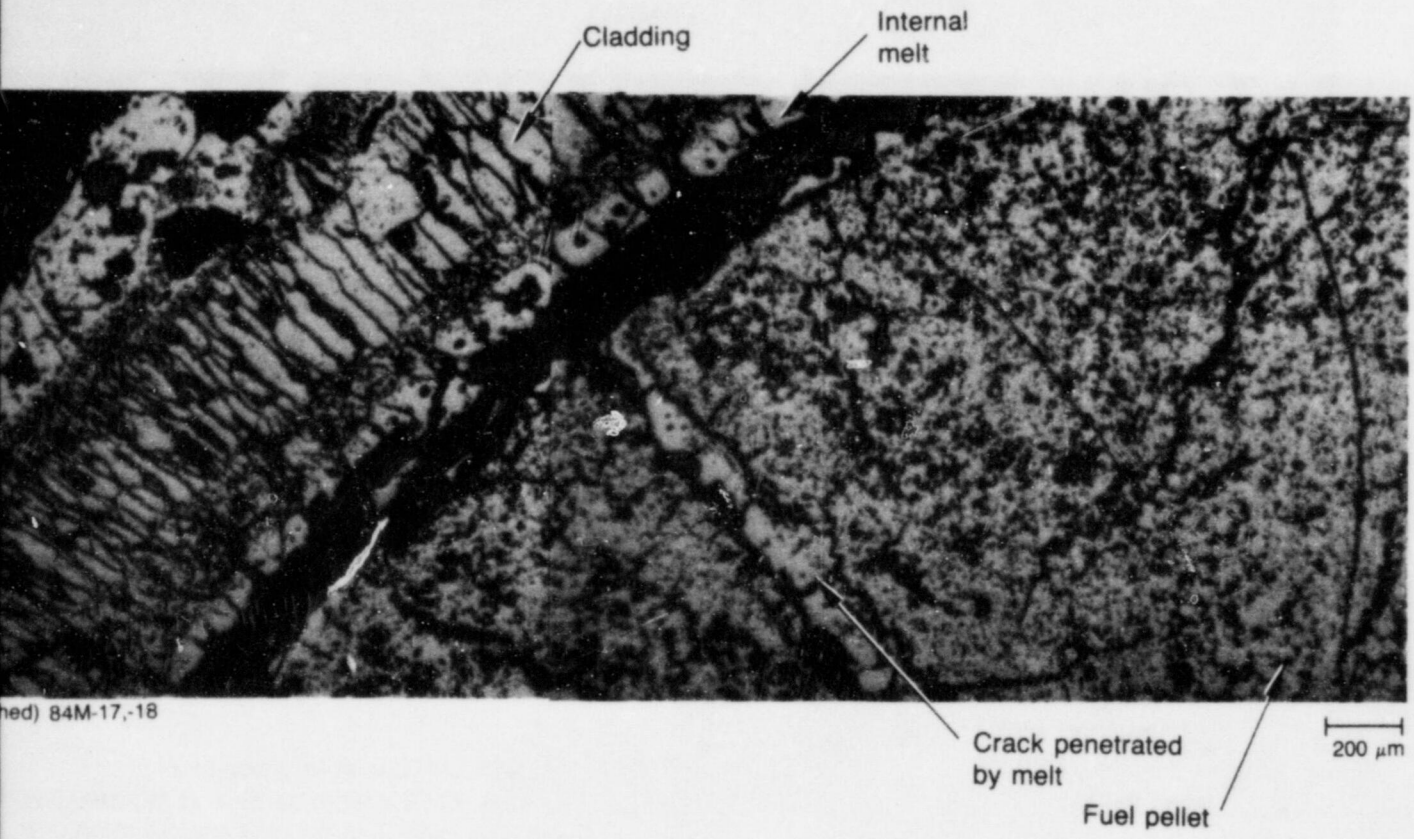

hed) 84M-17,-18

Zr x-ray image

unting
ment

quefaction in Sample 19R (0.915 m).

TI
APERTURE
CARD

Also Available On
Aperture Card

8609300386-14

Backscattered electron image

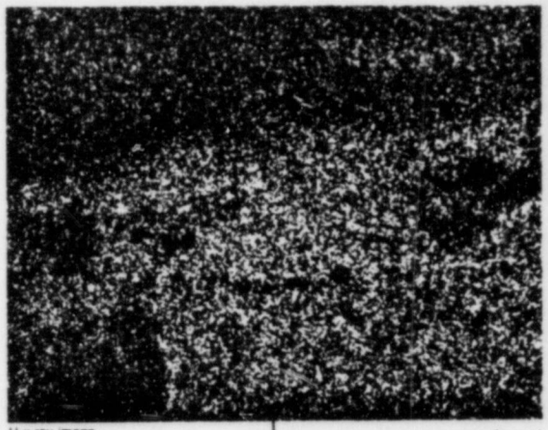

U x-ray image

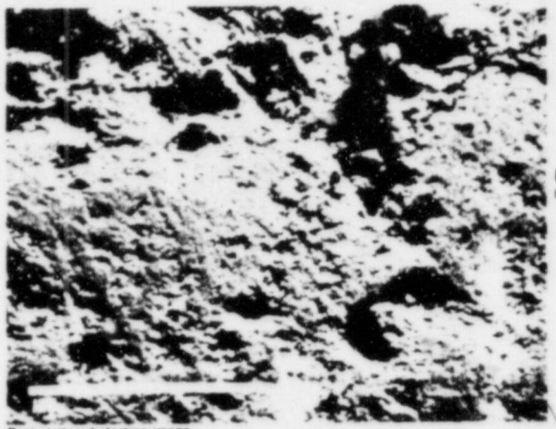

Backscattered electron image

Area A: U-100.0 wt %, trace of Zr
Area B: Zr-70.7 wt %, U-29.3 wt %, traces of Fe, Ni and Cr
Area C: Zr-85.2 wt %, U-14.5 wt %, Ni-0.2 wt %, traces of Fe and Cr
Area D: Zr-76.3 wt %, U-22.4 wt %, Ni-0.6 wt %, Cr-0.4 wt %, Fe-0.3 wt %,

Area F: Zr-60.8 wt %, U-36.3 wt %, Ni-1.2 wt %, Cr-1.0 wt %, Fe-0.7 wt %

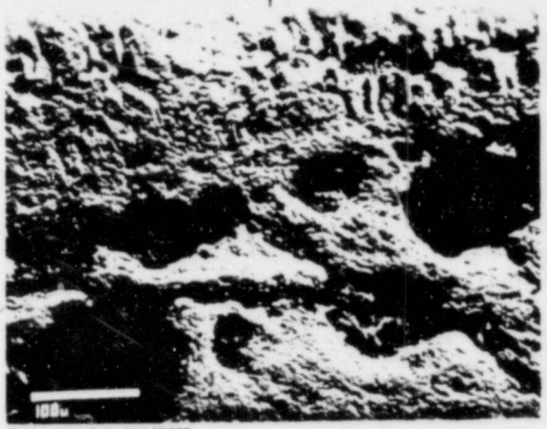

Backscattered electron image

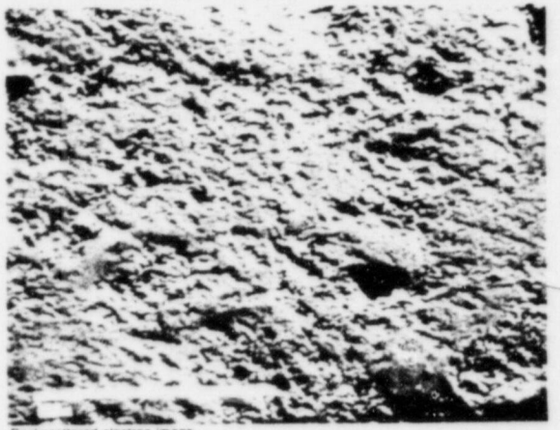

Backscattered electron image

Area G: U-53.3 wt%, Zr-42.9 wt%, Ni 1.7 wt%, Cr-1.4 wt%, Fe-0.7 wt%

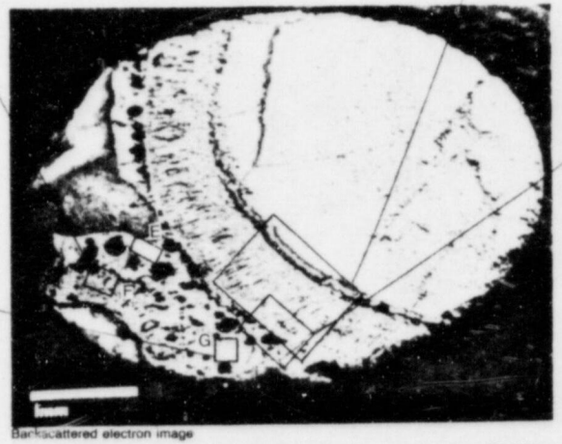

Backscattered electron image

Area E: U-51.0 wt %, Zr-44.9 wt %, Ni-1.7 wt %, Cr-1.5 wt %, Fe-0.8 wt %

Figure E-68. SEM/EDS findings from melt/cladding interaction zone near the bottom of Sample 19R.

TI
APERTURE
CARD

Also Available On
Aperture Card

8609300386 -15

Area H: U-97.5 , ' %, Zr-2.5 wt %, trac
Area I: U-60.7 wt %, Zr-38.5 wt %, Ni-
Area J: Zr-75.1 wt %, U-24.9 wt %, tra
Area K: Zr-87.3 wt %, U-12.6 wt %, tra
Area L: Zr-62.6 wt %, U-34.1 wt %, Ni
Area M: U-52.8 wt %, Zr-41.3 wt %, N

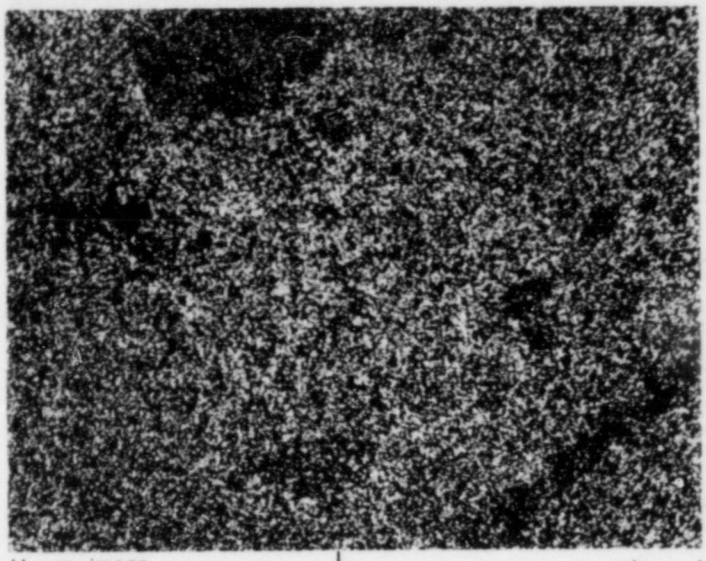

U x-ray image

12.5 μm

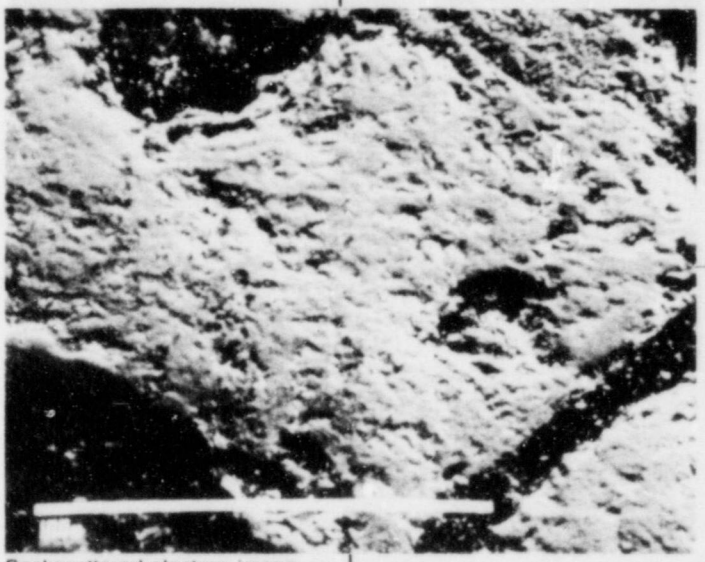

Backscattered electron image

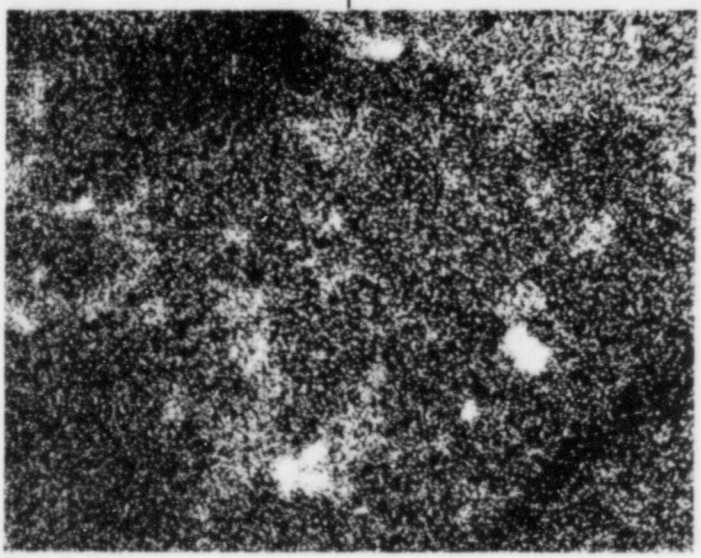

Ni x-rya image

12.5 μm

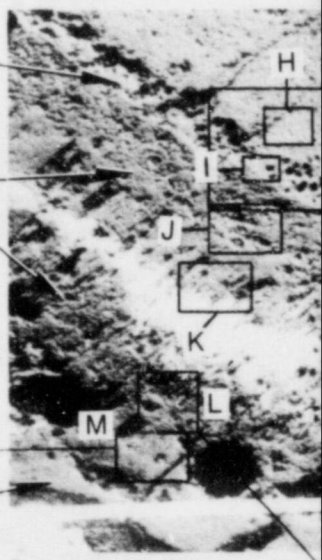

Backscattered electron image

Backscattered electron image

Figure E-69. SEM/EDS results from

es of Fe and Ni
0.3 wt %, Fe-0.3 wt %, Cr-0.2 wt %
ces of Fe, Ni and Cr
ces of Fe, Ni and Cr
1.5 wt %, Cr-1.1 wt %, Fe-0.7 wt %
-2.9 wt %, Cr-1.8 wt %, Fe-1.2 wt %

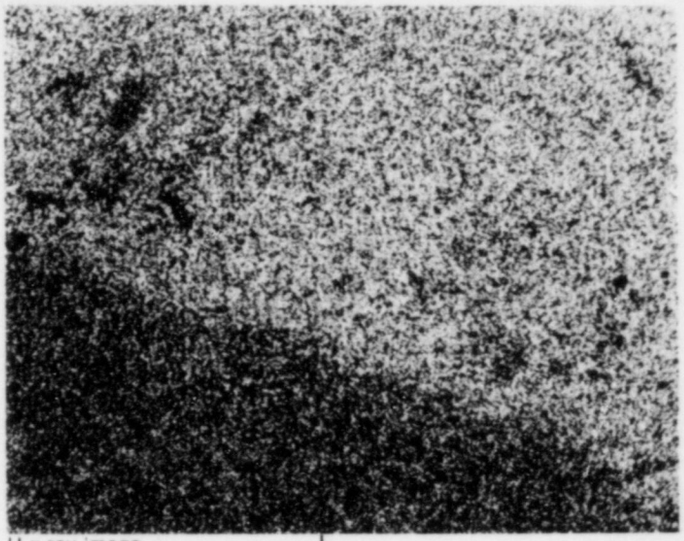

U x-ray image

25 μm

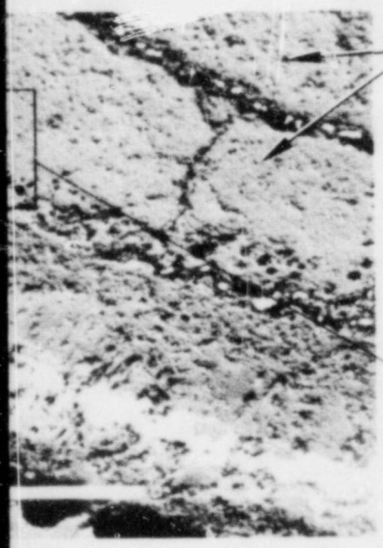

143 μm

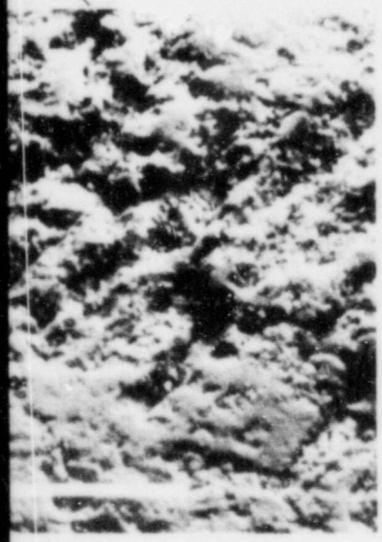

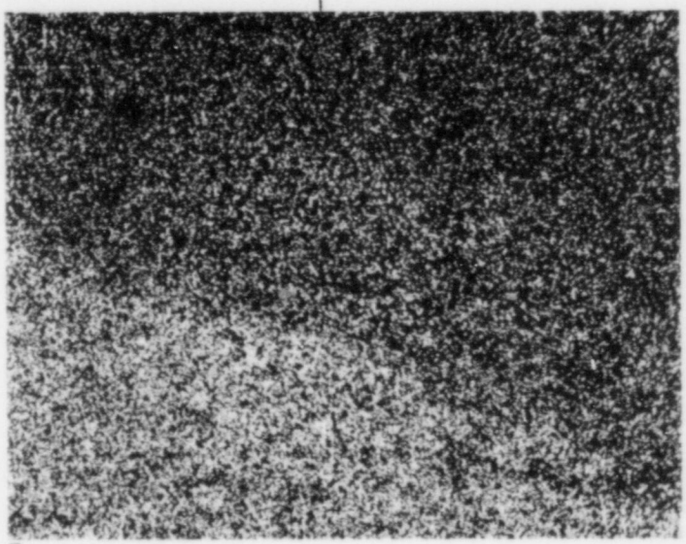

Zr x-ray image

25 μm

TI
APERTURE
CARD

Also Available On
Aperture Card

E-97

interaction zone near the top of Sample 19R.

8609300386-16

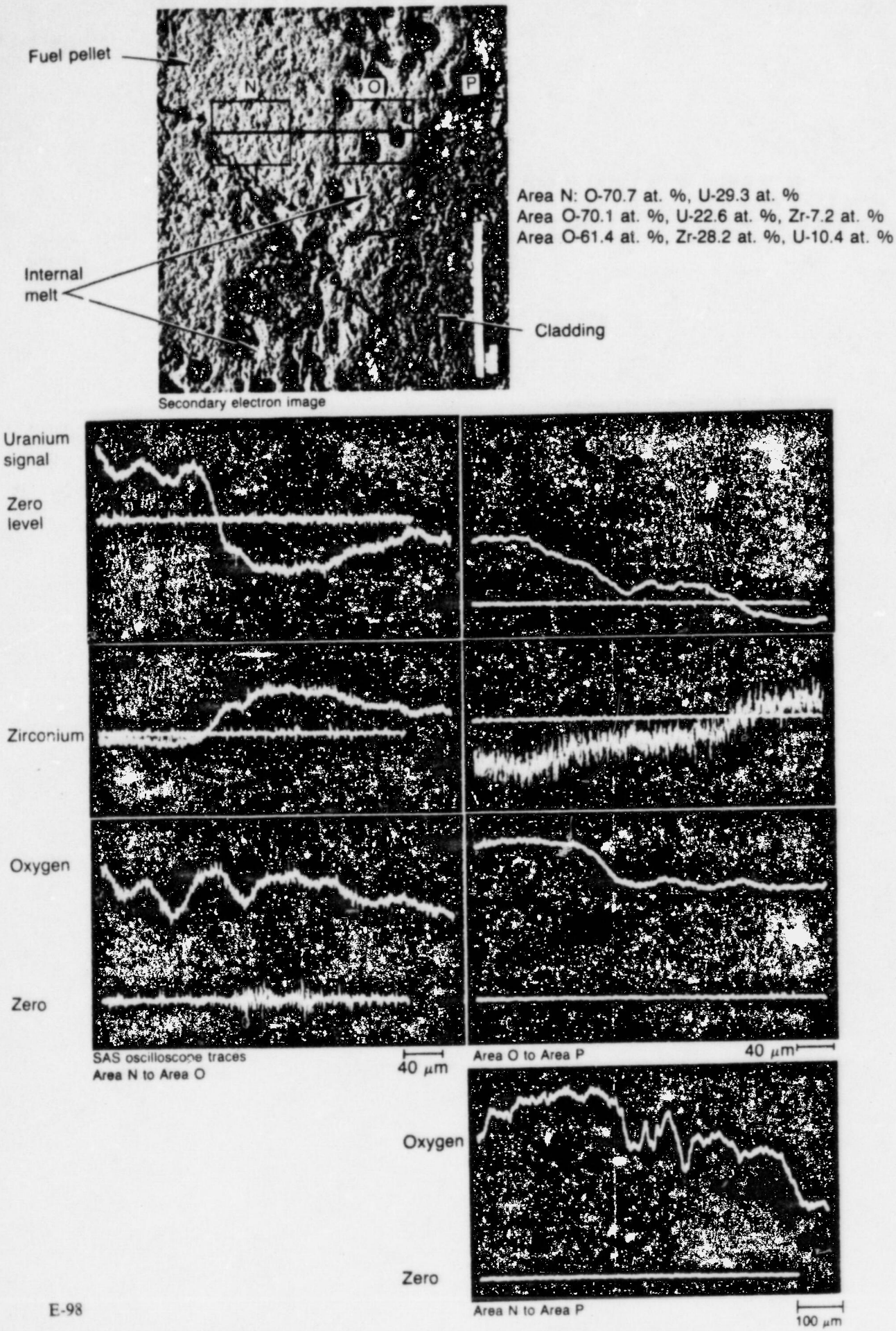

Figure E-70. SAS data across the fuel/melt cladding interface on Sample 19R.

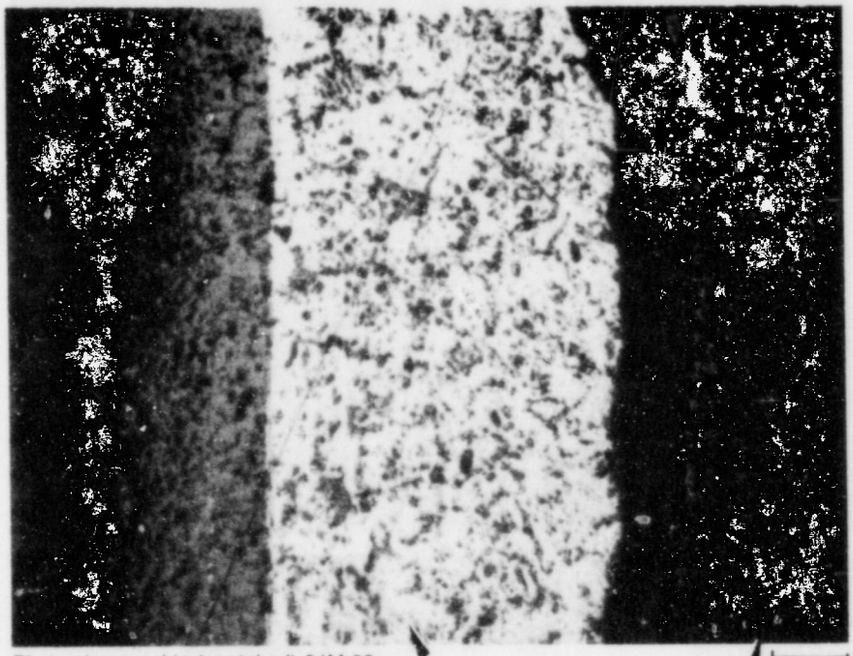

Photomicrographic (unetched) 84M-32

100 μm

Zr x-ray image

Backscattered electron image

100 μm

Shroud liner segment: Zr-100.0 wt %, no traces

Backscattered electron image

Area average: Zr-97.3 wt %, Fe-
Area A: Zr-97.8 wt %, Fe-1.2 wt
Area B: Fe-100.0 wt %, no trace

Figure E-71. Sample 19S (0.915

TI
APERTURE
CARD

Also Available On
Aperture Card

435 μm

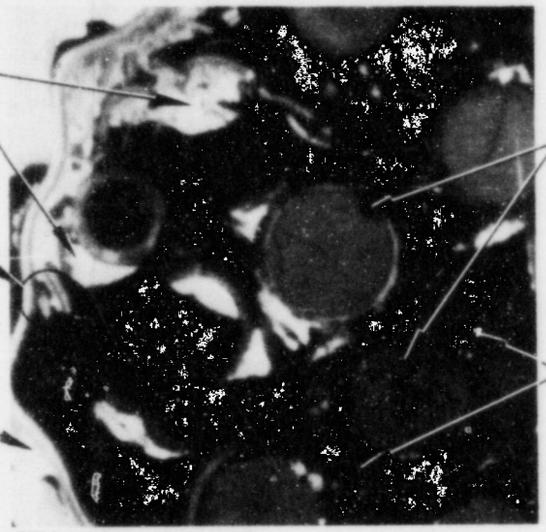

STM-19 macrophotograph

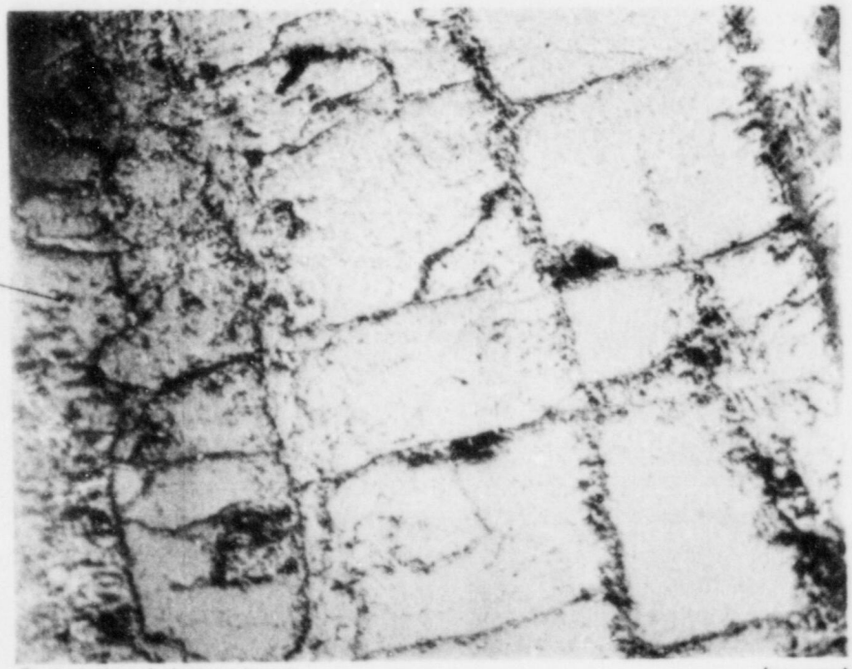

Backscattered electron image

100 μm

.4 wt %, Ni-1.3 wt. %
%, Cr-0.6 wt %, Ni-0.4 wt %, trace of U
s

Cladding segment: Zr-100.0 wt %, no traces

m), illustrating oxidation of the shroud liner.

8609300386-17

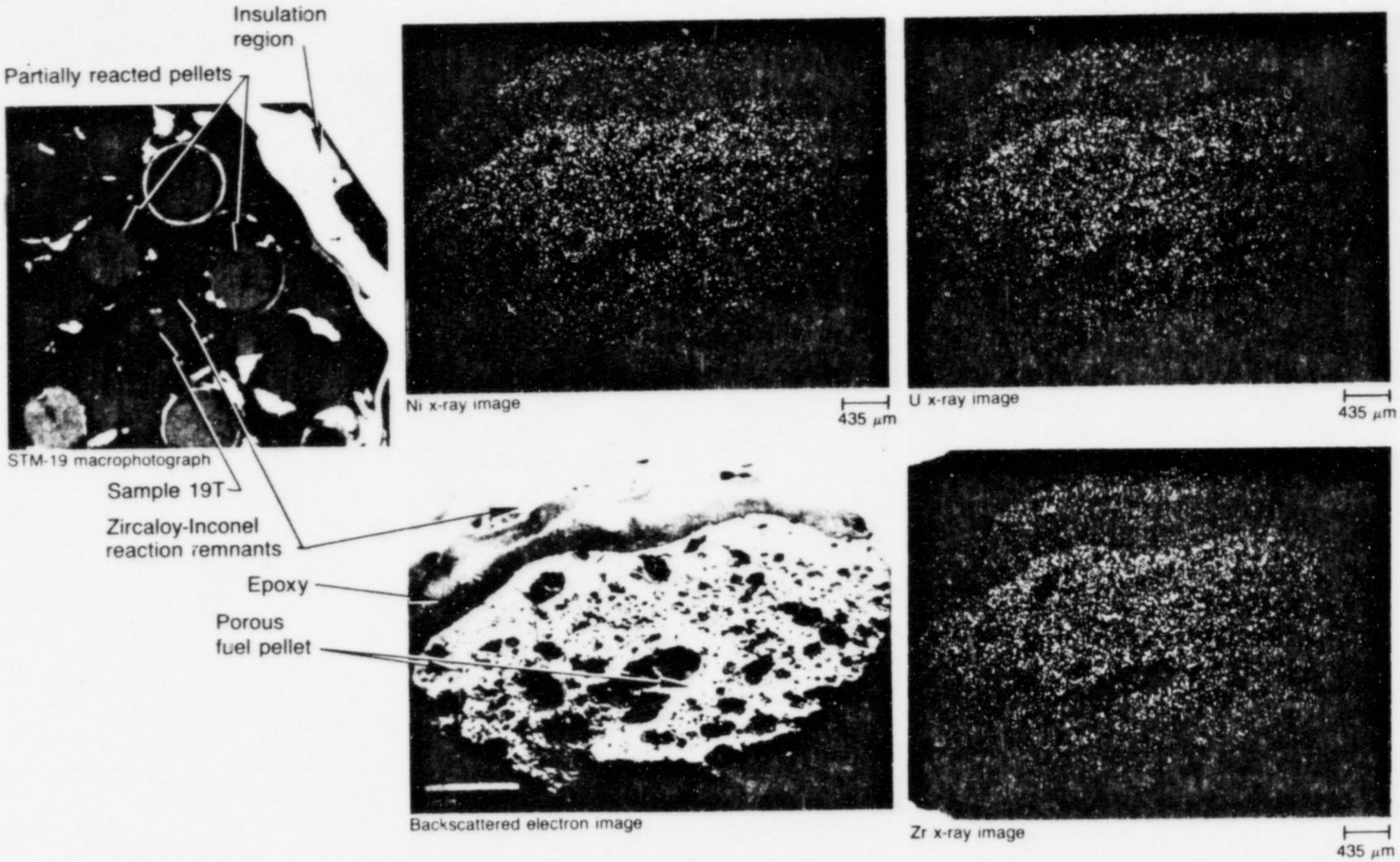

Figure E-72. Basic element distributions in liquefied fuel Sample 19T (0.195 m).

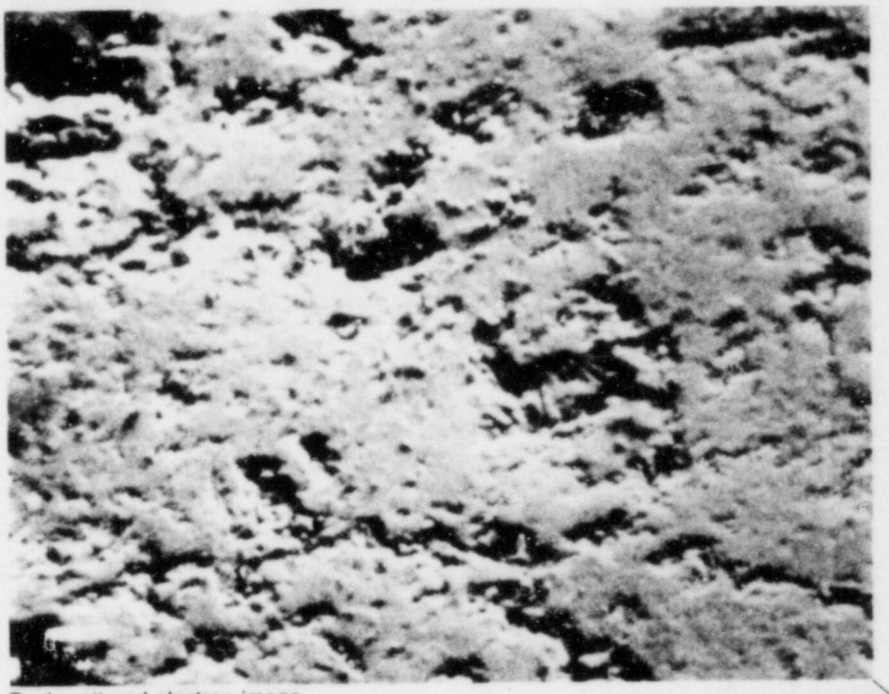

Backscattered electron image

12.5 μm

Area A: Zr-69.3 wt %, U-29.0 wt %, Ni-0.9 wt %, Cr-0.4 wt %, Fe-0.3 wt %

Secondary electron image

Area average: U-8
Fe

Backscattered electron image

12.5 μm

Area C: U-93.3 wt %, Zr-5.3 wt %, Ni-0.6 wt %, Fe-0.6 wt %, Cr-0.3 wt %

Figure E-73

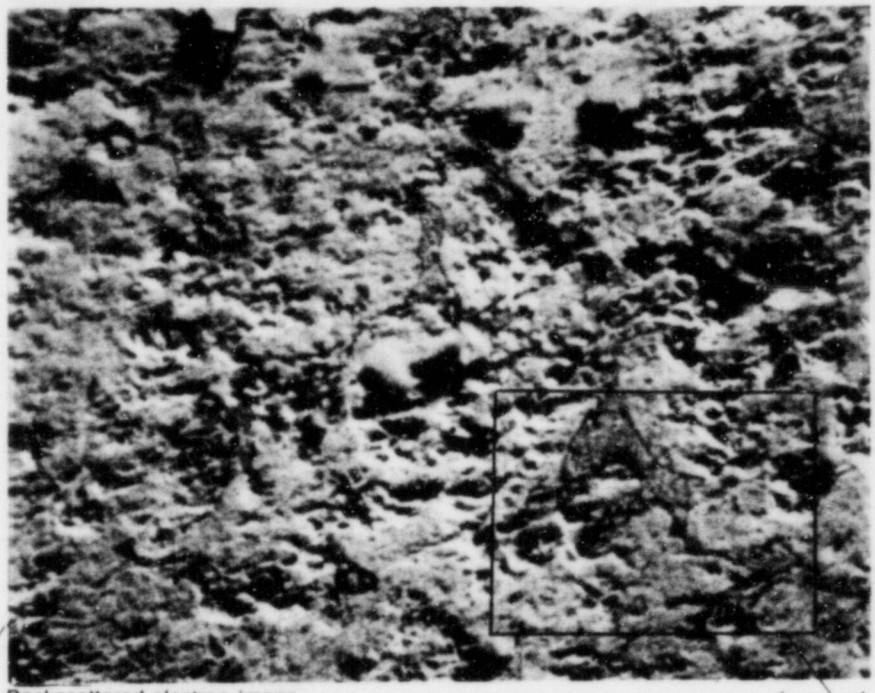

Backscattered electron image

12.5 μm

Area B: U-86.9 wt%, Zr-9.2 wt%, Ni-2.4 wt %, Cr-1.0 wt %, Fe-0.5 wt %

TI
APERTURE
CARD

Also Available On
Aperture Card

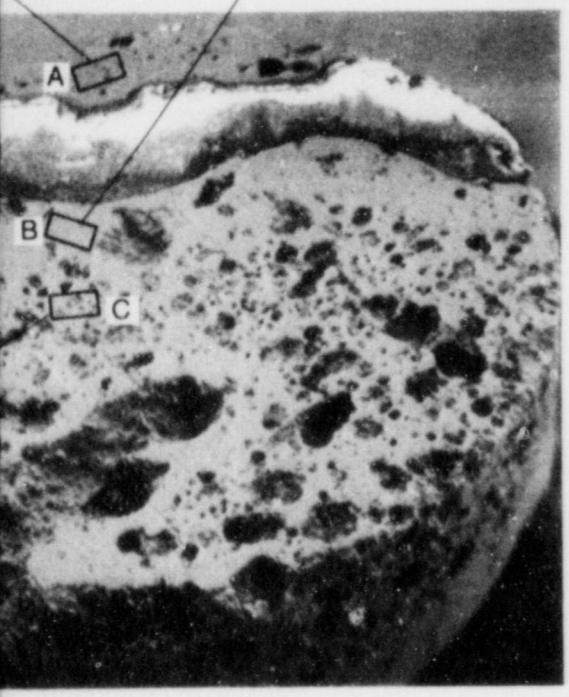

3.8 wt%, Zr-13.8 wt%, Ni-1.5 wt%,
-0.5 wt%, Cr-0.5 wt%

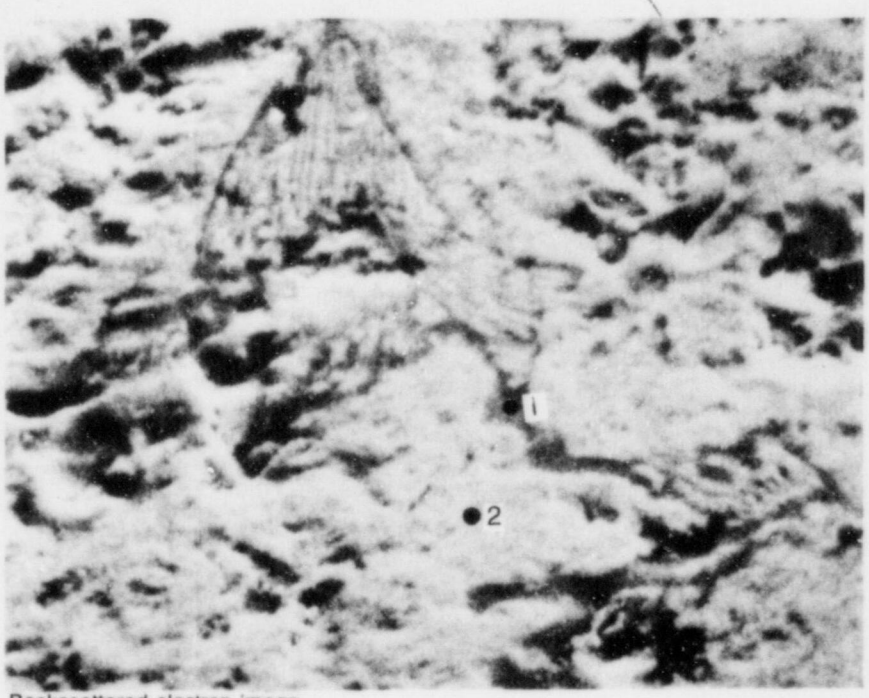

Backscattered electron image

50 μm

Point 1: U-76.4 wt%, Zr-9.2 wt %, Ni-7.6 wt%, Cr-4.8 wt%, Fe-2.0 wt %

Point 2: U-90.1 wt%, Zr-8.9 wt %, Ni-1.0 wt%, trace of Fe

E-101

SEM/EDS results from Sample 19T.

8609300386-18

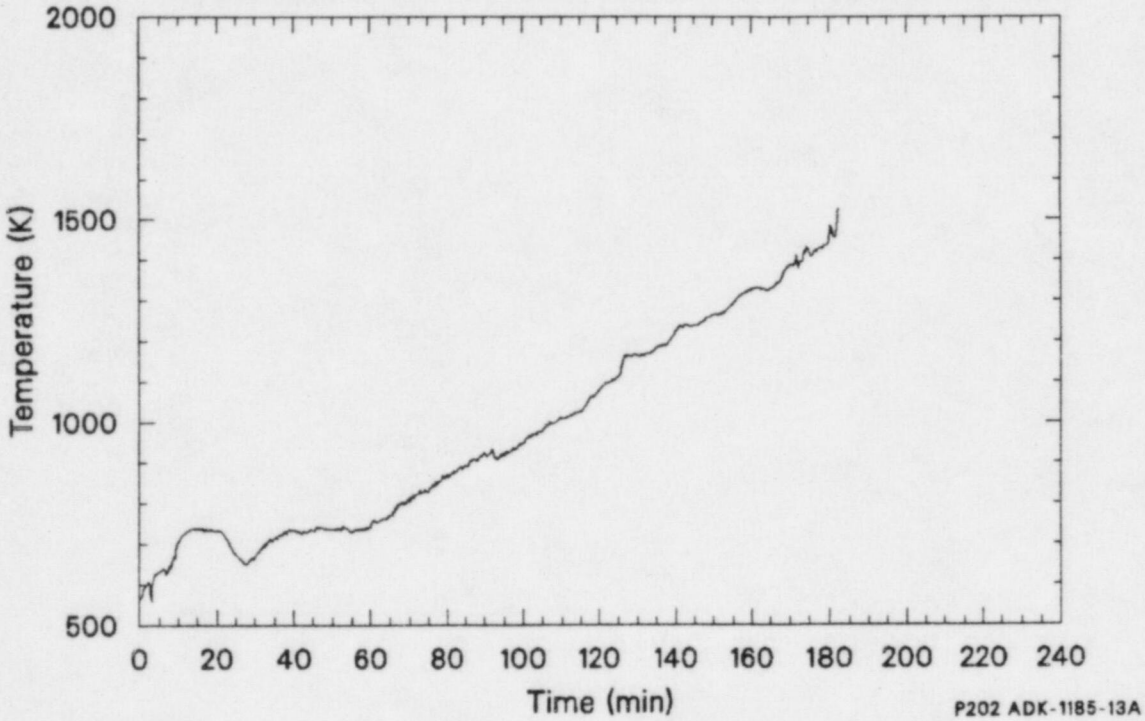

Figure E-74. Averaged thermocouple measurements of steam temperature within the fallback barrier.

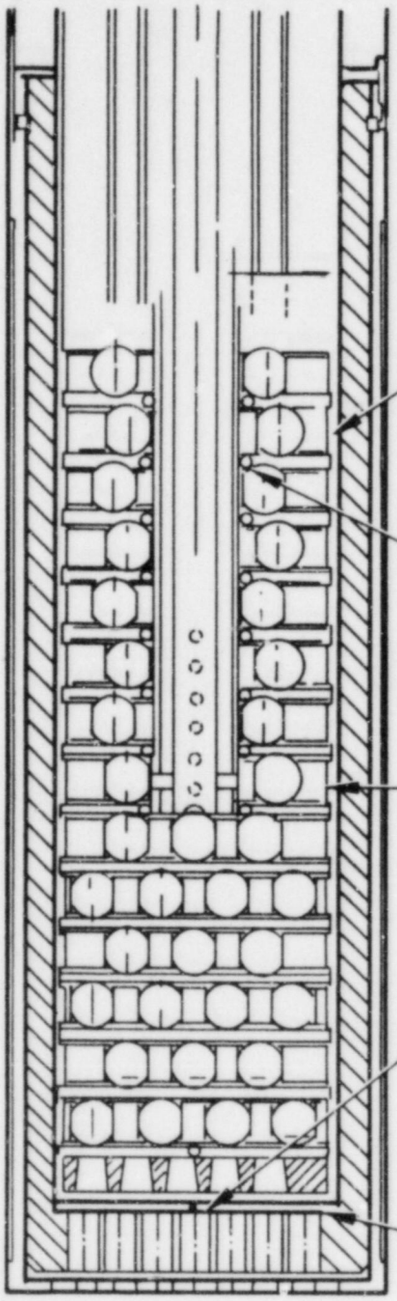

Sample	Temperatures (K) Effective isothermal	Metallography	COBILD peak
13	1400	<1850	1704
12	1380	<1850	1671
9B	1380	<1850	1680
5B	1550	<1850	1806
5D	1490	1850 < T < 2170	1724

5 12 050

Figure E-75. Estimated temperatures within the fallback barrier.

APPENDIX F

ANALYSIS OF BUNDLE-RETAINED FISSION PRODUCTS

APPENDIX F

ANALYSIS OF BUNDLE-RETAINED FISSION PRODUCTS

Ten retained fission product (RFP) samples were extracted from the SFD-ST fuel bundle after the bundle had been encapsulated with epoxy and sectioned for metallurgical examinations. Concentrations of detectable fission and daughter products were measured. In addition, fifteen samples were extracted from the fallback barrier. The primary objective was to estimate whole-bundle inventories remaining within the fuel region and fallback barrier, and combine with the on-line gamma spectrometer and effluent system sample data to provide a fission product mass balance. In the process, information was also generated on RFP variations between axial elevations and between different bundle materials for correlation to fuel behavior phenomena and transient release processes.

1. BUNDLE SAMPLING METHODS

The ten RFP samples consisted of two distinct types: fines abraded from five bundle cross sections, and small cylinders core-drilled from five isolated bundle positions. The ground RFP samples, with precision elevations and thicknesses, corresponded to metallographic macrophotographs and included both fuel and structural materials. These samples were suited to estimating fission product retention within morphologically distinct bundle regions (lower rod stubs, melt-covered pellets, central loose debris, upper rod remnants). However, the grinding process necessarily homogenized fission products localized in fuel pellets, solidified melts, and structural surfaces. The core-drilled samples were obtained to study fuel liquefaction, transport within the fuel region, and deposition on hot structural surfaces. In addition, these samples aided interpretation of the ground sample measurements.

The in-cell grinding apparatus designed for this purpose is displayed (during manual check-outs) in Figures F-1 and F-2. Each cross section was first remotely attached to a holding fixture by set screws. The holding fixture was then inserted into a leveling device and adjusted by a manipulator on a dial-indicator until the cross-sectional surface to be ground was parallel to the leveling device surface resting on the indicator. Meanwhile, a sheet of 400-grit abrasive paper was placed inside the polishing dish, which in turn was mounted on an adaptor attached to the grinder spindle. Demineralized water was added to the dish as a grinding lubricant, with a small amount of sodium nitrite added to improve wetting of the grinding disk and to trap volatile fission products in the aqueous solution. After lowering the sample assembly onto the grinding disk, and after attaching an eccentric spider to prevent the cross section from turning, the spindle was engaged to commence grinding.

The eccentric point of the spider was changed periodically to reduce formation of a central crown on each cross section and to prolong lifetimes of the grinding disks. Nevertheless, ten 400-grit disks were typically required to achieve the target removal thickness of 25 μm. To renew an abrasive disk, the sample assembly was raised and tilted such that any adherent fines could be rinsed into the polishing dish (see Figure F-2). The dish contents were then poured into a pre-labeled container, whereupon the grinding disk and dish were rinsed and decanted into the same container. Each grinding disk was placed in a second dry sample container for eventual fission product measurements, along with paper wipes used to clean measurement surfaces.

The dial-indicator was used to map the bundle cross sections at identical temperatures before and after grinding. A total of 25 reproducibly located points were measured on each cross-sectional surface (60-degree angular intervals) with a precision of 1.25 μm from gauge block calibrations. Nevertheless, the desired thickness tolerance of 2.5 μm could not be approached on a 25 μm grinding of initially flat surfaces, because of the preferential removal of material from cross-sectional peripheries, which was caused primarily by spindle wobbling. However, development efforts further determined that the crown contour would not change prohibitively once it had been established. Consequently, each cross section was pre-ground before RFP sampling, which had the additional benefit of removing the surface chemically etched during metallography.

The miniature core-drilling fixture, positioning templates, and thin-sectioning apparatus used to extract the cylindrical samples (5.6-mm diameter) are described in Appendix E. In this context, it is important to note that a 1.9-mm deep wafer was extracted for elemental composition measurements before each 5.1-mm deep RFP sample was sliced. Therefore, material distributions within the RFP specimens do not exactly match those shown at core-drilled positions on the cross-sectional macrophotographs (see Figures F-3 and F-4). However, these changes must be minor, because closely spaced neutron tomographs were reviewed before selecting positions to confirm that bundle structures were essentially constant within 10 mm of the metallographic plane.

2. MEASUREMENT TECHNIQUES

The fission products of primary interest were initially identified as ^{90}Sr, ^{95}Zr, ^{106}Ru, ^{127}Te, ^{129}I, ^{137}Cs, and ^{144}Ce. Later, ^{125}Sb was added because it was conveniently detectable and displayed unusual deposition behavior. In addition, ^{95}Nb (daughter product of ^{95}Zr) was quantified instead of ^{95}Zr. Within all samples ^{95}Zr was detected , but not separately quantified due to possible gamma interference with ^{154}Eu. The primary technique used to quantify RFP concentrations was gamma spectrometry. Chemical separation and calibrated beta counting was performed for ^{90}Sr because of the lack of gamma emission from this isotope. Accurate results demanded that as much sampled material as possible was dissolved into homogeneous solution in order that small representative aliquots could be placed in vials with calibrated geometries. By contrast, undissolved solids (grinding disks, insoluble sludge, etc.) had to be counted dry, with a point-source approximation the only recourse for concentration conversions.

The core-drilled RFP samples were first attacked by aqua regia, a mixture of nitric and hydrochloric acids. This approach dissolved most of two of the cylindrical samples. Dry counting of the remaining small amount of insoluble material introduced negligible additional uncertainty on the total concentrations. The other three cylinders required a second dissolution sequence with a mixture of nitric and hydrofluoric acids before the remaining solid chunks were reduced to tolerably small amounts of insoluble sludge.

The ground RFP samples were more complicated to prepare because of the presence of the grinding disks, paper wipes, and appreciable amounts of water lubricant and rinse. Concentrated nitric acid was first added to the containers of ground fines and rinse in an attempt to dissolve the fines. However, considerable sludge remained in each case and therefore another dissolution process using a nitric/hydrofluoric acid bath followed, leaving relatively little sludge for dry spectrometric counting. The grinding disks were immersed in dilute nitric acid to leach most fission products from them, and the disks were counted dry following the leaching process. The paper wipes resisted nitric acid leaching and had to be counted directly. Due to the small amounts of fission product-bearing material on the wipes, insignificant error was introduced to the total concentration results.

High quality results were achieved for ^{95}Nb (daughter of ^{95}Zr), ^{106}Ru (via ^{106}Rh), ^{125}Sb, ^{137}Cs, and ^{144}Ce (via ^{144}Pr) by calibrated spectral gamma counting. Strontium assays required chemical separation before beta counting to eliminate beta background from other radionuclides. Separation efficiencies were determined by adding a known weight of stable strontium carrier to each aliquot and by weighing the precipitate. Practical constraints restricted ^{90}Sr assays to the primary leaching samples.

Unfortunately, results were not as favorable for ^{129}I, that is a very long-lived (16 million-year half-life) daughter product of ^{129}Te (70-min half-life). The poor gamma yield and low (40-keV) gamma emission energy make ^{129}I essentially undetectable by direct gamma spectrometry, even with much larger concentrations than initially present in the SFD-ST fuel bundle. However, after chemical trapping, separation, and drying, ^{129}I can be neutron activated to ^{130}I, which has several strong gamma emissions. An iodine trapping apparatus was used during dissolution of the core-drilled samples. However, after neutron activation, only the ^{131}I spike (added tracer) was resolved on the gamma spectra.

Efforts to detect ^{127}Te by gamma spectrometry after chemical separation were similarly unsuccessful. Virtually all of the initial inventory of ^{127}Te was expected to have decayed to stable ^{127}I by the time the

spectrometry was performed, due to the 9-hr half-life. However, ^{127m}Te decays with a 109-day half-life into ^{127}Te. Thus, there was sufficient possibility of ^{127}Te gamma emission from this alternate decay path, even after more than two years, to justify the attempt. The tellurium separation process was not to blame, because ~95% of the ^{123m}Te tracer was recovered. Consequently, the brief SFD-ST irradiation, transient tellurium release and transport processes from the bundle region, and long decay times before sample extraction and processing, were jointly responsible for the inability to quantify ^{127}Te concentrations. Note that naturally occurring tellurium impurities preclude a neutron activation approach.

Several additional measurements, not directly related to fission products, were performed to assist conversion of the measured concentrations into retention percentages. The most direct approach was to normalize to the uranium concentration within each sample. To this end, a separate representative aliquot was taken from the primary leaching solution from each RFP sample, the uranium was chemically separated and neutron activated, and the ^{235}U concentration was measured by counting the delayed neutron emission. The total uranium concentration was calculated from the 6.19% posttest ^{235}U enrichment, wherever necessary.

While this method yielded reasonable results for the core-drilled samples, uranium concentrations within the ground samples were far below expectations (based upon both RFP concentrations and ground thickness measurements, as well as metallographic and elemental composition findings). Another aliquot was therefore taken from four of the five ground RFP solutions and analyzed directly (after dilution) for total uranium concentration by inductively coupled plasma spectrometry (ICP). The results of the ICP analyses confirmed the delayed neutron measurements and, as will be explained, required an alternative normalization process (macrophotographic planimetry) to be adopted for the ground samples.

Following delayed neutron counting, the chemically isolated uranium was analyzed for uranium isotopic distribution in an attempt to precisely determine the burnups. This information would have been very valuable for estimating the original fission product inventory of bundle materials that had slumped from otherwise poorly known bundle elevations during the transient. Unfortunately, the low bundle-average burnup of 91 MWd/T (~0.009 at.% burnup) did not permit local variations in ^{235}U depletion to be detected. That is, ^{235}U results from all samples were effectively identical (~6.2%) within instrument uncertainty (±0.25%), independent of sample position with respect to the PBF power profile.

3. MEASURED RFP CONCENTRATIONS

Measured RFP data from the five core-drilled samples are listed in Table F-1, along with the associated uncertainties and the ^{235}U results from delayed neutron counting. Samples 4D, 4F, and 4H were obtained by drilling upward into cross section STM-4, which was cut at the 0.145-m bundle elevation (Figure F-3). After allowance for a 2-mm thick elemental composition slice adjacent to the metallographic plane, each of the three 5-mm thick RFP samples was centered approximately at the 0.15-m bundle elevation. Similarly, Samples 19S and 19T were taken from cross section STM-19 (Figure F-4), whose metallographic plane was at 0.915 m, so these two specimens were centered approximately 0.92 m above the base of the fuel pellet stack. Fuel bundle elevations and associated morphologies are shown in Figures E-2a, b, and c, Appendix E.

Samples 4F (unreacted fuel pellet) and 19T (liquefied fuel with oxidized cladding and some structural material) dissolved readily in aqua regia, leaving only small amounts of sludge for direct gamma counting. Samples 4D (metallic mixture of liquefied fuel, molten cladding, and Inconel), 4H (oxidized, uranium-rich melt), and 19S (oxidized zircaloy liner and cladding) resisted aqua regia and left relatively large chunks of undissolved material. These remnants had to be broken down by HNO_3/HF to dissolve the majority of trapped fission products for calibrated gamma spectrometry and beta counting of representative aliquots. Note that beta counting for ^{90}Sr was not performed on the sludge residues because of the practical difficulties in chemically separating any strontium from this relatively inert material. The remaining Sr amounts (in parentheses on Table F-1) were estimated by assuming that Sr and Ce were leached from the solids with equal efficiencies. That is, the unmeasured fraction of ^{90}Sr was assumed identical to the known fraction of ^{144}Ce in the sludge.

Uncertainties listed in the first three data columns of Table F-1 are due purely to counting statistics. On a relative basis, these values provide inferences on peak fitting and background interference, and were generally small contributors to the overall uncertainties in the *Total MicroCurie* column. Besides counting imprecisions, each total uncertainty value includes a 5% calibration uncertainty for liquid samples and, where calibrated sample geometries could not be achieved for dry countings and a point-source approximation was necessary, a 10% calibration uncertainty. Uncertainties of 20% were assigned to the parenthetical ^{90}Sr quantities. All uncertainty terms were root-sum-squared (square root of the sum of squared terms) to calculate each 95% confidence interval.

Because the cylindrical samples were all of the same size (125 mm^3), the total μCi results could be compared directly on a volumetric basis. However, allowances had to be made for the variations in sample composition and epoxy content that are indicated by the major differences in sample weights. For example, pure UO_2 Sample 4F should be expected to contain much higher RFP concentrations than Sample 19S, which consists predominately of oxidized zircaloy and epoxy. Meaningful comparisons demand that the fission product values be normalized to a relevant quantity like the ^{235}U content of each sample, which is listed in the last column of Table F-1. The uranium normalization is conducted in the next section, along with corrections for axial and radial neutron flux distributions during the fuel conditioning phase.

The RFP results and related uncertainties from the ground samples are presented in Table F-2. Bundle locations and data implications are discussed later, along with fuel normalization. Considerably more sample processing was required, primarily due to the grinding disks and paper wipes. Uncertainties listed in the first five data columns reflect counting statistics. Uncertainties in the *Total MicroCurie* column include counting imprecisions, plus a 5% calibration uncertainty for counting liquid aliquots and a 10% uncertainty for direct countings of insoluble sludge, grinding disks, and paper wipes. All terms were root-sum-squared at the 95% confidence level, where the calibration uncertainties typically overwhelmed counting statistics in the overall uncertainty.

The *Total MicroCurie* results were normalized to a 25 μm thickness to account for the differences in average ground layer thicknesses listed under the *Sample* heading. However, because the ground thickness measurements varied about the averages between $\pm$ 7% and $\pm$ 17% at the 95% confidence level, each thickness uncertainty had to be factored into the final uncertainty values in the last column of Table F-2. With the exception of Sample STM-4 ($\pm$ 7%), thickness variability dominated all other sources of error combined in the root-sum-squaring.

As mentioned earlier, ^{90}Sr measurements were made only on aliquots from the primary leach solutions, where most of the strontium should have collected. Chemically separating and beta counting the relatively small ^{90}Sr amounts left in the HNO_3/HF solution, the insoluble sludge, the grinding disks, and the paper wipes would have been prohibitively expensive. Instead, an approximation was made, assuming that the fractions of the total ^{90}Sr remaining in these materials were the same as the separation efficiencies measured for ^{144}Ce over each cross section. Accordingly, the ^{90}Sr values listed in parentheses were computed by multiplying the ^{90}Sr in the primary leach by successive ^{144}Ce fractions. Uncertainties of $\pm$20% were arbitrarily assigned to the parenthetical ^{90}Sr values for calculating overall uncertainties. Due to the dominance of thickness variability and the relatively small estimated ^{90}Sr amounts, the 20% value had little influence on combined ^{90}Sr uncertainty quantities.

Results from ^{235}U determinations on primary leach solutions from the ground samples are not reported in Table F-2 because they are misleadingly small. After adjusting to 25 μm thicknesses, these values are 12.6 mg for STM-2, 8.6 mg for STM-4, 10.6 mg for STM-8, 5.4 mg for STM-13, and 8.6 mg for STM-19. By comparison, 24.6 mg (posttest) would be expected across a full array of 32 fuel pellets. Planimetry performed on the five cross-sectional macrophotographs revealed that only STM-2 maintained an as-fabricated bundle geometry, while fuel dissolution reduced pellet area fractions to 0.79 of nominal at STM-4, 0.73 at STM-8, 0.80 at STM-13, and 0.75 at STM-19. On this basis, the measured ^{235}U concentrations are 51% of that expected at STM-2, 44% at STM-4, 59% at STM-8, 28% at STM-13, and 47% at STM-19. Since all five cross sections contained appreciable area fractions of U-bearing melts (especially STM-4 and -8) besides fuel pellets, these ^{235}U results deviate even more than the above indications.

This planimetric comparison might suggest that the actual ground layer thicknesses were considerably smaller than those listed in Table F-2, despite the precise gauge block calibrations. However, this possibility can be eliminated because the fission products measured in each sample agree much better with the layer thicknesses than with the ^{235}U amounts. Normalizing the fission products in Table F-2 to the above ^{235}U values, plus factoring in the power profile and decay-corrected pretest inventories, produces apparent retentions between 150 and 250% for most RFP species at all five bundle elevations. Only one situation (^{125}Sb at STM-8) yielded a physically believable retention of 95%. Therefore, the ^{235}U values from the grindings cannot be valid normalizing agents, and thus the product of layer thicknesses and planimetric area fractions was used for this purpose.

This discrepancy was investigated further, due to potential impacts on the ^{235}U measurements from the core-drilled samples. Aliquots were taken from the STM-4, -8, -13, and -19 primary leach solutions and analyzed directly for elemental uranium concentrations by ICP, after multiple dilutions to preclude personnel exposure. The ICP analysis essentially confirmed the delayed neutron measurements, though ICP-derived amounts were between 18 and 26% higher. The positive ICP bias can be attributed to accumulated dilution errors, since both ICP and delayed neutron counting should be inherently accurate to approximately $\pm 5\%$. Moreover, normalizing to the ^{235}U concentrations from ICP still generates much higher fission product retentions than physically possible in the overwhelming majority of cases.

Consequently, the tentative conclusion was reached that HNO_3 did not extract uranium from the bundle fines and grinding disks with anywhere near perfect efficiency. Accordingly, the secondary HNO_3/HF leach from STM-8 was checked for ^{235}U by the same uranium separation/neutron activation/delayed neutron emission method used on the primary samples. However, only 3% of the primary leach ^{235}U content was found. By extension, the missing uranium must be in the grinding disks, paper wipes and/or the insoluble sludge.

Although not satisfactorily explained, this unanticipated difficulty is almost certainly an artifact of the grinding method and in no way invalidates the ^{235}U measurement approach. Furthermore, the ^{95}Nb, ^{106}Ru, ^{25}Sb, ^{137}Cs, and ^{144}Ce determinations were not compromised, because the disks, papers, and sludge were individually gamma counted, as well as the secondary leach solution. Nevertheless, the possibility cannot be discounted that more ^{90}Sr remained in these items than assumed by ^{144}Ce fractional comparisons. That is, strontium could conceivably have behaved like uranium and been HNO_3-leached with poorer efficiency than cerium.

4. FISSION PRODUCT RETENTION CALCULATIONS

Converting the measured RFP amounts into local percentages of initial inventories required several interrelated steps. Calculations were performed with the ORIGEN2 code for decay periods matching the actual dates of gamma and beta counting, producing decay-corrected whole-bundle inventories that assumed 100% retention.[F-1] The next step factored in an axial power profile adjusted for the 0.115 m of fuel stack extension. As shown in Figure F-5, this adjusted profile distributes the extra 0.115 m among the four most conspicuous gaps on the neutron radiographs (see Figures E-2a, b, and c), thereby providing axial peaking factors appropriate to the posttest sectioning elevations. Specific local-to-average factors determined were 0.605 for STM-2 grindings; 0.903 for STM-4 grindings and the 4D, 4F, and 4H cylinders; 1.087 for STM-8 grindings; 1.353 for STM-13 grindings; and 0.686 for the STM-19 grindings, plus the 19S and 19T cylinders. Uncertainties for these factors were estimated at $\pm 5\%$, based on sample elevation imprecisions. From this point, the conversion sequences for the cylinders and grindings proceeded by different paths.

Radial flux variations across the test bundle during the conditioning phase had to be incorporated into the cylinder retention calculations. Reactor physics calculations[F-2] for the relative flux were 0.929 for 4D, 1.113 for 4F, 0.929 for 4H, 1.113 for 19S, and 0.920 for 19T. Any lateral shifting from pretest positions was ignored, so 5% (relative) uncertainties were assigned to these radial peaking factors for all but 4F, a pellet segment from a stationary rod stub. Additional 5% uncertainties were applied to Samples 4D and 4H, due to possibilities for lateral melt spreading and mixing. The next phase was the ^{235}U normalization, where the ^{235}U measured in

each cylinder (Table F-1) was converted into a fraction of the whole-bundle ^{235}U inventory, 0.88 kg. Multiplying each ORIGEN2 whole-bundle μCi value by the ^{235}U fraction, and the axial and radial power factors, produced the fission product amounts that would be expected in each cylinder had no release occurred. Finally, the retention percentages listed in Table F-3 were generated by dividing the measured RFP amounts (Table F-1) by the calculated 100% retention values. Uncertainty terms from the RFP measurements, the power peaking factors, and the ^{235}U measurements were combined by root-sum-squaring. No uncertainty component was provided for the ORIGEN2 predictions, although an uncertainty of $\pm 10\%$ relative was added in Table 15 of the main text to account for this source.

5. DISCUSSION OF CYLINDRICAL SAMPLE RESULTS

The retention percentages determined for the core-drilled cylinders (Table F-3) must be interpreted with respect to the phenomena they represent. Detailed scanning electron microscopy/energy-dispersive x-ray spectroscopy (SEM/EDS) findings from the adjacent composition wafers are presented in Appendix E, along with the relevant fuel behavior context. Only the highlights of these elemental studies are given here.

Sample 4F represents a fuel pellet that neither reacted with molten cladding nor was exposed to temperatures much above 2000 K for a prolonged interval. Very little (if any) ^{144}Ce, ^{106}Ru, and ^{137}Cs were released, and the majority of the ^{95}Zr and ^{125}Sb was retained in the unreacted UO_2 matrix. However, Table F-3 indicates that roughly 90% of the ^{90}Sr escaped the pellet (though not necessarily the bundle region). While this anomalous result cannot be completely disregarded without a known cause and while it is used in forthcoming partitioning calculations for STM-4, it should be noted that it has negligible influence on whole-bundle ^{90}Sr retention determinations.

The inability to detect ^{129}I is meaningful on this particular sample. After allowing for iodine recovery and separation efficiencies, the detection threshold for ^{129}I by neutron activation and gamma spectroscopy is $\sim$10 ng. Based on the ORIGEN2 prediction for this isotope (plus radial and axial power peaking factors), at least 100 ng of ^{129}I would have been expected in Sample 4F without any iodine release. This implies that 90% of the ^{129}I escaped the pellet. However, 90% iodine release is difficult to reconcile with 2% cesium release indicated for Sample 4F in Table F-3, so performance of the iodine trapping apparatus must be questioned.

The Table F-3 retention values were derived by a ^{235}U normalization and the ^{235}U content measured in Sample 4F (6.96×10^4 μg) was accurately cross-checked. A pellet fragment consisting of pure UO_2 and weighing 1.333 g must contain 1.175 g of total uranium. Since 6.192% of this uranium is ^{235}U, 7.27×10^4 μg of ^{235}U would be expected, which is a difference of only 4% from the measured amount. This agreement eliminates the possibility of a large bias error in the ^{235}U measurements listed in Table F-1.

Sample 19T represents UO_2 melted by molten cladding, although appreciable amounts of Ni, Fe, and Cr from the upper spacer grid were included in the melt. Solidification occurred, either by oxidation or cooling, before the molten mixture could slump to a lower elevation. If fission products in the fuel pellet at the time of liquefaction were uniformly diluted by the melt along with ^{235}U, coarse agreement with Sample 4F retention percentages would be expected despite the lower temperatures achieved at the 4F position. Yet, only ^{95}Zr and ^{125}Sb data support this simplistic understanding. The relatively low 19T retention values for ^{106}Ru, ^{137}Cs, and ^{144}Ce might be explained by enhanced diffusional release prior to liquefaction, although chemical reactions during dissolution may also have contributed.

Sample 19S was extracted primarily to ascertain whether or not fission products were irreversibly deposited on hot structural surfaces in the upper bundle region during the transient. The companion composition slice mainly consisted of oxidized cladding and oxidized zircaloy liner, although one ZrO_2 object showed trace amounts of uranium from prior reaction with fuel-bearing material. A correspondingly small amount of ^{235}U was measured in the 19S cylinder. The ^{235}U-normalized retention percentages for 19S are generally similar to those for Sample 19T, and imply that most of the fission products in 19S can be attributed to the fuel-bearing material. However, ^{125}Sb is one outstanding exception, where most must have been deposited. Nevertheless, it is not certain that the deposition occurred on ZrO_2, because two small

inclusions of partially oxidized iron were also found during SEM/EDS investigations on the companion elemental composition sample. Also found was ^{95}Nb in slightly greater than expected amounts, and could therefore be due to neutron activation of ^{95}Zr (parent of ^{95}Nb) in cladding and ZrO_2 insulation.

Sample 4H represents the liquefied fuel that accumulated throughout the lower bundle region. The small retention values (Table F-3) for ^{106}Ru, ^{125}Sb, and ^{137}Cs indicate low melt absorption of these species, by comparison to uranium. Meanwhile, the percentages for ^{90}Sr, ^{144}Ce, and, to a lesser extent, ^{95}Nb are unrealistically high. Most of the extra ^{90}Sr, ^{144}Ce, and ^{95}Nb can be explained by the fact that the melt slumped from a higher neutron flux elevation. However, because the maximum axial power factor (1.36; see Figure F-5) is 150% of that at the STM-4 elevation (0.90), all of the melt had to originate at, or very near, the 0.5-m elevation to solely account for these large values. Although plausible, the possibility must be considered that the melt preferentially absorbed ^{90}Sr, ^{144}Ce, and perhaps ^{95}Zr.

Sample 4D was extracted from the metallic, Zr-rich melt concentrated within a narrow bundle range centered near the 0.14-m elevation. Retention percentages for ^{106}Ru, ^{125}Sb, and ^{137}Cs are conspicuously higher than in Sample 4H, which suggests higher solubilities for these species in melts of low oxygen content. Had the metallic melt been oxidized before cooling, additional releases might have occurred. The extraordinarily high retention values for ^{90}Sr and ^{144}Ce in 4D cannot be explained solely by higher neutron flux at the original melt elevation and therefore must have preferentially absorbed some strontium and cerium. The original melt elevation cannot be accurately determined and therefore the magnitude of the absorption cannot be precisely estimated. It is also probable that some ^{90}Sr and ^{144}Ce was absorbed into Sample 4H. However, the lower ^{95}Nb retention value in 4D makes it unclear whether or not ^{95}Zr (parent of ^{95}Nb) was preferentially absorbed into either melt specimen.

6. CROSS-SECTIONAL RFP RESULTS

Ground sample data from Table F-2 are more difficult to convert into meaningful retention percentages than the core-drilled cylinders. As noted earlier, the HNO_3 leach incompletely extracted uranium and the associated ^{235}U measurements proved far to small to use as normalizing agents. However, despite the leaching problem, the retention analyses would still have been complicated by the varying distributions of materials within the five bundle cross sections.

The general methodology used is as follows. The decay-corrected whole-bundle inventories from ORIGEN2 for ^{90}Sr (3.58 Ci), ^{95}Nb (0.332 Ci), ^{106}Ru (2.19 Ci), ^{125}Sb (0.237 Ci), ^{137}Cs (3.78 Ci), and ^{144}Ce (20.2 Ci) were divided by the pretest fuel stack length to produce average linear fission product concentrations. The next step was to superimpose the posttest-adjusted PBF power profile (Figure F-5) to generate the 25 μm layer concentrations at each cross-sectional elevation. These 100% retention concentrations were then adjusted for the difference from the nominal amounts of fuel on the five macrophotographs (measured by planimetry) that were caused by pellet liquefaction and axial shifting of fuel fragments. For those cross sections without appreciable fission product-bearing melts, the last basic step was to divide the measured RFP quantities from Table F-2 (normalized to 25 μm thickness) by adjusted 100% retention values, thereby producing posttest retention percentages for the six radionuclides.

However, the STM-4 and -8 cross sections contained larger area fractions of slumped melt than fuel pellets. Consequently, the approximation could not be made that all of the measured fission products were within UO_2. Instead, the fission products had to be partitioned by extrapolating local RFP concentrations from the core-drilled cylinders.

STM-2. Cross section STM-2 was cut through the bottom spacer grid at the 0.055-m bundle elevation. As shown in Figure E-10 (Appendix E), STM-2 includes a full fuel rod array, plus small amounts of oxidized and metallic melts that collected on the grid. This bundle elevation stayed relatively cool, so none of the fuel pellets were attacked by molten zircaloy cladding and Inconel.

Thirty-two fuel pellets nominally occupy a 0.199 fraction of the inter-saddle area (8.645×10^{-3} m^2). However, the combination of pellet dishes intersected the STM-2 cut, chipped pellet corners, and thermocouple holes reduced the actual UO_2 area fraction to ~0.185. This value was visually estimated, since precise planimetry was not performed on the STM-2 macrophotograph. The associated decrease in fission product content was partially offset by the oxidized and metallic melts that slumped from higher elevations, with respective area fractions of ~0.05 and 0.01.

In the first attempt at generating STM-2 retention percentages, the approximation was made that the fission product-bearing melts exactly compensated for the missing pellet portions. That is, STM-2 was treated as if no melt was present and a 0.199 UO_2 area fraction existed. This initial approach produced apparent retentions of 80% for ^{90}Sr, 91% for ^{95}Nb, 99% for ^{106}Ru, 80% for ^{125}Sb, 94% for ^{137}Cs, and 96% for ^{144}Ce.

The likelihood of actual releases from this low temperature elevation was minimal and it was considered that these values were small, evidently because the melts incompletely offset the less-than-nominal UO_2 area. Therefore, these values were arbitrarily divided by the ^{144}Ce retention (i.e. a 100% cerium retention was assumed, with other values scaled upward accordingly). This refinement yields best-estimate retentions of 83% ± 12% for ^{90}Sr, 95% ± 14% for ^{95}Nb, 103% ± 15% for ^{106}Ru, 83% ± 12% for ^{125}Sb, 98% ± 14% for ^{137}Cs, and 100% ± 14% for ^{144}Ce. The uncertainty bands are estimated at the 95% confidence level and include the combined uncertainties from Table F-2, a 10% (relative) uncertainty on the UO_2 area fraction, and a 5% uncertainty on the 0.605 local power factor (from sectioning elevation imprecisions). As with the core-drilled samples, ORIGEN2 was assumed here to have negligible uncertainty although a 10% relative uncertainty was added to Table 16 in the main text.

These calculated retentions should be interpreted in the following manner. No measurably significant transient releases occurred at this elevation for ^{95}Nb, ^{106}Ru, ^{137}Cs, and ^{144}Ce. The ^{90}Sr value suggests minor release, but the inability to gamma count this isotope indicates experimental effects that are not precisely incorporated into the uncertainty band. However, there is a strong indication that a small amount of ^{125}Sb escaped the fuel matrix. This deduction is partially confirmed by the 60% ± 5% retention of ^{125}Sb in intact pellet Sample 4F (Table F-3), which was also exposed to relatively mild conditions during the test.

STM-4. As shown in Figure F-3, the 0.145-m bundle elevation contained sizeable amounts of metallic and oxidized melts, both of which attacked the fuel rods. Planimetry estimated a metallic melt area fraction of 0.099, an oxidized melt fraction of 0.175 (excluding cracks and large pores), and a fuel pellet fraction of 0.157. Furthermore, roughly one-fourth of the fuel escaped melt damage and the associated high temperatures and chemical alterations. Thus, the Table F-2 RFP measurements must be divided among both melt types, partially reacted fuel, and intact UO_2 pellets. Samples 4D, 4F, and 4H were respectively core-drilled from the metallic melt, an intact fuel rod, and the oxidized melt to assist in this partitioning process.

The estimation of retention percentages for each fission product in the partially reacted fuel pellets was difficult because no core-drilled sample representing such material was extracted. To understand the STM-4 results, it is necessary to determine the portions of the total RFP amounts that can be explained by unreacted pellets and both melt types (Tables F-1 and F-2). After making the assumption that RFP concentrations in the 4D, 4F, and 4H cylinders validly represent bulk averages for these materials, the remaining fission products measured in the ground STM-4 sample were assigned to the UO_2 pellets exposed to high temperatures. Approximate retention percentages were estimated for these partially reacted pellets.

Each core-drilled sample had a radius of 2.8 mm and occupied a 2.85×10^{-3} fraction of the inter-saddle area. The 0.099 metallic melt area fraction converts to 34.7 Sample 4D equivalents and the 0.175 ceramic melt fraction to 61.4 Sample 4H equivalents. Meanwhile, planimetry estimated that 0.040 of the 0.157 UO_2 area fraction represented unreacted fuel pellets. The 0.040 fraction converts to 14.0 Sample 4F equivalents, leaving a 0.117 area fraction for partially reacted pellets. Each cylinder was also 5.1 mm in depth, so 25 μm layers would produce one two-hundredth of the RFP values listed in the *Total MicroCurie* column of Table F-1. Samples 4D, 4F, and 4H results were scaled upward accordingly and subtracted from the thickness-normalized STM-4 totals in Table F-2. The remaining fission products were divided by 100% retention values calculated from the

ORIGEN2 whole-bundle predictions (reduced to a 25 μm thickness), a 0.903 axial peaking factor, and a 0.117 area fraction for reacted fuel. The results of these calculations are summarized on Table F-4.

The uncertainties in Table F-4 were assigned and propagated in the following manner. Values in the first data column were taken directly from Table F-2. The second column values are the root-sum-square of the Table F-1 uncertainties for Sample 4D, a $\pm 5\%$ term for planimetry imprecisions, and an arbitrary 20% term to account for RFP inhomogeneities in the metallic melt. The oxidized melt uncertainties were similarly derived at the 95% confidence level. The unreacted fuel quantities include the 4F uncertainties, a $\pm 5\%$ term for planimetry errors, and a $\pm 10\%$ term for the subjectivity in separating unreacted and reacted fuels. The reacted fuel uncertainties are the root-sum-square of values in the preceding four columns, since all were involved in generating the nominal remainders. The predicted (100% retention) RFP column uncertainties include a $\pm 5\%$ term on the axial peaking factor and a $\pm 10\%$ quantity on the area fraction of reacted UO_2. The final 95% confidence intervals were produced by root-sum-squaring the fractional uncertainties from the preceding two columns and applying the resultant fractions to the nominal retention percentages.

STM-8. Figure E-13 (Appendix E) displays the posttest bundle condition at STM-8, where only partially reacted UO_2 pellets and oxidized melt are present. Planimetry estimated that melt-covered UO_2 occupies a 0.145 fraction of the inter-saddle area and oxidized melt (excluding cracks and macropores) fills a 0.330 fraction. The as-built insulation and inner liner area fraction of 0.312 was reduced to 0.121. Due to the large area fraction of melt, the RFP distributions are not obvious.

An attempt was made to segregate the STM-8 RFP contents (Table F-2) between the partially reacted pellets and the oxidized melt in the same manner as performed for STM-4. The assumption had to be made that Sample 4H results applied to the STM-8 oxidized melt (uncertainty unknown), since no RFP samples were core-drilled at the 0.245-m elevation. Remaining fission products in the STM-8 grindings were then assigned to the fuel pellets, and were finally divided by 100% retention values calculated from ORIGEN2 predictions for a 0.145 UO_2 area fraction and 1.087 axial power factor. The UO_2 retention percentages produced were 34% for ^{90}Sr, 78% for ^{95}Nb, 100% for ^{106}Ru, 44% for ^{125}Sb, 65% for ^{137}Cs, and 51% for ^{144}Ce. Again, due to the lack of core-drilled samples at STM-8, uncertainty bands cannot be legitimately calculated for these retention quantities.

These retention values do not agree very well with Table F-4 for STM-4 reacted fuel: 18% for ^{90}Sr, 91% for ^{95}Nb, 73% for ^{106}Ru, 65% for ^{125}Sb, 60% for ^{137}Cs, and 16% for ^{144}Ce. Thus, the assumption that Sample 4H accurately represented the STM-8 oxidized melt may not be valid, possibly because the STM-8 melt could have slumped from a more highly irradiated bundle elevation. Significant differences in elemental composition were also detected during SEM/EDS surveys. Sample 4H contained 65 wt% U wt% Zr (plus a substantial amount of undetected oxygen), while oxidized melts in STM-8 composition samples that were all adjacent to pellets ranged between 70 and 80 wt% U, with correspondingly less Zr than 4H. This composition difference may be related to the relatively advanced state of pellet dissolution at the 0.245-m elevation. (See Appendix E.)

STM-13. This cross section was cut at the 0.495-m bundle elevation, a region of partially melted and highly embrittled rods that fractured extensively. Planimetry on Figure E-16 established a UO_2 area fraction of 0.159, as compared to the nominal value of 0.199 for a nominal bundle cross section, plus a 0.492 area fraction of ZrO_2. Nevertheless, close inspection of the STM-13 macrophotograph and findings from composition samples suggest that the porous material outlining many pellets contains substantial Zr and is probably best regarded as liquefied fuel. Thus, the 0.159 UO_2 area fraction includes a small portion of chemically altered pellet material. Meanwhile, it is likely that the large ZrO_2 area fraction contains some pellet fragments and other types of fuel-bearing material that could not be separated by planimetry. These combined effects introduce a $\pm 10\%$ uncertainty in the UO_2 area fraction.

Since 0.159 is $\sim$80% of 0.199, the 100% retention values produced from the ORIGEN2 linear average predictions and a 1.353 local power factor must be reduced by this amount. Dividing the Table F-2 measurements by the above adjusted 100% retention quantities generated the following best-estimate

retention values for the STM-13 fuel pellets: 41% ± 7% for ^{90}Sr, 58% ± 11% for ^{95}Nb, 43% ± 8% for ^{106}Ru, 66% ± 13% for ^{125}Sb, 54% ± 10% for ^{137}Cs, and 48% ± 9% for ^{144}Ce. The uncertainty bands include the combined uncertainty from Table F-2, a 5% (relative) uncertainty on the local power factor, and a 10% (relative) uncertainty on the UO_2 area fraction.

STM-19. Despite the large axial separation, cross section STM-19 (0.915 m) resembles STM-13 in many important regards. As with STM-13, the vast majority of fission product-bearing material is in the form of partially reacted fuel pellets and therefore no complex partitioning studies are necessary. As shown in Figure F-4, many pellets are surrounded by a porous ceramic with appreciable Zr in solution plus some Ni, Fe, and Cr from the upper spacer grid. This material is regarded as liquefied fuel that solidified before it could slump to lower elevations. The major distinction from STM-13 morphology is that much of the STM-19 bundle geometry survived the transient, such that bundle materials did not mix with ZrO_2 insulation to any great extent.

Planimetry on Figure F-4 identified a UO_2 area fraction of 0.148, which primarily represents UO_2 exposed to high temperatures. This fraction also includes a small portion of fuel liquefied by molten cladding and Inconel. Area fractions of 0.109 for ZrO_2 and 0.064 for oxidized cladding/Inconel were also measured. However, elemental investigations on the STM-19 composition samples occasionally found small amounts of uranium in the cladding/Inconel mixtures, so a small fraction of the total STM-19 fission products were doubtless located outside the fuel pellet regions. Moreover, Sample 19S showed considerable ^{125}Sb deposited on oxidized structural surfaces. These effects cannot be quantitatively treated, but neglecting them is a substantial source of uncertainty with regard to retention within the fuel pellets. Accordingly, a ± 10% uncertainty was arbitrarily assigned to the 0.148 UO_2 area fraction.

The measured UO_2 area fraction is ~75% of the nominal pretest value of 0.199. As with STM-13, the local 100% retentions generated from the linear average ORIGEN2 predictions (decay-corrected) and a 0.686 local power factor (from Figure F-5) were reduced by this amount. Dividing the Table F-2 RFP measurements by the adjusted 100% retention quantities produced the following best-estimate retention quantities for STM-19: 56% ± 12% for ^{90}Sr, 87% ± 18% for ^{95}Nb, 52% ± 11% for ^{106}Ru, 92% ± 20% for ^{125}Sb, 54% ± 11% for ^{137}Cs, and 71% ± 15% for ^{144}Ce. Again, the uncertainty bands reflect the combined uncertainty in Table F-2, a 10% (relative) uncertainty on the UO_2 area fraction, and a 5% (relative) uncertainty on the power factor.

7. DISCUSSION OF CROSS-SECTIONAL RETENTIONS

Fission product retention results from the five SFD-ST bundle cross sections are summarized in Table F-5. Fission products contained within the STM-4 and -8 solidified melts have been subtracted, leaving those fission products estimated inside fuel pellets for relative comparison along the bundle length. Melt retentions could not be completely eliminated, however, because of the small area fractions within STM-2, -13, and -19. Furthermore, any fission product deposition that occurred on structural surfaces could not be separated from fuel retentions.

Several trends are immediately apparent in Table F-5. The relatively cool, chemically unaltered fuel at the 0.055-m elevation showed no release for most radionuclides. Nevertheless, when combined with intact fuel results from 0.145 m, there is evidence of measurably significant ^{125}Sb release. Since no equiaxed grain growth was discovered in these UO_2 pellets, this finding suggests high antimony volatility at temperatures below 2000 K.

As discussed in Appendix E, many fuel pellets at, and above the 0.145-m elevation were chemically attacked by molten oxygen-stabilized alpha-zircaloy (>2245 K). In many cases the melt was fully oxidized as a liquid, implying temperatures >2670 K. Melting of stoichiometric UO_2 (3120 K) may have occurred in at least one instance. These high temperature, chemically modified pellets, yield indications of appreciable release for all fission products measured in this study. Yet, as noted earlier, these released fission products did not entirely escape the bundle region. In particular, strontium and cerium were preferentially absorbed into the slumped

melts. More discussion on possible release mechanisms and perturbing measurement effects is provided after the whole-bundle retention estimates and fallback barrier results have been presented in the following two subsections.

It is also worthwhile to compare retentions between STM-13 and -19. Percentages are similar, especially for ^{137}Cs, but indicated retentions are generally smaller at the bundle mid-length, which probably experienced a longer time at elevated temperatures. The largest retentions at both elevations are for ^{125}Sb and ^{95}Nb, although neutron activation of ^{95}Zr could have biased the ^{95}Nb upward. This observation can be explained in part by irreversible deposition on structural surfaces, as suggested by Sample 19S (Table F-3). The agreement between the STM-19 best-estimate retentions and liquefied fuel Sample 19T is noteworthy. This suggests that the liquefaction process cannot be solely responsible for releasing these six fission products as solid fuel retentions would be considerably larger.

8. WHOLE-BUNDLE RETENTION ANALYSES

Results reported thus far apply only to small local portions of the SFD-ST bundle. Consequently, satisfying the primary objective of estimating whole-bundle retention percentages required extrapolating the locally measured values over relatively large axial regions. As shown by the full-length neutron radiographs (Figures E-2a, b, and c in Appendix E), the SFD-ST bundle could be crudely separated into axial segments containing mainly lower rod stubs, melt-covered fuel pellets, central loose debris, and upper rod remnants. These segment morphologies reflected varying extents of zircaloy oxidation, fuel liquefaction, and melt relocation induced by transient thermochemical processes, plus formation of embrittled rod segments. Since the associated times at temperature also influenced fission product releases from the fuel matrix, locally determined RFP percentages were extended over bundle portions exhibiting similar morphological characteristics, at least to a first approximation. Whole-bundle retention values were then generated by calculating appropriately weighted averages.

Figure F-6 shows the axial distribution of ^{235}U determined from neutron radiographs and closely spaced tomographic cross-sectional reconstructions. Benchmarks were supplied by planimetry on metallographic cross sections at the 0.055-, 0.145-, 0.170-, 0.245-, 0.270, 0.395-, 0.495-, and 0.915-m elevations. The ^{235}U concentration within intact and partially reacted fuel pellets was obtained directly from planimetric area fractions of UO_2 and the average posttest enrichment. Meanwhile, ^{235}U concentrations in the metallic and oxidized melts, added to the pellet ^{235}U distribution in Figure F-6 to form the total ^{235}U plot, were assumed equal to those measured in Samples 4D and 4H. That is, metallic and oxidized melt area fractions in each cross section were multiplied by 0.246 (4D/4F ^{235}U ratio) and 0.292 (4H/4F ^{235}U ratio), respectively, to achieve effective equivalences to ^{235}U in the UO_2 area fractions. An additional assumption was that negligible uranium escaped the bundle region, such that the integrated area under the total ^{235}U plot in Figure F-6 matched the pretest bundle loading, minus the insignificant burnup. Equivalently, the total ^{235}U curve had to average 88.8% of the initial linear concentration, after allowing for the stack growth from 0.915 to 1.03 m.

Considerable difficulty was encountered in satisfying the last constraint, because planimetry on the tomographic cross sections underestimated the UO_2 and melt area fractions by 20 to 50%. Appreciable manual adjustment of the plot was therefore required whenever metallographic benchmarks were not available. To legitimize this process, the gross gamma scan of the SFD-ST test train[F-3] was divided by the adjusted flux profile (Figure F-5) to produce the approximate axial distribution of fission product-bearing material (dashed plot on Figure F-6). This plot also had to satisfy the 100% ^{235}U retention condition, but this could be accomplished by simple vertical shifting of the entire normalized curve.

It must be recognized that the gross gamma scanner detected energetic gamma emissions from fission product decay several weeks after the transient, and that some of the prominent radionuclides at the time (^{95}Zr, ^{95}Nb, ^{103}Ru, ^{140}La, and ^{141}Ce)[F-4] could have been preferentially absorbed into the melts or irreversibly deposited on structural surfaces. Correspondingly, the depression in the normalized gamma plot between the 0.40- and 0.80-m elevations suggested that most of the slumped melt originated within this interval. In addition the scanner collimator opening was 51-mm wide and 38-mm high, and the scanner could not therefore detect

most rod fragments packed into the insulation region (i.e. outside the nominal bundle periphery) and not resolve small axial gaps. However, it is apparent that some downward shifting and settling of embrittled rod chunks occurred during bundle handling between gamma scanning and neutron radiography, forming the major peaks and valleys on Figure F-6. The shifts shown are approximate and are increasingly uncertain toward the top of the bundle because of the imprecision in the crane speed calibration discussed in Appendix E.

Despite the above complications, the normalized gamma scan served well as a baseline for adjusting the tomographically-derived ^{235}U content in UO_2 and melt area fractions. However, peak and valley magnitudes outside benchmarked areas still contain uncertainties of about $\pm 25\%$, and planimetric imprecisions on the metallographic macrophotographs, combined with any additional fuel shifting between neutron radiography and bundle sectioning induced uncertainties of at least $\pm 10\%$ at benchmarked positions. Thus, Figure F-6 should be interpreted as a trend-type best estimate, rather than exact information.

While individual points on Figure F-6 have large associated uncertainties, UO_2 and melt areas separately integrated over regions A through F should be accurate within $\pm 10\%$, due to the total ^{235}U retention condition. This permits converting the best-estimate ^{235}U profile into an idealized distribution better suited to whole-bundle RFP extrapolations. This idealized histogram is displayed in Figure F-7, where regions A through F respectively correspond to intact rod stubs (negligible equiaxed UO_2 grain growth and cladding melting), partially dissolved fuel pellets coated by oxidized and metallic melts, partially reacted pellets surrounded by oxidized melt, central loose rod fragments, a transition region where minor bundle geometry was maintained, and upper rod remnants with much of the original array geometry. Based on the assumption that fuel morphology is related to fission product retention, RFP percentages from cross sections STM-2, -4, -8, -13, and -19 can be applied directly to regions A, B, C, D, and F. RFP concentrations were not measured within region E, so the STM-13 and -19 values were averaged.

As shown in Figure F-7, the 0.115 m of overall stack growth is distributed among the four largest gaps in Figure F-6. Consequently, average power peaking factors for each region were extracted from Figure F-5 to produce, for each fission product, regional decay-corrected inventories product that neglected any release processes (100% retention values). Applying the locally determined fission product retention percentages generated posttest RFP concentrations for each bundle region. Finally, weighted whole-bundle averages were calculated by multiplying the regional RFP concentrations by the region lengths, summing the products, and dividing the total by the sum of the region lengths (0.915 m) to remove the stack growth artifact.

^{90}Sr. The best-estimate axial ^{90}Sr histogram and the posttest weighted average are presented in Figure F-8. The associated calculations are outlined in detail for this fission product to illustrate the methodology. Figures for the other five species can be followed by analogy in Table F-6, with substitution of appropriate ORIGEN2 predicted inventories and local retention fractions.

The region A magnitude in Figure F-8 (19.66 mCi/cm) is the product of the decay-corrected pretest bundle-average ^{90}Sr concentration (39.16 mCi/cm), the regional fraction of the nominal ^{235}U concentration (1.00, from Figure F-7), the regional average power factor (0.605, from Figure F-5), and the best-estimate ^{90}Sr retention fraction for cross section STM-2 (0.83, from Table F-5). Thus, 83% retention of ^{90}Sr was assumed over all of region A. Multiplying 19.66 mCi/cm by the region A length (0.113 m, from Figure F-7) produces 222.16 mCi, which is approximately 11.6% of the total occupied area in the Figure F-8 histogram.

Region B has ^{90}Sr partitioned into metallic and oxidized melts, as well as partially reacted fuel pellets. The fuel magnitude (4.94 mCi/cm) is the product of 39.16 mCi/cm, the regional fraction of nominal ^{235}U (0.751, from Figure F-7), the regional power factor (0.933, from Figure F-5), and the ^{90}Sr retention fraction in STM-4 reacted fuel (0.18, from Table F-5). The 25.86-mCi/cm oxidized melt magnitude was calculated with the above 39.16 and 0.933 factors, but used an equivalent ^{235}U area fraction of 0.472 (Figure F-7) and a ^{90}Sr retention fraction of 1.50 (Table F-3, from Sample 4H). The metallic melt magnitude (6.50 mCi/cm) was produced by multiplying 39.16 mCi/cm, 0.933, an equivalent ^{235}U area fraction of 0.083 (Figure F-7), and a 2.14 ^{90}Sr retention fraction (Table F-3, from Sample 4D).

Region C displayed similar ^{90}Sr behavior to region B, especially after allowing for the differences in incident neutron flux. The fuel magnitude (13.88 mCi/cm) was the product of the decay-corrected pretest inventory (39.16 mCi/cm), a 1.141 power factor (Figure F-5), a 0.914 fraction of nominal ^{235}U (Figure F-7), and a 0.34 estimated ^{90}Sr retention fraction for STM-8 reacted fuel (Table F-5). The oxidized melt magnitude (30.36 mCi/cm) was generated by assuming an identical ^{90}Sr concentration to Sample 4H from cross section STM-4, with factors 39.16 mCi/cm, 0.933 (region B), 1.50 (region B), and an equivalent ^{235}U area fraction of 0.554 (Figure F-7).

The region D ^{90}Sr magnitude of 17.73 mCi/cm was produced by multiplying 39.16 mCi/cm, a 1.304 power factor (Figure F-5), a 0.847 fraction of nominal ^{235}U (Figure F-7), and a 0.41 best-estimate retention fraction from STM-13 (Table F-5). Again, this amounts to assuming 41% retention throughout region D.

The 17.90 mCi/cm region E magnitude used factors of 39.16 mCi/cm, a 0.973 power average (Figure F-5), a 0.969 fraction of nominal ^{235}U (Figure F-7), and 0.485 ^{90}Sr retention fraction (average of STM-13 and -19 from Table F-5). Similarly, the region F magnitude (12.18 mCi/cm) was generated by multiplying 39.16 mCi/cm, 0.554 power factor (Figure F-5), a 1.002 fraction of nominal ^{235}U (Figure F-7), and a STM-19 best-estimate retention fraction of 0.56 (Table F-5).

Finally, the whole-bundle posttest average of 20.93 mCi/cm was calculated by multiplying each regional ^{90}Sr magnitude (histogram height) by the corresponding regional length (A:0.113 m, B:0.087 m, C:0.065 m; D:0.034 m, E:0.175 m, and F:0.135 m), summing the products, and dividing the total by 0.915 m. Comparing 20.93 mCi/cm to the decay-corrected pretest average (39.16 mCi/cm) yielded a whole-bundle ^{90}Sr retention value of 53%. Note that this whole-bundle value was largely determined by the retention percentages from STM-13 and STM-19, which jointly specify regions D, E, and F.

A rigorous whole-bundle uncertainty calculation is impossible without more RFP measurements. The known and estimated error sources previously described combine to produce an uncertainty of approximately ±30% relative, which neglects uniformity of fission product retention within each region. Several additional measurements within each region would be required to estimate regional retention variability, as well as to legitimately calculate valid average retention values.

The foremost implication of Figure F-8 is that a substantial fraction of the ^{90}Sr inventory escaped the fuel matrix due to transient release processes. However, the timing of the migration from the bundle region cannot be deduced from this analysis. The other prominent result from Figure F-8 is that a large portion of the posttest ^{90}Sr was retained by the metallic and oxidized melts (see Figure F-7). Were it not for this effect, overall bundle retention of this fission product would have been measurably smaller. Figure F-8 also implies that melt slumping to regions B and C was influential in releasing ^{90}Sr from the coated fuel pellets, although this observation is less definite.

^{95}Nb. The retention histogram for ^{95}Nb (^{95}Zr daughter product) is displayed in Figure F-9. All regional calculations used a decay-corrected pretest inventory of 3.63 mCi/cm, rather than the 39.16-mCi/cm ^{90}Sr value. The only other differences were the relevant ^{95}Nb retention fractions, as indicated on Table F-6.

The posttest weighted average of 2.66 mCi/cm is 73% of the pretest whole-bundle average, the highest overall retention value for the six RFP species measured. This may reflect some neutron activation of zircaloy. Figure F-9 shows 14.1% of the posttest ^{95}Nb within the melts, by comparison to 8.7% of the total ^{235}U (Figure F-7). However, this extra ^{95}Nb can largely be explained by melt slumping from a high flux elevation, unlike ^{90}Sr and ^{144}Ce, so there is no clear indication of preferential ^{95}Zr absorption by the melts. Figure F-9 also reveals very high retention within region F, after allowing for the low 0.554 power factor. This observation suggests irreversible deposition of ^{95}Zr on oxidized upper structural surfaces, as discussed earlier for the STM-19 results.

^{106}Ru. Figure F-10 presents the ^{106}Ru retention histogram. The 51% whole-bundle retention of ^{106}Ru is the lowest value of the six RFPs measured. Figure F-10 displays no evidence of melt absorption and irreversible deposition, which probably contributes to the small overall retention within the bundle region.

The ^{106}Ru content in UO_2 of Region C is unusually high and suggests that Sample 4H underestimated the ^{106}Ru content in the STM-8 oxidized melt. Figure F-10 does not infer that melt slumping to regions B and C stimulated ^{106}Ru release from coated fuel pellets. Thus, ^{106}Ru escape from the fuel matrix may have required particularly high temperatures that only occurred at higher bundle elevations.

^{125}Sb. The retention histogram for ^{125}Sb is presented in Figure F-11. Melt absorption is marginally lower for ^{125}Sb than ^{235}U, especially when allowance is made for melt slumping from a high flux elevation. Consequently, solubility of ^{125}Sb in the melts was relatively low, as with ^{106}Ru. However, upper bundle ^{125}Sb retention is quite large, by comparison to regions B and C. This finding indicates irreversible deposition on oxidized upper structural surfaces, as mentioned in the earlier discussion of results from STM-19 grindings and Samples 19S and 19T. Thus, overall retention within fuel pellets was probably somewhat smaller than the 66% posttest weighted average.

^{137}Cs. Figure F-12, the ^{137}Cs retention histogram, shows the most uniform retention over the bundle length of any RFP, after consideration of the average power peaking factors. Retention within region C reacted fuel appears unrealistically large, but this could be because of Sample 4H underestimating the ^{137}Cs content of region C oxidized melt (as with ^{106}Ru). Melt coating of region C pellets should have transferred sufficient heat for substantial release of this relatively volatile fission product from this elevation.

^{144}Ce. The Figure F-13 retention histogram for ^{144}Ce generally resembles Figure F-8 for ^{90}Sr. Strong melt absorption of ^{144}Ce is again the dominant profile indication. The 61% whole-bundle retention for ^{144}Ce is in the middle of the range for the six measured RFP species, and probably would have been lower without the preferential melt absorption.

9. FALLBACK BARRIER ANALYSIS

The SFD-ST test train incorporated a fallback barrier just above the fuel bundle, with the primary purpose of preventing any condensed steam droplets from returning to the bundle. The large surface area of the fallback barrier had the potential for significant fission product retention ($>0.5\ m^2$). Fifteen samples were extracted during initial disassembly of the lower test train (Figure F-14) and were counted as point sources directly.[F-5, F-6] No acid leaching/chemical separation was performed to permit ^{90}Sr assays due to the small likelihood of strontium deposition.

The gamma spectrometry results are presented in Table F-7, after normalization to visually estimated surface areas. Combined uncertainties are generally within $\pm 25\%$ relative. However, gamma self-absorption may have extensively perturbed values for tube sections L1, S1, S2, and S3, and samples with predominate deposition on sides facing away from the spectrometer. Note also that the area-normalization treatment presumes uniform deposition, but variations in flow impaction, horizontal surface accumulation, and vertical surface adhesion probably prevented consistent behavior.

The Table F-7 format is intended to facilitate comparisons at various fallback barrier positions, but is not suitable for listing the tellurium isotopic findings. Samples 4A, 5A, 5C, and 9A (counted on 14 June 1983) showed respective ^{129m}Te (459 keV) amounts of 4.1, 4.6, 3.0, and 2.4 μCi. However, this isotope was either not observed, or obscured on spectra obtained from the remaining samples after nearly seven additional months of decay. Meanwhile, ^{127m}Te (57 and 417 keV) emissions were not reported in Reference F-5, but are listed as minimum amounts for several samples in Reference F-6. These microCurie values are >5.5 for Sample 10, >3.4 for Sample 11, >55 for Samples S1 and S2, >13 for Sample L1, and >1.7 for Sample 14T. Peak interferences prevented quantification for remaining samples, apart from Sample 15 where no ^{127m}Te peak was detectable. Thus, measurably significant deposition of tellurium isotopes did occur within the fallback barrier.

Two key trends are apparent on Table F-7 with regard to fission products measured within the bundle. First, ^{95}Nb, ^{106}Ru, ^{125}Sb, and ^{144}Ce were found in much larger concentrations toward the bottom of the

fallback barrier and ZrO_2 steam inlet tube (see Figure F-14). Second, ^{137}Cs was evidently transported differently, because it was more commonly located in appreciable amounts on upper barrier and steam tube portions.

Only ^{95}Zr, ^{95}Nb, ^{103}Ru, ^{106}Ru, ^{125}Sb, ^{137}Cs, ^{140}Ce, ^{144}Ce, and ^{152}Eu (of the radionuclides in Table F-7) are fission products. Possible sources for the remaining activation products include zircaloy cladding, zirconia insulation, Inconel grids, bundle thermocouples, and water. None of the activation products clearly correlate with fission products, and therefore no inferences on transport media could be drawn. For example, ^{58}Co, ^{60}Co, and ^{113}Sn occurred in especially large concentrations on Sample 5A, along with ^{95}Nb, ^{106}Ru, ^{125}Sb, and ^{144}Ce, but this apparent relationship is not supported by Sample S3. Neutron activation of the fallback barrier base could also contribute significantly to the ^{95}Zr and ^{95}Nb counted on lower samples. However, Sample S3 (located much higher) demonstrated that some transport and deposition of ^{95}Zr did occur, although it is not clear whether the ^{95}Zr originated within the UO_2 fuel or was activated within zircaloy cladding and zirconia insulation.

However, one correlation with deposition of nonvolatile fission products could be tentatively established. Sample 5A contained relatively large amounts of a white scale prevalent at the fallback barrier base, as shown along the side powdery ZrO_2 fiberboard remnants at the top of Figure F-15. Substantial scale was also found on Samples 4A and 5C, whereas Sample 4A was shielded from transient flows by the bottom orifice plate and Sample 5C was radially removed from the flow stream. Meanwhile, samples from middle and upper barrier regions, like those at the base of Figure F-15, revealed only occasional white specks. The interior of Sample S3 could not be viewed, so this visual correlation to ^{95}Nb, ^{106}Ru, ^{125}Sb, and ^{144}Ce content cannot be extended further.

In retrospect, scrapings should have been taken from the barrier base for gamma counting and ^{90}Sr assays, since the scale possibly represents a transient accumulation of carrier particles. Much of the white material in Figure F-15 is zirconia insulation flushed from the bundle center during the transient, the reflood and flushing phases, and later flow testing. With its high surface area and initial proximity to UO_2 fuel, zirconia insulation would be a possible transport medium.

However, much of the loosely attached, compacted powder was dislodged, along with any attached fission products, during impact fracturing of Samples 4A, 5A, and 5C. (Impact separation is shown in Figure F-16). The white substance more prevalent on the extracted samples was the relatively adherent scale, which was most apparently deposited on the ZrO_2 pellets in Figure F-15. Limited bonding of the scale to ZrO_2 implies the presence of other compounds in the scale. Therefore, other chemical compounds may have been involved in transporting the measured ^{95}Nb, ^{106}Ru, ^{125}Sb, and ^{144}Ce. Again, without discrete samples of both the scale and powder from the barrier bottom, it is impossible to determine the base material compositions and fission product concentrations.

To provide some perspective on absolute fission product retention within the fallback barrier, the ^{95}Nb, ^{106}Ru, ^{125}Sb, ^{137}Cs, and ^{144}Ce concentrations (decay-corrected to 6 January 1984) from Table F-7 were averaged and scaled upward, assuming 0.52 m^2 total surface area within the barrier (including the ZrO_2 inlet tube). Results for these radionuclides were then compared to whole-bundle inventories calculated by ORIGEN2 for 29 October 1983, and decay-adjusted to 6 January 1984. The retention fraction estimates so produced are 4×10^{-3} for ^{95}Nb, 6×10^{-3} for ^{106}Ru, 3.2×10^{-2} for ^{125}Sb, 3×10^{-3} for ^{137}Cs, and 9×10^{-5} for ^{144}Ce.

These retention fractions are of very limited accuracy. The fifteen samples were strongly biased toward upper barrier regions (Figure F-14). As a consequence, ^{137}Cs retention may be overestimated, while deposition of nonvolatile fission products on lower barrier regions is underestimated. It is noteworthy that 34% of the ^{95}Nb, 56% of the ^{106}Ru, 48% of the ^{125}Sb, and 21% of the ^{144}Ce in the 15-sample area-normalized averages originated on Sample 5A, but only 1.6% of the total ^{137}Cs was found there. Again, the absence of gamma spectrometer data on both the adherent scale and the compacted powder at the bottom of the fallback barrier is a major shortcoming.

10. DISCUSSION OF WHOLE-BUNDLE INVENTORIES

The preceding calculations of whole-bundle posttest fission product inventories necessarily involved many approximations. The extrapolation of the local fission product concentrations and associated retention fractions over large axial regions of the SFD-ST bundle was a particularly large source of uncertainty. Many more local measurements would be required to produce accurate whole-bundle values. It should also be recognized that many techniques were adopted for the first time on the Scoping Test, so significant analytical improvements can be expected on posttest examinations of future SFD bundles.

Despite the above limitations, certain preliminary deductions have been made from the SFD-ST RFP measurements. The most obvious is that measurable fractions of the ^{90}Sr, ^{95}Nb, ^{106}Ru, ^{125}Sb, ^{137}Cs, and ^{144}Ce inventories escaped the bundle region. The actual whole-bundle fractions may differ from the nominal quantities indicated in Figures F-8 through F-13, due to accumulated bias errors. In addition, the assumption of morphological uniformity in fission product retention was probably more valid for some fission products than others, but the data base was not sufficient to establish any such trends.

The conclusion of significant bundle losses of all six RFP species is partially confirmed by on-line detection of several cesium radioisotopes in quantity. Approximately 30% of the ^{137}Cs inventory and 36% of the ^{136}Cs inventory were measured downstream of the bundle and fallback barrier.[F-7] These results qualitatively support the 47% overall bundle release indicated in Figure F-12 for ^{137}Cs. This agreement indicates the absence of any large systematic bias, that would apply to all six RFP species, in the calculated whole-bundle posttest values.

Reference F-7 also states that very little (<0.1%) of the strontium, zirconium (niobium parent), ruthenium, antimony, and cerium radioisotopes were detected at the spectrometers and in the effluent samples. Furthermore, ^{95}Nb, ^{106}Ru, ^{125}Sb, and ^{144}Ce were not found irreversibly deposited in large amounts within the fallback barrier assembly. Thus, apart from ^{137}Cs, large discrepancies exist between on-line measurements and the posttest retention determinations for all RFP species.

It is possible that substantial fractions of the missing ^{90}Sr, ^{95}Nb, ^{106}Ru, ^{125}Sb, and ^{144}Ce are located at the bottom of the fallback barrier. If this inference from Table F-7 is correct, it is reasonable to suppose that additional fission products were deposited on the upper rod plenums, Al_2O_3 spacer pellets, upper end caps, and the upper shroud liner. Recognizing that the upper gross gamma scan includes some axial position uncertainty, one indication of such deposition exists in Figure E-1 (Appendix E) where the cosine shape flattens briefly before falling off to zero activity. Fission product deposition on largely unsampled structural components, combined with bias errors in bundle retention values, could conceivably close the mass balances for ^{90}Sr, ^{95}Nb, ^{106}Ru, ^{125}Sb, and ^{144}Ce.

However, losses of these species from the bundle region may have occurred by other means. Bundle flow resistance testing was performed without spectrometer monitoring before test train disassembly, and the SFD-ST bundle was stored in the PBF canal for roughly two months before air storage began. Therefore, long-term leaching, separation, and settling processes could have had some influence on RFP concentrations. In addition, drying of the bundle before neutron radiography involved heating above the boiling point of water for several days with a purging flow of dry nitrogen gas. Although generally consistent with the unetched core-drilled cylinders, the ground RFP samples would have been affected by any metallographic etching damage that penetrated beyond the 25 μm pre-ground layer. Volatilization of these elements during acid dissolution is unlikely, especially because little cesium was apparently lost to the atmosphere. However, this possibility cannot be completely discounted. Similarly, any texture effects during grinding (e.g., preferential removal of grain boundary substances) should have been self-compensated by the pre-grinding step, but again this cannot be positively demonstrated.

Assuming that acid-dissolution losses of ^{90}Sr, ^{95}Nb, ^{106}Ru, ^{125}Sb, and ^{144}Ce were negligible, the above candidate loss mechanisms could not readily liberate fission products from within UO_2 grains. Consequently, it is probable that the missing fission products were at least released to grain boundaries during the transient. Moreover, ^{137}Cs and ^{125}Sb clearly escaped fuel pellets in substantial amounts, with

appreciable ^{125}Sb irreversibly deposited on hot structural surfaces. Thus, it is conceivable that some ^{90}Sr, ^{95}Zr, ^{106}Ru, and ^{144}Ce also escaped the UO_2 pellets before cooldown.

Releases of fission products from UO_2 pellets would not be too surprising where fuel liquefaction occurred. Approximately 9% of the total ^{235}U was found in the oxidized and metallic melts (Figure F-7), so at least this percentage of the initial pellet volume was dissolved. Approximately another 5% of the total UO_2 resided as liquefied fuel that solidified before slumping from regions D, E, and F. Furthermore, fuel liquefaction typically occurred at higher than average neutron flux elevations, so a significant fraction of the fission product inventories could conceivably have escaped the UO_2 pellets by this mechanism.

However, liquefaction-induced releases cannot satisfactorily explain the relatively small retentions indicated for the nonvolatile fission products. Liquefied fuel Sample 19T showed nearly the same retentions as solid fuel pellets at the STM-19 elevation. In addition, ^{90}Sr and ^{144}Ce retention values in the melts indicate that fuel liquefaction did not result in significant release of these species. It should be noted that melt retention was included in the mass balance calculations.

It is therefore necessary to explore potential fission product removal processes from UO_2 that stayed solid during the transient. Reference F-7 attributes most of the volatile releases to quench-shattering of UO_2 pellets, where fission products are presumed to be suddenly freed from grain boundaries exposed by thermal shock. However, this explanation was not supported by the posttest bundle examinations. Some embrittled rods did fracture over regions D and E during cooldown, but local pellet fragments are between one-tenth and one-half of the original volume. Nothing approaching the size of individual fuel grains was found, excepting remnants of the ZrO_2 insulation. Moreover, some of the observed fracturing occurred during bundle handling, in combination with axial shifting of the debris. Finally, although some evidence was found of fuel microcracking during metallography and SEM examinations, UO_2 grains were generally closely spaced. Thus, steam and water would not have had prompt access to the vast majority of fuel grain boundaries during the cooldown phase.

The explanation in Reference F-7 relies to a large extent on the observation that large amounts of volatile fission products did not reach the gamma spectrometers until approximately two minutes after scram, seemingly implying a burst release from grain boundaries. However, the thermocouple data indicated that the saturation temperature of 556 K was achieved throughout the bundle about 8 min after reactor scram. Therefore, the *quench* phase discussed in previous documents actually consisted of a gradual cooldown, due largely to the solidified melt mass low in the bundle, rather than sudden thermal shock. In addition, spikes from two absolute pressure transducers were used in Reference F-7 as evidence of sudden coolant-fuel interactions. However, a detailed examination of the transducer data was performed and it was concluded that the pulses were more likely to be electrical noise than the result of physical phenomena occurring in the fuel bundle.[F-8] The final high temperature and cooldown phases of the test, and the impact on fission product release, are discussed in more detail in the main text.

One phenomenon contributing to delayed arrival of fission products at the spectrometers was the fracturing of certain structural components that permitted previously released fission products to escape from dead spaces, either by gas flow or coolant washout. The largest such region was above the fallback barrier, as shown in Figure F-14. The holes in the ZrO_2 steam inlet tube were located 0.25 to 0.30 m below the transition to the zircaloy steamline. This ZrO_2 tube fractured apparently during reflood (along with the embrittled inner heat dissipation tube), which suddenly forced trapped gases above the original inlet elevation into the steamline. Although the gas mixture was predominately hydrogen molecules, krypton, xenon, and any gaseous forms of iodine, cesium, and tellurium would also have occupied this volume. A similar situation possibly existed in upper rod plenums and upper bundle insulation, where fracturing during reflood would have freed other trapped gases.

The bundle differential pressure was evidently sufficient to fracture the bundle along the embrittled rods coated by melt (between the 0.10- and 0.17-m elevations) and lift most of the bundle upward at least 0.115 m. Only the lowest melt-encrusted segment returned to its original elevation during posttest handling, while

other bundle segments were wedged in place against insulation strengthening tubes. The Appendix E radiograph (Figure E-2c) further illustrates extensive damage to upper fuel rod plenums that contrasts with preservation of bundle geometry in upper fueled regions. Thus, it is very likely that the upper rod end caps impacted the base of the fallback barrier, shattering both the embrittled upper plenum cladding and the ZrO_2 inlet tube within the barrier (see Section 4.10 of main text for more discussion).

One phenomenon conceivably involved in transporting nonvolatile fission products from solid fuel pellet interiors to available deposition surfaces is melt reduction of UO_2. Many pellet remnants were extensively penetrated along major pellet cracks by molten zircaloy fingers (see Appendix E and Reference F-9). Consequently, some of the fuel that stayed solid during the transient was chemically altered. Strontium, ruthenium, and cerium are generally regarded as stable within a solid UO_2 matrix, although this understanding may be invalid as fuel melting temperatures are approached. No data exists to support the stability of fission products in the UO_{2-x} formed at high temperatures by oxygen absorption into nearby molten zircaloy. Recent data suggest that rare-earth oxides will vaporize as monoxides in a reducing environment, with much higher effective volatilities.[F-10]

The scanning electron microscopy/energy-dispersive x-ray spectroscopy and scanning Auger spectroscopy data in Appendix E largely confirm deductions made in Reference F-9. However, these elemental composition studies uncovered two unexpected results, with implications on the phenomena governing the fission product releases measured during the Scoping Test.

The first finding was that hyperstoichiometric uranium oxides formed above the solidified melt region of the test bundle. Oxygen concentrations were measured on only three samples from the upper three-fourths of the bundle, but hyperstoichiometric fuel ($\sim UO_{2.6}$) was discovered on all three samples. The fuel oxidation apparently occurred during the cooldown phase, after rapid zircaloy oxidization had been terminated and after local melts had solidified. No firm deductions can be made on the total amount of hyperstoichiometric fuel, but this phenomenon may have been responsible for some delayed fission product releases from fuel microcrack networks that are apparently related to reduced grain boundary adhesion in oxidized fuel.

The second finding was of less definite significance and concerns the particularly high neutron attenuation of the metallic melt located near the 0.14-m bundle elevation. (Shown as very dark material in Figure E-5.) Reference F-3 deduced that the metallic melt was either very dense or contained large amounts of highly attenuating bundle elements (U, Ni, or thermocouple constituents). However, neither suggestion proved correct. The 4D core-drilled cylinder had a density of only 7.6 g/cm^3, (Table F-1) and volume of 0.125 cm^3. Appendix E determined that the material was mostly oxygen-stabilized alpha-zircaloy, with relatively small amounts of dissolved Inconel and uranium. The explanation for the strong neutron attenuation is believed to be an extraordinarily high hydrogen content (not detectable by EDS and SAS). Since the metallic melt is considered to have formed and slumped during a temporary flow reduction, the large hydrogen content implies that high temperature fuel was also exposed to an ambient hydrogen atmosphere over a significant duration. Due to the rapid hydrogen diffusion rates under such conditions, fission product hydrides, hydroxides, and monoxides could have formed both inside fuel grains and along grain boundaries.

Very little is known about volatilities of these chemical compounds at the fuel temperatures experienced during the SFD-ST. However, vapor transport of hydrides, hydroxides, and monoxides during a significant flow reduction could explain the observed deposition of ^{95}Nb, ^{106}Ru, ^{125}Sb, and ^{144}Ce on the fallback barrier base without these radionuclides being detected at the gamma spectrometers downstream. However, this phenomenon is highly speculative and is mentioned here mainly for the sake of completeness. Nevertheless, a similar situation could arise in a severe reactor accident during a sudden change from a steam-rich to a steam-starved environment, such as would occur after sufficient melt slumped into a lower plenum to completely evaporate the coolant. Accordingly, this candidate release mechanism may warrant further investigation.

11. CONCLUSIONS

Fission product retention was estimated for several prominent radionuclides within the SFD-ST fuel bundle region. The calculated retention values are 0.53 for ^{90}Sr, 0.73 for ^{95}Nb, 0.51 for ^{106}Ru, 0.66 for ^{125}Sb, 0.53 for ^{137}Cs, and 0.61 for ^{144}Ce. Numerous approximations were required, especially where local measurements were extrapolated on the basis of gross fuel morphology. Uncertainties in the above retention values cannot be estimated without many more samples.

The indicated fission product releases primarily occurred within solid fuel pellets, because at most, 15% of the fuel was liquefied during SFD-ST and because fuel liquefaction probably affected no more than 20% of the fission product inventories. Likely phenomena contributing to solid fuel releases are UO_2 reduction by molten cladding (melt absorption of oxygen) and postscram formation of hyperstoichiometric fuel (enhanced fuel oxidation). The possibility also exists that fission product hydrides, hydroxides, and monoxides formed and volatilized during a short significant flow reduction related to melt accumulation near the bundle base.

Most of the released ^{137}Cs was transported downstream to the gamma spectrometers during the high temperature transient and subsequent reflood. Meanwhile, ^{90}Sr, ^{95}Zr, ^{106}Ru, ^{125}Sb and ^{144}Ce evidently migrated only short distances. The last four species appear to be associated with deposition of a white scale on the base of the fallback barrier. Some cesium and tellurium were also found irreversibly deposited within the fallback barrier.

Oxidized and metallic melt samples showed strong absorption of ^{90}Sr and ^{144}Ce, by comparison to ^{235}U. This finding suggests high solubilities and permanent trapping of these species in (U,Zr,O) melts.

Evidence of irreversible deposition of ^{125}Sb was detected on oxidized structural surfaces within the bundle region. This isotope also displayed measurably significant release from relatively cool, chemically unaltered fuel pellets.

12. RECOMMENDATIONS

The grinding method of extracting retained fission product samples introduced several major problems. Uranium was apparently not leached from the ground fines and grinding papers with expected efficiency, and this difficulty could also have extended to strontium separations. In addition, the intended $\pm 10\%$ tolerance on ground layer thicknesses was not achieved on most samples, resulting in somewhat larger measurement uncertainties than desired. The grinding approach did, however, provide sufficiently small samples for developing sample processing techniques in a glove box environment. These techniques can now be adapted to hot cells that can accommodate much larger samples. Accordingly, 3-mm thick slices are being cut from the SFD 1-3 and 1-4 bundles during initial sectioning operations, thus eliminating complications from the grinding disks and paper wipes and reducing relative errors from thickness imprecisions. Furthermore, these slices will definitely be free of any possible alterations from metallographic etching. Slice-extraction of cross-sectional samples will not remove the necessity of determining area fraction of melts and different fuel types on the mating bundle faces to be studied metallographically. Manual planimetry proved barely adequate for this purpose, due to subjectivity and an inability to resolve small melts, fuel pellet fragments, and porosity on the macrophotographs. Digital image processing should ideally provide the required area fractions at higher precision. This technique was attempted on photographs of the SFD-ST cross sections, but the illumination was too uneven to convert gray level ranges into discrete material fractions. Thus, a suitable lighting procedure should be developed.

Manual planimetry experienced considerably greater difficulty on the cross-sectional reconstructions from neutron tomography than the macrophotographs. Preliminary efforts to digitally process the tomographic images were encouraging, but it became evident that the filtered back-projection algorithm introduced excessive noise. Nevertheless, with algorithm development targeted toward this objective, it is possible that accurate

posttest profiles of major bundle constituents would be produced at elevation separations of only 0.4 mm. It is even feasible that reduced, Zr-penetrated fuel and hyperstoichiometric fuel could be nondestructively separated from nominal UO_2, which would be invaluable for modeling transient fuel behavior and fission product release processes on a macroscopic scale.

The strong possibility of nonvolatile fission product deposition between the fuel column top and the fallback barrier base has not been confirmed. Due to the large associated mass balance gaps for these species, a sample should be extracted from this region and gamma counted. A ^{90}Sr determination should also be performed if appreciable gamma emissions from ^{95}Nb, ^{106}Ru, ^{125}Sb, and ^{144}Ce are detected on this sample.

Core-drilled samples for retained fission product analysis were arbitrary in location and too few in number. Consequently, fission product concentrations could not be clearly separated by the fuel pellet morphology (microcrack patterns, grain size distributions, melt penetration along cracks, inward Zr diffusion, etc.) to support modelling efforts. A small aperture gamma spectrometer able to scan over bundle cross sections is virtually essential for such studies.

For a variety of reasons (discussed in this Appendix and main text) it was not possible to establish a detailed correlation between events in the bundle and fission product release from the fuel. Out-of-pile induction-heating experiments on irradiated fuel pellets in pure steam and pure hydrogen at representative pressures (7 MPa, 15 MPa) over a range of temperatures are important to provide unambiguous information on the two processes. Gamma spectrometry should be used to study time dependent release variations between fission products, with deposition coupons employed for determination of as-released chemical forms and metallography for corresponding fuel morphologies and UO_2 grain size distributions. A similar experiment is recommended involving UO_2 dissolution by molten cladding, to determine which fission products are released before and during liquefaction and to measure delayed releases upon emergence of shrinkage pores and cracks in the cooling melts.

13. REFERENCES

F-1. B. G. Schnitzler, EG&G internal letter to S. A. Ploger, "Revised SFD Scoping Test Inventories," BGS-85, May 15, 1985.

F-2. J. D. Abrashoff, *Reactor Physics Analysis for the Phase 1 Severe Fuel Damage Experiments in the Power Burst Facility*, EG&G Internal Document, EGG-PHYS-5550, October 1981.

F-3. B. A. Cook, P. A. Kalish, and D. M. Tow, *Posttest Examination of the Severe Fuel Damage Scoping Test Bundle Geometry*, to be issued.

F-4. S. A. Ploger, EG&G internal letter to P. D. Randolph, "Design/Estimate Request for SFD Test Train Gross Gamma Scanner," OGER-6-82, April 14, 1982.

F-5. R. J. Gehrke, J. W. Rogers, EG&G internal letter to B. A. Cook, "Radioisotope Activities of PFB-SFD-ST Fallback Barrier Samples," GEH-14-83, June 29, 1983.

F-6. R. J. Gehrke, EG&G internal letter to D. J. Osetek, "Fallback Barrier Samples from PBF Scoping Test," GEH-4-84, February 2, 1984.

F-7. A. W. Cronenberg, J. K. Hartwell, D. L. Hagrman, and D. J. Osetek, *Fission Product Behavior During the Severe Fuel Damage Scoping Test*, to be issued.

F-8. R. D. McCormick, EG&G internal letter to P. E. MacDonald, "SFD-ST Bundle Pressure Pulses," RDMC-2-83, February 7, 1983.

F-9. P. Hoffman, *Metallographic Examination of the Severe Fuel Damage Scoping Test Fuel Rod Bundle Cross Sections*, to be issued.

F-10. R. P. Wichner and R. D. Spence, "A Chemical Equilibrium Estimate of the Aerosols Produced in an Overheated Light Water Reactor Core," *Nuclear Technology, 70*, September 1985.

Table F-1. Retained fission products in core-drilled samples[a]

Sample (Weight) Type	Fission Product[b]	Aqua Regia Dissolution (μCi)	HNO_3/HF Dissolution of Solids (μCi)	Direct Counting of Insoluble Sludge[c] (μCi)	Total Microcuries[d]		^{235}U in Aqua Regia (μg)	^{235}U in HNO_3/HF (μg)	Total ^{235}U (μg)
4D (0.953 g) Metallic Melt	^{90}Sr	2.58 ± 0.03	120.0 ± 1.2	(2.4)	125.0 ± 6.5	(±5.2%)	4380 ± 240	12,800 ± 600	17,180 ± 840 (±4.9%)
	^{95}Nb	0.33 ± 0.01	2.64 ± 0.07	0.04 ± 0.01	3.01 ± 0.16	(±5.3%)			
	^{106}Ru	16.22 ± 0.25	2.79 ± 0.29	0.23 ± 0.05	17.24 ± 1.03	(±6.0%)			
	^{125}Sb	2.99 ± 0.06	1.19 ± 0.09	~0	4.18 ± 0.24	(±5.7%)			
	^{137}Cs	9.05 ± 0.06	1.74 ± 0.06	0.03 ± 0.01	10.82 ± 0.55	(±5.1%)			
	^{144}Ce	105.5 ± 0.3	342.1 ± 1.0	97.3 ± 0.2	544.9 ± 24.4	(±4.5%)			
4F (1.333 g) Fuel Pellet	^{90}Sr	29.4 ± 0.3	Not Necessary	(0.4)	29.8 ± 1.5	(±5.1%)	69,600 ± 3600	Not Necessary	69,600 ± 3600 (±5.2%)
	^{95}Nb	10.51 ± 0.26		0.45 ± ~0	10.96 ± 0.59	(±5.4%)			
	^{106}Ru	151.5 ± 2.9		2.52 ± 0.03	154.0 ± 8.1	(±5.3%)			
	^{125}Sb	10.72 ± 0.65		0.20 ± 0.01	10.92 ± 0.84	(±7.7%)			
	^{137}Cs	287.5 ± 1.3		4.33 ± 0.01	291.8 ± 14.4	(±4.9%)			
	^{144}Ce	1525.6 ± 3.9		19.9 ± ~0	1445.5 ± 71.4	(±4.9%)			
4H (0.760 g) Oxidized Melt	^{90}Sr	29.4 ± 0.3	72.0 ± 0.7	(2.1)	103.5 ± 5.3	(±5.1%)	840 ± 60	19,500 ± 1000	20,340 ± 1060 (±5.2%)
	^{95}Nb	0.13 ± ~0	4.56 ± 0.06	0.01 ± ~0	4.70 ± 0.24	(±5.1%)			
	^{106}Ru	1.18 ± 0.04	0.67 ± 0.16	0.01 ± ~0	1.86 ± 0.19	(±10.2%)			
	^{125}Sb	0.62 ± 0.02	0.47 ± 0.06	~0	1.09 ± 0.08	(±7.3%)			
	^{137}Cs	1.88 ± 0.02	2.16 ± 0.04	0.02 ± ~0	4.06 ± 0.21	(±5.2%)			
	^{144}Ce	59.48 ± 0.12	430.20 ± 0.79	4.17 ± 0.01	493.85 ± 24.50	(±5.0%)			
	^{90}Sr	1.44 ± 0.01	0.04 ± ~0	(0.09)	1.57 ± 0.09	(±5.4%)			
19S (0.441 g) Oxidized Zircaloy	^{95}Nb	0.06 ± 0.01	0.09 ± ~0	0.02 ± ~0	0.17 ± 0.01	(±5.9%)	660 ± 60	156 ± 18	816 ± 78 (±9.6%)
	^{106}Ru	0.52 ± 0.04	0.08 ± 0.01	0.54 ± 0.01	1.14 ± 0.08	(±7.0%)			
	^{125}Sb	4.50 ± 0.03	0.37 ± ~0	0.09 ± ~0	4.96 ± 0.25	(±5.0%)			
	^{137}Cs	0.59 ± 0.01	0.36 ± ~0	0.03 ± ~0	0.98 ± 0.05	(±5.1%)			
	^{144}Ce	9.45 ± 0.05	0.26 ± ~0	0.58 ± 0.01	10.29 ± 0.49	(±4.8%)			
19T (0.988 g) Liquefied Fuel	^{90}Sr	106.0 ± 0.1	Not Necessary	(2.4)	108.4 ± 5.4	(±5.0%)	53,300 ± 2600	Not Necessary	53,300 ± 2600 (±4.9%)
	^{95}Nb	4.84 ± 0.09		0.24 ± 0.01	5.08 ± 0.26	(±5.1%)			
	^{106}Ru	30.92 ± 0.72		13.44 ± 0.20	44.36 ± 2.18	(±4.9%)			
	^{125}Sb	3.49 ± 0.17		0.32 ± 0.04	3.81 ± 0.25	(±6.6%)			
	^{137}Cs	49.90 ± 0.29		26.02 ± 0.09	75.92 ± 3.62	(±4.8%)			
	^{144}Ce	486.1 ± 1.2		10.8 ± 0.1	496.9 ± 24.4	(±4.9%)			

a. All uncertainties computed at the 95% confidence level. Values in first three columns from counting statistics only.

b. Peak energies used for counting: ^{95}Nb: 766 keV, ^{106}RuD: 622 keV, ^{125}Sb: 428 keV, ^{137}Cs: 662 keV, and ^{144}Ce: 133 keV. ^{90}Sr measured by beta emission after chemical separation.

c. ^{90}Sr estimated from fraction of total ^{144}Ce in the sludge.

d. Total uncertainty value includes weighted terms from spectrometer calibrations and dry counting of sludge residues.

Table F-2. Retained fission products in ground samples[a]

Sample (Elevation) Thickness (μm)	Fission Product[b]	HNO_3 Leach of Fines, H_2O, and Grinding Disks	HNO_3/HF Dissolution of Remaining Sludge[c]	Direct Counting of Insoluble Sludge[c]	Post-Leaching Count of Grinding Disks[c]	Direct Counting of Paper Wipes (no Leaching)[c]	Total[d] Microcuries	Normalized[e] to 25 μm Thickness (μCi)	
STM-2	^{90}Sr	31.0 ± 0.31	(0.5)	(∼0)	(0.2)	(2.5)	34.2 ± 1.7	48.3 ± 6.2	(± 13.0%)
(0.055 m)	^{95}Nb	2.9 ± 0.06	0.4 ± 0.01	∼0	∼0	0.3 ± 0.01	3.6 ± 0.18	5.1 ± 0.66	(± 12.9%)
17.70 ± 2.18	^{106}Ru	23.1 ± 0.48	0.7 ± 0.05	0.1 ± ∼0	∼0	2.0 ± 0.06	25.9 ± 1.30	36.5 ± 4.8	(± 13.2%)
	^{125}Sb	1.2 ± 0.09	0.8 ± 0.02	∼0	0.1 ± ∼0	0.2 ± 0.01	2.3 ± 0.14	3.2 ± 0.43	(± 13.4%)
	^{137}Cs	38.6 ± 0.20	0.4 ± 0.01	∼0	∼0	3.0 ± 0.02	42.0 ± 1.98	59.4 ± 7.7	(± 13.0%)
	^{144}Ce	208.1 ± 0.63	3.3 ± 0.04	0.4 ± ∼0	1.2 ± 0.01	16.6 ± 0.06	229.6 ± 10.7	324.3 ± 41.8	(± 12.9%)
STM-4	^{90}Sr	44.5 ± 0.45	(2.9)	(1.4)	(6.3)	(8.9)	64.0 ± 3.9	67.0 ± 6.4	(± 9.6%)
(0.145 m)	^{95}Nb	3.8 ± 0.06	0.8 ± 0.01	∼0	1.1 ± 0.01	1.0 ± 0.02	6.7 ± 0.32	7.0 ± 0.60	(± 8.6%)
23.88 ± 1.65	^{106}Ru	20.8 ± 0.43	1.6 ± 0.05	2.1 ± 0.03	6.2 ± 0.09	5.2 ± 0.13	35.9 ± 1.81	37.6 ± 3.3	(± 8.8%)
	^{125}Sb	1.6 ± 0.10	0.8 ± 0.02	∼0	1.0 ± 0.02	0.5 ± 0.03	3.9 ± 0.22	4.1 ± 0.37	(± 9.0%)
	^{137}Cs	45.3 ± 0.20	0.2 ± 0.01	∼0	2.0 ± 0.02	6.9 ± 0.05	54.4 ± 2.45	57.0 ± 4.7	(± 8.3%)
	^{144}Ce	268.0 ± 0.70	17.6 ± 0.07	8.5 ± 0.03	38.2 ± 0.08	53.3 ± 0.18	385.6 ± 17.5	403.8 ± 33.7	(± 8.4%)
STM-8	^{90}Sr	52.5 ± 0.53	(1.2)	(1.6)		(13.7)	69.0 ± 4.3	86.8 ± 15.7	(± 18.1%)
(0.245 m)	^{95}Nb	4.5 ± 0.08	0.3 ± ∼0	0.2 ± ∼0		1.7 ± 0.02	6.7 ± 0.32	8.4 ± 1.5	(± 17.9%)
19.88 ± 3.38	^{106}Ru	28.3 ± 0.64	0.1 ± 0.01	2.2 ± 0.03		8.4 ± 0.16	39.0 ± 1.89	49.1 ± 8.7	(± 17.7%)
	^{125}Sb	1.3 ± 0.12	0.2 ± 0.01	0.2 ± 0.01		0.6 ± 0.03	2.3 ± 0.17	2.9 ± 0.54	(± 18.6%)
	^{137}Cs	38.0 ± 0.24	0.4 ± 0.01	1.0 ± 0.06		5.6 ± 0.04	45.0 ± 2.05	56.6 ± 10.0	(± 17.7%)
	^{144}Ce	311.3 ± 0.97	7.1 ± 0.03	9.2 ± 0.02		81.3 ± 0.21	408.9 ± 18.3	514.3 ± 90.4	(± 17.6%)
STM-13	^{90}Sr	30.2 ± 0.30	(0.6)	(0.4)	(2.8)	(5.1)	39.1 ± 2.2	44.5 ± 6.8	(± 15.2%)
(0.495 m)	^{95}Nb	2.7 ± 0.07	0.6 ± 0.01	∼0	0.8 ± 0.01	0.6 ± 0.01	4.7 ± 0.23	5.4 ± 0.80	(± 14.8%)
21.98 ± 3.05	^{106}Ru	14.2 ± 0.48	0.7 ± 0.03	1.3 ± 0.01	4.4 ± 0.06	3.4 ± 0.06	24.0 ± 1.27	27.3 ± 4.1	(± 15.0%)
	^{125}Sb	1.1 ± 0.11	1.1 ± 0.02	0.4 ± 0.01	1.0 ± 0.02	0.5 ± 0.01	4.1 ± 0.25	4.7 ± 0.72	(± 15.3%)
	^{137}Cs	40.4 ± 0.26	3.6 ± 0.02	0.2 ± ∼0	5.4 ± 0.02	3.4 ± 0.02	53.0 ± 2.39	60.3 ± 8.9	(± 14.8%)
	^{144}Ce	193.5 ± 0.81	3.7 ± 0.03	2.6 ± 0.01	18.2 ± 0.01	32.5 ± 0.08	250.5 ± 11.3	285.0 ± 41.9	(± 14.7%)
STM-19	^{90}Sr	27.3 ± 0.28	(0.4)	(0.3)	(0.9)	(2.1)	31.0 ± 1.5	28.6 ± 5.1	(± 17.9%)
(0.915 cm)	^{95}Nb	2.7 ± 0.05	0.7 ± 0.01	0.1 ± ∼0	0.4 ± 0.01	0.3 ± ∼0	4.2 ± 0.20	3.8 ± 0.67	(± 17.6%)
27.05 ± 4.58	^{106}Ru	7.2 ± 0.23	0.4 ± 0.03	5.6 ± 0.04	2.8 ± 0.05	1.4 ± 0.02	17.4 ± 1.08	16.1 ± 2.9	(± 18.0%)
	^{125}Sb	2.0 ± 0.07	0.7 ± 0.01	0.2 ± 0.01	0.3 ± 0.01	0.2 ± 0.01	3.4 ± 0.17	3.1 ± 0.55	(± 17.7%)
	^{137}Cs	21.8 ± 0.12	4.5 ± 0.02	0.4 ± ∼0	2.4 ± 0.02	1.6 ± 0.01	30.7 ± 1.39	28.4 ± 5.0	(± 17.6%)
	^{144}Ce	189.2 ± 0.51	2.7 ± 0.02	2.1 ± 0.01	5.9 ± 0.03	14.9 ± 0.03	214.8 ± 9.88	198.5 ± 35.0	(± 17.6%)

a. All uncertainties computed at the 95% confidence level. Uncertainties in first five columns due to counting statistics only.

b. Peak energies used for counting: ^{95}Nb: 766 keV, ^{106}Ru: 622 keV, ^{125}Sb: 428 keV, ^{137}Cs: 662 keV, and ^{144}Ce: 133 keV. ^{90}Sr measured by beta emission after chemical separation.

c. ^{90}Sr estimated from fraction of total ^{144}Ce in each material.

d. Total uncertainty value includes weighted terms from spectrometer calibrations and dry counting of sludge, disks, and wipes.

e. Total uncertainty value includes nonuniformity in ground layer thicknesses.

Table F-3. Retention percentages in core-drilled samples[a]

Cylinder RFP	4F (Intact Fuel Pellet)	4H[b] (Oxidized Liquefied Fuel)	4D[b] (Metallic Melt)	19T (Molten Fuel)	19S (Oxidized Zircaloy)
^{90}Sr	10% ± 1%[c]	150% ± 17%	214% ± 24%	80% ± 8%	62% ± 6%
^{95}Nb[d]	74% ± 6%	122% ± 14%	99% ± 11%	67% ± 7%	120% ± 12%
^{106}Ru	100% ± 9%	5% ± 1%	54% ± 6%	59% ± 6%	82% ± 9%
^{125}Sb	60% ± 5%	25% ± 3%	113% ± 13%	44% ± 5%	3100% ± 310%
^{137}Cs	98% ± 9%	6% ± 1%	18% ± 2%	53% ± 5%	37% ± 4%
^{144}Ce	105% ± 10%	145% ± 16%	193% ± 22%	74% ± 7%	83% ± 8%

a. Normalized to ^{235}U measured within each cylinder. Uncertainties do not include contribution for ORIGEN2 inventory.

b. Values not corrected for downward melt relocation from higher flux elevations.

c. Value suspect, probable measurement error.

d. Mostly ^{95}Zr during the SFD-ST transient.

e. Pronounced deposition.

Table F-4. RFP partitioning in cross section STM-4

RFP	STM-4 Total μCi (25 μm thickness from Table F-2)	Metallic Melt Content [8.56 cm^2] (% of total μCi)	Oxidized Melt Content [15.14 cm^2] (% of total μCi)	Unreacted Fuel Content [3.46 cm^2] (% of total μCi)	Reacted Fuel Remainder [10.12 cm^2] (% of total μCi)	Predicted Content of Reacted Fuel [100% retention]	Reacted Fuel Retention
^{90}Sr	67.0 ± 6.4 μCi	21.7 ± 4.6 μCi (32.4%)	33.7 ± 7.2 μCi (50.3%)	2.1 ± 0.3 μCi (3.1%)	9.5 ± 10.7 μCi (14.2%)	52.8 ± 5.9 μCi	18% ± 20%
^{95}Nb [^{95}Zr]	7.0 ± 0.6 μCi	0.52 ± 0.11 μCi (7.4%)	1.53 ± 0.33 μCi (21.9%)	0.76 ± 0.09 μCi (10.9%)	4.19 ± 0.70 μCi (59.9%)	4.63 ± 0.52 μCi	91% ± 18%
^{106}Ru	37.6 ± 3.3 μCi	3.0 ± 0.6 μCi (8.0%)	0.6 ± 0.1 μCi (1.6%)	10.8 ± 1.3 μCi (28.7%)	23.2 ± 3.6 μCi (61.7%)	31.8 ± 3.6 μCi	73% ± 14%
^{125}Sb	4.10 ± 0.37 μCi	0.72 ± 0.15 μCi (17.6%)	0.35 ± 0.08 μCi (8.5%)	0.76 ± 0.10 μCi (18.5%)	2.27 ± 0.42 μCi (55.4%)	3.47 ± 0.39 μCi	65% ± 14%
^{137}Cs	57.0 ± 4.7 μCi	1.9 ± 0.4 μCi (3.3%)	1.3 ± 0.3 μCi (2.3%)	20.4 ± 2.5 μCi (35.8%)	33.4 ± 5.3 μCi (58.6%)	55.7 ± 6.2 μCi	60% ± 12%
^{144}Ce	403.8 ± 33.7 μCi	94.4 ± 19.9 μCi (23.4%)	160.7 ± 34.2 μCi (39.8%)	101.1 ± 12.4 μCi (25.0%)	47.6 ± 53.4 μCi (11.8%)	292.2 ± 32.7 μCi	16% ± 18%

Table F-5. Fission product retentions inside SFD-ST fuel pellets[a]

Cross Section (Elevation)	STM-2 (0.055 m)	STM-4 (0.145 m)		STM-8 (0.245 m)	STM-13 (0.495 m)	STM-19 (0.915 m)
Morphology	Intact	25% Intact[b]	75% Reacted[c]	Reacted[d]	Reacted	Reacted
Fission Product						
^{90}Sr	83% ± 12%	10% ± 1%[e]	18% ± 20%	34%	41% ± 7%	56% ± 12%
^{95}Nb[f]	95% ± 14%	74% ± 6%	91% ± 18%[g]	78%	58% ± 11%	87% ± 18%
^{106}Ru	103% ± 15%	100% ± 9%	73% ± 14%	100%[h]	43% ± 8%	52% ± 11%
^{125}Sb	83% ± 12%	60% ± 5%	65% ± 14%	44%	66% ± 13%	92% ± 20%[i]
^{137}Cs	98% ± 14%	98% ± 9%	60% ± 12%	65%	54% ± 10%	54% ± 11%
^{144}Ce	100% ± 14%	105% ± 10%	16% ± 18%[j]	51%	48% ± 9%	71% ± 15%

a. This table concerns only those fission product percentages within UO_2 pellets, since fission products absorbed into melts have been subtracted from cross-sectional measurements. Thus, pellet retention must be distinguished from bundle retention. Uncertainties do not include contribution from ORIGEN2 inventory.

b. From pellet sample 4F, as factored into Table F-4.

c. From Table F-4, after subtracting fission products in intact pellets and inside metallic and oxidized melts.

d. Sample 4H concentrations applied to STM-8 oxidized melt and then subtracted from STM-8 totals. Uncertainties cannot be accurately estimated, since no core-drilled samples were extracted from STM-8 cross section.

e. Suspect value, probable measurement error.

f. Mostly ^{95}Zr during SFD-ST transient.

g. Value appears somewhat large. Content of ^{95}Nb in metallic and oxidized melts probably underestimated.

h. Value too large. ^{106}Ru concentration in STM-8 oxidized melt was apparently underestimated by extrapolating results from core drilled sample 4H.

i. Reflects deposition of ^{125}Sb on upper structural surfaces.

j. Value too low. Content of ^{144}Ce in metallic and oxidized melts overestimated by extrapolating 4D and 4H concentration.

Table F-6. Whole Bundle posttest fission product inventory calculations[a]

Region	A: 0 to 0.113 m	B: 0.113 to 0.200 m			
(power factor)[b]	(0.605)	(0.933)	(0.933)	(0.933)	
[fraction of nominal ^{235}U][c]	[1.00]	[0.751]	[0.472]	[0.083]	
Morphology	Intact Pellets	Reacted Pellets	Oxidized Melt	Metallic Melt	Rea
Fission Product (ORIGEN2 av. conc.)					
^{9}Sr (39.16 mCi/cm)	83% retention 19.66 mCi/cm	18% retention 4.94 mCi/cm	150% retention 25.86 mCi/cm	214% retention 6.50 mCi/cm	34% 13.88
^{95}Nb (3.63 mCi/cm)	95% retention 2.09 mCi/cm	91% retention 2.31 mCi/cm	122% retention 1.95 mCi/cm	99% retention 0.28 mCi/cm	78% 2.95
^{106}Ru (23.94 mCi/cm)	103% retention 14.92 mCi/cm	73% retention 12.24 mCi/cm	5% retention 0.53 mCi/cm	54% retention 1.00 mCi/cm	100% 24.96
^{125}Sb (2.59 mCi/cm)	83% retention 1.30 mCi/cm	65% retention 1.18 mCi/cm	25% retention 0.29 mCi/cm	113% retention 0.23 mCi/cm	44% 1.19
^{137}Cs (41.34 mCi/cm)	98% retention 24.51 mCi/cm	60% retention 17.37 mCi/cm	6% retention 1.09 mCi/cm	18% retention 0.58 mCi/cm	65% 28.02
^{144}Ce (220.5 mCi/cm)	100% retention 133.4 mCi/cm	16% retention 24.7 mCi/cm	145% retention 140.8 mCi/cm	193% retention 33.0 mCi/cm	51% 117.3

a. Regional fission product inventory = ORIGEN2 average concentration x regional power factor x fraction of nominal ^{235}U x

b. From Figure F-5.

c. From Figure F-7.

d. Concentration assumed identical to oxidized melt in Region B.

e. Regions D, E, and F cover two-thirds of the SFD-ST bundle, so bundle-average retentions are dominated by results from the ST

$$\text{Whole-bundle retention percentage} = \frac{100 \times (\text{regional inventory magnitude} \times \text{region length})}{\text{fuel stack length (0.9144 m)} \times \text{ORIGEN2 average concentration}}$$

C: 0.235 to 0.300 m		D: 0.315 to 0.655 m	E: 0.685 to 0.860 m	F: 0.895 to 1.030 m	
1.141)	(0.933)[d]	(1.304)	(0.973)	(0.544)	
0.914]	[0.554]	[0.847]	[0.969]	[1.002]	
ted Pellets	Oxidized Melt	Reacted Pellets	Reacted Pellets	Reacted Pellets	Bundle Average[e]
retention	150% retention	41% retention	48.5% retention	56% retention	53% retention
mCi/cm	30.36 mCi/cm	17.73 mCi/cm	17.90 mCi/cm	12.18 mCi/cm	20.93 mCi/cm
retention	122% retention	58% retention	72.5% retention	87% retention	73% retention
nCi/cm	2.29 mCi/cm	2.32 mCi/cm	2.48 mCi/cm	1.75 mCi/cm	2.66 mCi/cm
retention	5% retention	43% retention	47.5% retention	52% retention	51% retention
mCi/cm	0.62 mCi/cm	11.37 mCi/cm	10.72 mCi/cm	6.91 mCi/cm	2.26 mCi/cm
retention	25% retention	66% retention	79% retention	92% retention	66% retention
nCi/cm	0.33 mCi/cm	1.89 mCi/cm	1.93 mCi/cm	1.32 mCi/cm	1.70 mCi/cm
retention	6% retention	54% retention	54% retention	54% retention	53% retention
mCi/cm	1.28 mCi/cm	24.65 mCi/cm	21.04 mCi/cm	12.39 mCi/cm	21.93 mCi/cm
retention	145% retention	48% retention	61% retention	59.5% retention	71% retention
mCi/cm	165.2 mCi/cm	116.9 mCi/cm	9123.7 mCi/cm	86.9 mCi/cm	135.4 mCi/cm

retention fraction

M-13 and -19 cross sections.

TI
APERTURE
CARD

Also Available On
Aperture Card

8609300386-19

Table F-7. Isotopic activities in fallback barrier samples (Microcuries per cm^2)[a,b]

Isotope	Gamma Energy (keV)	4A 4.92 cm^2	5A 2.00 cm^2	5C 10.5 cm^2	9A 2.99 cm^2	10 2.85 cm^2	11 2.85 cm^2	12A 0.45 cm^2	13A 3.63 cm^2	14B 3.90 cm^2	14T 5.25 cm^2	15 18.0 cm^2	S1 27.4 cm^2	S2 48.7 cm^2	S3 13.0 cm^2	L1 101 cm^2
^{46}Sc	889	5.41 (0.98)	NAN/NOB	NAN/NOB	NAN/NOB	0.34	0.34	NOB	NOB	NAN/NOB	NOB	NOB	0.06	0.03	NOB	NOB
^{54}Mn	834	0.05 (0.03)	0.06 (0.04)	0.02 (0.01)	0.01 (~0)	0.03	0.03	0.03	0.02	0.01	~0	~0	0.02	0.01	~0	0.01
^{58}Co	810	0.88 (0.12)	2.18 (0.29)	0.24 (0.03)	0.13 (0.02)	0.09	0.06	0.08	0.06	0.04	0.01	~0	0.04	0.03	0.03	0.04
^{60}Co	1332	0.24 (0.22)	0.56 (0.52)	0.09 (0.08)	0.05 (0.05)	0.19	0.13	0.17	0.14	0.08	0.02	0.01	0.08	0.06	0.06	0.08
^{95}Zr	724	5.79 (0.63)	20.45 (2.21)	9.06 (0.98)	2.02 (0.22)	0.28	0.26	0.29	0.36	0.10	0.02	0.02	0.03	0.03	0.64	0.25
^{95}Nb[c]	765	11.8 (1.25)	40.40 (4.39)	17.62 (1.95)	4.01 (0.44)	0.63	0.60	0.64	0.83	0.22	0.06	0.03	0.07	0.06	1.39	0.53
^{103}Ru	497	1.36 (0.04)	4.90 (0.13)	0.31 (0.01)	0.01 (~0)	0.01	~0	0.20	0.01	0.01	NAN	NOB	NOB	NOB	0.07	0.01
^{106}Ru[c]	622	1.00 (0.68)	3.85 (2.63)	0.15 (0.10)	NAN/NOB	0.04	0.03	0.16	0.07	0.04	0.01	NOB	NOB	NAN	0.85	0.06
^{113}Sn	391	0.10 (0.03)	0.91 (0.26)	0.40 (0.12)	0.10 (0.03)	0.07	0.02	0.07	0.07	0.04	0.03	0.06	0.02	0.03	0.01	0.03
^{125}Sb[c]	427	7.89 (6.85)	14.85 (12.89)	1.16 (1.01)	0.21 (0.18)	0.63	0.13	0.93	0.66	0.54	0.25	0.15	0.64	0.48	1.38	0.39
^{137}Cs[c]	661	0.10 (0.10)	0.50 (0.49)	0.05 (0.05)	0.04 (0.04)	8.42	1.23	0.98	0.72	0.27	0.99	10.50	2.51	4.28	0.25	0.23
^{141}Ce	145	0.05 (~0)	2.40 (0.03)	NAN/NOB	NAN/NOB	NOB	NAN	~0	NOB	~0	NOB	NOB	NOB	NOB	0.03	0.01
^{144}Ce[c]	2185	NAN/NOB	2.30 (1.39)	NAN/NOB	NAN/NOB	0.39	0.25	0.78	0.14	0.33	0.05	NOB	NAN	NAN	2.85	0.56
^{152}Eu	1408	0.20 (0.19)	NAN/NOB	NAN/NOB	NAN/NOB	0.07	0.07	NOB	NOB	NOB	NOB	NOB	0.02	0.01	0.01	NOB
^{181}Hf	482	12.20 (0.42)	0.68 (0.02)	0.10 (~0)	0.02 (~0)	0.15	0.16	NOB	~0	~0	NOB	NOB	0.02	0.01	0.01	~0
^{182}Ta	1121 1221	0.31 (0.01)	0.57 (0.02)	0.11 (~0)	0.02 (~0)	0.03	0.03	0.05	0.01	0.01	~0	NOB	0.01	0.01	0.02	0.01

a. Samples 4A, 5A, 5C, and 9A were counted on 6-14-83 (230 days decay). Remaining samples were counted on 1-6-84 (436 days decay). Parenthetical values in first four data columns are decay-corrected to 1-6-84 for direct comparison.

b. NAN means peak interference. NOB means not observed. Both means cause of peak rejection not determined.

c. Concentrations from the 15 fallback barrier samples were averaged, scaled upward assuming 5200 cm^2 of barrier surface area, and then divided by the decay-corrected whole-bundle inventories. The inventory fractions thus estimated within the entire fallback barrier are 4×10^{-3} for ^{95}Nb, 6×10^{-3} for ^{106}Ru, 3.2×10^{-2} for ^{125}Sb, 3×10^{-3} for ^{137}Cs, and 9×10^{-5} for ^{144}Ce.

TI
APERTURE
CARD

8609300386-2D

Also Available On
Aperture Card

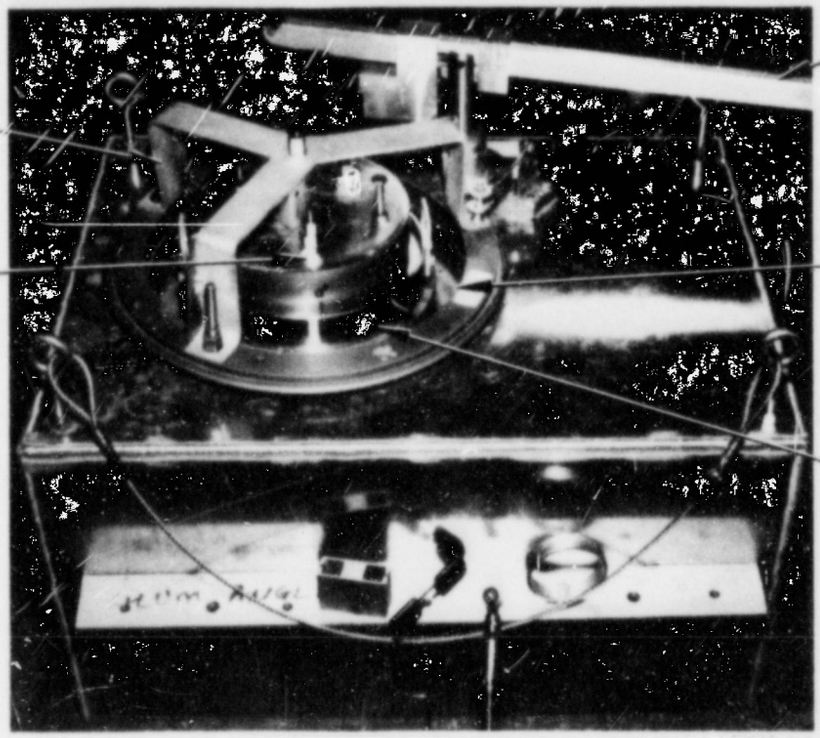

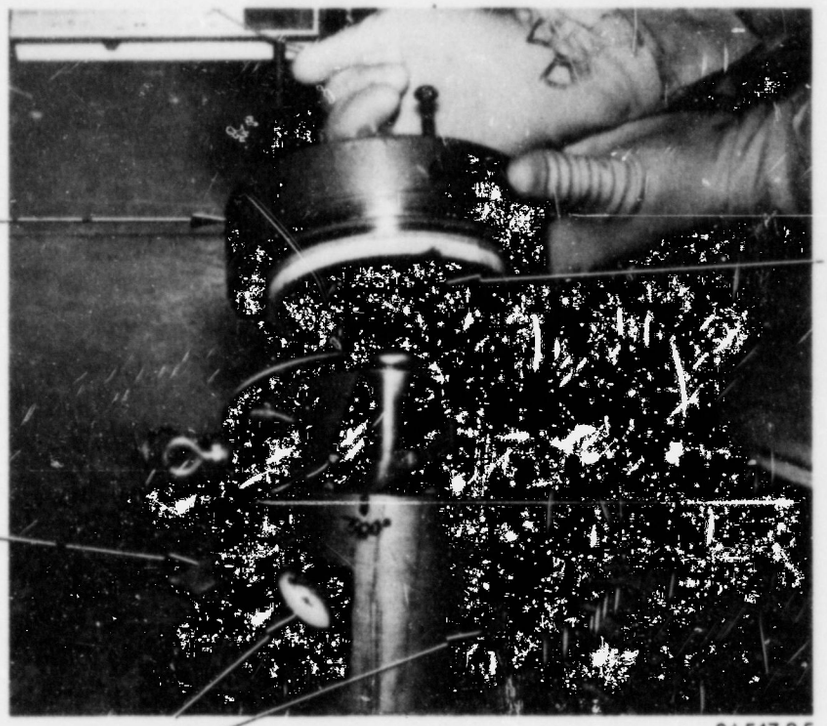

Figure F-1. Retained fission product grinding apparatus and dial-indicator fixture (before hot cell insertion.)

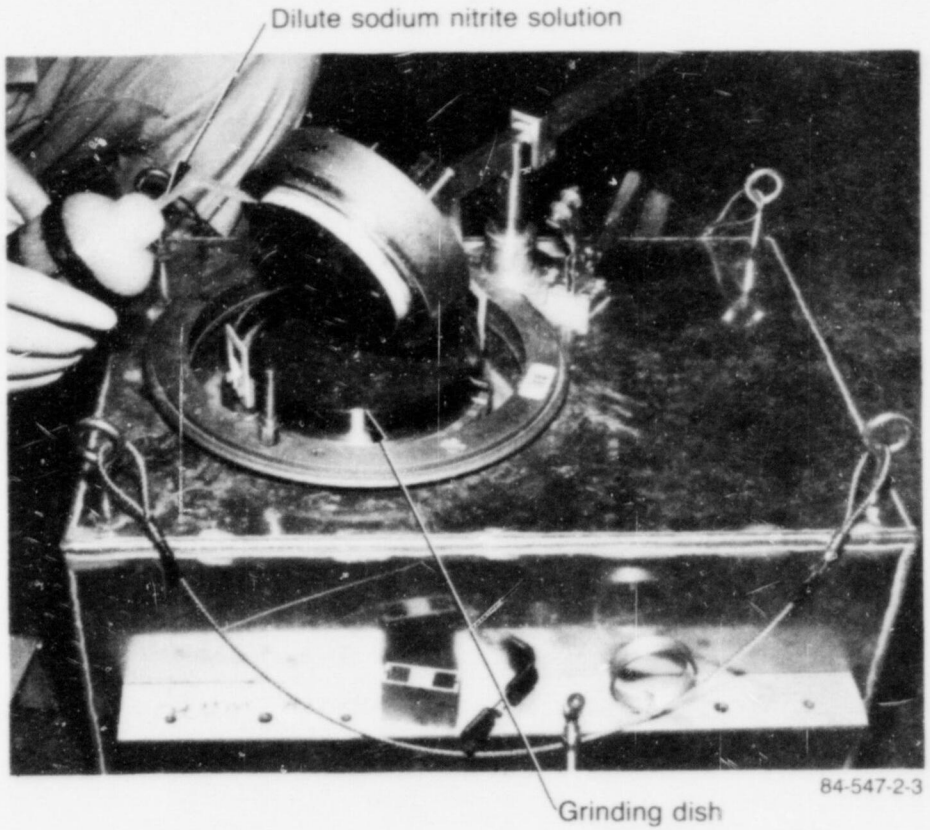

Figure F-2. Out-of-cell demonstration of (left) rinsing ground cross-sectional surface before dish removal and (right) decanting fines and lubricant before rinsing and changing grinding paper.

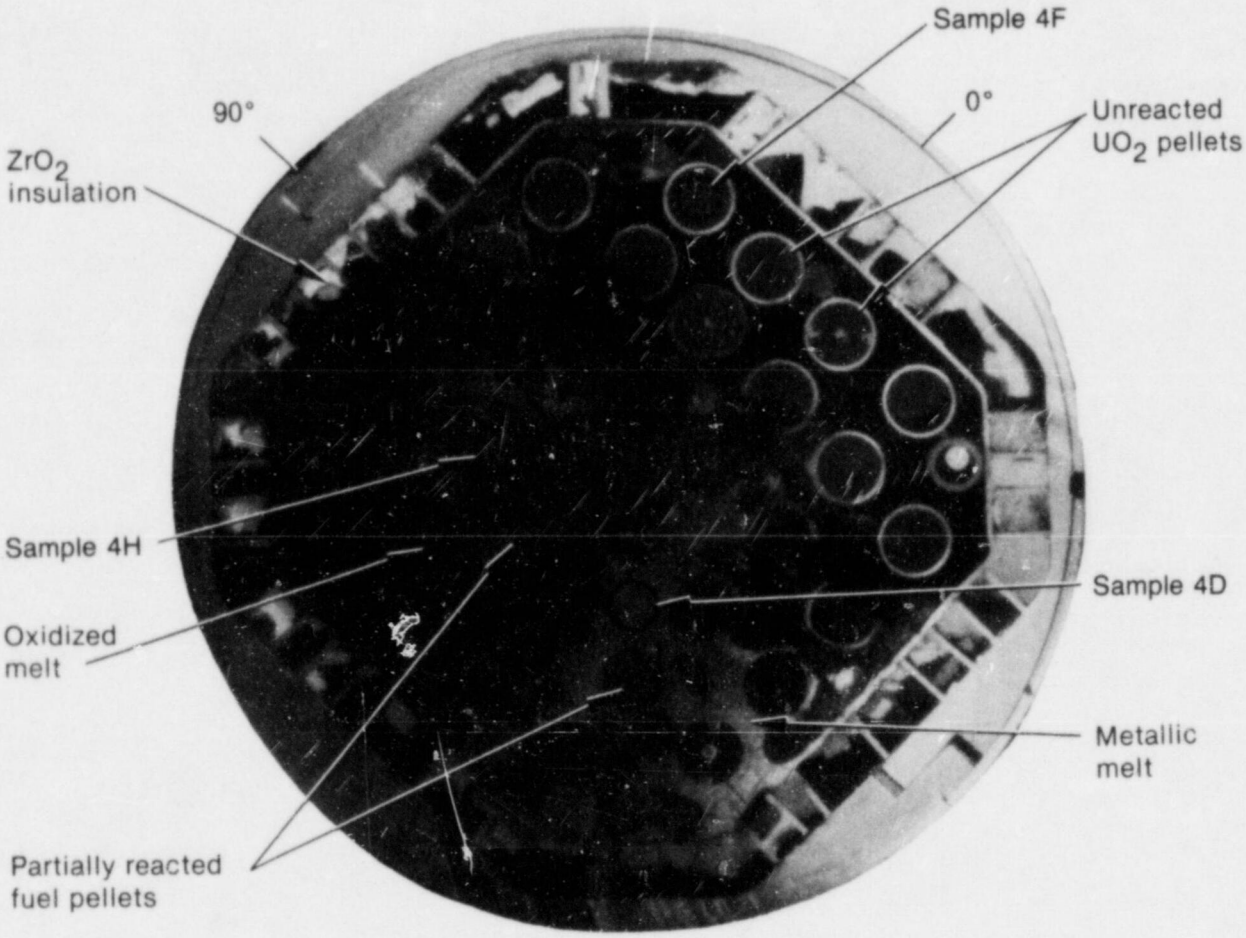

Figure F-3. Cross section STM-4 (0.145 m) showing core-drill positions.

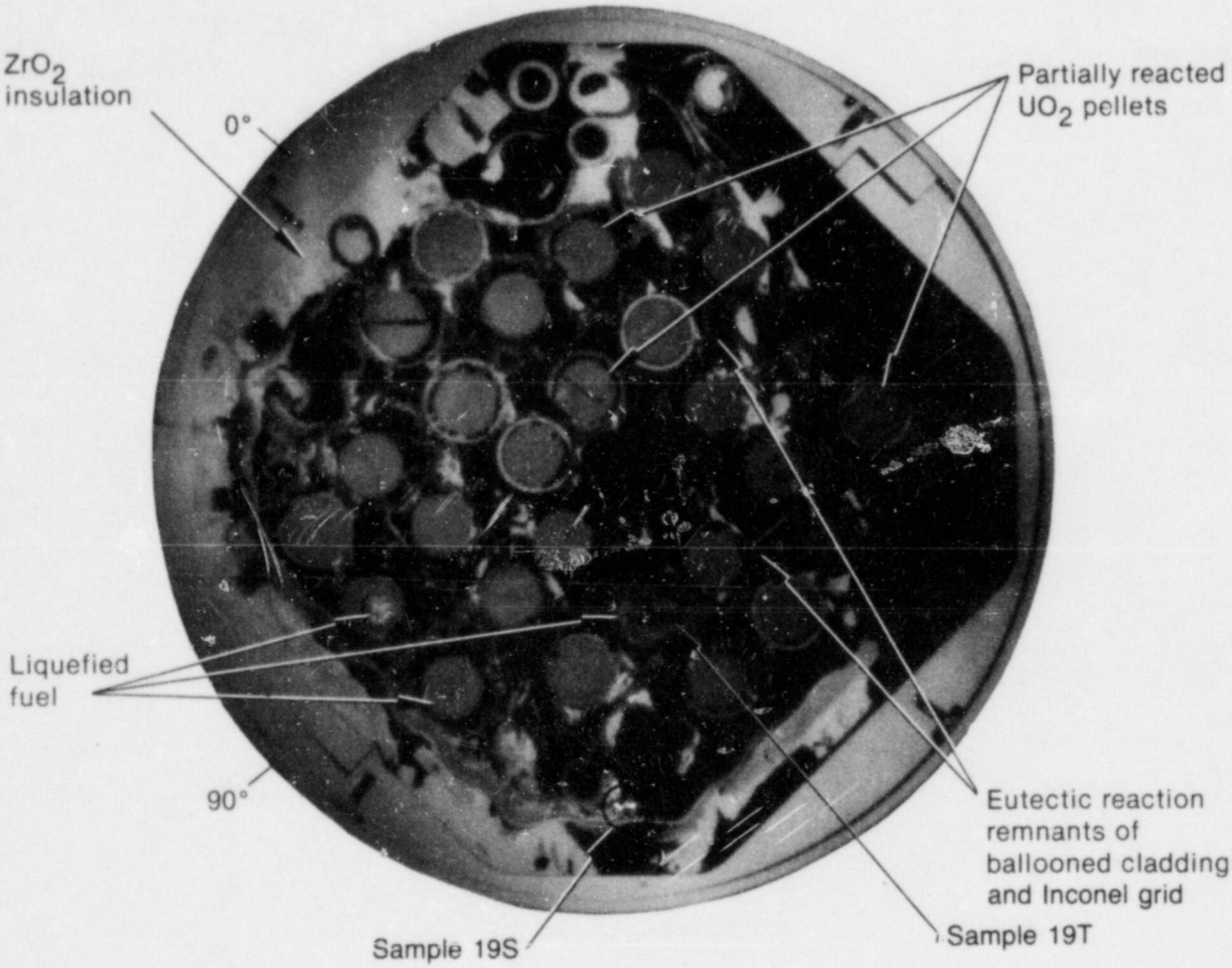

Figure F-4. Cross section STM-19 (0.915 m), illustrating core-drill positions.

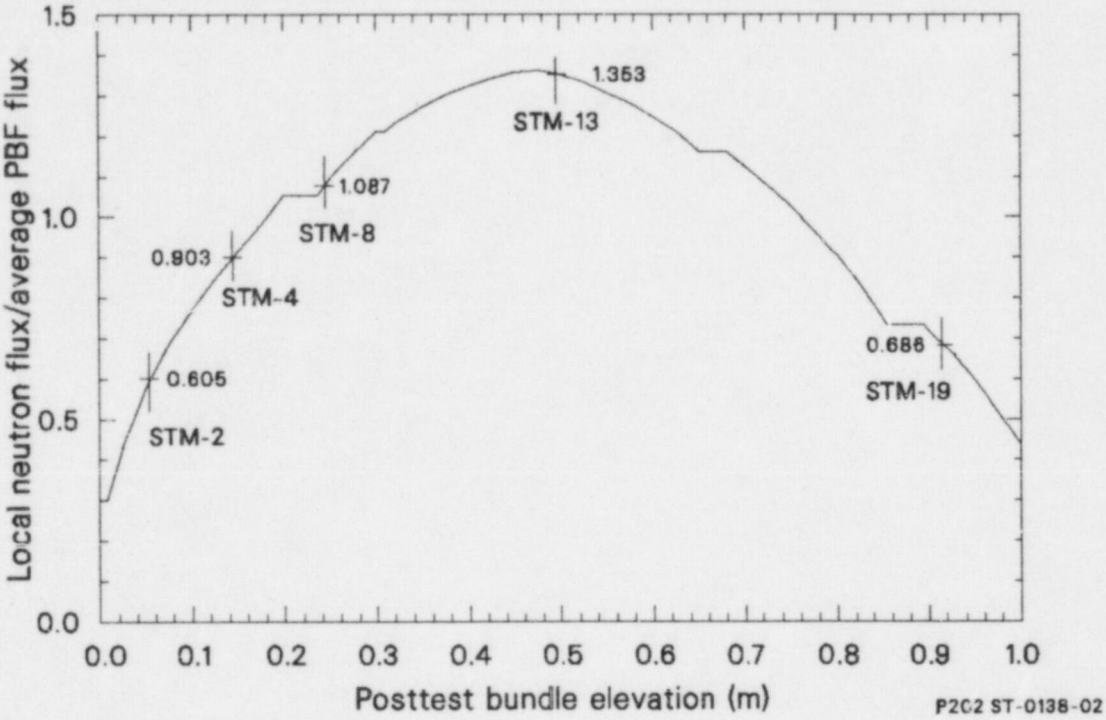

Figure F-5. Axial power profile adjusted for 0.115 m of stack growth according to neutron radiographs.

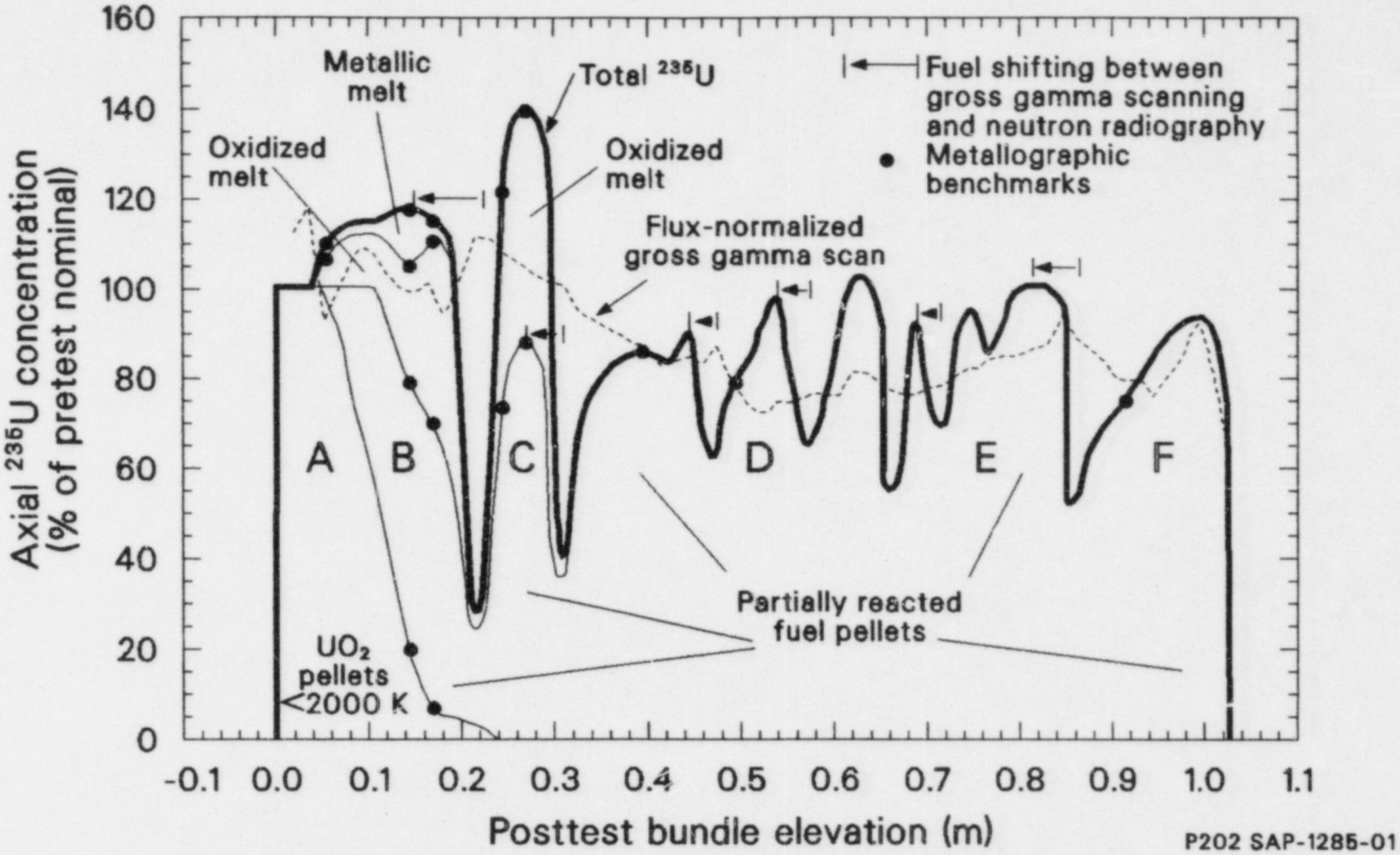

Figure F-6. Posttest distribution of ^{235}U estimated from neutron radiography and tomography, with assistance from metallographic planimetry and gross gamma scanning.

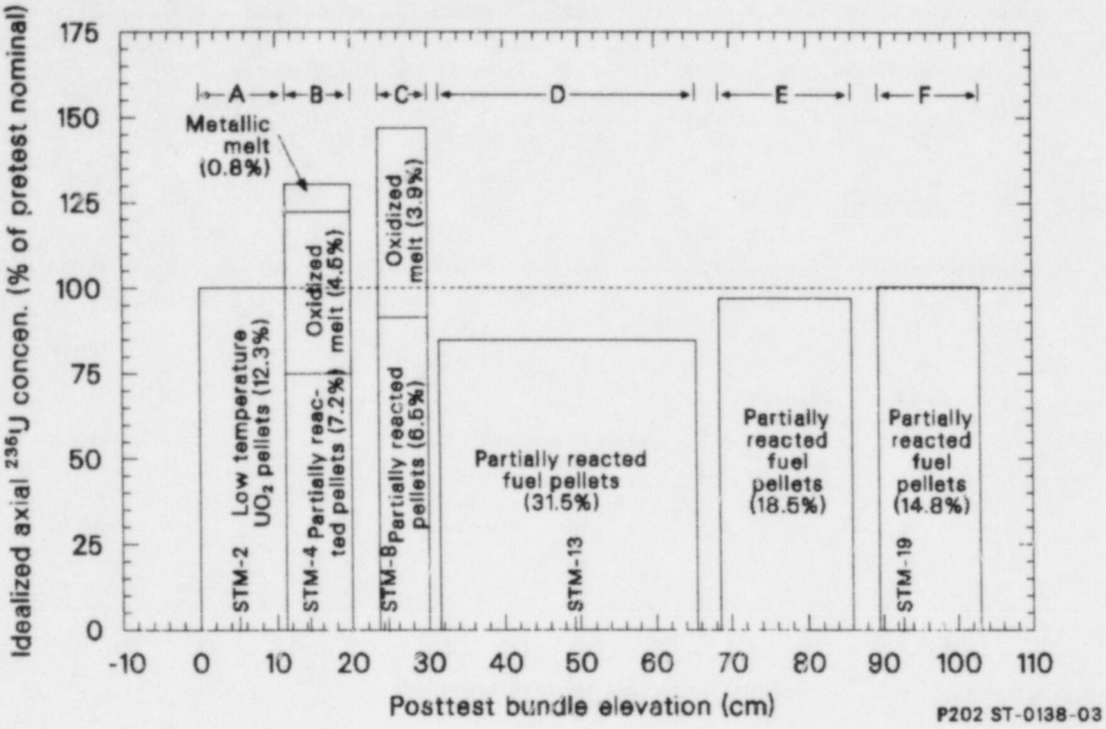

Figure F-7. Idealized ^{235}U distribution. (Regions D, E, and F contain small melt regions that could not be separated by planimetry.)

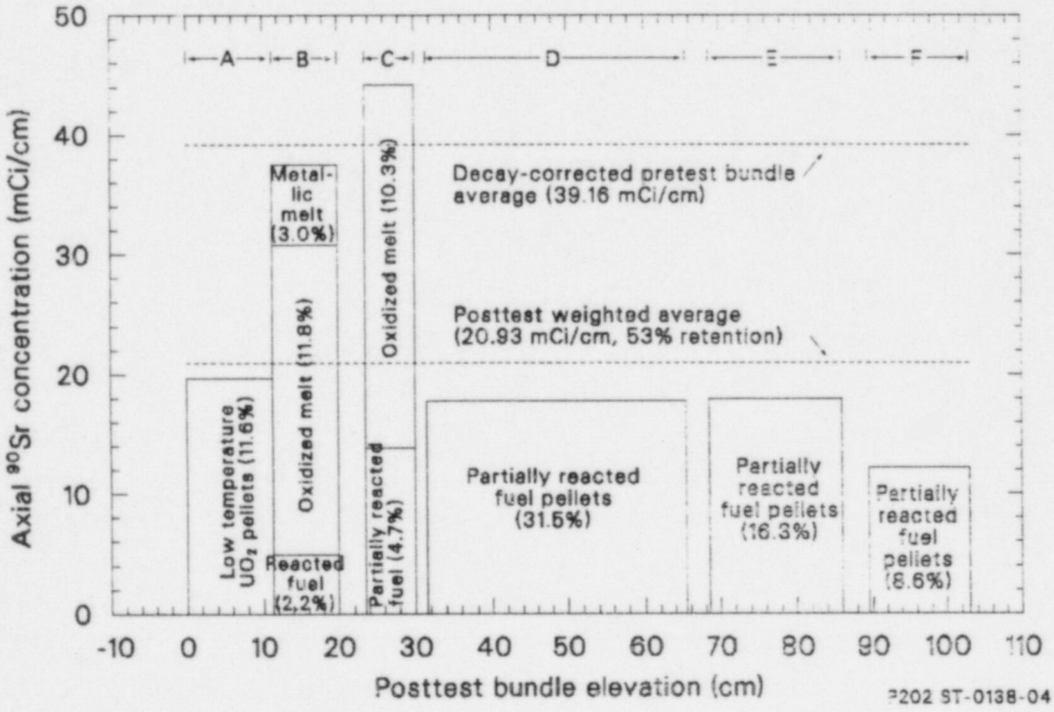

Figure F-8. ^{90}Sr distribution.

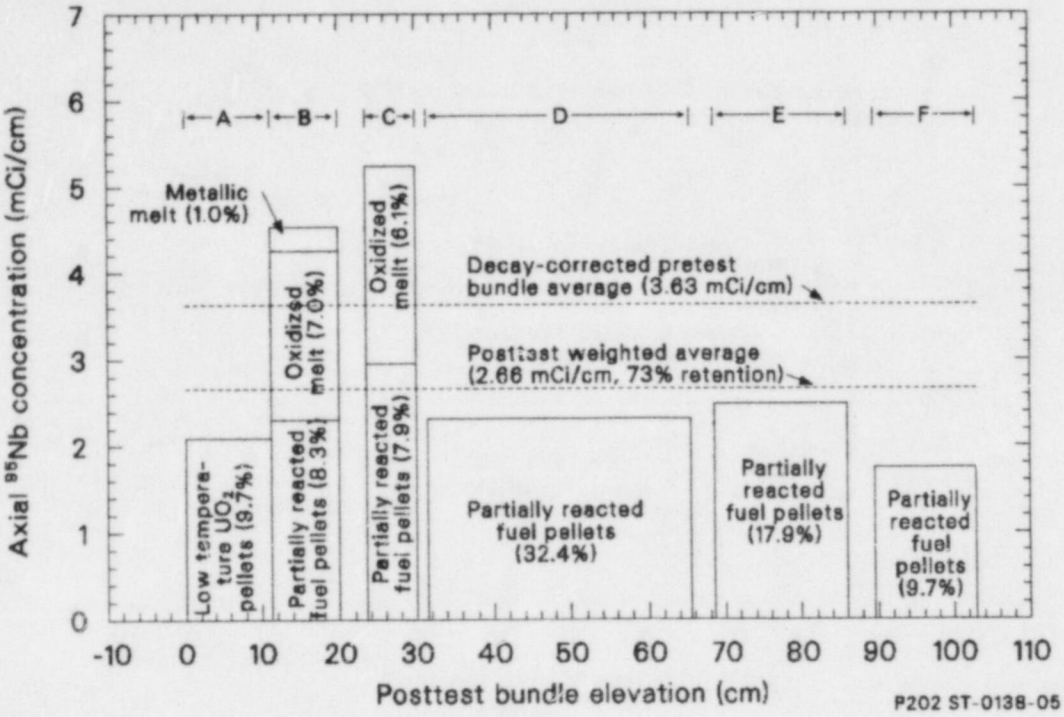

Figure F-9. ^{95}Nb distribution.

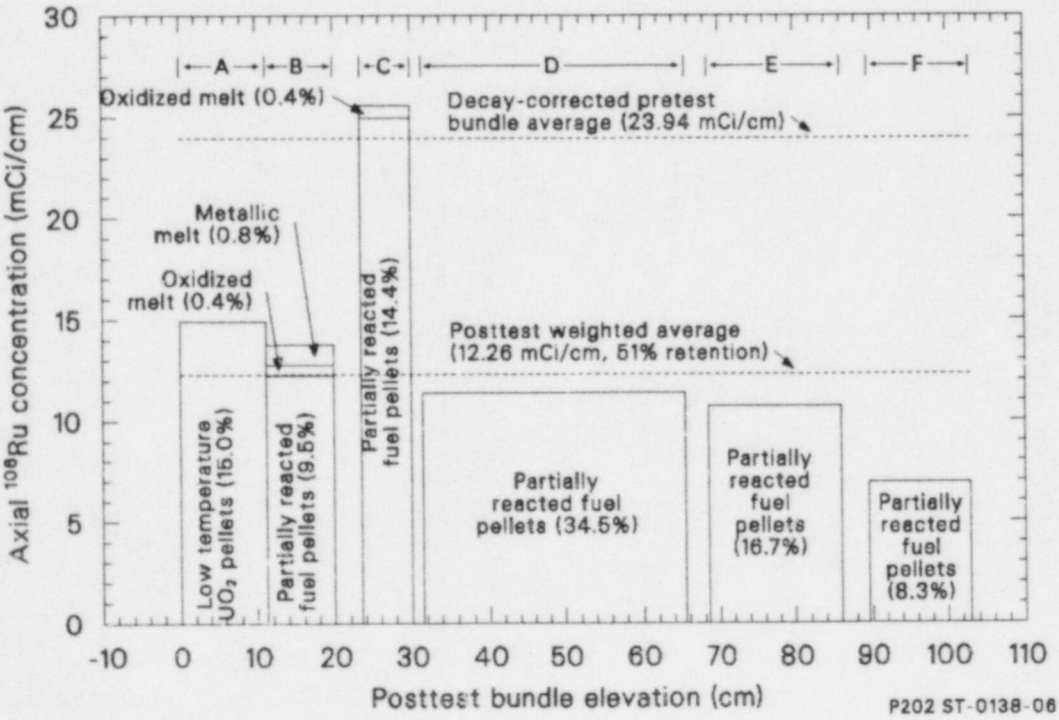

Figure F-10. ^{106}Ru distribution.

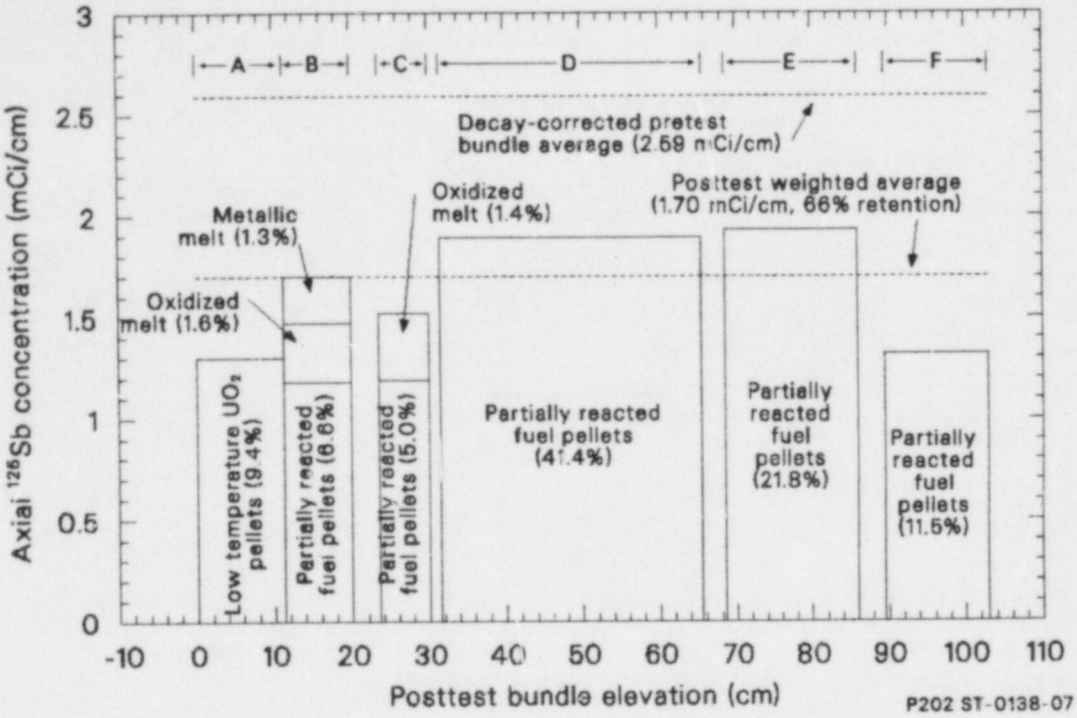

Figure F-11. ^{125}Sb distribution.

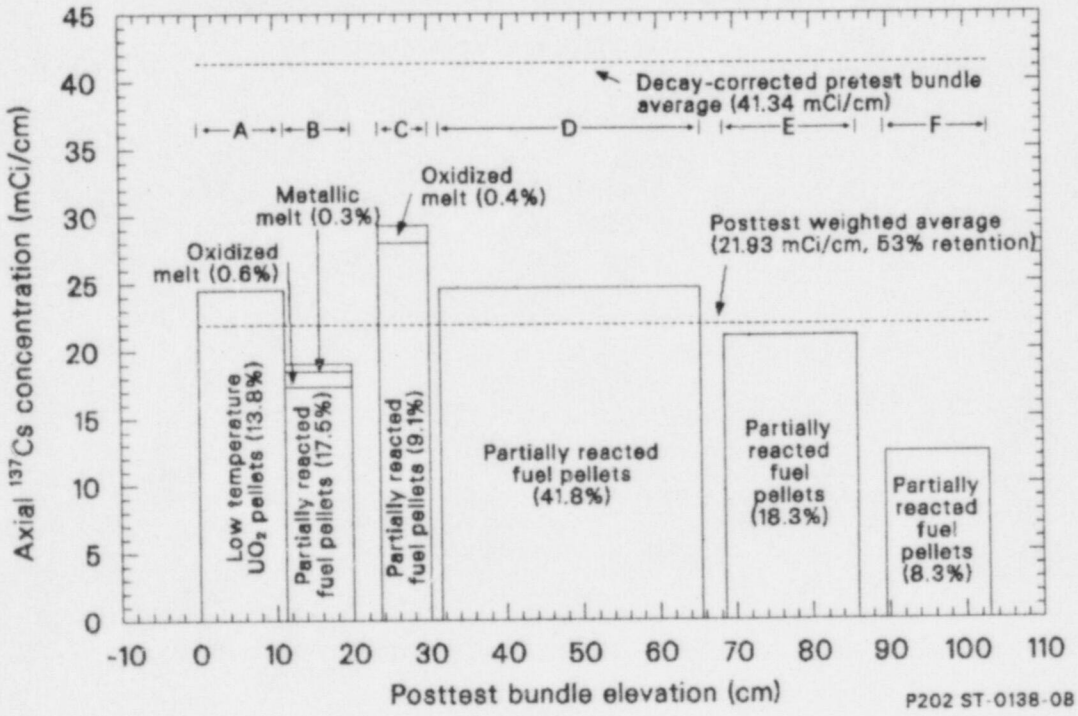

Figure F-12. ^{137}Cs distribution.

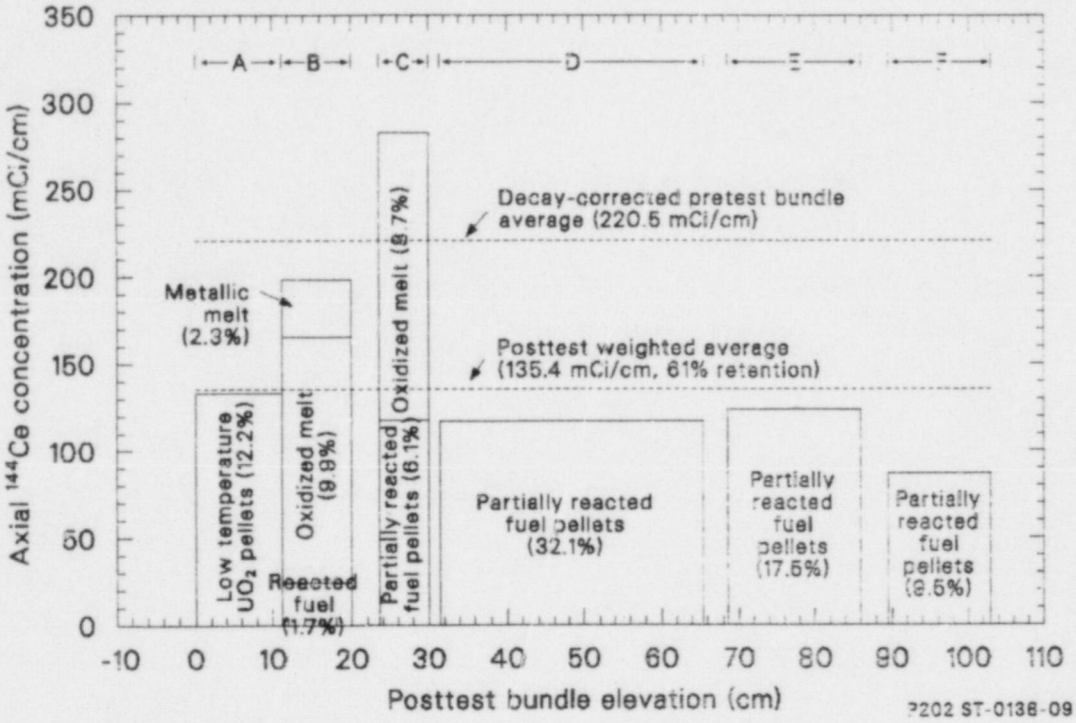

Figure F-13. ^{144}Ce distribution.

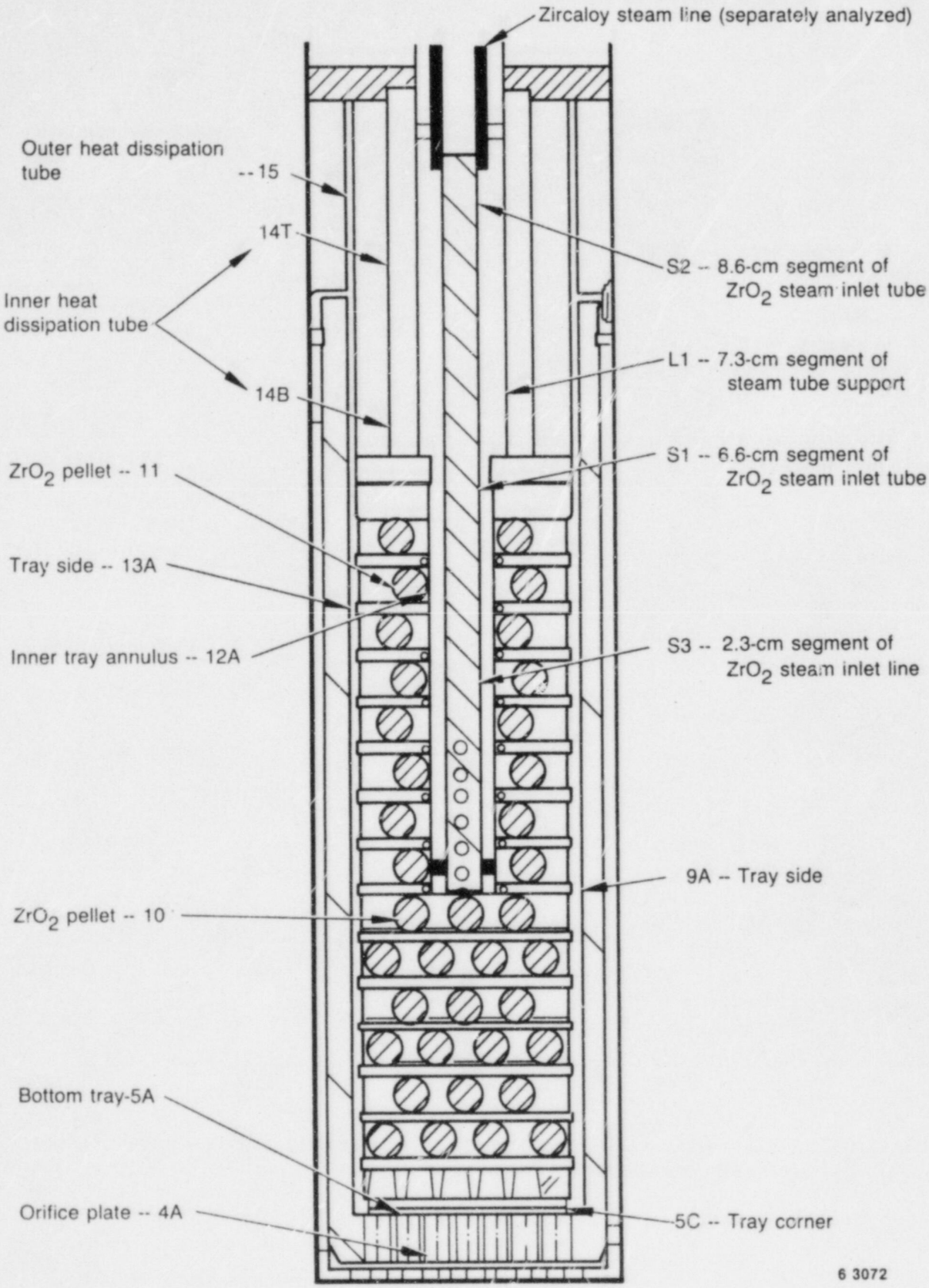

Figure F-14. Approximate positions of gamma counting samples extracted from fallback barrier. (Total height shown is approximately 0.42 m.)

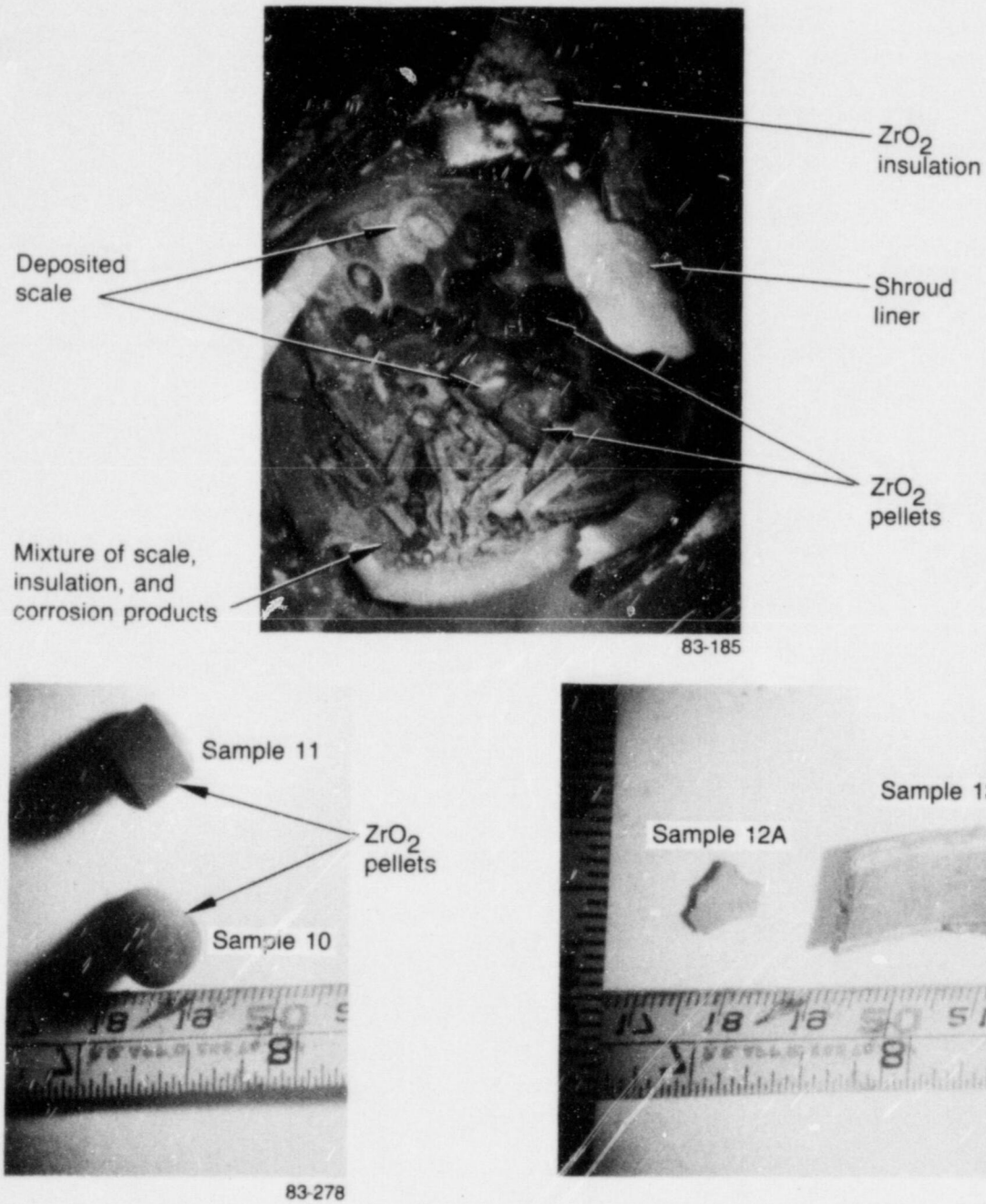

Figure F-15. Contrast in deposited scale and powder residue between the fallback barrier base and gamma counting samples from the middle and upper barrier regions.

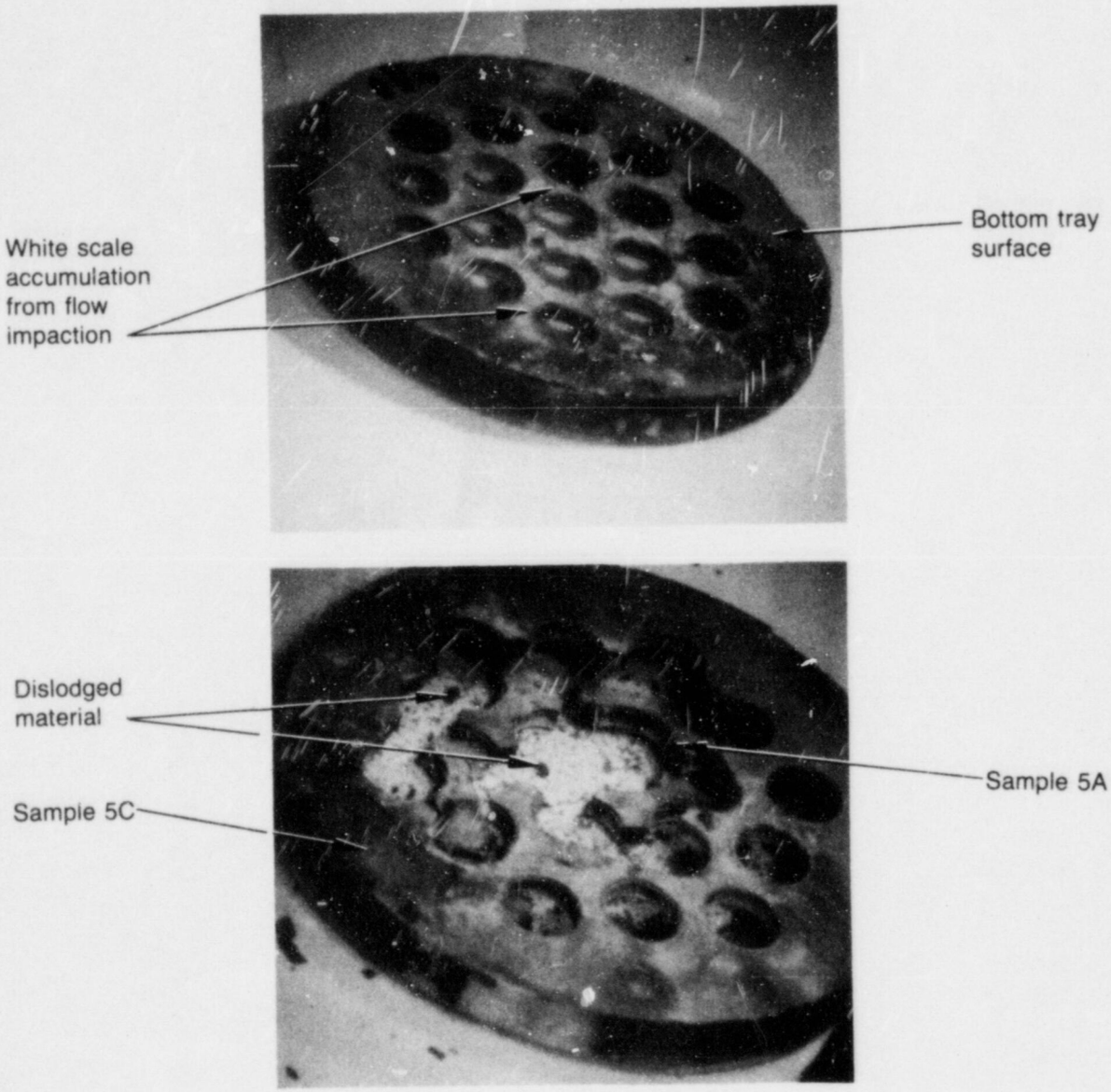

Figure F-16. Fallback barrier tray No. 5, before and after impact fracturing of gamma counting specimens.

APPENDIX G

FISSION PRODUCT AVERAGE AGE TRANSIT CALCULATIONS

APPENDIX G

FISSION PRODUCT AVERAGE AGE TRANSIT CALCULATIONS

1. INTRODUCTION

The correlation of the fuel bundle behavior during the transient, and the data recorded by the various spectrometers, was a major objective of the test. An assessment of the transit time for fission products released from the fuel to reach the detectors was provided using the spectral data.

Each spectrum accumlated during the test contained data from both short-lived ($t_{1/2} < \sim$a few min) and long lived ($t_{1/2} < \sim$a few h) noble gas isotopes. By investigating the ratio of short- to long-lived noble gas activities in each spectrum, the decay time since release of the noble gas material from the test fuel could be determined. This time, termed the average age of the material, is analogous to the calculated transit time but does not depend on assumptions concerning plug or mixed flow and includes the effect of any unmodeled holdup or mixing.

This appendix decribes the method developed for the fission product average age transit calculations. The procedure utilized the readily available parameters calculated from the on-line spectral data during the fission product behavior analysis.[G-1] The calculated transit times using this method are presented in Section 5.2 of the main text and compared with other estimates based on flowmeter data.

2. METHODOLOGY

The radioisotopes of interest, ^{90}Kr, ^{89}Kr, ^{85m}Kr, and ^{139}Xe, decay exponentially after release from fuel. This would not be true if parent feed to these nuclide from previously or concurrently released materials was important. The parent half-lives are 1.9 s, 4.4 s, 2.9 m, and 2.3 s respectively, thus no significant growth from the parent combinations was expected. The SFD-ST bundle inventories of short-lived ($t_{1/2} < \sim$a few min) and long-lived ($t_{1/2} > \sim$a few h) radionuclides were not changing strongly during the time period of interest. A strongly changing bundle inventory from time step to time step, would result in a postulated release of material with different initial ratios of short- to long-lived nuclides and an iterative procedure would therefore be required to determine the average age.

Short-lived inventories are sensitive to the instantaneous power and the SFD-ST bundle power was relatively constant for the final period before scram. Long-lived inventories increase linearly with the total power. The total power during the last 16 min of the transient amounted to ~5% of the previous 24 h. These observations imply that the inventories of both short- and long-lived nuclides were relatively constant over the last phase of the transient. The SFD 1-1 test, with its faster ramp rate and higher percentage of total power in the last few minutes, provided a worst-case estimate of the errors in this respect. ORIGEN2 calculations for SFD 1-1 showed deviations of ±6% (RSD) in the short- to long-lived released material ratios over the last seven minutes of the transient. Less deviation over the last 15 min of the SFD-ST are expected. It was assumed that the SFD-ST short- and long-lived noble gases were released in the same fractions from the test fuel. This assumption is supported by Figure 33 of Reference G-1 and by FASTGRASS calculations for trace irradiated fuel. FASTGRASS predicted 14.5% release for all noble gases during SFD 1-1 regardless of half-life.[G-2]

Conceptually the calculations are simple and only complicated by the need to use readily available parameters from the previous fission product behavior analysis. Specifically, it is not necessary to know the short- to long-lived inventory ratios explicitly, but only the ratios previously calculated for each isotope of the measured activities to those predicted by releasing a fraction of the inventory and decay correcting to the measurement time (i.e., the Measured-to-Predicted ratios of Reference G-1).

The ratio of short-lived to long-lived concentrations from a spectrum taken at time T_{MEAS} was compared with the inventory ratio. Using s and ℓ to denote short- and long-lived, respectively,

$$\frac{C_s}{C_\ell} = \frac{I_s e^{-\lambda_s t_{decay}}}{I_\ell e^{-\lambda_\ell t_{decay}}} \tag{G-1}$$

where C denotes a measured concentration at the detector, I is the fuel inventory at the time of release, λ is the appropriate decay constant and t_{decay} is the unknown time since release.

Since $\lambda_\ell t_{decay} << 1$

$$\frac{C_s}{C_\ell} \approx \frac{I_s e^{-\lambda_s t_{decay}}}{I_\ell} . \tag{G-2}$$

From analyses previously performed[G-1] Measured-to-Predicted ratios (R) were available for each isotope. These are formulated as

$$R_s = \frac{C_s \dot{f}}{I_s K e^{-\lambda_s t_{trans}}} \tag{G-3}$$

$$R_\ell = \frac{c_\ell \dot{f}}{I_\ell K e^{-\lambda_\ell t_{trans}}} \approx \frac{C_\ell \dot{f}}{I_\ell K} \tag{G-4}$$

where

R	=	Measured-to-Predicted ratio,
$\dot{f}$	=	volumetric flow rate,
K	=	elemental release rate constant for the appropriate time step,
t_{trans}	=	transit time assumed in the Reference G-1 model.

Based on Equations (G-3) and (G-4)

$$\frac{R_s}{R_\ell} = \frac{C_s}{C_\ell} \cdot \frac{I_\ell}{I_s e^{-\lambda_s t_{trans}}} . \tag{G-5}$$

Substituting from Equation (G-2)

$$\frac{R_s}{R_\ell} = \frac{I_s e^{-\lambda_s t_{decay}}}{I_\ell} \cdot \frac{I_\ell}{I_s e^{-\lambda_s t_{trans}}} \tag{G-6}$$

rearranging and solving for t_{decay}

$$t_{decay} = t_{trans} - \frac{\ln (R_s/R_\ell)}{R_\ell} \quad . \tag{G-7}$$

All of the values in Equation (G-7) are readily available.

Uncertainties on t_{decay} can be developed from statistical errors in the Measured-to-Predicted ratios as follows. Denoting R_s/R_ℓ as N and treating t_{trans} and λ_s as constants

$$\frac{d\, t_{decay}}{dN} = - \frac{1}{\lambda_s N}$$

$$d\, t_{decay} = - \frac{dN}{\lambda_s N}$$

or

$$\Delta\, t_{decay} = - \frac{\Delta N}{N \lambda_s} \tag{G-8}$$

indicating that the absolute error in t_{decay} is dependent on the decay constant of the short-lived nuclide and the relative error in N where $N = R_s/R_\ell$. For the uncertainties developed in this work the relative error in N was estimated by propagating the relative error in the measured concentrations of the short- and long-lived species in quadrature. The errors associated with the denominator of Equations (G-3) and (G-4) were small and therefore neglected.

Figure G-1 illustrates the calculational basis, given the assumption that the test fuel inventory contains ^{90}Kr ($t_{1/2} = 32.3$ s) and ^{85m}Kr ($t_{1/2} = 4.48$ h) in a 10-to-1 ratio. When these nuclides are released from the fuel their short-lived inventory is no longer being replenished, they decay with their natural half-lives. Consequently, if the fuel inventory ratio is known, the measured ratio of ^{90}Kr to ^{85m}Kr provides a direct correlation to the decay time since fuel release. In the example figure, the measured ratio is 1.17, resulting in a calculated decay time from fuel to detector of 100 s.

In practice, the time of measurement and not the time of fuel release is known. However, the SFD-ST power history provided inventories of both short and long lived nuclides that are relatively constant during the 16 min prior to scram. This avoided the iterative calculation required had each new decay time resulted in a time of fuel release that provided a different initial inventory ratio.

The calculation of average age since fuel release is not valid following reactor scram. When the fission source is removed, and the inventory of short-lived nuclides is not replenished, all radioactive materials, both in the fuel and exterior to the fuel, decay and the temporal relation to the fuel release time is lost. This can be better understood with reference to Figure G-1. The example figure presents the decay curve for an initial inventory ratio of 10. During a relatively constant irradiation period, the initial inventory may change slightly, but each curve will have the same slope since this was determined by the relative species half lives. Thus, over the course of a relatively constant irradiation period, the family of closely spaced curves of common slope provides the correlation of a measured activity ratio to decay time, and the correlation would be unambiguous. When the fission source is removed at reactor scram the initial inventory ratio decays eventually to nearly zero, producing a family of curves through which no unambiguous correlation of ratio to decay time can be derived.

Calculations for the gas spectrometer used both ^{90}Kr ($t_{1/2} = 32.2$ s) and ^{89}Kr ($t_{1/2} = 3.16$ min) for the short-lived isotopes. In both cases the long-lived isotope was ^{85m}Kr ($t_{1/2} = 4.48$ h). Krypton-90 was not detected reliably at either of the liquid spectrometers and consequently ratios of ^{89}Kr to ^{85m}Kr were used exclusively to calculated average age of the material at these spectrometer locations. The calculated transit times are presented in Section 5.2 of the main text and compared with other estimates based on flowmeter data. The uncertainties indicated on the plots provided in Section 5.2. were derived as described above and considered only the statistical error in the activity values.

3. REFERENCES

G-1. A. W. Cronenberg, J. K. Hartwell, D. L. Hagrman and D. J. Osetek, *Fission Product Behavior During the PBF Severe Fuel Damage Scoping Test*, to be issued.

G-2. J. Rest, D. J. Osetek and J. K. Harwell, "Isotopic Fission Product Release from Nuclear Fuel Under Severe Core Damage Accident Conditions," *IAEA International Symposium on Source Term Evaluation for Accident Conditions*, Columbus, Ohio, October 1985.

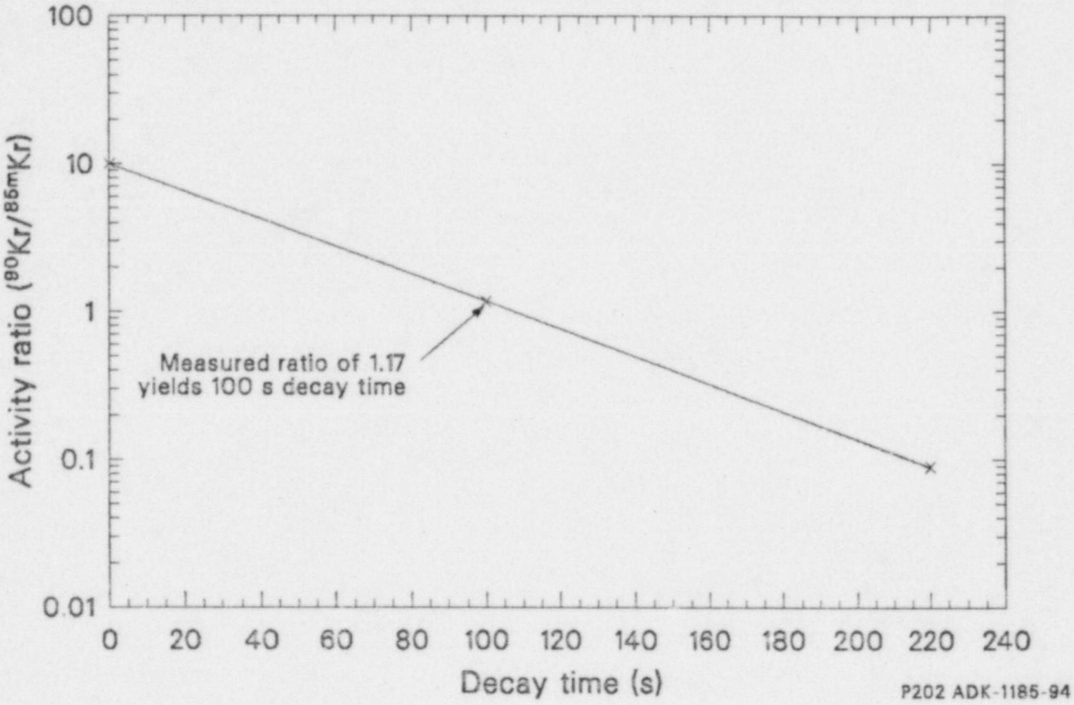

Figure G-1. Illustration of average age calculation method.

APPENDIX H

THE SCDAP MODEL FOR THE ANALYSIS OF THE SFD SCOPING TEST

APPENDIX H

THE SCDAP MODEL FOR THE ANALYSIS OF THE SFD SCOPING TEST

1. INTRODUCTION

SCDAP (Severe Core Damage Analysis Package)[H-1,H-2] is a computer code designed to characterize and quantify the fuel damage processes in a fuel bundle during severe reactor accidents. The code calculates the fuel bundle temperature response, cladding ballooning and oxidation, meltdown and fission gas release. The code has models for all of the major relevant phenomena occurring in a fuel bundle during a severe accident. A short description of the models in the code is given in Table H-1.

The SFD-ST analysis was performed using Version 18 of SCDAP. The input data to the code specifies bundle geometry, nodalization, initial conditions nuclear power distribution, and coolant boundary conditions. A user's guide to the input requirements is provided in References H-3 and H-4. However, certain parameters require additional explanation and this is provided in Section 2 of this appendix. Complete listings of the values used for the SFD-ST calculations are given in the microfiche attached to the back cover of this report. The final section of this Appendix outlines development of the fission product release model in SCDAP.

The 32 fuel rods in the test bundle were divided into three component groups as shown in Figure H-1. The shroud was described as a fourth component group. Each component group was divided axially into 10 equal regions (node units). The center of each node unit is referred to as an axial node, and the elevations are shown in Figure H-2 together with the thermocouple locations.

2. DERIVATION OF SCDAP INPUT DATA

2.1 Geometry Dependent Data

The linear dimensions of the fuel bundle and its constituent parts were obtained from the technical drawings. Definitions of various input parameters derived from the linear dimension data are provided below, where *italics* have been used to identify input description phrases used in the Users Guide.[H-3]

1. *Plenum void volume* = Total fill volume - Gap volume

   Total fill volume = Upper plenum volume + lower plenum volume + pellet end dish volume + pellet chamfer volume + fuel OD to cladding ID gap volume

2. *Helium gas inventory in the gap per rod* is the as-fabricated inventory calculated using the ideal gas law at a temperature of 300 K and the total fill volume

3. *Radii of each material layer assuming outer shroud = 0.0*

   The complex shroud configuration shown in Figure 3 of the main text is represented as slabs of dimensions equal to the *shroud height* x *shroud width* x effective thicknesses. The effective thickness of each region in the shroud, that are summed from the outside of the shroud to provide the required input radii, were established as follows

$$\text{Outer Zr wall thickness} = \left[\frac{\text{shroud width}}{2\pi}\right] \ln\left[\frac{\text{outer wall OR}}{\text{outer wall IR}}\right]$$

$$\text{Gap thickness} = \left[\frac{\text{shroud width}}{2\pi}\right] \ln\left[\frac{\text{outer wall IR}}{\text{inner wall OR}}\right]$$

$$\text{Inner Zr wall thickness} = \left[\frac{\text{shroud width}}{2\pi}\right] \ln\left[\frac{\text{inner wall OR}}{\text{outer wall IR}}\right]$$

$$\text{Zr saddle thickness} = \left[\frac{\text{shroud width}}{2\pi}\right] \ln\left[\frac{\text{outer wall IR}}{\text{inner saddle equivalent radius}}\right]$$

where the inner saddle equivalent radius = (cross-sectional area within saddle/π)$^{1/2}$

ZrO_2 insulator thickness = actual thickness of slab region

Zr inner liner = actual thickness of slab region.

2.2 Material Properties Data

It is necessary to specify for the shroud gap and the ZrO_2 insulator the specific heat capacity, density, and thermal conductivity at 10 temperature values *hard-wired* into the code. The input data to these two regions are described below.

1. The gap region contained a melt-through detector, consisting of a stainless steel/magnesium oxide thermocouple wire wound tightly around the inner Zr wall, and He filler gas at a pressure of 0.2 MPa (STP) (Figure H-3). The region was modeled with a material averaged specific heat and density that were constant with temperature. Temperature dependent thermal conductivity values were derived from the detailed heat transfer calculations described in Reference H-5.

2. The specific heat for the ZrO_2 insulator was obtained from the Materials Properties Handbook (MATPRO).[H-6] A constant valve of 700 J/kg K was used because the SCDAP *hard-wired* temperature points were unsuitable for the interpolation of the actual MATPRO values. The density of the ZrO_2 fiberboard and ZrO_2 strengthening tube composite was derived from the technical specification and drawings. The thermal conductivity as a function of temperature was estimated from the measured temperature difference across the insulating shroud and a local theoretical heat transfer coefficient based on fuel bundle and shroud inner wall temperature measurements. The comparisons were made for various shroud insulation temperatures to provide the following relationship

   $$\text{Conductivity} = -0{\cdot}42 + 0.00164T \text{ W/(m}\cdot\text{K)}$$

   Where T = shroud insulation temperature (K).

   The thermal conductivity of the shroud insulator determined prior to the test, from vendor-measured values and a geometrical interpretation for the composite ZrO_2 fiberboard and strengthening tubes, was represented by

   $$\text{Conductivity} = +0{\cdot}193 + 0.00031T \text{ W/(m}\cdot\text{K)} \ .$$

2.3 Bundle Power History and Spatial Power Distribution

The derivation of the preconditioning bundle power history and the transient power history was described in Section 4.3 of the main text. The bundle nuclear power profile given in Figure 11 (main text) provided the

basis for power representation input to SCDAP. The calculation used the automatic spatial power distribution option described in Reference H-4. The water-filled bundle axial power shape was taken from the reactor physics calculations[H-7] and confirmed by the fission chamber measurements. The relative component powers and the relationship between the relative bundle power and the coolant density were also deduced from the reactor physics calculations.

2.4 Gamma-Ray Heating in the Shroud

Reactor physics calculations provided estimates (± 50%) of the gamma-ray heating in the shroud for the water-filled and steam-filled situations of 0.016 kW/kg per reactor MW and 0.013 kW/kg per reactor MW respectively. The variation of the gamma-ray heating with time was derived from these values, the measured reactor thermal power profile and the coolant level reduction. The representation of the shroud described in Section 2.1 results in a significantly reduced volume. To ensure the correct total power was deduced by SCDAP the volumetric gamma-ray heating was increased appropriately.

2.5 Thermal-Hydraulic Model Data

The simple thermal-hydraulic model was used throughout these calculations. For the reference calculation the coolant had a constant pressure value of 6.66 MPa and enthalpy value of 1.07×10^6 J/kg corresponding to the measured inlet temperature. The coolant flow rate was obtained from the qualified experimental data. In Version 18 of SCDAP the bypass coolant boundary condition is *hard-wired* into the code at 400 K. The inlet bypass temperature of 518 K in the Scoping Test was sufficiently different to necessitate the *hard-wired* value to be overridden with a code update.

3. THE SCDAP VERSION 18 FISSION PRODUCT RELEASE MODEL

SCDAP Version 18 incorporates the PARAGRASS fission product release model PAR30228 developed by Rest et al.[H-8 to H-10] The fission product inventory is computed on the following basis:

1. The input volumetric power (Wm^{-3}) versus time (s) profile, and the fuel rod volume provides the integrated power (Ws).

2. The integrated number of fissions is derived with a conversion factor of 1 Ws = 3.1×10^{10} fissions.

3. The Xe + Kr inventory is estimated on the basis of 0.31 atoms produced per fission. The individual components are assumed produced in the proportion of 0.85 Xe and 0.15 Kr.

4. Cs is generated with an effective rate of 0.1882.

5. I is generated with an effective rate of 0.011.

The above Cs and I effective generation rates, coupled with their atomic weights of 0.132905 and 0.126904 kg/g mole respectively, always results in a Cs/I ration of 17.9. This compares with an ORIGEN2 value for the Scoping Test pretransient irradiation history of 7.7. Significant discrepancies exist between the simplified SCDAP model and the ORIGEN2 code for the absolute quantities of Xe, Kr, Cs and I predicted to be generated.

The coupled SCDAP/PARAGRASS model for fission product release from intact fuel rods was assessed during the Scoping Test analysis. The theoretical model incorporated in PARAGRASS to treat the release of Xe and Kr from solid fuel, and the empirical models for Cs and I, dictate an increasing release of fission

products with increasing fuel temperature. However, the coupled SCDAP/PARAGRASS code produces significant discontinuities in release as a function of temperature; the temperature range associated with the discontinuity varying with the prescribed irradiation history. The stand-alone version of PAR30228 showed no such effect. An investigation into the cause of the error in the coupled code was not undertaken as an updated intact rod fission product release model, based on the FASTGRASS-VFP code, was being incorporated into SCDAP to replace PAR30228. The update routine, PARAGRASS-VFP Version 50531, includes integral release models for the release and chemistry of the volatile fission products Cs, I and Te.[H-2]

As a result of the unsatisfactory inventory model, the reliability of the coupled code fuel release predictions and the current state of development of SCDAP/PARAGRASS-VFP, the SCDAP Version 18 predictions of fission product release for the Scoping Test have not been reported. In order to provide best-estimate code predictions of release, the SCDAP time and spatial dependent temperature histories were input to the stand-alone version of PARAGRASS-VFP. This work is described in Subsection 6.3 of the main text.

REFERENCES

H-1. C. M. Allison, E. R. Carlson, and R. H. Smith, "SCDAP: A Computer Code for Analyzing Light Water Reactor Severe Core Damage," *Proceedings of the International Meeting on Light Water Reactor Severe Accident Evaluation, Cambridge, Massachusetts, August 28-September 1, 1983.*

H-2. C. M. Allison, G. A. Berna and L. J. Siefken, *SCDAP/MOD1 Theory and Models*, EG&G Internal Document, January 1985.

H-3. G. A. Berna, C. M. Allison, and L. J. Siefken, *SCDAP/MOD1/VO: A Computer Code for the Analysis of LWR Vessel Behavior During Severe Accident Transients*, EG&G Internal Document, IS-SAAM-84-002, Rev. 1, July 1984.

H-4. B. L. Charboneau and A. D. Knipe, *Prompt Power Distribution Model (PROMPOW)*, EG&G Internal Document, SE-RSTD-85-002, February 1985.

H-5. R. G. Ambrosek, J. L. Jones, L. A. Stephan, and G. A. Tatar, *PBF SFD-ST Protective System Analysis*, EG&G Internal Document, RE-A-82-014, April 1982.

H-6. D. L. Hagrman et al., *MATPRO-Version 11 (Revision 2) A Handbook of Materials Properties for Use in the Analysis of Light Water Reactor Fuel Rod Behavior*, NUREG/CR-0497, TREE-1280 Rev. 2, August 1981.

H-7. J. D. Abrashoff, *Reactor Physics Analysis for the Phase I Severe Fuel Damage Experiments in the Power Burst Facility*, EG&G Internal Document, EGG-PHYS-5550, October 1981.

H-8. J. Rest, "Volatile Fission-Product Source Term Evaluation Using the FASTGRASS Computer Code," *Proceedings of the International Meeting on Thermal Reactor Safety, Chicago, Illinois, August 29-September 2, 1982*, pp. 111-121.

H-9. J. Rest, "Evaluation of Volatile and Gaseous Fission Product Behavior in Water Reactor Fuel Under Normal and Severe Core Accident Conditions," *Nuclear Technology, 61*, 1983, pp. 33-48.

H-10. J. Rest, "The Mechanistic Prediction of Xenon, Iodine, and Cesium Release from LWR Fuel Under Degraded-Core Accident Conditions," *ANS Topical Meeting on Fission Product Behavior and Source Term Research, Snowbird, Utah, July 15-19, 1984.*

Table H-1. Description of SCDAP models

Phenomenon	Model
Coolant boil-off	1-D quasi-steady drift flux model to calculate coolant swelling due to steam generation; quasi-steady heat transfer from fuel rods to coolant.
Heat and mass transport by coolant in uncovered region of core	One-dimensional quasi-steady model which assumes coolant is a mixture of steam and hydrogen; heat transfer by convection and radiation between fuel rods and coolant mixture; axially varying geometry with consideration of cladding ballooning and fuel rod meltdown.
Fission product release from fuel	PARAGRASS model derived from mechanistically based model developed at Argonne National Laboratory.
Cladding oxidation	Cathcart-Pawel (temperature less than 1850 K) and Urbanic parabolic rate equations. Model takes into account oxidation limitation due to oxygen starvation.
Dissolution of UO_2 by liquefied zircaloy	Transient dissolution is modeled by Turk's equation and saturation dissolution by MATPRO.
Dissolution of ZrO_2 by liquefied zircaloy	If temperature is below 2700 K, no dissolution occurs. If temperature is greater than 2700 K, complete dissolution instantly occurs.
Breach in cladding ZrO_2 shell	Calculation of stress applied to ZrO_2 shell by column of liquefied fuel and cladding. If stress exceeds MATPRO rupture stress breach occurs.
Relocation of liquefied (Zr,U,O) mixture flowing through breach in ZrO_2 shell and downward along outside of fuel rod	Motion of (Zr,U,O) mixture is calculated taking into account gravity and friction forces. Cooling and solidification of (Zr,U,O) mixture is calculated taking into account heat conduction from mixture into fuel rod.
Heat conduction in fuel rods and control rods	Stacked one-dimensional (radial) heat conduction is modeled using finite element method. Maximum of six nodes in fuel and cladding. Maximum of twenty radial nodes in flow shroud.

Table H-1. (continued)

Phenomenon	Model
Heat transfer at surface of fuel rods and control rods	Heat transfer by convection and radiation between fuel rods and coolant mixture is modeled. In addition heat transfer by radiation between fuel rods and control rods is modeled.
Cladding ballooning and rupture	Two models are used to calculate cladding deformation and time of rupture. Both models use anisotropic cladding material properties and strain rate and temperature dependent stress-strain relations. First model calculates axisymmetric deformation of cladding at all axial nodes. Second model calculates nonuniform circumferential temperature distribution and calculates localized nonaxisymmetric cladding deformation at the axial node having maximum cladding temperature.
Pressure change in fuel rods	Empirical model developed from FRAPCON-2 calculations.

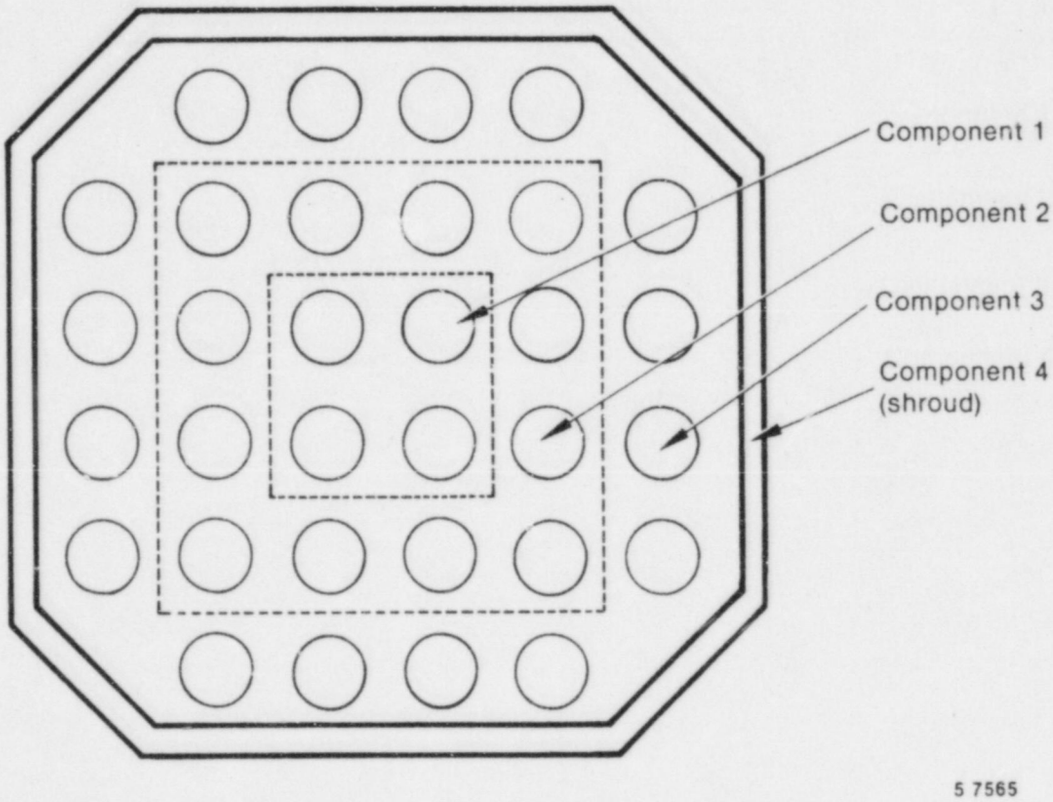

Figure H-1. Fuel bundle and shroud divided into component groups for SCDAP analysis.

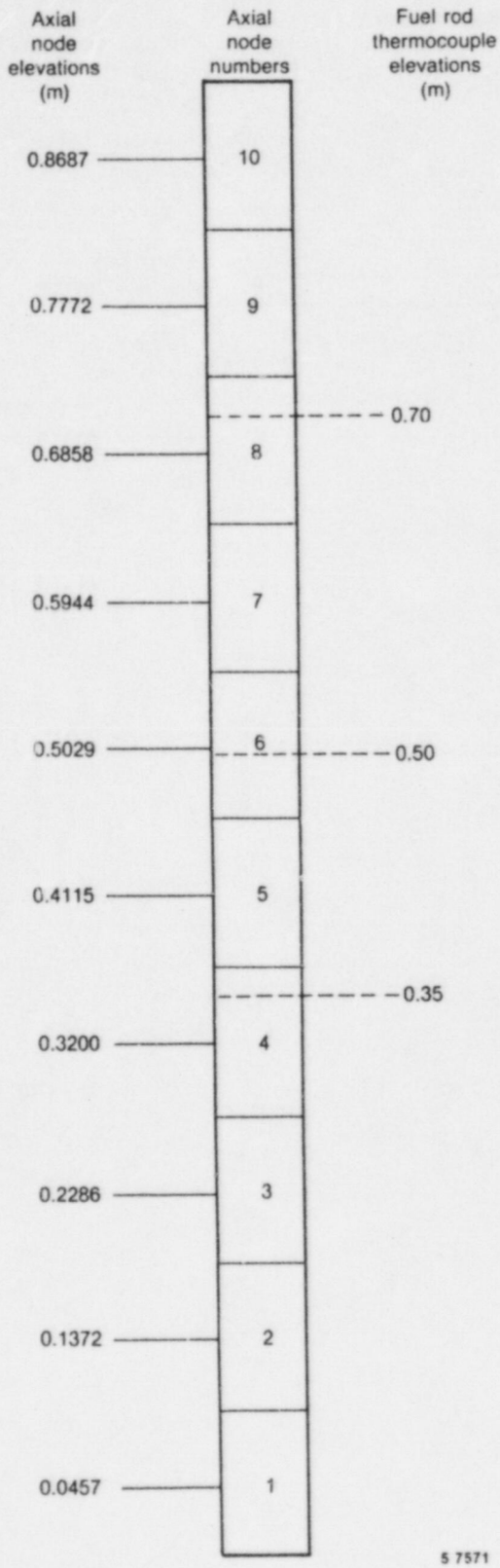

Figure H-2. Axial view of SCDAP model for fuel rod.

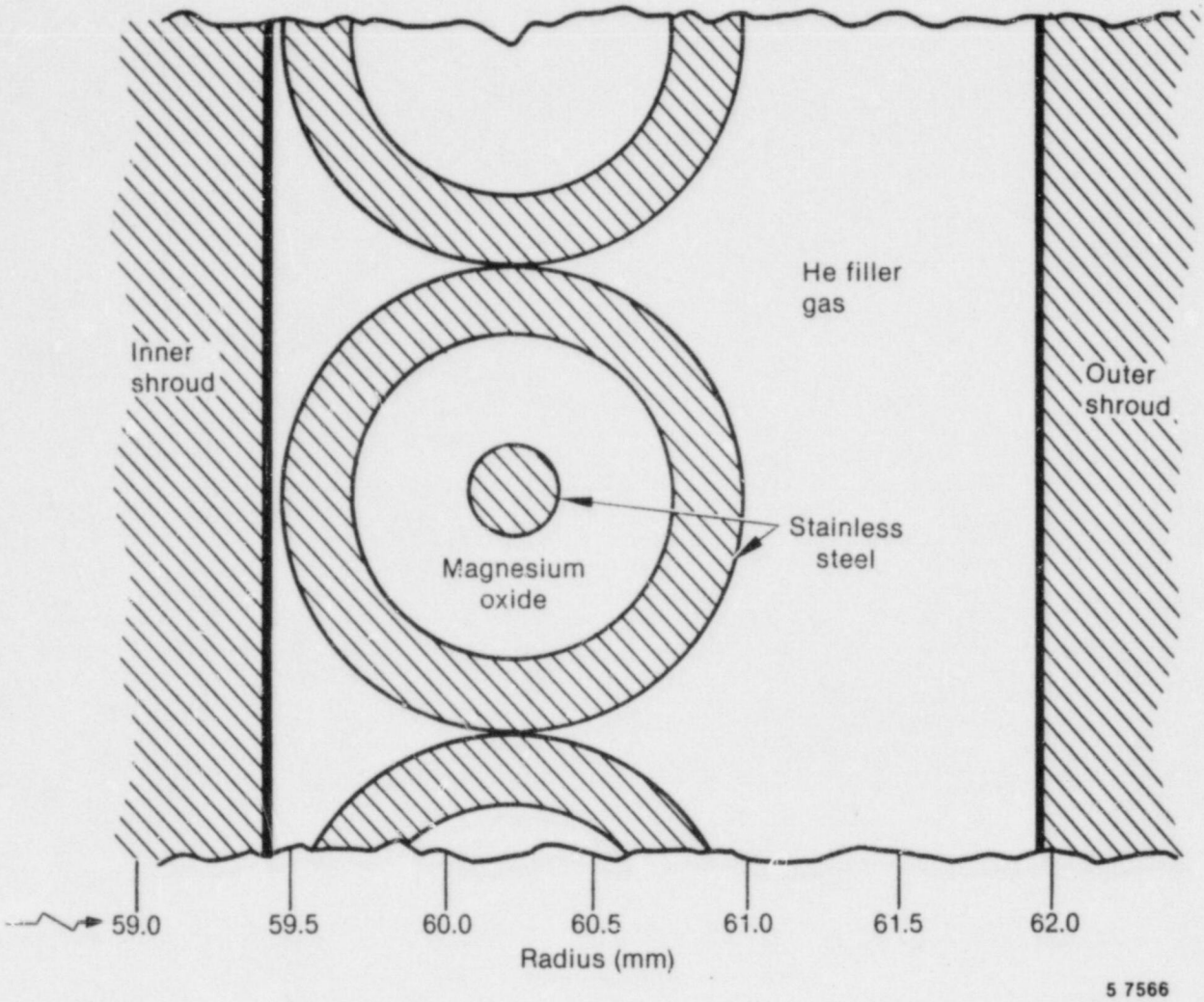

Figure H-3. Shroud gap region.

APPENDIX I

DOCUMENTATION AND RECORDS TRACEABILITY

APPENDIX I

DOCUMENTATION AND RECORDS TRACEABILITY

1. INTRODUCTION

The purpose of this appendix is to provide a set of instructions for retrieving records, documents, data tapes, etc., for the Severe Fuel Damage Scoping Test in order to (a) reconstruct the processing, correction, and presentation of data: (b) retrieve data tapes in the raw or corrected form; (c) determine the type and location of instruments used; (d) determine the calibrations, zero settings, offsets, etc., for the transducers and instruments used; (e) find details of the test train design, fabrication, and instrumentation; and (f) retrieve calculations used in the discussions presented in this report. Much of this information is contained in various reports, documents, files, and drawings produced during the planning, building, and operation of the test, as well as during the data processing and qualification procedure.

2. FILES, DOCUMENTS, AND RECORD SYSTEMS

There is no unified filing system and not all of the files and documentation are stored on a formal basis. This section lists the major files, documents, and record systems, as well as an explanation of what they contain. Some documents, materials, tapes, records, etc., maintained by a Department of Energy (DOE) contractor such as EG&G Idaho, Inc., are not generally available without either EG&G Idaho or Nuclear Regulatory Commission (NRC)/DOE assistance.

2.1 Interim and Informal Reports

These reports are prepared primarily for preliminary or internal use and are generally intended as working documents. They have not received full review and approval. Since these documents may undergo substantial changes, they should not be considered final.

2.2 Data Acquisition Specification (DAS)

This document is designed as a working tool for setting up the experiment instrumentation. It details the amplifiers to be used, gain settings, zero offsets, instrument ranges, patch panel connections, and provides a cross index between the measurement identifiers of the Experiment Operating Specification (discussed in Subsection 2.7), the working parameter channels, and the patch panel numbers. This document is used to set up and check out the facility instrumentation for each experiment. It does not have a unique number, but is filed in the Configuration Document Control (CDC) generic file (described in Subsection 2.12) for the particular experiment.

2.3 Transducer Report

Information on the transducers used in the particular experiment is contained in the Transducer Report. These reports list the transducers by serial number and by the measurement identifier. They also contain the basic equations necessary to translate transducer output voltage (current) into Engineering Units. These equations are based on calibration data if available. A brief description of the transducers is given and calibration techniques are discussed. These reports are contained in the Engineering Design Files (discussed in Subsection 2.9) and have a unique number.

2.4 Experiment Operating Procedure (EOP)

This document describes in detail how the experiment will be operated from the PBF control room. It includes instrument checklists to ensure proper operation at specific points in the experiments. This document is assigned a unique number by the CDC, and the original is retained in the CDC files.

2.5 Experiment Specification Document (ESD)

This document describes, in specific terms, the purpose of the experiment and, in general terms, the instrumentation required. These documents are interim reports.

2.6 Experiment Configuration Specification (ECS)

This document describes in specific terms how the test train will be constructed and instrumented. It is from this report that the experiment apparatus is designed and the Site Work Releases (described in Subsection 2.11) are prepared. This is an interim report.

2.7 Experiment Operating Specification (EOS)

This is an informal report, the purpose of which is to explain, in general, how the experiment will be performed, what data are to be recorded, and where measurements are to be made. In most cases, there is detail of the instrument locations, desired operating ranges, necessary response times, and measurement accuracy. This document also establishes the official identifiers that will accompany each measurement.

2.8 Experiment Predictions Document (EP)

This is an interim document that explains the objectives of the experiment as well as giving a general description of the test conduct, measurements to be made, and instruments to be used. The results of the test prediction calculations are presented, along with references to computer codes and input conditions.

2.9 Engineering Design File (EDF)

This is an informal file system maintained at the INEL. The purpose of this file is to record engineering work, done in support of the Power Burst Facility or experiments, which requires more formal recording.

2.10 Blue Book

This is an informal file system to record the design, instrumentation, fabrication, and checkout of the test train. The file consists of a number of looseleaf binders, each entitled according to subject. Each specific test has a Blue Book; however, no unique number is assigned. The Blue Books are on file at CDC and with the test train and experiment project engineers. Following is a list of the Blue Book contents:

1. Experiment Configuration Specification
2. Design Process Records (design documentation package provided by the cognizant design engineer with a cover letter describing section contents)
3. Assembly Site Work Releases

4. Indentured Parts List

5. Fuel Train Assembly Procedures (applicable Assembly Disassembly Procedures (ADPs) and hot cell Detailed Operating Procedures (DOPs) are listed by the cognizant assembly engineer)

6. Test Train Assembly Procedures (applicable ADPs are listed by the cognizant assembly engineer)

7. Test Train Disassembly Procedures (applicable ADPs are listed by the cognizant assembly engineer)

8. Quality Discrepancy Reports

9. Instrument Schedule.

2.11 Site Work Release (SWR)

The SWR is a document that can contain other documents, records, drawings, etc. It has a unique number issued by Configuration Document Control. A Site Work Release is issued to cover specific areas of work. These documents are on file at CDC.

2.12 Configuration Document Control (CDC)

The CDC is physically located at the Power Burst Facility. This is a formal control system that is used to file the Site Work Releases, drawings, plant operation manuals, PBF facility Technical Specifications, PBF System Design Documents, Experiment Operating Procedures, Detailed Operating Procedures, Engineering Design Files, and Document Revision Records. Many of these documents are filed by a unique number, but there are also generic files by test that contain items such as the Data Acquisition Documents and the Blue Books.

2.13 Drawing File

All drawings used in the construction and instrumentation of the test trains have a unique drawing number. The originals are filed in the EG&G Idaho drawing vault. Copies of particular test drawings are usually filed at CDC.

2.14 Data Tapes

All raw test data generated at the PBF are recorded on tape by the Data Acquisition and Reduction System (DARS) in pulse code modulated (PCM) form. These PCM tapes were kept at the PBF up until this Test Result Report was published. They were then sent to the EG&G Idaho central file where they are retained for about one year before being transmitted to the Federal Tape Storage Center in Seattle, Washington, where they are retained indefinitely. These tapes can be retrieved a. any time. Records of tapes and methods of retrieval are kept at the PBF. These tapes can only be used in conjunction with the DARS.

Data tapes are also stored at the INEL Computer Science Center in qualified (corrected) form in what is called the NRC/DOE Data Bank.

2.15 Data Processing History File

This informal file records the location of data tapes that have been processed. Microfiche of all processed data in graphical form, as well as all changes made to the data, are recorded here. Both raw and finished data fiche are stored.

2.16 Computer Code Configuration Control (CCCC)

This is a formal control system operated at the INEL. The system is designed for historical storage and retrieval of tapes or cards. Each stored item is given a unique number and is stored either to a specified date or indefinitely.

2.17 User-Supplied Configuration Control Log (USDCC)

This log is maintained at the INEL and is designed to ensure traceability and reproducibility of computer aided analyses and Cyber data processing. The USDCC lists references to computer codes in the CCCC, tapes in the INEL Tape Library, and support documents.

2.18 Photographs

Photographs are retrievable from either of two separate sources. Photographs identified by a letter followed by a number (e.g., A234), or the year followed by a letter and number (e.g., 79B-332), are on file at the Test Reactor Area hot cell organization. Photographs identified by the year followed by only a number (e.g., 79-4567) are on file with the EG&G Idaho Photography section.

APPENDIX J

SFD-ST DATA PLOTS

APPENDIX J

SFD-ST DATA PLOTS

The Qualified test data recorded during the SFD-ST are presented on microfiche attached to the back cover of this report. Qualified and Trend data appear as solid and dashed lines, respectively, on the plots. In cases where part of the data is classified as Failed there is no plot line.

The Qualified data on the microfiche contain error bars representing the 95% confidence level (2σ). The size of the error bars may not be constant on a given plot because uncertainties vary as a function of instrument readings or time. Data plots presented in the text of this report are from the same source but do not show the uncertainties.

NRC FORM 335 (2-84) NRCM 1102, 3201, 3202

U.S. NUCLEAR REGULATORY COMMISSION

BIBLIOGRAPHIC DATA SHEET

SEE INSTRUCTIONS ON THE REVERSE

1. REPORT NUMBER (Assigned by TIDC, add Vol. No., if any)

NUREG/CR-4683
EGG-2413

2. TITLE AND SUBTITLE

PBF SEVERE FUEL DAMAGE SCOPING TEST—
TEST RESULTS REPORT

3. LEAVE BLANK

4. DATE REPORT COMPLETED

MONTH	YEAR
August	1986

5. AUTHOR(S)

Alan D. Knipe
Scott A. Ploger
Daniel J. Osetek

6. DATE REPORT ISSUED

MONTH	YEAR
August	1986

7. PERFORMING ORGANIZATION NAME AND MAILING ADDRESS (Include Zip Code)

EG&G Idaho, Inc.
P.O. Box 1625
Idaho Falls, Idaho 83415

8. PROJECT/TASK/WORK UNIT NUMBER

9. FIN OR GRANT NUMBER

A6305

10. SPONSORING ORGANIZATION NAME AND MAILING ADDRESS (Include Zip Code)

Division of Accident Analysis
Office of Nuclear Regulatory Research
U.S. Nuclear Regulatory Commission
Washington, D.C. 20555

11a. TYPE OF REPORT

Technical

b. PERIOD COVERED (Inclusive dates)

12. SUPPLEMENTARY NOTES

13. ABSTRACT (200 words or less)

This report presents a comprehensive evaluation of the Severe Fuel Damage Scoping Test (SFD-ST) performed in the Power Burst Facility (PBF) at the Idaho National Engineering Laboratory. The test is part of an internationally sponsored light water reactor severe accident research program, initiated by the U.S. Nuclear Regulatory Commission. The experiment was the first of four, in-pile, multifuel rod tests performed in the PBF. The SFD-ST fuel bundle comprised 32, 0.9-m long, trace-irradiated (91 MWd/T) fuel rods. The bundle was surrounded by an insulating shroud, with the region maintained at a pressure of 7 MPa. The experiment consisted of a transient in which the inlet coolant flow to the test bundle was reduced to 16 g/s, and the nuclear power increased, until the peak temperature approached fuel melting. The ∿3 h transient was terminated by scram of the reactor, with the inlet coolant reflooding and cooling the bundle to saturation temperature within 8 min. The overall technical objective of the test was to contribute to the understanding of fuel bundle dynamics, and the related hydrogen and fission product behavior, during a high temperature transient. The report provides a description of the major observed phenomena. Interpretation of the test was based upon the response of on-line instruments, posttest fission product sample analysis, nondestructive and destructive postirradiation examination of the fuel bundle, and a calculational study using the Severe Core Damage Analysis Package (SCDAP).

15. AVAILABILITY STATEMENT

Unlimited

16. SECURITY CLASSIFICATION

(This page)

Unclassified

(This report)

Unclassified

17. NUMBER OF PAGES

18. PRICE

b. IDENTIFIERS/OPEN-ENDED TERMS